

ISSN 0288-4534
CODEN: KONA E7

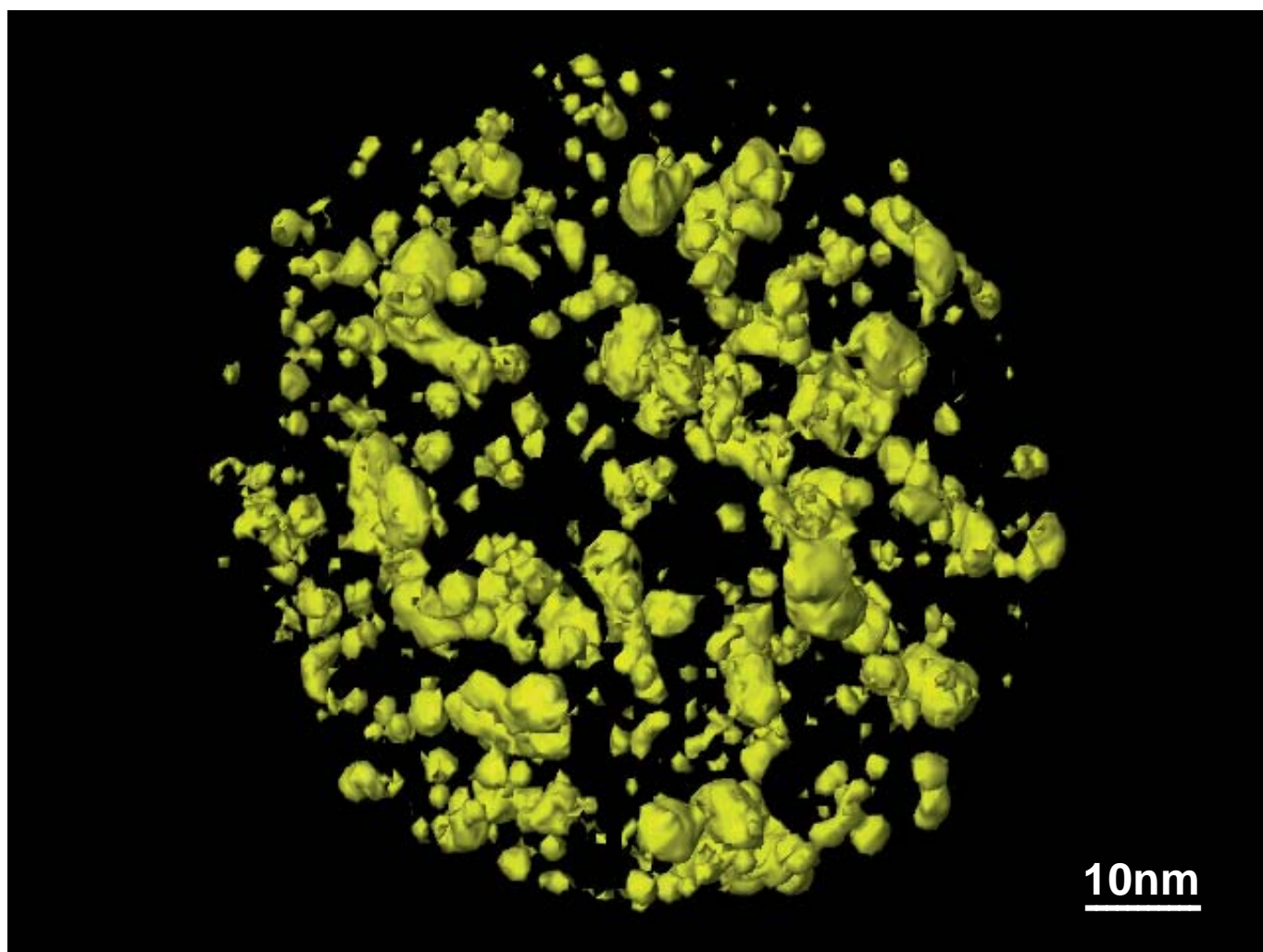
粉

KONA

POWDER AND PARTICLE

No. 22 (2004)

Published by Hosokawa Powder Technology Foundation



now available online – www.kona.or.jp

KONA

POWDER AND PARTICLE

<http://www.kona.or.jp>

KONA is a refereed scientific journal that publishes articles on powder and particle sciences and technology. KONA has been published annually since 1983 in Japan. KONA is distributed to researchers, members of the scientific community, universities and research libraries throughout the world.

About the Cover of Journal "KONA"

The Chinese character “粉” is pronounced “KONA” in Japanese, and means “Powder”. The hand written “粉” is after the late Mr. Eiichi Hosokawa, founder of the Hosokawa Micron Corporation.



Hosokawa Micron Corporation and its R&D Center

Editorial Board

Y. Tsuji Editor in Chief
(Osaka Univ., JAPAN)

Asia/Oceania Editorial Board

Y. Kousaka (Emeritus Professor of Osaka Prefecture Univ., JAPAN)

H. Masuda (Kyoto Univ., JAPAN)

H. Emi (Emeritus Professor of Kanazawa Univ., JAPAN)

K. Higashitani (Kyoto Univ., JAPAN)

K. Nogi (Osaka Univ., JAPAN)

Y. Fukumori (Kobe Gakuin Univ., JAPAN)

J. Hidaka (Doshisha Univ., JAPAN)

M. Takahashi (Nagoya Institute of Technology, JAPAN)

P. Arnold (Univ. of Wollongong, AUSTRALIA)

S.H. Kang (Yeungnam Univ., KOREA)

W. Tanthapanichakoon (National Science and Technology Development Agency, THAILAND)

T. Yokoyama (Hosokawa Powder Technology Research Institute, JAPAN)

M. Naito (Osaka Univ., JAPAN)

Secretariat

T. Kawamura (Hosokawa Powder Technology Foundation, JAPAN)

Europe/Africa Editorial Board

E. Forssberg Chairman (Univ. Lulea, SWEDEN)

J. Schwedes Vice Chairman (Univ. Braunschweig, GERMANY)

W. Peukert (Univ. Erlangen, GERMANY)

S.E. Pratsinis (ETH Zürich, SWITZERLAND)

H. Kalman (Ben Gurion Univ., ISRAEL)

J.F. Large (Univ. de Tech. de Compiègne, FRANCE)

N.Z. Lyakhov (Institute of Solid State Chemistry, RUSSIA)

M. Ghadiri (Univ. of Leeds, UNITED KINGDOM)

Secretariat

P. van der Wel (Hosokawa Micron B.V. NETHERLANDS)

P. Krubeck (Hosokawa Micron GmbH, GERMANY)

Americas Editorial Board

B.M. Moudgil Chairman (Univ. of Florida., U.S.A.)

D.W. Fuerstenau Vice Chairman (Univ. of California, U.S.A.)

R. Flagan (California Institute of Technology, U.S.A.)

L. Augsburger (Univ. of Maryland School of Pharmacy, U.S.A.)

P.S. Santos (Univ. of São Paulo, BRAZIL)

R. Hogg (Pennsylvania State Univ., U.S.A.)

D.J.W. Grant (Univ. of Minnesota., U.S.A.)

Secretariat

D.A. Scott (Hosokawa Micron Inter., U.S.A.)

Publication Office

Hosokawa Powder Technology Foundation (Japan) in Hosokawa Micron Corporation

No. 9, 1-chome, Shoudai Tajika, Hirakata-shi, Osaka 573-1132, Japan

Notes

○Hosokawa Powder Technology Foundation has entrusted the editorial duty to the editorial board organized by the Council of Powder Technology, Japan.

(Complimentary Copy)

Printed in Japan

The Letter from the Editor

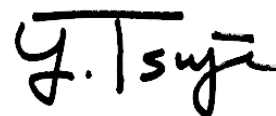


Yutaka Tsuji
Editor-in-Chief

It is my pleasure to issue KONA Number 22. KONA is an annual journal and thus it is printed once a year and distributed through the KONA web site. Paper-base KONA is also distributed to libraries although the number of paper-base KONA is limited. The season when you see the new volume of KONA is usually winter. Winter, particularly late December or early January, is the time to make general views of the year. Looking back over the year 2004, I really feel that unfortunate or sad things have happened far more than fortunate or glad things. The world of particle technology is not an exception. In September, Prof. Brian Scarlett, the world giant of particle technology, passed away. This sad news has spread all over the world. In Japan, we lost Prof. Kei Miyanami who was the editor-in-chief KONA from 1991 to 1999. Prof. Miyanami, 68, passed away on September 24th. He died of cancer. With numerous services rendered by both professors, we offer this token of our deepest sympathy.

Let me briefly describe Prof. Miyanami and his achievements. After graduating from the University of Osaka Prefecture in 1959, he was working at the Central Research Laboratory of Hitachi, Ltd. In 1965 he returned to work at the Department of Chemical Engineering of the university that he graduated from. His research areas were powder mixing, granulation and coating. He is well known as an expert of measurements of powder processing. Long time ago when computers were not so much developed as today, he was already very skillful to use computers for measurements. A unique optical sensor for powder mixing was developed in his laboratory. Many valuable experimental and theoretical results have been presented by himself and his group. Later, his main interest turned to environmental problems like management of waste and garbage processing. He filled various important roles in committees concerning these problems. Another feature of his activities that we know is his close and good relation with the Korean community of particle technology. His presence was very meaningful in that the Japanese community of particle technology has been able to develop good relation with Korean researchers and engineers. His contribution to KONA journal was great. He was respected as an excellent editor and liked by everyone who knows him because of his warm personality.

Besides these personnel losses in particle technology, many unfortunate things happened in 2004. In Japan, we suffered natural disasters such as typhoons and earthquakes. In the world, bad news and tragedies are countless. If we try to take an example of few good things, we might say that Japanese economy is becoming a little better. Powder industries receive this benefit and have been revitalized in 2004. I hope that this trend will continue and grow more in 2005.

A handwritten signature in black ink that reads 'Y. Tsuji'.



KONA

GENERAL INFORMATION

HISTORY OF THE JOURNAL

KONA journal has been published by the Council of Powder Technology, Japan. (CPT), from No.1 to No.12 issues, under the sponsorships of Hosokawa Micron Corporation (No.1 to No.9) and Hosokawa Powder Technology Foundation (No.10 to No.12).

The CPT has been established in 1969 as a non-profit organization to enhance the activities of research and development on powder science and technology in Japan under the sponsorship of Hosokawa Micron Corporation. In 1983, the CPT has decided to issue an international journal named "KONA", which publishes the excellent articles appeared in Japanese journals concerning powder science and technology, after translated into English, throughout the world. After the seventh volume issued in 1989, the CPT has changed its policy to internationalize the "KONA" from the 8th issue (1990) and on by incorporating the monographs originally written in English from the authors throughout the world. Immediately, the present editorial board including Asian, Americas' and European Blocks has been organized.

From the 13th issue and on, the Hosokawa Powder Technology Foundation has taken over the role of KONA publisher from the CPT in 1995 (No.13) and the Foundation has entrusted the editorial duty to the present KONA editorial board organized by the CPT without requesting any shift in our present editorial policies. This switching of publisher has been simply and only to make the aim and scope of the Foundation definite. Essentially no change has been observed in continuously editing and publishing this journal except in the designation on a part of the journal cover.

AIMS AND SCOPE OF THE JOURNAL

KONA Journal is to publish the papers in a broad field of powder science and technology, ranging from fundamental principles to practical applications. The papers discussing technological experiences and critical reviews of existing knowledge in specialized areas will be welcome.

These papers will be published only when they are judged, by the Editor, to be suitable for the progress of powder science and technology, and are approved by any of the three Editorial Committees. The paper submitted to the Editorial Secretariat should not have been previously published except the translated papers which would be selected by the Editorial Committees.

CATEGORY OF PAPERS

- Invited papers
Original research and review papers invited by the KONA Editorial Committees.
- Contributed papers
Original research and review papers submitted to the KONA Editorial Committees, and refereed by the Editors.
- Translated papers
Papers translated into English, which were previously published in other languages, selected by the KONA Editorial Committees with the permission of the authors and / or the copyright holder.

SUBMISSION OF PAPERS

Papers should be sent to each KONA Editorial Secretariat.

- Asia / Oceania Editorial Secretariat
T. Kawamura
Hosokawa Micron Corporation Micromeritics Laboratory 1-9,
Shoudai Tajika, Hirakata 573-1132 JAPAN
- Europe / Africa Editorial Secretariat
Dr. P. van der Wel or Mrs. P. Krubeck
Hosokawa Micron GmbH
Welsersstr. 9-11, 51149 Köln
P.O. Box 920262, 51152 Köln
GERMANY

- Americas Editorial Secretariat
D.A. Scott
Hosokawa Micron International Inc.
10 Chatham Road, Summit, NJ 07901 USA

PUBLICATION SCHEDULE

KONA is published once a year.

SUBSCRIPTION

KONA is distributed free of charge to senior researchers at universities and laboratories as well as to institutions and libraries in the field throughout the world. The publisher is always glad to consider the addition of names of those who wish to obtain this journal regularly to the mailing list. Distribution of KONA is made by each Secretariat.

Free electronic publication of KONA is available in
<http://www.kona.or.jp>

INSTRUCTIONS TO AUTHORS

- (1) Manuscript format
 - Two copies should be submitted to the Editorial Secretariat, in double-spaces typing on pages of uniform size.
 - Authorship is to give author's names, and the mailing address where the work has been carried out on the title page.
 - Abstract of 100-180 words should be given at the beginning of the paper.
 - Nomenclature should appear at the end of each paper. Symbols and units are listed in alphabetical order with their definitions and dimensions in SI units.
 - Literature references should be numbered and listed together at the end of paper, not in footnotes. Please give information as in the following examples:
 - 1) Carslaw, H.C. and J.C. Jaeger: "Conduction of Heat in Solids", 2nd ed., Clarendon Press, Oxford, England (1960).
 - 2) Howell, P.A.: US Patent, 3,334,603 (1963).
 - 3) Rushton, J.H., S. Nagata and D.L. Engle: *AIChEJ.*, 10. 294 (1964).
 - 4) Seborg, D.E.: Ph.D. Dissertation, Princeton Univ., N.J., U.S. A. (1969).
 - Original figures with each single copy should be submitted, on separate sheets. Authors' names and figure numbers are marked in the corner.
 - Figure numbers and captions are listed on a separate sheet.
 - Place of figure insertion is to be indicated in the margin of the manuscript.
 - Tables should be typed on separated sheets.
 - Author's short biography and photograph should be attached.
 - For data and text submissions we accept PC-format floppy and CD-ROM discs with unformatted text files in ASCII code. Files in Microsoft Word format are also acceptable. When submitting images, please insure that the files are compatible with Adobe Photoshop and have a resolution of at least 350 dpi.
- (2) Reprints
 - The authors shall receive 50 free reprints. Additional reprints will be furnished when ordered with return of galley proofs.
- (3) Publication policy
 - All papers submitted for publication become immediately the property of the CPT and remain so unless withdrawn by the author prior to acceptance for publication or unless released by the Editor. Papers are not to be reproduced or published in any form without the written permission of the CPT.

Obituary



It is my deep grief that I have to inform the death of Professor Kei Miyanami, the former editor-in-chief of KONA. On September 24th, 2004, Professor Dr. Kei Miyanami passed away in an age of 68. He died of cancer.

Towards the end of autumn in 2003, he felt strange around his belly and had difficulty in urination. The medical examination diagnosed his illness as disorder of urinary bladder muscle due to the autonomic ataxia. For nearly one year, he spent normal life with taking medicines for the illness. At the beginning of summer in 2004, he had medical examination again since he felt unexpected fatigue and lumber pain. The doctor found cancer on his prostate gland and advised him to take hormone therapy at home. At the end of August, he could not stand up anymore and his family brought him into a hospital. Three weeks later, he breathed his last, very gently like sleeping.

Prof. Kei Miyanami was born in Osaka (Japan) on July 22th, 1936. He graduated from Osaka Prefecture University (OPU) and obtained his bachelor (1959) and master degrees (1961). He studied chemical engineering at OPU. From 1961 to 1965, he worked in industry (Hitach Ltd.). He carried out research on computer control of chemical plants at the Central Research Laboratory, Hitach Ltd. His experiences in computer technology were of great use for his later research on powder technology.

In 1965, he obtained faculty position at Chemical Engineering, OPU. After several years research on

the dynamics of mixing process, he received PhD degree in Chemical Engineering from OPU in 1971. The next year (1972), he became Associate Professor of Chemical Engineering at OPU. He also had an experience of staying in the U.S. for one year as a visiting scholar. He worked with Prof. L.T. Fan at Kansas State University (U.S.A.). By using his excellent skills on computer, which he gained at Hitach Ltd., he carried out research intensively on developing mathematical models of complicated diffusion problems and chemical engineering themes. After coming back from the U.S., he became Professor of Chemical Engineering at OPU in 1979.

His major interest lied on measurement, control, and optimization of powder handling processes. In the early 1970', when the computer was very expensive and not so much developed as today, he developed many novel sensors including optical sensor for continuously detecting mixing degree and then applied to several powder handling processes. These technologies contributed very much to the progress of automated production of particulate materials. Later, his main interest turned to environmental problems such as recycling, waste management and pollution control.

Prof. Miyanami served on many committees, councils and working parties. He was member of many councils and committees in local governments for environmental assessment-protection-affairs and wastes management. In regard to the environmental assessment-protection field, he was one of the most famous scientists in Japan. He also served as editor-in-chief of KONA from 1991 to 1999. In 2000, he retired university (OPU) and became a professor emeritus.

He had a sharp brain and very good "eyes" of observation and insight; he always had an insight into the current trend and tried to be a frontier. Contrary to his serious attitude in the daytime, he behaved cheerfully after 5 o'clock. He loved alcohol, smoking and singing at Karaoke bar. He was a beloved and a requested partner in industry, university, local governments, committees and in private life. He had enormous number of friends, which he considered as his treasure. We lost "giant" of particle technology.

S. Watano
Professor, Osaka Prefecture University, Japan

Mourning the Passing of Professor Scarlett



The 2nd of September 2004 was a very sad day, as our dear friend Prof. Scarlett passed away. It was actually in November, two years ago, when I received an Email from Prof. Scarlett, saying “I have been diagnosed with rectal cancer, and will have an operation at the beginning of the New Year following radio/chemo therapy treatment.” In the Email, he also wrote “Do not worry. I have a plan to attend a meeting in Budapest in May of next year.” I was really touched by his courage and resolve in confronting the disease that had afflicted him, but hoped that he would concentrate on the treatment without trying to do too much. After that, I heard from some people that he was fine and attending various international meetings, including IFPRI and ISO. So when his death came so suddenly, I was really shocked and felt great sadness for he was only 66 years old, and was expected to take an even more important role as a world leader in the field of powder technology. His passing is a tremendous loss, and extremely difficult for us to come to terms with.

Prof. Scarlett was a great powder technology specialist, not only as an academic but also as a person who engendered trust, loyalty and love. It was in August 1983 in the party of an international conference held in Hawaii that I met Prof. Scarlett for the first time. As I remember, Prof. Jimbo introduced me to him, and I immediately thought him to have a kind and warm personality. I told him that I was looking for a place to study overseas, and he answered quite casually, “Why don’t you come to my place? I’ll contact you when I get funding.” However, there was no correspondence after that for at first six months, and then one year, so I almost gave up. Then in September 1984, I had an out-of-the-blue international call

from Prof. Scarlett in which he said “I met Prof. Emi and Prof. Kousaka recently at an international conference in Minneapolis, and heard that you would like to study in America. I have now managed to get funding, so please come to Holland, not America.” I still remember vividly that I was very moved by his sincerity as he had been trying for a year for me, a person he had only met once in his life before.

This is how I came to attend his laboratory at Delft University of Technology from November 1984 to March 1986. This was just after Prof. Scarlett had moved from England to Holland, and he was devoting all his energy to his work, which made the atmosphere of the laboratory very dynamic. As my research theme was static electricity, Prof. Scarlett asked me to gain knowledge of the electrostatic charging of powder from Prof. Senichi Masuda of our university, who was a world-class authority on electrostatics. After consulting with Prof. Masuda, he let me have the drawing of the “Boxer Charger”, which he was very proud of that time, along with other items as research souvenirs to take with me to Delft. That was how Prof. Scarlett and I came to start a profound relationship with Prof. Masuda. This story tells us how much Prof. Scarlett considered it important to have wide-ranging exchanges with people in different fields, in order to expand and nurture the scale of his research.

Being a lover of Japan, Prof. Scarlett respected Prof. Iinoya very much, and was also a close friend of Prof. Jimbo. Thanks to this, I had the opportunity to be taken under his wing at Delft, and he thereafter invited Japanese researchers to Delft almost every year, including Dr. Igasaki from AIST (National Institute of Advanced Industrial Science and Technology), and Prof. Mori and Prof. Hidaka from Doshisha University. He even said that he would be happy to receive any Japanese if they were introduced by Yamamoto. The Japanese persons who were directly looked after by him numbered more than ten. This was counted among his numerous achievements, which resulted in his receiving the Iinoya Award of The Society of Powder Technology, Japan in 1998. On the night of the award, Prof. Scarlett, his wife Joan, and I toasted this achievement at a hotel in Brighton, and I will never forget the wonderful look of happiness on his face at that time.

Prof. Scarlett always treasured opportunities to meet people, and treated everybody in an equal way. There are numerous such episodes one could men-

tion to describe his fine character, but one example was at a small international conference related to powder in Xian, China in May 2000. I decided to attend it as a lecturer because Prof. Scarlett was invited to give a lecture. During this three-day conference, there were a number of quite poor research presentations, to be honest, but the professor listened to every lecture with a sincere and serious manner, and also took part in question-and-answer discussions. He told me after that he had treated the discussions with respect, as they were young human resources who would forge the future of China's powder technology, and had attended and taken part fully in the conference. At that moment, I felt I had witnessed his earnest desires for the real prosperity of the world's powder technology future and would make any efforts to realize this.

Towards the end, I was determined to see Prof. Scarlett at any cost, and made great efforts to visit Gainesville, Florida two weeks before his death. At that time, the doctors were saying he had only 2 to 8 weeks left to live. The professor used to be a very large man, but his body was reduced to almost half its size after his heroic fight against his disease. However, his passion for powder technology was even stronger, perhaps even fierce. He appeared in the laboratory at the University of Florida dressed in a suit and tie to meet me and Dr. Matsuyama who accompa-

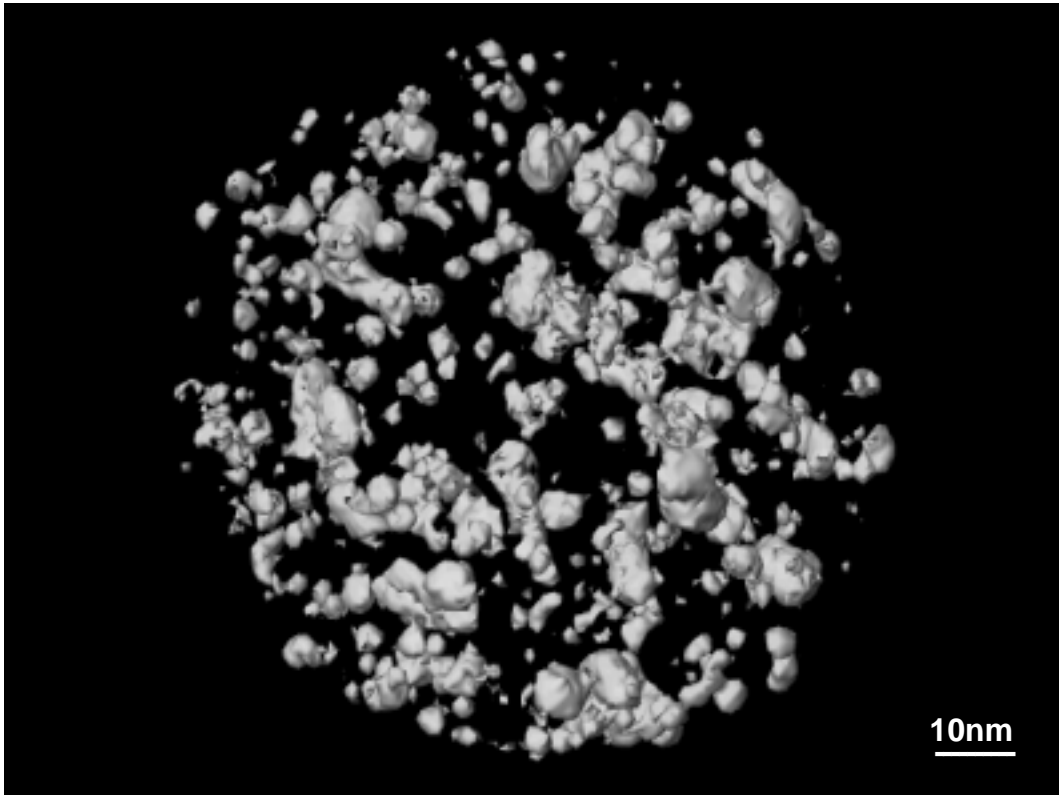
nied me, and talked enthusiastically in a dignified voice, which made his disease almost unnoticeable, about the procedure of the joint program of powder technology between America and Japan. He brought in some PhD students and had them explain the modeling of powder process, and had an intense discussion with them without compromising his condition. He was even worried about me, remarking "Hideo, are you all right? You look very serious." I guess my face was showing fatigue from jet lag and the stress of using English. Two weeks after that, he passed away. I would like to say, "I know you must have had a lot more things you wanted to do, but Prof. Scarlett, please do not worry and please rest in peace. We will try hard to take over your work."

This photo was taken at the Space Center in Florida, and shows the professor happily with his wife, Joan, at an event to commemorate his retirement from Delft University of Technology. It was taken with a digital camera that his disciples from Japan gave him as a memento. I would like to leave this photo of Professor Scarlett and his beloved wife whom he fell in love with in Sherwood Forest, as a true memory to the man.

Hideo Yamamoto
Dean of Faculty of Engineering
Soka University

Explanation of the Cover Photographs
Application of three-dimensional electron tomography
on a TiO₂-Ag composite powder

Kenji Kaneko
 University of Kyushu
 Department of Materials Science and Engineering



The movie shows a reconstructed three-dimensional image of a TiO₂-Ag composite powder.

It has been known that the bactericidal activity under dark conditions and very weak UV intensity, such as indoor UV light, TiO₂ should be deposited with antibacterial metals such as silver. TiO₂-25mol%Ag composite powders were successfully synthesized by ultrasonic spray pyrolysis from the solution of TiO₂ sol and AgNO₃.

Three-dimensional image, reconstructed from a series of projections from -60° to 60° with every 2° interval, clearly presents a clear morphology of a spherical shape TiO₂-Ag nanocomposite powder with finely dispersed Ag particles within the TiO₂ matrix (anatase).

KONA Powder and Particle No. 22 (2004)

Contents

< Review Papers >

- | | |
|--|--|
| * The Influence of Relative Humidity on Particle Adhesion – a Review of Previous Work and the Anomalous Behaviour of Soda-lime Glass | J.A.S. Cleaver and J.W.G. Tyrrell..... 9 |
| * Trends in Microencapsulation Research | H. Yoshizawa..... 23 |
| * Particle Size Analysis of Aerosols from Medicinal Inhalers | J.P. Mitchell and M.W. Nagel..... 32 |

< Original Research Papers >

- | | |
|--|--|
| * The Sevilla Powder Tester: A Tool for Characterizing the Physical Properties of Fine Cohesive Powders at Very Small Consolidations | A. Castellanos, J.M. Valverde 66
and M.A.S. Quintanilla |
| * Predicting Packing Characteristics of Particles of Arbitrary Shapes | M. Gan, N. Gopinathan, X. Jia 82
and R.A. Williams |
| * Characterization of Flow Properties of Powder Coatings Used in the Automotive Industry | C. Conesa, K. Saleh, A. Thomas, 94
P. Guigon and N. Guillot |
| * Liquid-fed Aerosol Reactors for One-step Synthesis of Nano-structured Particles | L. Mädler..... 107 |
| * Measurement of Adhesion Forces between Particles and Rough Substrates in Air with the Vibration Method | S. Ripberger and K. Hein 121 |
| * Methodology and Analysis of the Effect of Liquid Infiltration on the Hydrodynamic Dispersion of Silica Aerogel Agglomerates | N.S. Hudak, I. Manas-Zloczower 134
and D.L. Feke |
| * Aluminium Matrix Composites Reinforced with Si ₃ N ₄ , AlN and ZrB ₂ , Produced by Conventional Powder Metallurgy and Mechanical Alloying | J.B. Fogagnolo, M.H. Robert, 143
F. Velasco and J.M. Torralba |
| * Rational Design of Dispersants by Molecular Modeling for Advanced Ceramics Processing Applications | Pradip, B. Rai and P. Sathish 151 |

< **Translated Research Papers** >

* Surface Structure and Photocatalytic Activity of Ti Supported on Alumina Powder	<i>M. Fuji, Y. Sugiyama, T. Takei,.....</i> 159 <i>M. Chikazawa, K. Tanabe and K. Mitsuhashi</i>
* Effects of Oxidization and Adsorbed Moisture on Time Change in Tribo-electrification of Powder Particles	<i>H. Masuda, D. Yasuda,.....</i> 168 <i>A. Ema and K. Tanoue</i>
* Effect of Mixing Condition on Sol-Gel Synthesis of Barium Titanate Ultrafine Particles	<i>K. Gomi, K. Tanaka and H. Kamiya</i> 177
* Preparation of the Composite Thermoelectric Materials with Small Particles Dispersion by MA	<i>S. Katsuyama, M. Ito and H. Nagai</i> 186
* Size Effect for Barium Titanate Nano-particles	<i>T. Ohno, D. Suzuki, H. Suzuki and T. Ida</i> 195

The Influence of Relative Humidity on Particle Adhesion – a Review of Previous Work and the Anomalous Behaviour of Soda-lime Glass[†]

J.A.S. Cleaver* and J.W.G. Tyrrell
Chemical and Process Engineering
School of Engineering
University of Surrey**

Abstract

The adhesion of fine particles plays a significant role in the performance of particulate processes and in the quality of particulate products. The extent of adsorption of water on the particles from the surrounding atmosphere is governed directly by the relative humidity of the air. Published evidence suggests that changes in relative humidity of the air can have a profound influence on the adhesion of individual particles. However, there are numerous conflicting reports in the literature suggesting that adhesion can increase, decrease or pass through a maximum as the relative humidity increases.

A thorough review of the relevant literature is presented in which the experimental evidence relating to the influence of relative humidity on particle adhesion is gathered and discussed. Apart from the amount of water adsorbed on the surface, it is clear that the adhesion depends upon the surface roughness which prevents the formation of a complete capillary meniscus at the particle contact point until a critical relative humidity is reached. At this point, sufficient water is adsorbed to engulf the asperities and a marked increase in adhesion is noted. Many surfaces undergo some physical or chemical change in the presence of adsorbed water, e.g. solubility, softening, or phase change. This can lead to complex adhesion behaviour. Hysteresis of adhesion with increase/decrease of relative humidity is commonly observed. Theoretical approaches correctly recognise the role of the Laplace pressure in the capillary bridge as being dominant in controlling adhesion. However, evidence suggests that contributions from the solid-solid interaction, surface tension of the bridging film and disjoining pressure can also be important under certain circumstances.

As an illustration of complex behaviour, original data for the adhesion of a glass microsphere on a flat glass surface are presented. The data were obtained using a custom-built AFM instrument. Upon desorption, a critical relative humidity lying between 30% and 40% was observed. At this point, a singular peak in adhesion occurred which was accompanied by long-range repulsion between the surfaces prior to contact. The long-range repulsion was found to be an exponential function of separation distance. This phenomenon has been attributed to the spontaneous formation of glass corrosion products from the liquid layer on desorption when the two surfaces approach each other. According to published literature, these corrosion products can take the form of needle-like or dendritic structures. The resulting steric repulsion is observed to be exponential with respect to distance, in agreement with the established trend. Once contact is made between the surfaces, the strong adhesion may be due to either sintering or entanglement of the corrosion products. Further work is required to determine the precise chemistry of the process. At high humidities, the force-separation curves exhibit an extended pull-off region, suggesting that the adsorbed film is mobile. This effectively reduces the adhesion by increasing the volume of the liquid bridge as the surfaces are pulled apart. This may explain why some reports in the literature show decreases in adhesion at high humidity.

Key words: Humidity, particle adhesion, inter-particle force, AFM, soda-lime glass, corrosion products

* Author to whom correspondence should be addressed.

** Guildford GU2 7XH, England UK

† Accepted: August 26, 2004

INTRODUCTION

When ostensibly dry powders are exposed to the surrounding atmosphere, adsorption of water molecules takes place on the particle surface. The extent of adsorption will naturally depend upon the partial pressure of water vapour, the system temperature and the affinity of the particles for water molecules. The presence of an adsorbed water layer modifies the interactions between individual particles and has an effect on a number of process operations, *e.g.* fluidisation, compaction, agglomeration, conveying of powders and hopper flow. Adsorbed water can also influence the interaction between particles and a surface leading to unpredictable behaviour for processes such as gas filtration, coating, and deposition. The driving force for adsorption is usually expressed in terms of the relative humidity (RH) defined as follows:

$$RH = \frac{p}{P^o} \quad (1)$$

where p is the partial pressure of water vapour in the air, and P^o is the vapour pressure of water. Relative humidity therefore accounts for variation in temperature through the associated variation in P^o .

The influence of RH on various processes is discussed by Harriman and Simkins [1] and Bracken [2]. They advocate a pragmatic approach, recommending RH limits for certain processes and discussing the relative merits of various methods of RH control. Whilst this approach may solve practical problems, a fundamental understanding of the influence of adsorbed water on particle interactions will lead to the development of more efficient processes and more effective products. All too frequently, adsorbed water is seen to be problematic in processes, but it must be borne in mind that there are potential benefits which can be identified through understanding the fundamental mechanisms involved.

The significance of air humidity in powder processing is stressed by Harnby *et al.* [3]. They comment that small changes in RH can produce a drastic change in powder cohesion, leading to loss of process control. They review some experimental attempts to characterise the effect of RH on cohesion by studies on single particles and on bulk powder samples. The main conclusion of their study is that there are large discrepancies between the findings of various workers. Apart from differences in measurement techniques, they attribute the discrepancies to the large number of variables, the most significant of which

were thought to be the chemical nature of the surface, the particle size, shape and surface roughness.

The influence of adsorbed moisture on particle adhesion is not straightforward, and is expected to depend on the thickness of the adsorbed layer, the surface roughness, the surface chemistry, the contact geometry and any dissolution, intra-particle absorption or chemical changes that might arise due to the presence of water. To further complicate the issue, one can expect that some changes may happen over a long time scale whilst others may be instantaneous. There has therefore been much evidence in the literature that is apparently conflicting, whilst theoretical approaches have tended to oversimplify the issues. In the following sections we review the published evidence relating to the influence of humidity on particle adhesion, starting with pioneering experimental efforts in the first half of the last century, following the progress through to the present day. We report some original data for adhesion between glass surfaces that exhibit an anomalously high value of adhesion at a critical humidity. The singular peak in adhesion is accompanied by strong repulsion prior to contact that is not observed at any other humidity. It is this kind of behaviour that typifies the complexity of the influence of adsorbed water on particle adhesion.

A HISTORICAL PERSPECTIVE OF EXPERIMENTAL STUDIES

The first clues as to the influence of humidity on the force between surfaces came to light towards the end of the 1920s. Stone [4] made a qualitative study of the adhesion between pairs of glass spheres (diameter 1 – 2 mm) suspended on silk threads. He noted a significant decrease in adhesion when conducting the experiment in dry air, compared with the adhesion observed in ambient air. The difference was attributed to the presence of adsorbed water. From his adhesion observations he also inferred that adsorbed moisture could be removed from the spheres by a current of dry air provided the beads are separated. If the beads are in contact then adhesion still persists in spite of the dry air flow. This observation has implications for the storage and drying of static bulk powders. It is unfortunate that Stone made no report of relative humidities or force values for his otherwise carefully conducted experiments.

Tomlinson [5,6] conducted studies of the adhesion between pairs of quartz fibres and pairs of glass spheres by measuring the deflection of the fibres. He studied freshly formed surfaces in a vacuum, and noted

that on exposure to the atmosphere, the surfaces lost most of their adhesion in a few hours. He attributed the loss in adhesion to the accumulation of contaminating matter from the air, reducing the surface energy of the solid surfaces. The striking difference in the trend between the observations of Tomlinson and Stone no doubt stem from Tomlinson's use of freshly prepared surfaces in vacuum, which will maintain much higher surface energies compared with the dry air conditions of Stone.

Bradley [7] used a spring technique to study adhesion between two spheres of quartz. In contrast to the findings of Tomlinson, Bradley reported that the adhesion was independent of whether the measurement was made in a vacuum or in air. Experiments were also conducted with freshly fused sodium pyroborate ($\text{Na}_2\text{B}_4\text{O}_7$) spheres. The adhesion in air was found to be about twice that measured for quartz. Furthermore in a vacuum, the adhesion was observed to drop to about a third of its value measured in ambient air. The high value of adhesion in air was attributed to the adsorption of water. The difference between the adhesion of quartz surfaces and borate glass surfaces is most likely due to the glass being more hydrophilic than the quartz. In the work of Stone, Bradley and Tomlinson, it is unfortunate that no values of relative humidity were quoted.

A more systematic study of the influence of relative humidity was made by McFarlane and Tabor [8] for the interaction between a spherical glass bead on a glass plate using a pendulum technique similar to that of Tomlinson [5]. They produced direct verification of the expression for the adhesive force due to capillary action (F_c)

$$F_c = 4\pi R\gamma \cos \theta \quad (2)$$

between a sphere of radius R and a flat with a thin film of liquid interposed, having a specific surface energy γ and a contact angle θ . Note that equation (2) is an approximation which is strictly valid only when the film thickness is very much smaller than the sphere radius (R) and the contact angle is small [9]. McFarlane and Tabor found equation (2) applied at or close to 100% RH. The value of the surface tension for the air-water interface was calculated from the graph of adhesion versus R to be $67.3 \text{ mJ}\cdot\text{m}^{-2}$, which is less than the recognised value of $72.7 \text{ mJ}\cdot\text{m}^{-2}$. The discrepancy was attributed to a systematic experimental error. For McFarlane and Tabor's system, the adhesion was negligible at low RH values, only showing a notable increase at an RH of around 80%. This increase was shown to correspond closely to a notable increase

in experimental values for the adsorbed film thickness of water on glass. It is interesting that the maximum adhesion was observed to occur at RH values of 88% for glass on glass, even though the adsorbed film thickness is shown to carry on increasing until complete saturation is attained.

McFarlane and Tabor [8] studied the effect of surface roughness in the presence of adsorbed water, and concluded that increasing the roughness will decrease the adhesion. They proposed that adhesion falls as soon as the mean asperity height becomes comparable to the thickness of the adsorbed moisture film. At this point, multiple asperity contact was thought to occur with an associated decrease in adhesion.

A range of detailed studies of the influence of relative humidity on adhesion was made by Zimon in the 1960s and early 1970s, and these have been translated and summarised [10]. Zimon characterised the adhesion between glass spheres coated on to flat glass surfaces by the extent of particle detachment either in a centrifuge or by applying force *via* a pulsed vibration. This yielded an *adhesion number*, defined as the ratio of the number of particles remaining on the surface after an applied load to the number of particles originally present.

Zimon's experiments [10] showed that there was little change in adhesion over an RH range of 5 – 50%. Above an RH of 50%, Zimon noted a marked increase in adhesion. By comparison of experimentally determined values of adhesion with values predicted from equation (2), Zimon concluded that over an RH range of 50 – 65%, capillary forces are only beginning to take effect, whilst above 65% they prevail over other force mechanisms. This observation can be interpreted in terms of McFarlane and Tabor's inference [8] that capillary forces dominate once the adsorbed layer is sufficiently thick to engulf the surface asperities.

Zimon [10] modified the hydrophobicity of one or both contact surfaces by adsorption of various chlorosilanes. Compared with uncoated glass (adhesion numbers > 90%), the adhesion number dropped drastically to between 2% at an RH of 25% and 40% at an RH of 90% when both surfaces were rendered hydrophobic. When only one of the contact surfaces was coated, the adhesion number lay roughly midway between the two above extremes. In all cases, however, the adhesion number was observed to increase monotonically with increasing RH. Values of the contact angle for water on uncoated and coated glass were given by Zimon as 30° and 80° , respectively. This gives a factor of 0.2 between the two adhesive

forces predicted by equation (2). This factor is in broad agreement with the difference in the adhesion number for the uncoated and coated systems presented by Zimon.

Zimon observed in many cases that the adhesive force at saturation was significantly less than the corresponding theoretical values calculated from equation (2). He explained this phenomenon by invoking the concept of disjoining pressure exerted by the trapped film of water at the contact site. The disjoining pressure is a consequence of repulsive van der Waals forces that arise when the dielectric permittivity of the water is intermediate in value between the dielectric permittivity of the two solid surfaces, [9]. Zimon proposed that a finite separation distance will be established at mechanical equilibrium, the magnitude of which is determined by the disjoining pressure. He embodied this in the following equation for the force of adhesion F_{ad}

$$F_{ad} = F_c - F_{disj} \quad (3)$$

where F_c is the force due to capillary bridging and F_{disj} is the disjoining pressure. It is possible that disjoining pressure could account for the difference between the measured adhesion and the adhesion predicted from capillary bridging at saturation. However, there are many other factors that can influence the adhesion, *e.g.* mobility of the adsorbed film, viscous effects and uncertainty of the contact angle. It is worth noting also that disjoining pressure is only manifest for specific combinations of interacting components. Furthermore, disjoining pressure does not arise for the interaction between surfaces of the same material, irrespective of the interposing medium.

The final observation of Zimon [10] that is noteworthy relates to adhesion hysteresis with relative humidity. He reported higher adhesion on desorption than on adsorption for spherical glass particles interacting with a flat quartz surface. This is most likely due to the reduced tendency for water to evaporate from a capillary meniscus once it has formed. Thus for a given humidity, more water will be held at a particle contact point when desorbing compared with the amount of water present when adsorbing.

The centrifuge technique employed by Zimon [10] has been used with good effect by Podczeck *et al.* [11,12,13] to study the effect of relative humidity on the adhesion of pharmaceutical powders to various surfaces. In general, their findings were specific to each system studied, which were by nature very complex; their irregularly shaped particles ranged from hydrophobic to hydrophilic, with varying degrees of

solubility. Adhesion of the hydrophilic particles at high RH could be described by capillary bridging. This could not be applied to hydrophobic surfaces. They examined the effect of press-on force and contact time for their material. In some instances the press-on force had a profound effect, depending on the prevailing humidity. This set of work from Podczeck *et al.* successfully characterises the dependence of adhesion on humidity for these specific materials. It also gives an indication of the complexity of the underlying mechanisms, implying that broad generalisations regarding the effect of RH on adhesion cannot necessarily be transposed to other systems with success.

Further evidence relating to the fundamental nature of capillary menisci was gathered by Fisher and Israelachvili [14] and Christenson [15] using the surface force apparatus. This instrument and its applications to force measurement have been reviewed by Luckham [16]. The contacting surfaces comprise two crossed mica cylinders, which give an almost perfectly smooth contact with a geometry equivalent to a sphere on a flat surface. Christenson [15] found that the conclusions of Fisher and Israelachvili were in error in some instances by their use of a spring that permitted rolling and shearing of the surfaces in contact. The general trend observed by Fisher and Israelachvili, and Christenson, was that adhesion increased monotonically with increasing relative humidity to a maximum value corresponding to the value predicted by equation (2). Christenson identified this to occur at an RH of 70%, however, this is very system-specific, depending on the hydrophilicity and surface roughness, and the value is therefore somewhat arbitrary. The agreement between theory and experiment implied that the adhesion was dominated by the reduced Laplace pressure in the meniscus. Any other possible contributions to adhesion were negligible, *i.e.* solid-solid interaction, electrostatic double-layer force, disjoining pressure or the resolved component of the surface tension in the liquid neck. None of the authors attempted to address the adhesive mechanisms prevailing at lower RH values, prior to the onset of capillary formation. In a virtually saturated atmosphere, Fisher and Israelachvili observed that upon contact of the surfaces, the adsorbed moisture films become displaced from the contact region, leaving a residual monolayer of molecules sandwiched between the solids. This evidence must be taken into account when modelling the interaction between surfaces. It must be borne in mind that the surfaces used in these experiments had a smoothness verging on

the atomic, thus the effect of surface roughness is not apparent.

The issue of the prevailing mechanism of adhesion prior to the onset of capillary bridging has been addressed by Chikazawa *et al.* [17]. They used an electrobalance to measure the adhesion between surfaces of Pyrex glass, soda-lime glass, KCl and KBr. The potassium halide samples first showed notable adhesion at an RH of 20%. The configuration for the tests was sphere-on-flat. As the RH was increased, a sudden increase in adhesion was observed at around 65%, dropping sharply off again at an RH of 70%. A similar event occurred for the glass samples although the onset of adhesion was not detected until RH=40%, and the peak adhesion occurred between an RH of 70% and 85%.

Chikazawa *et al.* complimented their adhesion studies with measured adsorption isotherms of water on samples of the various materials studied. They concluded that there was insufficient coverage of water on the surfaces to facilitate capillary condensation at the onset of adhesion at an RH of 20% for the alkyl halides (40% for the glass samples). Between this point and the point at which adhesion was observed to peak, the authors proposed that hydrogen bonding was responsible for the interaction. The peak adhesion was proposed to coincide with the adsorption of sufficient water to allow capillary formation. No explanation was offered for the subsequent sharp drop in adhesion on increasing the RH. In the work of Chikazawa *et al.*, the issue of surface dissolution of the KCl and KBr is expected to add to the complex interplay of surface roughness, microporosity and hydrophobicity.

A novel technique for measuring the adhesion force between an array of individual particles and a flat surface has been developed by Harnby *et al.* [18]. Several thousand particles of either glass ballotini or sand were painstakingly positioned in the apertures of an electroformed microsieve. The adhesive force between the array and a flat surface of brass, glass or stainless steel was measured to within 0.1 mg using a top pan balance. The force between individual particles was then inferred by dividing the measured force by the total number of particles in the array. For example, the measured value for adhesion of a single glass ballotini particle (diameter=155 μm) on a glass surface was 1.7×10^{-7} N, at conditions approaching 100% RH. This is over two orders of magnitude lower than the result predicted from equation (2), *i.e.* 6.3×10^{-5} N, using Harnby *et al.*'s measured contact angle of 26° . This is in contrast to the majority of

other workers who find at least relatively good agreement close to saturation. It is therefore most likely that in spite of the careful efforts of Harnby *et al.* in the preparation of their array, there would have been some deviation in the height of the protruding particles. This would cause a significant reduction in the number of contacts compared with the number of particles present in the array, and hence is the most likely explanation for the low adhesion force measured.

In spite of the unrealistically small values of single particle adhesion reported by Harnby *et al.* [18], the overall trends are worthy of mention. No significant effect on adhesion was observed for different times of contact or predetermined loading values, implying that the contacts did not involve plastic deformation. However, the separation velocity was seen to exert a strong influence on adhesion, with the lowest separation velocities providing the strongest adhesion. It was concluded that low separation velocities allow the water sufficient time to flow into the liquid bridges, thereby strengthening them. In all conditions they observed an increase in adhesion with increase in RH, with no significant hysteresis. The critical value of RH at which the adhesion increased markedly was found to lie between 60% and 90%, which is broadly in agreement with the observations of Zimon [10].

The effect of surface roughness was also studied by Harnby *et al.* At close to 100% RH, sand particles contacting polished brass had only half the adherence of the same particles contacting roughened brass (4.4 μm). Harnby *et al.* consider this to be due to an increase in the contact area for the angular sand particles with the roughened surface. This is thought to be unlikely because the difference only manifested itself at close to 100% RH, whilst at all other values of RH, there is no discernible dependence of adhesion on roughness. It is more likely that the roughened surface promotes water condensation compared with the polished surface, and that the increase in adhesion is purely a result of more water present to form capillary bridges. The reverse trend was observed for glass ballotini on stainless steel. Smooth stainless steel resulted in significantly higher adhesion than roughened stainless steel. This trend was observed between RH values of 50% and 100%, suggesting that the roughened surface prevented effective contact between the glass ballotini and the adsorbed water layer, as previously identified by McFarlane and Tabor [8].

By analogy, the interaction between particles in a humid environment can be extended to the contact

between the read/write head and computer disk drives. This issue has been addressed by Li *et al.* [19], and Tian and Matsudaira [20], who examined the friction force as a function of lubricant addition and relative humidity. Both groups reported an increase in static friction coefficient with increasing thickness of adsorbed water film. Attempts have been made to derive a theoretical model for the contribution to static friction between the head and disk from capillary forces, taking into account surface roughness and adsorbed film thickness [21,22]. The model by Gao *et al.* [22] predicted critical conditions for the minimisation of static friction, but unfortunately the authors did not support their analysis with experimental observation.

ADHESION STUDIES USING ATOMIC FORCE MICROSCOPY

The study of particle adhesion entered a new phase with the development of the atomic force microscope (AFM). The high sensitivity of this instrumentation enabled the measurement of nano-scale forces and separations between particles with diameters of only a few micrometres. Sugawara *et al.* [23] used an AFM to measure the adhesion between a standard Si_3N_4 probe tip and a mica surface. They measured the adhesion under UHV conditions and under ambient pressure with relative humidities of between 23% and 65%. Their data revealed a smooth monotonic increase in adhesion with increasing humidity. The maximum adhesion they recorded was in the region of 1.7×10^{-8} N (at RH=65%), whereas the adhesion calculated from equation (2) is 2.3×10^{-8} N, given their quoted value of 25 nm for the probe tip radius. The authors attribute the discrepancy to the surface roughness of the cantilever probe. It is indeed likely that the effective tip radius is less than quoted due to irregularities or roughness. However, the agreement is close given that perfect wetting has been assumed.

Binggeli and Mate [24] used an AFM to study the adhesion and sliding friction between an AFM probe tip and a hydrophilic surface of silicon oxide as well as a hydrophobic surface of amorphous carbon. They assessed the amount of water adsorbed as a function of RH by studying the break-free length of the capillary meniscus when the probe tip is retracted from the surface. This method provides qualitative information regarding the film thickness. For more reliable measurements, account must be made of the film mobility and the fact that the presence of the probe tip on the surface will promote the localised conden-

sation of water [25]. The enhanced adsorption of water on the hydrophilic surface was shown to act as a lubricant, reducing the coefficient of friction. No reduction in friction coefficient was observed for the hydrophobic carbon surface, explained by the relative absence of water molecules on the surface. It is interesting to note that the adhesion for both surfaces was shown to decrease with increasing RH, over the range of 75% to 95%. The authors explained this reduction using a simple thermodynamic argument involving the chemical potential of the water film. This can be interpreted in terms of the decrease in adhesion that is predicted by a number of capillary bridge models as the volume of liquid between a sphere and a flat plate increases, *e.g.* [26,27]. The principle can be understood in terms of the reduction in Laplace pressure inside the bridge as the radius of curvature increases. It is worth noting that the opposite trend is predicted for conical geometry contacting a flat surface as the bridge volume (*i.e.* the RH) increases, *e.g.* [28,29]. This is due to the lessened dependence on the Laplace pressure for adhesion for this geometry, compared with the force required to overcome the surface tension of the film.

Tang *et al.* [30] also studied the adhesion between an AFM probe tip and various surfaces including mica, calcium fluoride (CaF_2) and potassium chloride (KCl). In contrast to Sugawara *et al.* [23], Tang *et al.* found that the adhesion for both mica and CaF_2 did not vary with humidity over the range 20% to 80% RH. The authors conclude that the surface tension of the adsorbed film is responsible for the adhesion. This is likely to be the case for these very smooth surfaces. Studies with the KCl revealed adhesion values of nearly an order of magnitude higher than those for CaF_2 . In addition, they observed an increase in adhesion between 60% and 80% RH. The authors explain the difference by the increased surface tension promoted by the dissolution of KCl which is readily soluble compared with the other components. It is likely that there are other effects occurring here. The surface tension of water does not increase by an order of magnitude when adding KCl [31]. Furthermore, there is evidence that at high concentrations, a solution of KCl in water becomes “capillary inactive”, refuting the fundamental mechanism underlying equation (2). It is more likely that the high adhesion observed with the KCl arises due to the tip embedding into the surface that has been softened by the presence of adsorbed water.

Sugawara *et al.* [23], Binggeli and Mate [24], and Tang *et al.* [30] used the AFM probe tip as a surro-

gate particle for studying interactions. However, it is possible to mount an individual particle on to an AFM cantilever using adhesive. Interactions between the probe particle and other surfaces or particles can then be measured directly. A number of researchers have used this principle to good effect. A study by Berard *et al.* [32] has looked at the interaction between the anti-influenza drug *Zanamivir* and α -lactose monohydrate. The interaction between active drug particles and carrier or excipient particles is important for the effective operation of dry powder inhalation devices. They reported a significant increase in adhesion as the humidity was increased from 0% to 85% RH. They attributed this to capillary bridging. However, they also observed modification of the surface of lactose due to adsorbed water. Smaller surface features preferentially dissolve and the resulting supersaturation promotes growth on larger features. This process, known as Ostwald ripening, has also been observed for boric acid particles [33]. It results in a significant change in surface roughness which is expected to modify adhesion. It may also lead to the production of a different phase on the particle surface which will modify its properties.

Using an AFM, Jones *et al.* [34] conducted a thorough study of adhesion between flat surfaces of glass or silicon and silicon AFM tips or glass microspheres. Adhesion as a function of relative humidity was observed over the range 5 – 90% RH. The flat substrates were treated to render them hydrophilic or hydrophobic. The interaction between the silicon probe tip and hydrophilic glass or silicon showed a steady increase in adhesion with RH that was reversible. The magnitude of adhesion agreed well with the Laplace-Kelvin theory of equation (2). The interaction between hydrophilic surfaces and glass microspheres (radius $\sim 20 \mu\text{m}$) also showed a steady and reversible increase in adhesion with increasing RH. However, these data fell at least three times below the adhesion predicted by equation (2), implying that full capillary formation was prevented by the surface roughness. Measurements of the surface profile of a glass microsphere revealed asperities of the order of 15 nm high and 50 nm across. Using the Kelvin equation, Jones *et al.* calculate the critical meniscus radii to range from 0.2 to 5 nm over the RH range 10 – 90%. This further supports the notion that full capillary meniscus formation was not achieved.

With hydrophobic flat surfaces, Jones *et al.* [34] observed a lower force, as expected, for all surfaces studied. However, they observed an anomaly for

experiments with glass (glass microsphere on glass flat, and silicon probe tip on glass flat) in the form of a high peak in adhesion at a relative humidity of between 20% and 40%. Their corresponding data are reproduced here in **Figure 1**. This adhesion peak was accompanied by a long-range attraction prior to contact, effective over a distance of around $2 \mu\text{m}$. The effect disappeared on repeating experiments at the same contact spot, but reappeared when moving to a new region on the surface. It was also shown to occur both during adsorption and desorption. The authors attribute the anomalous attraction to an electrostatic effect and acknowledge that it is likely to be a transient and dynamic in nature, rather than being a true equilibrium phenomenon. The presence of electrostatic charges on surfaces at this level of humidity is somewhat surprising. Visser [35] stated that humidity eliminates or greatly reduces the effect of electrical forces. This statement has been corroborated by Wan *et al.* [36], who measured adhesive forces and surface charges for surfaces of mica and silica. High values of adhesion were observed during experiments in dry nitrogen when the relative humidity was between 1 and 2%. Upon increasing the RH slightly (still with $\text{RH} < 10\%$), the adhesive force fell by about an order of magnitude. The drop in adhesion coincided with a decrease in the time taken for electrical charge dissipation from the surfaces; the exponential decay time constant fell by about two orders of magnitude.

In addition to their experimental study, Jones *et al.* [34] give a review of theoretical attempts to describe

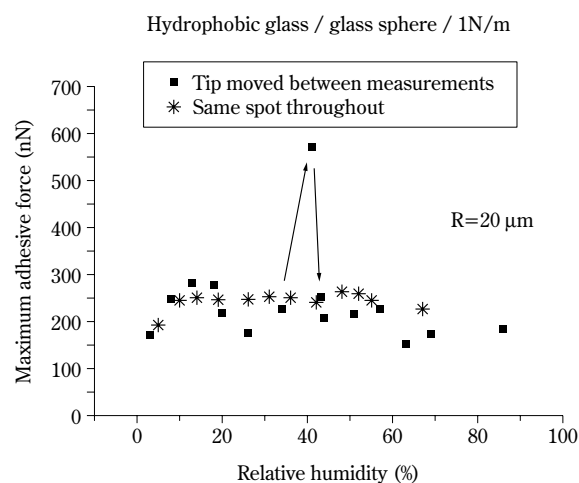


Fig. 1 Anomalous adhesion between a glass microsphere and a flat glass surface, both of which were rendered hydrophobic. Reproduced from Jones *et al.* [34].

particle adhesion, acknowledging the various contributions from solid-solid interaction forces, (van der Waals forces), capillary bridging and long-range electrostatic (Coulomb) forces.

In a later paper, Jones *et al.* [37] used an AFM to measure adhesion for powders of commercial interest. They observed a mix of behaviour with some powders exhibiting a marked increase in adhesion with increase in RH, whilst others showed no effect. This again confirms the complex nature of the prevailing phenomena. It is interesting to note that for the majority of powders tested, the adhesion was seen to increase with increasing maximum applied load (push-on force), suggesting that permanent deformation was occurring at contact areas.

A recent paper by Rabinovich *et al.* [38] addressed the transition between asperity contact and full capillary condensation for glass microspheres on a range of flat surfaces having varying degrees of roughness. The authors developed a model for the prediction of adhesion comprising two components. The first component accounts for the van der Waals forces between dry asperities, and incorporates the RMS roughness and the peak-to-peak distance between the asperities. The second component predicts the adhesion due to capillary bridging in an equation similar to equation (2) with a modification for the effective separation between the particle and the average surface plane, allowing for the presence of asperities on the surface. The first component was considered to be dominant prior to engulfment of the asperities by the capillary meniscus. Once engulfment occurred, the second component was considered to dominate. The transition between the components was shown to occur at a critical humidity. Experimental measurements gave excellent agreement with the theoretical approach. The critical humidity was observed to increase with increasing roughness. For the smoothest surfaces considered (RMS roughness 0.2 nm), the transition occurred at an RH of approximately 25%, rising to a value of 65% for a surface with an RMS roughness of 3 nm. Rabinovich *et al.* acknowledge the work of Coelho and Harnby [39,40] in predicting this critical humidity from a thermodynamic perspective involving the BET model for water sorption coupled with the Kelvin equation for liquid bridge stability. However, this model typically results in a critical RH in the region of 70 – 99%. Rabinovich *et al.* commented that a critical RH of 25% observed for smooth surfaces corresponds to a critical meniscus radius of approximately 0.4 nm as predicted by the Kelvin equation. This is an order of magnitude smaller than the

accepted lower limit for this macroscopic analysis [14,15], indeed it is of the same order as the nominal diameter of a water molecule. Doubt is therefore cast on the model of Coelho and Harnby for predicting critical humidity. Rabinovich *et al.* propose that a capillary meniscus existing at this low level of RH may well not be in thermodynamic equilibrium with the surrounding vapour, but may be in a metastable state. The work of Rabinovich *et al.* elegantly demonstrates the profound influence of nano-scale surface roughness on adhesion, and their modelling approach incorporating surface roughness shows great promise. Of course, the implication is that roughness data can be readily obtained in a form that realistically represents the specific physical situation.

The development of adhesion measurement as a function of relative humidity has been tracked, and the key experimental techniques have been identified. For fine powders, the centrifuge techniques give useful results that relate to the powder assembly. However, it is the AFM that enables detailed study of the relevant mechanisms at the level of the single particle. The disadvantage with the AFM technique is the large statistical variability that arises between individual measurements. In order to obtain statistically meaningful data, it is important to take sufficient measurements and apply some statistical criterion of confidence. The experimental evidence regarding the influence of humidity on particle adhesion has been presented. It is clear that the mechanisms responsible for adhesion are a complex interplay of surface roughness, amount of adsorbed water, electrical and mechanical properties of the solid, applied load and strain rate for separation. Further complexity is introduced for surfaces that interact with water in terms of solubility or plasticization. The modelling of particle adhesion as a function of relative humidity is still in its infancy.

ANOMALOUS BEHAVIOUR OF GLASS SURFACES

Jones *et al.* [34] have reported anomalously high values of adhesion for glass systems at certain values of relative humidity. Their data are reproduced here in **Fig. 1**. Note how a singularly high value of adhesion was observed at a relative humidity of 40%. We now report original data that are reminiscent of this anomaly. The study was conducted on a custom-built instrument based on the principle of an AFM with vertical displacement but no facility for scanning. A full description of the development and operation of

the instrument has been given in a previous publication [41], including details of cantilever spring constant determination and methodology for mounting particles on to the cantilever.

Adhesion was studied using single particles interacting with a flat surface. The particles repeatedly cycled in and out of contact with the surface at a frequency of 0.1 Hz, corresponding to an approach and retraction velocity of $\sim 0.5 \mu\text{m}\cdot\text{s}^{-1}$. The interaction between glass on glass and gold on gold was studied. The glass surfaces were cleaned in iso-propyl alcohol prior to measurement, to remove any organic contaminants. The gold surfaces were formed by sputter-coating gold on to a glass microsphere and glass slide. Sufficient time was allowed for sputtering to ensure a layer of gold in excess of 50 nm thick. Humidity control during an experiment was achieved by placing the entire instrument in a Perspex chamber and incorporating a beaker of distilled water or a tray of silica gel to raise or lower the RH accordingly. In practice, this gave a sufficiently slow change in RH such that instantaneous equilibrium could be assumed. This was tested experimentally by inducing a step-change in RH and observing that the adhesion force reached its equilibrium value directly.

Typical force-separation curves are shown in **Figures 2 and 3** for glass-on-glass at different values of RH. Each force curve, comprising 1000 data points, has been corrected to account for the cantilever deflection [41] to give true separation between the surfaces. The force data are therefore vertical for zero separation, as expected for rigid body contact. Both figures show the presence of attractive force prior to contact. The adhesion force was obtained from the minimum in the cantilever retraction curve, corresponding to the maximum deflection experienced by the cantilever prior to detachment from the surface. Note that at the moderate humidity shown in **Fig. 2**, there is little or no elongation of the liquid bridge when the particle is retracted from the surface. However, at the high humidity shown in **Fig. 3**, there is substantial elongation of the liquid bridge prior to complete detachment at a separation distance of ~ 1500 nm, suggesting that the liquid film is mobile at 83% RH. This mobility effectively increases the volume of the liquid bridge, and consequently reduces the measured adhesion for this geometry. If the film were not mobile, the adhesive force should correspond closely to that predicted by equation (2). It would be interesting to study the effect of strain rate on adhesion at this level of humidity to assess the contribution to adhesion from the vis-

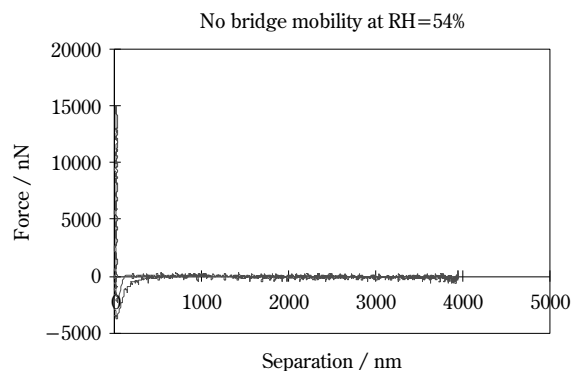


Fig. 2 Force-separation curve for the interaction between a glass microsphere (diameter=40 μm) and a flat glass surface at RH=54%.

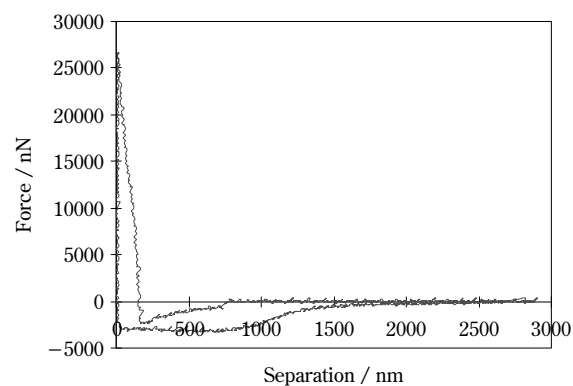


Fig. 3 Force-separation curve for the interaction between a glass microsphere (diameter=30 μm) and a flat glass surface at RH=83%. Bridge elongation is characterised by the extended separation distance in the retraction curve, (lower line).

cosity of the mobile film.

A typical plot of adhesion as a function of relative humidity is shown in **Figure 4** for glass-on-glass. Three data points were taken at each humidity, hence the scatter in the graph. Also superimposed on **Fig. 4** are the adhesion data for gold-coated surfaces. Adhesion values for the glass system and gold systems generally lay in the range 2000 to 6000 nN. This is well below the value of 17000 nN predicted by equation (2) for a sphere-on-flat configuration. On increasing the RH, little change in adhesion was observed with relative humidity for all surfaces studied. However, on desorption, a singular peak in adhesion was repeatedly observed to occur between a relative

humidity of 40 and 30%. This is apparent in **Fig. 4** at a relative humidity of 32.4%. The bizarre feature of this singular peak is that the strong adhesion is accompanied by a long-range (~ 300 nm) repulsion between the surfaces. The force curve corresponding to the peak in **Fig. 4** is shown in **Figure 5**. Repulsion is seen as the positive force prior to contact between the surfaces.

The nature of the strong adhesion and strong repulsion at this peak force is of great interest. Regarding

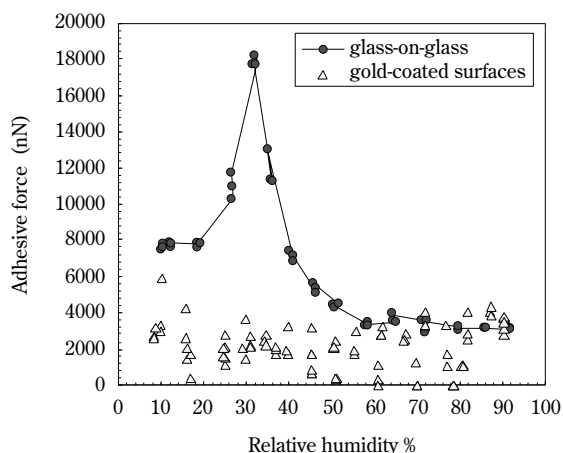


Fig. 4 Adhesion as a function of relative humidity for sphere (diameter $37\ \mu\text{m}$) interacting with a flat surface. The glass interactions are shown for decreasing humidity. The same peak in adhesion was not observed during increasing humidity. The data for gold-coated glass were obtained whilst increasing and decreasing humidity.

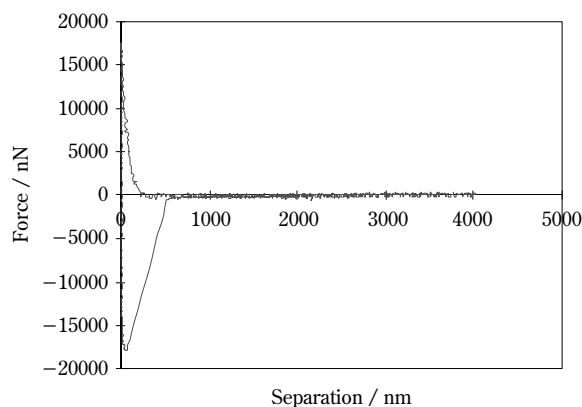


Fig. 5 Force-separation curve corresponding to the peak in adhesion shown in figure 4 for a $37\text{-}\mu\text{m}$ -diameter glass sphere interacting with a flat glass surface. Note the repulsion (positive force) prior to rigid body contact occurring at a separation distance of between 200 and 300 nm.

ing the repulsion prior to contact, the possibility of electrostatic repulsion was considered. Experiments were therefore repeated with an α -radiation source (Americium 241) in close proximity to the surfaces. This technique is advocated by Tomlinson [5] and Zimon [10] amongst others, to dissipate electrostatic charge. The strong repulsion pervaded even in the presence of the α -radiation source, suggesting that the force was not electrostatic in nature. Further evidence against electrostatic repulsion was gained by analysing the dependence of repulsive force on separation distance for a power law dependence. A log-log plot of repulsive force versus distance yielded a curve rather than a linear relationship, suggesting that electrostatic charging was not responsible for the observed repulsion.

Further analysis of the repulsive section of the curve revealed that the force decayed exponentially with separation distance. It is significant that others have also observed this dependence for repulsive forces between surfaces. Vigil *et al.* [42], examining the adhesion of silica surfaces in air, describe an exponentially decaying repulsion which they explain by the presence of a brush-like structure on the surface formed by the interaction between the silica surface and water vapour. Exponentially decaying steric repulsion has been observed by others working with polymer systems [43,44].

Vigil *et al.* [42] explain their brush-like structure on silica by growth of silanol and silicic acid chains on the surface which give rise to the steric repulsion on the surface and have a sintering effect when contact is made, giving rise to high values of adhesion. It is likely that a similar process can account for the repulsion and strong adhesion observed in the data presented here. A further possibility comes from the presence of glass corrosion products. It is well-established that soda-lime glass can undergo a range of water-induced surface reactions [45,46]. For example, soda (Na_2O) can react with water to give sodium hydroxide, which will in turn react with any carbon dioxide present to yield sodium bicarbonate and ultimately sodium carbonate [46]. We postulate that this kind of reaction can occur at high humidity in the relatively thick adsorbed liquid layer. Upon desorption, the water layer becomes supersaturated and the corrosion products precipitate out as a needle-like structure on the surface. Needles of this type up to $1\ \mu\text{m}$ in length have been reported by Arman and Kuban [47] for soda-lime glass stored in a humid environment. **Figure 6** shows a scanning electron microscope image of the contact region of a glass microsphere

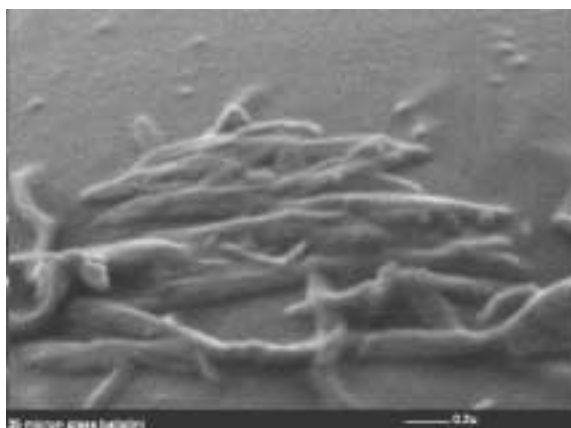


Fig. 6 SEM image of the contact site of a glass sphere directly after the repulsion and peak adhesion were observed. The features are proposed to be glass corrosion products that have spontaneously formed by crystallisation from the supersaturated liquid layer on decreasing the humidity.

taken immediately after it had experienced repulsion and peak adhesion. The features on the surface are thought to be corrosion products that have crystallised from the supersaturated water layer. They have subsequently been flattened by the forced contact between the surfaces. It is not clear at this stage exactly what reactions are occurring on the surface. Further work is required in this area to identify the precise chemistry that occurs on the surface of glass surfaces contacting in the presence of water vapour.

The anomalous adhesion for glass is reminiscent of the work of Jones *et al.* [34] who studied a similar system, see **Fig. 1**. However, Jones *et al.* observed this behaviour for glass surfaces that had been rendered hydrophobic. No anomalous peak was observed by them for untreated (hydrophilic) glass surfaces, on increasing or decreasing the relative humidity. They also observed similar behaviour to that in **Fig. 1** for a silicon probe tip interacting with hydrophobic glass. Note that Jones *et al.* observed their anomalously high force during both increases and decreases in relative humidity. In all cases, their peak in adhesion was accompanied by a strong attractive force prior to contact. This is in contrast to the work presented here, in which the peak adhesion was accompanied by strong repulsion prior to contact. In spite of the ostensible similarity in the adhesion peak between the work of Jones *et al.* and this present work, the large number of differences suggests that the responsible mechanisms may be different in each case.

CONCLUSION

A review of the literature relating to the influence of relative humidity on particle adhesion reveals that the behaviour is exceedingly complex. Adhesion is shown to depend on the thickness of the adsorbed layer of water, which in turn depends on the surface chemistry of the surfaces. Surface roughness plays a significant role, preventing the formation of a complete capillary meniscus at the particle contact point until a critical relative humidity is reached. At this point sufficient water is adsorbed to engulf the asperities. Some systems exhibit adhesion hysteresis with relative humidity. More complex behaviour can be expected if the surfaces experience some modification induced by adsorbed water, or if the surfaces are partially soluble. Theoretical approaches correctly recognise the role of the Laplace pressure in the capillary bridge as being dominant in controlling adhesion. However, evidence suggests that contributions from the solid-solid interaction, surface tension of the bridging film and disjoining pressure may also be important under certain circumstances. There is also evidence that water in the contact region may not necessarily be in thermodynamic equilibrium, existing instead in a metastable state. Adhesion data also have reportedly shown dependence on the separation strain rate in certain cases.

Original data have been presented for the adhesion of a glass microsphere on a flat glass surface. At high humidities, there is strong evidence that the adsorbed film is mobile, effectively reducing the adhesion by increasing the volume of the liquid bridge as the surfaces are pulled apart. Upon desorption, a critical relative humidity has been observed that yields a singular peak in adhesion, which is accompanied by long-range repulsion between the surfaces prior to contact. The long-range repulsion is an exponential function of separation distance. This phenomenon has been attributed to the formation of glass corrosion products which crystallise spontaneously from the liquid layer on desorption when the two surfaces approach each other. These are suspected to be in the form of needle-like structures that give rise to steric repulsion. Once contact is made, the strong adhesion may be due to either sintering or entanglement of the corrosion products. Further work is required to determine the precise chemistry of the process.

Table 1 Summary of experimental studies of the influence of relative humidity on particle adhesion.

Authors	Measurement technique	Contact geometry	Materials	RH range	Comments
Stone [4]	Pendulum	Sphere-sphere	Soda glass beads, diameter < 1.72 mm	Not specified	Adhesion in ambient air much greater than adhesion in dry air
Tomlinson [5,6]	Deflection of fibres	Sphere-sphere Fibre-fibre	Quartz fibres and glass spheres 0.12 – 1.22 cm diameter	Not specified	Reduction in adhesion of freshly formed surfaces after exposure to ambient air
Bradley [7]	Quartz spring balance	Sphere-sphere	Quartz beads and sodium pyroborate spheres of unequal size. $0.2 \text{ mm} < (d_1 d_2) / (d_1 + d_2) < 1.5 \text{ mm}$	Not specified	Quartz – no difference in adhesion measured in vacuum and ambient air. Borate – adhesion in vacuum one-third of the adhesion in ambient air
McFarlane and Tabor [8]	Pendulum	Sphere-flat	Glass spheres 0.25 – 1 mm diameter	78% – 100%	Equation (2) validated close to saturation. Role of surface roughness and adsorbed layer thickness demonstrated.
Zimon [10]	Centrifuge Pulsed vibration	Sphere-flat	Glass spheres 30 – 70 μm diameter Flat surfaces of glass, quartz and steel.	25% – 90%	Increase in adhesion observed above 50% RH. Reduction in adhesion for hydrophobic surfaces. Adhesion hysteresis reported.
Podczek <i>et al.</i> [11,12,13]	Centrifuge	Particle-flat Particle-particle	Lactose, salmeterol xinafoate	5% – 100%	Influence of press-on force and contact time studied. Difference between hydrophobic and hydrophilic surfaces identified.
Fisher and Israelachvili [14] Christenson [15]	Surface force apparatus	Crossed cylinders	Mica. Cylinder radii 14.6 – 24.1 mm	0% – 100%	Validation of equation (2) for capillary bridging above 70% RH.
Chikazawa <i>et al.</i> [17]	Electro-balance	Sphere-flat	Pyrex glass, soda-lime glass, KCl, KBr 2 mm – 16 mm diameter	3% – 98%	Capillary bridge formation observed above 60% RH. Adhesion below this value attributed to hydrogen bonding. Peaks in adhesion observed between 70% and 85%RH.
Harnby <i>et al.</i> [18]	Particle array and microbalance	Particle-flat	Glass and sand particles on brass, glass or stainless steel flat. Particle diameter range 85 – 460 μm	20% – 98%	Higher adhesion observed for low separation velocities. Onset of capillary bridging occurred between 60% and 90% RH. Poor agreement with equation (2). Surface roughness effects studied.
Sugarwara <i>et al.</i> [23]	AFM	Probe tip on flat	Silicon nitride on mica flat Tip radius 25 nm	23% – 65%	Increase in adhesion with RH. Measured adhesion was less than predicted by equation (2).
Binggeli and Mate [24]	AFM	Probe tip on flat	Tungsten tip ($r \sim 100 \text{ nm}$) on silicon oxide and amorphous carbon.	0 – 100%	Decrease in adhesion observed for increase in RH from 75% to 95%.
Tang <i>et al.</i> [30]	AFM	Probe tip on flat	Flat surfaces of mica, CaF_2 and KCl	20% – 95%	No influence of RH on adhesion for mica and CaF_2 surfaces. Higher adhesion values for KCl surface, showing increase from 60 – 80% RH.
Berard <i>et al.</i> [32]	AFM	Particle on flat	Zanamivir drug (10 – 100 μm) on lactose compact.	0%, 32% 85%	Increase in adhesion with increase in RH. Large scatter in data due to surface roughness. Modification of lactose surface observed at high RH.
Jones <i>et al.</i> [34]	AFM	Sphere on flat	Si probe tip and glass microsphere ($r=20 \mu\text{m}$ and 100 μm) on glass or silicon flat	0% – 90%	Effect of hydrophobic and hydrophilic surfaces, and surface roughness examined. Anomalously high adhesion observed for hydrophobic glass surface between 20% and 40% RH.
Jones <i>et al.</i> [37]	AFM	Particle on flat Particle on particle	Alumina, silica, limestone, titania, zeolite.	4% – 90%	Range of RH dependence of adhesion shown. Increase in adhesion observed with increase in push-on force.
Rabinovich <i>et al.</i>	AFM	Sphere on flat	Glass spheres (20 and 40 μm diameter) on treated silica flat surfaces	0% – 80%	Transition between dry adhesion and capillary bridge adhesion clearly identified and linked to surface roughness <i>via</i> theoretical model.

REFERENCES

- Harriman, L. and Simkins, D.: Don't sweat it, dehumidify. *Chem. Engng.*, Aug, pp.80-87 (1997).
- Bracken, E.: Combating humidity – the hidden enemy in manufacturing. *Sensor Rev.*, 17, no. 4, pp.283-290 (1997).
- Harnby, N., Hawkins, A.E. and Opalinski, I.: Measurement of the adhesional force between individual particles with moisture present, Part 1: A review. *Chem. Engng. Res. Des.*, 74, A6, part A, pp.605-615 (1996).
- Stone, W.: Some phenomena of the contact of solids. *Phil. Mag.*, 9, pp.610-620 (1930).
- Tomlinson, G.A.: Molecular cohesion. *Phil. Mag.*, 6, pp.695-712 (1928).
- Tomlinson, G.A.: Further experiments on the cohesion of quartz fibres. *Phil. Mag.*, 10, pp.541-544 (1930).
- Bradley, R.S.: The cohesive force between solid surfaces and the surface energy of solids. *Phil. Mag.*, 13, pp.853-862 (1932).
- McFarlane, J.S. and Tabor, D.: Adhesion of solids and the effect of surface films. *Proc. R. Soc. Lond. Series A*, 202, pp.224-243 (1950).
- Israelachvili, J.: Intermolecular and surface forces. 2nd Ed., Academic Press, (1991).
- Zimon, A.D.: Adhesion of Dust and Powder. Consultants Bureau, (Plenum Publishing Co.), New York, (1982).
- Podczec, F., Newton, J.M. and James, M.B.: The influence of constant and changing relative humidity of the air on the autoadhesion force between pharmaceutical powder particles. *Int. J. Pharmaceutics*, 145, pp.221-229 (1996).
- Podczec, F., Newton, J.M. and James, M.B.: Influence of relative humidity of storage air on the adhesion and autoadhesion of micronized particles to particulate and compacted powder surfaces. *J. Coll. and Interface Sci.*, 187, pp.484-491 (1997).
- Podczec, F., Newton, J.M. and James, M.B.: Variations in the adhesion force between a drug and carrier particles as a result of changes in the relative humidity of the air. *Int. J. Pharmaceutics*, 149, pp.151-160 (1997).
- Fisher, L.R. and Israelachvili, J.N.: Direct measurement of the effect of meniscus forces on adhesion: a study of the applicability of macroscopic thermodynamics to microscopic liquid interfaces. *Colloids and Surfaces*, 3, pp.303-319 (1981).
- Christenson, H.K.: Adhesion between surfaces in undersaturated vapours – a reexamination of the influence of meniscus curvature and surface forces. *J. Colloid Interface Sci.*, 121, no. 1, pp.170-178 (1988).
- Luckham, P.F.: The measurement of interparticle forces. *Powder Technol.*, 58, pp.75-91 (1989).
- Chikazawa, M., Kanazawa, T. and Yamaguchi, T.: The role of adsorbed water on adhesion force of powder particles. *Kona*, no. 2, pp.54-61 (1984).
- Harnby, N., Hawkins, A.E. and Opalinski, I.: Measurement of the adhesional force between individual particles with moisture present, Part 2: A novel measurement technique. *Chem. Engng. Res. Des.*, 74, A6, part A, pp.616-626 (1996).
- Li, Y., Trauner, D. and Talke, F.E.: Effect of humidity on stiction and friction of the head/disk interface. *IEEE Trans. Magnetics*, 26, no. 5, pp.2487-2489 Sept. (1990).
- Tian, H. and Matsudaira, T.: Effect of relative humidity on friction behaviour of the head/disk interface. *IEEE Trans. Magnetics*, 28, no. 5, pp.2530-2532 Sept. (1992).
- Tian, H. and Matsudaira, T.: The role of relative humidity, surface roughness and liquid build-up on static friction behaviour of the head/disk interface. *Trans. ASME J. Tribology*, 115, pp.28-35 Jan. (1993).
- Gao, C. Tian, X. and Bhushan, B.: A meniscus model of optimization of texturing and liquid lubrication of magnetic thin-film rigid disks. *Tribology Trans.*, 38, no. 2, pp.201-212 (1995).
- Sugawara, Y., Ohta, M., Konishi, T. Morita, S., Suzuki, M. and Enomoto, Y.: Effects of humidity and tip radius on the adhesive force measured with atomic force microscopy. *Wear*, 168, pp.13-16 (1993).
- Binggeli, M. and Mate, C.M.: Influence of capillary condensation of water on nanotribology studied by force microscopy. *Appl. Phys. Lett.* 65, (4), pp.415-417 July (1994).
- Dey, F.K., Cleaver, J.A.S. and Zhdan, P.A.: Atomic force microscopy study of adsorbed water on lactose particles. *Advanced Powder Technol.* 11, (4), pp.401-413 (2000).
- Mason, G. and Clark, W.C.: Liquid bridges between spheres. *Chem. Engng. Sci.* 20, pp.859-866 (1965).
- Orr, F.M., Scriven L.E. and Rivas, A.P.: Pendular rings between solids: meniscus properties and capillary force. *J. Fluid Mech.* 67, part 4, pp.723-742 (1975).
- Cahn, J.W. and Heady, R.B.: Analysis of capillary forces in liquid-phase sintering of jagged particles. *J. Am. Ceram. Soc.* 53, (7), pp.406-409 July (1970).
- Coughlin, R.W., Elbirli, B. and Vergara-Edwards, L.: Interparticle force conferred by capillary-condensed liquid at contact points. *J. Coll. Interface Sci.* 87, (1), pp.18-30 (1982).
- Tang, J., Wang, C., Liu, Maozi, Su, M. and C. Bai.: Effect of humidity on the surface adhesion force of inorganic crystals by the force spectrum method. *Chinese Sci. Bull.*, 46, no. 11, pp.912-914 June (2001).
- Sakong, Y., Hwang, J-E. and Son, M-Y.: A study of the surface tension of some electrolyte solutions. *J. Korean Chem. Soc.* 8, no. 1, pp.1-4 (1964).
- Berard, V., Lesniewska, E., Andres, C., Pertuy, D., Laroche, C. and Pourcelot, Y.: Dry powder inhaler: influence of humidity on topology and adhesion studied by AFM. *Int. J. Pharmaceutics*, 232, pp.213-224 (2002).
- Cleaver, J.A.S. and Wong, P.: Humidity induced surface modification of boric acid. *Surf. Interface Anal.* (2004). Accepted for publication.
- Jones, R., Pollock, H.M., Cleaver, J.A.S. and Hodges, C.S.: Adhesion forces between glass and silicon surfaces in air studied by AFM: effects of relative humidity, particle size, roughness and surface treatment. *Langmuir*,

- 18, pp.8045-8055 (2002).
35. Visser, J.: Adhesion of Colloidal Particles. *Surface and Colloid Sci.*, 8, pp.3-79 (1976).
 36. Wan, K-T., Smith, D.T. and Lawn, B.R.: Fracture and contact adhesion energies of mica-mica, silica-silica, and mica-silica interfaces in dry and moist atmospheres. *J. Am. Ceram. Soc.*, 75, (3), pp.667-676 (1992).
 37. Jones, R., Pollock, H.M., Geldart, D. and Verlinden, A.: Inter-particle forces in cohesive powders studied by AFM: effects on relative humidity, particle size and wall roughness. *Particle Technology*, 132, pp.196-210 (2003).
 38. Rabinovich, Y.I., Adler, J.J., Esayanur, M.S., Ata, A., Singh, R.K. and Moudgil, B.M.: Capillary forces between surfaces with nanoscale roughness, *Adv. Coll. and Interface Sci.*, 96, pp.213-230 (2002).
 39. Coelho, M.C. and Harnby, N.: The effect of humidity on the form of water retention in a powder. *Powder Technol.* 20, pp.197-200 (1978).
 40. Coelho, M.C. and Harnby, N.: Moisture bonding in powders. *Powder Technol.* 20, pp.201-205 (1978).
 41. Tyrrell, J.W.G. and Cleaver, J.A.S.: Development of an instrument for measuring inter-particle forces. *Advanced Powder Technol.* 12, (1), pp.1-15 (2001).
 42. Vigil, G., Xu, Z., Steinberg, S. and Israelachvili, J.: Interactions of silica surfaces. *J. Coll. Interface Sci.*, 165, pp.367-385 (1994).
 43. Biggs, S.: Steric and bridging forces between surfaces bearing adsorbed polymer: an atomic force microscopy study. *Langmuir*, 11, pp.156-162 (1995).
 44. Butt, H-J., Kappl, M., Mueller, H. and Raiteri, R.: Steric forces measured with the atomic force microscope at various temperatures. *Langmuir*, 15, pp.2559-2565 (1999).
 45. Clark, D.E., Pantano, C.G. and Hench L.L.: Corrosion of glass, books for industry and the glass industry, New York (1979).
 46. Trens, A., Denoyel, R. and Guilloreau, E.: Evolution of surface composition, porosity and surface area of glass fibres in a moist atmosphere, *Langmuir*, 12, pp.1245-1250 (1996).
 47. Arman, B. and Kuban, B.: Corrosion products encountered on glass surfaces, *Mat. Characterisation*, 29, pp.49-53 (1992).

Author's short biography



Dr Jamie Cleaver

Jamie Cleaver holds a first degree in Chemical Engineering from the University of Surrey, and a PhD in Chemical Engineering from the University of Cambridge. He has been active in particle technology research for over 10 years, focussing initially on powder flow and attrition. More recently he has developed expertise in micro-scale characterisation of particles, including measurement of inter-particle forces and nano-indentation, relating to issues such as powder cohesion and caking. He is currently a lecturer in Chemical Engineering at the University of Surrey.

James Tyrrell

Dr James Tyrrell is currently a science and technology writer for a business to business publication. Since receiving his BEng and PhD from the University of Surrey, he has worked on research contracts in South Australia and Germany, and as a development engineer in the UK. His expertise in scientific instrumentation spans a range of applications including nano-bubble imaging, thin film rheology, quantum dot metrology, interference microscopy, particle image velocimetry and inter-particle force measurement.

Trends in Microencapsulation Research[†]

Hidekazu Yoshizawa

*Department of Environmental Chemistry and
Materials, Faculty of Environmental Science
and Technology, Okayama University**

Abstract

A microcapsule is a tiny capsule and its preparation procedure, called microencapsulation, can endow various traits to the core material in order to add secondary functions and/or compensate for shortcomings. This paper first gives a general overview of microencapsulation technology and subsequent sections cover topics of microencapsulation research, including application of microcapsules to information and image technologies for microparticle-based paper-like display systems, a use that has attracted considerable attention recently. The research results of the project conducted by the Japan Chemical Innovation Institute under the commission of NEDO, as one of the projects of the METI Nanotechnology Program to develop microparticle-based paper-like display systems, are also introduced.

1. Introduction

Microencapsulation is a technique to prepare tiny packaged materials called microcapsules that have many interesting features. This technique has been employed in a diverse range of fields from chemicals and pharmaceuticals to cosmetics and printing. For this reason widespread interest has developed in microencapsulation technology.

The first industrial product employing microencapsulation was carbonless copy paper developed by Green and Schleicher in the 1950s. The microcapsules used in it were prepared by complex coacervation of gelatin and gum arabic [1]. To this day, carbonless copy paper is one of the most significant products to utilize microencapsulation technology, and is still produced commercially. The technologies developed for carbonless copy paper have led to the development of various microcapsule products in recent years.

Further function integration in microcapsules is essential to make products with excellent properties. Likewise, strategies should be considered to make

smaller microcapsules with thinner membranes. This direction of microencapsulation research is suited to current needs and matches the features of nanotechnology efforts initiated in the United States of America in 2000.

We have developed, so far, microcapsules with functions for separation and purification [2-7], controlled release of drugs [8-20], and the triboelectric property required by toner microparticles [21, 22]. Hollow microcapsules and microcapsules enclosing microorganisms have also been prepared [23, 24]. In this paper, after an introduction to microcapsules and microencapsulation, special attention is paid to research on a type of microparticle-based paper-like display, called the microencapsulated electrophoretic display system [25-27].

2. General features of microcapsules

Microcapsules are tiny microparticles with diameters in the range of nanometers or millimeters that consist of core materials and covering membranes (sometimes also called walls). The most significant feature of microcapsules is their microscopic size that allows for a huge surface or interface area. Through selection of the composition materials (core material and membrane), we can endow microcapsules with a variety of functions. Generally, membrane materials

* 3-1-1 Tsushima-Naka, Okayama 700-8530 Japan

Tel & Fax: 086-251-8909

E-mail: yhide@cc.okayama-u.ac.jp

[†] Accepted: July 21, 2004

are chosen in order to pronounce the effects of microencapsulation. Therefore, not only synthetic and natural polymers but also lipids and inorganic materials are used for the preparation of microcapsules.

Some well-known products prepared using microencapsulation techniques are artificial salmon roe and carbonless copy paper. Microcapsules can be classified into three basic categories according to their morphology as mono-cored, poly-cored, and matrix types, as shown in **Figure 1**. Morphological control is important and much effort has been given to controlling internal structures, which largely depend on the protocol and the microencapsulation methods employed.

Microcapsules have a number of interesting advantages and the main reasons for microencapsulation can be exemplified as (1) controlled release of encapsulating drugs, (2) protection of the encapsulated materials against oxidation or deactivation due to reaction in the environment, (3) masking of odor and/or taste of encapsulating materials, (4) isolation of encapsulating materials from undesirable phenomena, and (5) easy handling as powder-like materials.

More detailed features of microcapsules are summarized in books by Gutcho [28] and Arshady [29], and in review papers by Makino [30], Arshady [31], Kondo [32], Hatate, et al. [33], and Yoshizawa [34-36].

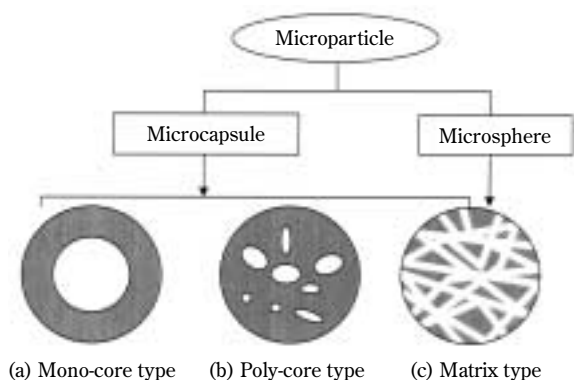


Fig. 1 Classification of microparticles from their morphology

3. Microcapsules in the information and imaging fields

The first successful application of microencapsulation technology in the information and imaging fields was the carbonless copy paper developed by the National Cash Register Company to solve the prob-

lems of solvent evaporation and diffusion of ink into paper substrate. Carbonless copy paper has become a \$5.5 billion business worldwide.

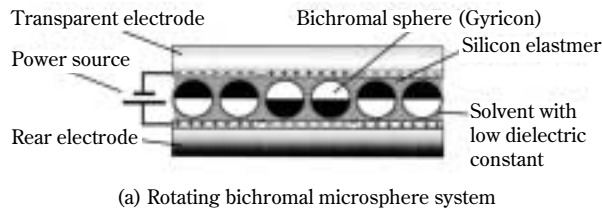
In the 1960s, microencapsulation of cholesteric liquid crystal by complex coacervation of gelatin and acacia was reported to produce a thermosensitive display material. J. L. Ferguson developed nematic curvilinear aligned phase (NCAP), a liquid crystal display system using microencapsulation of nematic liquid crystal [37]. Encapsulation technology has provided the enlargement of display areas and wider viewing angles.

The functions endowed by microencapsulation in the development of carbonless copy paper and NCAP can be summarized as the protection of core materials from deterioration such as oxidation and easy handling and treatment as powder-like substances.

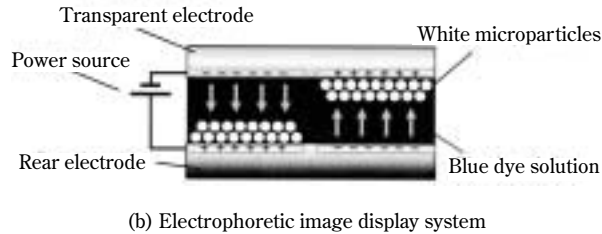
4. Why a microparticle-based display is desirable

Creation of a paper-like display with low power consumption has been an ambition of display researchers for many years. To realize this beneficial technology, many researchers have tried to make microparticle-based display systems. An electrophoretic image display system and a rotating bichromal microspheres system are representative of trials to create paper-like display systems [37, 38]. Particle-based display systems are attractive for their optical and electronic properties. These beneficial properties result from the highly scattering and absorbing microparticles that contain pigments like titanium dioxide and carbon black.

Figure 2 shows a schematic illustration of the rotating bichromal microspheres system (a) and the electrophoretic image display system (b). The rotating bichromal system called Gyricon has been developed by Nicholas K. Sheridan at the Xerox Palo Alto Research Center. In the rotating bichromal system, a microsphere with white and black hemispherical surfaces is in each cavity of a silicon polymer film that is placed between a transparent top electrode and a bottom electrode. The principle of the rotating bichromal microspheres system is the rotation of the microspheres to correspond to the addressed external electric field. That is, the positively-charged black hemispherical surface rotates toward the negatively-charged top electrode. In contrast, at the same moment, the negatively-charged white hemispherical surface has an electrostatic affinity to the positively-charged electrode. Thus, the color change is attributable to the



(a) Rotating bichromal microsphere system



(b) Electrophoretic image display system

Fig. 2 Schematic illustration of the rotating bichromal microsphere system (a) and the electrophoretic image display system (b)

rotation of bichromal microspheres. On the other hand, the fundamental aspect in the electrophoretic image display systems is caused by electrophoretic migration of charged microparticles in a fluid with a low dielectric constant. This system was presented by Isao Ota of Matsushita Electric Industrial Co., Ltd.

5. Microencapsulated electrophoretic display system

Despite many attractive features, however, the microparticle-based display systems mentioned above suffer from some shortcomings, including difficulty achieving perfect rotation (in the case of the rotating bichromal microspheres system) and short lifetime due to coagulation and agglomeration caused by colloidal instability (in the case of the electrophoretic image display system).

I had a chance to conduct research on paper-like display systems at the Media Laboratory of Massachusetts Institute of Technology with Prof. Joseph Jacobson, a key person in the development of paper-like display systems employing electrophoresis of microparticles. To overcome the previously mentioned shortcomings, we created E-ink, a new display system utilizing microencapsulation techniques with a fusion of chemistry, physics, electronics and other technologies [25]. The schematic illustration is shown in **Figure 3**. As this figure shows, the structure of E-ink is simple and each microcapsule, with about the diameter of a human hair, contains millions of tiny pigment

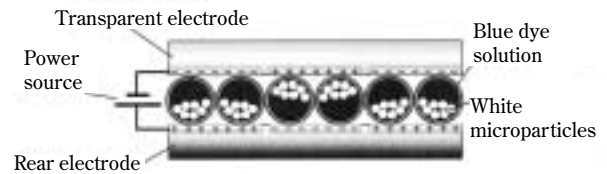


Fig. 3 Schematic illustration of the microencapsulated electrophoretic display system

microparticles that are well dispersed in an organic solution with a low dielectric constant. The microencapsulated electrophoretic display system prototype that we proposed in the journal *Nature* in 1998 was a one-particle system. Microcapsules contained one type of charged white microparticles dispersed in a blue dye solution. At present, we have developed a two-particle system that uses two kinds of microparticles (one white, one black) enclosed in a microcapsule. In the two-particle system, the dispersion medium in microcapsules is a transparent fluid.

When an electric field is applied between microcapsules, the microparticles move in the low dielectric constant solution toward the oppositely charged electrode in the phenomenon of electrophoretic migration. If the top transparent electrode is positively charged, white microparticles with negative charges should move toward the top electrode, making the surface appear white at that spot. At the same time, an opposite electric field pulls the black particles to the bottom of the microcapsules. By reversing this process, the black microparticles appear at the top of the microcapsules, which makes the surface become black at that spot. This is how microencapsulated ink (E-ink) forms letters and pictures on the display.

Figure 4 presents microphotographs of the microencapsulated electrophoretic display system at different magnifications, in which the letter 'k' was electronically induced. The prepared microcapsules were dispersed in UV-curable polymer and covered with a transparent electrode. The microcapsules were sieved to have an average diameter of about 40 μm . This diameter allows for a resolution of up to 600 dpi.

The contrast ratio and the reflectance of the prototype were 7:1 and 35%, respectively. Using the same measurement system, a newspaper had 5:1 contrast ratio and 55% reflectance. Furthermore, we observed the microencapsulated electrophoretic display system had bistability (image storage performance) for several months. Bistability is an important performance trait of rewritable paper and paper-like displays,

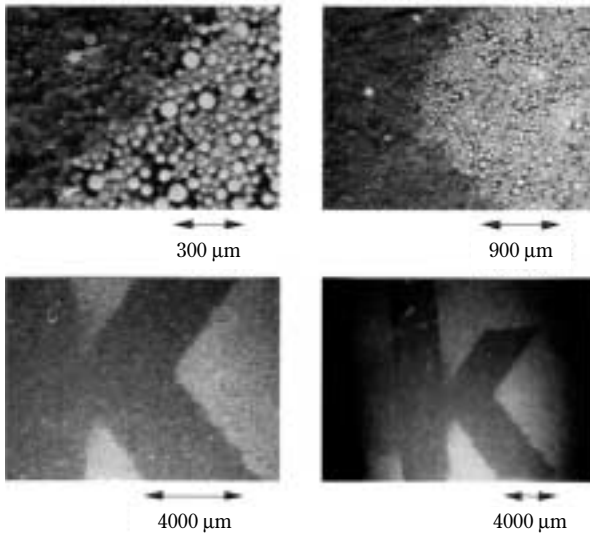


Fig. 4 Photograph of display image of microencapsulated electrophoretic display system

because it allows image retention even when the power is turned off. This trait allows for both portability and low-power consumption.

For electrophoretic image display systems, the remaining problems had been particle clustering, agglomeration and lateral migration. The benefit of microencapsulation in this case is the isolation of electrophoretic dispersion in discrete compartments. In other words, agglomeration of electrophoretic dispersion in a microcapsules has no influence on electrophoretic dispersion in neighboring microcapsules.

Prof. Joseph Jacobson and other cofounders established E Ink Corporation in Cambridge, Massachusetts in 1997 to produce a next-generation display which has many of the advantages of paper-like media, including the ability to access information anytime, anywhere [40]. This technology can be said to be the future of paper. E Ink advertises that paper-like displays have the following advantages. (1) *Paper-like readability* means that the display can be read in dim light with the same contrast as in bright sunlight, and at any angle without loss of contrast. (2) *Ultra-low power consumption* results from the performance of bistability, which allows a fixed image to be kept even when the power is turned off. (3) *Exceptional portability* because of the reduced use of both polarizer and glass compared to liquid crystal display systems.

E ink Corporation first demonstrated these systems as store signs under the brand name of Immedia in 1999. They were tested at various places including J. C. Penny retailing stores (**Figure 5**), and by the Arizona Republic newspaper for headline displays [27].



Fig. 5 Photograph of first commercial display with electrophoretic ink by E-ink's Immedia Technology in J.C. Penney stores

E ink Corporation recently announced that they have sold their first electronic paper display module for application in Sony's new e-Book reader, LIBRIé (**Figure 6**), produced in cooperation with Toppan Printing, Royal Philips Electronics and Sony Corporation [41-43]. They claim that more than 10,000 pages



Fig. 6 Photograph of Sony Corporation LIBRIé that uses the electrophoretic ink technology of E-ink Corporation

can be read with just four AAA Alkaline batteries. In fact, the LIBRIé is lightweight and displays images with a white/black contrast that is as high as a newspaper. The LIBRIé is reported to have reflectance of 50%, contrast ratio of 15:1, power requirements of 15 V, and a response time of 40 ms.

This milestone in microencapsulated electrophoretic display system development is the culmination of fundamental investigations of microparticle science and engineering, which have been conducted to make microcapsules with homogeneously transparent membranes, and microparticles enclosing pigment with superior dispersion stability, as well as the development of electronic parts.

6. Full color rewritable paper using functional capsules project

As mentioned above, the electrophoretic image display system shown in **Fig. 2** was developed by a company in Japan. A paper-like display system employing microparticle technology has also gathered much attention from companies in Japan in the fields of electronics and information. For example, a toner-type display system [44], an in-plain-type display system [45], a liquid powder display system [46] and a Gyricon-like cylindrical display system [47] have been developed by Fuji Xerox Co., Ltd., Canon Inc., Bridgestone Corporation, and Oji paper Co., Ltd., respectively. Powder engineers have also achieved marvelous results with the development of liquid powder that is 10 times smaller in bulk density (**Figure 7**). This allows for quicker response to polar change with a time of 0.2 ms, which is one-tenth of that of liquid



Fig. 7 Photograph of typical liquid powder developed by Bridgestone Corporation

crystal display systems.

Japan is one of the leading countries in microencapsulation technology. Creation of functional materials and achievement of high productivity are the final subjects of technology fusion with microencapsulation fabrication technology. The Japanese Ministry of Economy, Trade and Industry (METI) has created a national project concerning paper-like displays that employ microencapsulation, called the Full Color Rewritable Paper Using Functional Capsules Project. This project is conducted by JCII under the Commission of NEDO, as one of the projects in the METI Nanotechnology Program. In 2004, this project is also included as a special project to reinvigorate the economy in a program called Focus 21.

The paramount objective of this project is the development of a paper-like display prototype. The following three subjects have been identified as requiring research in order to achieve this goal.

- (1) Encapsulation technology
- (2) Nano-functional particle surface physical-properties control technology
- (3) Display material and functional evaluation technology using the encapsulation technology of nano functional particles

The goals of encapsulation technology research are the development of a microencapsulation procedure that achieves high efficiency for functional nanoparticle encapsulation, and the determination of factors that control microcapsule diameter, membrane thickness and membrane properties. Representative results are shown in **Figures 8~10**.

Fig. 8 shows a photograph of polyurea microcapsules that were prepared by interfacial polymerization

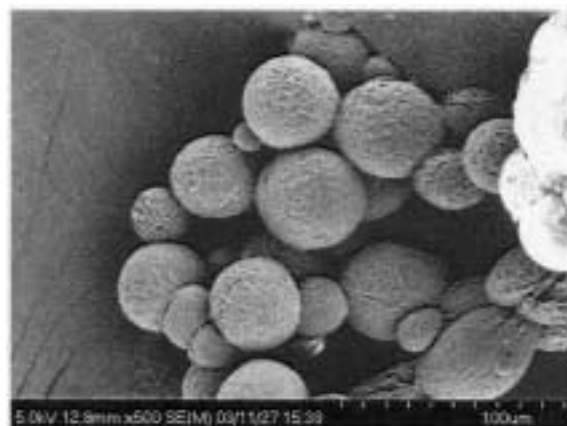


Fig. 8 SEM photograph of microcapsules prepared by interfacial *in situ* polymerization

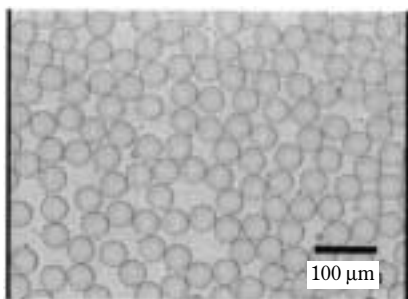
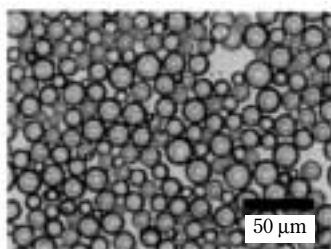
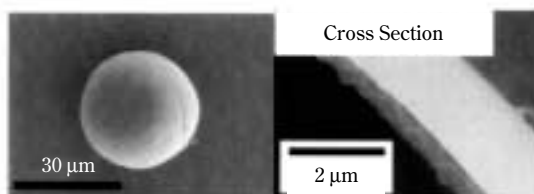


Fig. 9 Monodispersed microcapsules prepared by interfacial polyaddition after emulsification by the ink-jet method



(a) O/W emulsion



(b) Microcapsule

Fig. 10 Photographs of O/W emulsion and microcapsules prepared by phase-inversion emulsification and the subsequent hardening

between isocyanate groups of the acrylic resin and diamine substances. As the figure shows, the prepared microcapsules were found to be monodispersed satisfactorily because emulsification using an ink-jet apparatus provided fairly evenly monodispersed oil droplets. Membrane thickness can be controlled in a range of up to 800 nm.

Fig. 9 is an SEM photograph of microcapsules prepared by interfacial radical polymerization (interfacial *in situ* polymerization). In conventional *in situ* polymerization, the polymerization reaction occurs in liq-

uid droplets with dissolved monomers and initiators. Therefore, tiny microparticles dispersed in liquid droplets can be embedded in a polymer membrane to make a microencapsulated electrophoretic display system. By modifying the procedure with a reactive surfactant, the reaction site for radical polymerization of acrylonitrile was successfully localized at the O/W interface.

Phase-inversion emulsification was adopted to make monodispersed O/W emulsion. A photograph of a typical O/W emulsion is shown in **Fig. 10a**. At present, we can control monodispersion of prepared O/W emulsions by adjusting process parameters, including the polymer concentration, the degree of neutralization, and the rate of water addition. The prepared microcapsules are shown in **Fig. 10b**. Subsequent hardening with epoxy resin was useful to make the microcapsule membrane.

7. Systematization of capsule technology

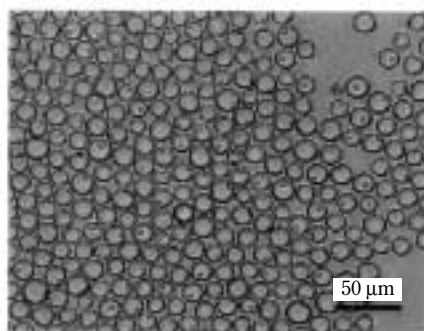
In this project, 6 research groups have joined forces and worked to systematize the knowledge of microencapsulation methods, including phase separation, solvent extraction, coacervation, *in situ* polymerization, and interfacial polymerization.

As an example of the results of these capsule technology systematization efforts, the microencapsulation by phase separation procedure is introduced in some detail below.

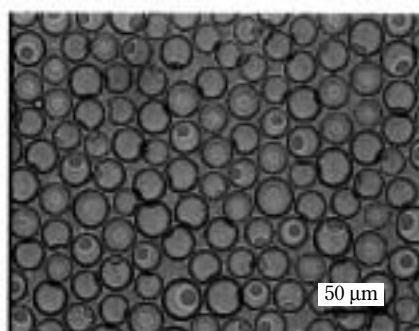
One objective was to establish a technique to control properties of crosslinked polyamino resin microcapsules prepared by the phase separation method. In order to develop a technique to control microcapsule diameter, membrane thickness and membrane morphology, the following investigations were carried out: (1) controlling the diameter of a microcapsule using the Shirasu Porous Glass (SPG) membrane emulsification technique, (2) controlling microcapsule membrane thickness with a mixture of two kinds of water-soluble polymeric surfactants.

(1) Investigation on controlling microcapsule diameter

Monodispersed emulsions having about 10% CV (coefficient of variation) were successfully prepared with the SPG membrane emulsification technique. Diameters of the prepared O/W emulsion were in proportion to the pore diameters of the SPG membrane. The diameters of the emulsion were five times as large as the pore diameters. Preparation of crosslinked poly-melamine microcapsules was attempted by using the monodispersed emulsions. Concentration of sodium



Pore diameter of SPG membrane is 2.6 μm



Pore diameter of SPG membrane is 4.8 μm

Fig. 11 Photographs of crosslinked polymelamine microcapsules prepared with the SPG membrane technique

dodecyl sulfate (SDS), which is a typical emulsifier in SPG membrane emulsification, was found to strongly affect the dispersion stability of the prepared microcapsules. Decreasing the SDS concentration by using the rich top emulsion phase allows monodispersed microcapsules to be prepared. **Figure 11** shows photographs of crosslinked polymelamine microcapsules prepared with the SPG membrane technique. The microcapsule diameter corresponded fairly well with the O/W emulsion diameter. The CV value was also about 10%. Through this investigation, control of microcapsule diameter was achieved in the range of 10–60 μm .

(2) Investigation on controlling microcapsule membrane thickness

Control of membrane thickness of crosslinked polyurea microcapsules was investigated by using several kinds of water-soluble polymeric surfactants, which were added in the continuous phase in microcapsule preparation. The relationship between membrane thickness and poly(E-MA) concentration is shown in **Figure 12**. It was found that the membrane thickness is related to the water-soluble polymeric surfactants used. When poly(E-MA), or poly(methyl vinyl ether-alt-maleic anhydride), was used as a water-soluble polymeric surfactant, membrane thickness of the prepared microcapsules were about 100 nm. When poly (acrylic acid) was used, the membrane thickness was about 400 nm. Control of membrane thickness was achieved by using a mixture solution of poly(E-MA) and poly (acrylic acid). **Fig. 12** shows that the membrane thickness could be controlled between 100–400 nm.

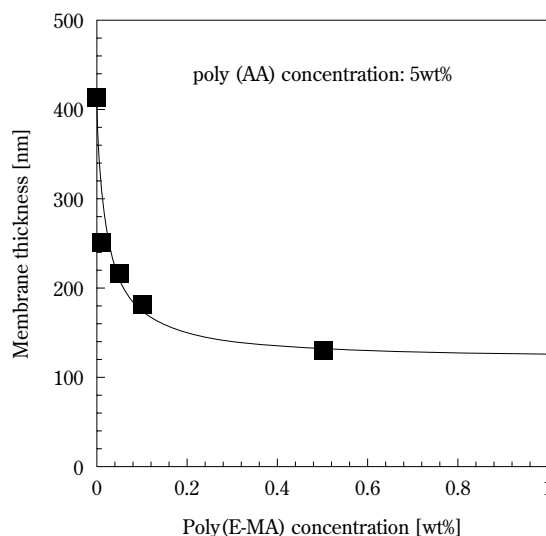


Fig. 12 Relationship between membrane thickness and poly(E-MA) concentration

Future development

This paper has reviewed the recent developments in microencapsulation technology, focusing on the topic of the development of the microencapsulated electrophoretic display system, a microparticle-based paper-like display. Much other research on microencapsulation has been conducted in recent years.

Microcapsules are not raw materials in most cases. Furthermore, microencapsulation is a technique to give raw materials advantageous traits in order to make superior products. This characteristic of the microencapsulation research means that periodically new developments lead to new products worthy of

public notice. The first remarkable product was carbonless copy paper, the second was controlled release of drugs, and at present, paper-like displays are receiving much attention.

In order to make microencapsulation technology more fruitful and to realize the sustainable development of microencapsulation, I believe that fundamental studies and reconsideration of base technologies for various microencapsulation procedures are strongly needed and that cooperation between academic and company researchers should be promoted. Fundamental research should include the elucidation of microcapsule membrane formation mechanisms, quantitative analysis of the effects of process parameters to control microcapsule properties, and the development of new microencapsulation procedures. These investigations would lead to the creation of new products with new functions.

Acknowledgement

In this paper, the author introduced some recent research results of the Nanotechnology Materials Program – Full Color Rewritable Paper Using Functional Capsules Project, which is supported by the New Energy and Industrial Technology Development Organization (NEDO), funded by the Japanese Ministry of Economy, Trade and Industry (METI), and administered by the Japan Chemical Innovation Institute (JCII). I would like to express my great thanks to my collaborators for many helpful discussions.

References

- 1) Green, B.K. and L. Schleicher: US patent, 2800457, CA 1957, 51:15842d (1957).
- 2) Yoshizawa, H., Y. Uemura, Y. Kawano and Y. Hatate: *J. Chem. Eng. Japan*, 26, 198 (1993).
- 3) Yoshizawa, H., Y. Uemura, Y. Kawano and Y. Hatate: *J. Chem. Eng. Japan*, 26, 692 (1993).
- 4) Yoshizawa, H., K. Fujikubo, Y. Uemura, Y. Kawano, K. Kondo and Y. Hatate: *J. Chem. Eng. Japan*, 28, 78 (1995).
- 5) Yoshizawa, H., Y. Uemura, Y. Kawano and Y. Hatate: *Solvent Extr. and Ion Exch.*, 13, 333 (1995).
- 6) Yoshizawa, H., M. Anwar, K. Motomura, Y. Uemura, K. Ijichi, T. Ohtake, Y. Kawano and Y. Hatate: *Solv. Extr. Res. Dev.*, Japan, 2, 185 (1995).
- 7) Shiomori, K., H. Yoshizawa, K. Fujikubo, Y. Kawano, Y. Hatate and Y. Kitamura: *Sep. Sci. Tech.*, 38, 4059 (2003).
- 8) Hatate, Y., K. Kasamatsu, Y. Uemura, K. Ijichi, Y. Kawano and H. Yoshizawa: *J. Chem. Eng. Japan*, 27, 479 (1994).
- 9) Yoshizawa, H., Y. Mizuma, Y. Uemura, Y. Kawano and Y. Hatate: *J. Chem. Eng. Japan*, 28, 46 (1995).
- 10) Tokuda, K., S. Natsugoe, T. Kumanohoso, M. Shimada, H. Yoshizawa, Y. Hatate, K. Nakamura, K. Yamada, S. Nadachi and T. Aikou: *Jpn J Cancer Chemother*, 22, 1641 (1995).
- 11) Goto, M., F. Nakashio, M. Iwama, H. Yoshizawa, K. Ijichi, Y. Uemura and Y. Hatate: *Kagaku Kogaku Ronbunshu*, 22, 923 (1996).
- 12) Yoshizawa, H., Y. Uemura, K. Ijichi, T. Hano, Y. Kawano and Y. Hatate: *J. Chem. Eng. Japan*, 29, 379 (1996).
- 13) Tokuda, K., S. Natsugoe, M. Shimada, T. Kumanohoso, H. Yoshizawa, Y. Hatate, K. Nakamura, K. Yamada, S. Nadachi and T. Aikou: *Jpn J Cancer Chemother*, 23, 1516 (1996).
- 14) Kiyoyama, S., K. Shiomori, Y. Baba, Y. Kawano, H. Yoshizawa and Y. Hatate: *Kagaku Kogaku Ronbunshu*, 23, 259 (1997).
- 15) Ijichi, K., H. Yoshizawa, Y. Uemura, Y. Kawano and Y. Hatate: *J. Chem. Eng. Japan*, 30, 793 (1997).
- 16) Tokuda, K., S. Natsugoe, M. Shimada, T. Kumanohoso, M. Baba, S. Takao, K. Nakamura, K. Yamada, H. Yoshizawa, Y. Hatate and T. Aikou: *International Journal of Cancer*, 76, 709 (1998).
- 17) Natsugoe S., K. Tokuda, M. Shimada, T. Kumanohoso, M. Baba, S. Takao, M. Tabata, K. Nakamura, H. Yoshizawa and T. Aikou: *Anticancer Research*, 19, 5163 (1999).
- 18) Nishino, S., H. Yoshizawa and Y. Kitamura: *J. Chem. Ind. Eng. China*, 53, 202 (2002).
- 19) Yoshizawa, H., S. Nishino, S. Natsugoe, T. Aikou and Y. Kitamura: *J. Chem. Eng. Japan*, 36, 1206 (2003).
- 20) Nishino, S., H. Yoshizawa, Y. Kitamura: *Pham. Tech. Japan*, 19, 2353 (2003).
- 21) Hatate, Y., S. Higo, Y. Uemura, K. Ijichi and H. Yoshizawa: *J. Chem. Eng. Japan*, 27, 581 (1994).
- 22) Hatate, Y., T. Nakaue, T. Imafuku, Y. Uemura, K. Ijichi and H. Yoshizawa: *J. Chem. Eng. Japan*, 27, 576 (1994).
- 23) Ijichi, K., H. Yoshizawa, T. Ashikari, Y. Uemura, Y. Hatate: *Kagaku Kogaku Ronbunshu*, 23, 125 (1997).
- 24) Uemura, Y., N. Hamakawa, H. Yoshizawa, H. Ando, K. Ijichi, Y. Hatate: *Chem. Eng. Comm.*, 177, 1 (2000).
- 25) Comiskey, B., J.D. Albert, H. Yoshizawa and J. Jacobson: *Nature*, 394, 253 (1998).
- 26) Yoshizawa, H. and E. Kamio: "Development and application of the micro/nano fabrication system of capsules and fine particles," M. Koishi ed., 56, CMC Books, Tokyo, Japan (2003).
- 27) Yoshizawa, H: "Current Technologies for Digital Paper," M. Omodani ed., 19, CMC Books, Tokyo, Japan (2003).
- 28) Gutcho, M.M.: "Microcapsules and Microencapsulation Techniques," Noyes Data Co., New Jersey, USA (1976).
- 29) Arshady, R.: "Microspheres, Microcapsules and Liposomes," Citrus Books, London, United Kingdom (1999).
- 30) Makino, K.: *Funtai to Kogyo*, 24, 43 (1992).
- 31) Arshady, R.: *J. Bioactive and Compat. Polym.*, 5, 315 (1990).
- 32) Kondo, T.: *Pharm. Tech. Japan*, 7, 263 (1991).
- 33) Hatate, Y., H. Nagata, H. Nagata and T. Imafuku:

- Kagaku Kogaku, 51, 519 (1987).
- 34) Hatate, Y. and H. Yoshizawa: "The Polymeric Materials Encyclopedia: Synthesis, Properties and Applications," 6, 4341, CRC Press, USA (1996).
 - 35) Yoshizawa, H. and Y. Hatate: Chemical Engineering, 38(5), 405 (1993).
 - 36) Yoshizawa, H. and Y. Hatate: Hyomen (Surface), 33, 552 (1995).
 - 37) Fergason, J.L.: SID Digest 85, 68 (1985).
 - 38) Ota, I., J. Ohnishi and M. Yoshiyama: Proc. IEEE, 61, 832 (1973).
 - 39) Sheridan, N.K., SID 77, 289 (1977).
 - 40) <http://www.eink.com/>
 - 41) <http://ne.nikkeibp.co.jp/members/NEWS/20031114/>
 - 42) <http://www.eink.com/news/release/pr70.html>
 - 43) http://www.sony.jp/products/Consumer/LIBRIE/products/products_01.html
 - 44) http://www.fujixerox.co.jp/research/category/eo/disp_tech/docs/jhc2001fall.pdf
 - 45) http://www.canon.co.jp/technology/future_tech/pl_display/content.html
 - 46) Hattori, R., S. Yamada, Y. Masuda and N. Nihei: SID 03 Digest, 846 (2003).
 - 47) Maeda, S., H. Sawamoto, H. Kato, S. Hayashi, K. Gocho and M. Omodani: Proc. Inter. Display Workshops '02, 1353 (2002).

Author's short biography



Hidekazu Yoshizawa

Dr. Hidekazu Yoshizawa is a professor of the Department of Environmental Chemistry and Materials at Okayama University. He received his BS (1985) and MS (1987) in Chemical Engineering from Osaka Prefecture University and his PhD (1995) from Kyushu University. He worked at Kagoshima University as Assistant Professor and Associate Professor in the field of microparticle science and technology. In 1997 and 1998, he was a postdoctoral associate at the Media Laboratory, Massachusetts Institute of Technology. He has worked at Okayama University from 1999. He now serves as a sub-leader of the Full Color Rewritable Paper Using Functional Capsules Project. His current research interests are synthesis and characterization of polymer colloids, synthesis and application of biodegradable polymers, and microparticulate drug delivery systems.

Particle Size Analysis of Aerosols from Medicinal Inhalers[†]

J.P. Mitchell*

Ph.D., F.R.S.C. (UK), C.Chem.

and M.W. Nagel

HBSc

Abstract

Methods currently in use for the in-vitro measurement of the particle size distribution of aerosols from medical inhalers are reviewed with emphasis on their applicability both for product development and quality control testing and for simulation of likely performance in clinical use. Key attributes and limitations of the various techniques are identified, and consideration is also given both to likely developments to improve the capabilities of these analyzers as well as to the procedures for their use.

Key words: Medical Aerosols, Particle Size Analysis, Inhaler Testing

WHY IS PARTICLE SIZE FROM MEDICAL INHALERS IMPORTANT?

Medical aerosols from pressurized metered-dose inhalers (pMDIs), dry powder inhalers (DPIs) and nebulizers are widely prescribed for treating 'traditional' diseases of the lung, particularly asthma and chronic obstructive pulmonary disease (COPD) [1]. In addition, such devices are of interest for the delivery of medications systemically, using the lung as a gateway [2]. In the case of oral delivery to the lower respiratory tract, it is widely recognized that particle size plays an important part in defining where the aerosol particles will deposit [3]. This is because the lungs together with the airways of the respiratory tract, have evolved to form a particle size-selective sampling system in which progressively finer particles are removed from the inhaled air-stream as they pass via the mouth, larynx and larger airways towards the alveolar spaces. If the model developed by Rudolph *et al.* is taken as an example for a tidally breathing adult [4], particles with aerodynamic diameter (d_{ae})

larger than approximately 6 μm deposit mainly in the oropharyngeal region, central (bronchial) airway deposition peaks with particles having d_{ae} between 4 and 6 μm , and peripheral (alveolar) deposition in the lung reaches a maximum with particles having d_{ae} between 2 to 4 μm (**Figure 1**). Aerodynamic particle size takes into account the influences of both particle density and shape and is related to particle physical size or volume equivalent diameter for a sphere (d_v) through the equation:

$$\sqrt{C_{ae}d_{ae}} = d_v \left[\frac{\rho_p C_p}{\chi \rho_0} \right]^{1/2} \quad (1)$$

where the Cunningham slip correction factors (C_{ae} and C_p) are close to unity when $d_v > 1.0 \mu\text{m}$, and the dynamic shape factor (χ) is unity for spherical particles [5]. Therapeutic aerosols are also delivered by the intra-nasal route both to treat topical disease [6] and target other organs, including the brain, via systemic delivery [7]. However, the particles are, in general, an order of magnitude or more larger than those useful for delivery to the lower respiratory tract [8]. Under these circumstances, there is also an interest in quantifying the size fraction finer than 10 μm aerodynamic diameter [9], since such particles may penetrate beyond the nasal cavity into the passage leading to the oro-pharynx or lower respiratory tract, where they may then deposit, possibly leading to unwanted local and/or systemic effects.

* Corresponding author.

Trudell Medical International, 725 Third Street, London, Ontario, Canada, N5V 5G4;

Tel: 519-455-7060 ext. 2296; Fax: 519-455-9053;

e-mail: jmitchell@trudellmed.com.

[†] Accepted: September 21, 2004

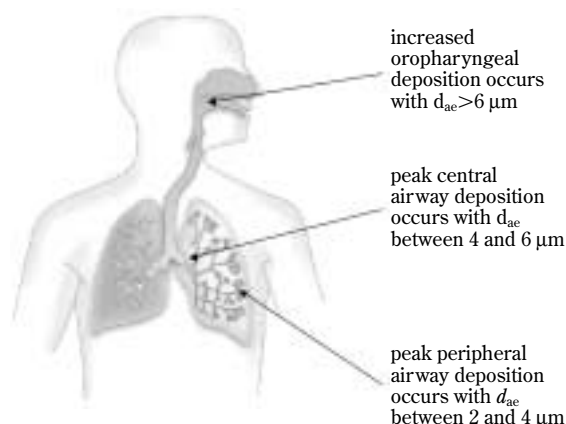


Fig. 1 Deposition of spherical particles of 1 g cm^{-3} density for slow, oral tidal-breathing by an adult patient (adapted from data in ref. 3)

From the above, it is self-evident that reliable techniques that measure the particle size of inhaled aerosols are an essential part of defining both oral [10] and nasal [11] inhaler performance in order to predict respiratory tract deposition as an indicator of clinical efficacy. In connection with oral delivery of medications to the lungs for either local or systemic effects, it is important to distinguish the proportion of the mass from the inhaler that is contained in so-called ‘fine’ particles that penetrate beyond the oropharynx from the total mass emitted by the inhaler. This component is often referred to as the fine particle or ‘respirable’ fraction (FPF) [12, 13]. The precise limits for FPF are debatable, depending upon the eventual destination of the medication, therapeutic action desired and category of patient (pediatric/adult). In the US Pharmacopeia [12], FPF is defined in terms of a size range appropriate to the formulation being tested. In Europe, only the upper limit of $5 \mu\text{m}$ aerodynamic diameter is stated explicitly [13], and the user is free to select a suitable lower limit. In practice, $4.7 \mu\text{m}$ is frequently chosen as the upper size limit for FPF, because this value corresponds with the cut-point size of stage 3 of the widely used Andersen 8-stage cascade impactor (Thermo Andersen, Franklin, MA) operated at 28.3 L/min . However, Newhouse [14] has proposed an upper limit of $2.0 \mu\text{m}$ aerodynamic diameter as being more appropriate for targeting the airways with a bronchodilator based on clinical evidence of efficacy. A similar limit may apply for the delivery of anticholinergics and corticosteroids, but larger particles may be more effective at achieving broncho-constriction in methacholine challenge testing [15]. A lower limit for FPF is rarely specified, but

should be, because a significant proportion of particles finer than about $1.0 \mu\text{m}$ aerodynamic diameter may be exhaled before depositing in the respiratory tract [3].

The fine particle mass (FPM) emitted by the inhaler per actuation is calculated as the product of the total emitted mass and FPF. This quantity should not be confused with so-called ‘fine particle dose’, as the clinically prescribed dose may require more than one actuation of the inhaler.

SCOPE OF THE REVIEW

The focus of this article is primarily on how particle size analysis equipment is used to evaluate the *in vitro* performance of inhalers, rather than on the assessment of the particle size of the constituents of formulations, which is a separate topic in itself. Thus the various methods involving optical or electron microscopy, though of great value in elucidating information about the physical size and microstructure of individual solid particles, are not included. Microscopy by itself does not determine particle aerodynamic size [5], and therefore is of little value as a predictor of the likely behavior of aerosol particles during inhalation. It is also of limited value to measure liquid droplet sizes, as assumptions have to be made about contact angle with the collecting surface and evaporation of volatile species including water can be difficult to control.

Both the choice of particle sizing equipment and how it is configured will depend on the purpose for which the data are required. The review examines two distinctly different approaches to the measurement of particle size of inhaler-produced aerosols that have developed in recent years. The first is the use of compendial methods for product development and quality control, and the second approach is the adoption of procedures that attempt to mimic more closely clinical use of the inhaler. An assessment is also included of the key attributes and limitations of the different types of particle size analysis equipment that are currently available to the user, and a brief summary of the state-of-the-art in terms of particle sizing is provided in conclusion.

TWO APPROACHES TO INHALER PARTICLE SIZE ASSESSMENTS: COMPENDIAL TESTING

The traditional particle size analysis methods for medical inhalers contained in the US (USP) [12] and European (Ph.Eur.) [13] Pharmacopias require that

some form of drug assay be undertaken of the collected size fractions, so that there is a direct link between measured particle aerodynamic size and the mass of active pharmaceutical ingredient (API). This link is especially important when excipients, such as surfactant particles, are present together with API. Non-invasive techniques that are based on light scattering or the time-of-flight principle that cannot distinguish between API and non-volatile, non-pharmaceutically active substances in the formulation (*e.g.* surfactant) will measure an overall particle size distribution that may not be reflective of the actual API-based size distribution [16].

The current compendial techniques listed in both USP and Ph.Eur. are summarized in **Table 1**. They are all based on the principle of inertial impaction that size-fractionates the incoming aerosol weighted in terms of API mass. In addition, this table also includes the Next Generation Pharmaceutical Impactor (NGI, MSP Corp., Shoreview, MN, USA), as this equipment will be adopted as apparatus 5 (DPIs) and 6 (pMDIs) in the USP [17] and also as apparatus E (both DPIs and pMDIs) in the Ph.Eur. [18]. It should

be noted that apparatuses A and B of the Ph.Eur. are the glass Twin Impinger and single-stage metal impactor respectively, both of which are likely to be shortly withdrawn, as although they are useful for rapid quantification of FPF, they provide insufficient size resolution in the critical range from 0.5 to 5.0 μm aerodynamic diameter [19].

In the case of DPI testing, a fixed volume of air is drawn through the inhaler with the valve to the pump downstream of the inertial impactor or impinger operated at critical flow, so that the resistance of the inhaler determines the precise flow rate-time profile once the solenoid valve is actuated to begin the process of sampling from the DPI [12, 13]. The final flow rate is achieved rapidly, and is therefore used to define the size-separating performance of the particle size analysis equipment. This process is closer to actual use by a patient, as it simulates the inhalation process, but there is no attempt to replicate actual inhalation flow rate-time profiles. In contrast, the impactor or impinger is always operated at constant flow rate (*i.e.* 28.3 L/min for the Andersen 8-stage CI) for the testing of pMDIs and nebulizers.

The twin emphases of compendial methods are on robustness and reproducibility. Both characteristics are required in order to optimize both accuracy and precision for the purpose of inhaler product development and quality control of production lots for batch release testing. The methodology is therefore highly standardized to minimize inter- and intra-operator and laboratory differences, and there is little scope for modification. However, minor adaptations to the basic methodology are frequently encountered. For instance, in a recently published standard by the Canadian Standards Association, the use of a low flow rate cascade impactor is specified for the purpose of evaluating spacer and valved holding chamber (HC) add-on devices with pMDIs that are intended for pediatric rather than adult use [20]. Precautions may also be taken to minimize the impact of surface electrostatic charge accumulation by the choice of metal to provide an electrically conductive surface, rather than non-conducting glass collection media in impactors [21], as well as by operating the equipment with climate control so that the ambient relative humidity is not too low. Control of relative humidity may also be important when testing spacers and holding chambers manufactured from non-conducting polymers, where electrostatic charge accumulation is important [22]. Local climate control may also be appropriate when testing DPIs, either where electrostatic charge associated with the powder particles may have a sig-

Table 1 Particle size analysis methods for medical aerosols listed in the current USP[†] and Ph.Eur.[‡]

Apparatus Description	USP	Ph.Eur. ^{note 1}
Andersen 8-stage impactor/ no pre-separator	Apparatus 1 for pMDIs	Apparatus D
Marple-Miller model 160 5-stage impactor	Apparatus 2 for DPIs	–
Andersen 8-stage cascade impactor/pre-separator	Apparatus 3 for DPIs	Apparatus D
Multi-stage liquid impinger (4-stages)	Apparatus 4 for DPIs	Apparatus C
Next Generation Pharmaceutical Impactor (7-stages)	Apparatus 5 for DPIs	Apparatus E
	Apparatus 6 for MDIs	

[†] US Pharmacopeia 28 – National Formulary 23, January, 2003, US Pharmacopeial Convention, Rockville, MD, USA

[‡] 4th Edition of the European Pharmacopeia, January 2002, European Directorate for the Quality of Medicine, Strasbourg, France

Notes:

1. Apparatus A is the glass Twin Impinger and apparatus B is the Metal Impinger that are both anticipated to be withdrawn in a future revision of the Ph.Eur.
2. All apparatuses listed in the table utilize the USP/Ph. Eur. Induction Port (throat).
3. The Next Generation Pharmaceutical Impactor is currently the subject of In-Process Revisions that are to be adopted in future editions of the USP [17] and Ph.Eur. [18].

nificant impact on aerosol behavior [23], or where hygroscopic substances are present [24].

In the case of nebulizer testing, a recently published European standard [25] specifies a fixed flow rate of 15 L/min for the withdrawal of aerosol for the measurement of droplet size distribution by multi-stage impactor, this flow rate being considered representative of a mid-inhalation flow rate during adult tidal breathing (500-ml, at 15 respiration cycles/min) [26]. An impactor with a flow rate ≤ 15 L/min may be used (the Marple Series 298/6 X impactor cited in the standard as an example CI, operates at only 2 L/min) by sampling a portion of the aerosol leaving the nebulizer, as long as the total flow rate exiting the device is maintained at 15 L/min. However, there is a risk that such an approach may not result in a representative size distribution, unless precautions are taken to sample isokinetically [5].

In compendial testing, there is no attempt to simulate the variable flow rate profile associated with the respiratory cycle [12, 13]. Furthermore, the inlet (induction port) to the size analyzing equipment is greatly simplified with respect to human anatomy, comprising in its most basic form, a right-angle tube made to very precise internal dimensions that are consistent between both European and US Pharmacopoeias. It is worth noting, however, that pharmaceu-

tical companies have independently developed several variants on the basic USP/Ph.Eur. design for their particular products [27], reflecting varying viewpoints on how inhaler aerosols should be sampled.

TESTING TO SIMULATE CLINICAL USE

In recent years, there has been a recent interest in developing and adapting *in vitro* particle size measurement techniques to be more predictive of the clinical situation, as an alternative to the use of compendial methods [28-38]. The systems that have been developed are inevitably more complex, as the particle sizing equipment (typically a cascade impactor) has to be operated at constant flow rate, whereas the variable flow rate profile associated with simulating part or all of the respiratory cycle is linked with the inhaler-patient interface. In many instances, tidal breathing is simulated [30-32, 34, 38], although actual patient-generated breathing patterns have also been recorded as a further refinement, and used to operate the breath simulation equipment [33, 35-37].

Pertinent details of some of the more important arrangements that have been developed are summarized in **Table 2**. Other refinements include the adoption of anatomically correct inlet geometries to resemble the human oro-pharyngeal region. These

Table 2 Studies in which particle sizing equipment has been linked with attempts to simulate oral breathing for testing medical aerosol inhalers*

Study	Particle sizing equipment	Description of interface with breathing simulator
Brindley <i>et al.</i> [35] Burnell <i>et al.</i> [36]	Andersen 8-stage impactor at 28.3 L/min	Electronic Lung™ used to test DPIs. Aerosol ‘inhaled’ into a sampling chamber by action of piston-in-tube. Recorded patient inhalation waveforms as well as standard (<i>e.g.</i> sinus) patterns can be used. Impactor samples from the chamber at the end of the inhalation maneuver.
Foss and Keppel [34]	Andersen 8-stage impactor at 28.3 L/min	Used for testing pMDI with HCs. Complete respiratory cycle simulated by piston-in tube pump connected to inhaler via ‘T’-piece. Other limb of ‘T’-piece goes to impactor. Pressurized air source supplies air via ‘T’-piece to enable impactor to operate without perturbing breathing pattern at inhaler.
Finlay [30], Finlay and Zuberbuhler [31, 32]	Andersen 8-stage impactor at 28.3 L/min	Used for testing pMDI with HCs. Piston-in-tube breathing simulator with electronic trigger to operate solenoid valve supplying compressed air at start of inhalation and terminate at start of exhalation, enabling impactor to operate continuously at 28.3 L/min.
Finlay and Gehmlich [33]	Virtual impactor (285 L/min) with MOUDI (MSP Corp.) operated at 30 L/min to size-classify 1 – 10 μ m particles	Used to test DPIs. Breathing simulator as described by Finlay and Zuberbuhler [32] connected to enclosure surrounding DPI. Air pushed through DPI at ‘inhalation’ to allow downstream collection of the aerosol by virtual impactor after passing through model oro-pharynx.
Fink and Dhand [37]	QCM 10-stage impactor (California Measurements, Sierra Madre, CA) at 0.24 L/min	Used for testing pMDIs with HCs. Ventilator-test lung used to derive breathing waveform. 1.5 L plenum located after HC from which sample is extracted to impactor.
Smaldone <i>et al.</i> [38]	Low flow impactor at 1 – 2 L/min	Used for testing nebulizers. Piston-in-tube pump simulates breathing waveform. Impactor samples from side-arm of ‘T’-piece connecting pump to nebulizer.

* This Table provides only basic information about complex arrangements for testing inhalers. The reader should refer to the original publications for complete method details.

models were based originally on cadaver casts, but more recently have been derived from imaging of live patients [39, 40]. The Sophia anatomical infant nose-throat (SAINT) model developed by Janssens *et al.* is an example of a clinically realistic representation that was developed from 3-dimensional computer tomography scans of the upper airways of an obligate nasal breathing 9-month infant [41]. The interior surfaces of such inlets/models can be wetted with a viscous agent such as Brij-35 (polyoxyethylene-23-lauryl ether [41]) or glycerol [42], as a further refinement to simulate mucosal surfaces.

Simulations of delayed or poorly coordinated pMDI actuation in the context of performance testing holding chambers are also attempts to bridge the gap between compendial testing and more closely simulating clinical use [43, 44]. Such studies indicate a developing trend towards improved evaluation of these so-called 'add-on' devices, since correct inhalation and exhalation valve function cannot be properly investigated under constant flow rate conditions [29].

From the foregoing, it is evident that when choosing the most appropriate approach to undertake particle size analysis, careful thought should be given to the purpose for which the data are required as well as considering the appropriateness of the technique for the class of inhaler that is being evaluated.

PARTICLE SIZE ANALYSIS TECHNIQUES WHICH METHOD TO CHOOSE

Table 3 contains a summary of the particle size analysis techniques that are currently in widespread use for the evaluation of medical inhalers, showing the operating principle, size range and inhaler types for which they are most applicable. Most particle sizing methods used for inhaler aerosol assessments are invasive, in that they require either a sample or the entire aerosol produced on actuation to be collected by the measurement equipment. Techniques that are based on either inertial impaction or time-of-flight (TOF) both determine aerodynamic diameter. However only multi-stage CIs or liquid impingers directly provides the mass-weighted data that are more relevant than the corresponding count/number-weighted size distribution results in predicting the mass of API likely to be delivered to different parts of the respiratory tract [10].

Ideally, the measurement technique should not perturb the inhaler aerosol being evaluated, since the process of moving the aerosol to the measurement instrument may alter the size distribution by enhancing processes that cause particles to deposit prematurely [45], or may result in droplet size reduction as a result of evaporation of volatile species, if care is not taken to minimize such behavior [46]. So-called non-invasive methods, which are all based on some form of particle-light interaction process, have not yet been

Table 3 Summary of particle sizing methods used to characterize medical aerosols from inhalers

Technique	Operating principle	Size Range (μm)	Assay for API	Direct Measure of Aerodynamic Diameter
Cascade impactor (CI) multi-stage liquid impinger (MSLI)	Inertial size separation in laminar flow	0.1 – 15 μm overall range, but varies from one instrument to another. CIs typically have 7 – 8 stages. The current MSLI has 4 stages + back-up filter.	YES	YES
Single stage impactors/ Twin Impinger (TI)	Inertial size separation in laminar flow	Cut size chosen to separate coarse from fine particles likely to penetrate the lower respiratory tract (<i>e.g.</i> 6.4 μm for TI at 60 L/min).	YES	YES
Particle time-of-flight (TOF)	Particle acceleration in ultra-Stokesian flow; transit time between two detectors	Aerosizer [®] (no longer available): 0.2 – 200 μm , extendable to 700 μm with larger nozzle. TSI 3603 PSD analyzer is successor: 0.2 – 700 μm TSI 3321 APS [®] with 3306 impactor inlet: 0.5 – 20 μm .	NO	YES
Laser diffractometry (LD)	Low angle laser light scattering	0.5 μm – 3 mm overall range, but varies from one instrument to another.	NO	NO
Phase-Doppler particle size analysis (PDA)	Phase shift observed by several detectors observing particle interaction with interference fringes formed from intersecting laser beams	0.3 – several hundred μm . Precise range depends upon the optical configuration chosen. Particle velocity can also be measured in 1-, 2- or 3-components of direction, depending on sophistication of measurement system.	NO	NO

refined to the point at which simultaneous chemical assay of the measured particles takes place to link the size measurement with mass of API delivered from an inhaler. However, a new generation of non-invasive instruments, such as the Ultra-Violet Aerodynamic Particle Sizer® aerosol spectrometer (TSI Inc., Shoreview, MN, USA) offer the potential for combining particle sizing with an assay procedure, in this instance by fluorescence intensity. The application of this instrument thus far has been to detect biologically active from inanimate particles in air quality monitoring, rather than distinguish API from non-therapeutically active particles in studies of inhaler-based drug delivery.

Non-invasive methods can be further sub-divided into TOF techniques that determine aerodynamic particle size directly by particle acceleration in a well-defined flow regime, and systems that are based on particle-light interaction. TOF-analysis is particularly useful for the assessment of powders in pre-formulation studies [47], as various methods for dry dispersion of powders into aerosol form are available. Light interaction methods can be further sub-divided into low angle (laser diffraction (LD)) and phase Doppler systems. LD systems measure orientation-averaged size that corresponds closely with volume equivalent diameter, at least for micronized, near spherical powder particles [48]. They are convenient to use, as they typically require few user defined parameters and enable size distribution measurements to be made in <1 min, compared with >1 h by cascade impactor. LD is especially applicable for sizing aqueous droplets produced either by nebulizers [49, 50] or nasal spray pumps [11], since the technique has a very wide dynamic range. Clark has shown that LD provides droplet volume median droplet diameter (VMD) as a measure of central tendency of the size distribution that is equivalent to mass median aerodynamic diameter (MMAD) for non-volatile dibutyl phthalate droplets produced by a jet nebulizer [51]. It is reasonable to expect this relationship to hold true for aqueous droplets, provided that care is taken to control evaporation [10]. Although the link between LD-measured size distribution and VMD may be appropriate for a homogeneous solution formulation, direct comparison between LD- and other techniques such as inertial impaction is unlikely to apply with suspension formulations. This is because LD quantifies droplet size distribution without reference to the mass content of API contained within the various sizes of droplets, in contrast to inertial methods where API mass is directly determined [10].

INERTIAL IMPACTORS, INCLUDING THE MULTI-STAGE LIQUID IMPINGER (MSLI)

Inertial size-separation by CI has been used as the 'gold standard' to size-analyze inhaler-derived aerosols for many years [12, 13] and is probably the widest used method today. The application of this class of particle size analyzer to the assessment of medical aerosols has recently been extensively reviewed, focusing on the types of impactor that are in current use together with their strengths and limitations for measurements with the different classes of inhalers [52].

The theory of impactors has been well developed by Marple and colleagues over several years, based on a 2-dimensional solution of the Navier-Stokes equations defining the gas flow field in the absence of particles, and then using Newton's equation of motion to model the passage of different sized particles through various stage geometries [53-55]. In its simplest form, a single stage impactor comprises a jet or nozzle plate containing one or more circular or slot-shaped orifices of diameter (W) located a fixed distance (S) from a flat collection surface that is usually horizontal (**Figure 2**). The stage functions by classifying incoming particles of various sizes on the basis of their differing inertia, the magnitude of which reflects the resistance to a change in direction of the laminar flow streamlines [53, 54]. As the incoming flow passes through the nozzle plate, the streamlines diverge on approach to the collection surface, whereas the finite inertia of the particles causes them to cross the streamlines. The dimensionless Stokes number (St), which is the ratio of the stopping distance of a particle to a characteristic dimension, in this case W (or aver-

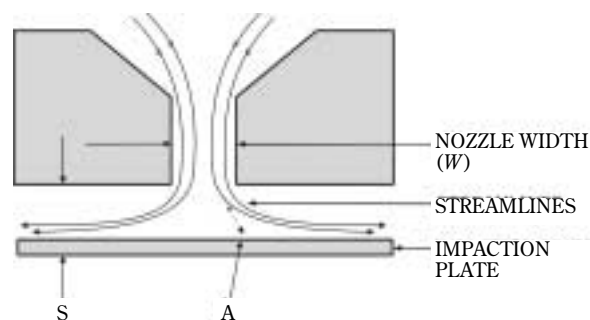


Fig. 2 Schematic of a single stage impactor, showing divergent streamlines in flow approaching collection surface, with particle trajectory meeting surface at point A

age diameter, \bar{W} , for a multi-orifice stage) describes the process, defining a critical particle size that will reach the collection surface for a particular stage geometry. For a single nozzle (jet) impactor, St is related to W through the expression:

$$St = \frac{\rho_{ae} C_{ae} d_{ae}^2 U}{9\mu W} \quad (2)$$

in which ρ_{ae} is particle density, C_{ae} is the Cunningham slip correction factor, U is the air velocity at the nozzle exit of impaction stage and μ is gas (air) viscosity [54].

The particle collection efficiency (E) of an ideal impactor stage, expressed as a percentage, will increase in a step-wise manner between limits of zero to 100% at a critical value of St . In practice, for a well-designed stage, E is a monotonic sigmoidal function of St or d_{ae} that increases steeply from $E \sim 0\%$ to $>95\%$, typically reaching its maximum steepness when E is 50% (**Figure 3**), corresponding to the stage effective cut-off diameter, also termed its d_{50} value, and:

$$\sqrt{C_{50}} d_{50} = \left[\frac{9\eta W}{\rho_{ae} C_{ae} U} \right]^{1/2} \sqrt{St_{50}} \quad (3)$$

or in terms of volumetric flow rate (Q):

$$\sqrt{C_{50}} d_{50} = \left[\frac{9\pi\mu n W^3}{4\rho_{ae} C_{ae} Q} \right]^{1/2} \sqrt{St_{50}} \quad (4)$$

for a multi-orifice stage comprising n circular nozzles. It is possible to take into account the shape of the

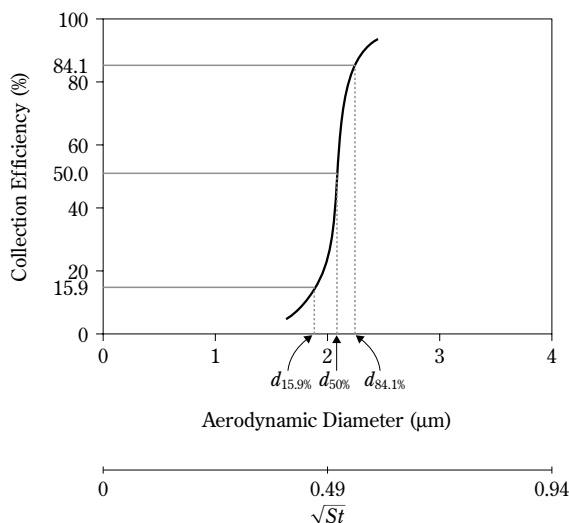


Fig. 3 Idealized collection efficiency curve for a single round-nozzle impactor stage

actual collection efficiency curve of the stage in the analysis of impactor data [56], but this refinement is rarely done for measurements of inhaler performance. Instead, the assumption is made that the mass of particles larger than d_{50} that penetrate the stage, is exactly compensated by the mass associated with particles finer than this size, that are collected [57]. Thus the d_{50} value is a constant for a given stage at a fixed flow rate. Marple and Liu [54] and more recently Rader and Marple [55], with an improved theory taking into account the effect of ultra-Stokesian drag, have identified that \sqrt{St} at E_{50} ($\sqrt{St_{50}}$) should be close to 0.49 for well-designed round-nozzle impactors (**Fig. 3**), where differences in particle inertia dominate the size separation process. $\sqrt{St_{50}}$ remains close to this value when the flow Reynolds number (Re), given by:

$$Re = \frac{\rho W V_0}{\mu} = \frac{4\rho Q}{n\pi\mu W} \quad (6)$$

is within the range from 500 to 3000 [54]. ρ is the gas (air) density.

The sharpness of cut of a given stage is defined in terms of the geometric standard deviation (GSD) of the collection efficiency curve, derived from the expression:

$$GSD_{stage} = \sqrt{\frac{d_{84.1}}{d_{15.9}}} \quad (7)$$

where $d_{84.1}$ and $d_{15.9}$ are the sizes corresponding to the 84.1 and 15.9 percentiles of the curve by analogy with the log-normal distribution function expressed in cumulative form, to which the shape of the collection efficiency curve approximates (**Fig. 3**). GSD for a well functioning stage should ideally be <1.2 (the GSD for an ideal size fractionator would be 1.0) [58]. However, in practice, values in many designs of commercial impactor can exceed this limit, especially with stages that classify particles larger than $5\ \mu\text{m}$ aerodynamic diameter, where gravitational sedimentation significantly contributes to the size-separation process [59]. The influence of gravity becomes especially evident at low flow rates with impactors such as the NGI that are designed to operate over a range of flow rates [60].

For multi-orifice impaction stages, Fang *et al.* [61] also identified the importance of the cross-flow parameter (X_c), as a parameter that affects stage GSD . X_c is defined as:

$$X_c = \frac{nW}{4D_c} \quad (8)$$

where D_c is the diameter of a cluster of nozzles on the

stage. If the value of this dimensionless parameter is greater than 1.2, the potential exists for spent air leaving the orifices closer to the centre of the nozzle plate to interfere with the flow exiting the outer orifices, thereby preventing their flow from reaching the collection surface.

A CI is assembled from several stages with progressively decreasing cut sizes (**Figure 4**), so that an incoming aerosol is size separated into the same number of fractions as there are stages. For inhaler testing, it is desirable to have at least 5 stages with d_{50} values located within the critical range from 0.5 to 5 μm aerodynamic diameter [62]. There is a link between the cut sizes of individual impactor stages and the likely deposition sites in the respiratory tract of the particles that are size-separated, but it is important to appreciate that diagrams, such as **Figure 5**, which relates to the Andersen 8-stage impactor, are only a guide, since the constant flow rate through a CI does not simulate the continuously varying flow rate associated with the respiratory cycle.

Technical details for the most widely used CIs for inhaler aerosol testing are summarized in **Table 4**. Stage d_{50} values for the Andersen 8-stage impactor, standard Marple-Miller impactor (MMI, MSP Corp., Shoreview, MN, USA) and the Multi-Stage Liquid Impinger (MSLI) (Copley Scientific Ltd., Nottingham, UK) have been taken from Marple *et al.* [63]. Size ranges appropriate to these and other CIs occasionally used for inhaler testing that are based on published cali-

bration data, are summarized in **Tables 5-9**. Cascade impactors are typically calibrated on a stage-by-stage basis using monodisperse aerosol particles [64-74] that are ideally electrostatically charge equilibrated

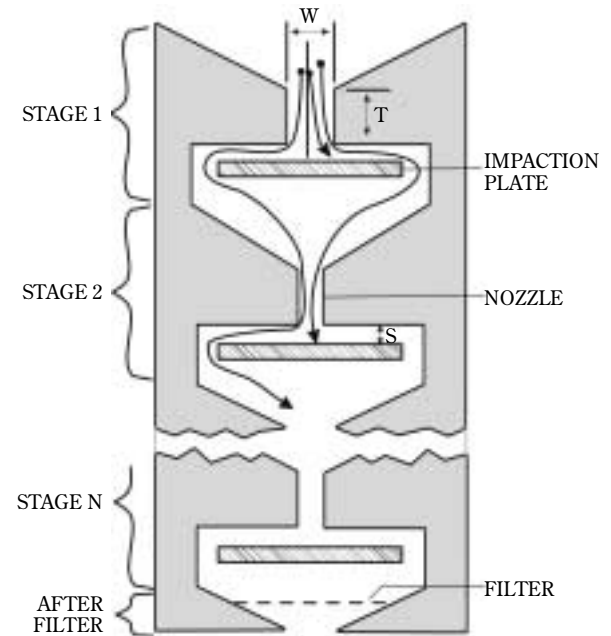


Fig. 4 Schematic of a multi-stage impactor, showing the separation of progressively finer particles as the aerosol passes through successive stages to the after filter

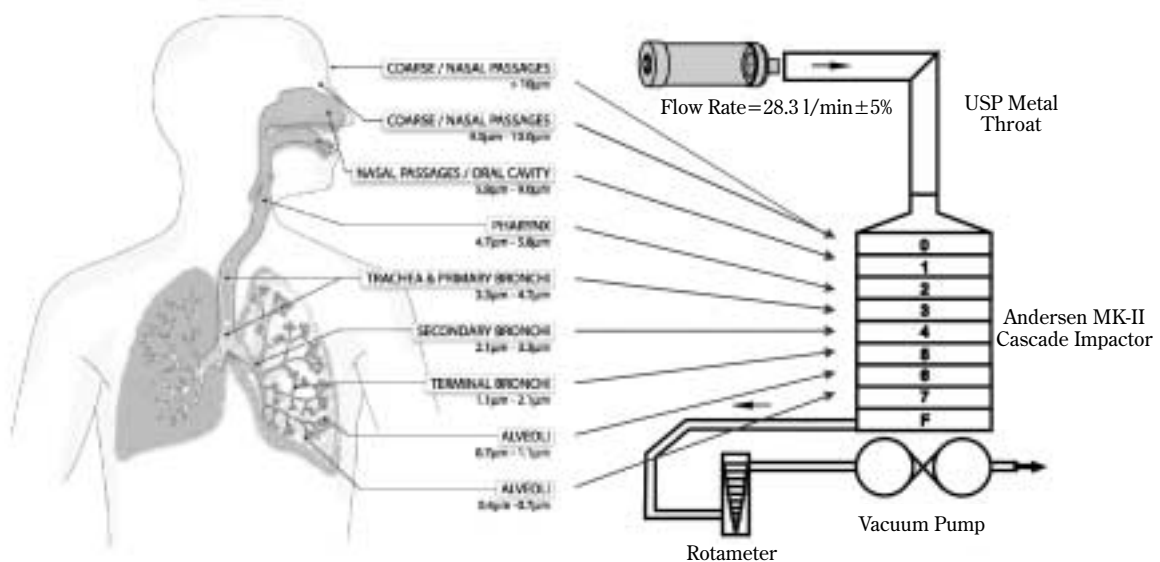


Fig. 5 Relationship between Andersen 8-stage CI cut sizes at 28.3 L/min and likely particle deposition in the respiratory tract

Table 4 Characteristics of cascade impactors used to size-analyze medical aerosols from inhalers

Impactor/ Impinger	Flow Rate (L/min)	Stages and Size Range	Reynolds number range	Calibration	Comments
Andersen 8-stage (ACI)	28.3	8 circular plates + after filter	110 – 782	Vaughan [65] Mitchell <i>et al.</i> [66]	ACI can be used at higher flow rates for DPI testing by modifying stages [54-55] – see Table 5.
Marple-Miller impactors (MMI)	Model 160 – 60	5 collection cups + after filter	1240 – 3160	Marple <i>et al.</i> [69]	Low flow version (model 150P) designed to operate at two discrete flow rates by interchange of single-jet nozzle to first stage.
	Model 150 – 30		1240 – 3160		
	Model 150P – 4.9 and 12.0		386 – 918 (4.9 L/min)	Olson <i>et al.</i> [70]	
			945 – 1951 (12.0 L/min)		
Next Generation Pharmaceutical Impactor (NGI)	15 – 100	7 collection cups + micro-orifice collector (MOC)	166 – 1482 (15 L/min – stages 1-7: MOC not recommended at this flow rate) 149 – 2938 (30 L/min) 298 – 5876 (60 L/min) 496 – 9793 (100 L/min)	Marple <i>et al.</i> [58] – 30 to 100 L/min Marple <i>et al.</i> [60] – 15 L/min	Horizontal inter-stage geometry with hinged lid access to aid auto- mation. MOC avoids use of after filter but an internal or external filter can be used for formulations with a significant portion of extra- fine particles that would otherwise penetrate the MOC.
Multi-Stage Liquid Impinger (MSLI)	60	4 impingement stages + after filter	3300 – 10310	Asking and Olsson [71]	Can be used at flow rates between 30 and 100 L/min.
Quartz crystal impactor (QCM)	0.24	10 flat collection sensors		Fairchild and Wheat [72] Horton <i>et al.</i> [73]	Other versions that operate at higher flow rates are available.
Micro Orifice Uniform Deposit Impactor (MOUDI)	30	8 plates (model 100) 0.8 – 10 µm 10 plates (model 110) 0.056 – 10 µm	350 – 1680	Marple <i>et al.</i> [74]	A version is available where continuous deposits are collected as a function of sampling time by rotating the nozzle plates relative to the collection surfaces.

Table 5 Stage d_{50} values (µm) for the various configurations of the Andersen 8-stage cascade impactor at different flow rates

Stage	Flow Rate (L/min)		
	28.3	60	90
–2	not used	not used	8.0
–1	not used	8.6	6.5
0	9.0	6.5	5.2
1	5.8	4.4	3.5
2	4.7	3.2	2.6
3	3.3	1.9	1.7
4	2.1	1.2	1.0
5	1.1	0.55	0.22†
6	0.7	0.26	not used
7	0.4	not used	not used

† Cut size reported by Thermo Andersen for this stage is 0.43 µm
Data at 28.3 L/min are nominal values supplied by the manufacturer,
data at 60 and 90 L/min are from [67] and [68].

[73]. The process is both labor intensive and time consuming, so that measurement of stage nozzle diameters (so-called stage mensuration) is currently

Table 6 Stage d_{50} values (µm) for various models of the Marple-Miller impactor

Stage	MMI model and flow rate (L/min)				
	150P 4.9	150P 12.0	150 30	160 60	160 90
1	10.0	10.0	10.0	10.0	8.1
2	7.2	4.7	5.0	5.0	4.0
3	4.7	3.1	2.5	2.5	2.0
4	3.1	2.0	1.25	1.25	1.0
5	0.77	0.44	0.63	0.63	0.5

Data for 4.9 and 12 L/min are from reference 57, and data at 30 and 60 L/min are from [64]. Data at 90 L/min are calculated assuming ideal inertial size separation.

regarded as an acceptable substitute to verify that impactor performance is maintained with use [12].

Although testing of pMDIs and nebulizers is conveniently undertaken at a fixed flow rates where calibration data are available, almost all DPIs require an inhalation maneuver to be simulated for the bulk powder to be dispersed and ejected from the inhaler. In

Table 7 Stage d_{50} values for the multi-stage liquid impinger at 60 L/min

Stage	Cut Size (μm)
1	13.0
2	6.8
3	3.1
4	1.7

Data from [71].

Table 8 Stage d_{50} values for the QCM impactor at 0.24 L/min

Stage	Cut Size (μm) from [72]	Cut Size (μm) from [73]
1	17.0	15.7
2	13.0	9.0
3	7.7	6.3
4	3.9	3.1
5	1.80	1.87
6	1.20	1.09
7	0.64	0.49
8	0.34	0.32
9	0.26	0.19
10	0.14 [†]	0.07

[†] Higher than expected cut size for stage 10 may have been influenced by calibration particle density being $>1 \text{ g}\cdot\text{cm}^{-3}$

Table 9 Stage d_{50} values for the Model 110[†] MOUDI at 30 L/min

Stage [‡]	Cut Size (μm) from [74]
1	9.9
2	6.2
3	3.1
4	1.8
5	1.00
6	0.56
7	0.32
8	0.18
9	0.097
10	0.057

[‡] The d_{50} value of the inlet is quoted as 18 μm , but this is not normally used as an impaction stage

[†] Model 100 MOUDI comprises stages 1 to 8

practice, the DPI is first attached to the induction port of the CI, flow rate adjusted until the pressure drop across the inhaler (measured at the induction port entry) is 4 kPa, chosen as being broadly representa-

tive of pressure drops produced by patients using DPIs [75]. Before simulating the inhalation maneuver, the volumetric flow rate is checked with the DPI replaced by a flowmeter that is capable of providing the volumetric flow rate either directly or through an appropriate Boyles' Law pressure correction [76]. This flow rate is often intermediate to one of the values for which cut off sizes have been obtained by calibration. For the ideal inertial separator, it can be shown by application of equations 3 or 4, that the stage cut-point size ($D_{50,1}$) at flow rate (Q_1) is related to the cut-point size ($D_{50,ref}$) at a reference flow rate (Q_{ref}) where calibration data are available, in accordance with:

$$D_{50,1} = D_{50,ref} \left[\frac{Q_{ref}}{Q_1} \right]^{1/2} \quad (9)$$

This relationship is the basis of the calculation provided in the current compendial methods, where $D_{50,ref}$ is fixed at 60 L/min [12, 13]. However, it is only strictly valid when inertial forces dominate the particle separation process so that \sqrt{St} is constant. This situation is not the case when gravity has a significant effect on the size-separation process, as occurs with components of CIs in which particles with $d_{ae} > 10 \mu\text{m}$ are being size-separated [77]. Under these circumstances, it may be more appropriate to fit calibration data, if acquired at several flow rates within the range of operation of the CI, by a power law expression of the form:

$$D_{50,1} = A \left[\frac{Q_{ref}}{Q_1} \right]^b \quad (10)$$

where Q_{ref} is a chosen reference condition (generally 60 L/min for DPI testing), and the parameters 'A' and 'b' are chosen to fit the calibration data. This more general approach was therefore adopted to predict stage cut-point sizes for the NGI between 30 and 100 L/min [17, 18, 58] (**Table 10**). Although not based on a model of the underlying physics of impactor operation, the approximation is practical to implement, and can also be applied to correct for other non-ideal behavior, such as the effect of the slip correction term describing particle motion, that can be significant with stages which separate particles finer than 0.5 μm .

Particle size measurements by cascade impactor can be affected by a number of factors that can introduce bias. Recently a working group of the US Product Quality Research Institute (PQRI), which is a collaborative process involving representatives from the pharmaceutical industry, academia and the FDA, developed a guide to aid those testing inhalers by the

Table 10 Values of constants 'A' and 'b' (Equation 10) for the NGI

Component	A	b
Pre-separator [†]	see footnote	see footnote
Stage 1	8.06	0.54
Stage 2	4.46	0.52
Stage 3	2.82	0.50
Stage 4	1.66	0.47
Stage 5	0.94	0.53
Stage 6	0.55	0.60
Stage 7	0.34	0.67

[†] Equation 10 was replaced by $D_{50,1} = 12.8 - 0.07(Q - 60)$ in order to account for the significant effect of gravity on its operation From [60]: used by permission, Mary Ann Liebert Inc.

cascade impaction method [21]. The underlying purpose of this document was to identify impactor-related contributions to the overall uncertainty of the mass balance of API that is used to validate the particle size measurement. However, the investigation tree con-

tained in this summary of 'good CI practice' (**Figure 6**), that identifies a way to trace the cause of a failed mass balance measurement, is also a useful guide when examining anomalous particle size data. The order of investigation has recently been validated by the outcome from a survey of impactor users within the pharmaceutical industry [78].

It is important to note that many of the issues listed in **Table 11** which has been derived from the PQRI publication, including the elimination of leakage pathways and correct alignment of components, can be eliminated in routine testing by careful adherence to protocols. Particular attention needs to be paid to the control of flow rate, as this parameter has a major influence on performance (equations 9 and 10) [76]. The choice of a suitable viscous surface coating to avoid particle bounce in a CI [79-82] is of critical importance when testing DPIs [83, 84], with the exception of the MSLI, where the liquid contained in each impaction stage fulfils this purpose. The decision whether or not to coat, and with whatever substrate, is normally made during the development of the method for a particular inhaler/drug product

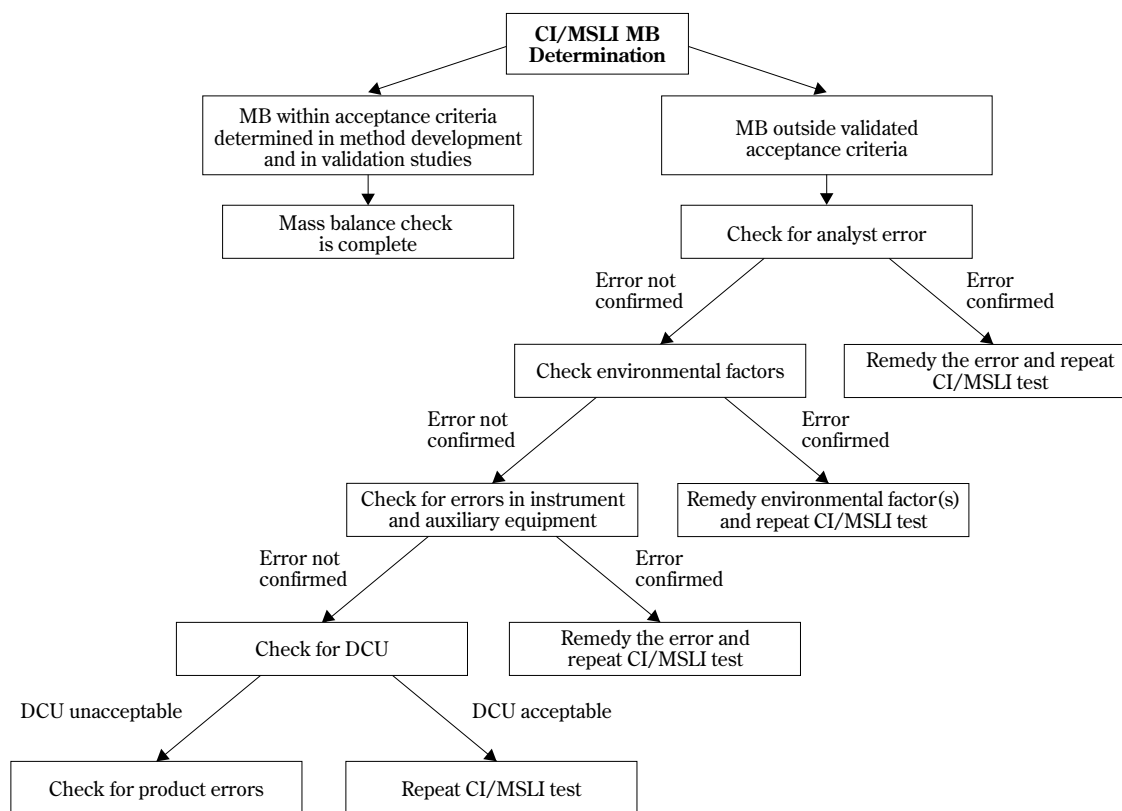


Fig. 6 Failure investigation tree for inhaler testing by cascade impactor (from [21]: used by permission, Mary Ann Liebert Inc.)

Table 11 Potential causes of bias in impactor-based particle size measurements – Impactor-related issues[†]

Factor	Potential Influence on Particle Size Distribution Accuracy
Correct location of collection surfaces	Large
Proper accounting for collection surfaces (and back-up filter)	Large
Assertion of stage order	Large
Air leakage into impactor	Small, unless leak is massive
Poor seal and orientation between induction port/impactor or between induction port/pre-separator/impactor	Small, unless leak is massive or components grossly out of alignment
Inadequate liquid volume or liquid missing from collection surfaces (MSLI)	More data needed to quantify risk of bias
Flow rate	Large
Timer operation of solenoid valve (DPI-testing)	Large
Cleanliness of stage nozzles	More data needed to quantify risk of bias
Worn/corroded stage nozzles	More data needed to quantify risk of bias
Electrostatic effects	Large, when non-metallic components are used
Use of collection surface coating	Large
Environmental factors (barometric pressure, relative humidity)	Potentially large, depending more on formulation (e.g. hygroscopic particles) than impactor

[†] adapted from [21]: used by permission, Mary Ann Liebert Inc.

[21]. A wide variety of such methods exist, and the European Pharmaceutical Aerosol Group (EPAG) has therefore recently published a summary of current procedures that are in use by member organizations [85]. Although pMDIs have customarily been tested using uncoated collection surfaces, recent data with the MMI [86], Andersen 8-stage CI [87] and NGI [88, 89] indicate that a surface coating may also be necessary when evaluating this class of inhaler with these impactors, especially if the formulation contains no surfactant and only 1 or 2 actuations of the inhaler are performed per measurement to simulate delivery of the clinically prescribed dose. Nevertheless, the outcome from a recent extensive multi-organization inter-comparison between the Andersen 8-stage CI and NGI testing a wide variety of both pMDI- and DPI-delivered formulations in which most measurements were undertaken with more than 2-actuations into the impactor, indicated that size distributions obtained by either impactor are substantially equivalent [90].

TIME-OF-FLIGHT AERODYNAMIC PARTICLE SIZE ANALYZERS

TOF particle size analyzers provide an attractive alternative method to cascade impactors or impingers for the determination of aerodynamic particle size dis-

tributions of inhaler-generated aerosols, as they operate in near real-time and are therefore rapid to use. They also have greater size resolution capability (>10 size channels per decade). These instruments each function on the principle of accelerating aerosol-based particles to the point at which their velocity temporarily lags behind that of the surrounding air molecules (ultra-Stokesian flow). During this period, the time it takes for individual particles to transit between two light beams is accurately measured, since this TOF is a unique function of aerodynamic size [91]. Two types of TOF analyzer have been widely applied to the measurement of medical aerosols.

1. The Aerosizer[®] family of TOF analyzers (Aerosizer[®] Mach 2 and Aerosizer[®] LD) were developed in the late 1980s and 1990s by Amherst Process Instruments Inc. Amherst Process Instruments Inc. was acquired by TSI Inc., Shoreview, MN, USA in 1998, who shortly thereafter replaced the previous systems with the DSP particle sizer. The PSD 3603 TOF analyzer superseded this instrument in 2003.
2. The Aerodynamic Particle Sizer (APS[®]) aerosol spectrometer developed by TSI Inc. in 1982 as the APS3300, followed by the APS3310 in 1987. These early instruments were superseded in 1997, initially by the model 3320 and in 2001 by

the currently available model 3321.

Both types of TOF analyzer operate effectively in the range of greatest interest for inhaler testing (0.5 to 20 μm aerodynamic diameter). Detailed descriptions of the operating principles of each technique together with their applications and limitations for the assessment of all types of inhaler-generated aerosols, have been reviewed in two previous publications [47, 92], so this summary focuses on the more important aspects that should be considered.

The underlying principle of the APS[®] family of instruments is based on the work of Wilson and Liu [93], that was further developed by Remiarz *et al.* [94]. The flow through the tapered nozzle does not reach sonic velocity, but the particles are accelerated in ultra-Stokesian flow. The 3300 and 3310 instruments comprised a sensor unit, which contains the sampling system, detector, preliminary data processor and flow sensing equipment (**Figure 7**). Although they offer a high degree of size resolution compared with CI/MSLI-based measurements, both instruments are susceptible to coincidence-related bias, when more than one particle is detected simultaneously. In addition, bias is caused by so-called 'phantom' particle detection because the laser beams defining the measurement zone were separated, so that individual particle transits are not detected [95, 96]. The 3320 and 3321 instruments therefore incorporate two overlap-

ping laser beams that define the measurement zone, combined with improved particle detection electronics. The time-of-transit of individual particles can therefore be followed by detecting a distinct double-crested signal as the particle traverses the illuminated pathway between both beams (**Figure 8**) [97]. Relative light scattering intensity can also be measured and correlated with the TOF-based aerodynamic size for each particle. Despite these improvements, accuracy in calculating mass-weighted size distributions most appropriate for medical inhaler assessments using the model 3320 was still limited by a very low-level background of false, large particle counts that were present even after the effects of particle coincidence and phantom particles had been eliminated [98, 99]. The cause was traced to small particles that re-circulated in the vicinity of the measurement zone, thereby re-entering at a much slower velocity and therefore being assigned a correspondingly larger size. This recirculation was eliminated in the model 3321 and minor improvements were also made to the detection electronics to optimize the time spent processing each particle transit event. Both models 3320 and 3321 can be equipped with a single stage impactor inlet ((SSI) model 3306) having a cut size of 4.7 μm aerodynamic diameter, for work with medical aerosols. A version is also available with a cut size of 2.5 μm aerodynamic diameter for measuring the fine

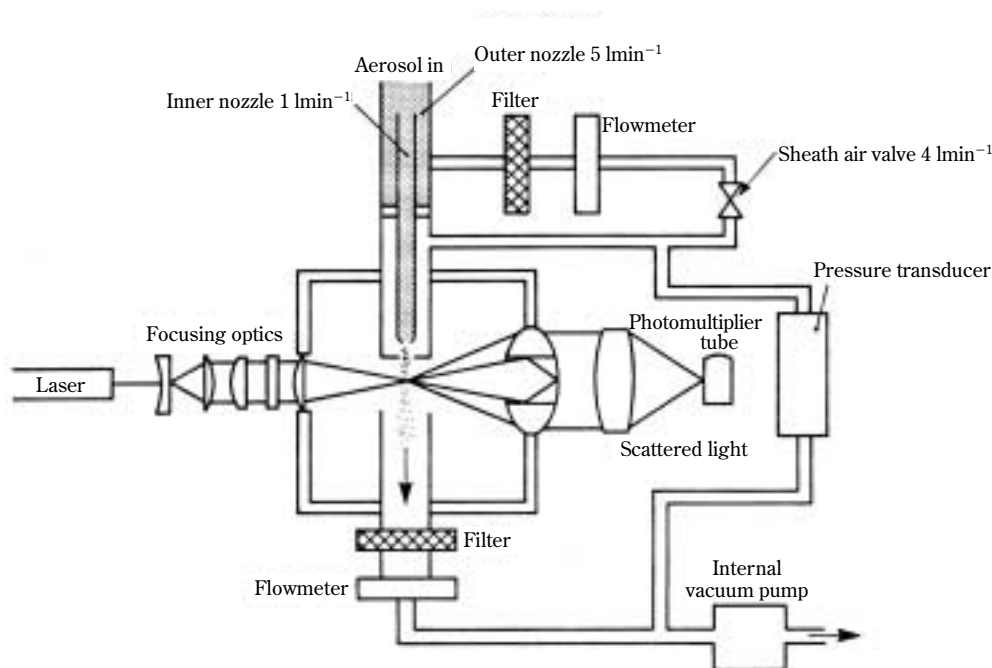


Fig. 7 Aerosol flow path and TOF detection system for the models 3300 and 3310 APS[®] aerodynamic particle sizer spectrometer (courtesy TSI Inc.)

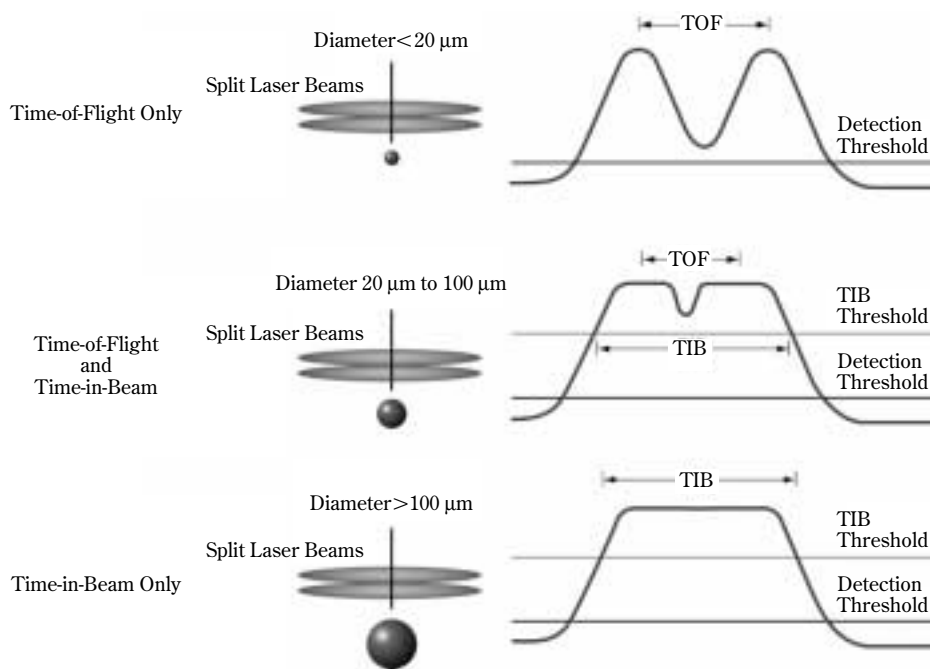


Fig. 8 'Double-crest' particle detection system utilized by models 3320 and 3321 of the APS[®] aerodynamic particle sizer spectrometer (courtesy TSI Inc.)

particle content of environmental aerosols, but which might also be useful for assessing extra-fine particle content of inhaler-generated aerosols. The entry to the SSI is a USP/EP induction port (**Figure 9**).

The Aerosizer[®] family of TOF analyzers operates by accelerating particles in a sonic expansion flow and measuring their time to transit a fixed distance defined by two parallel, but separated light beams located in the path of the flow close to the nozzle (**Figure 10**). Dahneke *et al.* [100] first described this operating principle, later amplified by Dahneke and Padiya [101], Dahneke and Cheng [102] and Cheng and Dahneke [103]. A cross-correlation technique is used to link measured TOFs between the two detectors to individual particle transits through the measurement zone, so that a meaningful size distribution can be constructed. However, the technique is complex and susceptible to non-ideal effects, particularly at high concentrations when several particles may be present simultaneously in the measurement zone [91]. The measurement range of the Aerosizer[®] is nominally from 0.2 to 200 μm aerodynamic diameter, making use of the standard 750 μm diameter tapered nozzle [91]. However, for research with DPIs in which the API is attached to larger lactose carrier particles, the measurement range can be shifted from approxi-

mately 0.2 to 700 μm aerodynamic diameter by the use of a larger (1500 μm diameter) nozzle. Various attachments were available to disperse bulk powder into aerosol form (Pulse-Jet Disperser[™], AeroDisperser[™]), sample fully expanded pMDI-generated aerosols from a large volume (AeroSampler[®]), simulate the inhalation portion of a breathing cycle (AeroBreather[®]) and dilute the incoming aerosol (AeroDiluter[®]) [47].

The PSD 3603 TOF analyzer successor to the Aerosizer[®] instruments utilizes a similar 'double-crest' particle detection arrangement as that developed for the more recent versions of the APS[®] TOF systems (**Fig. 8**). However, the flow path through the instrument more closely resembles that of the Aerosizer[®]. It can be used with a dry powder disperser attachment similar to that developed for the Aerosizer[®] for formulation development purposes. Other sampling devices that would be useful for inhaler testing, such as the AeroSampler[®] and AeroBreather[®], are not presently available, and no studies evaluating the PSD 3603 analyzer with inhalers have been published to date.

Table 12 is a comparison of the features of TOF- and CI-based analysis methods. In contrast with most impactors used to evaluate inhalers, TOF analyzers operate at flow rates that are too low for direct con-

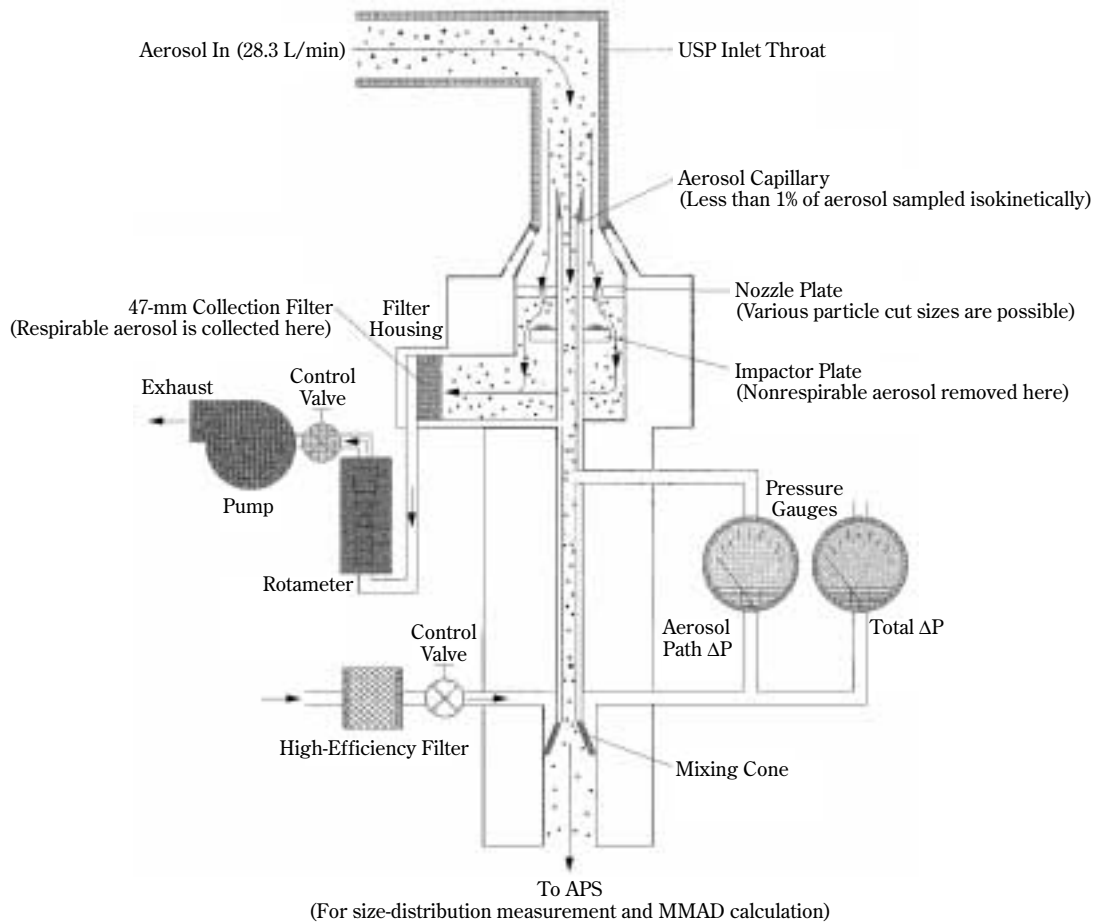


Fig. 9 Model 3306 single stage impactor for use with the APS[®] aerodynamic particle sizer spectrometer for the size characterization of medical aerosols (courtesy TSI Inc.)

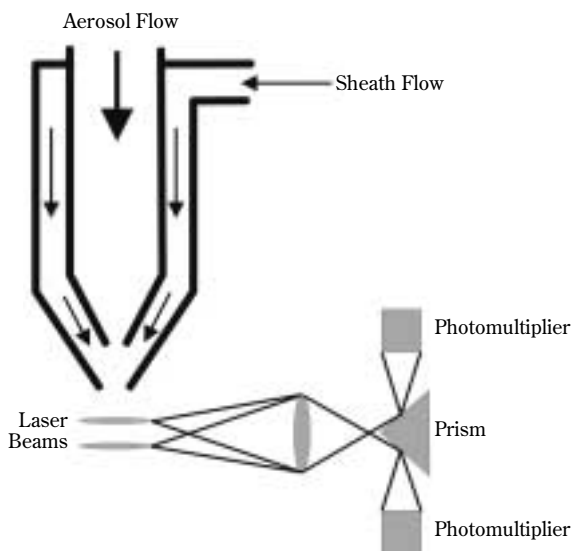


Fig. 10 Aerosol flow path and TOF detection system for the Aerosizer[®] particle size analyzer

nection to the inhaler, and therefore require the aerosol that is presented to the measurement zone to be sampled from the flow entering the analyzer. There is scant data on the variation of measurement efficiency as a function of particle size with these systems, largely because such measurements require a source of monodisperse particles in known number concentration. Such so-called ‘aerosol concentration’ standards are exceedingly difficult to achieve in practice, due to the several forces that act to remove suspended particles within the size range of interest [104]. The assumption is therefore made that particles of all sizes are sampled and measured with equal efficiency. However, recent publications by Armendariz and Leith [105] and Peters and Leith [106], who have established the measurement efficiency-aerodynamic size relationships for the APS[®] models 3320 and 3321 respectively, appear to indicate substantial differences between two superficially sim-

Table 12 Comparison of TOF analysis with cascade impaction

Cascade Impactor	TOF	
	Aerosizer [®] /PSD 3603	APS [®] /SSI
Direct assay for API	No assay possible	No assay possible by APS [®] , but SSI enables assay for API to validate FPF measurement (<4.7 μm aerodynamic diameter)
Typically 4-5 measurements/day/operator	1-measurement/minute is possible – replicates are easy to obtain	Similar measurement rate to Aerosizer [®] , but SSI samples (2 per measurement) take similar time to assay as equivalent number of impactor stages
Direct measure of API mass-weighted size distribution	Number-weighted size distribution requires transformation to mass-weighted basis with increased risk of bias by few very large particles if aerosol is polydisperse	Similar to Aerosizer [®] , but SSI provides FPF on a mass-weighted basis
Inhaler aerosol mass concentration is not a limitation	Particle concentrations >10 ⁴ cm ⁻³ may result in particle coincidence errors	Similar to Aerosizer [®]
Readily usable with variety of induction ports for inhaler testing	Aerosizer [®] has array of different sampling arrangements for different inhaler classes, but none are compendial based	SSI is supplied with USP/Ph.Eur. induction port
Precautions required to ensure particles are collected efficiently (<i>i.e.</i> eliminate bounce/blow-off)	Nothing is collected, so no precautions are necessary	Similar to Aerosizer [®] , but SSI collection surface below impactor requires precautions for efficient particle recovery
Particle density and shape are both incorporated in measurement of particle aerodynamic size because flow regime is Stokesian	Ultra-Stokesian flow introduces significant density- and shape-related biases	Similar to Aerosizer [®] , although effects are less pronounced because flow regime is closer to Stokesian
Inhalation maneuver can be simulated for DPI testing, and impactors have been linked with breathing simulators	AeroBreather [®] add-on option for Aerosizer [®] allows simulation of inhalation maneuver during sampling	No facility to simulate inhalation

ilar instruments. Although the efficiency of the model 3321 APS[®] in the range from 1 to 5 μm aerodynamic diameter was reported as approximately constant, equivalent data for the 3320 indicated a large decrease in efficiency between 2 and 5 μm, which would be expected to manifest itself as a bias towards the detection of finer particles within this range. Further work is therefore urgently needed to establish the cause of these differences, to extend the size range evaluated so that it ideally encompasses the full operating range of the instrument, and also to determine comparable data for the other TOF systems that are in use.

It is also important to appreciate that because TOF analyzers count individual particles as they transit between the light beams, the size distributions that are produced after transformation of TOF-data to particle size, are number-weighted. The subsequent conversion from a number- to mass-weighted basis may introduce ‘noise’ arising from the largest particles that may be present in a typical polydisperse inhaler-produced aerosol, and which are much fewer in number than particles that comprise the bulk of the size distribution [47, 92]. In the context of inhaler testing, this problem was encountered by Bouchicki *et al.* [107] with a pMDI-generated aerosol, in which an

APS[®]-measured count median aerodynamic diameter of an apparently unimodal size distribution with a tail extending past 2 μm aerodynamic diameter was reported as being close to 0.7 μm. However, on a mass-weighted basis, the same aerosol was distinctly bimodal, having one peak at 8 μm, a deep trough between 8 and 10 μm, followed by a second peak at 15 μm aerodynamic diameter. In this context, the SSI is a useful adjunct to the APS[®], as by virtue of being an impactor, it enables the FPF to be measured directly on a mass-weighted basis. The accuracy of the TOF-based size distribution can therefore at least be verified at either 2.5 μm or 4.7 μm aerodynamic diameter.

TOF analyzers are also sensitive to the high particle concentrations that can occur momentarily following actuation of inhalers, especially pMDIs [108]. The underlying causes of bias due to high particle concentrations are different between the Aerosizer[®] [109] and both earlier [95, 96] and later [98] APS[®] systems, on account of the different transit time detection methodologies. The Aerosizer[®] can be used with the AeroDiluter[®] to mitigate the problem, however a systematic study with a range of different pMDI-generated aerosols found that significant particle coincidence occurred with some formulations with

the maximum aerosol dilution that was available [108]. The steps taken with the latest generation of TOF analyzers utilizing 'double-crest' detection to minimize particle coincidence appear to have been effective, to judge from the agreement achieved between model 3320 and 3321 APS[®] measurements with cascade impactor data for pMDI-generated solution formulations [89, 99, 110]. However, testing with aerosols having a range of well-defined particle number concentrations is also necessary to confirm these observations. As a guide, the problem is likely to be of little concern if steps are taken to ensure that the particle concentration does not greatly exceed 10^4 particles cm^{-3} [47].

Size distribution measurements by TOF analyzers can also be biased by both particle shape and particle density, by virtue of the acceleration associated with particle motion through the measurement zone. Both types of inaccuracy have been detected in calibration studies making use of either monodisperse droplets [111, 112] or solid particles of well-defined shape (constant dynamic shape factor independent of aerodynamic size [113, 114]). In the case of liquid droplets, acceleration in the ultra-Stokesian flow regime is sufficient to distort liquid droplets larger than about 5 μm diameter, making them behave as oblate spheroids [111, 112, 115]. This process makes them appear to be smaller in aerodynamic size than is the case in reality. The issue of shape-related bias in TOF analyzers has not been investigated in a systematic manner in relation to the outcomes from medical inhaler performance testing. However, although shape-related bias might be of concern with nebulizer-based measurements where appreciable numbers of larger non-respirable droplets are present, very few studies with this class of inhaler have been undertaken with TOF analyzers to date, and the relatively high surface tension of aqueous liquids used in formulations that are currently delivered by nebulization, partially offsets droplet distortion. Shape-related bias is likely to be much more important when sizing DPI-based aerosols. In this context, studies with non-spherical, cube-shaped, single crystal-based reference particles having a well defined and size independent dynamic shape factor (1.19 ± 0.06) have demonstrated that both the APS[®] and Aerosizer[®] significantly undersize non-spherical particles. The magnitude of the bias associated with these shape standards varied from 20 to 27% in the APS[®], compared with between 21 and 51% in the Aerosizer[®] in the range from about 4 to 10 μm true aerodynamic diameter [113, 114]. In both investigations, the sizes measured by the TOF ana-

lyzer being evaluated were compared to corresponding particle aerodynamic size measurements by a reference Timbrell sedimentometer that operated under Stokesian conditions. On the basis of these data, it appears that quite small deviations from sphericity (dynamic shape factor of unity) may be associated with large errors by both types of TOF analyzer. However studies to quantify bias based on changes to the magnitude of the dynamic shape factor are difficult to perform, since very few standards having a range of well-defined shapes exist in the size range of interest [104].

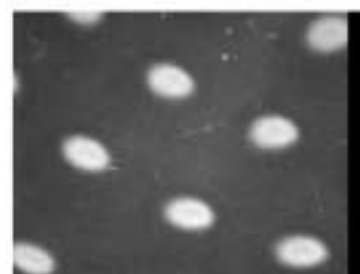
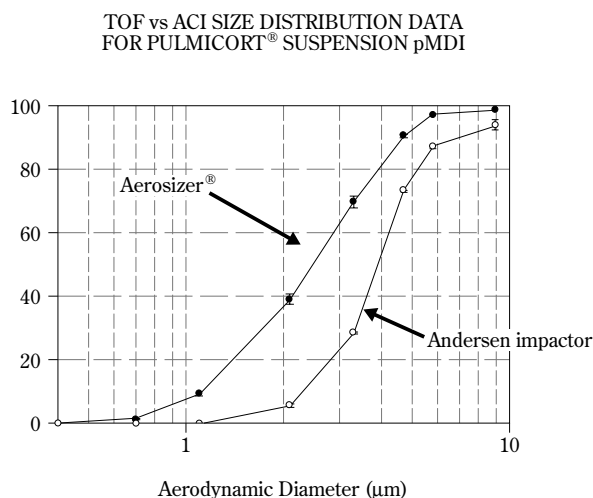
Increases in particle density from the reference value of 1.00×10^3 kg m^{-3} will result in an overestimation of aerodynamic diameter by TOF analyzers [114, 116]. Both the APS[®]/PSD and Aerosizer[®] are calibrated by their manufacturers with uniform sized polystyrene latex (PSL) particles, having a density of 1.05×10^3 kg m^{-3} . In the case of all versions of the APS[®], the software provides the user the option to correct the size distribution for particle density, based on the calculations of Wang and John [116]. The software for the Aerosizer[®] also offers the user the option of specifying particle density that enables a correction to be made, based on manufacturer-supplied curves, linking TOF values with reported particle aerodynamic diameter. The validity of these theoretical curves is supported by experimental data for PSL and glass microspheres [114] (density 2.45×10^3 kg m^{-3}). The user of either the APS[®] or Aerosizer[®] therefore has to provide a value for particle density in order for a correction to be made effectively. In many cases, especially for particles from pMDI/DPI systems, this value is unknown, so that the size distribution data are often presented assuming the particles to be similar to PSL (density 1.05×10^3 kg m^{-3}) or water (density 1.00×10^3 kg m^{-3}). However, the error introduced by this assumption might be significant, depending upon the actual particle density of the formulation being studied. As a guide, Cheng *et al.* showed that particle density-related bias was of the order of 10-15% for the APS[®] group of TOF analyzers within the range from 1.05×10^3 to 2.30×10^3 kg m^{-3} [117]. This finding compares with bias of 25% reported for the Aerosizer[®] family of instruments within the range from 1.05×10^3 to 2.45×10^3 kg m^{-3} [114]. Fortunately, in the case of measurements of non-spherical solid particles, bias introduced by increased density compared with that of water is offset by bias caused by deviations from sphericity, thereby reducing the overall impact of both effects [116].

In the context of inhaler performance testing, the

lack of an assay for API mass is probably the most significant limitation of current TOF instruments. This is largely why these techniques are unrepresented in the compendia. Tsou and Shultz, in a study of pMDI-based solution and suspension formulations, noted that since TOF analyzers do not quantify the mass of API contained in each particle that is detected, their accuracy with many pMDI-based formulations that contain excipients (surfactant) is degraded [118]. More recently, Mitchell and Nagel quantified the magnitude of the bias associated with Aerosizer[®]-based measurements of a budesonide containing suspension formulation, in which a significant proportion of the mass-weighted size distribution comprised particles of sorbitan trioleate [119]. The Andersen 8-stage CI-measured MMAD for this formulation was 3.9 μm , whereas the equivalent Aerosizer[®]-determined MMAD was only 2.4 μm (**Figure 11**). When the deposits on individual collection plates of the Andersen 8-stage CI were examined by microscopy, the surfactant particles were seen to have size-separated from the larger budesonide particles (**Fig. 11**). Tiwari *et al.*, also observed that the Aerosizer[®]-measured MMAD for a pMDI-based salbutamol formulation (1.90 μm) was much smaller than 6-8 μm that they obtained by CI [120]. The APS[®] appears to behave similarly to the Aerosizer[®] in this respect, since Mitchell *et al.*

observed that an APS[®] model 3321 undersized a suspension formulation containing fluticasone propionate, with TOF analyzer- and Andersen 8-stage CI-measured MMAD values being 1.8 μm and 2.8 μm respectively [89]. In contrast, in the same study, the APS-measured MMAD value for the solution formulation Qvar[™] (3M Health Care, UK), at 1.0 μm was very similar to MMAD values of 1.2 μm and 1.0 μm determined by Andersen CI and NGI respectively (**Figure 12**). Although Qvar[™] is surfactant-free, the API (beclomethasone dipropionate) is solubilized in ethanol. Gupta *et al.* have shown that care is required in the interpretation of SSI-measured fine particle fraction, when this accessory is used with the APS[®], as this solvent may not be completely evaporated before the aerosol is sampled by the SSI, if used with the APS[®], resulting in an underestimation of FPF [121]. Their recommendation is supported by recent data from Mitchell *et al.*, who found that FPF_{<4.7 μm} for Qvar[™] determined by the SSI was only 67.1 \pm 4.1%, compared with 96.4 \pm 2.5% by the APS[®] itself and 98.0 \pm 0.5% and 96.7 \pm 0.7% by Andersen CI and NGI respectively [89]. Either installing trace heating around the inlet pathway to the SSI [89], or increasing inlet length [121] have been proposed as solutions, but as yet neither have been implemented.

In addition to the evaluation of inhaler performance,



budesonide: 3–5 μm : stages 3/4



sorbitan trioleate: 0.7–2 μm : stages 6/7

Fig. 11 Undersizing of budesonide-based pMDI formulation by Aerosizer[®] TOF analyzer compared with Andersen 8-Stage impactor, caused by lack of discrimination between particles of API and surfactant (from [119] ordinate scale: cumulative mass % < stated size used by permission, Mary Ann Liebert Inc.)

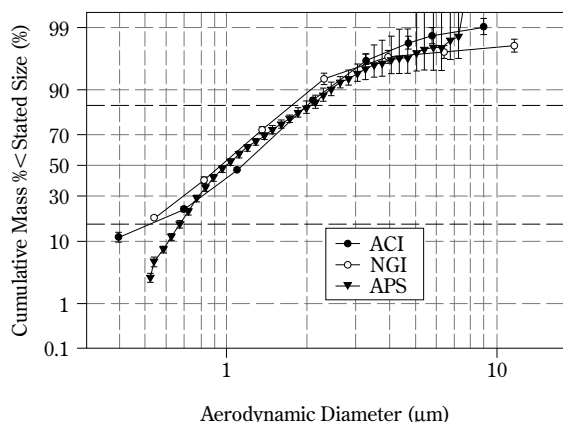


Fig. 12 Close agreement in TOF- and cascade impactor-measured particle size distributions for a solution formulation (Qvar™, 3M Pharmaceuticals) containing no surfactant (from [87]; used by permission, AAPS PharmSciTech)

TOF-based particle size analysis by Aerosizer®/DSP systems is an appropriate technique for characterizing powders used with DPIs during pre-formulation studies, as various tools, such as the Pulse Jet Disperser™ [92, 122] and AeroDipserser® [123] are available to facilitate the aerosolization process. As an example, Hindle and Byron used an Aerosizer®-Aero-Disperser® to size characterize a wide variety of powders used in DPI formulations, including terbutaline sulfate and salbutamol [123]. Their study is interesting in that they provided some guidance on how best to set up the powder disperser and TOF analyzer, and their methodology should in principle be transferable to the powder disperser used with the PSD 3603 analyzer. Firstly, they varied the shear force (pressure drop at the point of dispersion) applied to a sample of powder in the Aero-Disperser® from 3.5 kPa (low shear) to 27.6 kPa (high shear) to optimize de-aggregation, using the Aerosizer® to confirm whether or not aggregates were produced and measured. They then noted that if the powder feed in the Aero-Disperser® is set correctly, the sampling rate at the measurement zone of the Aerosizer® can be kept within the range from 5×10^2 to 10^4 particles s^{-1} , where the upper limit corresponded to 4.4% loss of 5 μm aerodynamic diameter particles from coincidence effects. They observed that conditions in the Aero-Disperser® must be optimized on a formulation-by-formulation basis to ensure the following:

- the sample analyzed is representative of the bulk powder,
- the sample is completely de-aggregated,

- de-aggregation does not comminute the sample.

The duration of the measurement appears to be critical, based on their measurements with micronized salbutamol base. This powder was readily de-aggregated, so that optimum measurement times were less than 200 s. As the sampling time was lengthened, the apparent number of particles in the range from 4 to 10 μm aerodynamic diameter increased, which was attributed to a gradual accumulation of electrostatic charge and resulting triboelectric agglomeration. They also noted that it is essential to clean the components of the Aero-Disperser® thoroughly between samples. They commented that it was also necessary to periodically clean exposed surfaces of the lenses at the measurement zone of the Aerosizer® to avoid both loss of sensitivity to the finest particles as well as a systematic shift in the distribution to larger sizes.

LIGHT INTERACTION METHODS OPTICAL PARTICLE COUNTERS (OPCs)

OPCs, in which particle size discrimination is based on differences in scattered light intensity within a well-defined angle, are widely used to characterize aerosols in the environment as well as in specialized applications, such as clean room monitoring, where particle concentrations are low. However, their applicability to study aerosols from medical inhalers is severely limited by sampling problems, as many instruments require focusing of individual particles in the light path as they are measured, which restricts the flow rate that can be achieved into the OPC. Like TOF-analyzers, they are also susceptible to particle coincidence when concentrated aerosols are sampled [124], a situation that is likely to occur with most inhalers. OPCs also measure particle number concentration, irrespective of particle chemical composition, rather than determine the mass of API as a function of particle size. However, in contrast with TOF-based systems, there is a lack of a direct relationship between OPC-measured particle size, and aerodynamic diameter. The size measured by OPCs is a complex function of the light scattering cross-section of the particle and the angle within which the scattered light is measured [5]. For particles larger than the wavelength of the illuminating light, the measured size is also dependent on refractive index [124], which is often unknown, particularly for formulations that are mixtures of API and excipients. These systems are also susceptible to a variety of environmental factors that alter either the light intensity of the illuminating beam or the detected scattered light, such as optical

window contamination if a sampling cell is present, as is almost always the case [124]. In spite of these limitations, Loffert *et al.* used a high volume light scattering single particle spectrometer (model CSASP-100, Particle Measuring Systems, Boulder, CO, USA) to measure size distributions of a variety of jet nebulizers delivering aqueous albuterol solution containing physiologically normal saline [125]. Their estimates of VMD ranged from 3.77 to 7.20 μm and they were able to discriminate differences in droplet size distribution from one nebulizer type to another. Unfortunately, this group did not provide any comparative measurements utilizing other techniques, in particular laser diffractometry, so it is not possible to judge the value of this approach by reference to the more commonly encountered nebulizer droplet sizing methods.

LASER DIFFRACTOMETRY (LD)

In recent years, a range of instruments based on the principle of laser light diffraction (low angle laser light scattering) has been developed from the original work of Swithenbank *et al.* [126]. In contrast with both TOF and OPC instruments, in which particles are ideally measured one at a time, LD analyzers determine the size distribution simultaneously of all the particles in the aerosol cloud present within the measurement zone during the course of a single measurement sweep (cloud ensemble particle sizing) [124]. The technique is very rapid, since several hundred sweeps are typically undertaken within a 1-s interval by modern instruments [127]. LD-particle size analysis can therefore be adapted to follow transient events, such as spray evolution following pMDI or nasal spray pump actuation [127-129]. In practice, however, most reported size distributions, particularly for continuous delivery nebulizers [51, 130] and nasal spray pumps [8, 131], are time-averages taken over several seconds, since these devices typically deliver a stable aerosol during this time period. Clark has reviewed the use of the LD technique for the measurement of nebulizer-generated aerosols [51], but many of the issues discussed therein are also applicable to the other inhaler types.

The principle of the LD method is well described in an international standard [132], and Scarlett has recently described the measurement process on a step-by-step basis [133], so only a brief description of the essentials follows here. In the classical set-up, an expanded laser beam is used to produce a parallel beam of coherent, monochromatic light of wavelength,

λ (Figure 13). A Fourier transform (range) lens is used to focus the diffraction pattern generated by the collection of particles entering the measurement zone onto a photodetector array located at the focal distance, F , from the range lens. This is the configuration of most relevance to medical inhaler applications, in which particles larger than about 0.5 μm are being size characterized. The undiffracted light is reduced to a spot of intensity I_0 at the center of the detector plane, with the diffraction pattern forming concentric, circular rings. Measuring the intensity pattern to deduce the particle size distribution is difficult, but measuring the light energy distributed over a finite area of the detector is easier to perform [134]. Large particles scatter most light energy at small angles, whereas finer particles scatter most energy at larger angles, and this differentiation in energy profiles provides a way to obtain information about particle size distribution from the light diffraction pattern.

The interaction of light with a particle involves four components:

1. diffraction at the contour of the particle,
2. internal and external reflection at the surface of the particle,
3. refraction at the interface coming from the support gas to the particle and vice versa as light exits the particle,
4. absorption inside the particle.

Scattering of unpolarized light of incident intensity I_0 by a single, spherical particle is described by the relationship:

$$I(\theta) = \frac{I_0}{2k^2a^2} [(S_1[\theta])^2 + (S_2[\theta])^2] \quad (11)$$

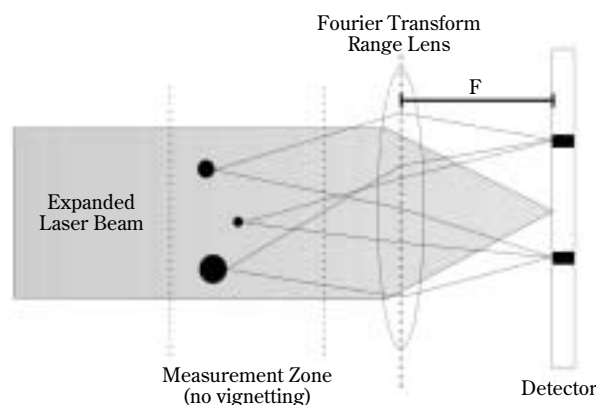


Fig. 13 Classical set-up for laser diffractometer-based particle sizing

where $I(\theta)$ is the total scattered intensity as a function of angle θ , k is the wavenumber defined by $[2\pi/\lambda]$, λ is the wavelength of light (assumed to be in air), and 'a' is the distance from the light scattering particle to the detector. $S_1(\theta)$ and $S_2(\theta)$ are dimensionless complex functions that describe the change of amplitude in the perpendicular and parallel polarized light components respectively as a function of angle θ with respect to the forward direction [132].

In the Fraunhofer approximation that only describes diffraction of light at the contour of the particle, it is assumed that all particles are much larger than λ and that only near forward scattering is considered (*i.e.* θ is small). Under these circumstances:

$$(S_1)^2 = (S_2)^2 = \alpha^4 \left[\frac{J_1(\alpha \sin \theta)}{\alpha \sin \theta} \right]^2 \quad (12)$$

and equation 11 simplifies to:

$$I(\theta) = \frac{I_0}{k^2 a^2} \alpha^4 \left[\frac{J_1(\alpha \sin \theta)}{\alpha \sin \theta} \right]^2 \quad (13)$$

where J_1 is a Bessel function of the first kind of order unity and the dimensionless size parameter, α , is given by:

$$\alpha = \frac{\pi d_{LD}}{\lambda} \quad (14)$$

d_{LD} is the particle size measured by the LD technique.

The analysis of the diffraction energy pattern can be complex for a 31-ring detector, such as is used by many LD instruments, since a 961-element matrix has to be solved. In practice, this procedure is undertaken by proprietary algorithms that involve matrix inversion involving the use of least-squares minimization criteria. These may assume a model for the size distribution, such as the Rosin-Rammler or log-normal functions. However, instruments since the early 1990s have also offered so-called 'model-independent' solutions in which it is initially assumed that the size distribution consists of one or more modes, each containing a finite number of fixed-size classes [135, 136]. The detector response is then simulated based on expectations for this relationship, optimizing the volume (mass)-fractions in each size class by minimizing the sum-of-squared deviations from the measured detector response. The reported size distribution is volume-weighted [132], making conversion to a mass-weighted basis straightforward on the basis that particle density is a constant irrespective of size. The choice of size distribution model is a critical step in the measurement process, and the use of a model-independent distribution is therefore recommended

for the initial analysis of aerosols [124].

The Fraunhofer approximation does not require knowledge of the optical properties (refractive index including light absorption coefficient) of the particles being studied, therefore its use is recommended when mixtures are being examined, assuming the underlying assumptions remain valid [132]. Annapragada and Adjei have concluded that the Fraunhofer approximation works well for unimodal size distributions, but may skew the reported distribution towards the mode that produces the strongest peak in the diffraction pattern for multimodal systems [137].

The more rigorous Lorenz-Mie (L-M) solution that describes light reflection, absorption and refraction besides scattering [138] should be used when d_{LD} approaches λ , [132]. The Fraunhofer approximation predicts only small differences in the intensity of light scattering energy as particle size decreases finer than about 10 μm . However, for such particles, L-M theory predicts strong fluctuations of the maximum light intensity in relation to changes in particle size, creating intensity values that are much higher than the corresponding Fraunhofer prediction for some sizes and much lower for others [132]. Merkus *et al.* have observed that the portion of fine particles $<2 \mu\text{m}$ diameter may be significantly greater when measuring nebulizer-generated aqueous droplets using the Fraunhofer approximation [139].

It is necessary to know the particle refractive index, if L-M theory is utilized [133], and it is usually assumed that the particles are smooth-surfaced spheres. These assumptions are relatively unimportant for dilute aqueous-based formulations, and the complex refractive index for water ($1.33+0i$ (*i.e.* no light absorption component)) is well defined. However, the matter does not appear to be so straightforward with dry powder inhaler-produced aerosols. In this context, de Boer *et al.* [48] commented that the L-M procedure is better (more rigorous) than the Fraunhofer technique. However, where $d_{LD} \gg \lambda$, they observed that the Fraunhofer approach may provide size distributions with micronized powders having diverse chemical composition as well as size, shape and surface appearance that correlate more closely with cascade impactor-based data, than data obtained applying L-M theory. This is because of the uncertainty that is inherent in the definition of complex refractive index required to implement L-M theory, together with the underlying assumption that the particles are smooth-surfaced spheres. Most modern instruments, such as the Mastersizer-S and Mastersizer-X (Malvern Instruments, UK) automatically arrive at the particle size

distribution by a rigorous solution of the L-M equations. However, the Helos LD (Sympatec GmbH, Clausthal-Zellerfeld, Germany) normally operates using the Fraunhofer solution, but a software option is available that applies L-M theory for applications where particle sizes are in the range from ca. 0.1 to 1.0 μm diameter.

The reported size scale based on d_{LD} approximates well with the size scale based on d_v for spherical particles (equation (1)). However, the applicability of LD for the size distribution measurement of dry powder aerosols that may comprise non-spherical particles may be questionable without data from an independent technique to validate the LD data. In this context, de Boer *et al.* noted that micronized powders for use in DPIs in most cases comprise particles that approach sphericity, under which circumstances, LD-based size is a measure of the geometric diameters of the particles at random orientation, and $d_{LD} \approx d_v$ [48]. They also commented that comparisons with d_{ae} obtained by cascade impactor or equivalent methods are in many cases possible, since the proportionality constant $(\rho_p/\rho_0\chi)^{1/2}$ in equation 1, ignoring the Cunningham slip correction factors, is between 0.96 and 1.22 for a range of particle shapes ranging from spherical ($\chi=1.0$) to cylindrical with aspect ratio (length/diameter) of 4 ($\chi=1.3$) and densities from 1.2 to 1.5 g cm^{-3} .

Various features of the LD technique are summarized in **Table 13**. Depending on choice of range lens, these instruments operate over a wide dynamic range, typically from 0.5 to 200 μm diameter for work with nebulizers [140-142]. However, they can be configured to size much larger droplets (*e.g.* from 20 to

1000 μm) for use when measuring the coarser aerosol produced by nasal spray pumps [8, 131]. Both the Malvern and Sympatec systems come with various attachments that assist in the measurement of inhaler-generated aerosols [128, 143]. Since LD is an absolute method based on fundamental principles, there is strictly no need to calibrate an instrument against a standard [144]. However, in practice to meet needs for validation in a regulatory environment, these instruments are normally checked by either the use of a suitable reticle containing a 2-dimensional profile of circles representing outlines of particles having well established diameters by microscopy [144, 145], or with standard reference materials having well defined optical as well as physical size properties [104, 133].

Apart from the ability to determine particle size distributions rapidly, the technique in its simplest form is non-invasive, in that a sample of the aerosol cloud need not be removed from where it is created to enable the measurement to take place. In a typical configuration used with nebulizers, the unconfined aerosol is generated in the pathway of the laser beam and subsequently removed by a vacuum system to prevent recirculation of droplets in the measurement zone (**Figure 14**) [141]. Care must be taken to avoid the phenomenon of ‘vignetting’ (**Table 14**), whereby light scattered at the widest angles (by the finest droplets) misses the range lens altogether [127]. It is therefore common practice to arrange that the aerosol flow passes as close as possible to the range lens without fouling its surface. Newer instruments, such as the Malvern Spraytec® LD have a more versatile optical bench layout so that the risk of vignetting is reduced [127]. It may also be necessary to minimize

Table 13 Particle size analysis by laser diffractometry – Features

Feature	Comment
Wide measurement range	LD systems typically measure more than 2-orders of magnitude in size with as many as 15 channels per decade. Precise range limits depend on configuration of optical bench. Overall range from 0.1 μm to several mm depending upon instrument type.
Volume (mass)-weighted size distribution	Possibility of bias arising from a few large particles that may not be representative of the true size distribution is avoided, since transformation of measured data from number-to a mass-weighted basis is not required.
Rapid	Several thousand measurements are possible in 1-s (<i>e.g.</i> one measurement is possible every 400 μs with the Malvern Spraytec® system). Can therefore be adapted to follow transient events, such as spray evolution following pMDI or nasal spray pump actuation. Most size distributions are time-averages over several seconds.
Non invasive	Measurements with many inhalers can be made by generating the aerosol in the path of the laser beam. More sophisticated arrangements are available in which the aerosol from the inhaler is introduced through a sample cell in the optical pathway to avoid re-circulation of particles in the measurement zone.
Excellent reproducibility between measurements of the same aerosol	Coefficients of variation \approx 1-2% in terms of size distribution parameters, such as volume median diameter are possible with currently available LD systems.

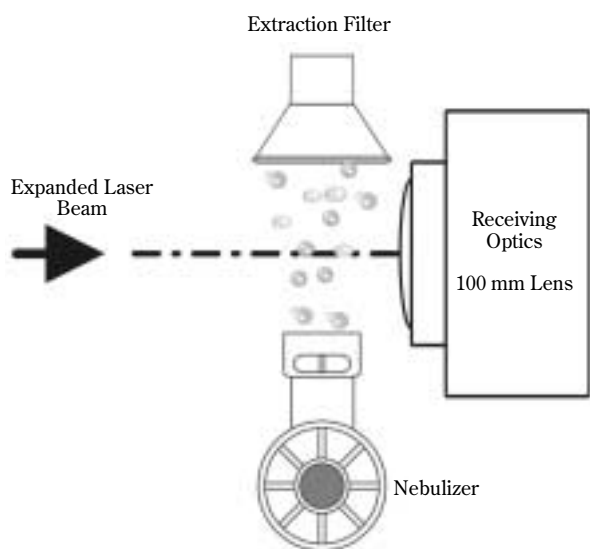


Fig. 14 Configuration for nebulizer droplet size analysis by laser diffractometer (from [141]; used by permission, Daedalus Enterprises Inc.)

droplet evaporation when working with aqueous droplets [10]. Sophisticated arrangements have therefore been developed so that laser diffractometer measurements can be made either through optical windows, for instance fitted to a USP/Ph.Eur. induc-

tion port attached to a CI [146, 147], or via a purpose-built sampling cell as part of the LD instrument [128, 148]. In one recently described configuration, the LD sample cell was located immediately downstream of a so-called 'inhaler module', comprising a USP/Ph.Eur. induction port and pre-separator of an Andersen CI to size analyze rapidly the fraction of aerosols from both pMDI- and DPI-based formulations that would penetrate as far as the entry to the CI in a conventional measurement [147]. In all of these configurations, the aerosol is confined within a defined volume, making control of local environmental conditions surrounding the aerosol readily achievable.

Care is needed to avoid the 'beam steering' phenomenon (**Table 14**), when applying the LD technique to study aerosols from pMDIs [149], since the refractive indices of both chlorofluorocarbon and hydrofluoroalkane propellants differ significantly from that of the surrounding air. The problem is particularly pronounced if the inhaler is actuated close to the laser beam so that the propellant released on actuation has little time for dilution with ambient air, and thereby local fluctuations in propellant/air composition erratically alter the path of the light diffracted by the particles [149]. Although Smyth and Hickey claimed that were able to distinguish a propellant-related mode in a tri-modal distribution resulting from a pMDI actuated close to the light path [129], great care is needed in interpreting the data that are measured in such ex-

Table 14 Particle size analysis by laser diffractometry – Limitations

Limitation	Comment
No assay for API is performed	Lack of a direct link between particle size and API mass limits LD use primarily with solution formulations. LD-size distributions of aqueous suspensions are a measure of water droplet sizes rather than the sizes of the API particles.
Particle sphericity is assumed	May be an issue when measuring DPI-generated aerosols, but many micronized powders have shapes that are close to spherical. LD is very suited to measurement of aqueous droplets from nebulizers and nasal spray pumps where this assumption is valid.
The phenomenon of 'vignetting' occurs, in which light scattered at wide angles misses the detector array, and therefore results in bias due to the absence of the finest particles in the distribution	Careful choice of range lens and optical bench set-up (where adjustable) can help minimize 'vignetting'. Otherwise, take steps to ensure that the total body of the spray plume is located within the working distance of the range lens (without being so close that the lens itself is fouled by droplet impaction).
Beam steering occurs as a result of changes in refractive index of the support gas for the aerosol being measured	Beam steering is difficult to avoid when working with pMDI-generated aerosols without some form of dilution so that the difference in propellant refractive index from that of air is minimized
Multiple scattering from highly concentrated aerosols, such as those generated locally by pMDIs results in bias due to over-broadening of the size distribution	Light obscurations as high as 35% can be tolerated with instruments, such as the Malvern Mastersizer LD systems. The Malvern Spraytec [®] system can permit measurements with light obscurations as high as 95% by the use of proprietary data analysis software.
Droplet evaporation during measurement results in a bias to finer sizes	This is more a limitation of the aerosol presentation arrangement than the LD technique. The use of a sample cell in which environmental conditions can be controlled may alleviate the problem.

periments, since the aerosol plume is highly dynamic in terms of particle size during formation.

The lack of a direct assay for API (**Table 14**) effectively precludes the use of LD for establishing the particle size of drug particles that are formulated in suspension [10], since the light scattering entity may, in the case of an aqueous formulation, be an empty water droplet, a droplet containing a single drug particle or a droplet containing more than one particle. However, despite this limitation, Sharpe *et al.* used LD to compare droplet size distributions from suspension oral and nasal pMDIs to see if they could detect changes in the droplet size distributions brought about by varying the size distribution of the API [150]. They actuated the inhaler being evaluated at a fixed distance from the laser beam (12 cm), and were able to detect changes in LD-measured droplet size distributions for formulations in which there was a 2.3-fold difference in mass median diameter of API (1.2 μm to 2.8 μm). However, they reported that their LD-technique could not discriminate between formulations when the mass median diameter difference was 1.5-fold (1.2 μm to 1.8 μm). Although this study demonstrates an innovative application of LD-based particle size analysis, their conclusions may not be of general application, as they are almost certainly formulation specific as well as being dependent upon the type of LD instrument (and data analysis method) chosen.

The light diffracted from one particle may be intercepted by one or more adjacent particles rather than being collected directly by the detector, if the particle number concentration in the laser beam is excessive. Particle-particle or 'multiple' scattering results in erroneous broadening of the particle size distribution and skewing towards finer sizes, the magnitude of which increases with increasing particle concentration [124]. Manufacturers provide a measure of multiple scattering by reporting the laser beam obscuration as a percentage for each measurement (an obscuration value of 100% represents a fully attenuated light beam). This effect is small for beam obscurations <ca. 50% [135], but efforts to dilute the aerosol should nevertheless be considered if obscuration exceeds about 30% with a conventional LD instrument, as can be the case with aerosols produced by air entrainment nebulizers or pMDIs. The Spraytec[®] LD system contains software that permits beam obscurations as high as 96% [127], thereby providing an alternative to aerosol dilution for studying more concentrated aerosols.

Although LD does not involve direct assay for API, its use as a rapid alternative to cascade impaction has become widespread in recent years, and numerous

comparisons with CI-generated size distributions have been undertaken as part of the validation process for particular inhaler types. In the case of nebulizers, where the aerosol generation process is continuous during the course of measurement, there is evidence that agreement between LD- and CI-based measurements is good, provided that precautions are taken to avoid heat and mass transfer from the droplets to the CI (*i.e.* by cooling the impactor so that its internal temperature matches that of the aerosol stream) [46]. Wachtel and Ziegler [146] and Ziegler and Wachtel [151] also arrived at this conclusion when evaluating a soft mist inhaler delivering an aqueous-based formulation by Sympatec HELOS/KF system. However, Smart *et al.* [142] observed that measurements of droplet volume median diameter (VMD) made by Mastersizer S LD analyzer were slightly, but significantly larger than corresponding MMAD values obtained by Andersen 8-stage CI for a continuously operating vibrating membrane atomizer generating aqueous sprays of solution and suspension formulations. The fact that the relationship between LD- and CI-measured median diameters was linear and constant within the range studied from 4 and 8 μm VMD (corresponding to 2 to 6 μm MMAD), is suggestive that the difference may have been caused by partial droplet evaporation in their CI, which was operated at $22\pm 2^\circ\text{C}$ and $60\pm 4\%$ RH. Ding *et al.* [152], studying the delivery of droplets of solution formulations of varying non-volatile concentrations in ethanol generated by electrohydrodynamic atomization also observed a consistent correlation ($r^2=0.83$) between LD-measured VMD (Mastersizer-X) and CI-measured MMAD (Andersen 8-stage CI). However, in their studies, VMD values ranging from 2.06 to 2.52 μm were between 10 and 20% finer than the corresponding CI-measured MMADs (2.2–2.9 μm). They attributed this slight difference between the two techniques to differing measurement principles. The poorer resolution of the CI may explain the significantly wider size distributions reported by this technique ($2.1 < \text{GSD} < 2.7$) compared with LD ($1.5 < \text{GSD} < 1.8$). Although the authors stated that the ethanol content had evaporated by the time that their LD measurements were made, they did not provide data in support of this claim. Incomplete evaporation in the LD analyzer compared with that taking place within their CI would explain the slight but consistently larger size measurements by the former technique.

The situation is even more complex where LD-measurements have been made with pMDIs, because of the presence of propellant in both vapor and liquid

droplet phases. Recently, Haynes *et al.* reported good correlations between Spraytec[®]-measured VMD and Andersen 8-stage CI-measured MMAD in the range of MMAD from 1 to 5 μm for pMDI solution formulations containing ethanol by heating the pMDI canisters to 40°C and 55°C [153]. This procedure increased the vapor pressure of the ethanol, resulting in faster rates of volatilization compared with room ambient conditions. However, apart from its undoubted value in demonstrating the importance of achieving comparable evaporation behavior in the LD and CI, it is questionable whether this approach is appropriate to characterize the inhaler as it might be used by a patient under normal climatic conditions.

Holmes *et al.*, [154] using a Spraytec[®] LD inhalation cell located between the exit of a USP/Ph.Eur. induction port and an Andersen 8-stage CI, observed that this technique significantly undersized a chlorofluorocarbon (CFC)-based beclomethasone dipropionate (BDP) formulation (VMD=2.65±0.37 μm) compared with Andersen CI-measured MMAD of 3.74±0.04 μm . However, the opposite behavior occurred when sizing the aerosol produced from a hydrofluoroalkane (HFA-134a) solution formulated BDP (Qvar[™]; VMD=2.39±0.06 μm ; MMAD=1.15±0.01 μm). In both instances, the LD-measurements indicated a wider spread of the size distributions compared with the equivalent CI-generated data. They attributed the differences between the two techniques as arising from differing evaporation behavior of the CFC- and HFA-propellants. However, the HFA-BDP formulation that they studied also contains ethanol as solubilizer. It is therefore also likely that the larger particle sizes measured by their LD was caused by partly evaporated ethanol, that would have been more complete by the time that the aerosol passed into the CI, similar to the situation with the study reported by Ding *et al.* [152]. Haynes *et al.* also reported similar findings with a variety of CFC- and HFA-based formulations operated at room ambient conditions [153]. Although they also attributed their observations to differences in propellant evaporation rates, they included variation of deposition in the USP induction port and the presence of excipients as other factors meriting further study.

Smyth and Hickey [155], working with a range of HFA-based solution formulations with ethanol as solubilizing agent for the API, observed LD-measured VMDs (Malvern 2600c) that were much larger (4 to 30 μm) compared with Andersen 8-stage CI measurements (0.48 to 1.54 μm) that are similar to the CI-data of Holmes *et al.* [154] for their HFA-based formula-

tion. Again, incomplete evaporation of propellant and ethanol may at least partly explain their findings, particularly as their LD measurements were made close (4 to 8 cm) from the pMDI actuator. However, it would be interesting to see if the differences between LD and CI measurements had persisted if a newer LD instrument had been used. Smyth and Hickey concluded that LD is particularly useful (in pre-formulation studies) in characterizing the plume as it leaves the pMDI actuator in a non-invasive manner. On the other hand, the CI-technique is better suited to distinguish small differences in particle size distribution of the (non-volatile) API brought about by changes in formulation. It follows that CI-based data are likely to be of more relevance in predicting the behavior of pMDI-based aerosols in the lower respiratory tract, since evaporation of volatile species is likely to be more complete by the time that the medication is inhaled, particularly if the patient uses a spacer or holding chamber [156].

PHASE DOPPLER PARTICLE SIZE ANALYSIS (PDA)

The Doppler effect can be utilized to obtain simultaneous information about particle size and velocity. Bachalo and Hauser [157] have described the fundamentals of the technique in detail, and therefore only a simplified explanation is provided here. The equipment consists of a coherent (laser) light source, transmitting optics, signal processors and data analysis and collection software. A fluctuating scattered light intensity-time profile is detected as individual particles traverse a series of interference fringes formed from intersecting laser beams that define a measurement volume (**Figure 15**). Several detectors arranged at different scattering angles are used to sample slightly different spatial portions of the scattered light signal per particle. In a two-detector system, the phase shift between detectors conveys information about particle diameter, refractive index and receiver geometry. PDA has a wide dynamic size range, typically from about 0.3 μm to 8 mm with accuracy of 5% for a particular optical configuration. Since the technique is an extension of laser Doppler anemometry, particle velocity can also be measured in the range from 1 to 200 m s^{-1} in 2- or 3-dimensions with accuracy typically of 1% [124]. However, care has to be exercised in setting up the technique, especially to ensure that the criteria used to validate particle transition correctly across the measurement zone are appropriately chosen so as to ensure representative

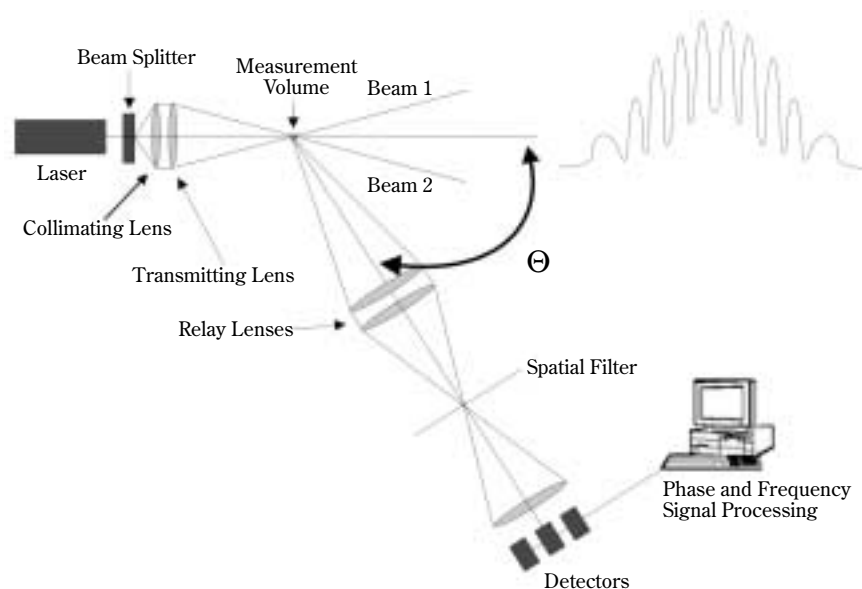


Fig. 15 Schematic of a phase Doppler particle size analysis system

measurement of the whole population of the size distribution.

PDA has traditionally been applied to the study of unconfined atomizer sprays and has thus far not widely been used for the assessment of medical inhaler aerosols. Two significant drawbacks are that PDA provides number-, rather than mass-weighted size distribution data, and no API assay is undertaken. Furthermore, the assumption of particle sphericity associated with the L-M solution to predict the phase shift as a function of particle size, limits its application to droplet rather than dry powder particle sizing. Nevertheless, Stapleton *et al.* [158] used PDA to measure droplet size distributions produced by jet nebulizers, as it was possible to make accurate and non-invasive size measurements at the immediate exit of the devices before the aqueous droplets were able to evaporate significantly in the ambient environment. Dunbar *et al.* [159] were able to obtain particle size distribution data from CFC-propelled pMDI formulations, locating the measurement zone as close as 25 mm from the actuator orifice in order to investigate aerosol plume development under room ambient conditions. It is important to note that the measurements by Dunbar *et al.* were undertaken as part of formulation development, rather than as a means of characterizing the likely behavior of the particles when inhaled.

Corcoran *et al.* [50] have provided the only systematic comparison to date between PDA-(Aerometrics,

Sunnyvale, CA), LD- and TOF-measured size distribution data, based on aqueous and relatively non-volatile propylene glycol droplets produced by two commercially available jet nebulizers. In general, for aqueous droplets they found a good agreement in both MMAD and size corresponding to the 90th volume-weighted percentile of the size distribution (d_{90}) estimated by PDA with the LD techniques that utilize the L-M model (Table 15). However, such agreement might be anticipated considering that a L-M solution was also applied in their PDA system. They further observed that TOF-analyzer measured narrower volume-weighted size distributions compared with the other techniques, but they were unable to assign a cause for this behavior. Interestingly, they were able to detect a small population of larger droplets (15-20 μm) by PDA with the nebulizer-produced propylene glycol droplets (data not shown here) that were not observed by the other techniques.

Currently, no systematic comparison between PDA- and CI-measured size distributions of inhaler aerosols is available. However, it is reasonable to anticipate fair agreement between these techniques, at least for aqueous solution-based aerosols that are homogeneous in terms of composition, on the basis of the findings of Corcoran *et al.* [50], as well as the similarity between LD- and CI-measured data already discussed for nebulizer-produced droplets (when precautions are taken to minimize evaporation).

Table 15 Comparison of MMAD and Size Corresponding to 90th Percentile of the Volume-Weighted Distribution (d_{90}) for Aqueous Droplets Produced by Two Jet Nebulizers (from [50]: Reprinted from *J. Aerosol Sci.* 31(1), Corcoran, T.E., Hitron, R., Humphrey, W. and Chigier, N., ‘Optical measurement of nebulizer sprays: A quantitative comparison of diffraction, phase Doppler interferometry, and time-of-flight techniques’, 35-50., Copyright (2000), with permission from Elsevier.)

Measurement Technique		Nebulizer 1		Nebulizer 2	
		MMAD (μm)	d_{90} (μm)	MMAD (μm)	d_{90} (μm)
PDA (Aerometrics)		4.9	10.5	3.7	8.1
TOF (Aerosizer [®])		6.4	9.6	5.4	8.3
LD	Spraytec [®] (Malvern Instruments)	5.0	10.9	3.4	7.8
	Mastersizer S (Malvern Instruments)	4.9	9.9	4.2	8.6
	M2600 (Malvern Instruments)	4.5	9.4	3.2	7.7

FUTURE DIRECTIONS IN INHALER PARTICLE SIZE MEASUREMENT

The statement made by Corcoran *et al.* [50] that various groups involved with inhaler aerosol particle size characterization rely on mechanical separation techniques, such as the CI method, regardless of recognized problems with these methods, illustrates the dilemma facing those trying to implement the most satisfactory methodology. On one hand, CI-methods are invasive, time consuming and are susceptible to various sources of bias that have been discussed previously. In contrast, light interaction techniques, including TOF analysis, offer rapid measurements and in many cases can be non invasive, making them attractive particularly when studying droplets where evaporation of volatile species is important. On the other hand, CI-based size analysis is the only current technique in which a direct assay of the mass of API is undertaken. Furthermore this technique provides a direct measure of aerodynamic diameter that is of most relevance in predicting likely deposition in the respiratory tract. TOF-analysis also determines aerodynamic size, but crucially lacks specificity in terms of relating this parameter unambiguously to API mass. TOF- and PDA-measured size distribution data also require transformation from number- to mass-weighting, a process that may result in significant error, particularly if a few large particles have been

unrepresentatively sampled. LD and PDA methods do not determine aerodynamic size, but various studies have indicated a broad degree of equivalence between light interaction measured size parameters and aerodynamic size at least for aqueous droplets. In summary, there is no single technique that meets all requirements, and for this reason all of the measurement methods that have been discussed in this review are likely to persist in future applications associated with the characterization of medical aerosol inhalers.

Looking ahead, it is reasonable to anticipate the following developments in the next five to ten years:

1. The CI is likely to remain the method of choice for CMC-type testing for regulatory purposes (batch release *etc.*). However, a widespread replacement of existing CIs by the Next Generation Pharmaceutical Impactor (NGI) will likely take place, driven by pharmaceutical companies seeking to submit regulatory applications for new chemical entities. At the same time, it is likely that existing CIs will continue to be used to characterize existing products to avoid unnecessary resubmission of data to regulatory agencies.
2. Efforts will continue to develop improved models of the human respiratory tract, differentiating not only by its development from neonate to adult, but also in terms of modifications caused by different disease modalities.
3. More emphasis will be placed on the importance of both measuring and controlling electrostatic charge, both associated with the inhalers themselves and also in some instances, with the measurement equipment. The use of climate controlled environments for making inhaler performance measurements will become more widespread, especially with increasing regulatory pressure to minimize measurement variability.
4. Methods will be developed that more effectively test breath-actuated inhalers, especially nebulizers and the new generation of electronically operated devices that deliver medication at the appropriate timing during the respiratory cycle.
5. Valved holding chamber used with pMDIs will be increasingly tested to simulate patient (mis) use (*i.e.* breath-holding, poor coordination between pMDI actuation, including delayed inhalation, rather than being evaluated merely at constant flow rate that does not test for inhalation/exhalation valve operation properly).
6. Currently available TOF-analyzers will continue to find limited use for size characterizing homo-

geneous solution-based formulations where the lack of assay for API is relatively unimportant. However, a new generation of TOF-based particle sizing instruments is likely to be developed in which single particle chemical assay is performed simultaneously with the TOF measurement. This equipment will have the capability to replace CI measurements for most types of formulation development where the speed of measurement is of greatest importance.

7. Moves by international bodies (CEN, ISO) to develop written standards defining both inhalers and the methods for characterizing their performance will continue, with most national standards being gradually replaced. This process is well under way in Europe with the general adoption of CEN 13544: 2001 for nebulizer performance testing. Approval has recently been given for a new ISO standard to be developed by committee TC84/JWG5, covering inhalers for medical use, with the exception of nebulizers already encompassed by the above CEN standard.

REFERENCES

1. Smith, S.J. and Bernstein, J.A. Therapeutic uses of lung aerosols. *In: A.J. Hickey Ed., Inhalation Aerosols: Physical and Biological Basis for Therapy*. Marcel Dekker, NY, USA, 1996, 233-269.
2. Farr, S.J. and Taylor, G. Insulin inhalation: Its potential as a non-parenteral method of administration. *In: A.L. Adjei and P.K. Gupta Eds., Inhalation Delivery of Therapeutic Peptides and Proteins*. Marcel Dekker, NY, USA, 1997, 371-387.
3. Heyder, J. and Svartengren, M.U. Basic principles of particle behavior in the human respiratory tract. *In: Bisgaard, H., O'Callaghan, C. and G.C. Smaldone Eds., Drug Delivery to the Lung*. Marcel Dekker, NY, USA, 2002, 21-45.
4. Rudolph, G., Gebhart, J., Heyder, J., Scheuch, G. and Stahlhofen, W. Mass deposition from inspired polydisperse aerosols. *Ann. Occup. Hyg.*, 196, 32(suppl. 1), 919-938.
5. Hinds, W.C. Properties, Behavior and Measurement of Airborne Particles, 2nd Ed., Wiley-Interscience, NY, USA, 1999.
6. Harris, A.S., Nilsson, I.M., Wagner, Z.G. and Alkner, U. Intranasal administration of peptides: nasal deposition, biological response and absorption of desmopressin. *J. Pharm. Sci.*, 1986, 75, 1085-1088.
7. Frey, W.H. Intranasal delivery: By-passing the blood-brain barrier to deliver therapeutic agents to the brain and spinal cord. *Drug Delivery Technol.*, 2002, 46-49.
8. Suman, J.D., Laube, B.L. and Dalby, R. Comparison of nasal deposition and clearance of aerosol generated by a nebulizer and an aqueous spray pump. *Pharm. Res.*, 1999, 16, 1648-1652.
9. Yu, C.D., Jones, R.E. and Henesian, M. Cascade impactor method for the droplet size characterization of a metered-dose nasal spray. *J. Pharm. Sci.*, 1984, 73, 344-348.
10. Clark, A. and Borgström, L. *In vitro* testing of pharmaceutical aerosols and predicting lung deposition from *in vitro* measurements. *In: H. Bisgaard, C. O'Callaghan, and G.C. Smaldone. Eds., Drug Delivery to the Lung*. Marcel Dekker, NY, USA, 2002, 105-142.
11. Suman, J.D., Laube, B.L., Lin, T-C., Brouet, G. and Dalby, R. Are *in vitro* tests of nasal solutions predictive of *in vivo* deposition? *In: R.N. Dalby, P.R. Byron, S.J. Farr and J. Peart. Eds., Respiratory Drug Delivery – VII*. Serentec Press, Raleigh, NC, USA, 2000, 137-144.
12. USP 28-NF 23. Chapter 601 – Physical tests and determinations: Aerosols. *United States Pharmacopeia*, Rockville, MD, USA, 2005, 2359-2377.
13. European Pharmacopeia. Section 2.9.18 – Preparations for inhalation: aerodynamic assessment of fine particles. *European Pharmacopeia: 4th Edn.*, Council of Europe, 67075 Strasbourg, France, 2002.
14. Newhouse, M.T. The current laboratory determination of ‘respirable mass’ is not clinically relevant. *J. Aerosol Med.*, 1998, 11S1, 122-132.
15. Zanen, P. and Laube, B. Targeting the Lungs with Therapeutic Aerosols. *In: Bisgaard, H., O'Callaghan, C. and G.C. Smaldone Eds., Drug Delivery to the Lung*. Marcel Dekker, NY, USA, 2002, 211-268.
16. Mitchell, J.P. and Nagel, M.W. Time-of-flight aerodynamic particle size analyzers: Their use and limitations for the evaluation of medical aerosols. *J. Aerosol Med.*, 1999, 12, 217-240.
17. US Pharmacopeial Convention. In-Process Revision <601> Aerosols, nasal sprays, metered-dose inhalers, and dry powder inhalers. *Pharm. Forum*, 2003, 29, 1176-1210.
18. European Pharmacopoeia Commission. Preparations for inhalation: Apparatus E, *PharmEuropa*, 2003, 15, 555-562.
19. Newman, S.P. and Kenyon, C.J. Asthma products bioequivalence. *Pharm. J.*, 1994, 253, 42.
20. Canadian Standards Association. Spacers and holding chambers for use with metered-dose inhalers. Canadian Standards Association, Mississauga, Ontario, Canada, 2002 CAN/CSA/Z264.1-02.
21. Christopher, D., Curry, P. Doub, W., Furnkranz, K., Lavery, M., Lin, K., Lyapustina, S., Mitchell, J., Rogers, B., Strickland, H., Tougas, T., Tsong, Y. and Wyka, B. Considerations for the development and practice of cascade impaction testing including a mass balance failure investigation tree. *J. Aerosol Med.*, 2003, 16, 235-247.
22. Dewsbury, N.J., Kenyon, C.J. and Newman, S.P. The effect of handling techniques on electrostatic charge on spacer devices: a correlation with *in vitro* particle size analysis. *Int. J. Pharm.*, 1996, 137, 261-264.

23. Byron, P.R., Peart, J. and Staniforth, J.N. Aerosol electrostatics I: Properties of fine powders before and after aerosolization by dry powder inhalers. *Pharm. Res.*, 1997, 14, 698-705.
24. Hindle, M., Jashnani, R.N. and Byron, P.R. Dose emissions from marketed inhalers: Influence of flow, volume and environment. In: R.N. Dalby, P.R. Byron, and S.J. Farr Eds., *Respiratory Drug Delivery – IV*. Interpharm Press Inc., Buffalo Grove, IL, USA, 137-142.
25. Comité Européen de Normalisation. Respiratory therapy equipment – Part 1: Nebulizing systems and their components. prEN 13544-1. CEN Brussels, Belgium, 2001, 33-38.
26. Dennis, J.H. Standardization issues: *In vitro* assessment of nebulizer performance. *Respir. Care*, 2002, 47, 1445-1458.
27. Dolovich, M. and Rhem, R. Impact of oropharyngeal deposition on inhaled dose. *J. Aerosol Med.*, 1998, 11(S1), 112-115.
28. Smaldone, G.C. and Le Soeuf, P. Nebulization: The device and clinical considerations. In: Bisgaard, H., O'Callaghan, C. and G.C. Smaldone Eds., *Drug Delivery to the Lung*. Marcel Dekker, NY, USA, 2002, 269-302.
29. Mitchell, J.P. and Nagel, M.W. Spacer and holding chamber testing *in vitro*: A critical analysis with examples. In: R.N. Dalby, P.R. Byron, S.J. Farr and J. Peart. Eds., *Respiratory Drug Delivery – VII*. Serentec Press, Raleigh, NC, USA, 2000, 265-273.
30. Finlay, W.H. Inertial sizing of aerosol inhaled during pediatric tidal breathing from an MDI with attached holding chamber. *Int. J. Pharm.*, 1998, 168, 147-152.
31. Finlay, W.H. and Zuberbuhler, P. *In vitro* comparison of salbutamol hydrofluoroalkane (Airomir) metered dose inhaler aerosols inhaled during pediatric tidal breathing from five valved holding chambers. *J. Aerosol Med.*, 1999, 12(4), 285-291.
32. Finlay, W.H. and Zuberbuhler, P. *In vitro* comparison of beclomethasone and salbutamol metered-dose inhaler aerosols inhaled during pediatric tidal breathing from four valved holding chambers. *Chest.*, 1999, 114(6), 1676-1680.
33. Finlay, W.H. and Gehmlich, M.G. Inertial sizing of aerosol inhaled from two dry powder inhalers with realistic breath patterns versus constant flow rates. *Int. J. Pharm.*, 2000, 210, 83-95.
34. Foss, S.A. and Keppel, J.W. *In vitro* testing of MDI spacers: A technique for measuring respirable dose output with actuation in-phase or out-of-phase with inhalation. *Respir. Care*, 1999, 44(12), 1474-1485.
35. Brindley, A., Marriott, R.M., Sumbly, B.S. and Smith, I.J. The Electronic Lung: A novel tool for the characterization of inhalation devices. *J. Pharm. Pharmacol.*, 1994, 45(S3), 1-35.
36. Burnell, P.K.P., Malton, A. Reavill, K. and Ball, M.H.E. Design, validation and initial testing of the Electronic Lung Device. *J. Aerosol Sci.*, 1998, 29(8), 1011-1025.
37. Fink, J.B. and Dhand, R. Laboratory evaluation of metered-dose inhalers with models that simulate interaction with the patient. *Resp. Care Clinics of North America*, 2001, 7, 303-317.
38. Smaldone, G.C., Fuhrer, J., Steigbigel, R.T. and McPeck, M. Characteristics of nebulizers used in the treatment of AIDS-related *pneumocystis carinii* pneumonia. *J. Aerosol Med.*, 1988, 1, 113-126.
39. Massoud, O., Martin, G.P., Marriott, C. and Nichols, S. The *in vitro* assessment of aerosolized drug deposition using novel oropharyngeal models. In: *Drug Delivery to the Lungs – XIII*. Aerosol Society, London, UK, 2002, 27-30.
40. Stapleton, K.W., Guentsch, E., Hoskinson, M.K. and Finlay, W.H. On the suitability of κ - ϵ turbulence modeling for aerosol deposition in the mouth and throat: A comparison with experiment. *J. Aerosol Sci.*, 2000, 31, 739-749.
41. Janssens H.M., De Jongste J.C., Fokkens W.J., Robben S.G.F., Wouters K., Tiddens H.A.W.M. The Sophia anatomical infant nose-throat (SAINT) model: a valuable tool to study aerosol deposition in infants. *J. Aerosol Med.*, 2001, 14, 433-441.
42. Olsson, B., Borgström, L., Asking, L. and Bondesson, E. Effect of inlet throat on the correlation between measured fine particle dose and lung deposition. In: R.N. Dalby, P.R. Byron and S.J. Farr, Eds., *Respiratory Drug Delivery – V*. Interpharm Press, Buffalo Grove, IL, USA, 996, 273-281.
43. Nagel, M.W., Schmidt, J.N., Doyle, C.C., Varallo, V.M. and Mitchell, J.P. *In Vitro* Performance of a New Non-Electrostatic Transparent Valved Holding Chamber (VHC). In: *Drug Delivery to the Lungs – XIV*, London, UK, December 2003, 71-74.
44. Fink, J.B., Dhand, R. Duarte, A.G., Jenne, J.W., and Tobin, M.J. Aerosol delivery from a metered-dose inhaler during mechanical ventilation: An *in vitro* model. *AM. J. Respir. Crit. Care Med.*, 1996, 154, 382-387.
45. Brockmann, J.E. Sampling and transport of aerosols. In: K. Willeke and P.A. Baron Eds., *Aerosol Measurement: Principles, Techniques and Applications*, Van Nostrand Reinhold, NY, USA, 1993, 77-111.
46. Finlay, W.H. and Stapleton, K.W. Undersizing of droplets from a vented nebulizer caused by aerosol heating during transit through an Andersen impactor. *J. Aerosol Sci.*, 1999, 30, 105-109.
47. Niven, R.W. Aerodynamic particle size analysis testing using a time-of-flight aerosol beam spectrometer. *Pharm. Technol.*, 1993, 72-78.
48. de Boer, A.H., Gjaltema, D., Hagedoorn, P. and Frijlink, H.W. Characterization of inhalation aerosols: A critical evaluation of cascade impactor and laser diffraction technique. *Int. J. Pharm.*, 2002, 249, 219-231.
49. Nerbrink, O., Dahlbäck, M. and Hansson, H-C. Why do medical nebulizers differ in their output and particle size characteristics? *J. Aerosol Med.*, 1994, 7, 259-276.
50. Corcoran, T.E., Hitron, R., Humphrey, W. and Chigier, N. Optical measurement of nebulizer sprays: A quanti-

- tative comparison of diffraction, phase Doppler interferometry, and time-of-flight techniques. *J. Aerosol Sci.*, 2000, 31, 35-50.
51. Clark, A.R. The use of laser diffraction for the evaluation of the aerosol clouds generated by medical nebulizers. *Int. J. Pharm.*, 1995, 115, 69-78.
 52. Mitchell, J.P. and Nagel, M.W. Cascade impactors for the size characterization of aerosols from medical inhalers; Their uses and limitation. *J. Aerosol Med.*, 2003, 16, 341-376.
 53. Marple, V.A. A Fundamental study of inertial impactors. Ph.D. thesis, University of Minnesota, Minneapolis, MN, USA, 1970.
 54. Marple, V.A. and Liu, B.Y.H. Characteristics of laminar jet impactors. *Environ. Sci. Technol.*, 1974, 8, 648-654.
 55. Rader, D.J. and Marple, V.A. Effect of ultra-Stokesian drag and particle interception on impaction characteristics. *Aerosol Sci. Technol.*, 1985, 4, 141-156.
 56. Picknett, R.G. A new method of determining aerosol size distributions from multistage sampler data. *J. Aerosol Sci.*, 1972, 3, 185-198.
 57. American Industrial Hygiene Association. J.Y. Young, Ed., Particle sampling using cascade impactors: Some practical application notes. AIHA Publications, Fairfax, VA, USA, 1995.
 58. Marple, V.A., Olson, B.A., Santhanakrishnan, K., Mitchell, J.P., Murray, S. and Hudson-Curtis, B. Next Generation Pharmaceutical Impactor. Part II: Calibration. *J. Aerosol Med.*, 2003, 16, 301-324.
 59. Rader, D.J. and Marple, V.A. Effect of gravitational forces on the calculation of impactor efficiency curves. In B.Y.H. Liu, D.Y.H. Pui and H.J. Fissan, Eds., *Aerosols*. Elsevier. N.Y., USA, 1984, 123-126.
 60. Marple, V.A., Olson, B.A., Santhanakrishnan, K., Roberts, D.L., Mitchell, J.P., and Hudson-Curtis, B. In: *Drug Delivery to the Lungs – XIV*, The Aerosol Society, London, UK, 2003, 37-40.
 61. Fang, C.P., Marple, V.A. and Rubow, K.L. Influence of Cross-flow on Particle Collection Characteristics of Multi-nozzle Impactors. *J. Aerosol Sci.*, 1991, 22, 403-415.
 62. Marple, V.A., Roberts, D.L., Romay, F.J., Miller, N.C., Truman, K.G., Van Oort, M., Olsson, B., Holroyd, M.J., Mitchell, J.P. and Hochrainer, D. Next Generation Pharmaceutical Impactor. Part 1: Design. *J. Aerosol Med.*, 2003, 16, 283-299.
 63. Marple, V.A., Olson, B.A. and Miller, N.C. The role of inertial particle collectors in evaluating pharmaceutical aerosol delivery systems. *J. Aerosol Med.*, 1998, 11S1, 139-153.
 64. Mitchell, J.P. Aerosol generation and instrument calibration. In: I. Colbeck Ed., *Physical and Chemical Properties of Aerosols*. Blackie Academic and Professional, London, UK, 1998, 31-79.
 65. Vaughan, N.P. The Andersen impactor: Calibration, wall losses and numerical simulation. *J. Aerosol Sci.*, 1989, 20, 67-90.
 66. Mitchell, J.P., Costa, P.A. and Waters, S. An assessment of an Andersen Mark-II cascade impactor. *J. Aerosol Sci.*, 1987, 19, 213-221.
 67. Nichols, S.C., Brown, D.R. and Smurthwaite, M. New concept for the variable flow rate Andersen cascade impactor and calibration data. *J. Aerosol Med.*, 1998, 11(S1), 133-138.
 68. Nichols, S.C. 2000. Calibration and mensuration issues for the standard and modified impactor. *Pharmeuropa.*, 2000, 585.
 69. Marple, V.A., Olson, B.A. and Miller, N.C. A low-loss cascade impactor with stage collection cups: Calibration and pharmaceutical inhaler applications. *Aerosol Sci. Technol.* 1995, 22, 124-134.
 70. Olson, B.A., Marple, V.A., Mitchell, J.P. and Nagel, M.W. Development and calibration of a low-flow version of the Marple-Miller impactor. *Aerosol Sci. Technol.*, 1998, 29, 307-314.
 71. Asking, L. and B. Olsson. Calibration at different flow rates of a multistage liquid impinger. *Aerosol Sci. Technol.*, 1997, 27, 39-49.
 72. Fairchild, C.I. and Wheat, L.D. Calibration and evaluation of a real time cascade impactor. *Am. Ind. Hyg. Assoc. J.*, 1984, 45, 205-211.
 73. Horton, K.D., Ball, M.H.E. and Mitchell, J.P. The calibration of a California Measurements PC-2 quartz crystal cascade impactor (QCM). *J. Aerosol Sci.*, 1992, 23, 505-524.
 74. Marple, V.A., Rubow, K.L. and Behm, S.M. A microorifice uniform deposit impactor (MOUDI): Description, Calibration and Use. *Aerosol Sci. Technol.*, 1991, 14, 434-446.
 75. Peart, J., Byron, P.R., Staehler, T.S., and Clarke, M.J. Pressure-drop measurements made during testing of dry powder inhalers. *Pharm. Forum*, 1997, 23, 3543-3546.
 76. Olsson, B. and L. Asking. Methods of setting and measuring flow rates in pharmaceutical impactor experiments. In: *Drug Delivery to the Lungs – XIII*. Aerosol Society, London, UK, 2002, 168-171.
 77. Huang, C-H and Tsai, C-J. Effect of gravity on particle collection efficiency of inertial impactors. *J. Aerosol Sci.*, 2001, 32, 375-387.
 78. Mitchell, J.P. Regarding the development and practice of cascade impaction testing, including a mass balance failure investigation tree. *J. Aerosol Med.*, 2004, 16, 431.
 79. May, K.R. The cascade impactor: An instrument for sampling coarse aerosols. *J. Sci., Instrum.*, 1945, 22: 187-194.
 80. Rao, A.K. and Whitby. K.T. Non-ideal collection characteristics of inertial impactors – Single stage impactors and solid particles. *J. Aerosol Sci.*, 1978, 9, 77-86.
 81. Rao, A.K. and Whitby. K.T. Non-ideal collection characteristics of inertial impactors – Cascade impactors. *J. Aerosol Sci.*, 1978, 9, 87-100
 82. Esmen, N.A. and Lee, T.C. Distortion of cascade impactor measured size distribution due to bounce and blow-off. *Am. Ind. Hyg. Assoc. J.*, 1980, 41, 410-419.
 83. Byron, P.R. Compendial dry powder testing: USP per-

- spectives. *In: P.R. Byron, R.N. Dalby and S.J. Farr Eds., Respiratory Drug Delivery IV*. Interpharm Press, Buffalo Grove, IL, USA, 1994, 153-162.
84. Dunbar, C.A., Hickey, A.J. and Holzner, P. Dispersion and Characterization of pharmaceutical dry powder aerosols. *KONA*, 1998, 16, 7-45.
 85. Mitchell, J.P. Practices of coating collection surfaces of cascade impactors: A survey of members of the European Pharmaceutical Aerosol Group (EPAG). *In: Drug Delivery to the Lungs – XIV*. Aerosol Society, London, UK, 2003, 75-78.
 86. Nasr, M.M., Ross, D.L. and Miller, N.C. Effect of drug load and plate coating on the particle size distribution of a commercial albuterol metered dose inhaler (MDI) determined using the Andersen and Marple-Miller impactors. *Pharm. Res.*, 1997, 14, 1437-1443.
 87. Nasr, M.M. and Allgire, J.F. Loading effect on particle size measurements by inertial sampling of albuterol metered dose inhalers. *Pharm. Res.*, 1995, 12, 1677-1681.
 88. Kamiya A, Sakagami M, Hindle M, Byron PR. Particle sizing with the next generation impactor: a study of Vanceryl™ metered dose inhaler. *J. Aerosol Med.*, 2003, 16, 216.
 89. Mitchell, J.P., Nagel, M.W., Wiersema, K.J., and Doyle, C.C. Aerodynamic Particle Size Analysis of Aerosols from Pressurized Metered-Dose Inhalers: Comparison of Andersen 8-Stage Cascade Impactor, Next Generation Pharmaceutical Impactor, and Model 3321 Aerodynamic Particle Sizer Aerosol Spectrometer, *AAPS PharmSciTech.*, 2003, 4, article 54 (available at <http://www.aapspharmscitech.org>).
 90. Asking, L. and Nichols, S. Next Generation Pharmaceutical Impactor (NGI): EPAG collaborative study. *In: Drug Delivery to the Lungs – XIV*. Aerosol Society, London, UK, 2003, 33-36.
 91. Baron, P.A., Mazumder, M.K. and Cheng, Y.S. Direct-reading techniques using optical particle detection. *In: K. Willeke and P.A. Baron, eds. Aerosol Measurement: Principles, Techniques and Applications*. Van Nostrand Reinhold, N.Y., 1993, 381-409.
 92. Mitchell, J.P. and Nagel, M.W. Time-of-Flight Aerodynamic Particle Size Analyzers: Their Use and Limitations for the Evaluation of Medical Aerosols, *J. Aerosol Med.*, 1999, 12, 217-239.
 93. Wilson, J.C. and Liu, B.Y.H. Aerodynamic particle size measurement by laser-Doppler velocimetry. *J. Aerosol Sci.*, 1980, 11, 139-150.
 94. Remiarz, R.J., Agarwal, J.K., Quant, F.R. and Sem, G.J. Real-time aerodynamic particle size analyzer. *In: V.A. Marple and B.Y.H. Liu Eds. Aerosols in the Mining and Industrial Work Environments. Vol. 3.*, Ann Arbor Science, Ann Arbor, MI., 1983, 879-895.
 95. Heitbrink, W.A., Baron, P.A. and Willeke, K. Coincidence in time-of-flight spectrometers: phantom particle creation. *Aerosol Sci. Technol.*, 1991, 14, 12-26.
 96. Heitbrink, W.A. and Baron, P.A. An approach to evaluating and correcting aerodynamic particle sizer measurements for phantom particle count creation. *Am. Ind. Hyg. Assoc. J.*, 1992, 53, 427-431.
 97. Hairston, P.P., Dorman F.D., Sem, G.J. and Agarwal, J.K. Apparatus for measuring particle sizes and velocities. 1996, U.S. Patent 5, 561, 515.
 98. Stein, S.W., Gabrio, B.J., Oberreit, D.R., Hairston, P.P., Myrdal, P.B. and Beck, T.J. An evaluation of mass-weighted size distribution measurements with the model 3320 Aerodynamic Particle Sizer. *Aerosol Sci. Technol.*, 2002, 36, 845-854.
 99. Stein, S.W., Beck, T.J. and Gabrio, B.J. Evaluation of a new aerodynamic particle sizer for MDI size distribution measurements. *In: R.N. Dalby, P.R. Byron, S.J. Farr and J. Peart. Eds., Respiratory Drug Delivery – VII*. Serentec Press, Raleigh, NC, USA, 2000, 283-286.
 100. Dahneke, B. Aerosol beam spectrometry. *Nature Phys. Sci.*, 1973, 244: 54-55.
 101. Dahneke, B. and Padiya, D. 1977. Nozzle-inlet design for aerosol beam. *In: J.L. Potter Ed., Rarefied Gas Dynamics*. A.I.A.A., N.Y., 1977, 51, 1163-1172.
 102. Dahneke, B. and Cheng, Y.S. Properties of continuum source particle beams. I. Calculation methods and results. *J. Aerosol Sci.* 1979, 10, 257-274.
 103. Cheng, Y.S. and Dahneke, B. 1979. Properties of continuum source particle beams. II. Beams generated in capillary expansion. *J. Aerosol Sci.*, 1979, 10, 363-368.
 104. Mitchell, J.P. Particle standards: Their development and application. *KONA*, 2000, 18, 41-59.
 105. Armendariz, A.J. and Leith, D. Concentration measurement and counting efficiency for the Aerodynamic Particle Sizer® 3320. *J. Aerosol Sci.*, 2002, 33, 133-148.
 106. Peters, T.M. and Leith, D. Concentration measurement and counting efficiency of the Aerodynamic Particle Sizer® 3321. *J. Aerosol Sci.*, 2003, 34, 627-634.
 107. Bouchikhi, A., Becquemin, M.H., Bignon, J., Roy, M. and Teillac, A. Particle size study of nine metered dose inhalers, and their deposition probabilities in the airways. *Eur. Resp. J.*, 1988, 1, 547-552.
 108. Mitchell, J.P., Nagel, M.W. and Cheng, Y.S. Use of the Aerosizer® aerodynamic particle size analyzer to characterize aerosols from pressurized metered-dose inhalers for medication delivery. *J. Aerosol Sci.*, 1999, 30, 467-477.
 109. Thornberg, J., Cooper, S.J. and Leith, D. 1999. Counting efficiency of the API Aerosizer®. *J. Aerosol Sci.*, 1999, 30, 479-488.
 110. Stein, S.W., Myrdal, P.B., Gabrio, B.J., Oberreit, D. and Beck, T.J. Evaluation of a new Aerodynamic Particle Sizer® spectrometer for size distribution measurements of solution metered dose inhalers. *J. Aerosol Med.*, 2003, 16, 107-119.
 111. Cheng, Y.S., Chen, B.T. and Yeh, H-C. A study of density effect and droplet deformation in the TSI Aerodynamic Particle Sizer®. *Aerosol Sci. Technol.*, 1990, 12, 278-285.
 112. Griffiths, W.D., Iles, P.J. and Vaughan, N.P. The behavior of liquid droplets in an APS® 3300. *J. Aerosol Sci.*, 1986, 17, 921-930.
 113. Marshall, I.A., Mitchell, J.P. and Griffiths, W.D. The

- behavior of regular-shaped non-spherical particles in a TSI Aerodynamic Particle Sizer[®]. *J. Aerosol Sci.*, 1991, 22, 73-89.
114. Cheng, Y.S., Barr, E.B., Marshall, I.A. and Mitchell, J.P. Calibration and performance of an API Aerosizer[®]. *J. Aerosol Sci.*, 1993, 24, 501-514.
 115. Ananth, G. and Wilson, J.C. Theoretical analysis of the performance of the TSI Aerodynamic Particle Sizer[®]. *J. Aerosol Sci.*, 1988, 9, 89-199.
 116. Wang, H. and John, W. Particle density correction for the Aerodynamic Particle Sizer[®]. *Aerosol Sci. Technol.*, 1987, 6, 191-198.
 117. Cheng, Y.S., Chen, B.T. and Yeh, H-S. Performance of an Aerodynamic Particle Sizer[®]. *Appl Occup. Environ. Hyg.*, 1993, 8, 307-312.
 118. Tzou, T-Z. and Schultz, R.K. Use and limitations of the Aerosizer[®] in measuring the aerodynamic particle size of MDIs. *Pharm. Res.*, 1993, 10, S167.
 119. Mitchell, J.P. Nagel, M.W. and Archer, A. Size analysis of a pressurized metered dose inhaler (pMDD)-delivered suspension formulation by the API Aerosizer[®] time-of-flight aerodynamic particle size analyzer. *J. Aerosol Med.*, 1999, 12, 255-264.
 120. Tiwari, D., Goldman, D., Malick, W.A. and Madan, P.L. Formulation and evaluation of abuterol metered dose inhalers containing tetrafluoroethane (P134a), a non-CFC propellant. *Pharm. Dev. and Technol.*, 1998, 3, 163-174.
 121. Gupta, A., Myrdal, P.B., Stein, S.W., Gabrio, B.J. and Beck, T.J. Comparison of the TSI model 3306 impactor inlet with the Andersen cascade impactor by testing solution metered dose inhalers. *In: R.N. Dalby, P.R. Byron, Peart, J. and S.J. Farr Eds., Respiratory Drug Delivery VIII.* Davis Horwood International, Raleigh, NC, USA, 2002, 659-662.
 122. Etzler, F.M. and Sanderson, M.S. Particle size analysis: a comparative study of various methods. *Part. Part. Syst. Charact.*, 1995, 12, 217-224.
 123. Hindle, M. and Byron, P.R. Size distribution control of raw materials for dry-powder inhalers using the Aerosizer[®] with the AeroDispenser[®]. *Pharm. Technol.*, 1995, 19, 64-78.
 124. Rader, D.J. and O'Hern, T.J. Optical direct-reading techniques: *In situ* sensing. *In: K. Willeke and P.A. Baron Eds., Aerosol Measurement: Principles, Techniques and Applications*, Van Nostrand Reinhold, NY, USA, 1993, 345-380.
 125. Loffert, D.T., Ikle, D. and Nelson, H.S. A comparison of commercial jet nebulizers. *Chest*, 1994, 106, 1788-1792.
 126. Swithenbank, J., Beer, J.M., Taylor, D.S., Abbot, D. and McCreath, C.G. A Laser Diagnostic Technique for the Measurement of Droplet and Particle Size Distribution, *Prog. Astronaut. Aeronaut.*, 1977, 53, 421-447.
 127. Ward-Smith, S. and Wedd, M. Determination of continuous particle size distributions of concentrated sprays. *Amer. Lab.*, 1999, 17-21.
 128. Krarup, H.G., Bumiller, M and Stauffer, T. The Malvern Spraytec[®] applied to pharmaceutical spray analysis. *In: R.N. Dalby, P.R. Byron, Peart, J. and S.J. Farr Eds., Respiratory Drug Delivery VIII.* Davis Horwood International, Raleigh, NC, USA, 2002, 505-508.
 129. Smyth, H.D.C. and Hickey, A.J. Dynamic particle size distributions emitted from pMDIs as determined by laser diffraction: A function of time and space. *In: R.N. Dalby, P.R. Byron, Peart, J. and S.J. Farr Eds., Respiratory Drug Delivery VIII.* Davis Horwood International, Raleigh, NC, USA, 2002, 727-730.
 130. Nerbrink, O., Dahlbäck, M. and Hansson, H-C. Why do medical nebulizers differ in their output and particle size characteristics? *J. Aerosol Med.*, 1994, 7, 259-276.
 131. Moslemi, P., Najafabadi, A.R. and Tajerzadeh, H. Evaluations of different parameters that affect droplet size distribution of nasal gel sprays. *In: R.N. Dalby, P.R. Byron, Peart, J. and S.J. Farr Eds. Respiratory Drug Delivery VIII.* Davis Horwood International, Raleigh, NC, USA, 2002, 619-622.
 132. International Standards Organization. Particle size analysis – laser diffraction methods: Part 1: General principles. ISO Geneva, Switzerland, 13320-1, 1999.
 133. Scarlett, B. Measuring and interpreting particle size distribution. *Am. Pharm. Rev.*, 2003, 6, 93-101.
 134. Brittain, H.G. Particle size distribution IV: Determination by laser light scattering. *Pharm. Technol.*, 2003, 102-114, available at www.pharmtech.com.
 135. Meyer, P. and Chigier, N. Dropsizes measurements using a Malvern 2200 particle sizer. *Atom. Spray Technol.*, 1986, 2, 261-298.
 136. Bayvel, L.P., Knight, J. and Robertson, G. Alternative model-independent inversion programme for Malvern particle sizer. *Part. Charact.*, 1987, 4, 49-53.
 137. Annapragada, A. and Adjei, A. An analysis of the Fraunhofer diffraction method for particle size distribution analysis and its application to aerosolized sprays. *Int. J. Pharm.*, 1996, 127, 219-227.
 138. Van de Hulst, H.C. Light Scattering by Small Particles. Dover, N.Y., 1981.
 139. Merkus, H.G., Marijnissen, J.C.M., Jansma, E.H.L. and Scarlett, B. Droplet size distribution measurements for medical nebulizers by the forward light scattering technique (laser diffraction). *J. Aerosol Sci.*, 1994, 25S1, 319-320.
 140. Kwong, W.T.J., Ho, S.L. and Coates, A.L. Comparison of nebulized particle size distribution with Malvern laser diffraction analyzer versus Andersen cascade impactor and low-flow Marple personal cascade impactor. *J. Aerosol Med.*, 2000, 13, 303-314.
 141. Mitchell, J.P., Nagel, M.W., Bates, S.L. and Doyle, C.C. An *in vitro* study to investigate the use of a breath-actuated small-volume, pneumatic nebulizer for the delivery of methacholine chloride bronchoprovocation agent. *Respir. Care*, 2003, 48, 46-51.
 142. Smart, J., Berg, E., Nerbrink, O., Zuban, R., Blakey, D. and New, M. Touchspray[™] technology: A comparison of the droplet size measured by cascade impaction and laser diffraction. *In: R.N. Dalby, P.R. Byron, Peart, J.*

- and S.J. Farr Eds. *Respiratory Drug Delivery VIII*. Davis Horwood International, Raleigh, NC, USA, 2002, 525-527.
143. Wolfgang, J. A laser diffraction particle size analyzer with integrated modules for use with various inhalation drug delivery devices. *In: R.N. Dalby, P.R. Byron, S.J. Farr and J. Peart. Eds., Respiratory Drug Delivery – VII*. Serentec Press, Raleigh, NC, USA, 2000, 535-537.
 144. Mühlenweg, H. and Hirleman, E.D. Reticles as standards in laser diffraction spectroscopy. *Part. Part. Syst. Charact.*, 1999, 16, 47-53.
 145. Hirleman, E.D., Oechsle, V. and Chigier, N.A. Response characteristics of laser diffraction particle size analyzers. *Opt. Eng.*, 1984, 23, 610-619.
 146. Wachtel, H. and Ziegler, J. Improved assessment of inhaler device performance using laser diffraction. *In: R.N. Dalby, P.R. Byron, Peart, J. and S.J. Farr Eds., Respiratory Drug Delivery VIII*. Davis Horwood International, Raleigh, NC, USA, 2002, 379-381.
 147. Davies, P., Derbyshire, D., Kotsokechagia, T. and Shaikh, T. Novel method for screening DPI and MDI formulations using experimental design and laser diffraction. *In: Drug Delivery to the Lungs – XIV*. Aerosol Society, London, UK, 2003, 144-147.
 148. De Boer, A.H., Gjaltema, D., Hagedoorn, P., Schaller, M., Witt, W. and Frijlink, H.W. Design and application of a new modular adapter for laser diffraction characterization of inhalation aerosols. *Int. J. Pharm.*, 2002, 249, 233-245.
 149. Ranucci, J. Dynamic plume-particle size analysis using laser diffraction. *Pharm. Technol.*, 1992, 108-114.
 150. Sharpe, S., Hart, J. and Sequeira, J. Effect of formulation and device on particle/droplet size distribution of metered dose inhaler (MDI) products measured by laser diffraction. *In: R.N. Dalby, P.R. Byron, Peart, J. and S.J. Farr Eds., Respiratory Drug Delivery VIII*. Davis Horwood International, Raleigh, NC, USA, 2002, 577-579.
 151. Ziegler, J. and Wachtel, H. Particle size measurement techniques for pharmaceutical device development. *In: Drug Delivery to the Lungs – XII*. Aerosol Society, London, UK, 2001, 54-57.
 152. Ding, J.Y., McVeety, B.D., Busick, D.R., Miller, P.R., Zimlich, W.C. and Placke, M.E. Correlation of particle size distribution measurements between optical and inertial impaction techniques using an ethanolic drug formulation for inhalation. *In: R.N. Dalby, P.R. Byron, Peart, J. and S.J. Farr Eds. Respiratory Drug Delivery VIII*. Davis Horwood International, Raleigh, NC, USA, 2002, 355-358.
 153. Haynes, A., Shaik, M.S., Krarup, H. and Singh, M. Evaluation of the Malvern Spraytec® with inhalation cell for the measurement of particle size distribution from metered dose inhalers. *J. Pharm. Sci.*, 2004, 93, 349-363.
 154. Holmes, C.E., Kippax, P.G., Newell, H.E., Southall, J.P. and Ward, D.J. Simultaneous analysis of respirable aerosols via laser diffraction and cascade impaction. *In: Drug Delivery to the Lungs – XII*. Aerosol Society, London, UK, 2001, 58-61.
 155. Smyth, H.D.C. and Hickey, A.J. Comparative particle size analysis of solution propellant driven metered dose inhalers using cascade impaction and laser diffraction. *In: R.N. Dalby, P.R. Byron, Peart, J. and S.J. Farr Eds., Respiratory Drug Delivery VIII*. Davis Horwood International, Raleigh, NC, USA, 2002, 731-734.
 156. Corr, D., Dolovich, M., McCormack, D., Ruffin, R., Obminski, G. and Newhouse, M. Design and characteristics of a portable breath actuated, particle size selective medical aerosol inhaler. *J. Aerosol Sci.*, 1982, 13, 1-7.
 157. Bachalo, W.D. and Hauser, M.J. Phase Doppler Spray Analyzer for Simultaneous Measurements of Drop Size and Velocity Distributions, *Opt. Eng.*, 1984, 23, 583-590.
 158. Stapleton, K.W., Finlay, W.H. and Zuberbuhler, P. An *In-Vitro* Method for Determining Regional Dosages Delivered by Jet Nebulizers, *J. Aerosol Med.*, 1994, 7, 325-344.
 159. Dunbar, C.A., Watkins, A.P. and Miller, J.F. An experimental investigation of the spray issued from a pMDI using laser diagnostic techniques. *J. Aerosol Med.*, 1997, 10, 351-368.

Author's short biography



J.P. Mitchell

Jolyon Mitchell is currently Scientific Director of Trudell Medical International, with responsibility for all aspects of *in vitro* aerosol testing. During the past 10 years, he has built up the laboratory to the point at which more than 130 publications have been produced for the open literature, many of which have appeared in peer-reviewed journals. He is involved in several industry-wide organizations involved with inhaled medical aerosol delivery, including the European Pharmaceutical Aerosol Group (EPAG) and the US Product Quality Research Institute (PQRI). He has participated in the development of a new Standard for Spacers and Holding Chambers, developed by the Canadian Standards Association, and is currently a Canadian delegate to ISO/TC84/WG5, involved with the development of a new standard for aerosol-based inhalers. He is a member of the American Association of Pharmaceutical Scientists (Inhalation Technology Focus Group) and is on the Editorial Advisory Board of *Journal of Aerosol Medicine*.

Since graduating from the University of Salford in the United Kingdom with a doctorate in physical chemistry in 1976, he has had approaching 20 years experience in the measurement and control of aerosols, initially as an experimentalist and more recently as coordinator of major projects involved with standards and calibration of aerosol measuring equipment. He joined the UK Atomic Energy Authority in 1980 to undertake research into the release and subsequent behavior of aerosols that might be released from severe nuclear reactor accidents. This work involved developing several measurement devices and tools for their calibration, and subsequently evolved into initiatives concerned with the development of new particle standards. As Manager of the Aerosol Science Centre, he coordinated the first phase of a UK government initiative to apply the principles of valid analytical measurement to the assessment of aerosols. He joined Trudell Medical International in 1994 to develop their medical aerosol laboratory. He played a significant part in the development and archival calibration of the Next Generation Pharmaceutical Impactor (NGI).

He has published more than 200 articles in the open literature, of which about 60 are in peer-reviewed journals and 6 are invited review articles. He has also contributed to two books on aerosol science, writing chapters concerned with aerosol measurement techniques and the calibration of aerosol measurement equipment.



M.W. Nagel

Mark Nagel currently holds the position of Laboratory Manager and is responsible for overseeing the operation of the Aerosol Laboratory for Trudell Medical International. In the past 11 years the laboratory he has contributed to several regulatory submissions and he has contributed to over 130 publications, many of which have been published in the peer reviewed literature.

After graduating from the University of Western Ontario with a bachelors degree in Toxicology with Environmental Science in 1993 he joined Trudell Medical International as a Laboratory Technician and 4 years later assumed the role of Laboratory Manager.

The Sevilla Powder Tester: A Tool for Characterizing the Physical Properties of Fine Cohesive Powders at Very Small Consolidations[†]

A. Castellanos, J.M. Valverde,
and M.A.S. Quintanilla
*Facultad de Física. Universidad de Sevilla**

Abstract

We present a fluidized bed apparatus that enables us to test the bulk mechanical properties such as the yield stresses and compressibility of fine cohesive powders. Every measurement is preceded by driving the powder into the bubbling regime in which the material loses memory of its previous history. Then the gas flow is set to a given value to take the powder into a well defined and reproducible initial state of low consolidation. Reverse flow is used to exert high compressive stress. A cornerstone of our technique is that the procedure is automatized, thus making results operator insensitive. Besides being a practical tool to diagnose the flowability of experimental powders, the Sevilla Powder Tester (SPT) also provides us with a powerful technique to research fundamental problems in powder mechanics.

1 Introduction

The mass flow of fine particles is relevant in many industrial fields. It is estimated that 60% of products in the chemical industry are manufactured as particulates and a further 20% use powders as ingredients [1]. In spite of this, most industrial powder processes are dependent on empirical correlations since the link between the physics of local grain interactions and their global mechanical behavior is still poorly understood. A clear example are fluidized beds, which are extensively used whenever a good solid-fluid contact is needed such as in the catalytic cracking of oil, the combustion of coal, drying, mixing, transport, etc. A precise knowledge of the fluidized bed structure and behavior is quite relevant not only from a theoretical point of view but also from the practical point of view.

The behavior of powders can be significantly influenced by particle size, particle deformation, distribution of forces, cohesive and frictional interaction, contact restructuring, aggregation, interstitial gas, etc. The presence of these multiple and usually cooperative features makes the problem of investigating powder behavior from a fundamental perspective a rather complicated challenge, thus empirical ap-

proaches prevail. Most of the empirical studies to characterize powder flow yield numbers which are not clearly related to the fundamental physical properties. More importantly, due to the hysteretic nature of interparticle contact forces, uniform powders are hard to create and the packing arrangement is a strong function of the previous history. Generally speaking, the techniques employed lack a satisfactory way of initializing the powder in order to have an initial reproducible state in which the memory of the powder has been erased. Moreover, the more cohesive the powder, the larger the memory effects are. Consequently, the wide experimental variations in bulk properties at low consolidations measured by the traditional testers preclude a reliable estimation of interparticle forces [2], which are ultimately responsible for the ability of a powder to flow [3].

In this paper we review a Powder Tester apparatus [4] in which the powder sample is conveniently initialized by the use of fluidization. This Powder Tester enables us to investigate fluidization properties such as bed expansion, sedimentation, aggregation of fine particles within the fluidized bed, onset of bubbling for sufficiently large gas flow, transition to a solid-like regime for gas flows smaller than a critical one, etc [5]. For the solid state, in which particle contacts are permanent, the tester measures the uniaxial tensile yield stress of the powder and its average particle volume fraction as a function of the consolidation stress,

* Avenida Reina Mercedes s/n, 41012 Sevilla. Spain.

[†] Accepted: August 26, 2004

which can be controlled in a range spanning from a few to thousands of Pascal by means of forward and reverse controlled gas flow. The behavior of powders during compaction yields information about the mechanism of density increase. From the bulk stresses, we estimate the interparticle contact forces that are well correlated to direct measurements of forces between isolated particles made using a Scanning Force Microscope (SFM) [6]. All the measurements can be done under complete computer control and are fully automated. A further advantage of the SPT for testing experimental powders is that the instrument only needs a small volume of powder (typically around 20 g.).

1.1 Some techniques of analysing powder flowability

Schwedes recently made an extensive review on testers for measuring the bulk flow properties of granular materials [7]. In this section, we highlight some of the most-used techniques in powders from a critical perspective.

1.1.1 Empirical techniques

A traditional way of testing powder flowability is to measure the ability of the powder to flow through standard devices. For example, we find in the *Book of the American Society for Testing and Materials Standards* a technique that consists of measuring the time that a given mass of powder takes to discharge through a hopper [8]. Even though this technique has been proved to be useful for metallic powders, an external energy source such as tapping is needed for very cohesive powders to help powder flow [9]. Vibration, however, may consolidate the powder and, especially in the case of fine particles, this enhances cohesiveness. A similar technique, frequently used for pharmaceutical tableting applications, consists of forcing the powder to pass through rings of decreasing diameters [10]. The flowability index is defined as the diameter of the smaller ring through which the sample can discharge three consecutive times. There is also a commercial rheometer similar to the ones employed to measure the viscosity of liquids, but that has been adapted to test powder flow [11]. The rheometer incorporates a blade with different sections in the opposite sides of a rotation shaft. The first section has its surface parallel to the rotation shaft whereas the second section is twisted relative to the rotation shaft. The Hosokawa Powder Tester [12] is another instrument that has been extensively employed in the xerographic industry to measure toner flowa-

bility. In the Hosokawa test, a number of screens of different sizes are placed vertically and are vibrated. An estimation of the toner flowability is given by the relative mass of powder that passes through each screen.

The success of these techniques is hindered by the difficulty of initializing the powder in an initial reproducible state. Therefore, results are dependent on the history of the powder: i.e. the filling procedure, previously applied stresses, etc. This is particularly important in the case of fine cohesive powders for which interparticle attractive forces may increase by several orders of magnitude with the applied external load [13]. An additional problem is that the interaction of the powder with mechanical parts, such as the blade of a rheometer, may produce a "heterogenous" cohesiveness since the load and shear applied can change abruptly from point to point within the sample. Thus the results achieved depend on the particular design of the device and on the experimental procedure. In addition, the correlation of the experimental results to fundamental physical parameters of the powder remains rather obscure. Therefore, it would be desirable to measure properties more directly linked to fundamental parameters, thus yielding more robust and confident results.

1.1.2 Techniques of analysing powder flowability based on fundamental properties

The powder compressibility has usually been taken as a measure of powder flowability [14]. Granular materials that flow well end up in very dense packings that are quite difficult to compress, whereas poorly flowing powders pack in open structures that can be further compressed with ease. Compaction tests in which a cylindrical plug of powder is compacted axially by a piston are commonly used in civil engineering [15]. A proposed number to classify powder flowability is the Hausner ratio, defined as the ratio of the tapped powder density to the untapped powder density [16].

Most of the situations involving the flow of powders imply the presence of shear stresses. Therefore, some techniques to test powder flowability are focused on measuring the yield stress as the powder sample is sheared. Consider an arbitrary plane through the powder sample and a shear stress τ acting on that plane; there will be a value of stress that will cause the powder to shear off in the plane and cause the powder to flow. This yield stress depends on the normal stress σ acting perpendicular to the plane. In general, τ increases with σ , and the relationship between

τ and σ defines the yield locus of the powder. At high stresses the yield locus can be approximated by a linear function known as Coulomb's law [17]

$$\tau = \sigma \tan \Phi + c \quad (1)$$

where c and Φ are the cohesion and the angle of internal friction. For many coarse granular materials c is negligible.

The point of the yield locus on the negative σ axis is the ultimate tensile strength σ_t . The linear theory is, however, inadequate to describe the behavior of fine cohesive powders at low values of σ and τ that occur in practice. Traditionally, the Jenike shear cell [18] has been used by engineers in powder technology to estimate the angle of internal friction of highly consolidated granular materials. Essentially, the technique consists of compacting a powder sample with a known external load into a cylindrical cell composed of two metal rings one upon the other. With the compaction load still applied, the minimum steady state shear stress necessary to displace the upper ring horizontally with respect to the lower one is measured. Steady state flow means flow at constant density and constant shear stress. These values of normal and shear stresses define the end point of the yield locus. Then the normal load on the powder is decreased and the new horizontal force necessary to initiate shearing of the powder is measured. In order to minimize the influence of the operator, the Jenike cell is commercialized with a reference material with which researchers can check both their equipment and experimental technique. The reference powder consists of "3 kg of limestone powder packed in a polyethylene jar" and is accompanied by a certificate that supplies the limiting shear stress for four different powder normal stresses [19]. However, in a great deal of powder processing equipment there is no significant compressive force while the Jenike cell is inappropriate for low consolidation stresses. The recently developed ring shear tester represents a technical improvement on the Jenike tester in order to measure the yield locus at smaller loads ($< \sim 100$ Pa) [20]. An experimental problem that besets the Jenike cell technique and its modified versions is the lack of a reliable method of producing reproducible initial states. Interparticle contact forces are very sensitive to small variations of the previous external loads. As a result, errors due to poor preparation methods can easily arise. Further disadvantages of the Jenike test are that it must be accepted that the slip plane coincides with a horizontal plane and that the shear process takes place uniformly throughout the sample in order

to relate the stresses to the real stresses inside the material. This is known to be false for overconsolidated materials [21]. A commercial alternative to the Jenike shear cell is the Peschl annular shear cell, in which the shear stress is applied by rotating the top part of an annular shear box containing the powder sample [21]. While this test allows for a constant area of shear and unlimited shear distance, making it useful for quantifying powder flow after failure, wall effects and strong uncertainty in stress distribution are major drawbacks.

Another property that has been employed to quantify powder flow is the angle of repose of a pile of powder [22]. Even though the angle of repose is a well defined property of noncohesive granular materials, it is meaningless when cohesive interaction becomes important. We may remember from our childhood that sand castles can sustain 90° slopes but when we tried to increase the size of the castle, landslides would probably happen that decreased the angle of repose to well below 90° . The influence of the size of the powder sample on the avalanching behavior of fine powders is well documented in the literature [23]. Therefore, the size of the pile, which is indeed an external parameter, must be specified in the testing procedure when dealing with cohesive powders.

A common tool to analyse the avalanching behavior of powders is a horizontal rotating drum partially filled with the granular sample [24]. In this device, intermittent and nearly reproducible avalanches are observed at low rotation speeds. For low-cohesive well-behaved granular materials, avalanches occur quite regularly with nearly uniform size and time spacing, whereas in the case of poorly flowing cohesive powders, the time spacing and size of avalanches shows a noisy behavior [24]. A rotating drum-based unit, developed by Kaye and coworkers [25], is now commercially available. In this device, avalanches are automatically detected by a change in the light intensity captured by a grid of photocells placed behind the drum. The avalanching behavior is characterized by the time interval between consecutive avalanches. The scatter of the points is a measure of the regularity of the avalanche process. With this technique, a gas conditioning system can be implemented [26] in order to control gas conditions inside the chamber that may have a profound effect on powder flowability. Testing cohesive powders is, however, difficult and the test usually yields inaccurate results. A source of error is that the powder sticks easily to the walls of the drum and this reduces visibility. As a result, the light intensity series can easily become

non-stationary whereas the number of avalanches per unit time detected decreases, thus complicating analysis of the data. In the case of very cohesive powders it is also likely that the powder slips as a whole. A further criticism is that merely the data on the time interval between consecutive avalanches cannot be enough to analyse cohesive systems with complex dynamics. For instance, Quintanilla et al. [24] have seen that for a class of cohesive powders, there is a regular sequence of large avalanches preceded by a number of two or three small precursors. In such cases, an in-depth statistical analysis is needed.

Since flowability is closely linked to interparticle forces, it can be thought that a good bulk test is to measure the powder tensile yield stress for which the interparticle attractive force is responsible. The split cell tester is a commercial device able to measure a tensile yield stress [21]. The sample is held in a ring-shaped cell and is compacted vertically using a plunger. Then a horizontal tensile stress is applied and steadily increased until the sample is pulled apart. In this way, the tensile yield stress for a given consolidation stress is measured. In the lifting lid tester, the sample is pulled vertically in the same direction of compaction [21]. These techniques present some inconveniences when applied to fine cohesive powders. One of them is again the lack of a mechanism for initializing the powder into a reproducible state of consolidation. As a consequence, results are of poor reproducibility. Another is the difficulty of measuring the tensile yield stress of fine cohesive powders at low consolidation stresses by means of piston consolidation [27]. It must be remarked that the way of preparation and compaction of the powder in the cell does not produce an isotropic state of stresses. Therefore, the tensile yield stress does not have to coincide with the tensile strength. Research tools such as triaxial tests achieve an approximated isotropic behavior by using hydrostatic compaction, but is applicable only to high compression loads.

1.1.3 Direct measurement of interparticle forces

A good estimation of the powder flowability should be based on direct measurement of the interparticle forces. The adhesion force between individual particles can be measured directly using a Scanning Force Microscope [6]. With this instrument, a probe particle is attached at the end of a V-shaped tipless cantilever. The probe particle is brought close to an isolated substrate particle under computer control and a loading-unloading cycle is applied. The largest down-

ward deflection achieved by the cantilever during unloading gives the adhesion force. **Figure 1** shows the statistical distribution of the adhesion force measured between two micrometer-sized toner particles. Another apparatus recently reported to measure interparticle forces [28] comprises a sensor unit composed of a contact needle that comes into contact with the powder and dislodges particles, measuring the adhesive force between the particle and sample substrate. This technique, however, does not have a way to control the previous load force on the particle that modifies adhesion substantially for plastic contacts [6]. The same criticism applies to the well-established centrifugal method [28].

As can be seen in **Fig. 1**, the SFM data obtained for the adhesive force between irregularly shaped particles such as xerographic toners has a broad dispersion. This is mainly due to the dependence of the adhesive force on the local surface properties of the contact. When two irregular particles are brought into contact, we can expect a wide range for the adhesive force measured depending on the exact location of the contact that determines the asperity size. This problem gets worse when flow conditioner additives are dispersed on the particle surface.

1.1.4 The fluidized bed method

A method to obtain the uniaxial tensile yield stress of the powder with high reproducibility consists of supplying a gas flow into a powder bed [27, 29]. The layout of the experimental system is shown schemati-

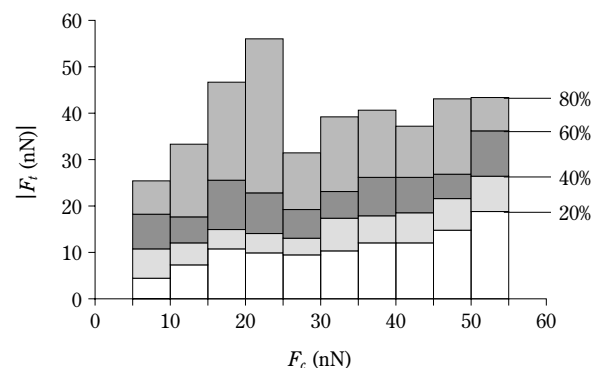


Fig. 1 Statistical distribution of the adhesive force (F_t) between two irregularly shaped toner particles with low surface additive coverage as a function of the load force (F_c). Forces are measured using a Scanning Force Microscope. The vertical bars indicate the cumulative distributions of the experimental measurements for every range of load force.

cally in **Figure 2**. Powder samples are supported on a porous plate in a vertically-oriented cylindrical vessel. Our experimental materials are xerographic toners made of polymer and with typical particle size $\sim 10 \mu\text{m}$. Pore size of the distributor plate is $\sim 5 \mu\text{m}$ to ensure that toner particles do not penetrate into the pores and that the gas stream is distributed uniformly over the lower boundary of the bed. A controlled flow of dry nitrogen is introduced into the lower part of the vessel. By using dry nitrogen, the complicating effect of humidity, which is known to affect particle adhesion [30], is minimized. The gas flow is controlled by a mass flow controller while the gas pressure drop across the bed Δp is measured by a differential pressure transducer. Readings of the pressure drop across the porous plate (without toner in the cell) are taken before each series of powder measurements. In all the range of gas flows we used, there is a linear dependence of the pressure drop across the plate on the gas flow velocity. The powder sample is weighed and then placed in the vessel; at this stage the sample is quite inhomogeneous, with some loose and some compacted areas. To homogenize the sample, the bed is driven into the freely bubbling regime by imposing a large gas flow. Once in the bubbling regime, the bed loses memory of its previous history [31]. In the case of highly cohesive powders, such as toners with very low additive concentration, it is necessary to shake the sample in order to break up channels that conduct fluidizing gas away from the bulk of the powder and prevent fluidization. For that purpose, an electromagnetic shaker can be incorporated into the set-up in the base of the bed [4]. The bed is allowed to bubble during a time period large enough to reach a stationary state and after that the gas flow is suddenly returned to zero. This gives a repeatable start-

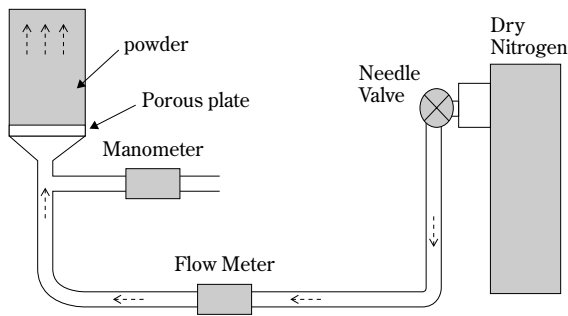


Fig. 2 Original apparatus used by us for measuring the uniaxial tensile yield stress of the powder.

ing condition for the powder. The height of the bed h provides an average value of the particle volume fraction

$$\langle \phi \rangle = \frac{m_s}{\rho_p A h} \quad (2)$$

where m_s is the powder mass, ρ_p is the particle density that must be known beforehand, and A is the cross-sectional area of the vessel. h is measured by means of an ultrasonic sensor placed on top of the vessel. The consolidation stress σ_c at the bottom of the bed is assumed to be the total weight of the sample divided by the area of the gas distributor. To measure the uniaxial tensile yield stress σ_t we subject the vertical layer of powder to an upward-directed flow of gas that is slowly increased to put the bed under tension. The total pressure drop is measured and the pressure drop across the gas distributor is subtracted from it. This is shown in **Figure 3**. When the gas passes through the packed bed of particles, the gas pressure drop is due to frictional resistance and increases linearly with increasing gas flow at low Reynolds numbers as described in general by the Carman-Kozeny equation [32]

$$\frac{dp}{dx} = \frac{E\mu}{d_p^2} \frac{\phi^2}{(1-\phi)^3} v_g^2 \quad (3)$$

where x is the vertical coordinate measured downward from the free surface of the bed, μ is the dynamic gas viscosity ($\mu = 1.89 \times 10^{-5} \text{ Pa}\cdot\text{s}$ at ambient temperature for dry nitrogen), v_g the superficial gas velocity, and $E \approx 180$ is an empirical constant. There is a critical

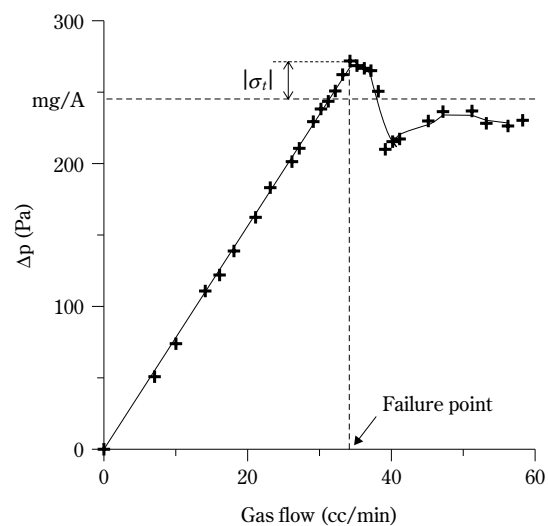


Fig. 3 Pressure drop across a bed of toner (Canon CLC500 cyan) consolidated by a consolidation stress $\sigma_c \approx 70 \text{ Pa}$. Cross-sectional area of the bed 20.3 cm^2 .

gas velocity at which the powder fractures and the gas pressure drop across the bed Δp falls abruptly. In order to find the tensile yield stress it is important to know how the powder fails. Close observations reveal that fracture of the bed always starts at the lowest point, the bottom of the bed. This was already predicted theoretically and later observed by Tsinontides and Jackson [33]. In their one-dimensional analysis, they neglected the wall effect and considered the uniaxial stress σ , local particle volume fraction ϕ and gas pressure depending only on the vertical coordinate x . Next, we give a slightly modified analysis from that of Tsinontides and Jackson [33] to show explicitly that the condition for tensile yield will be first met at the lowest point of the bed as the gas flow is progressively increased.

1.1.5 Location of fracture in the fluidized bed

In the consolidated equilibrium state, prior to the application of a gas flow, there are no external forces acting upon the particles except for the gravity force. Then we have a compressive stress $\sigma_c(x)$ across the bed that obeys the simple equation

$$\frac{d\sigma_c}{dx} = \rho_p \phi g \quad (4)$$

The vertical coordinate x is measured downward from the free surface of the bed. When the gas is forced to pass through the bed, we must also consider the drag force per unit total volume F_s exerted by the gas on the particles, which is given by the gas pressure drop per unit length $F_s = dp/dx$. Then the force balance equation is

$$\frac{d\sigma}{dx} = \rho_p \phi g - \frac{dp}{dx} \quad (5)$$

Since in fine powders, the gas flow is usually at small Reynolds numbers, it is admitted that F_s is proportional to the gas velocity $F_s \approx \beta(\phi)v_g$. For a sufficiently large gas velocity, the negative contribution of the drag force will turn the stress σ negative and equal to the tensile yield stress σ_t at some point within the bed. In order to find the yield condition, Eq. 5 must be integrated. There are several empirical equations in the literature for $\beta(\phi)$. Tsinontides and Jackson found it reasonable to adopt the Richardson-Zaki equation [34]:

$$\beta(\phi) = \frac{\rho_p \phi g}{v_{p0}} \frac{1}{(1-\phi)^{n-1}} \quad (6)$$

where n is ~ 5 for small Reynolds numbers and v_{p0} is the sedimentation velocity of a single particle, $v_{p0} =$

$(1/18)(\rho_p - \rho_g)d_p^2 g / \mu$ (ρ_g is the gas density), in the Stokes regime. While Eq. 6 describes well the behavior of fluidized beds at small values of the particle volume fraction, the Carman-Kozeny equation (Eq. 3) gives the best results for $\phi > 0.3$ [35]. Since we are looking for the yield point of the granular solids at large values of ϕ , Eq. 3 seems more appropriate to us for the pressure gradient. The integration of Eq. 5 yields

$$\sigma(x) = \int_0^x \rho_p \phi(\xi) g \left[1 - \frac{10\phi(\xi)}{[1-\phi(\xi)]^3} \frac{v_g}{v_{p0}} \right] d\xi \quad (7)$$

where we have used $E=180$ and the gas density has been neglected as compared to particle density.

Let us consider first the simplest case of a homogeneous bed in which $\phi = \phi_0$ and $\sigma_t = \sigma_{t0} < 0$ are constants throughout the bed. Then we have

$$\sigma(x) = \rho_p \phi_0 g x \left(1 - \frac{10\phi_0}{(1-\phi_0)^3} \frac{v_g}{v_{p0}} \right) \quad (8)$$

i.e. the uniaxial stress across the bed will increase linearly with a slope that decreases as the gas velocity is increased. Eventually the slope becomes negative and with a sufficiently large gas velocity, σ will equal σ_{t0} at the point where $|\sigma|$ is maximum, which is always the bottom of the bed. Note that if σ_t increases with the depth of the bed (due to an increase in consolidation, for example) the fracture will occur also at the base of the sample as long as there is a non-vanishing σ_{t0} , at the free surface (tensile yield stress at zero consolidation).

A more realistic approach is to take into account that $\phi(\xi)$ increases with the depth of the bed as a result of the increase of the local consolidation stress. In the whole range of consolidations tested, we obtain a good fit to the experimental data on the average particle volume fraction $\langle \phi \rangle$ by the modified hyperbolic law (see as an example **Figure 4**)

$$\langle \phi \rangle(\xi) = a - \frac{b}{(1+c\xi)^d} \quad (9)$$

For the commercial toner Canon CLC700, we have $a=1.366$, $b=1.088$, $c=3.968$, and $d=0.02454$ with a regression coefficient $R=0.9954$. To apply this formula, we need to assume that the average particle volume fraction $\langle \phi \rangle(\xi)$ from the free surface to a depth ξ in a bed of total height x is equal to the measured $\langle \phi \rangle$ in a bed of total height ξ . From the definition of $\langle \phi \rangle$

$$\langle \phi \rangle(\xi) = \frac{1}{\xi} \int_0^\xi \phi(\lambda) d\lambda \quad (10)$$

we derive the local particle volume fraction $\phi(\xi)$

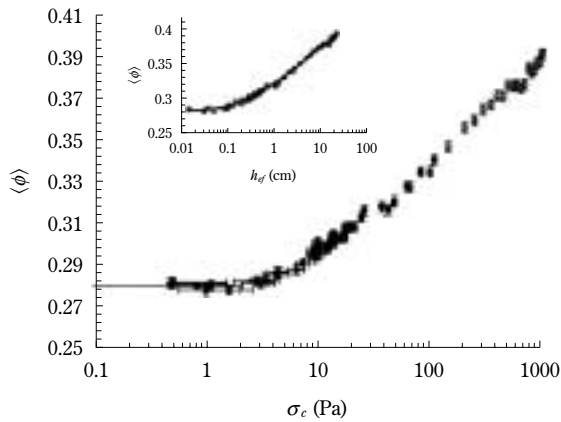


Fig. 4 Average particle volume fraction of a consolidated bed of Canon CLC700 toner as a function of the consolidation stress. The data obtained by reducing consolidation by means of an upward-directed gas flow (see below, solid symbols) are plotted jointly with data obtained by increasing consolidation by means of a downward-directed gas flow (see below, open symbols). The inset shows the whole set of data of the average particle volume fraction as a function of the effective depth measured from the top free surface, defined as $h_{ef} = \sigma_c / (\rho_p \langle \phi \rangle g)$ (the continuous curve represents the modified hyperbola fit equation $\langle \phi \rangle = a - \frac{b}{(1 + ch_{ef})^d}$, with $a = 1.366$, $b = 1.088$, $c = 3.968$, $d = 0.02454$, and a regression coefficient $R = 0.9954$).

$$\phi(\xi) = \langle \phi \rangle(\xi) + \xi \frac{d\langle \phi \rangle(\xi)}{d\xi} \quad (11)$$

to be used in Eq. 7. **Figure 5** shows the new profiles of the uniaxial stress obtained by numerical integration of Eq. 7 for different values of the gas velocity. The essential difference with respect to the uniform case is the convex shape of $\sigma(x)$ due to the increase of the drag force with depth. The consequence is that the yield condition is more neatly met at the base of the sample.

According to Eq. 5, the total gas pressure drop across a bed of height h at yield, $(\Delta p)_Y$, is given by the powder weight per unit area plus the tensile yield stress at the bottom

$$(\Delta p)_Y = \rho_p \langle \phi \rangle gh + |\sigma_t(h)| \quad (12)$$

Thus the overshoot of Δp beyond the bed weight per unit area when the powder fails gives us a quantitative measure of the uniaxial tensile yield stress $\sigma_t(h)$. For practical purposes, we checked that the tensile yield stress is not sensitive to the rate of increase of the gas flow. **Figure 6** shows results of σ_t for a given sample obtained using different rates. It is

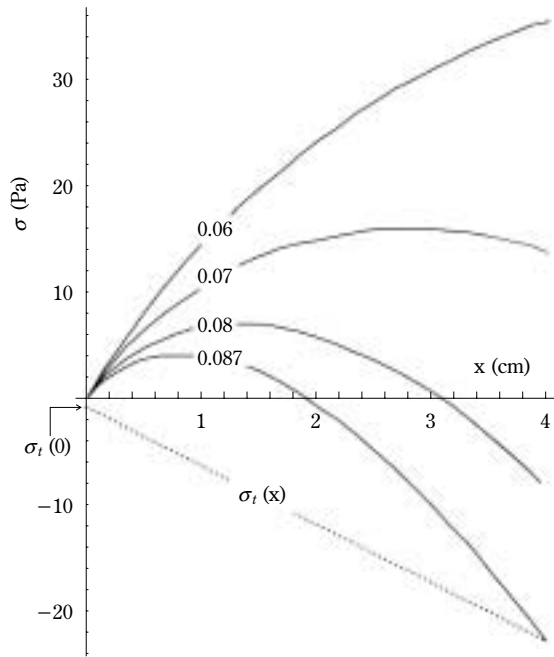


Fig. 5 Continuous lines: Uniaxial tension (σ) across a non-homogeneous bed of powder as the gas flow is increased (the ratio of the gas velocity to the sedimentation velocity of an individual particle v_g/v_{p0} is indicated for each curve). The free surface is at $x=0$ and the bottom at $x=4$ cm. The calculation is performed for a non-homogeneous bed with average particle volume fraction $\langle \phi \rangle = 1.366 - 1.088 / (1 + 3.968\xi)^{0.02454}$ (fit curve to Canon CLC500 toner experimental data) and particle density $\rho_p = 1199$ kg/m³. The dotted line is the experimental tensile yield stress ($\sigma_t = 1 + 5.5x$ Pa) for Canon CLC500. The yield condition ($\sigma = \sigma_t$) is met at the bottom of the powder ($x=4$ cm) for $v_g/v_{p0} \approx 0.087$.

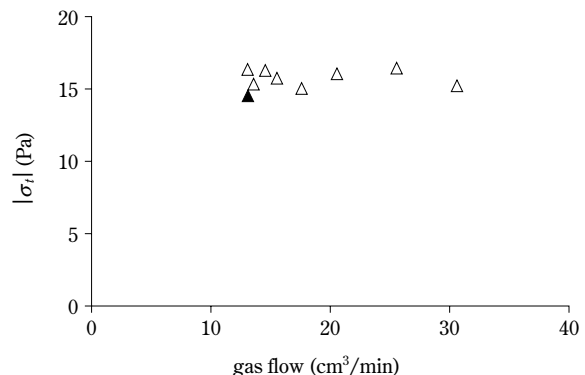


Fig. 6 Uniaxial tensile yield stress measured by increasing quasi-statically the gas flow (solid triangle) and by imposing instantaneous values (void triangles) of the gas flow represented in the horizontal axis.

seen that the deviation between the results is within the experimental scatter (± 1 Pa).

As noted by Tsinontides and Jackson [33], the condition for tensile yield can be met either at the lowest point within the powder bed or at the contact between the bed and the gas distributor plate. However, we have consistently observed that the gas distributor surface remains always covered by a thin layer of powder after the break. Thus the measurement is indeed that of the tensile yield stress of the powder rather than a measure of the interface strength between the distributor plate and the powder. As further proof, we present in **Figure 7** experimental measurements of σ_t using both metallic and ceramic gas distributor plates. Within the experimental scatter, the results fit to a single curve.

The yield condition will be more neatly met at the base of the powder for the most cohesive toners ($|\sigma_t|$ large) while a large portion of powder remains far from the yield condition. In contrast, for low-cohesive systems ($|\sigma_t|$ small), the uniaxial stress will be close to the tensile yield stress throughout all the material at the yield point, therefore, in practice, the fracture will be less clearly visible at the base. In our experimental work, we observe a variety of behaviors at the yield point depending on the magnitude of the tensile yield

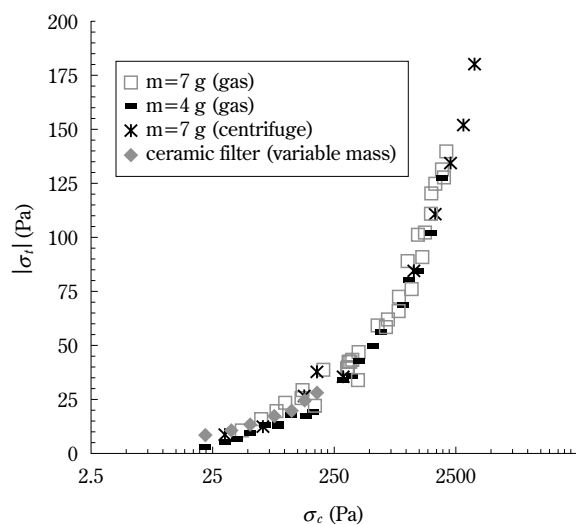


Fig. 7 Uniaxial tensile yield stress as a function of the consolidation stress for an experimental xerographic toner with 0.2% concentration by weight of additive. The data from different tests using consolidation by gas (two tests with samples of different masses) and centrifuging in a bed with a metallic gas distributor are plotted jointly with data obtained in a bed with a ceramic gas distributor where consolidation was increased by adding new mass to the sample.

stress and in agreement with this theoretical prediction. For most cohesive powders, the fracture at the bottom is clean and the powder rises in the bed as a plug. Furthermore, the bottom of the plug does not erode as it rises in the bed. The toner without flow additives behaves in this way. For powders of medium-large cohesiveness, fracture of the bed is still clearly visible and plugs are still formed, but the plug erodes as powder agglomerates fall away from its lower surface. The plug then becomes unstable and collapses at a certain height. Examples of this behavior are the toners with 0.01% and 0.05% Aerosil concentration by weight (12.5 μm particle size). For powders of low cohesiveness, plugs are rarely visible. After the break at the bottom of the bed, the fracture propagates until it reaches a certain height. Then, the gas escapes from the powder through channels which erupt like miniature volcanoes. The lower the cohesiveness of the toner, the less stable are the channels. These effects are observed, for example, in the toners with 0.1% and 0.2% Aerosil concentration. Finally, for the least cohesive powders, for example, the experimental toner with 0.4% Aerosil concentration or the Canon CLC500 toner, plugs do not develop, channels are very unstable, and a state of homogeneous fluidization is easily reached. We note, however, that this type of behavior depends also on the consolidation stress σ_c that influences the tensile yield stress – as we will see. In that sense, beds of small σ_c favor the formation of channels, whereas highly consolidated beds favor the formation of stable plugs.

Valverde et al. [27] found that wall effects are negligible for particles with a typical size of $\sim 10 \mu\text{m}$ in beds with typical heights not larger than their diameter, as can be seen in **Figure 8**. Data of the average particle volume fraction from circular beds and from a rectangular bed fit within the experimental scatter to a single curve.

In our early investigations, two techniques were employed in order to test the powder under different consolidation stress. In the first one, the powder mass was varied by adding powder to the bed [27] (see, for example, **Fig. 8**). In the second one, the vessel with the powder inside was centrifuged prior to measuring the tensile yield stress [36], thus increasing the apparent gravity by $g_a = (g^2 + \omega^4 r^2)^{0.5}$, where ω is the angular velocity and r the average radius at which the bed is rotating (see, for example, **Fig. 7**). These techniques needed to be performed by human operators and therefore none of them allowed for automation of the measurements. Furthermore, there are some difficulties related to testing the powder under very

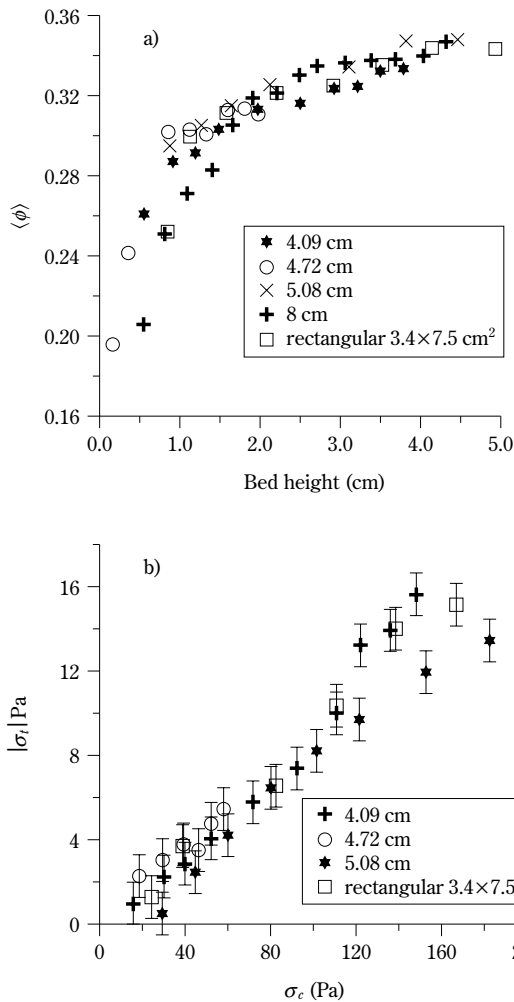


Fig. 8 (a) Average particle volume fraction as a function of the bed height. (b) Test of the uniaxial tensile yield stress versus consolidation stress. Data obtained for toner with 0.4% of additive obtained with different bed diameters (4.09 cm, 4.72 cm, 5.08 cm, 8.0 cm) and with a rectangular bed.

low/high consolidations. For very small consolidation stresses, beds of extremely low height must be used. In such cases, it was likely that non-uniform consolidation allowed the gas to flow preferentially through regions of high porosity such as channels. In the other extreme, if we wanted to achieve high consolidations by adding mass to the bed, its height should be increased up to values larger than the bed diameter for which wall effects are not negligible. In those cases, the tensile yield stress measured had an important contribution from the wall friction as shown by **Figure 9**. We will see that these inconveniences are solved by using the gas flow as an agent to compress or decompress the powder.

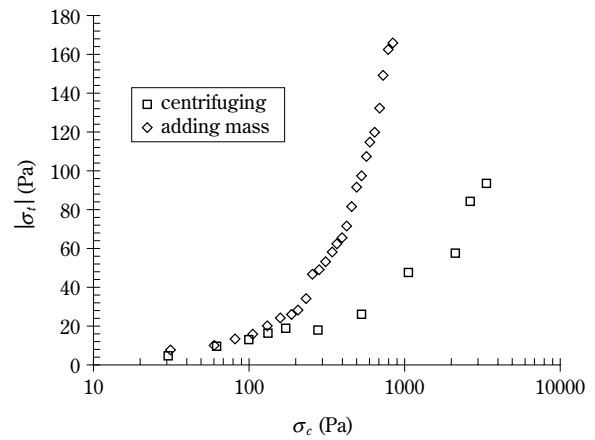


Fig. 9 Uniaxial tensile yield stress as a function of the apparent consolidation stress for the xerographic toner Canon CLC700 using different techniques of consolidation. One of them consists of adding mass to the sample contained in a cylindrical bed (diameter $D=5.08$ cm), where σ_c at the bottom would be given by $\rho_p \langle\phi\rangle gh$ if wall effects are neglected. The other way of consolidation consists of centrifuging the bed. With the technique of adding mass, wall effects are not negligible for $\sigma_c > \sim 200$ Pa, corresponding to bed heights typically larger than the bed diameter ($h = \sigma_c / (\rho_p \langle\phi\rangle g) \sim 5$ cm).

2 The automated Sevilla Powder Tester (SPT)

In **Figure 10** a schematic view of the automated SPT is shown. The main novelty is that by means of a series of computer-controlled valves, a controlled dry nitrogen flow can be pumped upward or downward through the bed while the gas pressure drop across the bed is read from the differential pressure transducer. In this way, the gas flow can be used to automatically vary the consolidation stress on the powder while at the same time avoiding wall effects and inhomogeneous gas distribution through shallow layers.

To compress the powder over the sample weight per unit area after the powder has settled, the valves are operated to change the gas flow path to the reverse mode. Then the downward-directed gas flow is slowly increased from zero to a given value. The gas imposes a distributed pressure over the granular assembly pressing it against the distributor plate. The consolidation stress at the base of the bed is thus increased up to

$$\sigma_c = W + \Delta p_0 \quad (13)$$

where $W = \rho_p \langle\phi\rangle gh$ and Δp_0 is the downward-directed gas pressure drop. Further increasing the compressing gas flow imposes further pressure on the sample.

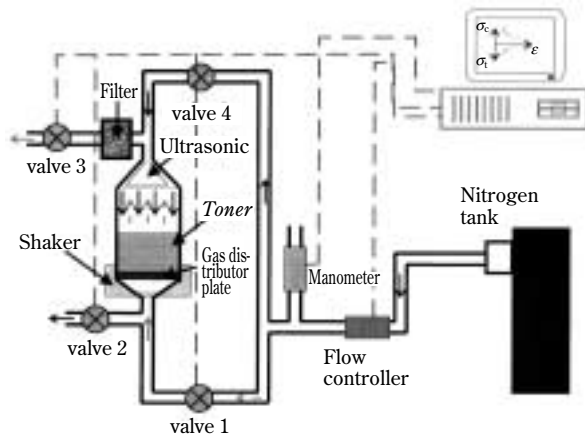


Fig. 10 Schematic diagram of the automated Powder Tester. The powder sample is held in a 4.45-cm diameter, 17-cm high cylinder made of polycarbonate, the base of which is a sintered metal gas distributor of 5 μm pore size. The cylinder is placed on a shaker used to help powder fluidization. Dry nitrogen is supplied from a tank of compressed gas and a mass flow controller is used to adjust the flow. The pressure drop across the bed is measured by a differential pressure transducer. A series of computer-controlled valves are used to control the gas flow path through the bed. The bed height is read from an ultrasonic sensor. All these components are connected to a computer by means of a data acquisition board. A filter is placed upstream of valve 3 to catch elutriated particles and prevent valve 3 from damage.

On the other hand, the automatic Powder Tester provides us with a useful technique to test the powder under very low confining pressures like in microgravity. To decrease σ_c below the powder weight per unit area, we allow the powder to settle under a remaining upward-directed flow. In this way, σ_c is lowered down to

$$\sigma_c = W - \Delta p_0 \quad (14)$$

where Δp_0 is the pressure drop of the remaining gas flow reducing consolidation.

As before, the uniaxial tensile yield stress of the consolidated sample is measured by slowly increasing an upward-directed gas flow that subjects the bed to a tensile stress. The bed height is automatically measured by means of an acoustic pulse technique. **Figures 11 and 12** show the gas pressure drop across the bed during the breaking process for overconsolidated and underconsolidated states, respectively. As consolidation is increased, it is clearly seen that the slope of the linear part increases as a consequence of the increase of the average particle volume fraction. The overshoot of the pressure over the weight per

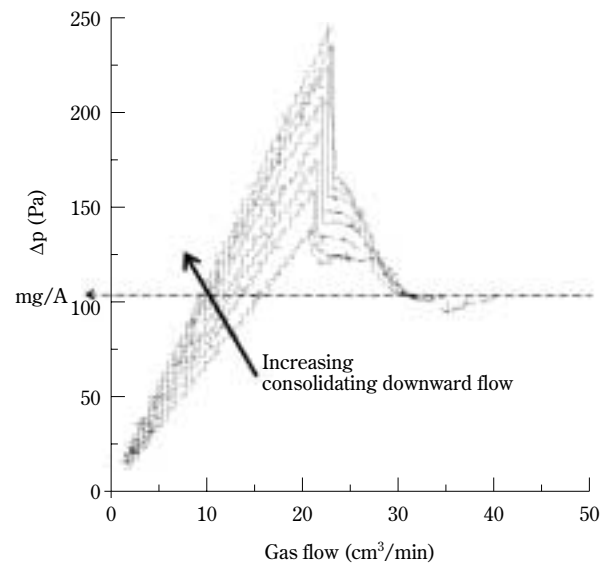


Fig. 11 Gas pressure drop versus gas flow for a given mass of xerographic toner (with 0.05wt of silica) previously consolidated with a downward-directed gas flow. Curves in the left-hand direction correspond to increasing values of the compressing gas flow and hence to increasing values of the consolidation stress σ_c .

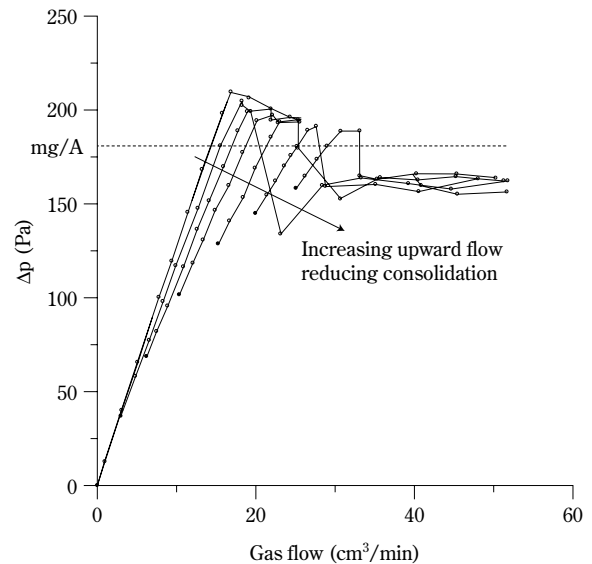


Fig. 12 Gas pressure drop versus gas flow for a given mass of xerographic toner (with 0.2wt of silica) in states of reduced consolidation obtained by allowing the powder to settle under an upward-directed gas flow. Curves in the right-hand direction correspond to increasing values of the decompressing gas flow and hence to decreasing values of the consolidation stress σ_c .

unit area (i.e. the uniaxial tensile yield stress) also increases. Conversely, when the sample consolidation

is subsequently decreased, the average particle volume fraction decreases and hence the slope of the linear part decreases and the uniaxial tensile yield stress decreases.

Figure 13a is an example of the complete diagram that can be obtained from the SPT. It shows the interdependence between the consolidation stress, the tensile yield stress and the particle volume fraction for two powders with different levels of surface additive coverage, SAC, concentration. Clearly, a higher consolidation implies larger particle volume fraction and tensile yield stress. In the upper part of the figure it is seen that for a given consolidation stress, the particle volume fraction has a larger value for a higher additive level. This is a direct result of the increase in flowability with increasing additive, which increases the ability of the toner particles to rearrange themselves at a given stress. For a constant value of the consolidation stress, the tensile yield stress increases

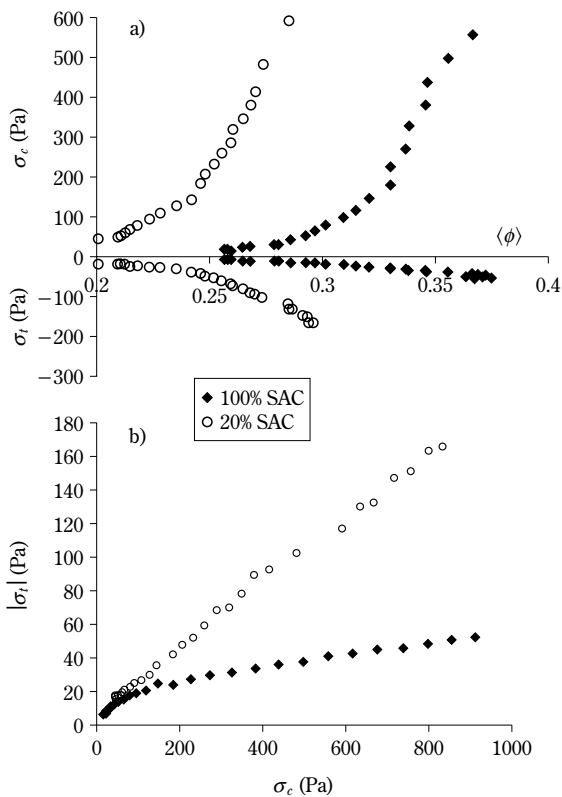


Fig. 13 (a) Relationship between the average particle volume fraction $\langle\phi\rangle$, uniaxial tensile yield stress σ_t and consolidation stress σ_c as measured by the SPT. (b) Tensile yield stress as a function of the consolidation stress. Results for two xerographic toners of $\approx 7 \mu\text{m}$ particle size and with different surface additive coverage (SAC) levels are shown.

with decreasing additive concentration (**Figure 13b**). This is directly related to the increase in interparticle force with decreasing additive concentration [6].

The SPT has been fully automated and yields highly repeatable results [4]. This was also shown previously in **Fig. 7**, where the experimental curves $\sigma_t - \sigma_c$, obtained by means of gas consolidation and centrifugation, overlap. The data plotted in **Figure 14** also show that we cannot differentiate the results for the average particle volume fraction as a function of the consolidation stress obtained from both compaction techniques.

Figures 15 and 16 give an idea of the sensitivity of the SPT to differentiate the flowability of apparently similar powders. In **Fig. 15**, we present the phase diagrams yielded by the aeroflow meter for two samples of different color of the toner Canon CLC700 (magenta and cyan). It is difficult to establish a quantitative difference in the flowability of both samples. **Fig. 16** shows the average particle volume fraction of both samples as a function of the consolidation stress applied by the downward gas flow (Eq. 13). Now both toners are well separated. As a consequence of their better ability to flow, the magenta toner particles are able to pack in a more compact structure for the same consolidation stress and this is clearly captured by the SPT. A straightforward extension of the SPT consisting of using nitrogen with controlled relative humidity enables the characterization of powder flow under well-controlled ambient conditions.

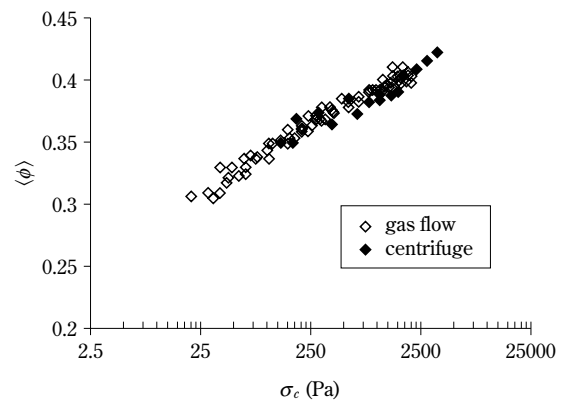


Fig. 14 Average particle volume fraction as a function of the consolidation stress for a toner of $12.5 \mu\text{m}$ particle size and 40% SAC. The external pressure is applied by means of a gas flow (void symbols) and by means of centrifugation of the cell (solid symbols).

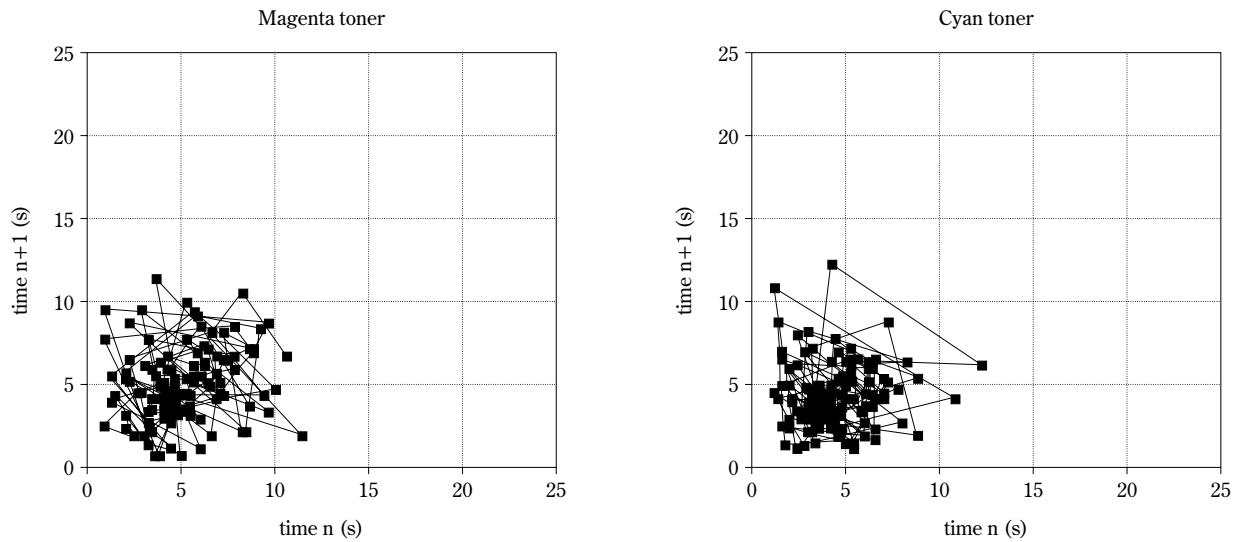


Fig. 15 Delay map for two samples of different color (magenta and cyan) of the commercial xerographic toner Canon CLC700. The points of time T_n at which an avalanche occurs are represented against the points of time T_{n+1} of the next avalanche.

2.0.6 Viscoplastic flow of interparticle contacts

An interesting experiment that can be performed automatically with the Powder Tester is to subject the sample to a fixed value of the consolidation stress for a controlled period of time. After this time period, the consolidation stress is removed and the tensile yield stress is measured. The increase of the tensile yield stress gives us an insight into the viscoplastic behavior of the interparticle contacts. From a practical point

of view, the increase of strength with time of consolidation during storage is a relevant issue. Our measurements for xerographic toners indicate that the estimated adhesion force [6] rises exponentially to a maximum in a time scale that depends on the load imposed and on the surface additive coverage. **Figure 17** indicates that as the load is increased while keeping the surface additive coverage constant, the relative increase of the adhesion force becomes more

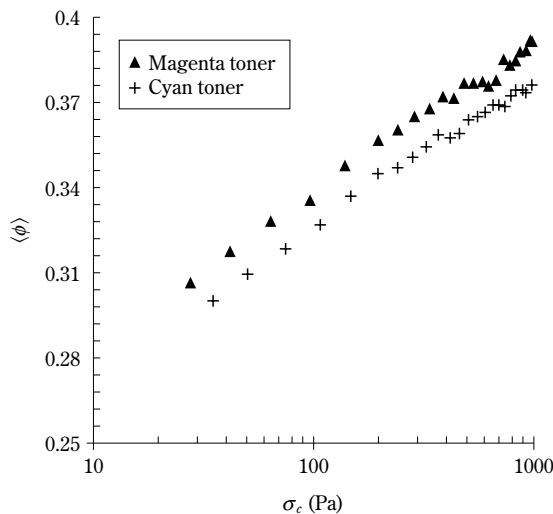


Fig. 16 Average particle volume fraction as a function of the consolidation stress measured using the SPT for two samples of different color (magenta and cyan) of the commercial xerographic toner Canon CLC700.

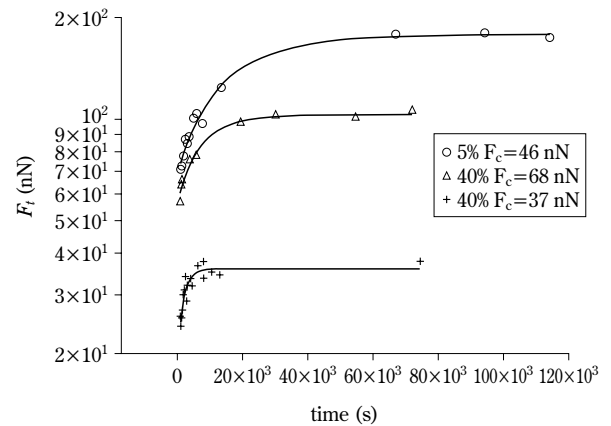


Fig. 17 Estimated interparticle adhesion force as a function of the time during which the powder is consolidated. Examples are shown for toner particles with different surface Aerosil coverage and subjected to different load forces.

pronounced. A similar behavior is obtained if the surface additive coverage is decreased while keeping the load constant. Therefore, not just the actual value of the adhesive force for a given load force but also the time of application of the force plays a role in the compression process, suggesting a viscoplastic deformation of the contact in large time scales. To avoid viscoplastic flow, the data presented in the previous sections of this paper were taken from measurements made within a short time scale ($t < \sim 5$ min.).

3 The tilted fluidized bed: a technique for measuring the incipient flow of a sheared cohesive powder

Our fluidized bed technique provides a convenient method of generating a reproducibly consolidated powder and can be adapted to measure the limiting shear stress of the powder subjected to a controlled and small consolidation stress. After initializing, the next step is to apply a shear stress to the sample by slowly tilting the bed. As the angle of tilt increases, this generates a shear stress in the powder layer. For deep beds, the location of the shear plane and the angle of tilt α at which failure occurs depend on the width of the bed D [23]. If we restrict our samples to shallow layers of height $h \ll D$, it is observed that the width of the bed has no major influence and that powder failure occurs near the base of the sample. We then have

$$\tau_1 \approx \rho_p \langle \phi \rangle gh \sin \alpha \quad (15)$$

Similarly, the consolidation stress is related to the weight of the sample and to the angle of tilt

$$\sigma_1 \approx \rho_p \langle \phi \rangle gh \cos \alpha \quad (16)$$

Thus, from the angle at which the sample fails in shear, we calculate the coordinates of one point (σ_1, τ_1) on the yield locus. In order to generate more data for the yield locus we need to be able to vary the compressive stress on the sample. As before, we do this by means of a small remaining gas flow reducing consolidation. If we now tilt the apparatus, the shear stress at the bottom of the sample is given by Eq. 15 since the component of the buoyancy force acting on the shear direction is zero. On the other hand, the consolidation stress σ acting perpendicular to the shear plane is reduced by the gas pressure drop Δp , and so Eq. 16, modified to take account of Δp , becomes

$$\sigma \approx \rho_p \langle \phi \rangle gh \cos \alpha - \Delta p \quad (17)$$

As the consolidation stress is decreased, the angle

of failure decreases and for zero tilt, we recover the measurement of the uniaxial tensile yield stress σ_t . Thus, by combining gas flow and tilt, we can generate a range of conditions of shear stress and normal stress. **Figure 18** shows the incipient yield locus obtained in this way for the Canon CLC500 toner. Two sets of experimental results obtained with experimental toners of different cohesivity are shown in **Figure 19**. For the cases illustrated in **Fig. 19**, the Aerosil concentrations are 0.02% and 0.2% by weight. Clearly, the yield loci of the two materials at low stresses are very different. For a given normal stress, the critical shear stress needed to make the powder flow decreases when the flow additive is increased as a consequence of the decrease of adhesion force.

Another remarkable feature of the yield loci is their convex shape at small stresses. This is a well-known

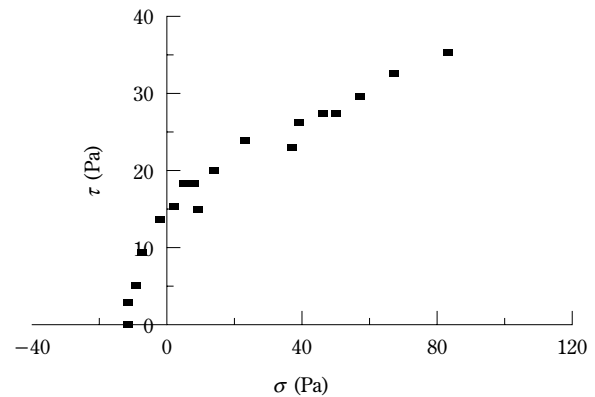


Fig. 18 Yield locus of the Canon CLC700 toner determined by the tilted fluidized bed technique.

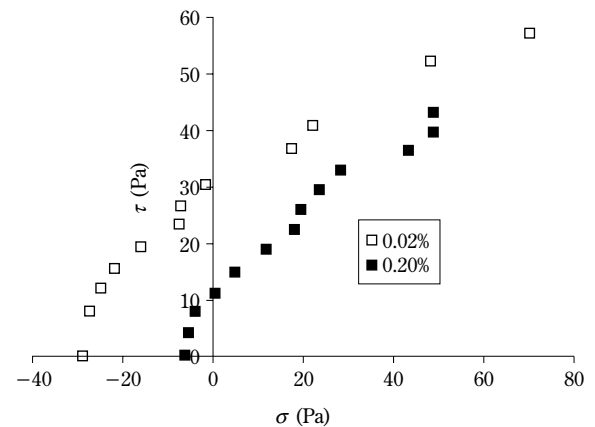


Fig. 19 Yield locus of experimental toners (12.7 μm particle size, 0.02% and 0.2% by weight of Aerosil) determined by the tilted fluidized bed technique.

common aspect of the yield locus of fine powders at low stresses [7]. Moreover, we see that the cohesion c of the powder, defined as the critical shear stress for zero consolidation stress, is comparable to the uniaxial tensile yield stress.

If we approximate the yield loci obtained at high stresses by a Coulomb's linear law (Eq. 1), we see in **Fig. 19** that our results predict an increase of the angle of the internal friction with the percentage of flow conditioner, as observed by Steeneken et al. [37] in potato starch powders, due to the roughening of the powder particles by the additive. We derived the same trend on the effect of additive on the angle of internal friction from experiments where the angle and depth of avalanches were measured in tilted beds of varying width and the results were fitted by a wedge model [23].

In the tilted fluidized bed technique, the yield locus is not defined for a "presheared" sample and the end Mohr circle for steady state flow cannot be determined. Therefore, the initial states in the classical shear testers and our tester are different. Nevertheless, a comparison of the yield loci obtained using our technique with the yield loci obtained from other standard testing devices such as the recently developed ring shear tester [20] is of great interest, and no doubt it will contribute to deepen our understanding of the behavior of powders subjected to very small shear and normal stresses.

4 Conclusions

In this paper we have described a Powder Tester instrument whose main advantages are i) results are operator-insensitive since measurements are automatically taken, and ii) fluidization provides a convenient method to have the sample in a reproducible initial state. Every step in the process is determined by gas flow, and by means of a set of valves and flow controllers, we are able to run the entire process by a computer. The measurements involving gas flow velocity, pressure difference, and bed height are accessed by the same computer, and from these sets of measurements, the values of consolidation stress, average particle volume fraction, and uniaxial tensile yield stress are automatically calculated. An upward/downward-directed gas flow is used for deconsolidating/consolidating the powder, and an ultrasonic device measures the bed height giving an average value of the particle volume fraction. By quasistatically tilting the bed, the SPT also serves to measure the yield shear stresses. This technique is especially feasible to

measure the yield locus of cohesive powders, which are difficult to initialize, subjected to very small consolidation stresses.

As a concluding remark we want to stress that the usefulness of the SPT is not just restricted to flowability diagnosis. Our experimental work shows that the tester is a powerful instrument of research in powder technology.

Acknowledgements

This research has been supported by the Xerox Foundation, the Xerox Corporation, and the Spanish Government Agency Ministerio de Ciencia y Tecnologia (DGES) under contract BMF2003-01739. We acknowledge P.K. Watson, M. Morgan, F. Genovesse, A. Ramos, and A. T. Perez for their valuable contributions to this work.

References

- [1] B.J. Ennis in *Powders & Grains 97* (Balkema, Rotterdam, 1997) p. 13.
- [2] R. Jones, H.M. Pollock, D. Geldart, and A. Verlinden: *Powder Technol.*, **132**, 196 (2003).
- [3] A. Castellanos, J.M. Valverde, A.T. Prez, A. Ramos and P.K. Watson: *Phys. Rev. Lett*, **82**, 1156 (1999).
- [4] A. Castellanos, A. Ramos, and J.M. Valverde: *Device and method for measuring cohesion in fine granular media*. Patent no. WO9927345-A. Patent Assignee: University of Seville. Publication date: June 3, 1999. J.M. Valverde, A. Castellanos, A. Ramos, A.T. Perez, M.A. Morgan and P.K. Watson: *Rev. Sci. Instrum.* **71**, 2791 (2000).
- [5] J.M. Valverde, A. Castellanos and M.A.S. Quintanilla: *Phys. Rev. Lett.* **86**, 3020 (2001). A. Castellanos, J.M. Valverde and M.A.S. Quintanilla: *Phys. Rev. E.* **64**, 041304 (2001). J.M. Valverde, M.A.S. Quintanilla, A. Castellanos, and P. Mills: *Phys. Rev. E* **67**, 016303 (2003). J.M. Valverde, A. Castellanos, P. Mills and M.A.S. Quintanilla: *Phys. Rev. E* **67**, 051305 (2003).
- [6] M.A.S. Quintanilla, A. Castellanos, and J.M. Valverde: *Phys. Rev. E* **64**, 031301 (2001).
- [7] J. Schwedes: *Granul. Matter* **5**, 1 (2003).
- [8] Book of ASTM Standards, Part 9, *American Society for Testing and Materials*, Philadelphia, 45, 1978.
- [9] D.A. Hall and J.G. Cutress: *J. Inst. Fuel*, **33**, 63 (1960).
- [10] Cole Parmer 1997-1998 catalog, p. 541.
- [11] C.M. Iles, Bateson I.D., Walker J.A.: *Rheometer for testing flow characteristics of materials such as powders, liquids and semisolids such as pastes, gels and ointments*. Patent no. EP1102053-A2, May 23, 2001.
- [12] R.L. Carr: *Chem. Engng*, **18**, 163 (1965).
- [13] P.K. Watson, J.M. Valverde and A. Castellanos: *Powder Technol.* **115**, 44 (2001). J.M. Valverde, A. Castellanos and P.K. Watson, *Powder Technol.*, **118**, 240 (2001).

- [14] R.L. Carr: Chap. 2, Gas-Solids Handling in Process Industries, Marcel Dekker, NY, 1976.
- [15] British Standard 1377, *Methods of tests for soils for civil engineering purposes* (1975).
- [16] H.H. Hausner: Int. J. Powder Metallurgy, **3**(4), 7 (1967).
- [17] C.A. Coulomb: *Mémoires de Mathématiques et de Physique présentés à l'Académie des Sciences par divers savants et lus dans les assemblées, Année 1773* (Académie Royale des Sciences, Paris, 1776) Vol. 7, p. 343.
- [18] J. Schwedes: *Fließverhalten von Schüttgütern in Bunkern.*, Verlag Chemie GmbH, Weinheim, 1968.
- [19] Institute for Reference Materials and Measurements. Directorate General Joint Research Centre of the European Commission.
- [20] D. Schulze and A. Wittmaier: Chem. Eng. Technol. **26**, 2 (2003).
- [21] L. Svarovsky: *Powder Testing Guide: Methods of Measuring the Physical Properties of Bulk Powders* (Elsevier Applied Science, England 1987).
- [22] *Classification and Symbolization of Bulk Materials* ISO 3435-1977-E-.
- [23] J.M. Valverde, A. Castellanos, A. Ramos and P.K. Watson: Phys. Rev. E **62**, 6851 (2000).
- [24] M.A.S. Quintanilla, J.M. Valverde, A. Castellanos, R.E. Viturro: Phys. Rev. Lett. **87**, 194301 (2001).
- [25] Kaye, B.H., Gratton-Liimatainen, J. and Faddis, N.: Part. Part. Syst. Charact., **12**, 232 (1995).
- [26] Poole T.A.: *Apparatus for determining powder flowability*. Patent no. WO9738297-A1, Oct 16, 1997.
- [27] J.M. Valverde, A. Ramos, A. Castellanos and P.K. Watson: Powder Technol., **97**, 237 (1998).
- [28] Y. Shimada, Y. Yonezawa, H. Sunada, R. Nonaka, K. Katou, and H. Morishita: KONA **20**, 223 (2002).
- [29] T. Hiroyuki: *Method and instrument for measuring adhesion of granular body*. Patent no. JP3269340, Nov 29, 1991.
- [30] H. Schubert: Powder Technol. **37**, 105 (1984).
- [31] J.M. Valverde, A. Castellanos and M.A.S. Quintanilla: Contemp. Phys. **44**, 389 (2003).
- [32] P.C. Carman: Trans. Inst. Chem. Engrs. **15**, 150 (1937).
- [33] S.C. Tsinontides and R. Jackson: J. Fluid Mech., **255**, 237 (1993).
- [34] J.F. Richardson and W.N. Zaki: Trans. Inst. Chem. Engrs. **32**, 35 (1954).
- [35] K. Rietema: *The Dynamics of Fine Powders* (Elsevier, London 1991).
- [36] A. Castellanos, J.M. Valverde, and P.K. Watson: ZAMM **80**, S423 (2000).
- [37] P.A. Steeneken and A.J. Woortman: Powder Technol. **47**, 239 (1986).

Author's short biography

Antonio Castellanos Mata

Antonio Castellanos received his doctoral degree in nuclear physics in 1972. Actually he is Professor of Electromagnetism at the University of Seville, Spain. His current research interests are in the coupling of electric fields to fluids (electrohydrodynamics, EHD), in control of bio-particles and liquids in microelectrodes structures (AC electrokinetics and EHD in MEMS), in gas discharges (ozonizers, pollution control), and in the physics of cohesive granular media.

José Manuel Valverde Millán

José Manuel Valverde Millán obtained a Bachelor Science degree in Physics at the University of Seville in Spain in 1993, and a Ph.D. in Physics from the same University in 1997. He teaches electromagnetism at the department of Electronics and Electromagnetism, University of Seville. His main research topic is the fundamental physics of cohesive powders. He has published around 25 papers in international journals and is co-author of the patent on the Seville Powder Tester described in this paper. In most of his research projects he has worked in collaboration with Xerox Co.

He is married with Isabel, has a beautiful little daughter (Sofia) and a beloved 13 years old son (Manuel), and lives in San José de La Rinconada (Spain).

Miguel Angel Sánchez Quintanilla

Miguel Angel Sánchez Quintanilla received the B.S. degree in Physics from the University of Seville in 1998 and the Ph.D. degree in 2003 also in the University of Seville. His research interests are in the mechanics of cohesive granular materials and fluidization of powders, and in particular the relation between the mesoscopic and continuum approaches.

Predicting Packing Characteristics of Particles of Arbitrary Shapes[†]

M. Gan, N. Gopinathan, X. Jia*
and R.A. Williams

*Institute of Particle Science and Technology
School of Process, Environmental and
Materials Engineering, University of Leeds***

Abstract

A computer model for particle packing is of importance in both theories and applications. By taking a very different approach from existing packing algorithms, our digital packing algorithm – called DigiPac – is able to avoid many of the difficulties normally encountered by the conventional algorithms in dealing with non-spherical particles. Using the digital approach, it is easy to pack particles of arbitrary shapes and sizes into a container of any geometry. This paper briefly describes the digital packing algorithm, but the focus is on validation of the DigiPac model through several case studies involving mono-sized non-spherical particles and also powders with different size distributions. Packing densities from DigiPac simulations are compared with those measured experimentally by ourselves in some cases and in others with data published in the literature using other models. The results show a good agreement in all the cases, which enhances our confidence in DigiPac that despite being a geometrical packing algorithm with no explicit consideration of particle interactions, it is able to predict quite accurately the packing structure of particulates whose shapes are commonly encountered in both industry and everyday life.

1. Introduction

The packing of particles is of importance in both theoretical and practical terms. For example, the random packing of spheres has been used as a model to represent the structure of liquids and glassy materials; to study phenomena such as electrical conductivity, fluid flow, stress distributions and other mechanical properties in granular materials; and to investigate processes such as sedimentation, compaction and sintering [1]. Since the 1960s, computer simulation algorithms have been widely used to simulate the packing of granular materials mainly on the basis of either sequential addition or collective rearrangement. The computer-generated random packing of particles is obtained either by using a so-called packing algorithm or by adopting a dynamic simulation model. Packing algorithms usually neglect

the physical process of packing in order to provide a computationally efficient method to generate the structure. Particle dynamics models, on the other hand, are designed to simulate the process of a particulate system and, when used to simulate the packing process, produce the packing structure as a result.

It has been recognised for many years that both particle size and shape have a strong effect on the packing characteristics of granular materials. Most attempts at computer simulation assume a spherical shape, although some simulations of non-spherical particles have been reported [2-7]. The main reason for this is the inherent complexity of representing and handling geometries of asymmetric particles. The effects of particle size and size distribution on the packing of particles [1,8-13] have been extensively investigated based on the packing of spheres, and the literature is full of results in this field [11-13]. In contrast, the study of the effects of particle shapes is very limited and mostly focused on the identical particles with simple analytical geometries such as cylinders or discs [2,4], ellipsoids [3,4,14,15] and parallelepipeds [4].

* Corresponding author.

Tel.: ++44-113-343-2346; fax: +44-113-343 2781.

E-mail address: x.jia@leeds.ac.uk

**Leeds, LS2 9JT, UK

[†] Accepted: August 26, 2004

In reality, particles with irregular geometries constitute the majority of powders. In these cases, how to simulate the packing of particles with the real shape had been a challenge. Traditionally, the shape of a non-spherical particle may be represented by a sphere-composite. In principle, the sphere-composite method may be used for arbitrary shapes to any predefined accuracy. In practice, the immense effort required to construct arbitrary shapes using small spheres and the subsequent computational costs of the simulations have so far limited its application to only a few relatively simple shapes. Using a polygonal mesh to map over the surface of a solid object is another possible way to represent irregular shapes. This surface presentation is widely adopted in 3D computer graphics to render photo-realistic scenes [16] and has also been used in particle packing simulations [17,18]. The main obstacles that prevent its widespread application are the same as for the sphere-composite approach, plus two added difficulties. One lies in collision and overlap detection, the other in the coding effort required to make the simulation program robust and efficient. Recently, by taking a very different approach from the traditional packing algorithms, a new, digital packing algorithm called DigiPac [19] avoids many of the difficulties associated with the traditional approaches, and makes it easy to pack particles of arbitrary shapes in containers of an arbitrary geometry. Even though in DigiPac, consideration of particle interactions is limited to the geometric constraints, it can be shown to be able to predict the packing characteristics of irregularly shaped particles. This is the focus of this paper.

Since the full details of DigiPac have been reported elsewhere [19,20], Section II only gives a brief description of the algorithm and emphasis will be on comparing and contrasting DigiPac with traditional approaches. Section III describes the case studies performed, including experimental and simulation set-ups, shape modelling and methods of calculation to obtain packing densities. Section IV presents results and comparison of DigiPac simulations with experiments and other simulation models.

2. Methodology of DigiPac

2.1 Particle representation

In DigiPac, shapes are digitised and represented by pixels (in 2D) or voxels (in 3D). A particle is just a coherent collection of pixels or voxels after the particle is digitised, as shown in **Figure 1**. These pixels (or voxels) can be stored and manipulated as integers or

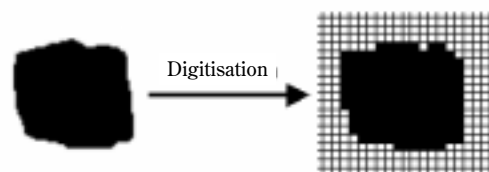


Fig. 1 Schematics in 2D showing digitisation of particle shape and the packing space.

as bits, making DigiPac quicker and potentially less storage-demanding than the traditional approaches for complex shapes. In addition, apart from the initial errors in digitisation, the digital algorithm does not suffer from rounding errors as traditional approaches do. The number of pixels or voxels to be used for a shape does not depend on the complexity of shape, which again translates to substantial savings in storage when dealing with complex shapes.

Using the pixel/voxel representation also means that the real shapes can be taken directly from the digital images of the real particles. There are 3D optical and X-ray scanners that can scan 3D objects and output the structure in digital formats.

2.2 Digitisation of packing space and particle movements

In DigiPac, the packing space or the container is also digitised and mapped onto a grid. Thus, a container of arbitrary geometry is easily incorporated into the packing model. Since both particles and the packing space (the container) are digitised, it follows that particles must also move in discrete steps. In other words, particle movements are also digitised. As a result, collision/overlap detection becomes a simple matter of detecting whether two particles occupy the same site(s) at a given time step. The time taken to check overlaps is a linear function of the particle number and does not increase with the complexity of particle shapes. Computationally, this is an important advantage of DigiPac over traditional methods.

In the current DigiPac model, particles are allowed to move randomly, one grid cell at a time, on a square lattice. In 2D, there are 8 possible directions, 4 orthogonal and 4 diagonal, to choose from, all with equal probability. In 3D, the possible directions are 26, i.e. 6 orthogonal and 20 diagonal. In order to encourage particles to settle, upward moves are accepted with a so-called rebounding probability. This diffusive motion helps the particles to penetrate and explore every available packing space.

2.3 Control parameters of simulation

In DigiPac, there are several ways to control how particles are added and how particles move in packing space. For example, during a packing process, particles are allowed to rotate in addition to translation. Rotation usually, but not always, results in a denser packing structure since it often increases the chance of a better fit.

Particles can be introduced either from a specified point (point source) or randomly across a specified area (rain mode or hopper mode), above the container at a predefined rate. The former results in a heap, the latter fills the container more evenly. The rate of particle addition affects the packing density. Generally, slow addition leads to denser packing structure, and a high addition rate leads to a less dense structure [21]. Laterally, the boundaries can be either solid walls or periodical.

3. Particle packing case studies

The purpose of this paper is to demonstrate the ability of the DigiPac algorithm to predict correctly and accurately the packing density of non-spherical particles. The case studies reported here form part of the model validation exercise we have been performing over the past few years. We first report several simple yet illustrative case studies involving mono-sized objects of a non-spherical shape in each case. The objects used are tubes, polyhedrons, oblate spheroids (M&M candies), cylinders and spherocylinders. The packing properties for these simple case studies were obtained either from experiments carried out by ourselves or from published results by other researchers [4,6,7,22,23].

We then report packing results for nine industrial powders and compare them with measured packing densities in eight of the nine cases and with the prediction of an empirical model [25] in the last case. For reasons of confidentiality with industrial collaborators, the identities of the powders are withheld and they will simply be referred to as **PWD1** to **PWD9** in the following text.

3.1 Methods of digitising particles

There are many ways to digitise particles, of which we have used three in the present work. Particles with a regular and well-defined geometry (including sphere, tube, polyhedron, M&M candy, cylinder and spherocylinder) were generated directly in the digital format using DigiPac utility software. They are shown in **Figure 2a**.

The industrial powders PWD1 to PWD8 are used in the case studies. They are chemically pure. Therefore, given their measured bulk density by weight and their true particle density, the volume bulk packing density can easily be derived. Random samples were taken and imaged using X-ray Micro Tomography (XMT). Their shapes were obtained by stacking the XMT images. Two examples of digitised powder particles are shown in **Figure 2b**. The number of individual particles scanned and digitised using XMT ranged between 59 and 175. Size distribution was deemed to be adequately represented by the sample particles for each powder. These digital particles were multiplied to make up the population used for the packing simulations. Therefore, with the DigiPac approach, predetermined size distributions and shape factors become redundant. Particles in some of these powders were porous – they were themselves agglomerates of smaller primary particles. The internal porosity of these particles was estimated by analysing XMT images of individual particles.

For practical reasons, particles from PWD9 were modelled rather than digitised directly. SEM images of PWD9 powder show that particles may be regarded as round in form and rough in texture. To model such particles, we used a so-called sphere-on-sphere (SOS) method. With the SOS method, a given number of small spheres are mounted and half buried on the surface of a large core sphere. An example is given in **Figure 2c**. The small spheres are primarily used to simulate surface roughness. To some extent, they also change the particle shape away from that of a perfect sphere. The use of small spheres has the effect of increasing the distance between the centres of adjacent particles as well as increasing inter-particle frictions. In essence, the SOS method is similar to the random sphere construction (RSC) method used by Smith and Midha [26] to model the iron powder particles produced by water atomization. Although both SOS and sphere-composite methods use small spheres to make up a non-spherical particle, a crucial difference is that in SOS, spheres can overlap whereas in the sphere-composites used for DEM simulations [5,27], they are not allowed to overlap.

Size distribution for PWD9 was extracted from SEM images. In addition, eight variations from the original distribution were used in the simulations in order to assess if and how the bulk density may be enhanced by varying the size distribution. These distributions are shown in **Figure 3**. Results from DigiPac simulations were compared with those from a so-called linear packing model (LPM) developed elsewhere [25].

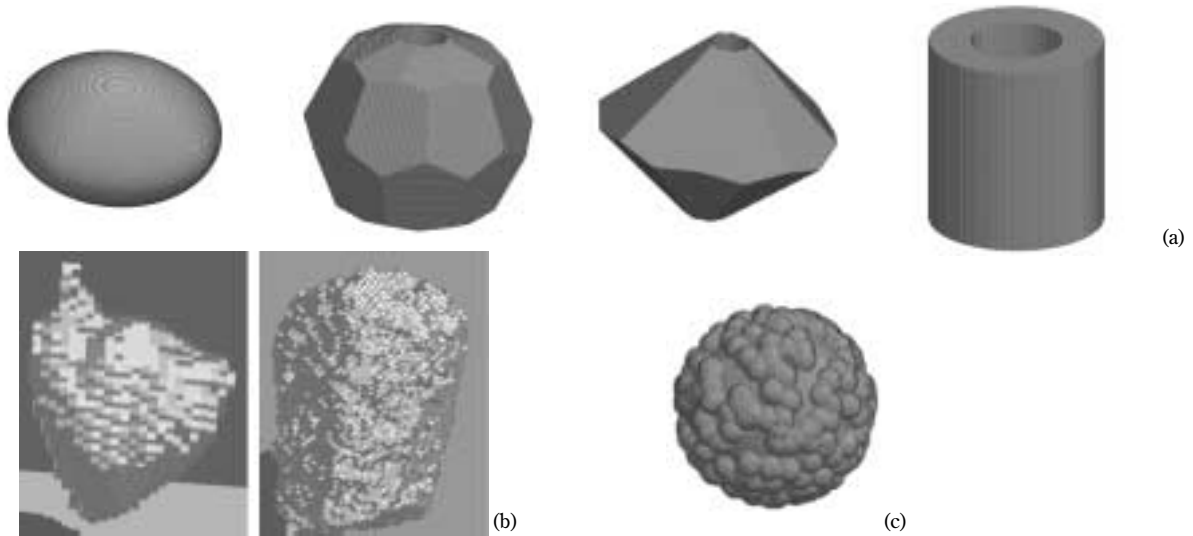


Fig. 2 Examples of digitised shapes used in the case studies. (a) Computer-generated replica of everyday objects. (b) XMT digitised shapes. (c) Shape generated using the SOS method.

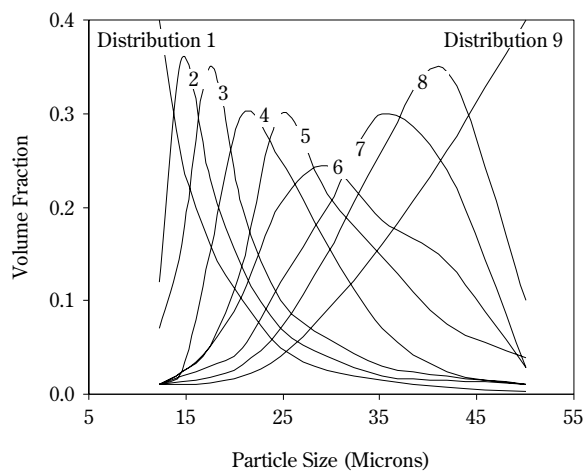


Fig. 3 Particle size distribution of PWD9 (No. 6) and its eight variations.

LPM is a semi-empirical model for estimating the packing density of multi-component mixtures, requiring only experimental data for the packing of mono-sized particles and binary mixtures to determine the model parameters used. To use LPM, the initial packing density of each component was set to 0.523. This was based on the mean value simulated in the packing of mono-sized surface-roughed spheres. The particle diameters are set equal to the equivalent volume diameters. It is noted that these equivalent volume diameters are conceptually different from the equivalent

packing diameters used in LPM, and they may differ in value as well.

3.3 Method of calculating bulk packing density in DigiPac

Volume packing density is one of the most important and commonly measured structural properties of a packing. It is defined and calculated as the ratio of the volume of the solids to the total volume of the packed space. Where bulk density is to be calculated, a cubic simulation box was used as the container with periodic boundary conditions in the lateral (X and Y) directions. The regions affected by solid walls and free surfaces are excluded, and the bulk density is estimated using the central part of the density distribution profile along the vertical (Z) direction, as shown in **Figure 4**.

3.4 Details of packing experiments and simulations

Seven simple but illustrative case studies were performed using the following shapes: tube, 16-face-polyhedron, 32-face-polyhedron and oblate spheroid (M&M candy). Except for the M&M candies, the particles are all made of plastics and obtained from toy shops. During each experiment, particles were poured into a container. Two short cylinders and a small baby food jar were used as containers. The two cylindrical containers had a flat bottom. The bottom of the baby food jar is domed. Dimensions of the particles and container are summarised in **Table 1**.

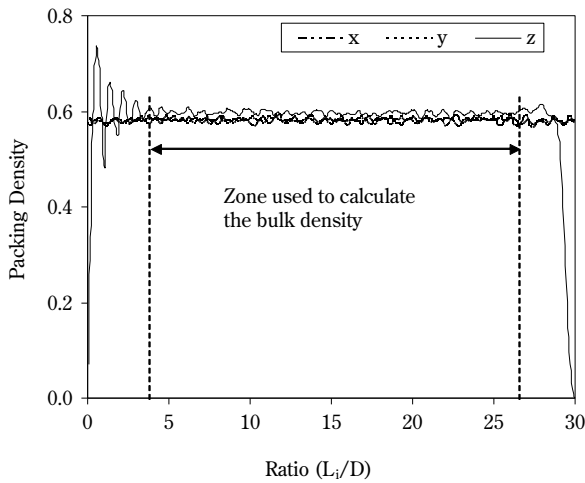


Fig. 4 Packing density profiles along X, Y and Z directions in a cubic simulation box with periodical boundary conditions in the lateral (X and Y) directions. The bulk density is calculated by taking the average over the central part in the profiles to avoid wall effect and the influence of free surface. L_i is the dimension of the simulation box along direction i and D the average particle diameter.

The simulation conditions were set to match the experimental set-up as much as possible. For instance, the number of particles and the particle-container size ratio were the same in both experiments and simulations. The real particles were not exactly identical but had small (<3%) deviations in both dimension and shape. These differences were ignored in the simulations where each shape is replicated exactly to make up the required number.

To encourage particles to find a better fit, they were allowed to rotate randomly during the packing. The rebounding probability was set to a value between 0.2 and 0.5. The number of particles used ranged from 5000 to 15000. The length-to-diameter aspect ratio of the cylinders varied from 0.1 to 30, and covers the range considered by Coelho et al. [4]. The spherocylinder particles had the same volume in all the

cases but their aspect ratio changed between 0.125 and 3.5, which is in line with the work of Abreu et al. [7]. The geometry of these particles is given in **Table 2**. **Table 3** summarises the conditions used for DigiPac simulations.

Table 1 Geometric parameters of objects and containers and number of particles used

Particle	Particle size (mm)	Number of particles
Sphere	$d=6$	660 (in C4)
Short tube	$d_{out}=4.6, d_{in}=2.4, h=5.1$	534 (in C1)
		721 (in C4)
32-face polyhedron [†]	$d=8.2, d_{hole}=2.0$	176 (in C1)
16-face polyhedron [*]	$d=4.1, d_{hole}=1.5$	546 (in C2)
		1113 (in C4)
M&M candy	$d_1=d_2=9.3, d_3=4.8$	126 (in C3)
Cylindrical container 1 (C1)	$D=44.8, h=50.9$	
Cylindrical container 2 (C2)	$D=44.8, h=25.7$	
M&M candy container (C3)	$D=27.5, h=97.1$	
Baby food jar (C4)	$D_{in}=5.8, h=6.8$	

Table 2 Geometric parameters of the spherocylinders

Diameter (D)	Length (L)	Aspect Ratio (r)
19	2	0.125
18	4	0.250
17	8	0.500
16	12	0.750
14	16	1.100
14	20	1.500
12	30	2.500
11	38	3.500

NB: L is the length of the cylindrical part, i.e. excluding the hemispherical ends.

Table 3 Summary of simulation conditions for cylinders, spherocylinders and powders

Parameter	Study case			
	Cylinder	Spherocylinder	PWD1 - PWD8	PWD9
Simulation box size	500×500×600	400×400×400 to 700×700×700	200×200×200	600×600×600
Number of particles	5000-8000	5000-13000	5900-17500	10000-100000
Number of components	1	1	59-175	9
Rebounding probability	0.3-0.5	0.3-0.6	0.1	0.2
Particle rotation	Yes	Yes	Yes	No

4. Results and discussion

The packing densities of mono-sized non-spherical particles and of mixtures of polydisperse particles are reported in this section. The scale and other settings used for DigiPac simulations are selected to give very good reproducibility of the results. For example, under the same conditions but changing the random number sequences, 12 simulations were performed, and the standard deviation was 0.001 and the maximum difference in density was 0.004. When DigiPac is applied to sphere packing, the packing density of 0.615 is obtained. This value is consistent with the experimental observation ($\rho=0.61$) carried out by Oweberg et al. [29], but lower than 0.637 – an accepted value for random dense packing [30]. This difference may be attributed to different packing methods and material properties.

4.1 Packing of aspherical particles with defined geometries

Table 4 compares results for the simulated and physical packed beds used in the simple case studies involving spheres, short tubes, 16-face polyhedrons, 32-face polyhedrons and M&M candies. Since, geometrically speaking, the particles and containers used for both simulations and physical tests are, within the measurement limits, identical, comparing the heights of the packed beds is equivalent to comparing their mean packing densities. The former is much easier to do than the latter, and, more importantly, it avoids more calculations which may introduce extra errors. Therefore, the packing height rather than density was used for comparisons. From **Table 4**, it is clear that the predictions are in good agreement with the measurements.

Table 4 Comparison of the measured and simulated packing heights of packed beds

Particles	Height of the packed bed (cm)			
	Cylinder container		Jar container	
	Measured	Simulated	Measured	Simulated
Spheres			5.8	5.3
Short tubes	5.1	5.0	5.6	5.1
16-face polyhedrons	2.6	2.8	3.8	4.3
32-face polyhedrons	5.1	5.2		
M&M candies	8.5	8.8		

4.2 Packing of cylinders

The packing of cylinders was investigated by many authors [2,4,22-24,32,33]. All studies showed that the packing density depends only upon the aspect ratio r (length-to-diameter). Although the mechanism of cylinder packing is not yet fully understood, some empirical equations have been formulated under certain conditions.

Zou and Yu [22] proposed an empirical equation (referred to as ZY model) to quantify the relationship between the porosity and sphericity of cylindrical particles in dense random packing, based on the experiments of wood cylinder packing. For cylinders ($r>1$), the equation of dense packing reads:

$$\ln \varepsilon_{0d,cyl} = \psi^{6.74} \exp[8.00(1-\psi)] \ln 0.36 \quad (1)$$

and for discs ($r<1$):

$$\ln \varepsilon_{0d,Disk} = \psi^{0.63} \exp[0.64(1-\psi)] \ln 0.36 \quad (2)$$

The sphericity ψ is defined as the ratio of the surface area of a sphere having the same volume as the particle to the actual surface area of the particle [34]. By this definition, the sphericity of a cylinder is related to the aspect ratio by:

$$\psi = 2.621 \frac{r^{\frac{2}{3}}}{1+2r} \quad (3)$$

Rahli et al [23] also proposed an empirical equation (referred to as RTB model), based on the excluded volume model elaborated by Onsager [35], as:

$$\varepsilon = 1 - \frac{11}{2r+6+\frac{\pi}{2r}} \quad (4)$$

Parkhouse and Kelly [36], based on the statistical approach to the distribution of the pores in the stacks, gave the following equation about the relationship between the porosity and the aspect ratio ($r>7$) of a cylinder (called PK model here):

$$\varepsilon \approx 1 - 2 \frac{\ln(r)}{r} \quad (5)$$

Figure 5 shows the porosity as a function of the aspect ratio r simulated by DigiPac. The results of other investigations [4,22,23,36] are included for comparison. It is clear that the porosity increases with the increase of the aspect ratio r . The porosities simulated by DigiPac are lower than those obtained by using the sequential deposition algorithm (RSA) carried out by Coelho et al. [4], but higher than those obtained by the empirical equations (1) to (5). The differences

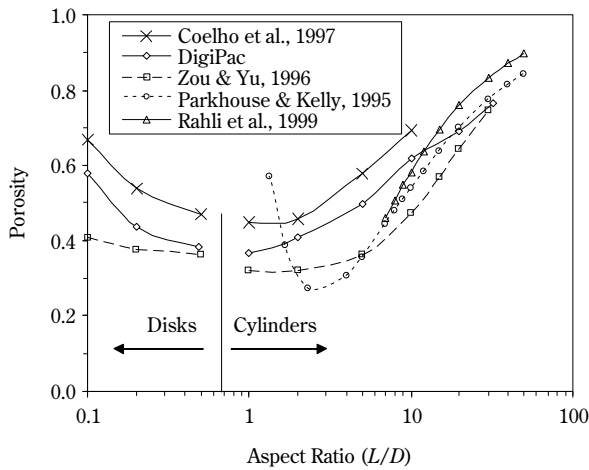


Fig. 5 Porosity versus aspect ratio for the packing of cylinders.

can also be observed in the ϵ - r curves investigated by different authors or methods, as can be seen in the curves from the work of Zou and Yu (ZY Model), Rahli et al. (RTB model), Parkhouse and Kelly (PK model) in Fig. 5. Especially, big differences can be observed when $r < 5$. This indicates that there is no universal model for a wider range of cylinders. The data also imply that particle packing is a complicated process and involves many factors such as packing methods and conditions and particle properties. For example, Evans and Ferrar [2] observed that a small degree of out-of-plane randomness enhances packing compared with both in-plane and 3D random orientation distribution.

One of the important factors in the simulation of particle packing is how quickly particles are introduced to the system, i.e., the particle addition rate. It is known [14,21] that the slower the rate, the higher the packing density. The particle addition rate could therefore be one of the reasons for the porosity differences in our Digipac simulations and the empirical estimations. In the present simulations, it has not been observed that the packing density of dense random packing of cylinders with a certain value of aspect ratio r is higher than that of spheres; but this feature has been reported in the literature [22,23]. This phenomenon needs further investigation to understand the mechanism. However, we observed it in the packing of spherocylinders described in the next section.

4.3 Packing of spherocylinders

Compared with cylinders, the packing of sphero-

cylinders is less investigated. Part of the reason for that is that spherocylinders are less common in reality. However, the study of spherocylinders can provide unique information for characterisation of the particle shape with packing density of the non-spherical particles [37-39].

Figure 6 plots the relationship between the porosity and aspect ratio of the spherocylinders. Again for the purpose of comparison, the simulated results, investigated by Abreu et al [7] and Williams and Philipse [6], are also given in Fig. 6. The porosity simulated by DigiPac is consistent with the results given by Abreu et al. [7] for a vibration amplitude of 2.0×10^{-3} m (twice the sphere diameter); but higher than the values given by Williams and Philipse [6]. Generally speaking, the porosity decreases and then increases with increasing aspect ratio. Similar trends have also been observed by Sherwood [3] and Donev et al [40] for ellipsoids, as well as by Aoki and Suzuki [32] and Zou and Yu [22] for cylinders. It shows that a small deviation in shape from that of a perfect sphere can lead to more efficient packing. Direct application of this result is in the field of powder storage and transportation. As noted by Donev et al [40], this has potential applications for a broad range of scientific disciplines such as ceramics, glass formation, etc.

When the aspect ratio $r=0.5$, the porosity is at its minimum. This aspect ratio is the same as that given by Abreu et al [7]. It is close to the value ($r=0.4$) given by Williams and Philipse [6]. For sphere packing, the porosity in Abreu's simulation is 0.425, higher than the 0.388 simulated by DigiPac. However, the differences in porosity among different approaches decrease with increasing r for $r > 2$. The reason is not

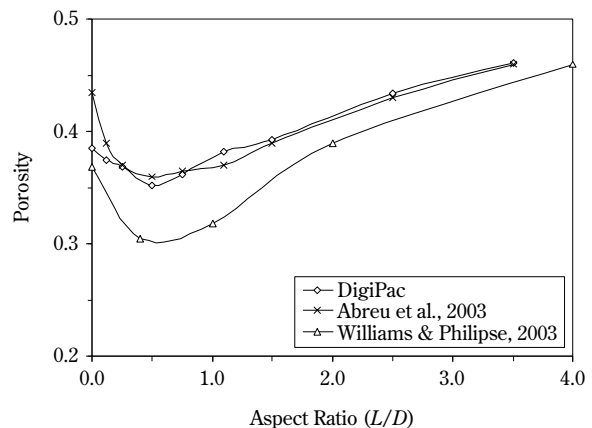


Fig. 6 Porosity versus aspect ratio for the packing of spherocylinders.

clear at the present and needs further investigation.

4.4 Packing of Powders

4.4.1 Experimental validation

Figure 7 compares the bulk packing densities of eight powders obtained by DigiPac simulations and measurements. It is clear that the simulated results are in good agreement with the measurements with an average error of less than 6%. When the eight powders were mixed and formed a composite powder, the packing density of the composite was 0.45 by simulation and 0.47 by measurement. These results directly demonstrate that DigiPac can predict very accurately the packing density of polydispersed non-spherical mixtures with real shapes encountered in industry.

As shown above, DigiPac is especially valuable for solving the packing problems of irregularly shaped particles. Conventionally, to investigate the packing of irregularly shaped particles, the characteristics of particle shape, angularity, etc. must be quantified first [41]. This is a tedious job and there is no universal method to quantify these parameters for real, complex-shaped particles. Obviously, one of the advantages of DigiPac over the conventional approaches is that no shape factors are required. This avoids the difficulty in the analysis of the complex shape of non-spherical particles. This is very useful for the particle systems in which particle shapes are difficult to quantify.

4.4.2 Validation by comparing with model predictions

As noted by Yu et al [25], their linear packing model (LPM) developed for spherical particles may

be applied to mixtures of non-spherical particles if the particle shapes are not too different from spherical. The LPM was used to calculate the packing density of the powders, because it was successfully used to predict the packing density of irregular particles based on the concepts of equivalent packing size and initial porosity of mono-sized irregular particles [42]. Although there are a few packing models to predict the packing density of spheres [9,43,44], they cannot be used for the present system.

Figure 8 gives the packing densities of different distributions of the powder obtained by both DigiPac and LPM. Although simplifications were made to permit use of DigiPac and LPM, the bulk densities obtained by the two approaches are generally quite close. It was observed that the variation of packing density of the investigated size distributions is small, because of the narrow size range (10 to 50 microns). The results in Section 4.4.1 and this section clearly demonstrate that DigiPac can very accurately predict the packing density of powders with the real size distributions and shapes. This conclusion was also supported by the work of Gopinahan [45].

Whilst DigiPac can predict directly the packing density of a multi-component mixture, LPM needs as input the packing density of each individual component and of each binary mixture of the components under different compositions to determine the empirical constants used in the model before it can be used to predict the packing density of a multi-component mixture. On the other hand, since LPM is basically an analytical formula with empirical constants to be determined, once established, it can be used to quickly and easily predict the packing density for all

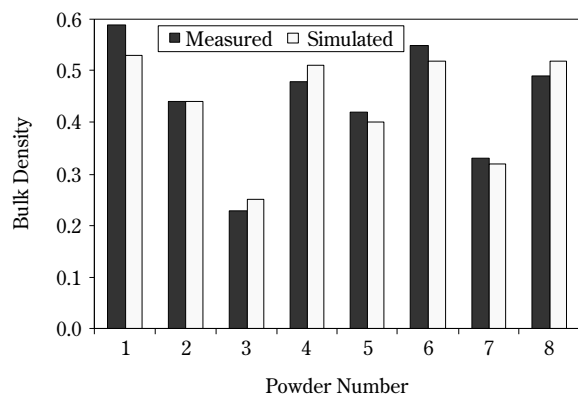


Fig. 7 Comparison of measured and simulated packing densities for PWD1 to PWD8.

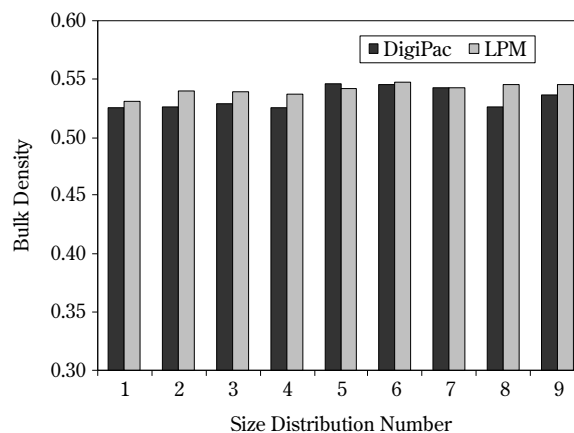


Fig. 8 Comparison of bulk packing densities obtained using DigiPac and LPM for PWD9 with nine different size distributions.

possible compositions involving the same components; whereas each run of DigiPac simulation only gives the packing density for a particular composition it is set up to simulate. Generally speaking, to use LPM for non-spherical particles, the equivalent packing size and initial packing density of each component [25,42] must be obtained first. These parameters are usually obtained from the experiments. It is tedious and time-consuming to determine these parameters experimentally. In DigiPac, the difficult part is digitisation of irregular shapes. Fortunately, with the help of a 3D optical scanner or X-ray tomography, 3D images of real particles are easily obtained. It is expected that DigiPac will become an attractive method for a number of applications [46].

Since the interactions of particles are limited to geometric constraints, the limitations of DigiPac are obvious in the present version. Therefore, further work should be carried out by integrating other interactions into the algorithm. However, as demonstrated above, DigiPac gives accurate predictions for the packing of not only mono-sized nonspherical particles but also of nonspherical mixtures with polydispersed sizes. The potential application of DigiPac may be found in ceramics, powder storage and transportation, multiphase flow, etc.

5. Conclusions

Through the case studies, DigiPac, a newly developed packing algorithm based on digitisation technology, has been validated by using non-spherical particles of uniform sizes and powders of different size distributions. Although the particles with well-defined geometries are used in simulations of mono-sized particle packing, the results are illustrative for the purpose of validation. The porosity obtained is consistent with the measurements and other model predictions.

Our simulation results indicate that the maximum packing density may also be obtained under the condition of minor particle shape deviations from that of a sphere, which is in line with the results reported recently by a number of investigators. The results have implications for a wide range of applications of scientific disciplines.

The DigiPac-simulated results of the packings of industrial powders with size distributions are in good agreement with the measurements; using DigiPac, the simulated packing density is also well comparable to the prediction from the accepted packing model – the linear packing model. These results give direct

evidence to confirm the validity of DigiPac in solving particle packing problems encountered in industry.

The case studies demonstrate that DigiPac is readily applicable in the packing of both mono-sized non-spherical particles and multi-component non-spherical mixtures. Such a successful packing algorithm provides a powerful means to solve various packing problems in a range of applications.

More work needs to be done to extend DigiPac to solve more complicated systems, such as particles where cohesive forces are involved.

Acknowledgement

M. Gan would like to acknowledge the financial support from British Nuclear Fuels PLC.

Nomenclature

D or d	Diameter of spherical particle	(m)
r	Ratio of length to the diameter in cylinder and spherocylinder	(–)
Ψ	Particle sphericity	(–)
Φ	Cylinder diameter	(m)
ϵ	Porosity of a packed bed	(–)
ρ	Packing density in a packed bed	(–)

References

- German, R.M.: "Particle packing characteristics", Metal Powder Industries Federation, NJ, (1989).
- Evans, K.E. and M.D. Ferrar: "The packing of thick fibres", *J. Phys. D*, 22 (1989), 354-360.
- Sherwood, J.D.: "Packing of spheroids in three-dimensional space by random sequential addition", *J. Phys. A*, 30 (1997), L839-L843.
- Coelho, D., J.F. Thovert and P.M. Adler: "Geometrical and transport properties of random packing of spheres and aspherical particles", *Phys. Rev. E*, 55(2) (1997), 1959-1978.
- Thomas, P.A. and J.D. Bray: "Capturing non-spherical shape of granular media with disk clusters", *J. Geotech. & Geoenviron. Eng.*, 125(3) (1999), 169-178.
- Williams, S.R. and A.P. Philipse: "Random packing of spheres and spherocylinders simulated by mechanical contraction", *Phys. Rev. E*, 67 (2003), 051301-9.
- Abreu, C.R.A., F.W. Tavares and M. Castier: "Influence of particle shape on the packing and on the segregation of spherocylinders via Monte Carlo simulations", *Powder Technol.*, 134 (2003), 167-180.
- Yu, A.B. and N. Standish: "Porosity calculation of multi-component mixtures of particles", *Powder Technol.*, 52 (1987), 233-241.
- Yu, A.B. and N. Standish: "Estimation of the porosity of particle mixtures by a linear-mixture packing model,"

- Ind. Eng. Chem. Res. 30(6) (1991): 1372-1387.
10. He, D.N., E.N. Ekere and L. Cai: "Computer simulation of random packing of unequal particles", *Phys. Rev. E*, 60 (1999), 7098-7104.
 11. Kong, C.M. and J. Lannutti: "Effect of agglomerate size distribution on loose packing fraction", *J. Am. Ceram. Soc.*, 83(9) (2000), 2183-88.
 12. Liu, L. and Y. Yuan: "Dynamic simulation of powder compact by random packing of monosized and polydisperse particles", *J. Mater. Sci. Lett.* 19 (2000), 841-843.
 13. Torquato, S., T.M. Truskett and P.G. Debenedetti: "Is random close packing of spheres well defined?" *Phys. Rev. Lett.* 84(10) (2000), 2064-2067.
 14. Buchalter, B.J. and R.M. Bradley: "Orientational order in random packings of ellipses", *Phys. Rev. A*, 46(6) (1992), 3046-3056.
 15. Wang, C.Y., C.F. Wang and J. Sheng: "A packing generation scheme for the granular assemblies with 3D ellipsoidal particles", *Int. J. Numer. and Analyt. Meth. in Geomech.*, 23 (1999), 815-828.
 16. Foley, J.D., A.V. Dam, S.K. Feiner and J.F. Hughes: "Computer Graphics, Principles and Practice", 2nd Edition, Wesley, New York, (1990).
 17. Dickinson, J.K., and G.K. Knopf: "Generating 3D packing arrangements for layered manufacturing", *Proc. Intern. Conf. on Agile, Intel. & Computer-Integrated Manuf. Sys.* Troy, New York: 7 October 1998-8 October 1998. Rensselaer Polytechnic Institute. 1-13. CD ROM.
 18. Latham, J.P., A. Munjiza and Y. Lu: "On the prediction of void porosity and packing of rock particulates", *Powder Technol.*, 125(1) (2002), 10-27.
 19. Jia, X. and R.A. Williams: "A packing algorithm for particles of arbitrary shapes", *Powder Technol.*, 120 (2001), 175-186.
 20. Jia, X., N. Gopinathan and R.A. Williams: "Modeling complex packing structures and their thermal properties", *Adv. Powder Technol.*, 13(1) (2002), 55-77.
 21. Zhang, Z.P., L.F. Liu, Y.D. Yuan, and A.B. Yu: "A simulation study of the effect of dynamic variables on the packing of spheres", *Powder Technol.*, 116 (2001), 23-32.
 22. Zou, R.P. and A.B. Yu. "Evaluation of the packing characteristics of mono-sized non-spherical particles", *Powder Technol.*, 88 (1996), 71-79.
 23. Rahli, O., L. Tadrist and R. Blanc: "Experimental analysis of the porosity of randomly packed rigid fibers", *C. R. Acad. Paris*, 327(2) (1999), 725-729.
 24. Novellani, M., R. Santini and L. Tadrist: "Experimental study of the porosity of loose stacks of stiff cylindrical fibers: influence of the aspect ratio of fibers", *Eur. Phys. J. B13* (2000), 571-578.
 25. Yu, A.B., R.P. Zou and N. Standish: "Modifying the linear packing model for predicting the porosity of non-spherical particle mixtures", *Ind. Eng. Chem. Res.* 35 (1996), 3730-3741.
 26. Smith, L.N. and P.S. Midha: "Computer simulation of morphology and packing behaviour of irregular particles, for predicting apparent packing density", *Comput. Mat. Sci.*, 7 (1997), 377-383.
 27. Abou-Chakra, H, J. Baxter and U. Tuzun: "Three-dimensional particle shape descriptors for computer simulation of non-spherical particulate assemblies", *Adv. Powder Technol.* 15(1) (2004), 63-77.
 28. Reyes, S.C. and E. Iglesia: "Monte Carlo simulations of structural properties of packed beds", *Chem. Eng. Sci.*, 46(4) (1991), 1089-99.
 29. Oweberg, T.G., R.L. McDonald and R.J. Trainor: "The packing of spheres", *Powder Technol.*, 3 (1969/70), 183-188.
 30. Bideau, D. and A. Hansen (Eds.): "Disorder and granular media", Elsevier, North-Holland, (1993), (Chaps. 2 and 4).
 31. Svarovsky, L.: "Powder testing guide: methods of measuring the physical properties of bulk powders", Elsevier Applied Science Publishers LTD, England (1987).
 32. Aoki, R. and M. Suzuki: "Effect of particle shape on the flow and packing properties of non-cohesive granular materials", *Powder Technol.*, 4 (1970/71), 102-104.
 33. Milewski, J.V. and H.S. Katz: "Handbook of fillers and reinforcements for plastics", Van Nostrand Reinhold, NY, (1987), 14-33.
 34. Allen, T.: "Particle size measurement", Chapman & Hall, London, 3rd ed., (1981).
 35. Onsager, L.: "The effect of shape on the interaction of colloidal particles", *Ann. NY Acad. Sci.* (1948), 627-569.
 36. Parkhouse, J.G. and A. Kelly, "The random packing of fibers in three dimensions", *Proc. R. Soc. Lond. A*, 451 (1995), 737-746.
 37. Veerman, J.A.C. and D. Frenkel: "Phase diagram of a system of hard spherocylinders by computer simulation", *Phys. Rev. A*, 41(6) (1990), 3237-3244.
 38. McGrother, S.C., D.C. Williamson and G. Jackson: "A re-examination of the phase diagram of hard spherocylinders", *J. Chem. Phys.*, 104(17) (1996), 6755-6771.
 39. Bolhuis, P.B. and J.D. Frenkel: "Tracing the phase boundaries of hard spherocylinders", *Chem. Phys.*, 106(2) (1997), 666-687.
 40. Donev, A., I. Cisse, D. Sachs, E.A. Variano, F.H. Stillinger, R. Connelly, S. Torquato and P.M. Chaikin: "Improving the density of jammed disordered packings using ellipsoids", *Science*, 303 (2004), 990-993.
 41. Kuo, C. and R.B. Freeman: "Imaging indices for quantification of shape, angularity, and surface texture of aggregates", *Transport. Res. Record* 1721, No. 00-0686 (2000), 57-65.
 42. Yu, A.B. and Z.P. Zou: "Prediction of the porosity of particulate mixtures", *KONA*, 16 (1998), 68-81.
 43. Ouchiyama, N. and T. Tanaka: "Porosity estimation for random packings of spherical particles," *Ind. Eng. Chem. Fundam.* 23(4) (1984), 490-501.
 44. Suzuki, Y.A., T. Watanabe and T. Oshima: "Estimation of the void fraction in a bed randomly packed with particles of three sizes," *Int. Chem. Eng.* 26(3) (1986), 491-497.
 45. Gopinathan, N.: Ph.D. Dissertation, University of Leeds, England, (2004).

46. Williams, R.A. and X. Jia: "A new method for prediction of bulk particle packing behavior for arbitrary-shaped

particles in containers of any shape", *Particulate Sci. and Technol.*, 21(2) (2003), 195-205.

Author's short biography



Mingle Gan

Mingle Gan received his bachelor degree in physics (1987), master degree in materials science (1990) both in Sichuan University, China and PhD in University of New South Wales, Sydney, Australia in 2002. He worked as an engineer and a senior engineer in Southwestern Institute of Physics in Chengdu, China during 1990 – 1997. His research interests included materials property measurements, materials processings, surface coatings, ion beam materials analyses, ion implantations, interactions of plasma with materials. His PhD study and later the post-doctoral research in University of Leeds focus on mathematical modelling and computer simulations of granular media.



Nishanth Gopinathan

Nishanth Gopinathan is currently a post-doctoral research associate at the Particle Engineering Research centre, University of Florida. His PhD was from University of Leeds, UK where he worked in "Packing of complex shaped particulates and property prediction of porous media". He completed his Bachelors from Calicut University in India in 1998 and Masters form Indian Institute of Technology, Kanpur. After this he worked in Unilever Research India, Bangalore, India as a Research Officer where he studied surfactant-structurant synergistic effects. His research expertise has been in several areas including discrete element modeling, lattice Boltzmann technique, particle packing and segregation. He has worked in consultancy projects for several companies including Proctor and Gamble, Johnson Matthey Catalysts, Imerys, etc.



Xiaodong Jia

Xiaodong Jia obtained his BSc in Engineering Physics from Tsinghua University, China in 1986 and PhD in Chemical Engineering from the now University of Manchester in 1992. He is a senior research fellow in the Institute of Particle Science and Engineering, University of Leeds. His interests are particle and powder characterisation and modelling.

Author's short biography



Richard A. Williams

A graduate in Mineral Technology and PhD from Imperial College of Science and Technology, he holds the Anglo American plc Chair in Mineral and Process Engineering and is a Keyworth Professor of Manufacturing and Information Systems Engineering at the University of Leeds and Visiting Professor at the University of Exeter. He was formerly The Royal Academy of Engineering-Rio Tinto Professor of Minerals Engineering at University of Exeter at Camborne School of Mines (1995-1999), and a Senior Lecturer in Chemical Engineering at UMIST (1986-1994). He is a Fellow, Council Member and Trustee of The Royal Academy of Engineering. He has worked in the engineering of colloidal and particulate systems across a range of industrial sectors, with emphasis on in-process measurement and modelling of particulate systems. His specialist research areas include: formation of ultrafine particles, production of nanofluids, particle aggregation and colloidal stability, precision emulsification. A further major interest has been the development and application of in-process measurements using process tomographic sensors.

Characterization of Flow Properties of Powder Coatings Used in the Automotive Industry[†]

Cyril Conesa^{1,2}, Khashayar Saleh¹,
Aline Thomas¹, Pierre Guigon¹,
Nicolas Guillot²

¹ Chemical Engineering Department, Compiègne
University of Technology

² Department of Materials and Painting Processes,
PSA Peugeot Citroën

Abstract

The aim of this work was, on the one hand, to gain a better understanding of the effect of flow additive content on the powder flowability, and on the other hand, to point out the most suitable tests to characterize the flow properties of industrial powder paints used in automotive industries. The flow properties of 5 powder coatings, containing 0, 0.12, 0.30, 0.53 and 0.96 w/w%, respectively, of a flow additive and an industrial batch, were tested using both conventional and novel characterization techniques. The lubricant used was a silica powder. Test methods employed were a packing test, a circular shear cell (Peschl), a powder rheometer and a fluidization/de-aeration test. The flowability of powder batches is significantly improved with increasing lubricant content up to an optimal value of about 0.53%. SEM images of different powder samples showed that the optimal point corresponds to a critical additive content where the amount of additive is high enough to form a continuous film around the particles. Beyond this critical content, the particle-lubricant contacts are replaced by lubricant-lubricant contacts. This phenomenon leads to a degradation of flowability due to a higher cohesivity of additive particles.

INTRODUCTION

Among all manufacturing processes for automotive production, the painting operation contributes most to direct environmental emissions. As a consequence of recent restrictions in European legislation concerning the volatile organic compounds (VOC) emissions, the trend in almost every finisher industrial field is to replace the conventional solvent-borne paints by new low-emission paint systems, including powder coating systems. Powder paints are very finely divided solvent-free polymer coatings, which present important advantages over conventional paints from ecological and economical points of view [1].

There are many ways to apply powder coating materials, as reported in the “technical” literature.

The most important ones are without doubt the fluidized bed technique and the electrostatic spraying of powders.

The fluidized bed was the first application method used to apply powder coatings. Powder paint is suspended inside a fluidized reservoir by blowing air through it from a porous base. Workpieces, preheated to a temperature above the melting point of the powder, are then immersed in the fluidized powder, and powder particles in contact with the substrate melt and adhere to the surface. This technique is still used in many applications such as wire products or electrical busbars. However, the development of this process has been limited by large drawbacks: the relatively high thickness of the final layer on the one hand, and the impossibility of handling on the other hand.

Compared to fluidized bed coating, the powder electrostatic spraying technique is much more versatile and can be applied to a wide variety of workpieces with different shapes and sizes. Furthermore, this technique provides thinner and more homogeneous

¹ CNRS-UMR 6067, BP 20529, 60205 Compiègne cedex

² Vélizy Technical Center, CC.09, 78943 Vélizy – Villacoublay cedex

[†] Accepted: August 26, 2004

films.

These advantages explain in part the great interest shown in this technique among industrial finishers and more particularly the automotive sector. Since the introduction of this technique in 1962, the electrostatic powder spray process outstripped the fluidized bed technique.

As shown schematically in **Figure 1**, in electrostatic powder coating processes, powder paint is fluidized in a reservoir and is then blown through a feed pipe to a special charging corona bell. After passing through the corona bell, in which particles are electrostatically charged, the powder is sprayed toward a grounded workpiece [2]. The adhered powder is then heated, whereupon it melts and cross-links to form a uniform layer over the workpiece. In addition, unlike the liquid paint systems in which non-deposited paint is lost, the oversprayed powder during the electrostatic application process can be reclaimed for further use.

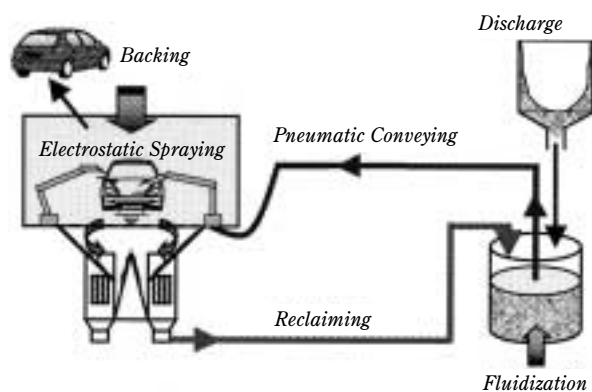


Fig. 1 Schematic diagram of industrial application process

In the automotive industry, a very high-grade appearance is required for a minimal thickness of finished film. However, powder coatings commonly suffer from the so-called “orange peel” effect, a subtle surface unevenness of the solidified coating, which influences the final appearance. In the case of powder coatings, the finished film quality can be reached by very specific physical properties of powder: small and narrow particle size distributions [3]. Unfortunately, as is well-known in powder technology, the handling properties of these fine powders present some problems such as blocking during storage and poor powder flowability that cause application problems such as poor fluidization, irregular feed rates and increased powder hold-up in the transport hose [4]. In powder

technology, one of the most common solutions to overcome this problem is to add a flow additive: particles of submicron size located between large particles, resulting in a reduction of inter-particle forces [5].

The aim of this work was, on the one hand, a better understanding of the effect of flow additive content on the powders’ flowability and, on the other hand, to point out the most suitable tests to characterize the flow properties of industrial powder coatings used in automotive industries. The flow properties of 5 powder coatings, containing 0, 0.12, 0.30, 0.53 and 0.96 w/w% of a flow additive and an industrial batch, respectively, were tested using current and novel characterization techniques. The lubricant used was a silica powder. Test methods employed were the packing test, circular shear cell (Peschl), powder rheometer and fluidization/de-aeration tests.

EXPERIMENTAL

1. Materials

A powder based on polyester/epoxy thermosetting hybrid resin was chosen for this study. It is a gray powder coating used for the primer coat in the automotive industry. It has an angular particle shape. The mean particle size is close to 29 μm and the true density 1310 kg/m^3 . According to Geldart’s classification, the original powder, which does not contain the flow additive, falls within group C [6]. Powders that are in any way cohesive belong in this category. Fluidization of such powders is extremely difficult and they flow poorly.

The additive used is a commercial, very fine spherical silica powder (10 nm in diameter). This kind of additive is frequently used in order to improve the flowability of cohesive powders. A silica component was added to the fresh powder in weight percentages of 0; 0.25; 0.50; 1.00 and 2.00%. Each powder mixture was prepared in two steps inside a fluidization column. A first blend is carried out in a 1.10^{-2} m^3 fluidization column in order to pre-dilute the flow additive in 4 kg of fresh powder coating. The mixing time was 4 hours under mild fluidization. Then, the mixture was added again to 16 kg of fresh powder paint into a 1.10^{-1} m^3 stainless steel column. The mixing time was then 12 hours. The final batch weight was therefore 20 kg. During fluidization, oil-free air dried through a bed of silica gel was used. The use of a mechanical stirrer improved the fluidization and enabled the use of a low superficial air velocity close to $2.10^{-3} \text{ m}\cdot\text{s}^{-1}$ in order

Table 1 Characteristics of powder paints

Product	AGF 1	AGF 2	AGF 3	AGF 4	AGF 5	Industrial Batch
Additive content, %w/w, (based on added amount)	0	0.25	0.50	1.00	2.00	–
Additive content, %w/w, (measured)	0	0.12	0.30	0.53	0.96	–
Mean diameter, d_v (μm)	29.2	–	–	–	–	28.8
Mean diameter, d_{sv} (μm)	21.6	–	–	–	–	21.2
Shape factor	0,8	0,8	0,8	0,8	0,8	–
True density ($\text{kg}\cdot\text{m}^{-3}$)	1310	1310	1310	1310	1310	1310
Blaine specific area ($\text{m}^2\cdot\text{kg}^{-1}$)	2501	2531	2656	2766	3386	2448

to limit the loss of fine particles. Finally, each batch was sieved through a 75- μm mesh. In this work, an industrial batch of powder primer was also studied in order to assess the suitability of the test for industrial use.

The six powder coatings containing different amounts of additives were fully physically characterized. The particle size distribution was measured by laser diffraction using a Malvern Mastersizer (manufactured by Malvern Instruments), and the true density of solids by a Helium Pycnometer Accupyc 1330 (manufactured by Micromeritics). The true percentage of flowability additive contents in the final batches was also determined using the ICP-AES method [7]. The specific surface area was assessed using a Blaine permeameter.

Table 1 summarizes some physical characteristics of the 6 batches used in this work.

2. Methods

2.1. Aerated and tap density measurements

The bulk density of a powder is its mass divided by the bulk volume it occupies. The value of bulk density depends tremendously on the consolidation state of the powder. So both the aerated and tap densities of a powder have very different values [8,9].

Measurement of the bulk volume variation of the powder during tapping was performed using a tap density volumeter (manufactured by Quantachrome). It consists of a graduated 100-ml vessel and a tapping apparatus. The simple experimental procedure was the following: the powder was first poured into the 10^{-4} m^3 graduate cylinder through a suitable vibrating sieve such that most of the material would pass readily. The vibration amplitude was such that the time necessary to fill the vessel was at least 10 s. Before

weighing, the excess powder was scraped from the top of the vessel using a ruler, without disturbing or compacting the loosely settled powder. The vessel was then subjected to successive vertical taps, and volume measurements were obtained after a different number of taps. For each sample, the operation was continued up to 2000 taps, whereupon a steady state was reached indicating that the packing was achieved. The bulk density of a powder, ρ_N , at each tapping number N was determined by dividing the mass of the sample by the volume it occupies. Three tests were conducted on each sample for aerated density and tapped density. The average values were taken to be the aerated and tapped bulk density. The powder volume decrease was assessed by several parameters.

The first one is the ratio of aerated and tap density, known as the Hausner Ratio, HR, calculated using the following equation:

$$HR = \frac{\rho_N}{\rho_0} = \frac{V_0}{V_N} \quad (1)$$

where ρ_0 is the bulk density of unpacked powder, V_0 the initial apparent volume and V_N the powder volume at tapping number N . Typically, a powder that is difficult to fluidize will have an HR greater than 1.4. A powder that exhibits excellent flow and fluidization will be around 1.25 or less.

The second parameter is the compressibility C (introduced by Carr [10]) of the powder, which is the degree of volume reduction given by:

$$C = \frac{V_0 - V_N}{V_0} \quad (2)$$

Both Hausner's ratio and compressibility are commonly used as qualitative indicators for determining whether or not a powder is cohesive. They reflect the friction conditions in a moving mass of powder rather

Table 2 Carr's classification

$0.05 < C < 0.15$	good flow
$0.15 < C < 0.18$	fair flow
$0.18 < C < 0.22$	passable flow
$0.22 < C < 0.35$	poor flow
$0.35 < C < 0.40$	very poor flow

than in a static situation. Generally, the structure of a cohesive powder will collapse significantly on tapping while the free-flowing powder has little scope for further consolidation. The powder particles are forced to jump and to lose contact with each other for a moment while tapping. When the friction between the particles is reduced, the particles rearrange, and thus tapping results in improved packing conditions. So, a drop in Hausner ratio or compressibility corresponds to a decrease in the cohesiveness of the powder [8].

Concerning the compressibility C , the simplified Kawakita and Lüdde equation [11] leads to a relationship between the tapping compaction of powders and their compression:

$$\frac{N}{C} = \frac{1}{a} \cdot N + \frac{1}{ab} \quad (3)$$

a and b are constants, characteristic of the powder. The linear relationship between N/C and N allows the constants to be evaluated graphically.

The constant a stands for the degree of volume reduction at the limit of tapping and represents the maximal compressibility and the fluidity of a powder [12].

Conversely, b represents the tapping compressibility of a material. Its reciprocal $1/b$ is a measure of the resistance of the material to tapping. Hence, $1/b$ is considered as the constant relating to the cohesive forces of powder particles [12]. In this work, $1/b$ has not been taken into account because a specific experimental method is necessary to obtain an accurate value.

2.2. Shear cell measurement

Yield locus and failure functions of the six powders under investigation were established using a Peschl circular shear test (RO-200, IPT), **Figure 2**. The device consists of a 60-mm rotating bottom ring with a roughened base, an open upper ring of equal diameter and a round roughened lid prolonged by a horizontal arm permitting measurement of the shear force during experiments [13].

Firstly, the sample was compressed for 45 minutes under predetermined consolidation pressure (16, 12, 8; 4 and 2 kPa) before performing the shear test. Commonly, this step is called the “preconsolidation step”. In order to compensate the volume decrease of the consolidated powder, an extension ring is used to permit the addition of extra powder. When the consolidation time is completed, the extension ring is removed and the powder is carefully scraped level. The shear cell is then set up over the rotational base.

The rotational base is then activated in the direction of the shear. When the horizontal arm contacts the force sensor, the lid motion is stopped. Consequently, by rotating the shear cell relative to the lid, a shear deformation is developed leading to a shear stress, acting in the assumed shear plane located between the upper ring and bottom ring. Generally, the shear stress increases until failure takes place and then remains constant.

The first shear step is a conditioning step, which has the purpose of bringing the sample to critical conditions (shear without change of volume). We can call this step the “consolidation step”. This consolidation step has to be repeated by using a constant vertical load until the maximum top stress value is reached. After reaching the steady-state shear stress, the sample is relieved of the shear stress by reversing the direction of the rotating base until the shear stress becomes zero.

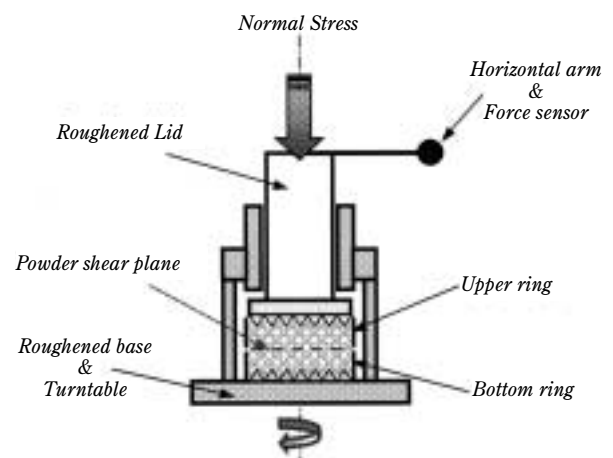


Fig. 2 Schematic diagram of circular shear stress apparatus (Peschl)

In the period where the shear stress is equal to zero, the vertical load is changed in order to prepare

the sample for the measurement in the next step. A shearing test which includes 10 steps starts with the same vertical load as the preconsolidation step and continues decreasing the normal load step by step. So the shear stress (τ), necessary to cause failure and create flow under 10 applied normal stresses (σ), can be measured for a given consolidation. The curve obtained is the so-called yield locus. Two further important parameters may be extracted from these results:

- Unconfined yield strength (f_c): this parameter is obtained by plotting the Mohr semicircle which passes through the origin and is at a tangent to the yield locus.
- Major principal stress (σ_1): it is obtained by a Mohr semicircle which is at a tangent to the yield locus at its end point.

According to Jenike [14], the ratio of the major principal stress σ_1 at steady-state flow to the unconfined yield strength f_c called the flowability index is a good indicator of powder flowability under load:

$$i = \sigma_1 / f_c \quad (4)$$

Table 3 Classification of flowability index

$i < 2$	very cohesive
$2 < i < 4$	cohesive
$4 < i < 10$	easy flowing
$10 < i$	free flowing

In this work, five yield loci (2, 4, 8, 12 and 16 kPa) were established for each sample from which the corresponding value of f_c and σ_1 were determined. A curve of (f_c) vs (σ_1), known as the flow function (FF), is then plotted and the flowability index determined.

2.3. Powder rheometer measurement:

The FT4 powder rheometer (manufactured by Freeman Technology) is a new device that is able to classify powders regarding their flowability. The aim of this device is to provide an automated testing program that is relatively independent of the operator and is quick.

The device principle, which is represented in **Figure 3**, is simple [15]. A powder sample, after being weighed, is placed in a glass cylindrical vessel. A specific twisted blade, with a diameter of 60 mm, moves along a helical path through the powder column. The controlled parameters are helical path angles, blade

tip speed, starting height and final height. As the parameter values are changed, the helical path has more or less revolution and the blade moves downward or upward, in clockwise or anti-clockwise direction. Therefore, it is possible to choose the direction of the blade tip displacement. Different regimes are possible: a shearing regime (the blade tip is parallel to the trajectory) or a compaction regime (the blade tip is perpendicular to the trajectory). The blade motion imposes the forces, causing the deformation and the flow of the powder. The axial forces and rotational forces acting on the blade during the cycle through the powder are measured continuously and used to derive the work done, or energy consumed, in displacing the powder. A typical test program alternates two steps. The first step is preparation of the sample for testing in a conditioning process in which the blade gently displaces the powder to establish a consistent and reproducible packing density. During the second step of the test cycle, the blade moved along a downward helical path, but in the opposite direction, to impose a compaction regime, thereby forcing the powder to flow around the blade.

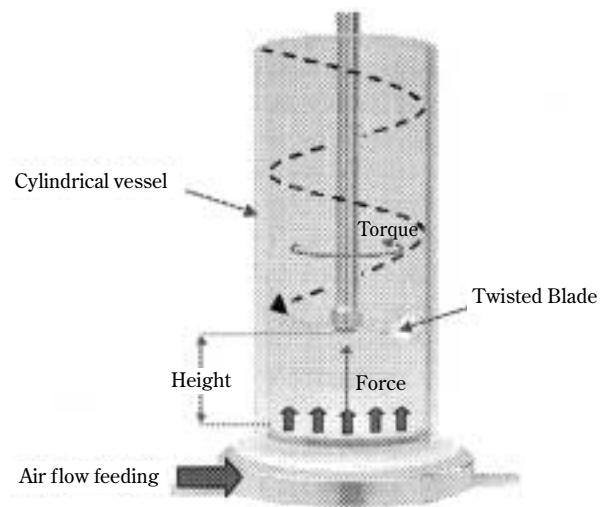


Fig. 3 Schematic diagram of FT4 powder rheometer from Freeman Technology

In this study, a specific test called the aeration test was developed. The bottom of the cylindrical test vessel is made of a stainless steel porous plate 62 mm in diameter. During the test, an air flow controlled by a mass flow controller passes from the bottom to the top through the column of powder. Dependent on the air velocity, the powder bed is either fluidized or sim-

ply aerated.

Approximately 100 g of powder paint is loaded into the translucent vessel. For the same sample, the measurements were achieved at 5 superficial air velocities (1, 2, 4, 6, 8 mm/s). A complete test is carried out with the air flow varying from the highest to the lowest value. In between each new air velocity, the testing stage is preceded by a conditioning cycle in order to obtain a steady state of aerated powder. During the aeration test, the normal force developed by the blade is very low. So for this study, only the torque energy was analysed.

2.4. Fluidization/De-aeration measurement:

A fluidization test and a bed collapsing technique were used in order to assess the fluidization and the cohesiveness of the six powders and to classify them. Virtually, the structural or inter-particle forces that affect flowability also affect fluidization.

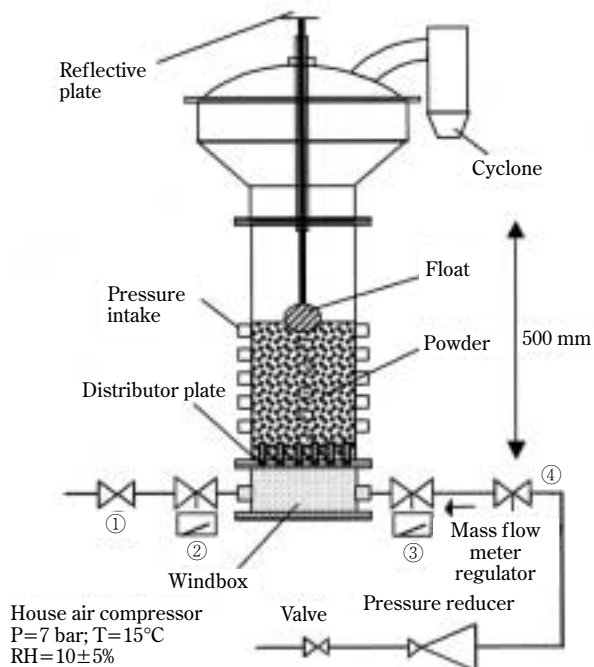


Fig. 4 Schematic diagram of experimental apparatus

The equipment to assess fluidization behavior in this study consisted of a rather standard fluidized test column. Three main parts comprise this experimental apparatus: the column, the air flow circuit and the acquisition device. **Figure 4** shows a schematic diagram with the dimensions of the experimental appara-

tus. The trials were carried out in a Pyrex column 100 mm in diameter and 500 mm in height built on an aluminum frame to make transport of the apparatus easier. At the top of the column, an expanded disengaging section minimizes particle entrainment and a cover surmounted by a cyclone recovers the finest particles. The distributor was made of two overlapping filter papers supported by a metallic porous plate. It is supported by the windbox, which was made deliberately small ($7,85 \cdot 10^{-4} \text{ m}^3$) in order to reduce the escape time and resistance during the de-aeration tests. Compressed air was fed to the bed of powder through a filter, a pressure regulator, a computerized mass flowmeter regulator (4), a solenoid valve (3), the windbox and the distributor plate. Transducers continually recorded the relative humidity (5% HR) and the temperature (22°C) in the windbox. During the tests, the overall pressure drop of the powder bed was measured by a relative pressure transducer (Kobold 3277-BO15) connected to a pressure tap at the windbox.

By means of an acquisition system, a program was created to increase and decrease the air flow rate for a certain time period. So, fluidization trials were carried out more than three times to automatically determine the minimum fluidization velocity for the different tested powders.

The powders' cohesiveness can also be quantified by the de-aeration method. For example, it is usual to foresee the ability of a powder to be conveyed in a pneumatic dense phase or lean phase by a de-aeration test. Initially, a known weight of solids (750 g) was filled into the column. The powder was then fluidized by compressed air at 2 times U_{mf} . When the system reached steady state, the air supply was suddenly cut off by a solenoid valve and the collapse height was recorded as a function of time using a device comprising a float and a laser beam. With the float system, the rapidly collapsing bed height could be determined with "reasonable" accuracy. The residual gas in the windbox was purged to the atmosphere through a solenoid valve (2) and a needle valve (1) installed on the windbox [16]. Without this device, after the sudden cut-off of the air supply, the residual gas in the windbox will be purged through the bed of particles and will disturb its collapsing. Thanks to an optimum valve opening factor, this phenomenon is limited. Because the bed height at $t < 0$ fluctuates considerably due to bubbling, up to 5 repeat tests were made and a numerical average taken which was then plotted. Collapse tests were done with the six powders over a range of velocities above U_{mf} .

RESULTS AND DISCUSSION

1. SEM

By using Scanning Electronic Microscopy (SEM), the surface of a powder coating host particle can be

explored in order to look at the surface coverage by submicronic silica particles.

The micrograph in **Figure 5** gives an overview of paint particles. The angular shape is the shape of ground particles. The micrographs in **Figures 6 to 10** compare the surface coverage for various amounts of

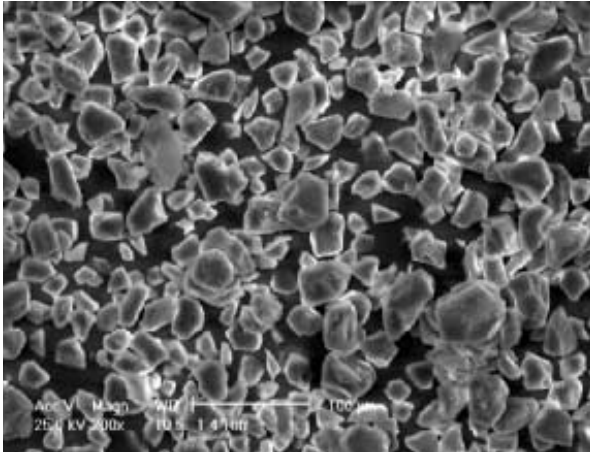


Fig. 5 Powder paint particles

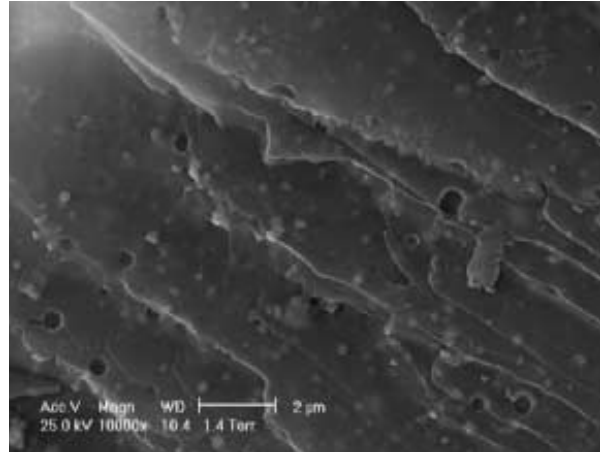


Fig. 6 Particle surface without flow additive

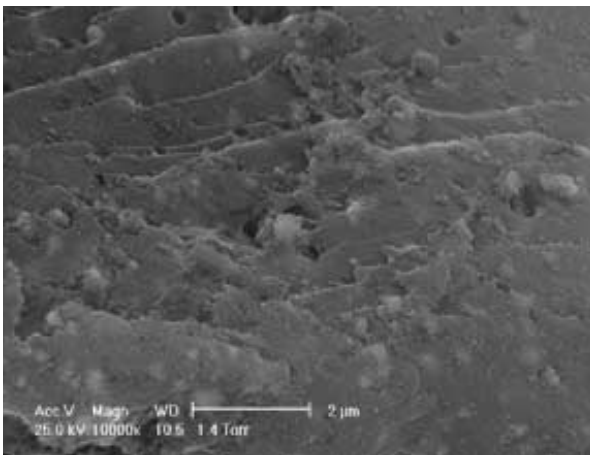


Fig. 7 Particle surface with 0.12% of flow additive

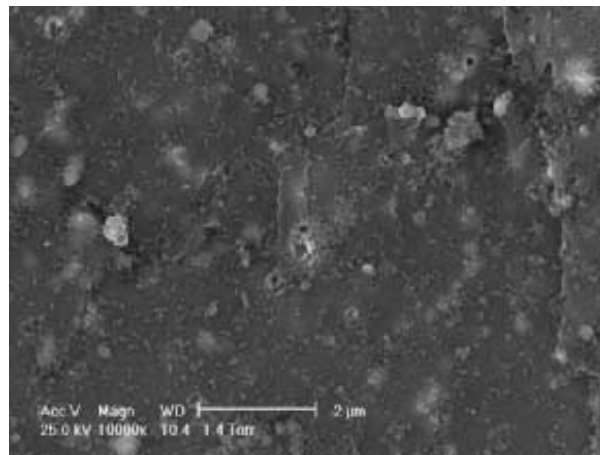


Fig. 8 Particle surface with 0.30% of flow additive

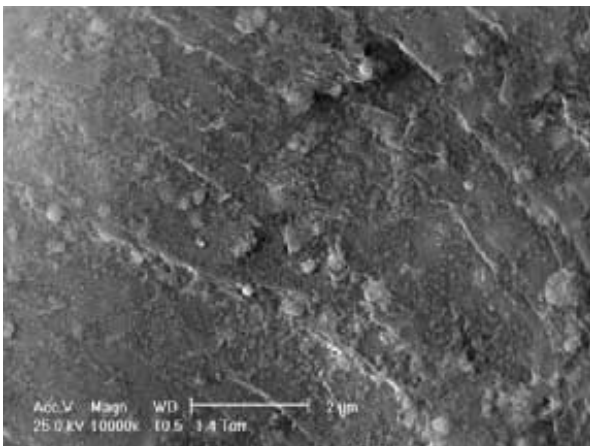


Fig. 9 Particle surface with 0.53% of flow additive

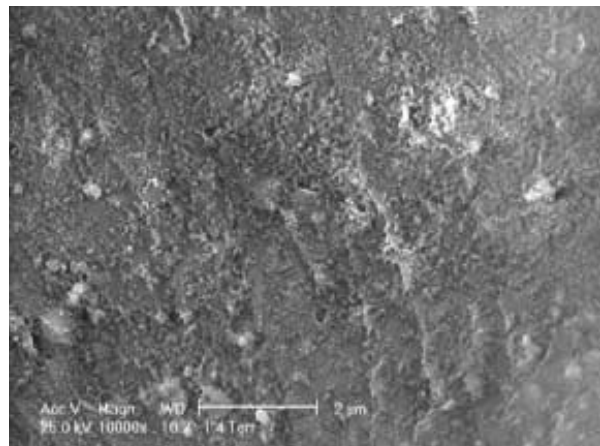


Fig. 10 Particle surface with 0.96% of flow additive

added additives. The nature of the attached particles was checked by the X-ray probe of the SEM.

2. Packing measurements

A greater inter-particle porosity indicates the presence of more air entrapped between the particles and consequently a high compressibility, which corresponds to a cohesive powder and thus poor flowability. In contrast, a low compressibility denotes lower cohesiveness.

A drop in the Hausner ratio or in the compressibility C involves a decrease in cohesiveness of the powder [8]. According to Carr's classification [9,10], the results presented in **Table 4** and in **Figure 11** highlight the flow property improvement when the flow additive percentage increases. *AGF 1* is therefore classified as having poor flow whereas *AGF 4* has a good flow. Nevertheless, it is interesting to see that the flowability improvement reaches a maximum. Beyond an optimal amount of silica, the flowability of powder drops again. This is indicated by the deterioration of *AGF 5* flow properties. The *AGF 5* flowabil-

ity hovers between *AGF 1* and *AGF 2*. This result also shows the important cohesion of the industrial batch which has a compressibility close to *AGF 1*.

3. Shear cell measurements

Figure 12 shows the results obtained using the circular shear cell for the unlubricated powder in comparison with mixtures containing silica. The best flow properties are obtained for a silica concentration which gives the highest value of flowability index (i).

As expected, the increase of the flow additive percentage from 0% (*AGF 1*) to 0.53% (*AGF 4*) improves the flow properties of the powder paint, since the flow function FF moves to the "easy-flowing" area. These results show also that above 0.96% of flow additive (*AGF 5*), the flowability drops. The *AGF 5* flow properties are very similar to *AGF 3*. However, the effect of lubrication appears less clearly than with the flowability index. This technique is less suitable and less sensitive for characterizing the powders. This result also shows the important cohesiveness of the powder of the industrial batch.

Table 4 Packing test results

Powder	AGF 1	AGF 2	AGF 3	AGF 4	AGF 5	Industrial Batch
a (Kawakita and Lüdde)	0.244	0.165	0.148	0.122	0.190	0.210
RH	1.32	1.20	1.18	1.14	1.23	1.26
C (%)	24	16.3	14.7	12.0	18.7	20.8
Carr's Classification	Poor flow	Fair flow	Fair flow	Good flow	Passable flow	Passable flow

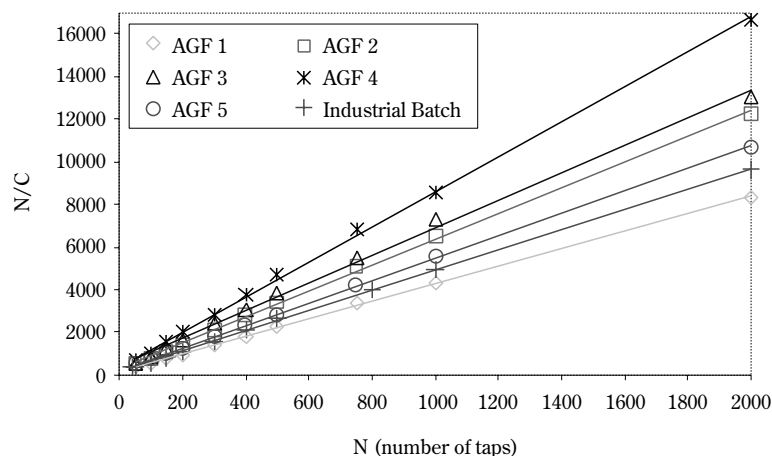


Fig. 11 Relation between N/C and the number of taps N

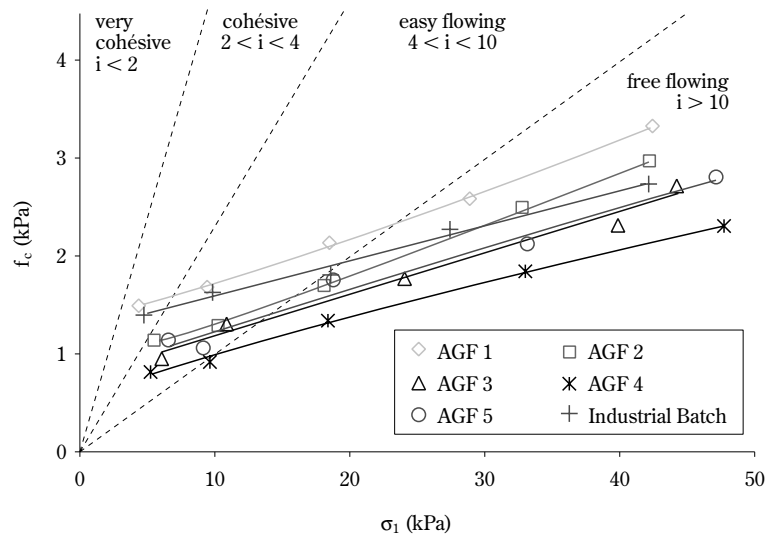


Fig. 12 Flow function and classification according to the flowability index (i)

4. Powder rheometer measurements

In **Figure 13**, results show the total torque energy consumed during a downward test traverse as a function of the superficial air velocity through the distributor. Raw data recorded between a height of 60 and 20 millimeters from the bottom of the vessel were used for the analysis.

Generally speaking, for the highest air velocities, an easy-flowing powder leads to homogeneous fluidization and the torque energy measured is very low. In contrast, fluidization is very difficult for a cohesive

powder and leads to channeling of the powder bed. The torque energy value is increased. When the gas velocity is decreased, the powder bed goes from the fluidized state to the consolidate state and the energy increases. These plots show that the torque energy decreases whereas the flow additive percentage increases up until 0.53% (*AGF 4*). This test did not show differences between *AGF 5*, *AGF 4* and *AGF 3*. The very low torque energy values of these three blends reveal good fluidization properties. However, at a low air velocity ($1 \text{ mm}\cdot\text{s}^{-1}$), the flow properties of *AGF 5* are slightly lower than *AGF 3*. These results

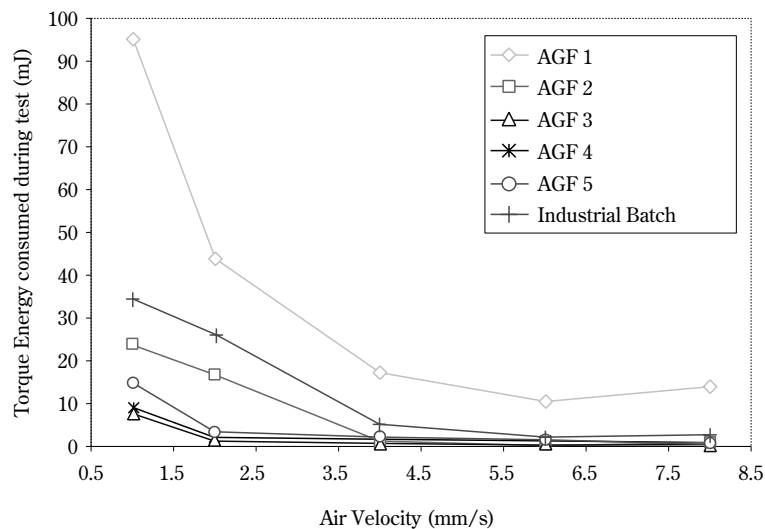


Fig. 13 Energy as a function of aeration air velocity

show that the powder paint without lubricant (*AGF 1*) is very cohesive. For each air flow rate, the torque energy values are much greater than for other mixtures with silica. Regarding the torque energy value at an air velocity of $1 \text{ mm}\cdot\text{s}^{-1}$, *AGF 5* takes its place between *AGF 2* and *AGF 3*. In addition, these results also show the stronger cohesiveness of industrial powders. The very low energy values recorded at higher air velocities indicate that fluidization of this powder is possible. Thus, this method seems suitable for industrial application.

5. Fluidization/De-aeration measurements

In a first stage, the minimum fluidization velocities U_{mf} of the six powder coatings were measured experimentally (**Table 5**). No measurements could be obtained for the powder *AGF 1*, (without flow additives), because fluidization was not possible. It denotes the very cohesive nature of this powder.

Table 5 Fluidization results

	Experimental U_{mf} (mm/s)
AGF 1	—
AGF 2	2.82
AGF 3	1.06
AGF 4	1.06
AGF 5	1.12
Industrial Batch	3.67

The other powders provide very different values of U_{mf} . The *AGF 2* powder (0.12% of additive) displays an U_{mf} nearly 3 times greater than the powders with higher additive content. Materials that exhibited good flow characteristics (0.30, 0.53 and 0.96%) provide a U_{mf} value close to $1 \text{ mm}\cdot\text{s}^{-1}$ and are difficult to differentiate, although the flow additive quantity increased. Moreover, in comparison with the other flowability test results, the *AGF 5* powder did not display a significant gap of behavior with regard to the other powders.

The powder from the industrial batch deviated clearly from the other powders with a more significant U_{mf} value. It shows the very cohesive nature of the powder coating used by the automotive industry. However, the fluidization of such a powder improved by the use of vibrations is quite suitable in the industrial application process.

In a second phase, de-aeration tests were undertaken. The total times for the de-aeration process and the total heights of initial expansion recorded for a superficial air velocity of 2 times U_{mf} are listed in **Table 6**. The curves in **Figure 14** display the kinetics of de-aeration of five of the six powders. The *AGF 1* powder, which did not contain a flow additive, is not fluidizable and has thus not been studied. The results show different behavior among the powders.

Regarding the curves in **Fig. 14**, 2 groups of de-aeration rate are observed. When fluidized at 2 times U_{mf} , the *AGF 2* powder and the industrial batch present a greater initial expansion, and the presence of channeling is visible particularly for the industrial

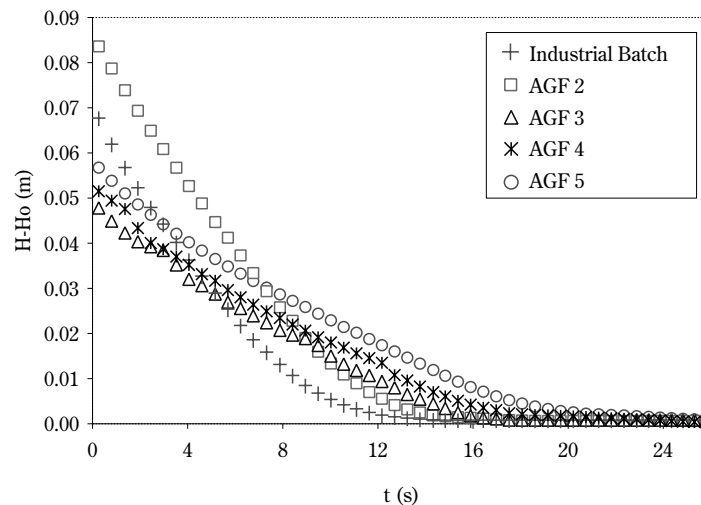


Fig. 14 Bed collapse curves

batch. When the air is cut off suddenly, they de-aerate more rapidly than the other powders, as the air escapes through the channels formed within the bed of powder. This affects the rate of de-aeration as shown in **Fig. 14**. The collapse curves are close to those of the cohesive group-C powders of the Geldart classification [17]. Powders which are intrinsically more cohesive de-aerate quickly because of channeling. After an initial rapid collapse of the bed caused by cracks caving in, the rate of collapse is controlled by the rate at which air can escape to vertical channels formed in the bulk of the powder. Regarding the *AGF 3*, *AGF 4* and *AGF 5* powders no channeling was observed, but the bubbling near the surface of the bed was more pronounced. Besides this, after the air was shut off, the collapsing of the powder bed is slower and the kinetic of de-aeration recorded is close to one of the group-A powders of the Geldart classification, which presents the height decreasing almost linearly [17].

Table 6 Collapsing results

	Total Expansion (mm)	Time (s)
AGF 1	–	–
AGF 2	85	20
AGF 3	49	22
AGF 4	52	26
AGF 5	58	27
Industrial Batch	69	18

The initial expansion height of the different powders did not provide a direct classification correlated to their flowability. In contrast, the total time for the de-aeration process leads to a classification directly correlated to both the flowability and fluidization properties of the six powders as indicated by the different characterization techniques. However, the deterioration of the flow properties of the *AGF 5* powder found by other methods was not observed. The fluidization properties of *AGF 5* appear very close to that of *AGF 4*.

CONCLUSION

Different methods were used to investigate the effect of flow additive content on the flow properties of powder paint. The addition of silica was followed by particle size and permeability measurements, as well as SEM analysis. The accurate quantification of silica

contents was achieved by ICP-AES.

Not every test showed the same sensitivity. Meaning that the classification of the powders according to their flowability or fluidization is slightly different depending on the method used. Moreover, not all of these techniques are suitable for use as a simple bench-top test as required by industry.

The tapping test, shearing test, powder rheometer, fluidization and de-aeration tests show as expected [18-19] that the flowability improves with the lubricant content up to a percentage of 0.30%.

Beyond 0.30%, the tests with some consolidation (tapping test and shearing test) show that an optimum in additive concentration exists, corresponding to the amount suitable to cover the whole particle surface. The tapping test shows greater resolution, is less time-consuming and less tedious.

Fluidization/de-aeration and powder rheometer tests are discriminating only for poorly fluidizable powders, which is the case for industrial powder paints where usually the flow additive content added is rather low in order not to adversely affect other properties. These tests are fully automatic and relatively fast, which is a plus for an industrial bench-top test.

LIST OF SYMBOLS

a	constant of Kawakita and Lüdde equation	
C	compressibility of a powder	
$d_{4,3}$	particle size diameter	(m)
$d_{3,2}$	particle size diameter	(m)
f_C	unconfined yield stress	(Pa)
FF	flow function	
H	height of bed at any time t	(m)
H_0	height of settled bed of powder	(m)
HR	Hausner Ratio	
i	flowability index	
N	tapping number	
t	time	(s)
U_{mf}	minimum fluidization velocity	(m·s ⁻¹)
V_N	powder volume at tapping number N	(m ³)
V_0	initial apparent powder volume	(m ³)
ρ_N	bulk density of a powder at each tapping number	(kg·m ⁻³)
ρ_0	initial bulk density of a powder	(kg·m ⁻³)
σ_1	major principal stress	(Pa)

REFERENCES

- [1] Lovano S.: Automotive applications for powder coating, Metal Finishing, (1996), 20-24
- [2] Bailey A.: The science and technology of electrostatic

- powder spraying, transport and coating, *Journal of Electrostatic*, 45 (1998), 85-120
- [3] Zhisong H., Scriven L.E., Davis H.T.: Film formation in powder coatings, *Waterborne Higher solids and powder coatings symposium*, (1997)
- [4] Satoh H., Harada Y., Libke S.: Spherical particle for automotive powder coatings, *Progress In Organic Coatings*, 34 (1998), 193-199
- [5] Fluck D., Fultz J., Darsillo M.: Fluidization additives in powder coatings, *Paint & Coatings Industry*, (1998), 214-220
- [6] Geldart D.: Type of gas fluidization, *Powder Technology*, 7 (1973), 285-292
- [7] Hermmelin M., Mermet J.M., Bertucci M., Zydowicz P.: Determination of additives in PVC material by UV laser ablation inductively coupled plasma atomic emission spectrometry, *Spectrochimica Acta*, B52 (1997), 421-430
- [8] Abdullah A.C., Geldart A.: The use of bulk density measurements as flowability indicators, *Powder Technology*, 102 (1999), 151-165
- [9] Viana M., Gabaude-Renou M.D.C, Pontier C., Chulia D.: The packing coefficient: a suitable parameter to assess the flow properties of powders, *KONA*, 19 (2001), 85-93
- [10] Carr R.: Evaluating flow properties of solids, *Chemical Engineering*, 18 (1965), 163-168
- [11] Kawakita K., Lüdde K-H: Some consideration on powder Compression Equations, *Powder technology*, 11 (1970), 61-68
- [12] Yamashiro M., Yuasa Y: An experimental study on the relationship between compressibility, fluidity and cohesion of powder solids at small tapping numbers, *Powder technology*, 34 (1983), 225-231
- [13] Peschl I.A.S.Z.: Measurement and evaluation of mechanical properties of powders, *Powder handling & processing*, 1 (1989), 135-141
- [14] Schwedes J.: Testers for measuring flow properties of particulate solids, *Powder handling & processing*, 12 n°4 (2000), 337-354
- [15] Freeman R.: The classification of powders in relation to flowability, *Powder Handling and Processing*, 12 n°2 (2000), 194-197
- [16] Park J.J., Park J.H., Chang I.S.: A new bed-collapsing technique for measuring the dense phase properties of gaz-fluidised beds, *Powder technology*, 66 (1991), 249-257
- [17] Geldart D., Wong A.C.Y.: Fluidization of powder showing degrees of cohesiveness – II. Experiments on rates of de-aeration, *Chemical Engineering Science*, 40 (1985), 653-661
- [18] Podczek F., Miah Y.: The influence of particle size and shape on the angle of internal friction and the flow factor of unlubricated and lubricated powders, *international journal of pharmaceuticals*, 144 (1996), 187-194
- [19] Feliw G.: *Écoulement de milieux granulaires en tambour tournant*, Thèse de doctorat, Institut National Polytechnique de Lorraine – Nancy, (2002)

Author's short biography

Cyril Conesa

Cyril CONESA is a PhD student working in a joint venture between the department of Chemical Engineering of the Compiègne University of Technology (France) and the department of Materials and Painting Processes of the PSA Peugeot-Citroën automotive company. The subject of his research deals with the physical behavior of powder coatings in order to characterize their handling and flow properties with regard to industrial applications.

Khashayar Saleh

Khashayar SALEH received a B.S. degree in Chemical Engineering from Sharif (Aryamehr) University of Technology (Tehran, Iran) in 1992. He prepared a PhD thesis on the coating of fine powders in the Chemical Engineering Laboratory of Toulouse and obtained his doctor's degree in 1998 from the Institut National Polytechnique de Toulouse (France). Dr Saleh is currently an associate professor in the chemical engineering department of the Compiègne University of Technology. His work is focused on powder technology including size enlargement technology and powder characterisation methods.

Aline Thomas

Aline THOMAS is a master-degree student in chemical engineering at the Compiègne University of Technology. The subject of her research deals with powder coatings fluidisation behaviour.

Pierre Guigon

Pierre GUIGON is a chemical engineer from ENSIGC Toulouse (France 1971). Master of Engineering Science, UWO London Ontario (Canada 1974), Docteur Ingénieur UTC Compiègne (France 1976), Docteur es Science UTC Compiègne (France 1978), Fellow of the Institution of Chemical Engineers. He is head of the Particle Technology Group at the Technical University of Compiègne. His research is in the field of particle suspensions (fluidization, pneumatic transport) and particle technology (comminution and agglomeration).

Nicolas Guillot

Nicolas GUILLOT was in charge of powder primer development in the Department of Materials and Painting Processes within the PSA Peugeot Citroën automotive company (Vélizy, France) from July 1998 and since 2001, is now also in charge of innovation.

Liquid-fed Aerosol Reactors for One-step Synthesis of Nano-structured Particles[†]

L. Mädler

Particle Technology Laboratory
ETH Zürich, Switzerland

Abstract

Aerosol technology is the key process for large-scale production of nano-structured materials such as carbon black, titania and silica. The understanding of gas-phase synthesis was transferred successfully from classic vapor-fed flames to liquid-fed aerosol reactors, enabling now also the one-step production of demanding and highly functional products. Such aerosol-derived nano-structured metal oxides, mixed metal oxides, and metals on metal oxides find application in the fields of catalysis, sensors, fillers, and electronics, and have advanced the research and development of these reactors in recent years. The four main spray methods include spray pyrolysis in a tubular reactor (SP), spray pyrolysis using a vapor flame reactor (VFSP), the emulsion combustion method (ECM) and flame spray pyrolysis (FSP). These methods are discussed and key concepts are compared such as the energy source driving the solvent/fuel evaporation and precursor reaction, final particle formation. Advances in fundamental understanding, scaling and simulation are highlighted. Specific strategies for the production of homogeneous products are presented in context with existing methods and specific applications. Finally, research needs are discussed with respect to new flame-made materials, instrumental strategies for their production and process optimization, including diagnostic techniques and process simulation.

1 Introduction

The potential of nano-sized clusters or particles has been recognized in recent years since processes for the synthesis of these entities and devices for nanoparticle characterization became established and new commercial applications were clearly identified [1, 2, 3, 4, 5, 6, 7, 8, 9]. Nano-grained materials or particles have distinctly different properties compared with bulk materials, because the number of surface atoms or molecules can become comparable to the number inside the particles [10].

Nano-sized powders can be synthesized by wet-chemical routes and gas-phase processes. However, gas-phase processes are often advantageous compared to liquid-phase processes since washing, drying, and calcining process stages are redundant. Furthermore, the use of high liquid volumes and surfactants, which are necessary to produce high purity materials at high yields, can be avoided [11].

Aerosol reactors that have been developed for the

manufacture of ultrafine powders include flame reactors [12], furnace reactors [13], gas-condensation methods [14, 15], plasma reactors [16], laser ablation [8] (the precursor of the previous three examples is preferentially a highly pure metal rod) and spray pyrolysis [17], to name just a few. Today, through the use of these methods, it is possible to make virtually all kinds of inorganic materials at the nano size level, giving potential for new or more cost-efficient applications in addition to existing industrial processes such as pigment generation, optical fiber fabrication, and carbon black production [7, 9]. In summary, the specific aerosol methods differ primarily in the technology of how thermal energy is transferred to the precursor species; how the precursor is delivered to the reaction site; economic aspects; and the final product characteristics.

The workhorses of the aerosol processes, flame reactors for the synthesis of nanoparticles from gaseous precursors, were first investigated in detail using diffusion and premixed flames [12, 18, 19, 20, 21]. By producing fumed silica and titania from chloride precursors, the competition between particle

[†] Accepted: August 26, 2004

coagulation and sintering was studied. Research in this field accelerated, however, when industrial flame reactors were introduced in the large-scale manufacture of optical fibers. Since the early 1990s, the pace of research has been further intensified with a renewed interest in flame technology for manufacturing advanced materials, emphasizing nano-structured particles for a large variety of applications [1].

Today, flame reactors are widely used for the manufacture of commercial quantities of nanoparticles such as carbon black (made by Cabot, Columbia, Degussa., etc.), fumed silica (Cabot, Degussa., Wacker, etc.), pigmentary titania (DuPont, Ishihara, Millennium, Kerr-McGee, etc.) and optical fibers (Corning, Hereaus, Sumitomo, etc.) [2]. Industrial flame reactors are reasonably well understood for the synthesis of particles with closely controlled particle size characteristics through control of the particle concentration and residence time, temperature history, reactant mixing, external fields and additives [22, 23]. Interfacing particle dynamic models with computer fluid models [24] has led to the prediction of a product powder's specific surface area within 3% even for industrial-scale systems [25].

Using vapor flame reactors, the variety of products is limited by the choice of metal precursors with sufficient vapor pressure to deliver the desired amount of the metal species into the reactor. Problematic examples include the low production rates for bismuth

oxide [26] or Pt/TiO₂ catalysts [27] from vapor flame reactors. Furthermore, it is difficult to produce multi-component materials with homogeneous chemical composition because differences in the chemical reaction rate and vapor pressure of the reactants, or different nucleation and growth rates may lead to non-uniform composition within and/or between particles and often yield segregated mixed-component particles [28]. However, in spray pyrolysis, each droplet contains the precursor in the exact stoichiometry as desired in the product [17, 29]. The droplet essentially serves as a discrete microreactor [30]. This is a huge advantage over vapor-phase routes since in the latter, several reactants have to be vaporized simultaneously with special care to obtain the desired stoichiometry.

Nielsen et al. [31] performed pioneering work in the field of the spray synthesis of metal oxides, mixed metal oxides, and ferrite powders from metal chloride, sulfate, acetate, and nitrate solutions. By atomizing the liquids into oxygen or air-fuel flames, they produced flakes, hollow-shaped, as well as submicron particles. The spray pyrolysis process took place over a wide range of conditions. A further distinction is made in the present paper between processes in which the powder is formed inside the droplet (spray pyrolysis) and processes where the precursor transport into the gas-phase occurs or the droplet explodes (see also **Figure 1** for reference). The latter can be

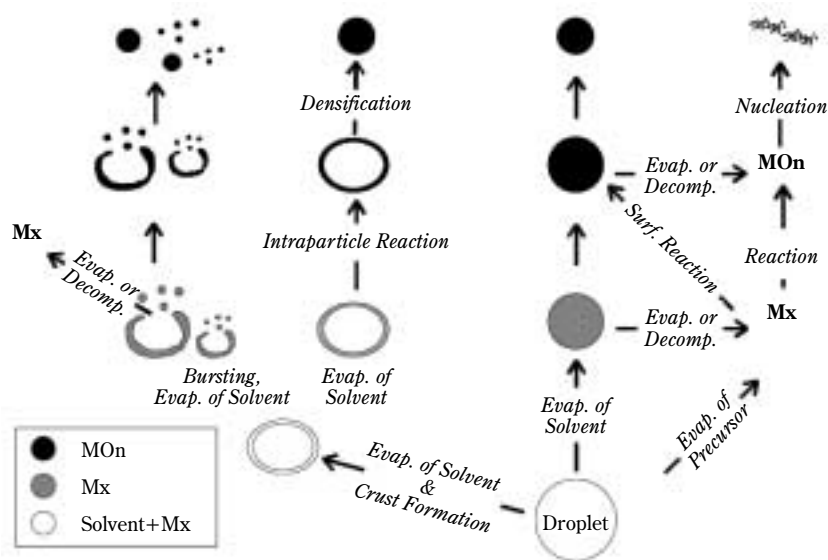


Fig. 1 Various mechanisms for metal oxide formation from dissolved metal precursors sprayed into a high-temperature reaction zone. Only mechanisms on the right-hand side lead to nano-grained particles (by precursor evaporation or decomposition at high temperatures), while formation of the product within the droplet environment often leads to hollow and/or larger particles (partly adapted from Kodas and Hampden-Smith [32]).

achieved by an external non-reactive heat supply (e.g. tubular reactor); in flames formed by additional reactant gases (e.g. vapor-flame-supported); or by the spray itself (droplet fuel burning, e.g. emulsion combustion method or flame spray pyrolysis).

2 Spray processes for nanoparticle production

Spray-supported methods for nanoparticle production differ mainly by how thermal energy is provided to the precursor species, influencing main particle formation parameters such as temperature profile and residence time within the high-temperature environment. **Figure 2** summarizes the four main spray methods discussed in this paper, namely spray pyrolysis in a tubular reactor (SP), spray pyrolysis using a vapor flame reactor (VFSP), the emulsion combustion method (ECM) and flame spray pyrolysis (FSP). In all four processes, the precursor is delivered under ambient pressure to the reactive environment by dispersing it into fine droplets. The main difference, however, is the energy source driving the solvent or fuel evaporation and precursor reaction (in some cases also liquid fuel reaction). As shown in **Fig. 2**, reactors with an external energy supply (energy which is not provided by the spray itself as in SP and VFSP) are less sensitive to the choice of precursors and solvents.

Water is often chosen as the solvent in systems with an external energy supply (SP, VFSP, ECM) due to economic aspects, ease of handling and the excellent

dissolution ability for many metal-containing precursors (e.g. nitrates, chlorides, acetates). In contrast, the combustion of the entire solution (as in FSP) results in higher maximum reactor temperatures and significantly larger temperature gradients compared with other methods. In the following sections, the resulting influences on final product properties will be discussed and highlighted.

2.1 Spray pyrolysis using tubular reactors (SP)

During the spray pyrolysis (SP) process, the precursor solution is atomized into a hot-wall reactor (or series of reactors) with well defined temperature fields. The aerosol droplets undergo evaporation, concentration of the solute within the droplet, drying, thermolysis of the precipitate particle to form a microporous particle, and finally sintering to form dense spheres [17]. The final product powder is formed within the atomized droplet through precipitation. Compared to liquid-phase precipitation, powders produced by SP are advantageous since they are more crystalline, less agglomerated (compared to calcined sol-gel-derived powders), of high purity and rarely require post-calcination [32].

Development of the spray pyrolysis process was driven largely by the need to address the lack of control of the calcination process in conventional solution-based techniques (e.g. co-precipitation, hydrolysis of organometallic compounds, sol-gel, freeze drying and spray drying) resulting in intermediate salts or hydroxide products. This led to development of the so-called “evaporative decomposition of solutions” (EDS) [33] or “spray roasting”. The EDS process has been successfully used for the production of single- and mixed-oxide powders (ferrite and chromite powders) on industrial scales [34]. A detailed investigation of the effect of the metal salt on the characteristics of EDS-derived MgO, ZnO and NiO powders, and in particular their morphology, was carried out by Gardner and Messing [35] and Gardner et al. [36]. The authors report fine-grained, high surface area, aggregate-free powders when using metal acetate precursors, whereas strongly aggregated powders were obtained from nitrate precursors. The difference was attributed to the exothermic decomposition of the acetate salt in the reaction. Similar results were obtained for γ -Fe₂O₃ by Gonzalez-Carreno et al. [37]. They report iron-oxide nanoparticles (about 5 nm) formed from acetylacetonate precursors (dissolved in methanol) due to the exothermic reaction of breaking individual crystals apart from the droplet skeletal structure. In the absence of exothermic decomposi-

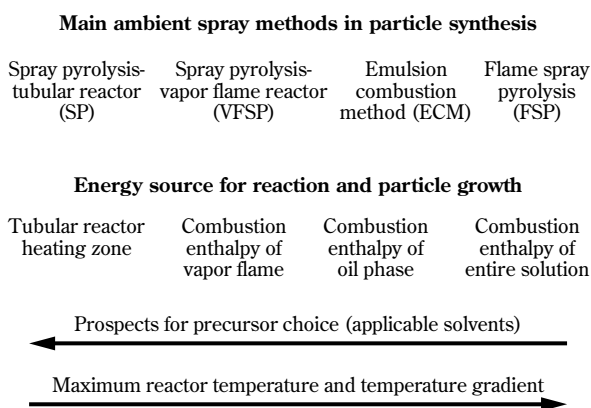


Fig. 2 Main spray methods operated at ambient pressure for gas-phase nanoparticle production from metal precursors. Precursors are delivered within a solvent into a reaction zone where reaction and the final product formation occurs.

tion (nitrate, ammonium citrate, chloride precursors), the skeletal structure of the droplet was retained [37].

Drawing on the advantage of the excellent spatial mixing of the reactants, the spray pyrolysis process was also established for multicomponent systems. Examples include the preparation of small particles of yttrium-stabilized zirconia from nitrates, where particles in the size range of 400 nm with an average crystal size of about 100 nm were formed [38]. Further examples include barium and strontium titanate synthesized from the organometallic titania tetraisopropoxide (TTIP) and the acetates and nitrates of barium and strontium [39, 40]. The formation of perovskites is a challenging task and often results in the formation of barium carbonate and/or irregularly shaped particles. However, the previous examples show that stoichiometry is well conserved during the spray pyrolysis process. Luminescent materials for the next generation of flat panel displays with high efficiency at low operating voltage (e.g. Y_2SiO_5 : Tb, non-aggregated Y_2O_3 : Eu phosphor particles) have also been produced from organometallic silica and corresponding nitrate precursors [41, 42]. Lenggono et al. [43] demonstrated a one-step synthesis for Zn_2SiO_4 : Mn particles (0.3-1.3 μm) with spherical, non-aggregated morphology and homogeneous phase. They applied long residence times (around 4 seconds) at high temperatures (1300°C) for final product formation. The authors highlighted the advantages of the aerosol route and the possibility of extending the production for multicomponent phosphor particles.

Another promising area for particles made by aerosol processes is catalysis. Spray pyrolysis was used to produce metal-supported catalysts resulting in well-dispersed metals (silver, platinum) on ceramic materials (e.g. alumina). The surface area of the catalyst was rather low (about 10 m^2/g), but direct catalytic studies showed that the metal components were available on the surface and that they were quite active for catalysis. The performance of aerosol-made catalyst was clearly identified by Moser et al. [44] (e.g. for conversion of methylcyclohexane). With this leading contribution to aerosol-derived metal/ceramic systems, it still took another 8 years to demonstrate that these systems are promising alternatives to conventional wet-phase-made ones using vapor flame and spray flame technology, respectively [27, 45].

Gas sensor materials can also be synthesized by spray pyrolysis. Spray-pyrolyzed Pt/SnO₂ particles have been demonstrated to exhibit high sensitivity for carbon-monoxide and ethanol [46]. The additional post-synthesis calcination step and the dilute process

conditions or low mass loading (low production rate) are still disadvantages of this specific SP process, but further developments in this area are expected [47].

One of the limitations of the spray pyrolysis process is evident during the synthesis of ceria particles [48]. In this instance, the process is not capable of producing nanometer-sized CeO₂ particles unless the solution concentration is extremely low [49]. To overcome this problem, Xia et al. [49] developed the salt-assisted ultrasonic aerosol decomposition where an inert salt can be used to control crystallite size and product aggregation. The disadvantages encountered with this technique are the required washing to remove the salt from the final product and purity issues similar to those experienced in wet-phase processes. Other examples of the salt-assisted method include the production of NiO, ZnS and $(\text{Ba}_{1-x}\text{Sr}_x)\text{TiO}_3$ [50]. Spray pyrolysis has also been used for the synthesis of well-ordered spherical silica particles with stable pore mesostructure of hexagonal or cubic topology [51]. Applications of this method include catalysis, chromatography, and controlled drug release. It should be mentioned that by using a hot-wall reactor and an inert carrier gas for the precursor delivery, non-oxide ceramic nanopowders such as the Si(N,C) systems [52] can be synthesized as well.

A deeper understanding of the droplet-to-particle formation mechanisms was achieved by modeling the solid particle formation during solution aerosol thermolysis combined with evaporation. Models accounting for the evaporation of such aerosol thermolysis have been successfully applied to study the effect of various parameters on the final product morphology as demonstrated by Jayanthi et al. [53], Yu [54] and Lenggono et al. [55]. However, more detailed knowledge is needed on multicomponent evaporation and precursor reaction/decomposition and particle formation to enable ab initio product design.

2.2 Vapor-flame-supported spray pyrolysis (VFSP)

The success of producing functional metal oxides, mixed-metal oxides and metals on metal oxides from cheap precursors (e.g. nitrates) in an economical aerosol process has triggered the evolution of the reactor design. Tubular reactors used in SP provide a well-controlled temperature zone over long residence times for conversion of the precursor to the final product. It was realized, however, that the synthesis of a variety of products requires higher maximum temperatures (above 1300°C) and shorter residence times. The established vapor flame method for the

production of silica and titania clearly showed the advantages of high temperature and large temperature gradients and their control [23]. This led to the development of vapor(gaseous)-flame-supported spray pyrolysis (VFSP). In VFSP, the energy is supplied by a vapor flame where a fuel (mainly hydrogen, methane or propene) reacts with air or oxygen, forming the reaction and particle formation zone. The precursor is sprayed directly into the flame. Most of the precursor reactions are endothermic and since mainly aqueous solutions are used to dissolve the precursor (e.g. nitrates), the spray itself also cools the flame.

One of the first applications of this technique was the synthesis of YBaCuO high T_c superconductors [56, 57]. Three years earlier, Kodas et al. [58] used spray pyrolysis in a tubular reactor to decompose the nitrate salts. Their product showed chemically homogeneous micron-sized particles of high purity and superconductivity at 90 K when produced at high temperature (1000°C) with a post-calcination step. The flame reactor offered the possibility of synthesis without an additional post-calcination step. Different flame reactor configurations and conditions were tested, and it was shown that a diffusion flame in which particles do not pass through the flame front was the best way to control the temperature in order to avoid preferential volatilization while minimizing water vapor content [56, 57]. The VFSP-produced powder displayed superconductivity at 92 K without post-processing.

Aggregated ultrafine spinel powders of NiMn_2O_4 and SrMnO_3 were obtained by dissolving the carbonate precursors in dilute acetic acid and spraying this solution into a hydrogen/oxygen diffusion flame [59]. The successful preparation of nano-grained ternary oxides in the flame process similar to established methods for titania and silica was a major step towards the aerosol-based, large-scale production of functional nanoparticles. Kriegel et al. [59] further demonstrated that the prepared $\beta\text{-SrMnO}_3$ powders were catalytically active (temperature-dependent CO_2 formation from methane) and had higher conversion rates compared with powders derived using a conventional solid-state reaction. This performance was mainly attributed to the high specific surface area in the absence of micropores of the aerosol-derived powder. The same technique was used for the production of ultrafine $\gamma\text{-Fe}_2\text{O}_3$ from iron(III) acetylacetonate dissolved in ethanol or toluene by Grimm et al. [60]. The authors compared their results with the established and patented combustion of the volatile $\text{Fe}(\text{CO})_5$ and found no significant difference. They further studied

the development of the iron-oxide crystalline phases by varying the reactor conditions (oxygen content within the flame) and highlighted the importance of high maximum temperatures and steep temperature gradients during synthesis of the $\gamma\text{-Fe}_2\text{O}_3$ phase, while higher residence times were necessary to obtain the $\alpha\text{-Fe}_2\text{O}_3$ phase. It is worth noting that in this study, the precursor solution itself supplied thermal energy to the process upon evaporation and reaction. The authors reported only the formation of ultrafine particles which most probably left the droplet environment during particle formation.

Brewster and Kodas [61] synthesized dense, spherical, unagglomerated BaTiO_3 by the VFSP approach, spraying acetate and lactate precursors dissolved in water into a hydrogen/oxygen flame. They demonstrated that various morphologies can be produced by varying the flame temperature and/or particle residence time in the flame. Furthermore, the authors state that vapor-flame-supported spray pyrolysis is the only way to produce dense barium titanate particles via an aerosol route (although comparison is made only with spray pyrolysis in a tubular reactor). They claimed that the high temperatures and heating rates within the flame reactor densified the particles more rapidly compared with the tubular reactor [61].

An important contribution was made by Helble and coworkers [30, 62], who explicitly introduced the concept of the “droplet micro-reactor” and the use of a reactive organic aerosol spray (similar to Grimm et al. [60]) while the main energy source was still a vapor flame reactor (or in some cases a tubular furnace); the resulting powder was of nano-scale size and crystalline as demonstrated for MgO and yttrium-stabilized zirconia (YSZ). The narrow size distribution, high purity and lowered sintering temperature of the produced ceramics were superior compared with state-of-the-art materials. Examples of complex powders produced by VFSP are phosphor particles such as $\text{SrTiO}_3 : \text{Pr}$ and $\text{Y}_2\text{O}_3 : \text{Eu}$ [63, 64].

Metal nanoparticles were also produced in the VFSP process for glass coloring (Co, Cu, Ag) [65] or catalytic applications (Pt nanopowders) [66], but no distinct testing was reported. The process of spraying a precursor solution into a hydrogen/oxygen flame was characterized with respect to the atomization of the liquid feedstock, characterization of the flame, and flame droplet interaction by Tikkanen et al. [67]. Laser diffraction anemometry was used to obtain the droplet size distribution of the spray within the flame, laser doppler velocimetry traced the droplet velocity, the flame temperatures were measured with pulsed

laser Rayleigh backscattering, and Schlieren photography determined the flame structure. Significantly, Tikkanen et al. [67] showed how the solvent affected the flame structure especially when using water instead of organic solvents. Detailed measurements of this kind, together with particle dynamic models (as done for vapor flame reactors [24]) would give detailed insights into the particle formation mechanisms and particle growth dynamics in VFSP flame reactors.

2.3 Emulsion combustion method (ECM)

A further step of applying the energy source in closer proximity to the reaction zone is the embedding of the aqueous precursor solution (mainly derived from nitrates) in a combustible droplet environment. This was achieved by preparing a water (with precursor) in oil (fuel) emulsion which was atomized into micron-sized droplets and subsequently ignited. This self-sustaining spray flame method is called the emulsion combustion method (ECM). Developed at Toyota labs in 1997 [68], this technique has been successfully applied to titania, silica, alumina, zirconia, barium titanate and zirconia-ceria, as well as electronic, catalytic and ceramic applications [69, 70]. A major limitation of this method can be the lack of control with respect to product morphology (e.g. hollow particles are often produced). A comparison between the ECM method and the flame spray pyrolysis (FSP) method (discussed in the next paragraph) revealed enhanced gas-phase mixing and reaction in the latter case [71]. The ECM was also used for the synthesis of gold coatings by flame spraying a micro-emulsion of an aqueous solution of $\text{HAuCl}_4 \cdot \text{H}_2\text{O}$ and a surfactant solution in hexane [72]. The authors report nanoparticles of up to several nanometers in size with good control of size and shape but do not identify specific applications of their product.

2.4 Flame spray pyrolysis (FSP)

It was previously mentioned that endothermic precursor reaction pathways often lead to hollow or fragmented product particles [36, 37]. The utilization of the endothermic species (mainly metal-nitrates and metal-chlorides dissolved in water) is driven by low cost, availability and solubility (achievement of high concentrations). However, when using these precursors, the final product particle formation takes place very often within the droplet due to insufficient energy needed to vaporize, sublime or disruptively decompose the precursor, in order to facilitate reaction and particle formation in the gas phase surrounding the

droplet. In most of the processes and applications introduced so far, the sprayed precursor solutions contained species which require external energy for their reaction. In EMC, the very high energy content of the kerosene in close proximity to the endothermic-reacting precursor (less than a micrometer) could not avoid the formation of hollow particles [69].

Taking this into account leads to the exclusive use of exothermic-reacting species and the design of self-sustaining spray flames that provide the temperature and the residence time profiles intrinsically similar to vapor flame reactors [23]. This similarity is illustrated in **Figure 3** which shows a comparison between the temperature profiles of a premixed vapor flame (open symbols) and a spray flame reactor (full symbols), each producing silica at similar production rates. One of the first studies using these principles was the formation of ceramic Al_2O_3 aerosol from aluminium(III) acetylacetonate dissolved in an azeotropic mixture of benzene and ethyl alcohol [73]. The mixture was sprayed and combusted with no soot formation giving ultrafine (3-100 nm) alumina particles. In this profound work, the authors investigated parameters influencing the crystal structure of alumina and targeted studies for the synthesis of α -alumina in flames. The authors demonstrated that an increase in the water vapor content decreases the formation of the

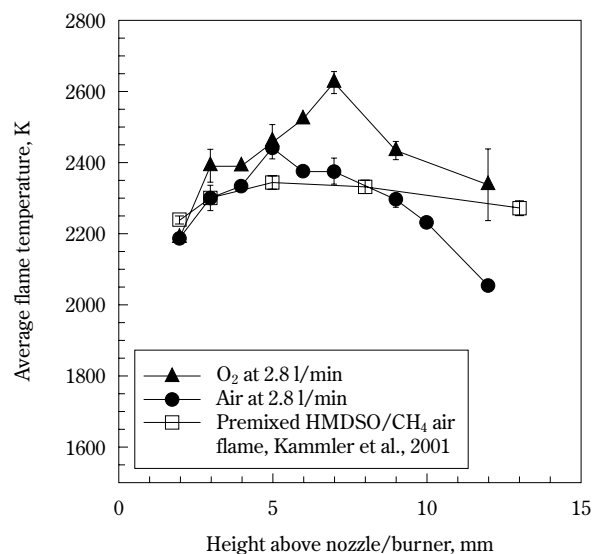


Fig. 3 Comparison of the measured axial temperature profiles of a silica-producing premixed vapor flame [2] and a self-sustaining spray flame [74]. The maximum flame temperature in both flames is very high and rather similar. The high velocities in the spray flame leads to faster cooling compared with the premixed vapor flame.

α -phase. This was implemented commercially with the vapor flame approach using vaporized AlCl_3 in carbon monoxide (Degussa, EP0395925, 1990).

It took twenty years to follow up on this initial idea of flame spray pyrolysis when Bickmore et al. [29] and Karthikeyan et al. [75] reported on the formation of MgO , Al_2O_3 , ZrO_2 and YSZ ceramics. Ultrafine particles were mainly produced from organic precursors and solvents (exothermic), while nitrates dissolved in water (endothermic) resulted in larger particles. This was also reported for the FSP preparation of yttria-stabilized zirconia (YSZ) powders from zirconium n-propoxide and ytterbium nitrate (with crystal water) [76].

An important step toward the economic application of spray flame pyrolysis for the production of functional and complex nanoparticles was the work by Bickmore et al. [29], where they report the preparation of ultrafine crystalline spinel powders (MgAl_2O_4). The authors realized the importance of the precursor formulation and accordingly prepared stoichiometric amounts of $\text{Al}(\text{OH})_3$ and MgO with the amine base, tri-ethanolamine in ethylene glycol. The as-produced precursor (including ethylene glycol) was diluted with dry ethanol. With this dilution, they adjusted the metal content and the viscosity for good atomization while at the same time the ethanol served as the fuel source for combustion. The spray was atomized with oxygen and ignited with a natural gas/oxygen torch. Production rates were up to 100 g/h and the minimum average particle diameter obtained from specific surface area measurements of the products was 25 nm. This precursor preparation/FSP process was further investigated for the production of titania from titanium tetrachloride that forms titanatrane glycolate when reacting the hydrosol in triethanolamine and ethylene glycol. The derived precursor was dissolved in different alcohols, and products with specific surface areas up to 45 m^2/g and a 9:1 anatase to rutile composition were produced. The materials had similar characteristics to commercial products of flame-made TiO_2 [77]. Another example of the success of this precursor strategy (triethanolamine and ethylene glycol) is the preparation of $\text{Na}_{1.67}\text{Al}_{10.67}\text{Li}_{0.33}\text{O}_{16.33}$ called β'' -alumina ($\text{Na}_2\text{O} \cdot x \text{Al}_2\text{O}_3$) serving as a high-temperature solid electrolyte [78, 79]. The flame-spray-pyrolyzed nanopowder expressed preferentially the β'' -phase, which was attributed to the rapid heating and cooling within the flame spray reactor favoring this specific reaction pathway. Further examples are group II metal aluminates (MeAl_2O_4) with $\text{Me} = \text{Mg}, \text{Ca}, \text{Ba}, \text{Sr}$ [80] as well as $3 \text{Al}_2\text{O}_3 \cdot 2 \text{SiO}_2$ [81,

82], CeO_2 and $\text{SrO} \cdot \text{Al}_2\text{O}_3 \cdot 2 \text{SiO}_2$ [82], n-phosphors ($\text{Y}_{(1-x-y)}\text{Yb}_x\text{Re}_y$) $_2\text{O}_3$ with $\text{Re} = \text{Er}, \text{Tm}$ and Pr [83] and $\text{CeO}_2/\text{ZrO}_2$ [83, 84]. The complexity and functionality for very different applications of the products summarized in this paragraph is worth noting. All the products are characterized by an average particle diameter below 100 nm derived from specific surface area measurements, and no hollow structures are reported.

Commercial organic precursors (aluminum-sec-butoxide) (zirconium-n-butoxide and zirconium-n-propoxide) dissolved/diluted in their parent alcohols were used in a high-production-rate flame spray process (180 g/h) for nano-scale alumina and zirconia [85]. Use of the rather volatile exothermal-reacting species resulted in spherical nanoparticles typical for flame processes [23]. Particle diameters ranged from 4 – 100 nm with an average of about 40 nm.

The control of primary particle size, crystal size, morphology and composition using the options of the spray flame reactor similar to vapor flame reactors was first investigated for silica [74] and then later for a variety of functional products such as zinc oxide [86] and bismuth oxide [87]. It was shown that the decomposition behavior and the subsequent reaction path of the precursor/solvent systems influences the morphology and homogeneity of the products. Using ethanol and nitric acid as the solvent of the nitrate precursor resulted in the formation of hollow (1 μm in diameter) and sintered dense spheres (50 – 100 nm in diameter) as well as aggregates of primary particles, each of 10 nm in diameter. In contrast, dissolution of the bismuth nitrate in acetic acid led to synthesis of solid nanoparticles. The acetic acid solvent may have favored the formation of an acetobismuth complex, facilitating enhanced precursor evaporation and gas-phase formation of the oxide particles [87]. The importance of the precursor mixture was further demonstrated when producing ceria in the FSP process. Here, the addition of iso-octane/2-butanol to the acetic acid/acetate solution accelerated precursor evaporation and gas-phase reaction, resulting in homogeneous powders [88]. Powders with an average BET diameter as small as 5 nm were produced. Similar studies were performed for the alumina system [89]. It was further shown that in mixed-oxide systems, control of the product structure and morphology can be obtained in flame spray pyrolysis such as for ZnO/silica [90], zinc silicate [91] and ceria/zirconia [92]. Especially in the latter example, Stark et al. [92] highlighted the importance and specifics of the exothermal reaction of the precursor solution when using carboxylic acid mixtures, where

the precursor composition offered a very fast precursor delivery by the sudden onset of decarboxylation. The ceria/zirconia system was tested for its oxygen exchange capacity [93] and was later modified with dopants [94]. Precise control of process and product powder characteristics enabled the formation of zinc-oxide quantum dots [95] and the simultaneous deposition of noble metals on the formed ceramic particles, for example, gold on silica and titania [96] and platinum or palladium on alumina and titania [45, 97, 98] (see **Figure 4**). It was further shown that precise control is not restricted to lab-scale reactors and that even at production rates up to 1.1 kg/h, particle sizes and morphology can be closely controlled [99, 100] (see **Figure 5**).

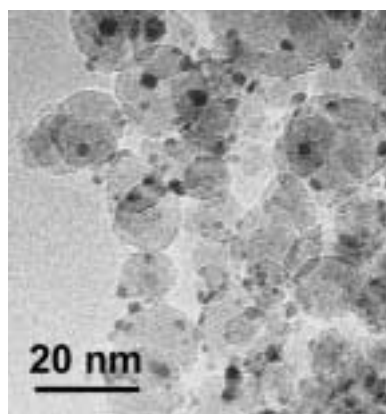


Fig. 4 HRTEM-image of 7.5 wt% Pt on open structured-alumina made by the single-step flame spray pyrolysis (courtesy of R. Strobel, adapted from Strobel et al. [45]).

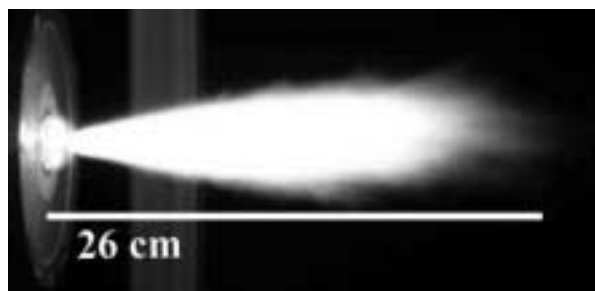


Fig. 5 Spray flame producing 250 g/h of silica (specific surface area of 96 m²/g) from a 1.26 M HMDSO/ethanol solution (courtesy of R. Mueller, adapted from Mueller et al. [99]).

2.5 Plasma-supported spray processes for nanoparticle synthesis

One important technique for pyrolyzing liquid precursor droplets to obtain nano-structured materials is plasma assisted droplet to particle conversion. These processes differ from the previous methods in terms of a closed (non-ambient) reactor design and significantly higher set-up expenditure and will therefore be mentioned only briefly here. Similar to conventional spray pyrolysis, the energy source is located externally of the reactor (mainly radio frequency inductively coupled or microwave cavity plasmas). Although the external energy source enables the utilization of a wide range (mainly aqueous) of precursor solutions, at the same time high energy densities from the plasma are required, leading to solvent evaporation (or droplet disruption), precursor conversion and particle formation. Consequently, all reported products are nano-grained powders with high crystallinity comprising a wide range of metal ceramics. Detailed overviews of the technique are given by Suzuki et al. [16], Vollath and Sickafus [101] and Hasegawa et al. [102]. The technology is also used commercially (e.g. for zinc oxide), while the reactor design focuses mainly on the utilization of pure metal precursors rather than spraying metal-containing solutions.

3 Applications of powders produced by spray pyrolysis methods

Spray pyrolysis in its different forms as introduced in Sections 2.1 to 2.4 finds application in various fields of modern technology. The high specific surface area, texture, morphology, crystal structure, composition, purity and environmental benefits (minimal liquid wastes) can be advantageous compared with powders prepared by wet chemical methods. Furthermore, the ability to produce nano-structured materials of single oxides, mixed oxides, and noble metals on ceramic supports has broadened the potential range of applications. **Table 1** gives a structured overview of the application for the examples described in Sections 2.1 to 2.4. Applications are categorized in the fields of ceramics, electronics, optics and catalysis. The morphology of the powders, mainly divided here into hollow and solid particles, is crucial for most of the applications and special attention is paid to this property in **Table 1**.

There is a broad variety of applications and specific powders made by ambient pressure spray processes, and only a small selection is given in **Table 1**. How-

Table 1 Summary of Sections 2.1–2.4

General	Application	Process [§] /Morphology	Reference
	Specific Remarks		
Ceramic	Al ₂ O ₃ , CaAl ₂ O ₄	SP/m	Roy et al. [33]
Ceramic	Al ₂ O ₃	FSP/u/n	Sokolowski et al. [73]
Ceramic	MgO	SP/m	Gardner and Messing [35]
Ceramic	YSZ	SP/m	Pebler [38]
Ceramic	MgAl ₂ O ₄	FSP/u	Bickmore et al. [29]
Ceramic	MgO, ZrO ₂ , YSZ	FSP/m,u,n	Karthikeyan et al. [75]
Ceramic	(MeAl ₂ O ₄) with Me=Mg, Ca, Ba, Sr	FSP/u/n	Narayanan and Laine [80]
Ceramic	YSZ	FSP/m	Yuan et al. [76]
Ceramic	TiO ₂	FSP/u/n	Bickmore et al. [77]
Ceramic	MgO, YSZ; sugar solution	VFSP/n	Helble [30]
Ceramic	ZrO ₂ , Al ₂ O ₃	ECM/m/h	Takatori et al. [68]
Ceramic	SrO · Al ₂ O ₃ · 2 SiO ₂	FSP/u	Laine et al. [82]
Ceramic	3 Al ₂ O ₃ · 2 SiO ₂	FSP/u	Baranwal et al. [81]
Ceramic	ZrO ₂ , Al ₂ O ₃ ; high production rate	FSP/u	Kilian and Morse [85]
Ceramic	ZrO ₂	VFSP/u/n	Limaye and Helble [62]
Ceramic	SiO ₂	FSP/n	Mädler et al. [74]
Ceramic	SiO ₂ ; high production rate	FSP/n	Mueller et al. [99]
Electronic	Ferrite and chromite powders	SP/m/u/n	Ruthner [34]
Electronic	YBaCuO	SP/m	Kodas et al. [58]
Electronic	BaTiO ₃ , SrTiO ₃	SP/m	Nonaka et al. [40]
Electronic	YBaCuO	VFSP/m	Zachariah and Huzarewicz [57]
Electronic	γ-Fe ₂ O ₃	SP/h/u/n	Gonzalez-Carreno et al. [37]
Electronic	γ-Fe ₂ O ₃ ; energy supply from the liquid	VFSP/n	Grimm et al. [60]
Electronic	BaTiO ₃	VFSP/m/u	Brewster and Kodas [61]
Electronic	Na _{1.67} Al _{10.67} Li _{0.33} O _{16.33}	FSP/u	Treadwell et al. [78]
Electronic	BaTiO ₃	SP/m	Ogihara et al. [39]
Electronic	Pt on SnO ₂	SP/m	Cabanas et al. [46]
Electronic	BaTiO ₃	ECM/m/h	Tani et al. [70]
Electronic	(Ba _(1-x) Sr _x)TiO ₃ , NiO, ZnS; salt-assisted	SP/u/n	Xia et al. [50]
Electronic	Au	ECM/n	Bonini et al. [72]
Electronic	ZnO	FSP/n	Tani et al. [86]
Electronic	Bi ₂ O ₃	FSP/n	Mädler and Pratsinis [87]
Electronic	ZnO/SiO ₂	FSP/n	Tani et al. [90]
Electronic	Au on TiO ₂ and SiO ₂	FSP/n	Mädler et al. [96]
Electronic	SnO ₂	FSP/n	Sahm et al. [47]
Optics	Y ₂ O ₃ : Eu	SP/m	Kang et al. [42]
Optics	Y ₂ SiO ₅ : Tb	SP/m	Kang et al. [41]
Optics	Co, Cu, Ag	VFSP/m/h	Gross et al. [65]
Optics	Y ₂ O ₃ : Eu	VFSP/m	Kang et al. [63]
Optics	SrTiO ₃ : Pr	VFSP/m	Kang et al. [64]
Optics	Zn ₂ SiO ₄ : Mn	SP/m	Lenggoro et al. [43]
Optics	(Y _(1-x-y) Yb _x Re _y) ₂ O ₃ with Re=Er, Tm and Pr	FSP/u	Laine et al. [83]
Catalysis	NiMn ₂ O ₄ , SrMnO ₃	VFSP/n	Kriegel et al. [59]
Catalysis	Pt, Ag, Ir, Sn on Al ₂ O ₃	SP/m	Moser et al. [44]
Catalysis	CeO ₂	SP/m	Vallet Regi et al. [48]
Catalysis	Ce _x Zr _(1-x) O ₂	ECM/m/h	Takatori et al. [68]
Catalysis	SiO ₂ , specific topology	SP/m	Lu et al. [51]
Catalysis	CeO ₂	FSP/u	Laine et al. [82]
Catalysis	CeO ₂ , salt-assisted	SP/u/n	Xia et al. [49]
Catalysis	Pt	VFSP/n	Oljaca et al. [66]
Catalysis	CeO ₂	FSP/n	Mädler et al. [88]
Catalysis	Pt on TiO ₂	FSP/n	Stark et al. [97]
Catalysis	Ce _x Zr _(1-x) O ₂	FSP/u	Sutorik and Baliat [84]
Catalysis	Ce _x Zr _(1-x) O ₂	FSP/n	Stark et al. [92]
Catalysis	SiO ₂ , Al ₂ O ₃ /Ce _x Zr _(1-x) O ₂	FSP/n	Schulz et al. [94]
Catalysis	Pt on Al ₂ O ₃	FSP/n	Strobel et al. [45]
Catalysis	Pd on Al ₂ O ₃	FSP/n	Strobel et al. [98]

[§]SP=Spray pyrolysis using tubular reactor; VFSP=Vapor-flame-supported spray pyrolysis; ECM=Emulsion combustion method; FSP=Flame spray pyrolysis; m=micron-sized aggregate (larger than 500 nm) composed of nano-crystallites (smaller than 100 nm); h=hollow particles; u=powders with distinct primary particles below 100 nm; n=powders with distinct primary particles below 20 nm

ever, the list shows that all spray techniques introduced in Section 2 are used for many different applications. All techniques are capable of producing metal oxides, mixed metal oxides and noble metal on metal oxides. It should be noted that powders with distinct primary particles below 20 nm are only produced when the liquid feed supplies the reaction energy to the reactor, as for example in exceptional cases of VFSP by Kriegel et al. [59], Grimm et al. [60], and more generally in FSP. Another point to note is that most of the techniques were first introduced 30 years ago, while it is only in the last four years that research has intensified in this area, driven by the increasing demand for functional nano-structured materials. This can further be seen in the pertinent patent literature (not reviewed here) as well as in the flourishing of commercial activity in this area.

4 Future directions

The capabilities and know-how of gas-phase synthesis were successfully transferred from classic vapor-fed flames to liquid-fed aerosol reactors, enabling the one-step production of demanding and highly functional products. Such aerosol-derived nano-structured metal oxides, mixed metal oxides and metals on metal oxides find application in the fields of catalysis, sensors, fillers, and electronics, and have advanced the research and development of these reactors in recent years. However, in the process of synthesizing these materials and controlling their functionality, many questions remain open. Examples include the formation mechanisms of mixed structures, such as two or multiple mixed oxides or metals on a metal oxide, further the formation of hollow structures in comparison with solid ones. Current research is addressing these questions with spatially resolved diagnostic methods to obtain droplet, gas and product kinetics in these complex multiphase systems. Such understanding will only be achieved by the combination of theoretical analysis and experimental data. In theoretical research, the challenge is the adaptation of established models, such as for nanoparticle growth in vapor(gas)-fed flames or droplet combustion in engines. The chemistry involved during the transformation of the dissolved precursor to the first stable clusters is probably one of the keys in further understanding this technology.

For numerous applications, coatings are applied to nanoparticles in order to improve their functionality. Modern sun creams make use of titania nanoparticles which absorb light in the ultraviolet region of the sun-

light spectrum and are small enough in size to avoid the scattering of visible light. However, in order to reduce photocatalytic activity and to improve the compatibility of the particle surface when immersed in liquid or solid matrixes, silica coatings are added. New protective coatings for optical filtering and thermal barriers, nano-structured polymers, and catalysts are already starting to enter the market. Nano-structured coatings show good corrosion/erosion resistance and could be used as possible replacements for environmentally troublesome chromium-based coatings. Coatings also assist the blending of materials such as boron nitride which has a very high thermal conductivity, making nanoparticles of this kind of material interesting for heat conduction in electronic devices. Here, the surface inertness has to be overcome by an alumina surface coating before embedding into the epoxy matrix.

Another largely unexploited field in this area is the direct utilization of as-produced particles being suspended and well-dispersed as an aerosol. Further processes such as immobilization and controlled deposition offer many exciting possibilities for further modifying the particles and new technologies of this kind are close at hand.

5 Summary

The utilization of liquid-fed reactors for the aerosol-based production of nano-sized powders has been reviewed. Growing awareness of the potential of aerosol processes and the increasing demand for functional metal oxides, mixed metal oxides and metals on metal oxides has driven the research and development of these reactors in recent years. The four main spray methods, namely spray pyrolysis in a tubular reactor (SP), spray pyrolysis using a vapor flame reactor (VFSP), the emulsion combustion method (ECM) and flame spray pyrolysis (FSP), were discussed and main concepts were compared such as the energy source driving the solvent/fuel evaporation and precursor reaction. Strategies for the production of homogeneous products were presented in context with existing methods and specific applications.

Acknowledgement

Stimulating discussions with Prof. S.E. Pratsinis, H.K. Kammler and M.J. Height (ETH Zurich) are gratefully acknowledged.

References

- [1] W.J. Stark and S.E. Pratsinis. Aerosol flame reactors for manufacture of nanoparticles. *Powder Technol.*, 126(2): 103-108, 2002.
- [2] H.K. Kammler, L. Mädler, and S.E. Pratsinis. Flame synthesis of nanoparticles. *Chem. Eng. Technol.*, 24(6): 583-596, 2001.
- [3] J. Schoonman. Nanostructured materials in solid state ionics. *Solid State Ion.*, 135(1-4): 5-19, 2000.
- [4] C.N.R. Rao. Novel materials, materials design and synthetic strategies: Recent advances and new directions. *J. Mater. Chem.*, 9(1): 1-14, 1999.
- [5] F.E. Kruis, H. Fissan, and A. Peled. Synthesis of nanoparticles in the gas phase for electronic, optical and magnetic applications – A review. *J. Aerosol Sci.*, 29(5-6): 511-535, 1998.
- [6] H. Hahn. Gas phase synthesis of nanocrystalline materials. *Nanostruct. Mater.*, 9(1-8): 3-12, 1997.
- [7] A. Gurav, T. Kodas, T. Pluym, and Y. Xiong. Aerosol processing of materials. *Aerosol Sci. Technol.*, 19(4): 411-452, 1993.
- [8] H. Gleiter. Nanocrystalline materials. *Prog. Mater. Sci.*, 33(4): 223-315, 1989.
- [9] A. Gutsch, M. Krämer, G. Michael, H. Mühlenweg, M. Pridöhl, and G. Zimmermann. Gas-phase production of nanoparticles. *KONA*, 20: 24-37, 2002.
- [10] N. Ichinose, Y. Ozaki, and S. Kashu. Superfine particle technology. Springer Verlag, Berlin, Heidelberg, New York, 1991.
- [11] S.E. Pratsinis and S.V.R. Mastrangelo. Material synthesis in aerosol reactors. *Chem. Eng. Prog.*, 85(5): 62-66, 1989.
- [12] G.D. Ulrich. Theory of particle formation and growth in oxide synthesis flames. *Combust. Sci. Technol.*, 4: 47-57, 1971.
- [13] H.G. Scheibel and J. Porstendorfer. Generation of monodisperse Ag-aerosol and NaCl-aerosol with particle diameters between 2-nm and 300-nm. *J. Aerosol Sci.*, 14(2): 113-126, 1983.
- [14] A.H. Pfund. Bismuth-black and its applications. *Phys. Rev.*, 35(2): 1434, 1930.
- [15] R.W. Siegel. Cluster-assembled nanophase materials. *Annu. Rev. Mater. Sci.*, 21: 559-578, 1991.
- [16] M. Suzuki, M. Kagawa, Y. Syono, and T. Hirai. Synthesis of ultrafine singlecomponent oxide particles by the spray-ICP technique. *J. Mater. Sci.*, 27(3): 679-684, 1992.
- [17] G.L. Messing, S.C. Zhang, and G.V. Jayanthi. Ceramic powder synthesis by spraypyrolysis. *J. Am. Ceram. Soc.*, 76(11): 2707-2726, 1993.
- [18] G.D. Ulrich, B.A. Milnes, and N.S. Subramanian. Particle growth in flames, II: Experimental results for silica particles. *Combust. Sci. Technol.*, 14: 243-249, 1976.
- [19] G.D. Ulrich and N.S. Subramanian. Particle growth in flames, III: Coalescence as a rate-controlling process. *Combust. Sci. Technol.*, 17(3-4): 119-126, 1977.
- [20] G.D. Ulrich and J.W. Riehl. Aggregation and growth of sub-micron oxide particles in flames. *J. Colloid Interface Sci.*, 87(1): 257-265, 1982.
- [21] M. Formenti, F. Juillet, P. Meriaudeau, S.J. Teichner, and P. Vergnon. Preparation in a hydrogen-oxygen flame of ultrafine metal oxide particles. *J. Colloid Interface Sci.*, 39(1): 79-89, 1972.
- [22] K. Wegner and S.E. Pratsinis. Aerosol flame reactor for the synthesis of nanoparticles. *KONA*, 18: 170-182, 2000.
- [23] S.E. Pratsinis. Flame aerosol synthesis of ceramic powders. *Prog. Energy Combust. Sci.*, 24(3): 197-219, 1998.
- [24] A. Schild, A. Gutsch, H. Muehlenweg, D. Kerner, and S.E. Pratsinis. Simulation of nanoparticle production in premixed aerosol flow reactors by interfacing fluid mechanics and particle dynamics. *J. Nanoparticle Res.*, 1: 305-315, 1999.
- [25] A. Gutsch, A. Schild, H. Riemenschneider, and S.E. Pratsinis. In AICHE Annual Meeting, Los Angeles, CA, Los Angeles, CA, 1997.
- [26] A.T. Liu and P. Kleinschmit. Production of fumed oxides by flame hydrolysis. In R.W. Davidge, editor, *Novel ceramic fabrication processes and applications*, volume 38, pages 1-10. The Institute of Ceramics, U.K., 1986.
- [27] T. Johannessen and S. Koutsopoulos. One-step flame synthesis of an active Pt/TiO₂ catalyst for SO₂ oxidation – A possible alternative to traditional methods for parallel screening. *J. Catal.*, 205(2): 404-408, 2002.
- [28] C.H. Hung and J.L. Katz. Formation of mixed-oxide powders in flames: TiO₂-SiO₂. *J. Mater. Res.*, 7(7): 1861-1869, 1992.
- [29] C.R. Bickmore, K.F. Waldner, D.R. Treadwell, and R.M. Laine. Ultrafine spinel powders by flame spray pyrolysis of a magnesium aluminum double alkoxide. *J. Am. Ceram. Soc.*, 79(5): 1419-1423, 1996.
- [30] J.J. Helble. Combustion aerosol synthesis of nanoscale ceramic powders. *J. Aerosol Sci.*, 29(5-6): 721-736, 1998.
- [31] M.L. Nielsen, P.M. Hamilton, and R.J. Walsh. Ultrafine metal oxides by decomposition of salts in a flame. In W.E. Kuhn, H. Lamprey, and C. Sherr, editors, *Ultrafine Particles*, pages 181-195. John Wiley & Sons, Inc., New York, 1963.
- [32] T.T. Kodas and M.J. Hampden-Smith. *Aerosol Processing of Materials*. Wiley-VCH, New York, first edition, 1999.
- [33] D.M. Roy, R.R. Neurgaonkar, T.P. O'Holleran, and R. Roy. Preparation of fine oxide powders by evaporative decomposition of solutions. *Am. Ceram. Soc. Bull.*, 56(11): 1023-1024, 1977.
- [34] M.J. Ruthner. Industrial production of multicomponent ceramic powders (metal oxides) by means of the spray roasting technique. In P. Vincenzini, editor, *Ceramic Powders: Preparation, Consolidation, and Sintering*, pages 515-531. Elsevier Scientific Publishing Company, Amsterdam, 1983.

- [35] T.J. Gardner and G.L. Messing. Preparation of MgO powder by evaporative decomposition of solutions. *Am. Ceram. Soc. Bull.*, 63(12): 1498-1501, 1984.
- [36] T.J. Gardner, D.W. Sproson, and G.L. Messing. Precursor chemistry effects on development of particulate morphology during evaporation decomposition of solutions. In C.J. Brinker, D.E. Clark, and D.R. Ulrich, editors, *Better Ceramics Through Chemistry*, volume 32 of *Materials Research Society Symposia Proceedings*, pages 227-237, Pittsburgh, PA, 1984. Noth-Holland.
- [37] T. Gonzalez-Carreno, M.P. Morales, M. Gracia, and C.J. Serna. Preparation of uniform γ -Fe₂O₃ particles with nanometer-size by spray-pyrolysis. *Mater. Lett.*, 18(3): 151-155, 1993.
- [38] A.R. Pebler. Preparation of small particle stabilized zirconia by aerosol pyrolysis. *J. Mater. Res.*, 5(4): 680-682, 1990.
- [39] T. Ogihara, H. Aikiyo, N. Ogata, and N. Mizutani. Synthesis and sintering of barium titanate fine powders by ultrasonic spray pyrolysis. *Adv. Powder Technol.*, 10(1): 37-50, 1999.
- [40] K. Nonaka, S. Hayashi, K. Okada, N. Otsuka, and T. Yano. Characterization and control of phase segregation in the fine particles of BaTiO₃ and SrTiO₃ synthesized by the spray pyrolysis method. *J. Mater. Res.*, 6(8): 1750-1756, 1991.
- [41] Y.C. Kang, I.W. Lenggoro, K. Okuyama, and S.B. Park. Luminescence characteristics of Y₂SiO₅: Tb phosphor particles directly prepared by the spray pyrolysis method. *J. Electrochem. Soc.*, 146(3): 1227-1230, 1999.
- [42] Y.C. Kang, S.B. Park, I.W. Lenggoro, and K. Okuyama. Preparation of nonaggregated Y₂O₃: Eu phosphor particles by spray pyrolysis method. *J. Mater. Res.*, 14(6): 2611-2615, 1999.
- [43] I.W. Lenggoro, F. Iskandar, H. Mizushima, B. Xia, K. Okuyama, and N. Kijima. One-step synthesis for Zn₂SiO₄: Mn particles 0.3-1.3 μ m in size with spherical morphology and non-aggregation. *Jpn. J. Appl. Phys. Part 2 - Lett.*, 39(10B): L1051-L1053, 2000.
- [44] W.R. Moser, J.A. Knapton, C.C. Koslowski, and R.H. Rozak, J.R. Vezis. Noble metal catalysts prepared by the high-temperature aerosol decomposition (HTAD) process. *Catal. Today*, 21(1): 157-169, 1994.
- [45] R. Strobel, W.J. Stark, L. Mädler, S.E. Pratsinis, and A. Baiker. Flame-made platinum/alumina: Structural properties and catalytic behaviour in enantioselective hydrogenation. *J. Catal.*, 213(2): 296-304, 2003.
- [46] M.V. Cabanas, G. Delabouglise, M. Labeau, and M. Vallet-Regi. Application of a modified ultrasonic aerosol device to the synthesis of SnO₂ and Pt/SnO₂ for gas sensors. *J. Solid State Chem.*, 144(1): 86-90, 1999.
- [47] T. Sahm, L. Mädler, A. Gurlo, N. Barsan, S.E. Pratsinis, and U. Weimar. Flame spray synthesis of tin dioxide nanoparticles for gas sensing. *Sens. Actuator B-Chem.*, 98(2-3): 148-153, 2004.
- [48] M. Vallet Regi, F. Conde, S. Nicolopoulos, C.V. Ragel, and J.M. Gonzalez Calbet. Synthesis and characterization of CeO₂ obtained by spray pyrolysis method. In *Synthesis and Properties of Mechanically Alloyed and Nanocrystalline Materials*, Pts 1 and 2 - Ismanam-96, volume 235-279 of *Materials Science Forum*, pages 291-296. Transtec Publications Ltd, Zurich-Uetikon, 1997.
- [49] B. Xia, I.W. Lenggoro, and K. Okuyama. Synthesis of CeO₂ nanoparticles by salt-assisted ultrasonic aerosol decomposition. *J. Mater. Chem.*, 11(12): 2925-2927, 2001.
- [50] B. Xia, I.W. Lenggoro, and K. Okuyama. Novel route to nanoparticle synthesis by salt-assisted aerosol decomposition. *Adv. Mater.*, 13(20): 1579-1582, 2001.
- [51] Y.F. Lu, H.Y. Fan, A. Stump, T.L. Ward, T. Rieker, and C.J. Brinker. Aerosol-assisted self-assembly of mesostructured spherical nanoparticles. *Nature*, 398(6724): 223-226, 1999.
- [52] D. Segal. Chemical synthesis of ceramic materials. *J. Mater. Chem.*, 7(8): 1297-1305, 1997.
- [53] G.V. Jayanthi, S.C. Zhang, and G.L. Messing. Modeling of solid particle formation during solution aerosol thermolysis - The evaporation stage. *Aerosol Sci. Technol.*, 19(4): 478-490, 1993.
- [54] H.F. Yu. Simulation of spray-pyrolysis for ceramic powder preparation. *Particul. Sci. Technol.*, 13(2): 149-167, 1995.
- [55] I.W. Lenggoro, T. Hata, F. Iskandar, M.M. Lunden, and K. Okuyama. An experimental and modeling investigation of particle production by spray pyrolysis using a laminar flow aerosol reactor. *J. Mater. Res.*, 15(3): 733-743, 2000.
- [56] M.R. Zachariah and S. Huzarewicz. Aerosol processing of YBaCuO superconductors in a flame reactor. *J. Mater. Res.*, 6(2): 264-269, 1991.
- [57] M.R. Zachariah and S. Huzarewicz. Flame synthesis of high-T_c superconductors. *Combust. Flame*, 87(1): 100-103, 1991.
- [58] T.T. Kodas, E.M. Engler, V.Y. Lee, R. Jacowitz, T.H. Baum, K. Roche, S.S.P. Parkin, W.S. Young, S. Hughes, J. Kleder, and W. Auser. Aerosol flow reactor production of fine Y₁Ba₂Cu₃O₇ powder - Fabrication of superconducting ceramics. *Appl. Phys. Lett.*, 52(19): 1622-1624, 1988.
- [59] R. Krieger, J. Töpfer, N. Preuss, S. Grimm, and J. Böer. Flame pyrolysis: A preparation route for ultrafine powders of metastable β -SrMnO₃ and NiMn₂O₄. *J. Mater. Sci. Lett.*, 13: 1111-1113, 1994.
- [60] S. Grimm, M. Schultz, S. Barth, and R. Muller. Flame pyrolysis - A preparation route for ultrafine pure-Fe₂O₃ powders and the control of their particle size and properties. *J. Mater. Sci.*, 32(4): 1083-1092, 1997.
- [61] J.H. Brewster and T.T. Kodas. Generation of unagglomerated, dense, BaTiO₃ particles by flame-spray pyrolysis. *AIChE J.*, 43(11): 2665-2669, 1997.
- [62] U.A. Limaye and J.J. Helble. Morphology control of zirconia nanoparticles through combustion aerosol synthesis. *J. Am. Ceram. Soc.*, 85(5): 1127-1132, 2002.

- [63] Y.C. Kang, D.J. Seo, S.B. Park, and H.D. Park. Morphological and optical characteristics of Y_2O_3 : Eu phosphor particles prepared by flame spray pyrolysis. *Jpn. J. Appl. Phys. Part 1 – Regul. Pap. Short Notes Rev. Pap.*, 40(6A): 4083-4086, 2001.
- [64] Y.C. Kang, D.J. Seo, S.B. Park, and H.D. Park. Direct synthesis of strontium titanate phosphor particles with high luminescence by flame spray pyrolysis. *Mater. Res. Bull.*, 37(2): 263-269, 2002.
- [65] K.A. Gross, J. Tikkanen, J. Keskinen, V. Pitkanen, M. Eerola, R. Siikamaki, and M. Rajala. Liquid flame spraying for glass coloring. *J. Therm. Spray Technol.*, 8(4): 583-589, 1999.
- [66] M. Oljaca, Y. Xing, C. Lovelace, S. Shanmugham, and A. Hunt. Flame synthesis of nanopowders via combustion chemical vapor deposition. *J. Mater. Sci. Lett.*, 21(8): 621-626, 2002.
- [67] J. Tikkanen, K.A. Gross, C.C. Berndt, V. Pitkanen, J. Keskinen, S. Raghu, M. Rajala, and J. Karthikeyan. Characteristics of the liquid flame spray process. *Surf. Coat. Technol.*, 90(3): 210-216, 1997.
- [68] K. Takatori, T. Tani, N. Watanabe, and N. Kamiya. Preparation and characterization of nano-structured ceramic powders synthesized by emulsion combustion method. *J. Nanopart. Res.*, 1: 197-204, 1999.
- [69] T. Tani, K. Takatori, N. Watanabe, and N. Kamiya. Metal oxide powder synthesis by the “emulsion combustion” method. *J. Mater. Res.*, 13(5): 1099-1102, 1998.
- [70] T. Tani, K. Takatori, and N. Watanabe. Characteristics and sintering behavior of barium titanate powder synthesized by emulsion combustion method. *J. Ceram. Soc. Jpn.*, 109(12): 981-985, 2001.
- [71] T. Tani, N. Watanabe, and K. Takatori. Emulsion combustion and flame spray synthesis of zinc oxide/silica particles. *J. Nanopart. Res.*, 5(1-2): 39-46, 2003.
- [72] M. Bonini, U. Bardi, D. Berti, C. Neto, and P. Baglioni. A new way to prepare nanostructured materials: Flame spraying of microemulsions. *J. Phys. Chem. B*, 106(24): 6178-6183, 2002.
- [73] M. Sokolowski, A. Sokolowska, A. Michalski, and B. Gokiel. The “in-flame-reaction” method for Al_2O_3 aerosol formation. *J. Aerosol Sci.*, 8: 219-229, 1977.
- [74] L. Mädler, H.K. Kammler, R. Mueller, and S.E. Pratsinis. Controlled synthesis of nanostructured particles by flame spray pyrolysis. *J. Aerosol Sci.*, 33(2): 369-389, 2002.
- [75] J. Karthikeyan, C.C. Berndt, J. Tikkanen, J.Y. Wang, A.H. King, and H. Herman. Nanomaterial powders and deposits prepared by flame spray processing of liquid precursors. *Nanostruct. Mater.*, 8(1): 61-74, 1997.
- [76] F.L. Yuan, C.H. Chen, E.M. Kelder, and J. Schoonman. Preparation of zirconia and yttria-stabilized zirconia (YSZ) fine powders by flame-assisted ultrasonic spray pyrolysis (FAUSP). *Solid State Ion.*, 109(1-2): 119-123, 1998.
- [77] C.R. Bickmore, K.F. Waldner, R. Baranwal, T. Hinklin, D.R. Treadwell, and R.M. Laine. Ultrafine titania by flame spray pyrolysis of a titanatrane complex. *J. Eur. Ceram. Soc.*, 18(4): 287-297, 1998.
- [78] D.R. Treadwell, A.C. Sutorik, S.S. Neo, R.M. Laine, and R.C. Svedberg. Synthesis of β'' -alumina polymer precursor and ultrafine β'' -alumina composition powders, chap. 14. In *Synthesis and Characterization of Advanced Materials*, volume 681 of ACS Symposium Series, pages 146-156. Amer. Chemical Soc., 1998.
- [79] A.C. Sutorik, S.S. Neo, D.R. Treadwell, and R.M. Laine. Synthesis of ultrafine β'' -alumina powders via flame spray pyrolysis of polymeric precursors. *J. Am. Ceram. Soc.*, 81(6): 1477-1486, 1998.
- [80] R. Narayanan and R.M. Laine. Synthesis and characterization of precursors for group II metal aluminates. *App. Organomet. Chem.*, 11(10-11): 919-927, 1997.
- [81] R. Baranwal, M.P. Villar, R. Garcia, and R.M. Laine. Flame spray pyrolysis of precursors as a route to nano-mullite powder: Powder characterization and sintering behavior. *J. Am. Ceram. Soc.*, 84(5): 951-961, 2001.
- [82] R.M. Laine, R. Baranwal, T. Hinklin, D. Treadwell, A. Sutorik, C. Bickmore, K. Waldner, and S.S. Neo. Making nanosized oxide powders from precursors by flame spray pyrolysis. *Key. Eng. Mat.*, 159-160: 17-24, 1999.
- [83] R.M. Laine, T. Hinklin, G. Williams, and S.C. Rand. Low-cost nanopowders for phosphor and laser applications by flame spray pyrolysis. In *Metastable, Mechanically Alloyed and Nanocrystalline Materials, Pts 1 and 2*, volume 343-3 of Materials Science Forum, pages 500-510. Trans Tech Publications Ltd, Zurich-Uetikon, 2000.
- [84] A.C. Sutorik and M.S. Baliat. Solid solution behavior of $Ce_xZr_{1-x}O_2$ nanopowders prepared by flame spray pyrolysis of solvent-borne precursors. In *Metastable, Mechanically Alloyed and Nanocrystalline Materials*, volume 386-3 of Materials Science Forum, pages 371-376. Trans Tech Publications Ltd, Zurich-Uetikon, 2002.
- [85] A. Kilian and T.F. Morse. A novel aerosol combustion process for the high rate formation of nanoscale oxide particles. *Aerosol Sci. Technol.*, 34(2): 227-235, 2001.
- [86] T. Tani, L. Mädler, and S.E. Pratsinis. Homogeneous ZnO nanoparticles by flame spray pyrolysis. *J. Nanopart. Res.*, 4(4): 337-343, 2002.
- [87] L. Mädler and S.E. Pratsinis. Bismuth oxide nanoparticles by flame spray pyrolysis. *J. Am. Ceram. Soc.*, 85(7): 1713-1718, 2002.
- [88] L. Mädler, W.J. Stark, and S.E. Pratsinis. Flame-made ceria nanoparticles. *J. Mater. Res.*, 17(6): 1356-1362, 2002.
- [89] T. Hinklin, B. Toury, C. Gervais, F. Babonneau, J.J. Gislason, R.W. Morton, and R.M. Laine. Liquid-feed flame spray pyrolysis of metalloorganic and inorganic alumina sources in the production of nanoalumina powders. *Chem. Mat.*, 16(1): 21-30, 2004.
- [90] T. Tani, L. Mädler, and S.E. Pratsinis. Synthesis of zinc oxide/silica composite nanoparticles by flame spray pyrolysis. *J. Mater. Sci.*, 37(21): 4627-4632, 2002.

- [91] T. Tani, L. Mädler, and S.E. Pratsinis. Synthesis of γ -willemite nanoparticles by post-calcination of flame-made zinc oxides/silica composites. Part. Part. Syst. Charact., 19(5): 354-358, 2002.
- [92] W.J. Stark, L. Mädler, M. Maciejewski, S.E. Pratsinis, and A. Baiker. Flame synthesis of nanocrystalline ceria-zirconia: effect of carrier liquid. Chem. Commun., (5): 588-589, 2003.
- [93] W. J. Stark, M. Maciejewski, L. Mädler, S.E. Pratsinis, and A. Baiker. Flame-made nanocrystalline ceria/zirconia: structural properties and dynamic oxygen exchange capacity. J. Catal., 220(1): 35-43, 2003.
- [94] H. Schulz, W.J. Stark, M. Maciejewski, S.E. Pratsinis, and A. Baiker. Flame-made nanocrystalline ceria/zirconia doped with alumina or silica: structural properties and enhanced oxygen exchange capacity. J. Mater. Chem., 13(12): 2979-2984, 2003.
- [95] L. Mädler, W.J. Stark, and S.E. Pratsinis. Rapid synthesis of stable ZnO quantum dots. J. Appl. Phys., 92(12): 6537-6540, 2002.
- [96] L. Mädler, W.J. Stark, and S.E. Pratsinis. Simultaneous deposition of Au nanoparticles during flame synthesis of TiO_2 and SiO_2 . J. Mater. Res., 18(1): 115-120, 2003.
- [97] W.J. Stark, S.E. Pratsinis, and A. Baiker. Heterogeneous catalysis by flame-made nanoparticles. Chimia, 56(10): 485-489, 2002.
- [98] R. Strobel, F. Krumeich, W.J. Stark, S.E. Pratsinis, and A. Baiker. Flame spray synthesis of $\text{Pd}/\text{Al}_2\text{O}_3$ catalysts and their behavior in enantioselective hydrogenation. J. Catal., 222(2): 307-314, 2004.
- [99] R. Mueller, L. Mädler, and S.E. Pratsinis. Nanoparticle synthesis at high production rates by flame spray pyrolysis. Chem. Eng. Sci., 58(10): 1969-1976, 2003.
- [100] R. Mueller, R. Jossen, S.E. Pratsinis, M. Watson, and M.K. Akhtar. Zirconia nanoparticles made in spray flames at high production rates. J. Am. Ceram. Soc., 87(2): 197-202, 2004.
- [101] D. Vollath and K.E. Sickafus. Synthesis of nanosized ceramic oxide powders by microwave plasma reaction. Nanostruct. Mater., 1: 427-437, 1992.
- [102] M. Hasegawa, Y. Kato, M. Kagawa, and Y. Syono. Effect of additive oxides on ultrafine CeO_2 particles synthesized by the spray-ICP technique. J. Mater. Sci. Lett., 15(18): 1608-1611, 1996.

Author's short biography



Lutz Mädler

Lutz Mädler studied Technical Physics at the Technical University of Zwickau, Germany, from 1991 to 96 and received an engineering diploma in Physics. He also holds Diploma and Doctoral degrees in Process Engineering from the Technical University of Freiberg, Germany. From 1996 till 1999 he worked for the Fraunhofer Institute of Toxicology and Aerosol Research Hannover, Germany, in the field of particle characterization and particulate source apportionment. In 1999 he joined the Particle Technology Group at the Swiss Federal Institute of Technology (ETH) Zurich. He received his Habilitation from ETH Zurich in 2003 and serves as Privatdozent (senior lecturer) for Particulate Processes. His research developed the area of spray processes for materials manufacture. He focuses on the design, control, and theoretical understanding of spray flame reactors for the production of functional and tailor-made nanoparticles for applications in composites, sensors, catalysts, and electronic materials.

Measurement of Adhesion Forces between Particles and Rough Substrates in Air with the Vibration Method[†]

Siegfried Ripperger¹, Konrad Hein²

¹ Lehrstuhl für Mechanische Verfahrenstechnik,
Technische Universität Kaiserslautern*

² Lehrstuhl für Mechanische Verfahrenstechnik,
Technische Universität Dresden**

Abstract

Pull-off forces were measured using the vibration method at 30-50% relative humidity for glass and tin spheres on a variety of substrates. The results were compared with those obtained through the colloidal probe technique. Both methods show good agreement for small particle sizes. Since the vibration method causes sinusoidally alternating stresses, the method yields detachment and contact forces between particles and substrate of the same order of magnitude. Alternating contact forces of the vibration method can cause an increase in the adhesion force through flattening of asperities, which also depend on the surface roughness and the mechanical properties of particle and substrate.

Pull-off force measurements with the colloidal probe technique and special attention to the influence of the contact force also show an adhesion force intensification with increasing contact forces depending on the surface roughness. No significant adhesion force intensification caused by increasing contact time to 30s at several contact forces was observed. For theoretical predictions based on van der Waals adhesion, an approach presented by Rabinovich and approximations of plastic micro-asperity flattening were combined.

1 Introduction

The accuracy of dosing procedures with fine powders in the pharmaceutical industry or the removal of abrasive particles after polishing operations are examples for industrial operations which are significantly influenced by adhesion phenomena in particle-wall systems. Such adhesion phenomena can arise from several adhesion mechanisms such as van der Waals adhesion, capillary or electrostatic adhesion forces, whose intensity depends on the topography, the chemical composition of the interacting surfaces, environmental conditions such as relative humidity and temperature, and the stresses between the surfaces in contact in combination with their mechanical properties.

Different techniques have been developed to measure the adhesion forces between particles and substrate. The so-called “colloidal probe technique” [1,

2], based on the atomic force microscope (AFM) [3], and the centrifuge technique [4, 5] have become well-established tools for studying adhesion forces. The vibration method [6, 7] with its technical conversion described later represents a complementary and practical method for the measurement of adhesion forces. Its alternating detachment and contact forces have a practical counterpart in the dynamic stresses acting on particles during frequently used operations of process engineering.

The paper presents adhesion force measurements between particles and rough substrates obtained through the vibration method at room temperature and moderate relative humidity between 30% and 50%. Under these ambient conditions, van der Waals adhesion represents the dominating adhesion mechanism. The results of the vibration method are compared with those obtained by the colloidal probe technique. We focus on the influence of surface roughness and contact forces on adhesion forces, while taking deformations of micro-asperities through alternating contact forces of the vibration method into account.

* 67653 Kaiserslautern, Germany

** 01062 Dresden, Germany

[†] Accepted: August 26, 2004

2 Methods

Pull-off forces between particles and substrate were measured using the vibration method and the colloidal probe technique (Nanoscope 3A, Digital Instruments, USA). The topography and surface roughness of the particles and substrates were characterized using tapping mode AFM (Nanoscope 3A, Digital Instruments, USA) and SEM (Gemini 982, Zeiss, Germany). Mode shape and acceleration of the vibrating surface were measured spectrally with a laser-scanning vibrometer (PSV 200, Polytec, Germany).

2.1 The vibration method

The measuring principle of the vibration method, first described by Deryaguin [6], is based on particle detachment from a vertical-sinusoidally vibrating surface caused by its inertia at a certain acceleration. Therefore, the vibration of the substrate not only yields a detachment force to overcome the adhesion force, but also causes contact forces between particles and substrate of the same order. Particle detachment events are continuously recorded and correlated with acting acceleration and particle mass, allowing the pull-off forces to be calculated.

2.1.1 Technical conversion

Our technical conversion differs in several aspects from that of Deryaguin. The use of a laser-scanning vibrometer (LSV) for the spectral measurement of the mode shape and acceleration of the vibrating substrate can be seen as the main difference. **Figure 1** shows the experimental set-up for the measurement of adhesion forces between particles and substrate. In contrast to our earlier investigations [7], the sinusoidal oscillation of the substrate is realized by a pre-loaded open-loop ultrasonic piezo actuator (UPA 25, US 100, LC 100; Cedrat Technologies, France) with adjustable frequency and excitation voltage as well as a temperature sensor. The test substrate (5×5 mm) is mounted above an adapter which is attached to the actuator over a prestressed screwed fastening and a small amount of epoxy resin, thus preventing additional vibration modes between the three components. The actuator provides a maximum acceleration of approximately 100000 g at its resonance frequency, which also depends on the actuator temperature and the mass of the mounted substrate. For that reason, the acceleration calibration of the sinusoidally oscillating substrate was carried out as a function of the excitation voltage U_{ex} and actuator temperature at fixed frequency f as shown in **Figure 2**.

Single particles were placed on the substrate using gentle sieve vibration to disperse the particles from the powder, avoiding any appreciable triboelectrical loading. The actuator with the mounted substrate was placed at the end of the laminar inlet zone of a grounded aluminium flow channel with rectangular cross-section over a drilling at the bottom side of the channel. With increasing acceleration of the substrate, the acting detachment force exceeds the adhesion force. Particle detachment events are continuously

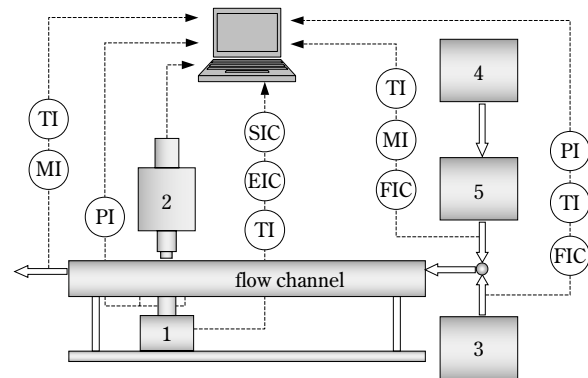


Fig. 1 Experimental set-up: (1) oscillation system with attached substrate; (2) optical unit with microscope, CCD camera and image analysing software; (3) compressed air with $T_{dew} = -60^\circ\text{C}$; (4) laminar flow box; (5) climatic exposure test cabinet and flow channel ($L \times W \times H$: 1700×40×4 mm).

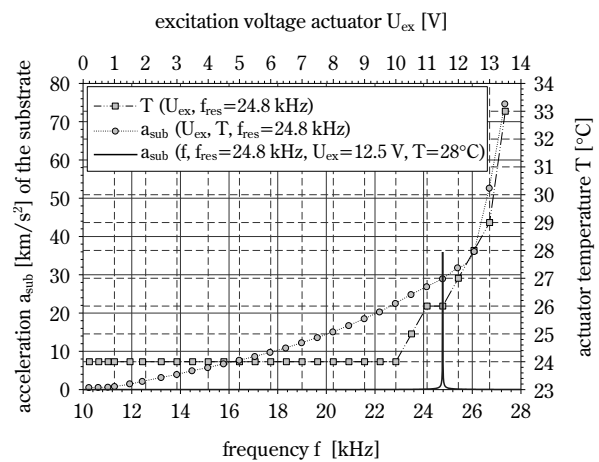


Fig. 2 Acceleration calibration curve $a_{sub}(U_{ex})$ of an electropolished stainless steel substrate. Additionally, the frequency-dependent course of $a_{sub}(f)$ and the heating of the actuator as a function of the excitation voltage $T(U_{ex})$ at fixed frequency are plotted.

recorded through a glass plate attached over the substrate at the top side of the flow channel with a microscope (Axiotech, Zeiss, Germany), a CCD camera and an image analysis software (Image Pro Plus, Media Cybernetics, USA). For horizontal dislocation of detached particles, the substrate is exposed to a laminar air flow ($Re_{channel}=1514$) parallel to the substrate. The air flow was cleaned and conditioned with a laminar-flow box (VMK 06.15, Steag, Germany), a climatic exposure test cabinet (KPK 200, Feutron, Germany) and a frequency-controlled fan. Optionally, compressed air with a dew point temperature of $T_{dew}=-60^{\circ}C$ can be used to realize very low relative humidity conditions. Flow rate, air temperature and humidity were measured continuously with a mass flowmeter (3063, TSI, USA), and a humidity sensor (FH A646, Ahlborn, Germany). Velocity profiles over the channel cross-section at different air flow rates were quantified with a hot-wire probe (8465, TSI, USA).

The adhesion force between particle and substrate can also be measured using particle re-entrainment in a turbulent air flow. In this case, a turbulent flow regime parallel to the nonvibrating surface is used to apply drag and lift forces to the adhering particles.

2.1.2 Principle of force measurement

Figure 3 shows a schematic diagram of the forces acting on a single particle exposed to a laminar air flow and adhered to a sinusoidally oscillating surface. Particle re-entrainment caused by fluid forces is determined by the stresses within the linear sublayer of the laminar flow ($Re_{channel}=1514$). The estimation of acting lift (F_{lift}) and drag (F_{drag}) forces for a particle fully submerged in the linear sublayer in contact with

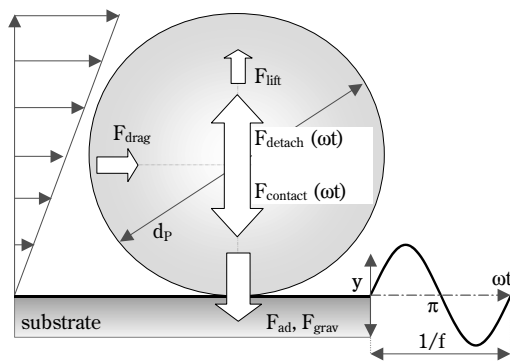


Fig. 3 Forces acting on a single particle exposed to a laminar air flow and adhered to a sinusoidally oscillating substrate (schematic).

a wall based on approaches by Leighton [8] and O'Neill [9] is described in detail by Hein et al. [7]. Under the given laminar flow conditions and particle size range, the contribution of both lift and drag forces to particle detachment as well as the gravitational force are negligible in relation to the adhesion forces and detachment forces. This was confirmed by force measurements with particle re-entrainment in a turbulent air flow at the same particles and nonvibrating substrates under otherwise unchanged environmental conditions. Under laminar flow conditions, fluid forces are only used for the horizontal dislocation of detached particles.

The maximum detachment force F_{detach} and contact force $F_{contact}$ are sinusoidally alternating inertial forces of the same order of magnitude acting on the particle at the top and bottom dead centre of the sinusoidally oscillating substrate.

$$|F_{detach}| = |F_{contact}| \quad (1)$$

Hence, the acceleration of the particle acts in the direction opposite to the acceleration of the vibrating surface, which is given by:

$$a_{sub}(t) = -a_p(t) \quad (2)$$

The absolute value of the maximum detachment and contact force results from the particle mass and the acceleration of the sinusoidally oscillating substrate at particle detachment, which is measured and calibrated with the LSV (Laser-scanning-vibrometer) as described in Section 2.1.1.

$$|F_{detach}| = |F_{contact}| = |a_{sub}| \cdot m_p \quad (3)$$

The mass of a spherical particle is calculated from its projected area and density. A simplified force balance at the top dead centre of the sinusoidally oscillating substrate under the assumptions of negligible small fluid forces permits calculation of the pull-off force between particle and substrate as follows:

$$F_{detach} = F_{ad} \quad (4)$$

The maximum contact force acts on the particle at the bottom dead centre. Its order of magnitude can be approximated under the assumption of an additive superposition of adhesion force and contact force [10] and substituting F_{ad} and $F_{contact}$ from Eq. (1) and (4).

$$F_{contact_max} \approx F_{ad} + F_{contact} \approx |F_{detach}| + F_{contact} \approx 2 \cdot |F_{detach}| \quad (5)$$

2.2 Comparison with other methods

As discussed in Section 1, the adhesion force and

the underlying adhesion mechanisms are influenced by various factors. The different measurement principles of each technique and their technical conversion result in different stresses and contact times between the interacting surfaces. This leads to a wide range of reported values for adhesion between the same particle-substrate system depending on the technique employed. In the light of this aspect, we give a brief comparison of the colloidal probe technique, centrifuge method and vibration method.

The measuring principle of the vibration method causes alternating detachment and contact forces of the same order of magnitude at the top and bottom dead centre of the sinusoidally oscillating substrate. In contrast, the colloidal probe technique or the centrifuge method apply a uniform and incremental detachment force to the particles and a contact force can be applied independently, just before particle detachment.

The maximum rotational speed of the ultra-centrifuge and the maximum oscillation amplitude of the sinusoidally oscillating piezo actuator limits the maximum detachment force especially for the vibration method. Depending on the acting adhesion force, particle density and the optical acquisition of the single particles, measurements with both methods are restricted to a minimum particle size of a few micrometres. Since the particles cannot be monitored continuously during the increase of the centrifuge's rotational speed, the precise moment of particle detachment events or the precise adhesion force cannot be determined. In most cases, the centrifuge must be stopped after each run at constant centrifugal acceleration. Since the attachment of particles to the AFM cantilever is usually done using micromanipulators under an optical microscope, the minimal particle size is limited to approximately 1 μm [11]. This comparatively tedious and high effort for sample preparation also limits the number of separate particles used within one study for practical reasons [11]. In contrast, the centrifuge technique and the vibration method usually measure the detachment force between various particles at different substrate locations in a single experiment, resulting in good statistical evaluation of the data. The colloidal probe technique allows the use of the same particle for several experiments at different substrate locations, and the particle surface topography can be subsequently examined. A further difference can be seen in the contact time between particle and substrate before particle detachment. With the centrifuge technique and the vibration method, the interacting surfaces usually remain in

contact for more than 1 minute, whereas the colloidal probe technique normally uses a measuring frequency of 1 Hz for repeated force measurements.

3 Test Particles and Substrates

Adhesion force measurements were carried out for glass spheres (Potters-Ballotini, UK), and tin spheres (Nanoval, Germany) on ground and electropolished stainless steel substrates (Lehrstuhl für Maschinen- und Apparatekunde, TU München, Germany) as well as a silicon wafer substrate (Institut für Halbleiter- und Mikrosystemtechnik, TU Dresden, Germany). The topography and surface roughness of the test particles and the substrate were characterized by SEM (**Figure 4**, **Figure 5**) and AFM (**Figure 6**). Particles and substrates were cleaned with ethanol in an ultrasonic bath, rinsed in deionised water and dried in an exsiccator. The substrates were additionally cleaned carefully with a low-pressure stream of compressed air before each measurement. Further attempts to clean the surfaces were not made to match its practical use. **Table 1** presents relevant material properties and results of the AFM roughness analysis.

3.1 Roughness analysis of particles and substrates

The root mean square roughness (rms) represents one possibility of quantifying the surface topography by means of an average value. This standardized roughness parameter was incorporated by Rabinovich [12] into the classic approach of Rumpf [13], to account for roughness effects on van der Waals adhesion (see Section 4). Since the rms values themselves do not indicate the frequency of the roughness or their characteristic peak-to-peak distance between the asperities, it is dependent on scale. Further approaches have been developed to account for this dependency and an asperity shape differing from the hemisphere [12]. Especially for real, technical surfaces with inhomogeneities caused by the manufacturing process, determination of the dominating roughness scale(s) and their associated roughness parameters out of a three-dimensional surface topography remains demanding. The box plot of the rms roughness against the scanning area allows information to be extracted about the dependency of the surface roughness on scale, taking variations of surface roughness caused by the manufacturing process into consideration. **Figure 7** shows the relationship between rms roughness and the area of scanning for stainless steel substrates and particles measured by AFM at

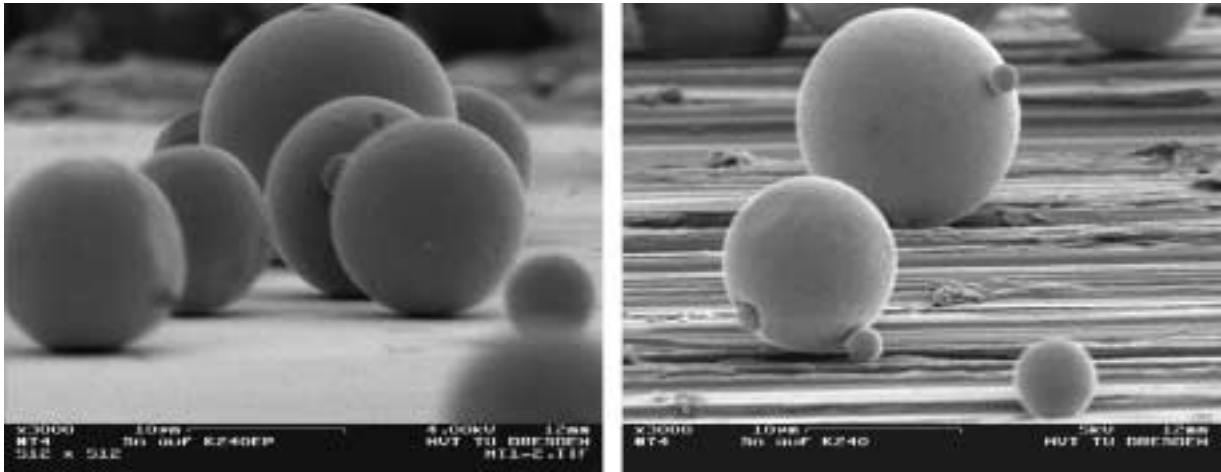


Fig. 4 SEM images of tin particles placed on an electropolished stainless steel substrate (left) and of tin particles placed on a ground stainless steel substrate (right).

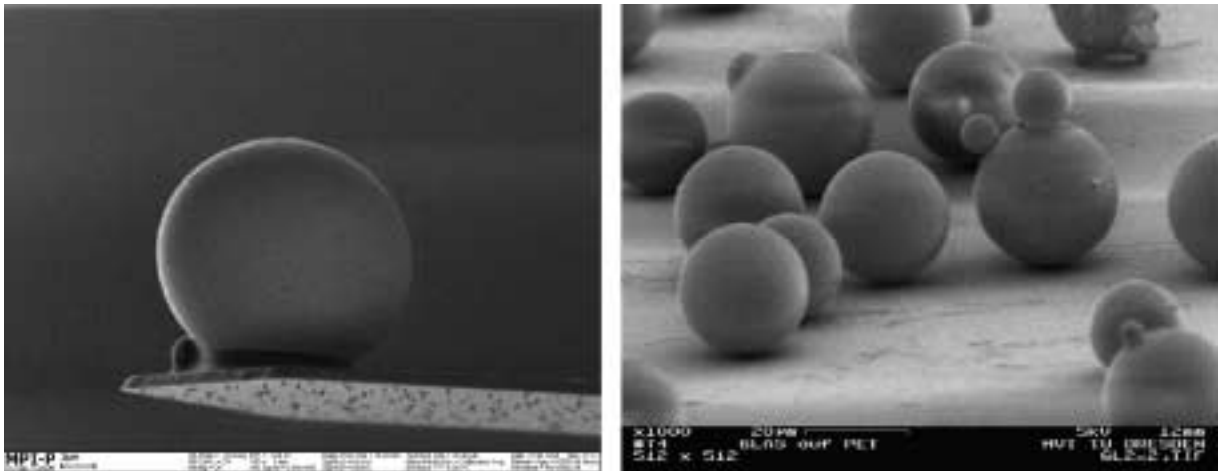


Fig. 5 SEM images of a tin particle attached to an AFM cantilever (left, MPI for Polymer Research, Mainz) and glass spheres on a PET substrate (right).

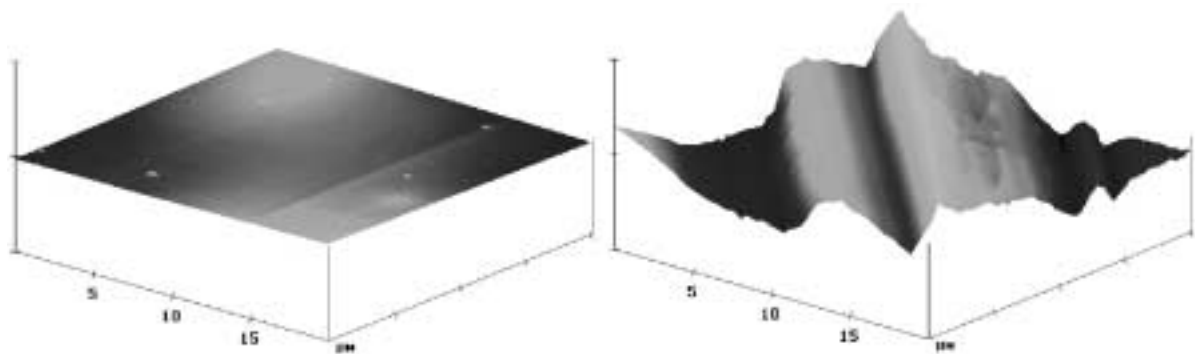


Fig. 6 AFM images of $20 \times 20 \mu\text{m}$ area with a vertical scale of 3000 nm/division of electropolished (left) and ground stainless steel substrate (right).

Table 1 Measured average surface roughness rms and material properties of particles and substrates

Material	rms [nm]	A [10 ⁻¹⁹ J]	ν [-]	ρ [gcm ⁻³]	H [GPa]	E [GPa]
tin spheres	Fig. 7	2.56	0.33	7.3	0.045	55
glass spheres	Fig. 7	1.1	0.2	2.4	10	70
silicon wafer substrate	~ 0.13	2.02	0.27	–	13	130
ground stainless steel substrate	Fig. 7	2.32	0.29	–	12	200
ground stainless steel substrate	Fig. 7	2.32	0.29	–	12	200

various positions. Depending on the asperity distribution and size, the scanned surfaces show an increase in rms roughness with increasing scanning area tending toward a characteristic maximum rms roughness. Similarly, a characteristic minimum scanning area exists, where only a nanoscopic roughness scale is dominant, as described previously by Kiely [14]. Despite the large variations in surface roughness for the ground stainless steel substrate, a significant reduction in rms roughness for very small scanning areas can be observed. This possibly indicates the existence of a “microscopic” roughness within the macroscopic dimension. Owing to its dependency on scale, use of the rms roughness in the approaches presented by Rabinovich raises the issue of a proper

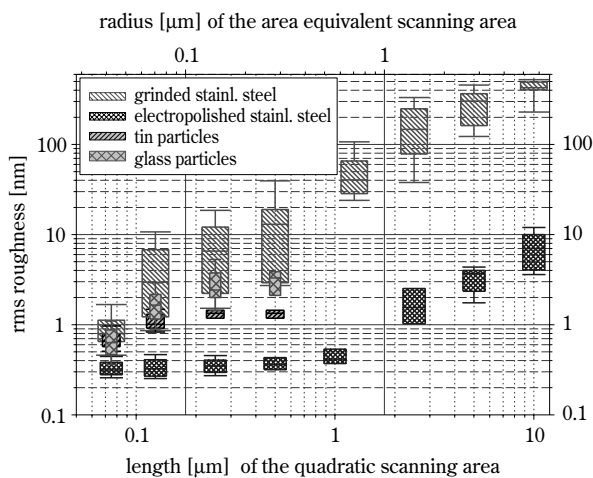


Fig. 7 rms-roughness analysis for ground and electropolished stainless steel substrates and tin and glass particles at different scanning areas and different positions calculated from AFM images.

choice of the scanning area to reflect the topography of the interacting surfaces in the real area of contact during force measurements.

4 Prediction of Adhesion Forces

A number of approaches exist for the prediction of particle-substrate interactions for ideally smooth surfaces, based on van der Waals adhesion [15], or derived from surface-energy-based approaches such as Derjaguin-Muller-Toporov (DMT) [16], or Johnson-Kendall-Roberts (JKR) [17] adhesion theory. The DMT and JKR theory take the elastic flattening effect into account. A major drawback towards the applicability of the DMT and JKR model lies in the need for an estimation of surface energy. Surface energy values vary depending on the source and its measurement technique, since influences of surface roughness or plastic deformation are often coupled within the surface energy parameter [18]. For a van-der-Waals-based approach, the fundamental interaction parameters are much better established. Although not accounting for polar forces, it can be assumed that the major contribution to surface energy results from van der Waals attraction.

With real surfaces, the roughness influence on the real area of contact and the magnitude of the force of adhesion limits the application of these models. A possibility of overcoming this problem is by simulating the influence of roughness on the force of adhesion, based on the local topography and chemical composition of the interacting surfaces [19, 20]. Other approaches try to quantify the surface topography by means of average values. Rabinovich [12] incorporated the rms roughness in the approach by Rumpf [13] to account for the effects of hemispherical asperities on van der Waals adhesion:

$$F_{vdw} = \frac{A_{12} \cdot d_p}{12 \cdot a_0^2} \cdot \left(\frac{1}{1 + \frac{d_p}{2.97 \cdot rms_{12}}} + \frac{1}{\left(1 + \frac{1.48 \cdot rms}{a_0}\right)^2} \right) \quad (6)$$

The effective Hamaker constant A_{12} between material 1 and 2 in vacuum can be calculated from the individual Hamaker constants of the adhesion partners as follows:

$$A_{12} = \sqrt{A_1 \cdot A_2} \quad (7)$$

The effective rms_{12} roughness of the interacting surfaces is calculated from the rms values of the substrate rms_{sub} and the particle rms_p (Fig. 7), assuming

an independent statistical combination of the contact surfaces.

$$\text{rms}_{12} = \sqrt{\text{rms}_p^2 + \text{rms}_{\text{sub}}^2} \quad (8)$$

This approach was enhanced repeatedly to account for an asperity shape differing from the hemisphere, superposition of roughness scales and finally elastic flattening of asperities [12], resulting in closer predictions of experimental adhesion values. On the other hand, these approaches are associated with more roughness parameters whose prediction might be complex and prone to subjective error, especially for anisotropic surfaces stemming from the manufacturing process. In the light of these findings, we use the approach of Eq. (6) in combination with a statistical and scale-dependent roughness characterization (section 3.1) of the particle and substrate to account for the topography of the interacting surfaces in the real area of contact. This should allow for the prediction of adhesion forces with a minimum of individual interpretation error during roughness characterization of the surfaces.

4.1 Influence of contact forces

Since the vibration method causes alternating detachment and contact forces of the same order of magnitude, the influence of contact forces on the adhesion forces should be regarded. According to Rumpf and co-workers [14], an adhesion force intensification caused by the elastic flattening of micro-asperities is only possible through an increase of the points of contact, however, a visco-elastic [21] or plastic flattening of the contact area can also intensify the adhesion force.

An estimation of plastic deformation can be based on various criteria. Kogut [22] and Maugis [23] suggested a comparison of a critical flattening or a critical contact radius with the corresponding elastic values. Depending on the degree by which the critical value is exceeded, elastic or elasto-plastic deformations take place. Rumpf [14] proposes a comparison of the contact pressure and yield strength Y or material hardness H to detect the elasto-plastic or plastic deformation of the contact area.

To consider the effect of micro-asperity plastic flattening on van der Waals adhesion we combine the Rabinovich approach (Eq. (6)) together with an estimation of plastic deformation by Rumpf. Because of the mechanical properties of the adhesion partners (Table 1), we discuss in all cases the adhesion between a soft, deformable particle and an approximately rigid substrate. Under this assumption, micro-

asperity plastic flattening can be considered to be a plastic flattening of the particle $h_{\text{flat_plast}}$, expressed through a modified effective roughness rms_{12_plast} in Eq. (6):

$$\text{rms}_{12_plastic} = \sqrt{(\text{rms}_p - h_{\text{flat_plast}})^2 + \text{rms}_{\text{sub}}^2} \quad (9)$$

Assuming only normal stresses and elastic contact at the circular interface between a smooth soft particle and a smooth rigid substrate, the contact pressure distribution $p_{\text{contact}}(r)$ over the contact radius r , the maximum elastic contact radius r_{contact} and the elastic flattening h_{flat} for a given contact force F_{contact} can be estimated with the Hertz theory [24].

$$p_{\text{contact}}(r) = \frac{3 \cdot F_{\text{contact}} \cdot \sqrt{1 - \left(\frac{r}{r_{\text{contact}}}\right)^2}}{2 \cdot \pi \cdot r_{\text{contact}}^2} \quad (10)$$

$$r_{\text{contact}}^3 = \frac{F_{\text{contact}} \cdot d_p}{2 \cdot K_{\text{elast}}(E_p, E_{\text{sub}}, \nu_p, \nu_{\text{sub}})} \quad (11)$$

$$h_{\text{flat}} = \frac{2 \cdot r_{\text{contact}}^2}{d_p} \quad (12)$$

According to Rumpf [14], the maximum contact force $F_{\text{contact_max}}$ consists of the adhesion force of the unstressed system and the external contact force F_{contact} . In the case of the vibration method, the maximum contact force $F_{\text{contact_max}}$ can be estimated with Eq. (5). For the condition

$$p_{\text{contact}}(r, F_{\text{contact_max}}) \geq H_p \quad (13)$$

a plastically deformed contact radius $r_{\text{contact_plast}}$ ($p_{\text{contact}} = H_p$) and a plastic flattening $h_{\text{flat_plast}}$ of the particle can be calculated, rewriting Eq. (10) and substituting r_{contact} in Eq. (12) by $r_{\text{contact_plast}}$. For real surfaces, roughness will decrease the real area of contact $A_{\text{contact}} = 2 \cdot \pi \cdot r_{\text{contact}}^2$ and thus increase the contact pressure, resulting in a stronger plastic flattening. One attempt to account for this effect, considering the deformable particle only, uses the bearing function available in the standard software of the AFM. This function uses AFM topography images to calculate the ratio $a_{\text{real}}(h)$ of the real contact area A_{real} to the scanning area A_{scann} , dependent on the height h of the roughness profile, and is therefore also dependent on scale. Figure 8 exemplifies a bearing analysis for the flattened AFM image of the spherical cap of a tin particle.

$$a_{\text{real}}(h) = \frac{A_{\text{real}}}{A_{\text{scann}}} \quad (14)$$

This ratio $a_{\text{real}}(h)$ can be incorporated in Eq. (10) to estimate the real contact pressure in dependency of maximum contact force $F_{\text{contact_max}}$ and elastic flattening h_{flat} .

$$p_{\text{contact_real}}(r) = \frac{3 \cdot F_{\text{contact}} \cdot \sqrt{1 - \left(\frac{r}{r_{\text{contact}}}\right)^2}}{a_{\text{real}}(h_{\text{flat}}) \cdot 2 \cdot \pi \cdot r_{\text{contact}}^2} \quad (15)$$

The further procedure for estimation of the plastic flattening $h_{\text{flat_plast}}$ of the particle described above, which is incorporated in Eq. (9), remains identical. The consideration of the real area of contact leads to a nearly complete plastic deformation of the contact area calculated with the Hertz theory with Eq. (11) and (12).

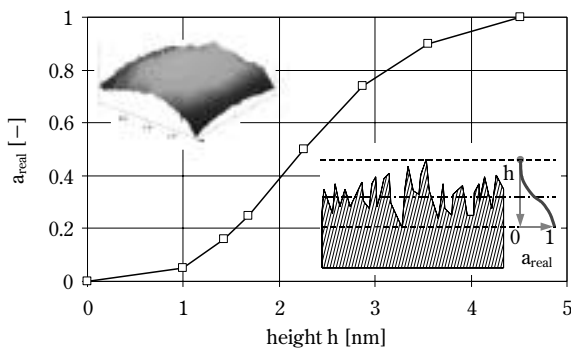


Fig. 8 Bearing analysis for a tin particle based on a flattened AFM image of 250×250 nm area and schematic of the bearing procedure (lower right picture).

5 Experimental Results and Discussion

The results of the vibration method represent the pull-off forces between various particles, each at different substrate locations. In contrast, the results of the colloidal probe technique (referred to as AFM) represent either repeated measurements between one particle at the same substrate location (referred to as 1 location) or at 200 different locations of the substrate (matrix). For a theoretical prediction based on van der Waals adhesion, we used the Rabinovich model of Eq. (6). To account for the variations in surface roughness of different particles and substrate

locations, an upper and lower limit of the theoretical adhesion force was calculated. The lower limit was computed using the 90% percentile of particle and substrate rms roughness in Eq. (8), whereas for the upper limit, the 10% percentile (upper and lower error bar in **Fig. 7**) was used. Based on estimations of the circular contact area between particle and substrate, with Eq. (11) we assume the box plot at 75×75 nm scanning area in **Fig. 7** to be the best representation of the contact area. The effect of micro-asperity plastic flattening at the particle, caused by alternating contact forces of the vibration method, was considered through the modified effective roughness rms_{12_plast} of Eq. (9), taking into account a reduced area of contact stemming from surface roughness as described in Section 4.1. For theoretical predictions of the maximum contact pressure force $F_{\text{contact_max}}$ of Eq. (13), we used twice the van der Waals adhesion force F_{vdW} of the unstressed system of Eq. (6) as described in Section 2.1.2, assuming particle detachment for $|F_{\text{vdW}}| \leq |F_{\text{detach}}|$, $|F_{\text{detach}}| \approx |F_{\text{contact}}|$ and $|F_{\text{contact_max}}| \approx |F_{\text{vdW}}| + |F_{\text{contact}}|$. The surface-energy-based approaches of DMT as well as JKR overestimate the measured values.

5.1 Tin particles on electropolished stainless steel substrates

Pull-off forces for tin spheres on an electropolished stainless steel substrate are shown in **Figure 9**. The colloidal probe technique (AFM) (Lehrstuhl für Maschinen und Apparate Kunde (MAK), TV München) and vibration method show relatively good agreement. For small particle sizes, the results of both methods are for the most part within the range defined by the

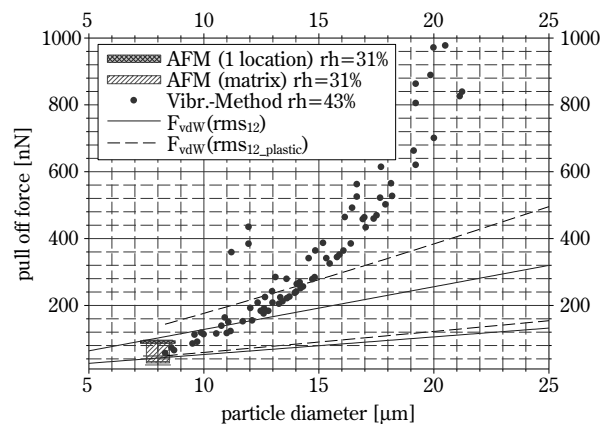


Fig. 9 Pull-off force for tin spheres on electropolished stainless steel substrates and predicted upper and lower limit of van der Waals adhesion using Eq. (6) with $\text{rms}_{12_upper} = 0,54$ nm and $\text{rms}_{12_lower} = 1,05$ nm of Eq. (8) and $\text{rms}_{12_plastic}$ of Eq. (9).

Rabinovich approach of Eq. (6), using the 90% and 10% percentile of particle and substrate rms roughness in Eq. (8) as a lower and upper limit of the predicted van der Waals adhesion force. With increasing particle size, the adhesion forces measured with the vibration method exhibit a stronger increase than predicted, showing a tendency to lower rms roughness values of the harder substrate with the higher Young's Modulus and hardness. Since the vibration of the substrate also causes contact forces between particle and substrate of the same order, higher adhesion forces and particle diameters represent higher contact forces. It is therefore possible that micro-asperities of the tin spheres with the comparatively lower Young's Modulus and hardness undergo an increasing flattening with increasing particle diameter, whereas the harder asperities of the substrate remain unchanged. This would result in a lower rms value which corresponds to a more intimate contact and an increase in adhesion force. To consider possible micro-asperity plastic flattening, the modified rms value $rms_{12_plastic}$ of Eq. (9) was used in Eq. (6). Especially for higher particle diameters and contact forces, the adhesion force intensification observed with the vibration method cannot be explained by plastic flattening only. Further reasons for this effect might be seen in an increase in the points of contact caused by rearrangements and elastic flattening of the particle not incorporated in the approach. Furthermore, the influence of the high-frequency alternating stresses might prevent a relaxation of the elastically flattened asperity, causing a kind of visco-elastic behaviour. Pull-off force measurements with the colloidal probe technique at an elevated measuring frequency of 5 Hz presented by Zhou [25] showed a significant adhesion force intensification with increasing measuring sequence. Resonant particle oscillation before particle detachment might be another source of adhesion force intensification. It can be caused by sinusoidally alternating elastic deformation of micro-asperities through high-frequency alternating detachment and contact forces of the vibration method for $F_{adhesion} > F_{detach}$. Estimations of this effect based on approaches by Ziskind [26] will be presented elsewhere.

Figure 10 shows successive pull-off force measurements for two tin particles on an electropolished stainless steel substrate under variation of the contact force measured with the colloidal probe technique (MPI for Polymer Research, Mainz, Germany) at 1 Hz measuring frequency. The measuring sequences tend toward increasing adhesion force with increasing contact force. Variations in the surface roughness of

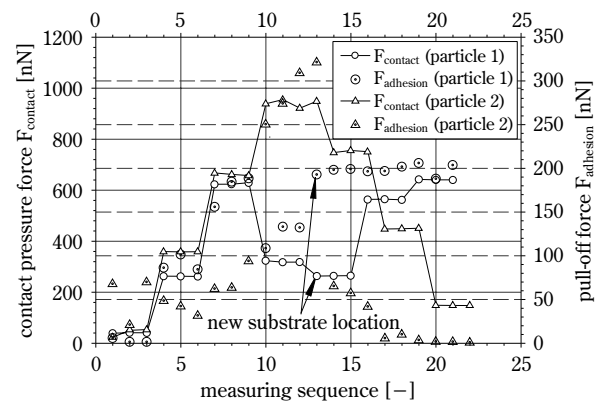


Fig. 10 Pull-off force for two tin particles on electropolished stainless steel substrates under variation of the contact force measured with the colloidal probe technique (particle 2 measured at 2 different substrate locations; particle 4 measured at the same location).

particle and substrate dependent on the substrate location influence the intensity of this effect and cause variations in the measured pull-off force for equal contact forces. Variations might also be attributed to impurities remaining on the adhesion partners after the cleaning procedure described in Section 3. In order to match the practical use of the surfaces, no further cleaning procedures were applied. After reducing the applied contact force, the measured pull-off force also decreased, indicating no significant plastic deformation of the micro-asperities.

5.2 Tin particles on ground stainless steel substrates

Figure 11 presents the pull-off forces for tin spheres on a ground stainless steel substrate. Again, the results of the vibration method and the colloidal probe technique (MAK, TV München) show relatively good agreement. In contrast to the comparatively smooth electropolished substrate, both measuring techniques show stronger variations. These fluctuations are primarily caused by large variations of the surface roughness of the ground substrate dependent on the location (**Fig. 7**). Compared to the electropolished substrate, adhesion force intensification caused by contact forces of the vibration method as explained in Section 5.1 can be observed on a smaller scale, which might be attributed to the higher surface roughness of the substrate. Since adhesion force intensification is not considered in the approach represented by Eq. (6) which relies on the rms roughness of particle and substrate rms_{12} only, the measured pull-off forces

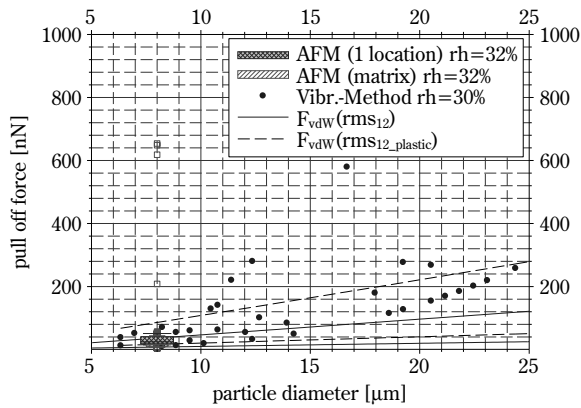


Fig. 11 Pull-off force for tin spheres on ground stainless steel substrates and predicted upper and lower limit of van der Waals adhesion using Eq. (6) with $rms_{12_upper}=0,7$ nm and $rms_{12_lower}=1,9$ nm of Eq. (8) and $rms_{12_plastic}$ of Eq. (9).

are underestimated. Another reason might be seen in the existence of a microscopic roughness scale on the ground substrate superimposed on the macroscopic roughness scale as described in Section 3.1, since the “non-contact” force between the macroscopic asperity and the surface is neglected. The use of an approach which accounts for this additional interaction [9] might improve the approximation. The approximation of the results with Eq. (6) can be improved considering possible micro-asperity plastic flattening with the modified rms value $rms_{12_plastic}$ of Eq. (9).

Successive pull-off force measurements for two tin particles on a ground stainless steel substrate under variation of the contact force measured with the colloidal probe technique (MPI for Polymer Research, Mainz, Germany) are presented in **Figure 12**.

Compared with the measuring sequences on the electropolished substrate (**Fig. 10**), adhesion force intensification caused by increasing contact forces can be observed on a much smaller scale. This tendency is in agreement with our measuring results with the vibration method. Again, variations in particle and substrate surface roughness dependent on the substrate location have a great influence on the intensity of this effect.

5.3 Dependency off the pull-off force on the contact time

As already mentioned in Section 2.2, the differences in the contact time between particle and substrate before particle detachment might lead to diverging measuring results for the same particle-substrate system caused by visco-elastic effects [10, 21]. For that

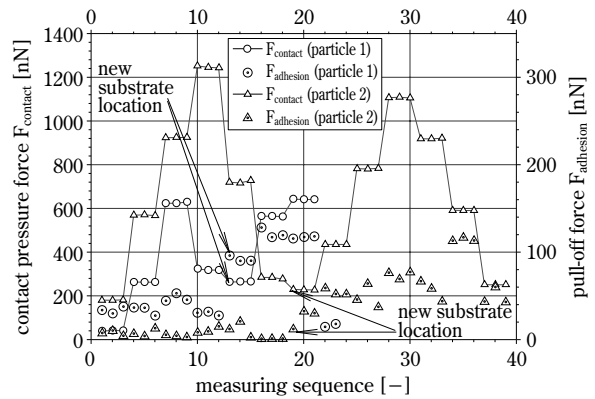


Fig. 12 Pull-off force for two tin particles on ground stainless steel substrates under variation of the contact force measured with the colloidal probe technique.

reason, the pull-off force was measured with the colloidal probe technique (MPI for Polymer Research, Mainz) at contact times of 1 s (1 Hz measuring frequency) and 30 s under a given contact pressure force. **Figure 13** shows the results of pull-off force measurements for tin particles on ground and electropolished stainless steel substrates at various substrate locations under variation of contact time and contact force. Within this time scale, no significant adhesion force intensification caused by increasing contact time at several contact forces was observed.

5.4 Glass particles on silicon wafer substrate

The pull-off force for glass particles on a silicon

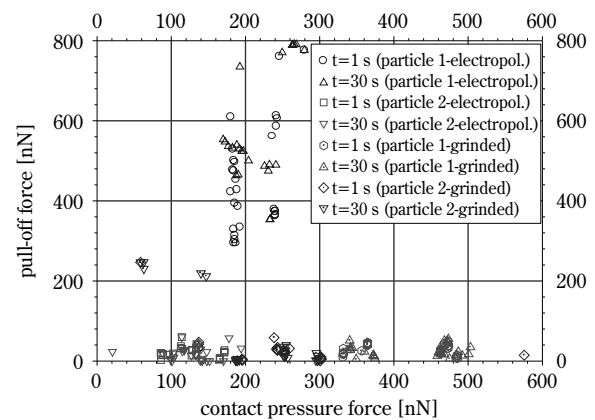


Fig. 13 Pull-off force for two tin particles on ground and electropolished stainless steel substrates at various substrate locations under variation of contact time and contact force measured with the colloidal probe technique.

wafer substrate measured by the vibration method and the colloidal probe technique (MAK, TV München) are shown in **Figure 14**. For small particle sizes, both methods show relatively good agreement. With increasing particle size, the vibration method exercises higher pull-off forces than the colloidal probe technique. Possible explanations for this effect were already described in Section 5.1. Analogous to the results for tin particles on the electropolished substrate, the comparatively smooth substrate seems to increase the effect of adhesion force intensification. The higher hardness and Young's Modulus (**Table 1**) of the glass particles in comparison with the tin particles reduce this effect. For small particle sizes, the results of the vibration method are generally within the range of the Rabinovich approach of Eq. (6). With increasing particle diameter and contact forces, the pull-off forces measured with the vibration method exceed the theoretical values for the unstressed system. With the modified rms roughness of Eq. (9), the adhesion force intensification observed with the vibration method can be explained – to some extent – by plastic flattening.

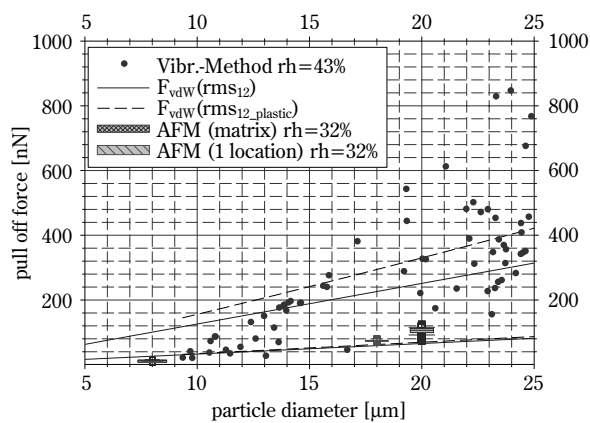


Fig. 14 Pull-off force for glass spheres on silicon wafer substrates and predicted upper and lower limit of van der Waals adhesion using Eq. (6) with $rms_{12_upper}=0,38$ nm and $rms_{12_lower}=0,97$ nm of Eq.(8) and $rms_{12_plastic}$ of Eq. (9).

6 Conclusions

Pull-off forces were measured using the vibration method and the colloidal probe technique. Both methods show relatively good agreement for small particle sizes. Alternating contact forces of the vibration method can cause an increase in the adhesion force

through flattening of micro-asperities. This effect was observed on a larger scale for the substrates with a comparatively smaller rms roughness and also found to be dependent on the mechanical properties of particle and substrate. Pull-off force measurements with the colloidal probe technique on the same adhesion systems with special attention to the influence of contact force also tended toward increasing adhesion force with increasing contact forces, exposing no significant indication of micro-asperity plastic flattening. Conforming with the results of the vibration method, the adhesion force intensification caused by increasing contact force was observed on a much smaller scale for the ground metal substrate with higher rms roughness values. At several contact forces, no significant adhesion force intensification caused by increasing contact time of 30 s was observed. Variations of the measuring results which were observed with both measuring techniques are predominantly caused by variations of the surface roughness, which in turn depend on the particle and substrate location. For small particle sizes, the results of both methods are generally within the range defined by the Rabinovich approach, using the 90% and 10% percentile of particle and substrate rms roughness as a lower and upper limit of the predicted van der Waals adhesion force. With increasing particle size, the adhesion forces measured with the vibration method show a stronger increase than predicted. The possible effect of micro-asperity plastic flattening of the particle was considered through the modified effective roughness in the Rabinovich approach, resulting in a better approximation of the results. Especially for higher particle diameters and contact forces, the adhesion force intensification observed with the vibration method cannot be explained by plastic flattening only. Further reasons for this effect might be seen in an increase of the points of contact caused by rearrangements or high-frequency alternating stresses which might prevent a relaxation of the elastically flattened asperity, thus causing visco-elastic behaviour.

7 Acknowledgements

We express our gratitude to the Deutsche Forschungsgemeinschaft, which supported this work within the Research Programme Ri 776/9-3. We are furthermore grateful to Dr. Michael Kappl and Dr. Lars Oliver Heim (MPI for Polymer Research, Mainz, Germany) and Dr. Bernhard Weigl (Lehrstuhl für Maschinen- und Apparatekunde, TU München, Germany) for performing force measurements with the

colloidal probe technique.

Nomenclature

a	: acceleration	[m/s ²]
A	: Hamaker constant	[J]
AFM	: atomic force microscope	[–]
d _p	: particle diameter	[μm]
E	: Young's Modulus	[GPa]
f	: frequency	[Hz]
F _{ad}	: adhesion force	[nN]
F _{contact}	: inertia force=contact force for $\pi < \omega t < 2\pi$	[nN]
F _{detach}	: inertia force=detachment force for $0 < \omega t < \pi$	[nN]
F _{grav}	: gravitational force	[nN]
F _{inertia}	: inertia force	[nN]
H	: hardness	[GPa]
h	: flattening	[nm]
K _{elast}	: $K_{elast} = \frac{4}{3} \cdot \left(\frac{1-v_p^2}{E_p} + \frac{1-v_{sub}^2}{E_{sub}} \right)^{-1}$	[Pa]
LSV	: laser scanning vibrometer	[–]
m _p	: particle mass	[kg]
Re _{channel}	: Reynolds number of the flow channel	[–]
rms	: root mean square	[nm]
SEM	: scanning electron microscope	[–]
T	: temperature	[°C]
t	: time	[s]
U _{ex}	: excitation voltage of the actuator	[V]
v	: Poisson's ratio	[–]
ρ	: density	[gcm ⁻³]
ω	: angular frequency	[Hz]

References

- 1) W.A. Ducker, T.J. Senden, R.M. Pashley: Direct measurement of colloidal forces using an atomic force microscope, *Nature* 353 (1991), 239-241.
- 2) H.-J. Butt: Measuring electrostatic, van der Waals, and hydration forces in electrolyte solutions with an atomic force microscope, *Biophys. J.* 60 (1991), 1438-1444.
- 3) G. Binning, C.F. Quate, C. Gerber: Atomic force microscope, *Phys. Rev. Lett.* 56 (1986), 930-933.
- 4) R.I. Larsen: The adhesion and removal of particles attached to air filter surfaces, *Am. Indust. Hyg. J.* 19 (1958), 265-270.
- 5) H. Krupp: Particle adhesion. Theory and experiment, *Adv. Coll. Interf. Sci.*, 1 (1967), 111-239.
- 6) B.V. Deryaguin, A.D. Zimon: Adhesion of Powder Particles to Plane surfaces, *Kolloidnyi Zhurnal*, Vol. 23, No. 5 (1961), 544-552.
- 7) K. Hein, T. Hucke, M. Stintz, S. Ripperger: Analysis of Adhesion Forces between Particles and Wall based on the Vibration Method, *Part. Part. Syst. Charact.* 19 (2002), 269-276.
- 8) D. Leighon, A. Avcrivos: The lift on a small sphere touching a plane in the presence of a simple shear flow, *J. Appl. Phys. (ZAMP)* 36 (1985), 174-178.
- 9) M.E. O'Neill: A sphere in contact with a plane wall in a slow linear shear flow, *Chem. Eng. Sci.* 23 (1968), 1293-1298.
- 10) H. Rumpf, K. Sommer, K. Steier: Mechanismen der Haftkraftverstärkung bei der Partikelhaftung durch plastisches Verformen, Sintern und viskoelastisches Fließen, *Chem.-Ing.-Techn.*, 48 (1976), 300-307.
- 11) M. Kappl, H. Butt: The Colloidal Probe Technique and its Application to Adhesion Force Measurements, *Part. Part. Syst. Charact.* 19 (2002), 129-143.
- 12) Y.I. Rabinovich, M. Moudgil et al.: Adhesion between nanoscale rough surfaces, *J. Colloid Interface Sci.*, 232 (2000), 10-24 .
- 13) H. Rumpf: Die Wissenschaft des Agglomerierens. *Chem.-Ing.-Tech.* 46 (1974), 1-11.
- 14) J.D. Kiely, D.A. Bonnell: Quantification of topographic structure by scanning probe microscopy, *J. Vac. Sci. Technol. B*15 (4), 1483-1493 (1997).
- 15) H.C. Hamaker: *Physica* 4 (1937), 1058.
- 16) B.V. Deryaguin, V.M. Muller, Y.P. Toporov: Effect of Contact Deformations on the Adhesion of Particles, *J. Coll. Int. Sci.* 53 (2), 314 (1975).
- 17) K.L. Johnson, K. Kendall, A.D. Roberts: Surface energy and the contact of elastic solids, *Proc. R. Soc. London A* 324, 301 (1971).
- 18) Y.I. Rabinovich, J.J. Adler, M.S. Esayanur, A. Ata, R.K. Singh, B.M. Moudgil: Capillary forces between surfaces with nanoscale roughness, *Adv. Coll. Int. Sci.* 96 (2002), 213-230.
- 19) K. Cooper et. al: Simulation of Adhesion of Particles to Surfaces, *J. Coll. Int. Sci.* 234 (2001), 284-292.
- 20) W. Peukert, C. Mehler, M. Götzinger: Application of Adsorption and Adhesion Measurements for Particle Surface Characterization, *Part. Part. Syst. Charact.* 18 (2001), 229-234.
- 21) Wei Hsuin Yang: The contact problem for viscoelastic bodies, *J. Appl. Mech.*, *Trans. ASME* 33 (1966), 395-401.
- 22) L. Kogut, I. Etsion: Adhesion in elastic-plastic spherical microcontact, *J. Coll. Int. Sci.* 261 (2003), 372-378.
- 23) D. Maugis, H.M. Pollock: Surface Force, Deformation and Adherence at metal microcontacts, *Acta metal.* 32 (1984), 1323-1334.
- 24) H.J. Hertz: *Reine Angewandte Math.* 92, 156 (1881).
- 25) H. Zhou et. al: Tailoring Particle-Substrate Adhesion, Oral Presentation 25.5 at the International Congress for Particle Technology 2004, Nuremberg.
- 26) G. Ziskind: Particle Behaviour on Surfaces subjected to external excitations, *J. Aerosol Sci.*, Vol. 31, No. 6 (2000), 703-719.

Author's short biography



Siegfried Ripperger

Born 1950 in Bous/Saarland. Studied mechanical and chemical engineering at the University of Applied Science at Saarbrücken and at the University of Kaiserslautern. Dr.-Ing. 1982 at Kaiserslautern with a thesis on the adsorption of organic compounds and water out of air at activated charcoal. 1983-1989 with Akzo AG at Wuppertal. Since 1987 head of the development and application department for technical membranes.

1989-1993 professor for chemical engineering and environmental technology at the University of Applied Science at Fulda. Since 1990 dean of the Faculty of Food Technology. 1993-2004 professor at the Technical University of Dresden, chair for mechanical process engineering. Since 1997 director of the Institute of Chemical Engineering and Environmental Technology at Dresden. Since April 2004 professor at the Technical University of Kaiserslautern, chair for mechanical process engineering.

More than 140 publications. Main research activities: the separation of fine particles out of gases and liquids, membrane separation, in-line particle measurement, characterization of dispersed systems and product development.



Konrad Hein

K. Hein graduated in process engineering from the Technical University of Dresden, Germany, in 1999. After carrying out his diploma thesis on the detection of small amounts of coarse particles in highly concentrated suspensions using a laser backscattering technique, he started working as a research assistant on a Ph.D. project in Prof. Ripperger's process engineering group at the Technical University of Dresden. His project deals with particle adhesion phenomena on vibrating surfaces in air.

Methodology and Analysis of the Effect of Liquid Infiltration on the Hydrodynamic Dispersion of Silica Aerogel Agglomerates[†]

Nicholas S. Hudak^{1*}, Ica Manas-Zloczower¹
and Donald L. Feke^{2**}

¹Department of Macromolecular Science and
Engineering

²Department of Chemical Engineering
Case Western Reserve University

Abstract

The processing characteristics of agglomerates of silica aerogel particles (surface treated to possess either hydrophilic or hydrophobic nature) have been examined. Although these agglomerates were purported to be highly uniform in terms of internal structure, fluid infiltration studies performed via direct visualization revealed significant heterogeneities. Dispersion studies performed under both steady and time-varying flow conditions, revealed additional non-uniformities among the population of agglomerates. Despite these difficulties, discernable trends linked to the duration of time the agglomerates were allowed to soak in the processing medium prior to the application of the shear flows were discovered. Additional experiments, in which the agglomerates were presoaked with a different, low viscosity fluid prior to shearing, revealed that dispersion could be promoted through this processing strategy. The experimental approaches and analyses presented in this study should be of interest to particle technologists faced with understanding and characterizing dispersion phenomena when the agglomerates being dispersed exhibit significant variability in properties.

Key words: Silica aerogels, agglomerates, dispersion, infiltration, wetting behavior

INTRODUCTION

Dispersive mixing of particulate clusters into liquids is an important step in a variety of materials and chemical processing applications. In dispersive mixing, mechanical forces, typically applied through hydrodynamic shear, are used to break the clusters into smaller size units or even down to the individual particle size. An understanding of the fundamental physical and chemical factors that govern hydrodynamic dispersion can lead to process optimization and ultimately better performance of the materials in which the particles are dispersed. It is common, however, that agglomerates encountered in practice exhibit

a range of physical characteristics, even though they may be prepared under very controlled manufacturing conditions. Such variability makes determination and prediction of processing behavior difficult. In this paper, we describe characterization techniques that can provide information on the modes and kinetics of hydrodynamic dispersion of particle clusters, and how these dispersion characteristics are linked to processing history, even when the agglomerates being studied exhibit non-uniform properties.

In experimental studies of the dispersion of agglomerates of carbon black [1], two distinct breakage mechanisms were observed. One was denoted as “rupture” in which an abrupt fragmentation of the cluster into a small number of relatively large pieces takes place. The second breakup mode, termed “erosion,” is characterized by the continuous detachment of small fragments from the outer surface of the agglomerate. The erosion process typically initiates at a lower applied shear stress than does rupture.

^{1,2} Cleveland, OH 44106 USA

* Current Address: Department of Chemical Engineering,
Columbia University, New York, NY

** Corresponding author; email donald.feke@case.edu

[†] Accepted: September 21, 2004

Bolen and Colwell [2] first proposed that dispersion occurs whenever hydrodynamic drag forces acting on the surface of the particle cluster induce internal stresses exceeding the cohesivity of the cluster. Therefore, the dispersion properties are affected by the cluster cohesivity and the geometry and intensity of the flow field.

Cluster cohesivity is related to both the strength of the interparticle forces between its constituent particles and the structural details of the particle packing within the cluster [3]. Since particle clusters are porous, capillary-pressure driven infiltration of liquid into the cluster can occur upon immersion of the cluster into the processing media. This infiltration may cause some rearrangement of the packing structure as well as alter the cohesive forces acting within the cluster. Additionally, the presence of fluid within the cluster can modify the manner in which hydrodynamic stress is transmitted from the external fluid to the cluster. Thus, knowledge of the extent of infiltration of the fluid medium, which is directly linked to the processing history, is an important factor in understanding the outcome of dispersion attempts.

The geometry and dynamics of the applied flow field is also expected to influence the dispersion kinetics of clusters. Many of the previous experimental studies on dispersion were performed under steady shear flow conditions. Dispersion in non-steady flows is more representative of the complex shear history experience by particle clusters in practical processing equipment [4].

In this study, we examine the synergies between fluid infiltration and flow conditions as they influence the dispersion of particle clusters. Specifically, we report on experiments to analyze the dispersion behavior of clusters of silica aerogels sheared within polydimethyl siloxane (PDMS) fluids. These particles were selected to represent a typical, non-ideal situation encountered in practice, namely one in which agglomerates with non-uniform structure and significant agglomerate-to-agglomerate variability are used. Still, we are able to discern trends in the dispersion results that can be interpreted in the context of fundamental chemical and physical concepts.

Different surface treatments applied to the aerogel particles, which modify the magnitude of the capillary pressure driving infiltration, enable some degree of control over the extent of fluid infiltration. In addition to using steady shear for dispersion, we report on experiments performed under oscillatory shear-flow conditions. Both the mode of dispersion and dispersion kinetics are reported, and these results can be

linked to the extent of infiltration of the processing fluid.

EXPERIMENTAL

Materials

Two types of non-commercial silica aerogel particles, provided in the form of clusters by the Cabot Corporation, were used in this study. These clusters, carefully prepared using standard forming techniques, were nominally of high uniformity, both in terms of packing structure within an individual agglomerate, and in terms of consistency between different agglomerates. One type (grade P346) is reported by the manufacturer to be treated (in an unspecified manner) to make the agglomerate hydrophobic while the other (grade P597) was treated to result in a hydrophilic surface. Each cluster ranged from 1 to 2 mm in diameter and was composed of individual particles in the 10–100 μm range. The BET surface area was ~ 700 m^2/g , which indicates a high degree of fine structure within these aerogels. Information on the composition and structure of the clusters is not available, and clusters were tested as received.

PDMS fluids of varying viscosities were used in the infiltration and shearing experiments. In the steady shear experiments, both 10 and 30 Pa-s PDMS were found to be effective in inducing dispersion. For the range of shear rates examined in the oscillatory shear experiments, the use of 60, 100, and 600 Pa-s PDMS fluids were necessary to cause dispersion. Before being used in the shearing experiments, fluids were placed under vacuum to aid the removal of entrapped air bubbles. In the range of shear rates employed in the experiments, these fluids exhibit Newtonian rheological behavior.

Dispersion Experiments in Steady Shear Flow

Figure 1 shows a schematic diagram of the cone-and-plate shearing device used for the steady shear experiments. The set-up procedure involved removing the transparent plate from the instrument and filling it with PDMS. A single agglomerate was submerged into the polymer and positioned within the plate. The plate was raised up under the cone, and the fluid slowly surrounded the cone. The motor was set to a particular speed N (in rotations per minute) and turned on to start the application of shear. The time between submersion of the agglomerate and application of shear is called the presoaking time; the polymer infiltrated into the agglomerate during this time.

The steady shear rate $\dot{\gamma}_{\text{steady}}$ that the agglomerate

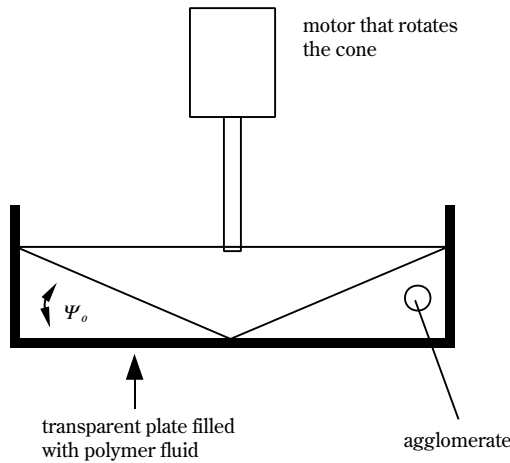


Fig. 1 Schematic of the cone-and-plate device used for the steady-shear experiments. Cone angle $\Psi_o=4^\circ$; maximum gap between cone and plate ~ 4 mm

experiences is related to the angular velocity of the cone Ω and the cone angle Ψ_o according to the following equation:

$$\dot{\gamma}_{steady} = \frac{\Omega}{\Psi_o} \quad (1)$$

Since the fluid exhibits Newtonian behavior in the range of shear rates used here, the nominal shear stress can be computed from the shear rate and viscosity:

$$\tau_{steady} = \mu \dot{\gamma}_{steady} \quad (2)$$

The results of dispersion experiments were recorded with a video camera connected to a computer. The agglomerate moves with the flow and passes through the focal point of the camera once per orbit. Scion image software was used to measure the average radius of the agglomerate as a function of shearing time.

Dispersion Experiments in a Non-Steady Shear Flow

Dispersion experiments were also performed in an oscillatory shear flow device (OSD) illustrated in **Figure 2**. In preparation for an experiment, the transparent lower container was removed from the instrument and filled with PDMS. Then the agglomerate was submerged into the polymer and positioned laterally. The container was raised up under the oscillating plate, and the fluid surrounded the plate. The motor was set to a particular speed N (in rotations per minute) and

turned on to start the application of shear. The transmission mechanism results in the rotational motion of the motor being converted to an oscillatory motion of the moving plate. The maximum shear rate $\dot{\gamma}_o$ over one cycle of oscillation is related to the position of the transmission linkage on the motor (A), motor rotation rate N , and gap between plates G according to the following equation:

$$\dot{\gamma}_o = \frac{2\pi AN}{G} \quad (3)$$

From this equation the mean shear stress over a cycle $\dot{\gamma}_{mean}$ can be calculated:

$$\dot{\gamma}_{mean} = \frac{2}{\pi} \dot{\gamma}_o \quad (4)$$

For the experiments reported here, we used $A=10$ mm, $G=4.83$ mm, and N ranging from 100 to 1500 s^{-1} .

As in the steady shear experiments, the process of dispersion was viewed directly through the transparent plate and recorded with a VCR. Using the OSD, the entire dispersion process can be viewed continuously, unlike in the cone-and-plate device where the

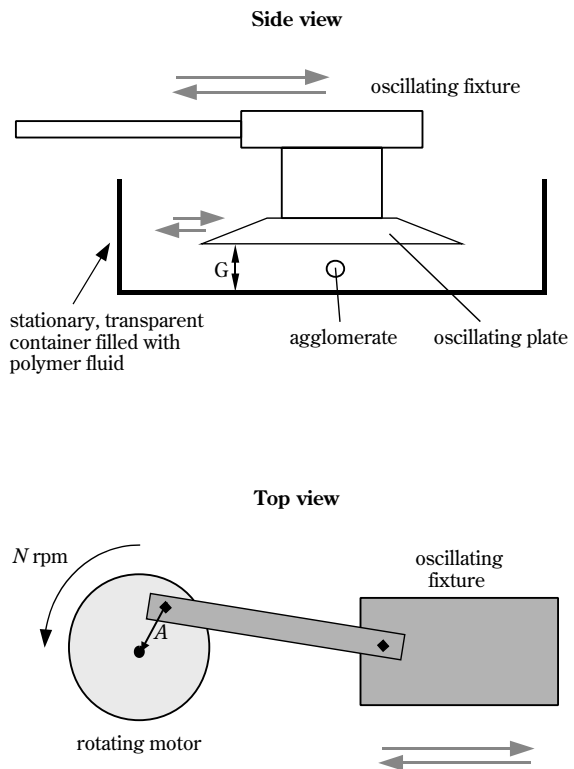


Fig. 2 Schematic of the oscillatory shear device used for the unsteady shear experiments. $G=4.83$ mm and $A=10$ mm.

agglomerate only enters the field of view of the camera once per rotation.

Preparation Procedures for the Clusters of Hydrophilic Silica

Humidity present in the ambient air could alter the hydrophilic agglomerates and affect their dispersion behavior. Therefore, precautions were taken to ensure that these agglomerates were not exposed to air before they were used in infiltration and shearing experiments. The container of silica and a dish of PDMS were placed in a glove bag flushed with dry nitrogen. In this environment, the container of agglomerates was opened, and a single cluster was selected and submerged in the PDMS. Subsequently, this dish was removed from the glove bag and placed in the cone-and-plate (steady shear) device or oscillatory device.

Infiltration Experiments

As mentioned, infiltration of the polymeric fluid into the agglomerate has a large effect on its dispersion properties. Therefore, a study of infiltration can help explain dispersion properties. Furthermore, an infiltration study can be used to probe agglomerate structure since the most porous regions of an agglomerate tend to become infiltrated first.

Since the silica agglomerates and the PDMS fluids have nearly identical indices of refraction, direct visualization of infiltration is possible. A transparent container was filled with 10 Pa-s PDMS. The agglomerate was removed from the sample container and submerged in the fluid. A video camera was used to view and record the agglomerate through the wall of the container. The camera and VCR were attached to a computer, where periodic images of the agglomerate were captured and analyzed. The infiltrated portion of the agglomerate was assumed to be that which became transparent, while the dry portions remained opaque. The extent of infiltration was quantified by measuring the apparent area of the infiltrated region using the Scion Image software.

RESULTS AND DISCUSSION

Infiltration Study

Hydrophobic Silica Agglomerates

The extent of infiltration as a function of time is shown in **Figure 3a** for a representative set of eight different clusters. The extent of infiltration is reported as the fraction of the cross-sectional area of the cluster apparently occupied by infiltrated fluid. As shown, there is a large amount of scatter among the various

agglomerates, even though they had ostensibly identical structures. The time for complete infiltration ranged from 15 min to approximately 1 hr. No strong correlation between cluster diameter and infiltration rate was observed. **Figure 3b** shows images of some

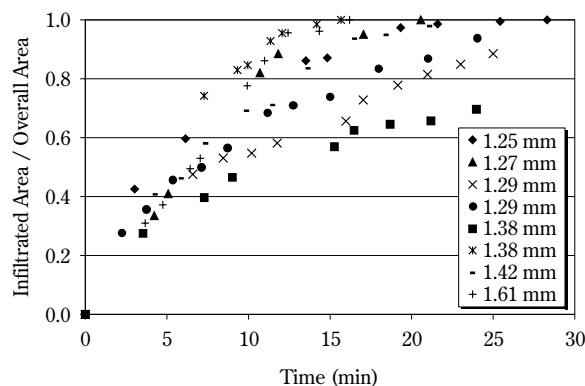


Fig. 3a Extent of infiltration as a function of time for the hydrophobic agglomerates. The diameter of each agglomerate is indicated in the legend.

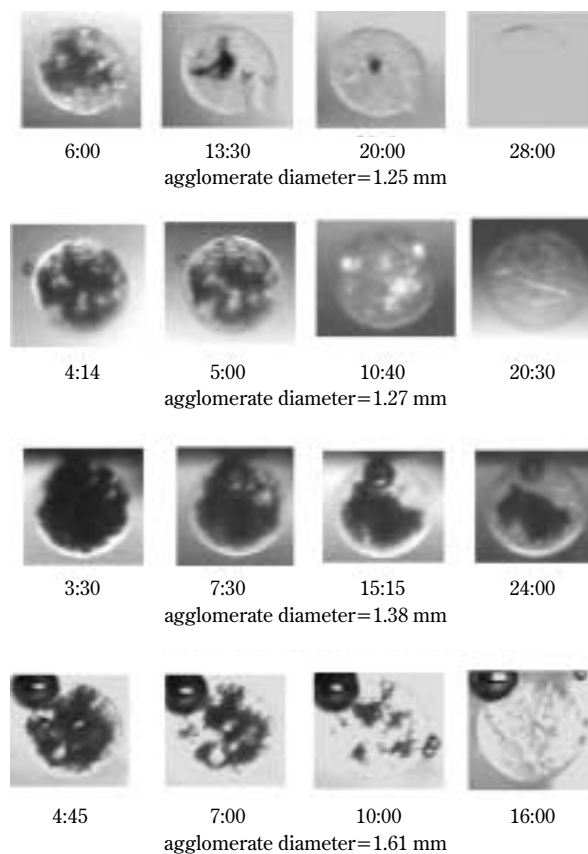


Fig. 3b Examples of the hydrophobic agglomerates as they become infiltrated. The time in seconds and minutes is indicated.

agglomerates as they were being infiltrated. In most cases, the infiltration did not occur uniformly from the outside surface to the inner core. For many agglomerates, fluid was observed to reach the center of the agglomerate long before the periphery was fully infiltrated. The infiltration patterns suggest a large degree of non-homogeneity in the structure of these clusters.

Hydrophilic Silica Agglomerates

The extent of infiltration as a function of time is shown in **Figure 4a** for representative sample of seven hydrophilic clusters. As with the hydrophobic agglomerates, there is a large amount of scatter among the samples. The total infiltration time ranged from 3 hr to several days. **Figure 4b** shows images of some agglomerates as they were being infiltrated. Unlike the hydrophobic agglomerates, these samples tended to infiltrate uniformly from the outer surface inward. This suggests a more homogeneous structure for the hydrophilic agglomerates by comparison with the hydrophobic ones.

Despite the large scatter in the observed infiltration behavior, some trends can still be discerned. For example, **Figure 5** shows a comparison of the median and extreme infiltration rates observed for the hydrophobic and hydrophilic agglomerates. In all cases, the infiltration of PDMS into the hydrophilic agglomerates was much slower than that of hydrophobic agglomerates. This can be attributed to a combination of the higher packing density in the hydrophilic agglomerates which was revealed in the infiltration studies, plus the expected strong interaction expected between the hydrophobic agglomerates and the PDMS.

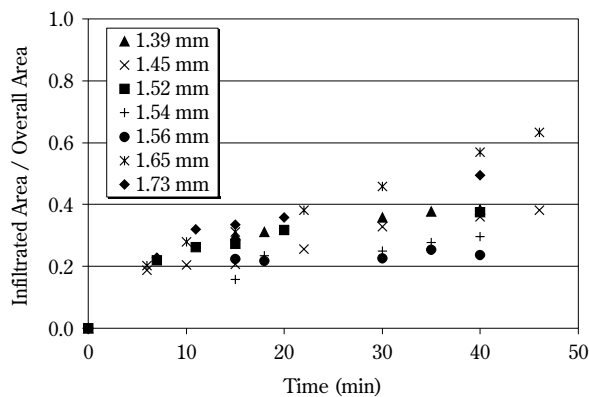


Fig. 4a Extent of infiltration as a function of time for the hydrophilic agglomerates. The diameter d of each agglomerate is indicated in the legend.

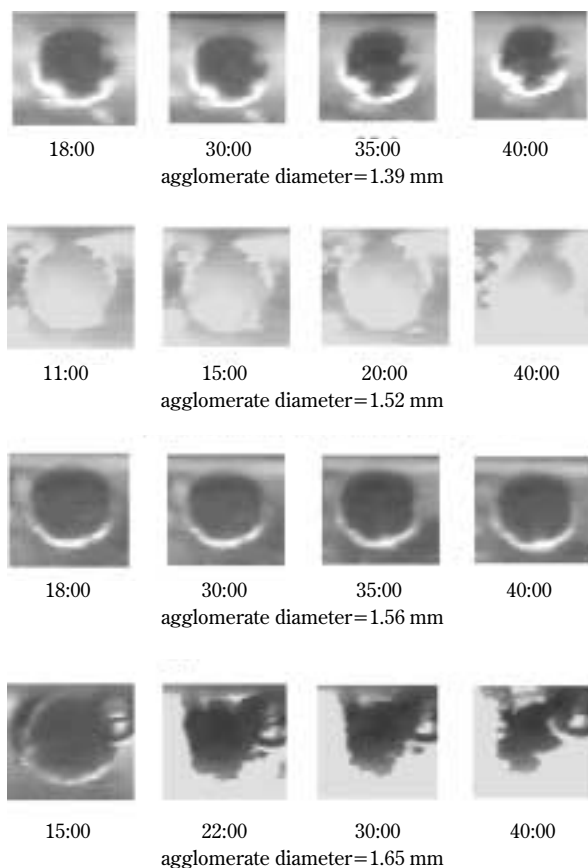


Fig. 4b View of the hydrophilic agglomerates as they become infiltrated. The time in seconds and minutes is indicated.

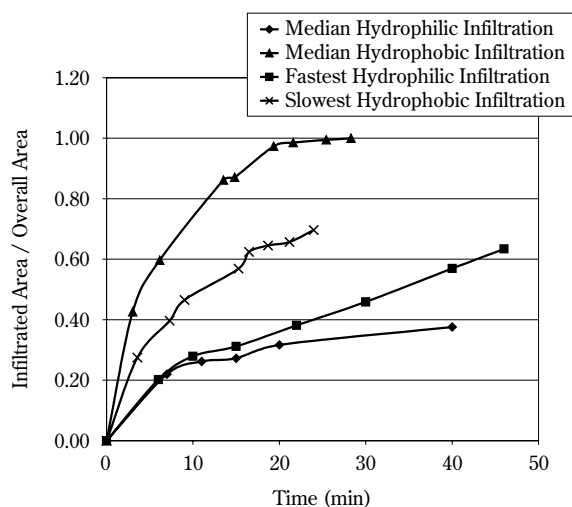


Fig. 5 Comparison of observed infiltration rates among the two types of agglomerates studied.

Dispersion of Hydrophobic Silica Agglomerates

Steady Shear

Table 1 presents a statistical summary for the results of steady shear experiments for the dispersion of the hydrophobic aerogels. The agglomerates were allowed to presoak for various periods of time before shear was applied, and shear stresses necessary to initiate a dispersion event were observed. Shown are the relative frequencies of rupture, erosion, and “no dispersion” events observed at the various applied shear strengths. Although shear conditions were carefully controlled, the agglomerates show a range of dispersion behavior. Generally, rupture was more likely to occur at higher shear stresses, but there was no clearly identifiable threshold value above which rupture would occur. Extended infiltration tended to suppress dispersion, most likely due to reinforcement of powder through the formation of liquid bridges.

The erosion mechanism was rarely observed for the hydrophobic agglomerates. For those cases in which erosion did occur, a large variation in erosion rates was observed. Furthermore, there was no apparent correlation between the presoaking time and the observed dispersion kinetics.

Oscillatory Shear

Table 2 provides a statistical summary of the results of the oscillatory shear experiments for hydrophobic silica. Erosion was not observed in any case. Rupture was less likely to occur after a long pre-soaking time, suggesting that extended infiltration enhances agglomerate cohesivity. For experiments with a 1.5-minute presoak, 500 Pa appeared to be the threshold stress above which dispersion will occur. For longer infiltration times, no definite trends were observed.

Table 1 Summary of the results of steady shear experiments with hydrophobic agglomerates. The relative frequency of the three possible dispersion outcomes are shown as a function of presoak time. Also shown are the ranges of shear stress used to achieve the dispersion events.

Presoak Time	No Dispersion	Erosion	Rupture
3–5 min	6 agglomerates	3 agglomerates	4 agglomerates
	100–600 Pa	600 Pa	450–600 Pa
10 min	2 agglomerates	2 agglomerates	3 agglomerates
	600, 1000 Pa	1100 Pa	1000–1100 Pa
15 min	9 agglomerates	2 agglomerates	4 agglomerates
	450–1200 Pa	800 Pa	450–800 Pa

Table 2 Summary of the results of oscillatory shear experiments with hydrophobic agglomerates. The erosion mode of dispersion was never observed.

Presoak Time	No Dispersion	Rupture
1.5 min	5 agglomerates	15 agglomerates
	≤ 500 Pa	≥ 500 Pa
2.0–2.5 min	5 agglomerates	18 agglomerates
	≤ 4300 Pa	≥ 415 Pa
3.0–6.0 min	5 agglomerates	11 agglomerates
	≤ 4400 Pa	≥ 1725 Pa

Dispersion of Hydrophilic Silica Agglomerates

Steady Shear

Thirteen experiments were carried out in the cone-and-plate device using the hydrophilic agglomerates. Rupture was observed only once, and erosion was never observed. Even at shear stresses as high as 4500 Pa, no dispersion occurred. In the case of the hydrophobic agglomerates, dispersion occurred at stresses between 450–600 Pa. This indicates that the hydrophilic agglomerates are more cohesive than the hydrophobic agglomerates in PDMS fluids.

Because of experimental limitations, the presoaking time for these experiments was around four minutes. However, the extent of infiltration of 30,000-cSt PDMS in four minutes is not significant and is most likely not the reason for the resistance to erosion.

Oscillatory Shear

Table 3 summarizes the results of the oscillatory shear experiments for the hydrophilic aerogels. Erosion was not observed in any case. Rupture was more likely to occur after shorter presoaking times, again suggesting that infiltration impedes dispersion by

Table 3 Summary of the results of oscillatory shear experiments with hydrophilic agglomerates. The erosion mode of dispersion was never observed.

Presoak Time	No Dispersion	Rupture
1.5–1.75 min	4 agglomerates	2 agglomerates
	≤ 3500 Pa	≥ 2600 Pa
2.0–2.5 min	9 agglomerates	5 agglomerates
	≤ 3800 Pa	≥ 2500 Pa
3.0–6.0 min	11 agglomerates	4 agglomerates
	≤ 7600 Pa	3150 Pa

increasing cohesivity. Stresses of 2500 Pa or higher were required for rupture to occur, whereas only 500 to 2000 Pa was required in the case of the hydrophobic samples.

Dispersion of Fully Infiltrated Agglomerates

As is sometimes done in practice, low viscosity fluids can be used to impregnate agglomerates prior to dispersing them in high viscosity media. Presumably, the soaking of the agglomerates with the low viscosity fluids can result in a lower overall agglomerate cohesivity or provide additional compatibility with the intended dispersion media. To study the effect of saturating agglomerates with liquids on its dispersion behavior, we carried out additional experiments in the oscillatory shear device. Relatively low viscosity fluids were used to presoak the agglomerates prior to the application of shear. Hydrophobic agglomerates were soaked in hexane for 15 s (enough for complete infiltration) and then tested at different stress levels in PDMS. Hydrophilic agglomerates were soaked in water or glycerin for 5 min (enough for complete infiltration) and then tested in the same way. After soaking, the excess water was removed from around the hydrophilic agglomerates in one of two different ways: (1) by placing the agglomerate on a towel; or (2) by carefully removing the water with an eyedropper. More water remained in the hydrophilic agglomerates when the excess was removed with an eyedropper instead of a towel.

Table 4 displays a summary of the results of these experiments. Dispersion of soaked agglomerates contrast the previous results reported. For both the hydrophobic and hydrophilic agglomerates, complete

fluid saturation seems to promote dispersion at lower shear stresses. These results are consistent with expectations.

CONCLUSIONS

Experimental observations in the infiltration and dispersion studies indicate a large degree of non-homogeneity for the agglomerates as received from the manufacturer. However, despite of this complication, useful observations regarding general trends of infiltration/dispersion behavior for these agglomerates could be made.

In the case of hydrophobic agglomerates, the infiltration patterns suggest a very non-uniform structure for the agglomerates. Such non-uniformity may be responsible for initiating rupture at the locus of weak, less dense spots in the cluster. Partial infiltration of these agglomerates seemed to suppress dispersion, most likely due to reinforcement of powder through the formation of liquid bridges.

In the case of hydrophilic agglomerates, infiltration studies suggest more dense and homogeneous agglomerates, which resist dispersion to a larger extent than their hydrophobic counterparts. Also, partial infiltration of these agglomerates seems to impede dispersion by increasing cluster cohesivity.

In contrast with the results obtained with partially infiltrated agglomerates, complete saturation of the agglomerates using low viscosity fluids that interact favorably with the constituent solids seems to reduce overall agglomerate cohesivity, thereby enhancing dispersion.

The experimental approaches outlined in this pa-

Table 4 Summary of dispersion experiments on agglomerates saturated with a low viscosity fluid prior to shearing. The two entries labeled “dry” represent control experiments in which no low-viscosity fluid was present within the agglomerate.

Type of Agglomerates	Procedure	Lowest stress at which rupture occurred (Pa)	Highest stress at which no dispersion occurred (Pa)	Presoak time in PDMS prior to shear (min)	Number of tests run	Range of stresses tested (Pa)
Hydrophobic	dry	414	4306	1–3	55	331–16500
Hydrophobic	soaked in hexane for 15 s; excess hexane removed with eyedropper	15	773	1.5–2	35	1–911
Hydrophilic	dry	2526	5963	1–6	35	1077–22360
Hydrophilic	soaked in water for 5 min; excess water removed with towel	1408	3975	2	19	538–6874
Hydrophilic	soaked in water for 5 min; excess water removed with eyedropper	311	828	2	28	75–2551
Hydrophilic	soaked in glycerin for 5 min; excess glycerin removed with eyedropper	331	795	2	7	124–1284

per provide a means of characterizing the behavior of particle agglomerates, even though there may be experimental difficulties associated with non-uniform agglomerate structures.

ACKNOWLEDGEMENTS

The authors would like to acknowledge support of this work through the ACS-PRF grant 35561-AC9. The authors are also grateful to IFPRI (International Fine Particle Research Institute) for supporting the development of the OSD technique.

NOMENCLATURE

A	amplitude of oscillation	(m)
G	gap between parallel plates in the oscillating shear device	
N	rotation speed of the motor	(rotations/min)
Greek		
$\dot{\gamma}_o$	maximum shear rate over one cycle in the oscillating flow experiments	(s^{-1})
$\dot{\gamma}_{steady}$	shear rate in the steady-flow experiments	(s^{-1})
$\dot{\gamma}_{mean}$	mean shear rate over one cycle in the oscillating flow experiments	(s^{-1})
Ω	rotation rate of the cone	(s^{-1})
Ψ_o	cone angle	(radians)
μ	fluid viscosity	(Pa)

REFERENCES

- [1] Rwei, S. P., D. L. Feke, and I. Manas-Zloczower, *Polymer Engineering and Science* **30**(12), 701 (1990).
- [2] Bolen, W. R. and R. E. Colwell, *Soc. Plast. Eng. J.*, **14**, 24 (1958).
- [3] Yamada, H. I. Manas-Zloczower, and D.L. Feke, *Powder Technology*, **92**, 163-169 (1997).
- [4] Levesse, P., I. Manas-Zloczower and D. L. Feke, *Rubber Chemistry and Technology*, **75**(1), 119 (2002).

Author's short biography



Nicholas S. Hudak

Nicholas S. Hudak received his B.S. degree in Polymer Engineering and Science from Case Western Reserve University in 2002. He is currently a Ph.D. candidate in Chemical Engineering at Columbia University.



Ica Manas-Zloczower

Ica Manas-Zloczower is Professor of Macromolecular Science and Engineering at Case Western Reserve University. She received her D. Sc. in Chemical Engineering from the Technion-Israel Institute of Technology in 1983. Professor Manas-Zloczower's research interests are in the structure and micromechanics of fine particle clusters, interfacial engineering strategies for advanced materials processing and dispersive mixing mechanisms and modeling. Her research focuses also on non-linear dynamics in polymer processing equipment and entropic measures of mixing tailored for specific system property assessment. Professor Manas-Zloczower is the Editor-in-Chief for the Journal of Polymer Engineering and serves on the Book Advisory Board for Hanser publisher. She is also the International Representative for the Americas of the Polymer Processing Society.



Donald L. Feke

Donald L. Feke is Professor of Chemical Engineering at Case Western Reserve University. He received his Ph.D. in Chemical Engineering from Princeton University in 1981. Professor Feke's research interests are in colloidal phenomena; particle processing, transport phenomena and separation processes for particulate systems.

Aluminium Matrix Composites Reinforced with Si_3N_4 , AlN and ZrB_2 , Produced by Conventional Powder Metallurgy and Mechanical Alloying[†]

J.B. Fogagnolo^{1,2}, M.H. Robert¹,
F.Velasco², J.M. Torralba²

¹ Department of Materials Engineering,
Mechanical Engineering Faculty,
State University of Campinas, Brazil

² Materials Science and Engineering Dept.
Universidad Carlos III de Madrid, Spain

Abstract

The homogeneous distribution of the reinforcement phase is a prime requisite for a composite material to present its superior performance. Powder metallurgy can produce composite materials in the whole range of matrix reinforcement composition, without the segregation typical of the casting process, and mechanical alloying serves to optimise the particle mixing stage, enhancing the reinforcement distribution. This work investigates the use of mechanical alloying plus hot extrusion to obtain Al6061 matrix composites reinforced with Si_3N_4 , AlN and ZrB_2 , and compares the result with the same composite materials obtained by more conventional powder metallurgy techniques. The incorporation of the reinforcement does not suffice to produce a significant improvement of the mechanical properties of the conventional powder metallurgy composites. Mechanical alloying breaks the reinforcement particle clusters, eliminates most of the defects present in these particles, decreases their size and enhances their distribution, which together with the metallurgical phenomena that change the metallic matrix, such as work hardening and oxide and carbide dispersion, produces an increase of about 150% in the hardness of the powder, when compared with the hardness of the as-received, non-reinforced aluminium powder alloy; and of 100% in the hardness and ultimate tensile strength of the consolidated materials, when compared with material of same composition processed by conventional powder metallurgy.

Key words: Aluminium, Powder Metallurgy, Mechanical Alloying, Hot Extrusion

1. INTRODUCTION

In recent decades, new manufacturing processes have been developed to produce metal matrix composites (MMC) that give composites with higher properties, or even to maintain the same level of properties at lower cost [1]. The manufacturing process is of great importance, since with the same matrix reinforcement system, it is the manufacturing process that will determine the property/cost relation [2].

Powder metallurgy can produce metal matrix composites in the whole range of matrix reinforcement compositions [3, 4] without the segregation phenomena typical of the casting processes. However, the matrix and reinforcement mixing process is the critical step towards a homogeneous distribution throughout the consolidated composite material, although subsequent processes, such as powder extrusion, can help to eliminate the clustering of reinforcement particles and therefore achieves their more uniform distribution throughout the metal matrix [5-7].

High-energy ball milling has been used to improve particle distribution throughout the matrix [8-14]. This technique, first developed by John Benjamin [15] to produce nickel superalloys hardened by oxide

¹ jfoga@iris.ufscar.br

² Avenida de la Universidad, 30-28911-LEGANÉS-SPAIN

[†] Accepted: September 21, 2004

dispersion, is now known as mechanical alloying or mechanical milling. The process in which mixtures of powders are milled together is denominated Mechanical Alloying; it involves material transfer to obtain a homogeneous alloy by repeated deformation/welding/fracture mechanisms. On the other hand, milling of powders of uniform composition, in which material transfer is not required for homogenisation, is termed Mechanical Milling [16].

The use of hot extrusion in powder metallurgy avoids the sintering process and results in a full density final product. Hot extrusion of powders allows a high shear strain rate, which promotes high strength bonding between particles and a microstructure very similar to that of a wrought product. In the case of aluminium and its alloys, hot extrusion breaks the typical oxide layer that coats the powder, and hence gives better bonding of the particles [17].

The purpose of this work is to investigate the effect of mechanical alloying on the characteristics of composite materials obtained by powder metallurgy. Composites obtained by hot extrusion of mechanical-alloyed composite powders are compared with materials of the same composition but processed by conven-

tional mixing of matrix and reinforcement powders.

2. EXPERIMENTAL PROCEDURE

Aluminium AA6061 powder alloy (Alpoco – The Aluminium Powder Co. Ltd., England) was used as the matrix. This powder was produced by gas atomisation, and displays an equiaxed or quasi-spherical morphology. Si_3N_4 , AlN and ZrB_2 (ART – *Advanced Refractory Technologies, Inc.*, USA) were used as reinforcement materials. The fraction of reinforcement was 5% by weight. **Figure 1** shows the powders used as raw material in this work. **Table 1** shows the chemical composition of the matrix powder, and **Table 2** the average diameter size and the theoretical density of the reinforcement powders.

To mix the matrix and the reinforcement powders, two processes were used: a conventional low-energy mixing and high-energy milling, i.e. mechanical alloying. The conventional mixing does not alter the original characteristics of the raw materials, and merely homogenises the reinforcement throughout the matrix. A horizontal ball mill rotating at 150 rpm for 90 minutes was used. The mechanical alloying was per-

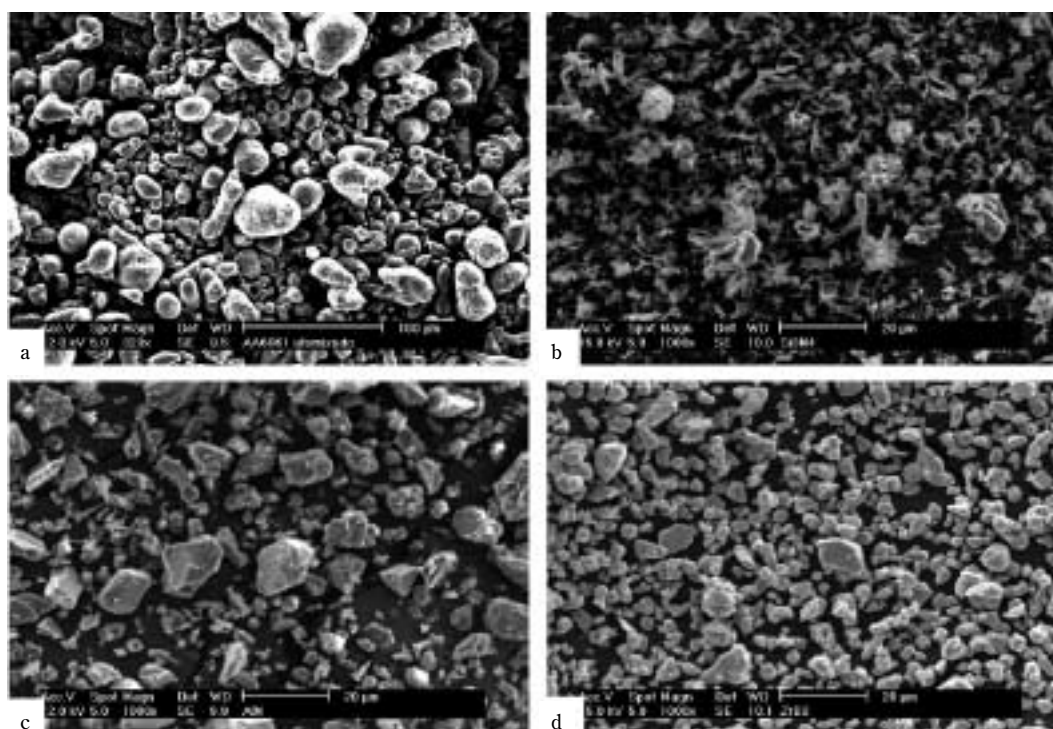


Fig. 1 Raw materials Al6061 aluminium alloy (a), Si_3N_4 (b), AlN (c) and ZrB_2 (d).

Table 1 Chemical composition of the as-received PM 6061.

Mg	Si	Cr	Cu	Fe	Others	Al
0.96	0.69	0.24	0.19	0.06	<0.3	Bal.

Table 2 Average diameter size and theoretical density of the matrix and reinforcement powders.

Material	Average particle size (μm)	Theoretical density (g/cm^3)
Si_3N_4	8.6	3.44
AlN	8.0	3.26

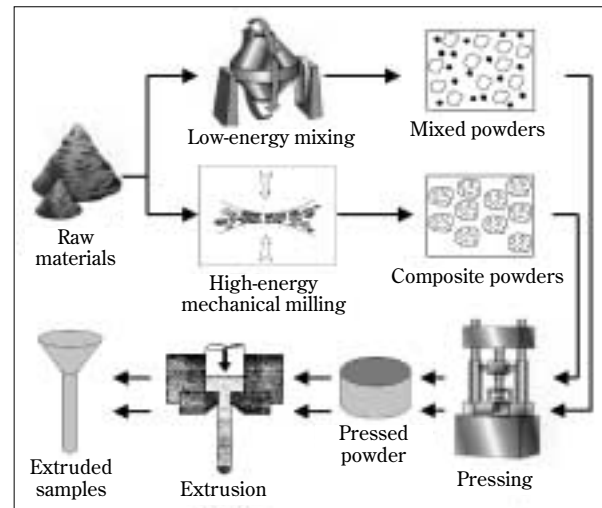


Fig. 2 Routes used to obtain the composite materials.

formed in an eccentric high-energy ball mill (*Fritsch GmbH, model "Pulverisette 6"*) with the following parameters: charge ratio: 6 : 1 (wt); ball diameter: 20 mm; ball material: AISI 420 stainless steel; speed 700 rpm. 1% (wt) of microwax was added to control the process (PCA). The high-energy milling time was that required to complete the mechanical alloying process, from the point of view of the phenomenological aspects [18], and was determined for each composition: 10 hours for the composite reinforced with Si_3N_4 and 12.5 hours for the composites reinforced with AlN and ZrB_2 . The mixed powders (low-energy mixing process) and composite powders (high-energy mechanical alloying) were examined by Scanning Electron Microscopy. Microhardness was determined in the as-received aluminium alloy and in the composite powders.

The powders were uniaxially cold-pressed at 300 MPa, and cylindrical samples of 25 mm diameter and around 16 mm were obtained. The cold-pressed samples were then hot extruded at 500°C, at a strain rate of 5 mm/s, without canning or degassing. The extrusion die was maintained inside a resistive furnace, which ensured good temperature control of the test. The sequence of the extrusion tests was randomly organized, in order to avoid systematic interference on the results. **Figure 2** shows the various stages of the production of the composite materials.

The extruded materials were examined by optical microscopy and by density measurements; ultimate tensile strength (UTS) (1 mm/min) and hardness (Vickers, 10 KN) were determined.

3. RESULTS AND DISCUSSION

3.1. Obtaining composite powders by mechanical alloying

Figure 3 compares the PM6061 with 5% AlN mixed powders with the composite particle obtained from the same composition after mechanical alloying. The AlN particles are bigger in the low-energy mixed powders (**Fig. 3a**) than in the mechanical-alloyed composite particle (**Fig. 3b**), and also show defects, such as cracks. The high-energy milling process reduces the reinforcement size, and tends to eliminate reinforcement clustering as well as reinforcement defects and sharp edges, producing a rounder reinforcement morphology, which will result in better composite properties. After mechanical alloying (**Fig. 3b**), each particle is a composite, displaying a uniform distribution of the reinforcement phase in the whole particle.

The degree of influence of the distinct reinforcement materials used in this work on the milling mechanisms can be attributed to their individual characteristics. Each kind of reinforcement material shows a different tendency to fragmentation when submitted to milling: the Si_3N_4 showing the highest tendency to fragmentation and the ZrB_2 the lowest. This difference is attributed to their different hardness and morphology.

As shown in **Fig. 1**, Si_3N_4 particles have an irregular morphology, while AlN and ZrB_2 particles have a more regular, polygonal morphology. These morphologies can in part explain the difference in the tendencies to fragmentation during milling: a more regular, polygo-

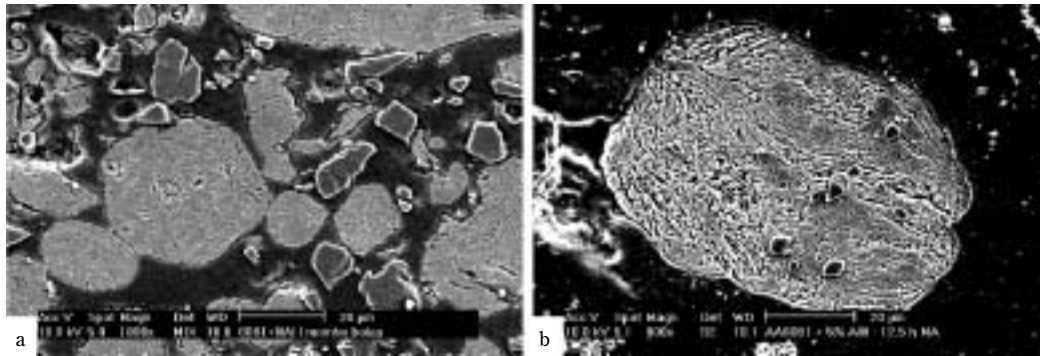


Fig. 3 PM6061 plus 5% AlN mixed powders (a) and the composite particle (b) obtained with the same composition after mechanical alloying.

nal morphology has a better inherent resistance to impact, while an irregular one has a larger surface area and sites that concentrate the stress and propagate cracks. From the point of view of the particle hardness, technical data in the ceramic literature [19] state known that Si_3N_4 is harder than AlN, and the results obtained in this work confirm the greater brittleness of the harder particle.

Figure 4 shows the composite powders reinforced with (a) Si_3N_4 and (b) ZrB_2 after mechanical alloying. The higher tendency to fragmentation during milling of Si_3N_4 particles produces a finer distribution of the reinforcement particles into the aluminium matrix.

Mechanical alloying promotes structural refinement, high dislocation density, and oxide and carbide dispersion (the aluminium carbide is derived from the PCA contamination), which should result in a great increase of the matrix hardness. In addition to this, the effect of reinforcement of the harder ceramic par-

ticles also contributes to raising material hardness. **Table 3** shows the microhardness of the as-received aluminium powder alloy and the composite powder produced by mechanical alloying. The great increase of hardness, around 150%, confirms the effectiveness of the process.

As mentioned above, Si_3N_4 is the reinforcement with the highest tendency to fragmentation during milling, and the composite powder reinforced with this material is the one that presents the finest distribution of the reinforcement throughout the matrix. ZrB_2 shows the least tendency to fragmentation during milling, and the composite powder reinforced with ZrB_2 is the one that presents the coarsest distribution of the reinforcement throughout the matrix. So the composite reinforced with Si_3N_4 displays the highest hardness among the composites analysed in this work, and the composite reinforced with ZrB_2 , the lowest one. A more extended description of the pro-

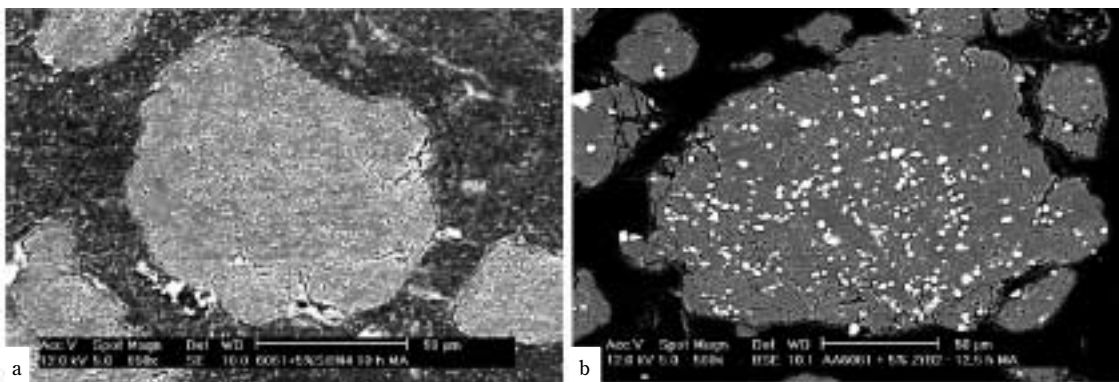


Fig. 4 Composite powders reinforced with (a) Si_3N_4 and (b) ZrB_2 after mechanical alloying.

Table 3 Microhardness of the as-received aluminium powder and the mechanically alloyed composite powders.

Material	Microhardness (HV)	Standard deviation
As-received PM6061	65,25	15,22
PM6061/5% AlN after 12,5 hours of milling	191,7	14,6
PM6061/5% ZrB ₂ after 12,5 hours of milling	186,9	19,6
PM6061/5% Si ₃ N ₄ after 10 hours of milling	208,9	13,4

duction of composite powders reinforced with Si₃N₄ and AlN by mechanical alloying is given elsewhere [18].

3.2. Powder consolidation by cold pressing and hot extrusion

Table 4 shows the pressures necessary to extrude the mixed and composite powders reinforced with Si₃N₄ and AlN; the reported values are the mean of eight tests. As the extrusion of powders consists in deforming and bonding the powder particles [20, 21], the higher the hardness of the powder to be extruded, the higher the pressure required to extrude. As a consequence, the pressure required to extrude the mixed powders is lower than those required to extrude the composite powders. A more extended description of the extrusion of the mechanical-alloyed powders is given elsewhere [21].

The density of the extruded materials is always between 98 and 100% of the theoretical density, whichever the process used, which confirms the effectiveness of the cold pressing plus hot extrusion to obtain full density products from powder material.

Table 4 Pressures necessary to extrude the mixed and the composite powders.

Reforcement	Powder	Average pressure (MPa)	Standard deviation (MPa)
Si ₃ N ₄	Mixed powder	441	23
	Composite powder	510	23
AlN	Mixed powder	503	32
	Composite powder	579	30

3.3. Characterization of the extruded materials

Figure 5 shows the microstructures of PM6061 reinforced with Si₃N₄ (**Fig. 5a** and **b**), AlN (**Fig. 5c** and **d**), and ZrB₂ (**Fig. 5e** and **f**), extruded from the mixed powders (**Fig. 5a**, **c** and **e**) and from the composite powders (**Fig. 5b**, **d** and **f**). These microstructures are observed in the transverse section of the extruded bars.

The materials extruded from the composite powders display a more homogeneous distribution of the reinforcement particles in the aluminium matrix. Also, the reinforcement particle is smaller in the mechanical-alloyed materials. As the Si₃N₄ is the reinforcement with the highest tendency to fragmentation, the composite reinforced with this material presents the finest dispersion of the reinforcement particles, as already observed in the powder characterization.

Table 5 shows the ultimate tensile strength (mean of eight tests) and the hardness (mean of twelve tests) of the composite materials obtained in this work. The UTS and the hardness of the mechanical-alloyed composites increases by around 100% above that of composite materials obtained by conventional powder metallurgy.

The increases observed are due to the extremely refined microstructure, oxide and carbide dispersion, reduction of the reinforcement particle size, elimination of the particle defects such as cracks and sharp edges, which reduce the tension concentration at critical points and the appearance of cracks during pressing or extrusion. All these effects are promoted by mechanical alloying.

As shown in **Table 3**, the hardness of the mechanical-alloyed composite powder is some 150% higher than that of the as-received aluminium powder alloy. However, the increase in the hardness of the extruded material due to the use of mechanical alloying is not so high: the hardness of the material extruded from the composite powders is around 100% higher than that extruded from the mixed powder, as shown in **Table 5**. It is well known that extrusion enhances the material strength by work hardening, but the composite powders obtained by mechanical alloying have already an extremely deformed structure, and the effect of the temperature of extrusion on this deformed structure promotes recuperation. The effect of oxide and carbide dispersion throughout the matrix on the material hardness is not influenced by the temperature of extrusion.

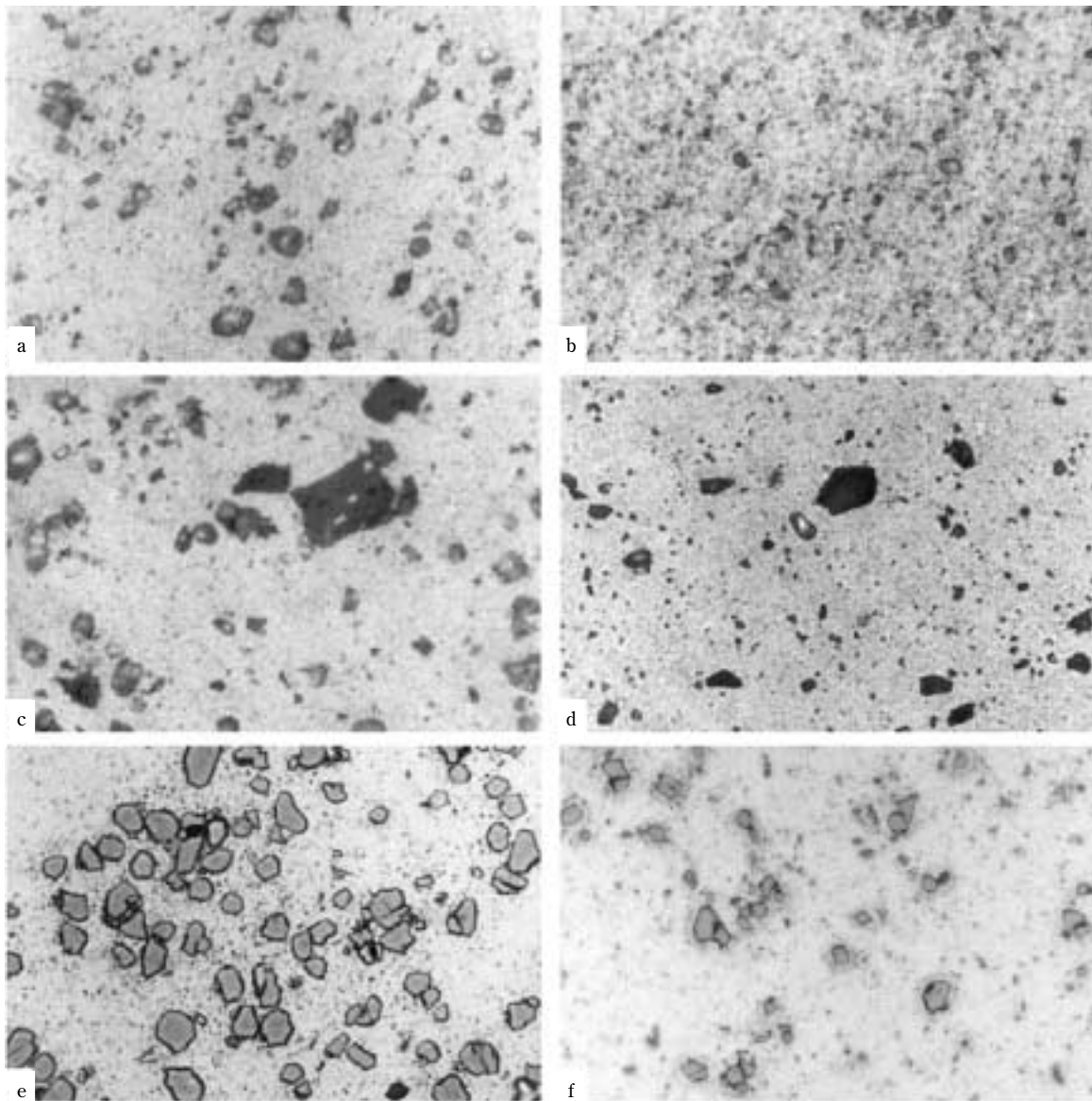


Fig. 5 Microstructures of PM6061 reinforced with Si_3N_4 (a and b), AlN (c and d), and ZrB_2 (e and f), extruded from the mixed powders (a, c and e) and from the composite powders (b, d and f).

Table 5 Ultimate tensile strength and hardness of the composite materials.

Reinforcement	Mixing process	UTS (MPa)	Standard deviation	Hardness (HV)	Standard deviation
AlN	Conventional	206	2	63	2
	Mechanical alloying	402	22	126	6
Si_3N_4	Conventional	214	3	63	1
	Mechanical alloying	422	6	119	4
ZrB_2	Conventional	192	1	59	2
	Mechanical alloying	320	20	110	4

4. CONCLUSIONS

The results obtained in this work confirm the efficiency of mechanical alloying and hot-extrusion to produce composite materials with highly refined structures, strengthened by oxide and carbide dispersion, with homogeneous distribution of the reinforcement particles, fully densified and showing better mechanical properties.

The use of mechanical alloying increases the powder hardness by about 150% when compared with the as-received non-reinforced aluminium powder alloy, and the UTS and hardness of the extruded materials by about 100%, when compared with the same materials, processed by conventional powder metallurgy.

Among the reinforced materials used in this work, the silicon nitride has the highest tendency to fracture during milling and promotes the highest increase in the composite strength.

5. ACKNOWLEDGEMENTS

The authors would like to thank CAPES – Brasil (Fundação Coordenação de Aperfeiçoamento de Pessoal de Nível Superior) for financial support.

REFERENCES

1. Kaczmar JW, Pietrzak K, Wlosinski W, J. Mater. Proc. Tech. 106 (2000) 58.
2. Harrigan Jr WC, Mat. Sci. Eng. A244 (1998) 75.
3. Smagorinski ME, Tzantrizos PG, Grenier S, Cavasin A, Brzezinski T, Kim G. Mat. Sci. Eng. A244 (1998) 86.
4. O'Donnell G, Looney L. Mat. Sci. Eng. A303 (2001) 292.
5. Jain MK, Bhanuprasad VV, Kamat SV, Pandey AB, Varma VK, Bhat BVR, Mahajan YR, Int. J. Powder Metall. (1993) 29, 267.
6. Hanada K, Murakoshi Y, Negishi H, Sano T, J. Mater. Process Tech. (1997) 63, 405.
7. Tan MJ, Zhang X, Mat. Sci. Eng A244 (1998) 80.
8. Tiwari AN, Gopinathan V, Ramakrishnan P, Mater. Manuf. Process. (1991) 6, 4, 621.
9. Lee J, Kim S, Park C, Bae C, J. Mater. Process. Manu. (1995) 4, 55.
10. Lu L, Lai MO, Zhang S, Key Eng. Mater. (1995) 104-107, 111.
11. Hanada, K, Khor KA, Tan MJ, Murakoshi Y, Negishi H, Sano T, J. Mater. Process Tech. (1997) 67, 8.
12. Gingu O, Rosso M, Ubertaini G, Proc. Powder Metallurgy World Congress and Exhibition, Granada, Spain, 1998, 5, 162.
13. Lu L, Lai MO, Ng CW, Mat. Sci. Eng. A252 (1998) 203.
14. Ruiz-Navas EM, Costa CE, Ruiz-Roman JM, Cambroner LEG, Ruiz-Prieto JM, Proc. Powder Metallurgy World Congress and Exhibition, Granada, Spain, 1998, 5, 146.
15. Benjamin JS, Metall. Trans. (1970) 1, 2943.
16. Suryanarayana C, Prog. Mater. Sci. (2001) 46, 1.
17. Schaffer GB, Sercombe TB, Lumbey RN, Mater. Chem. Phys. 67 (2001) 85.
18. Fogagnolo JB, Velasco F, Robert MH, Torralba JM, Mat. Sci Eng. A342 (2003) 131.
19. James F. Shackelford, CRC Materials Science and Engineering Handbook, CRC Press, 1994.
20. Roberts PR, Ferguson BL, Inter. Mater. Rev. 36 (2) (1991) 62.
21. Fogagnolo JB, Ruiz-Navas EM, Robert MH, Torralba JM, J. Mat. Sci., 37 (21) (2002) 4603.

Author's short biography



J. B. Fogagnolo

Dr. João Batista Fogagnolo, born in 1964, received his degree in Materials Engineering from the Federal University of São Carlos, Brazil, in 1990, his M.Sc degree in Mechanical Engineering from the State University of Campinas, Brazil, in 1996, and his doctor's degree in Mechanical Engineering from the State University of Campinas, in 2000. He worked in Carborundum of Brazil, from 1991 to 1996, and in University Carlos III of Madrid, Spain, from 1998 to 2001. Since 2002 he is researcher of the Materials Engineering Department at the Federal University of São Carlos. His research interests include: powder metallurgy, synthesis of aluminium matrix composites, synthesis of amorphous and nanostructured alloys, mechanical alloying, severe plastic deformation, powder consolidation by hot extrusion.

Author's short biography



M. H. Robert

Prof. Maria Helena Robert is Materials Science Engineer – Federal University of São Carlos (UFSCar), Brazil, 1975; Master in Mechanical Engineering (Materials & Manufacturing Processes) – State University of Campinas, (UNICAMP), Brazil; 1979; and PhD in Mechanical Engineering (Materials & Manufacturing Processes) – UNICAMP; 1983. She has made pos-doctoral studies at Dept. of Metallurgy, working on Semi-solid Processing; University of Sheffield, UK and Dept. of Materials Science and Engineering, working on Composite Materials; University of Liverpool, UK. Her Research Interests are Solidification of Metals and Alloys – structure control; Thixoforming – processes development/structures characterisation/mechanical properties of thixoformed products and Metal Matrix Composites – production and characterisation.



F. Velasco

Prof. Francisco Velasco is Metallurgical Eng., PhD in Materials Engineering in 1995 at Universidad Politecnica de Madrid. He works in powder metallurgy, mainly in the frames of wear and corrosion. He's got about 40 articles (SCI journals) and near 100 communications at congresses.



J. M. Torralba

Prof. José M. Torralba, born in 1959, Professor of Materials Science and Engineering, at Materials Science and Engineering Department, Universidad Carlos III de Madrid (Spain). He got the degrees of Metallurgical Engineer (1982, Technical University of Madrid), Dr. Eng (1985, Technical University of Madrid), Armament Engineer (1996, School of Engineering of Spanish Army), Dr. Eng. (1994, School of Engineering of Spanish Army). His main field of scientific interest is Powder Metallurgy. Since 1982, has worked in different sintered materials. These materials could be jointed in the following families: 1) Low alloyed steels: the main contribution was in the study of new alloying systems looking for the improvement of sinterability of the steels and as a consequence the structural properties. 2) Special sintered steels (stainless steels): studies promoting the increase in properties related to the behavior under service conditions of these materials, as corrosion or wear behavior. 3) Metal matrix composites: including aluminum matrix composites as well as stainless steel and high-speed steel matrix composites. In the last years the research group has been involved in Projects related to techniques close to advanced materials forming, like mechanical alloying or metal injection molding. He has published more than 250 scientific papers on these topics and supervised 10 PhD Thesis. In 1999 he received the Honorary Award “Professor Fryderyk Staub” by the Silesian University of Technology (Poland) and in 2001 the Honoris Causa Dr. degree by the Technical University of Cluj-Napoca (Romania).

Rational Design of Dispersants by Molecular Modeling for Advanced Ceramics Processing Applications[†]

Pradip, Beena Rai and P. Sathish

Tata Research Development & Design Centre*

Abstract

A molecular modeling based approach to design/selection of dispersants for colloidal processing of ceramics powders is presented. The validity and the utility of the proposed approach are illustrated with two case studies. The relative strength of interaction of dispersants belonging to two known family of dispersants namely, hydroxy aromatics (phenol derivatives) and aliphatic/aromatic carboxylic acids with alumina are found to correlate well with the experimental trends reported in literature. The dispersibility of BaTiO₃ nanoparticles as determined by the sediment density in different organic liquids are observed to match well with the corresponding interaction energies computed theoretically.

INTRODUCTION

The benefits of very fine-grained microstructures with submicron grain sizes for obtaining ceramic components with improved hardness, wear resistance, strength or optical performance is well known [1, 2]. More recently nanocrystalline materials have been shown to possess unique physical and mechanical properties including enhanced ductility and superplasticity even in traditionally brittle materials and optical transparency in otherwise opaque ceramics [3-5]. A whole new field of nano-ceramics promises to revolutionize the industry. Rocco and Bainbridge [6] project that more than \$1 trillion worth of products will be affected by nanotechnology and half of the newly designed advanced materials and manufacturing processes will be built using control at the nanoscale. Considerable progress has been made in the area of nanoparticle synthesis and processing. It is however well recognized that the conversion of these nanopowders into fully dense commercial products that retain a nanocrystalline grain size is not yet established [3, 4]. A better theoretical understanding

of the fabrication processes is needed in order to manufacture high-density products without microstructural coarsening [4]. Colloidal processing methods appear to be promising in consolidating nanopowders into fully dense products [7-20].

Dispersion of colloidal particles, in particular nanoparticles in aqueous and non-aqueous suspensions is crucial for the success of manufacturing processes for advanced ceramics applications. Colloidally stable suspensions are known to produce higher average packing densities and finer pore size distributions in green/sintered compacts than poorly dispersed or flocculated suspensions [12, 21-23]. The selection of appropriate dispersants is thus important for achieving the advantages of lower sintering temperature and/or significant enhancement of performance in industrial applications, as a consequence of employing colloidal/nano particles. Commonly used dispersants include menhaden fish oil, poly vinyl butyral (PVB), phosphate esters, fatty acids & fatty acid derivatives and several varieties of polymeric dispersants [15-21, 24, 25]. Depending on the nature of the dispersant, the mechanism of dispersion could be either electrostatic, steric or electrosteric [17-22].

Design, development and selection of dispersants for different applications remain an art. Most currently available commercial dispersants are selected primarily by trial and error methods based on rules of

* 54 B, Hadapsar Industrial Estate, Pune – 411 013, India

Email: pradip.p@tcs.com

[†] Accepted: October 26, 2004

thumb and past experience. The time and resources required to come up with an acceptable formulation is therefore prohibitively expensive for difficult-to-disperse nanoparticles based systems. Additionally, because of the high cost of empirical search for novel dispersants, the search envelope is severely restricted to a few well-known families of dispersants. There is thus a need for devising a more cost-efficient strategy and scientifically robust framework for design/selection of dispersants in order to derive maximum advantage from using more expensive nanoparticles in industrial practice. With recent advances in the understanding of molecular level phenomena governing adsorption of dispersants at interfaces, accessibility of application oriented molecular modeling tools and availability of relatively inexpensive computing power, it is possible to design dispersants customized for specific applications that are based on theoretical computations. We have elucidated the building blocks of this novel paradigm through our recent publications on this topic [26-33]. Two key features of the proposed approach are: one, identification of the molecular recognition mechanisms underlying the adsorption of dispersants at the interface and two, use of advanced molecular modeling techniques for theoretical computations of the relative magnitude of interaction. The molecular modeling thus provides a quantitative search technique for screening and identifying the most promising molecular architectures from a large set of candidates available for a particular application. As a consequence, considerable saving in time and effort needed for developing new dispersant formulations is possible.

We present in this paper our recent work on the rational design of dispersants for colloidal processing of ceramics powders in order to illustrate the power and the utility of our molecular modeling approach. Two case studies have been selected for discussion in this communication namely, (i) the dispersion of alumina in aqueous suspensions using hydroxy aromatics (phenol derivatives) and aliphatic/aromatic specialty chemicals belonging to carboxylic acids family of reagents and (ii) the prediction of dispersion characteristics of barium titanate nanoparticles in different organic solvents. We describe very briefly the molecular modeling methodology followed by examples.

MOLECULAR MODELLING METHODOLOGY

Force field calculations (Atomistic Simulations)

Force field methods are most appropriate for rela-

tively larger systems consisting of hundreds of atoms such as oligomers, polymers, condensed phases etc., which are of great interest in ceramics. Some of the generalized force fields currently available are Universal Force Field (UFF) [34-37], COMPASS [38] and DREIDING [39]. We have found UFF to be more suitable for the computations of the type presented in this paper. We have successfully demonstrated through our earlier work that UFF can be used to model such systems with reasonable accuracy [27-33]. The UFF is a purely diagonal and harmonic force field in which bond stretching is described by a harmonic term, angle bending by a cosine-Fourier expansion, and torsion and inversion by the cosine-Fourier expansion terms. The van der Waals interactions are modeled as Leonard-Jones potentials, and electrostatic interactions as a screened (distance-dependent) Coulombic term. All atomistic simulations in this study were carried out using the molecular modeling simulation program Cerius² [40].

Ceramics Surface

Surface Energy

The surface energy was calculated from the expression:

$$[U_s - U_b]/A$$

where U_s is the energy of the surface block of the crystal, U_b the energy of an equal number of atoms of the bulk crystal, and A the surface area.

Alumina (001) Surface

The Al-terminated (001) basal plane of α -alumina (corundum) has been found to be energetically most stable [21]. The hexagonal unit cell was cleaved at (001) plane to create an eighteen atomic layer thick surface cell. This surface cell was replicated in x and y planes to create a super cell of $21.22 \times 21.22 \text{ \AA}$. While relaxing the surface, top nine atomic layers were allowed to move and rest of the nine layers were constrained. The calculated surface energy (1.37 J/m^2) was comparable to reported values (2.42 J/m^2) [41].

Barium Titanate (001) Surface

We have recently reported [33] our work on molecular modeling of dispersion of nanoparticles of barium titanate using a variety of commercial dispersants including fatty acids and phosphate esters. The systematic force field and ab initio calculations were performed to arrive at the most stable BaTiO_3 surface. Based on the surface energies, BaO terminated (001) surface 0.83 J/m^2 was found to be more relaxed com-

pared to TiO₂ terminated (001) surface 2.65 J/m². The surface thus obtained was converted into a three dimensional periodic structure by adding a vacuum of 50 Å in Z-direction. This computer representation of BaTiO₃ was used in the present study as well.

Dispersant Molecules

Three family of dispersants namely, aromatic alcohols, aromatic carboxylic acids and aliphatic carboxylic acids were selected for the study. The molecules were optimized using UFF method.

Ceramics-Dispersant Complex (in vacuum)

The optimized dispersant molecule was docked on the ceramics surface. The initial geometry of ceramics-dispersant complex was created physically on the screen with the help of molecular graphics tools, taking into consideration the possible interactions of dispersant functional groups with surface atoms. The dispersant molecule was then allowed to relax completely on the surface. Several initial conformations (~20) were assessed so as to locate the minimum energy conformation of dispersant molecule at the ceramics surface.

Static Energy Minimization (Simulation Details)

The partial charges on the atoms were calculated using charge equilibration method [42]. The intramolecular van der Waal interactions were calculated only between atoms which are located at distances greater than fourth nearest neighbors. A modified Ewald summation method [43] was used for calculating the non-bonded coulomb interactions while for van der Waal interactions atom based direct cut off method was employed. Smart minimizer as implemented in Cerius² was used for geometry optimization. The optimization was considered to be converged when a gradient of 0.0001 Kcal/mole is reached.

Solvent Box

A three dimensional periodic box of solvent molecules was constructed and optimized so as to match the density in the box to that of the experimental density of the selected solvent. NVE molecular dynamics (MD) simulations were run for 300 ps to equilibrate the solvent box at 300 K at its experimental density.

Ceramics Surface – Dispersing Medium

Bulk solvent molecules, equilibrated as described in the previous section, were introduced over the ceramics surface. The ceramics surface-solvent complexes thus created were subjected to energy mini-

mization and molecular dynamics simulation.

Molecular Dynamics (MD) Simulations (in presence of solvent)

Structure of the complex obtained through static energy minimization method represents only a local minimum energy structure, which was used as initial configuration to find a global minimum energy structure through molecular dynamics (MD) simulations. MD calculations were run using constant energy microcanonical ensemble method (NVE) at 300 K with time step of 1 fs. Total run length was ~100 ps. During the simulations, the temperature was controlled by velocity scaling method. During simulations, atom-based cut-off method was employed for calculating both Van der waals and electrostatic forces. A typical optimized ceramic surface – dispersant complex in presence of the solvent is shown in **Figure 1**.

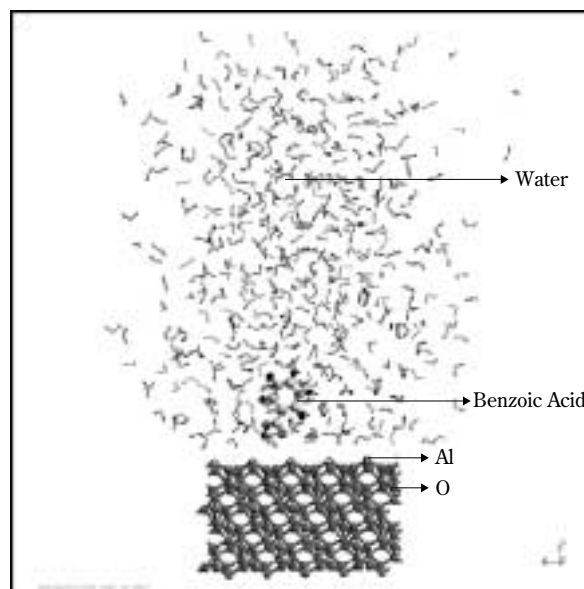


Fig. 1 Alumina (001) – benzoic acid complex in presence of water optimized by MD simulation.

Computation of Interaction Energy

The relative affinity of interaction of different dispersants with ceramics surface in presence or absence of the solvent can be quantified in terms of the interaction energy defined as follows:

In vacuum, (absence of dispersing medium):

$$IE_{(\text{in vacuum})} = E_{\text{complex, vacuum}} - \Sigma (E_{\text{surface}} + E_{\text{dispersant}}) \quad (1)$$

In the presence of dispersing medium:

$$IE_{(\text{in solvent})} = \Delta E_{\text{combined}} - \Sigma (\Delta E_{\text{solvent-dispersant}} + \Delta E_{\text{surface-solvent}}) \quad (2)$$

$$[\Delta E_{\text{combined}} = E_{\text{complex, solvent}} - \Sigma (E_{\text{surface}} + E_{\text{dispersant}} + E_{\text{solvent}})] \quad (3)$$

where $\Delta E_{\text{combined}}$ is the total interaction energy calculated using Eqn. 3. $E_{\text{complex, solvent}}$ is the total energy of the optimized surface-dispersant complex in the presence of solvent, E_{surface} , $E_{\text{dispersant}}$ and E_{solvent} are the total energies of free surface, dispersant and solvent molecules, computed separately. $\Delta E_{\text{solvent-dispersant}}$ is the interaction energy computed for the interaction of solvent and dispersant molecules and $\Delta E_{\text{surface-solvent}}$ is the contribution due to interaction of solvent molecules with the surface. These energies are subtracted from $\Delta E_{\text{combined}}$ to get the final interaction energy [$IE_{(\text{in solvent})}$] of dispersant molecule with the ceramic surface (Eqn. 2).

It is worth noting that the more negative magnitude of interaction energy indicates more favorable interactions between the dispersant and surface. The magnitude of this quantity is thus an excellent measure of the relative intensity/efficiency of interaction amongst various dispersants.

RESULTS AND DISCUSSIONS

BaTiO₃ dispersions in organic media

Mizuta et. al. [44] studied the fundamental properties of BaTiO₃ dispersions in pure organic liquids including alcohols, aldehydes, acids, ketones, hydrocarbons and water by sediment volume and contact angle measurements using four different powders namely, TAM-C, TAM-COF, Transelco (219-3) and Fuji BT-100PL. The experimental trends with respect to wettability and dispersion were found to be similar for all the four powders. We have taken the data for a typical powder, Fuji BT-100PL for comparing with our theoretical findings. Benzaldehyde was found to be the best dispersing medium. Based on their experimental work, the authors inferred that the intensity of interactions between organic functional groups and BaTiO₃ surface was as follows

Acid > aldehyde
 = alcohol > ester > ketone > ether > hydrocarbon

We have calculated interaction energies for some of the solvents with BaTiO₃ surface. Our results are compared with experimental results of Mizuta et al.

(Figure 2). The authors defined a dispersibility index in percent based on sediment volume measurements. Higher the value of this index the better is the dispersion. The theoretical predictions match well with the experimental findings.

Aqueous alumina suspensions

Hideber et. al. [45] studied the relation between the molecular structure of low-molecular weight organic dispersants namely, hydroxy aromatics and aliphatic/

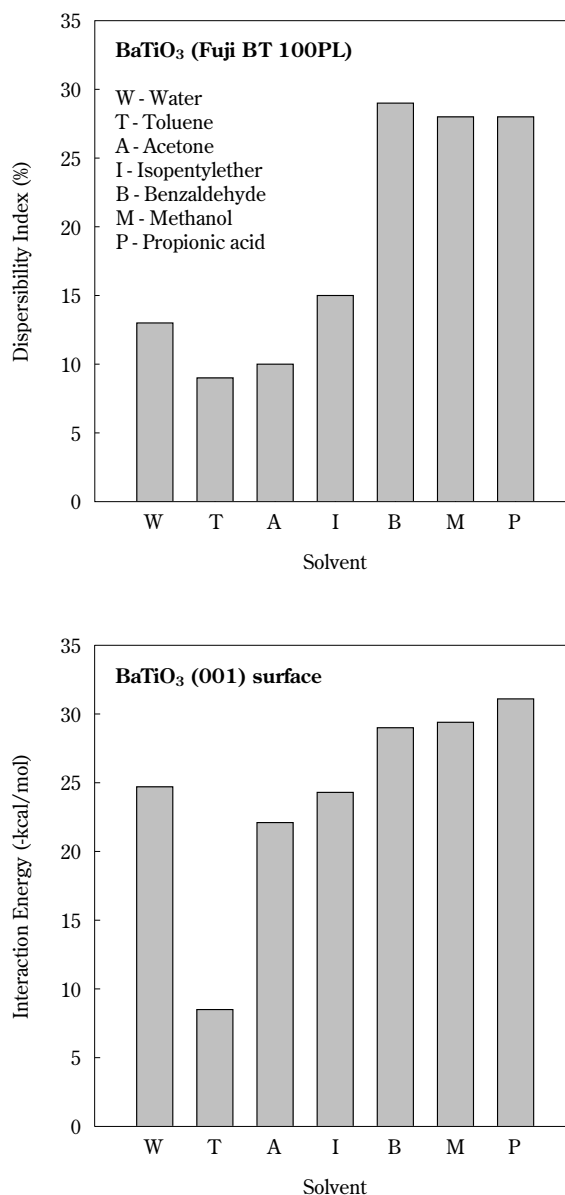


Fig. 2 (a) Percent dispersibility index of the Fuji BT 100PL powder (data taken from Ref. [44]), (b) Theoretically computed interaction energies obtained using MD simulations.

aromatic carboxylic acid and their influence on the dispersion behavior of alumina suspensions. In particular, the effect of the nature, number and position of the functional groups attached to the benzene ring were studied through adsorption and electrophoretic mobility experiments on aqueous alumina suspensions. The amount adsorbed was calculated from the difference between the amount of dispersant added and that remaining in the supernatant. The results were plotted in terms of adsorption as percent of the amount added. The initial concentration was maintained at 10^{-3} mole per litre.

The degree of adsorption (that is, the efficiency) of a dispersant increased with its ability to form one or more chelate rings with the ceramic surface. It also increased with increasing number of functional groups in a homologous series.

We have modeled the interactions of these dispersants with alumina surface. Our theoretical findings are compared with experimental results in **Figures 3, 4 and 5**.

Aromatic Alcohols

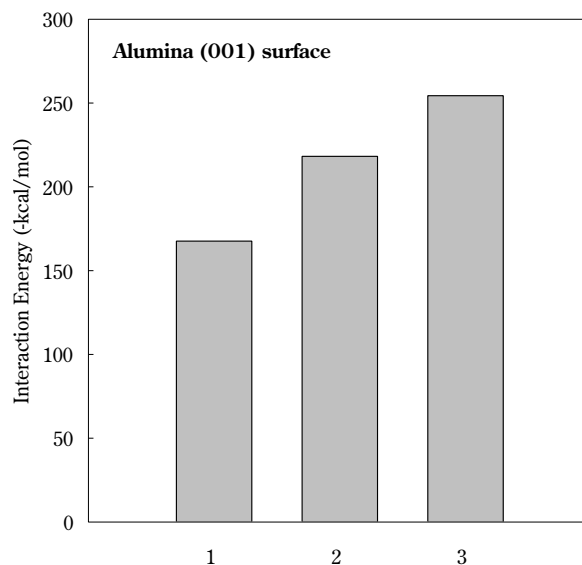
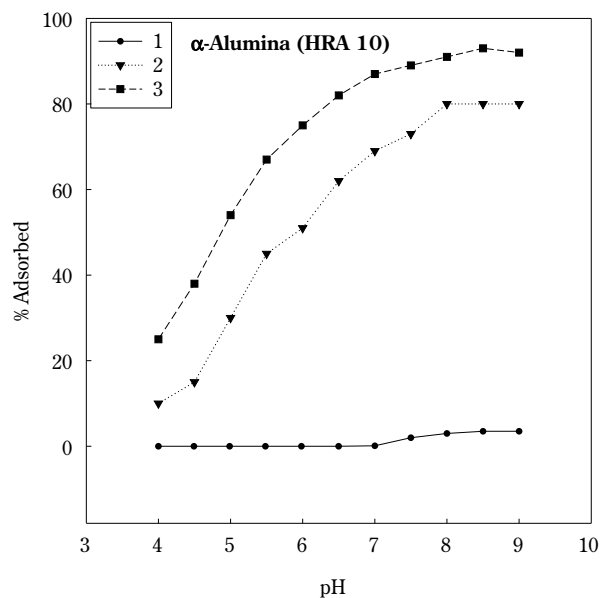
Computed interaction energies of phenol, catechol and pyrogallol with alumina are plotted and compared with experimental percent adsorption in **Fig. 3**. The predicted trends match well with experimental findings. As expected, the interaction energy becomes more negative with increasing number of -OH groups in the dispersant molecule.

Aromatic Carboxylic acids

The calculated interaction energies of benzoic, phthalic and hemimellitic acids with alumina are plotted in **Fig. 4b**. The corresponding experimental adsorption data compares well with the theoretical findings (**Fig. 4a**). The interaction energy is most favorable for the molecule with the highest number of functional groups in the benzene ring.

Aliphatic Carboxylic Acids

As shown in **Fig. 5a** the adsorption of propionic acid is lowest (only one carboxylic group). The presence of a hydroxyl group in α -position (lactic acid) enhances the adsorption. The adsorption at alumina surface increases with increasing number of functional groups: citric acid (three carboxyl) > malic acid (two carboxyl) > lactic acid (one carboxyl with α -hydroxyl) > propionic acid (one carboxyl). Based on the computed interaction energies, predicted order of adsorption was found to be: citric acid > malic acid > lactic acid > propionic acid (**Fig. 5b**).



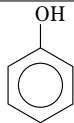
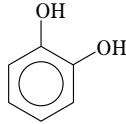
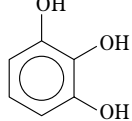
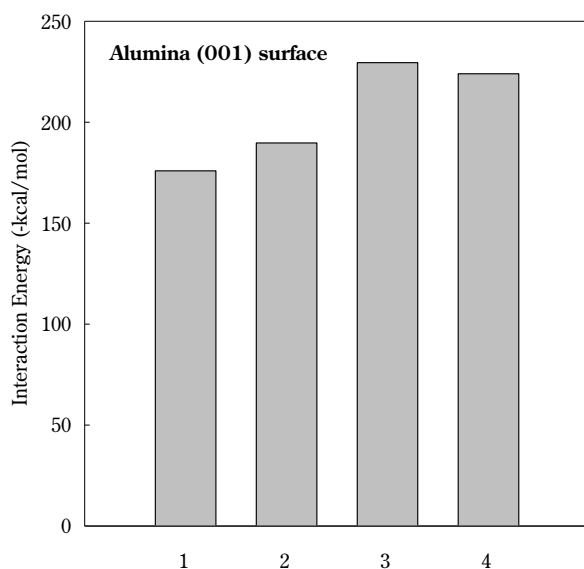
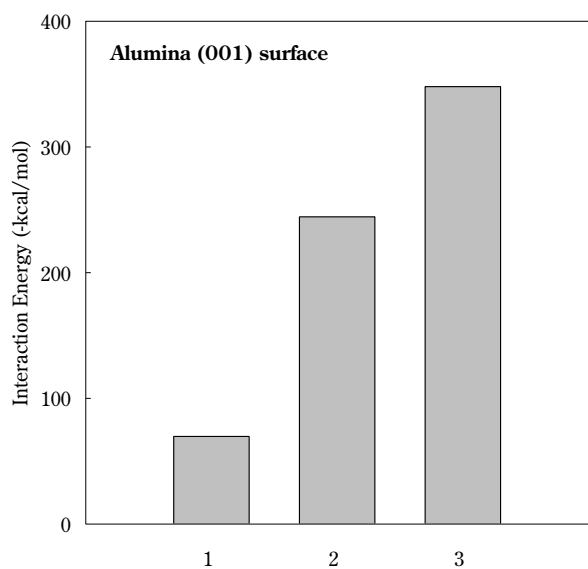
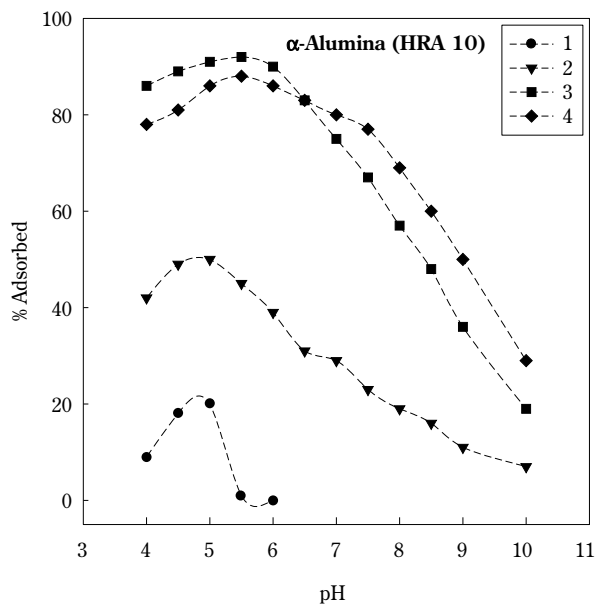
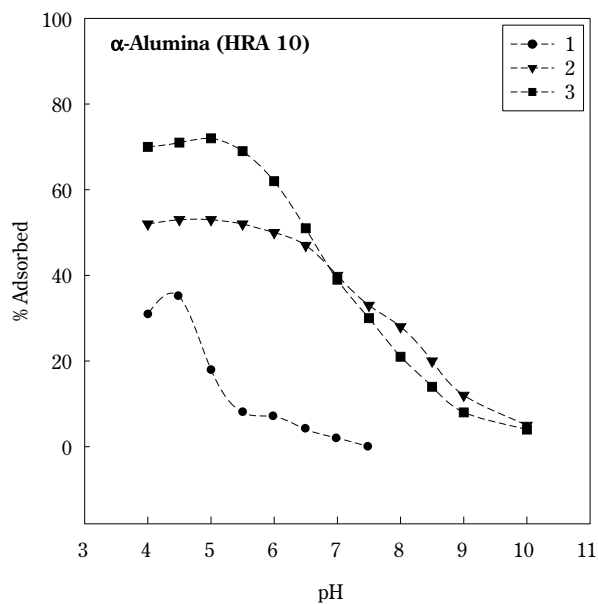
1	Phenol	
2	Catechol	
3	Pyrogallol	

Fig. 3 (a) Adsorption curves for phenol, catechol and pyrogallol on α -alumina (data taken from Ref. [45]), (b) Theoretically computed interaction energies obtained using MD simulations in presence of water.



1	Benzoic acid	
2	Phthalic acid	
3	Hemimellitic acid	

1	Propionic acid	
2	Lactic acid	
3	Malic acid	
4	Citric acid	

Fig. 4 (a) Adsorption curves for aromatic carboxylic acids on α -alumina (data taken from Ref. [45]), (b) Theoretically computed interaction energies obtained using MD simulations in presence of water.

Fig. 5 (a) Adsorption curves for aliphatic carboxylic acids on α -alumina (data taken from Ref. [45]), (b) Theoretically computed interaction energies obtained using MD simulations in presence of water.

CONCLUDING REMARKS

The utility of currently available molecular modeling tools in the design and screening of different molecular architectures for dispersion of ceramic powders is demonstrated through this communication. The relative efficiency of specialty chemicals for a particular ceramic powder-solvent system can thus be theoretically predicted. The molecular modeling based theoretical approach thus provides a scientifically robust framework for the design/selection of appropriate solvent and/or dispersant for a given application. With steady advancements being made in the theory and practice of molecular modeling approach, it is anticipated that even more complex design problems can be solved, in particular with respect to the optimization of the molecular architecture in order to develop performance chemicals tailor-made for the desired application.

ACKNOWLEDGEMENTS

The authors gratefully acknowledge the kind help, encouragement and support received from Prof. Mathai Joseph during the course of this work.

REFERENCES

- [1] A. Krell and H. Ma (1999), *Nanostuctur. Mater.* **11**, 1141-53.
- [2] A. Krell, P. Blank, H. Ma, T. Hutzler and M. Nebelung (2003), *J. Am. Ceram. Soc.* **86**, 546-53.
- [3] S. Seal, S. C. Kuiry, P. Georgieva and A. Agarwal (2004), *MRS Bulletin* **29**, 6-21.
- [4] J. D. Kuntz, Guo-Dong Zhan and A. K. Mukherjee (2004), *MRS Bulletin* **29**, 22-27.
- [5] J. Brinker (2004), *MRS Bulletin* **29**, 631-640.
- [6] M. C. Roco and W. S. Bainbridge (Eds.), "Technologies for improving human performance", *NSF-DOC Report* (also published by Kluwer Academic Publishers) Boston, pp. 468 (2003).
- [7] B. C. Yu, P. M. Biesheuvel and F. F. Lange (2002), *J. Am. Ceram. Soc.* **85**, 1456-60.
- [8] R. Zeng and B. Rand (2004), *Int. J. Materials and Product Technology* **21**, 435-442.
- [9] N. S. Bell, J. Cesarano III, J. A. Voigt, S. J. Lockwood and D. B. Dimos (2004), *J. Mater. Res.* **19**, 1333-1335.
- [10] N. S. Bell, J. A. Voigt, B. A. Tuttle and D. B. Dimos (2004), *J. Mater. Res.* **19**, 1341-1347.
- [11] H. Kamiya, Y. Fukuda, Y. Suzuki and M. Tsukuda (1999), *J. Am. Ceramic Soc.* **82**, 3407-3412.
- [12] G. H. Kirby, D. J. Harris, Q. Li and J. A. Lewis (2004), *J. Am. Ceramic Soc.* **87**, 181-186.
- [13] J. A. Lewis (2000), *J. Am. Ceramic Soc.* **83**, 2341-2359.
- [14] F. F. Lange (1989), *J. Am. Ceramic Soc.* **72**, 3-15.
- [15] L. B. Garrido and E. F. Aglietti (2001), *Ceramics International* **27**, 491-99.
- [16] J. Cesarano and I. A. Aksay (1988), *J. Am. Ceramic Soc.* **71**, 1062-1067.
- [17] V. A. Hackley (1997), *J. Am. Ceramic Soc.* **80**, 2315-2325.
- [18] V. A. Hackley (1998), *J. Am. Ceramic Soc.* **81**, 2421-2428.
- [19] M. J. Solomon, T. Saeki, M. Wan, P. J. Scales, D. V. Boger and H. Usui (1999), *Langmuir* **15**, 20-26.
- [20] Z. Zhou, P. J. Scales and D. V. Boger (2001), *Chemical Engineering Science* **56**, 2901-2920.
- [21] L. Bergstrom, K. Shinozaki, H. Tomiyama and N. Mizutani (1997), *J. Am. Ceram. Soc.* **80**, 291-300.
- [22] Pradip, R. S. Premachandran and S. G. Malghan (1994), *Bulletin of Material Science* **17**, 911-920.
- [23] M. Subbanna, P. C. Kapur and Pradip (2002), *Ceramics International* **28**, 401-405.
- [24] S. Mizuta, M. Parish and H. K. Bowen (1984), *Ceramics International* **10**, 43-83.
- [25] K. Mikeska and W. R. Cannon (1985), Advances in Ceramics, (Eds.) J. A. Mangels and G. L. Messing, *The American Ceramic Society Publication* **9**, pp. 164.
- [26] Pradip (1992), *Current Science* **63**, 180-186.
- [27] Pradip, B. Rai, T. K. Rao, S. Krishnamurthy, R. Vetrivel, J. Mielczarski and J. M. Cases (2002), *Langmuir* **18**, 932-940.
- [28] Pradip and B. Rai (2002), *Colloids and Surfaces* **205**, 139-148.
- [29] Pradip, B. Rai, T. K. Rao, S. Krishnamurthy, R. Vetrivel, J. Mielczarski and J. M. Cases (2002), *Journal of Colloid & Interface Science* **256**, 106-113.
- [30] J. A. Mielczarski, E. Mielczarski, J. M. Cases, B. Rai and Pradip (2002), *Colloids and Surfaces* **205**, 73-84.
- [31] Pradip and B. Rai, *Intl. Journal of Mineral Processing* **72**, 95-110.
- [32] B. Rai and Pradip (2003), *Proceedings, XXII International Mineral Processing Congress (IMPC), CapeTown*, eds. L. Lorenzen and D. J. Bradshaw (South African Institute of Mining & Metallurgy (SAIMM), CapeTown), **Vol. 2**, 1085-1093.
- [33] Pradip, B. Rai, P. Sathish and S. Krishnamurthy (2004), *Ferroelectrics* **306**, 195-208.
- [34] A. K. Rappé, C. J. Casewit, K. S. Colwell, W. A. Goddard and W. M. Skiff (1992), *J. Amer. Chem. Soc.* **114**, 10024-10035.
- [35] C. J. Casewit, K. S. Colwell and A. K. Rappé (1992), *J. Am. Chem. Soc.* **114**, 10035-10046.
- [36] C. J. Casewit, K. S. Colwell and A. K. Rappé (1992), *J. Am. Chem. Soc.* **114**, 10046-10053.
- [37] A. K. Rappé, K. S. Colwell and C. J. Casewit (1993), *Inorg. Chem.* **32**, 3438-3450.
- [38] H. Sun (1998), *J Phys. Chem. B* **102**, 7338-7364.
- [39] S. L. Mayo, B. D. Olafson and W. A. Goddard (1990), *J. Phys. Chem.* **94**, 8897-8909.
- [40] Cerius², Version 4.6; available from Accelrys limited, 9685 Scranton Road, San Diego, CA 92121-3752, USA.
- [41] N. H. de Leeuw and S. C. Parker (1999), *J. Am. Ceram. Solids* **82(11)**, 3209-3216 and references cited therein.

- [42] A. K. Rappe, and W. A. Goddard (1991), *J. Phys. Chem.* **95**, 3358-3363.
- [43] N. Karasawa, and W. A. Goddard III (1989), *J. Phys. Chem.* **93**, 7320-7327.

- [44] S. Mizuta, M. Parish and H. K. Bowen (1984), *Ceramic International* **10**, 43-48.
- [45] P. C. Hidber, T. J. Graule and L. J. Gauckler (1997), *J. of Europ. Ceram. Soc.* **17**, 239-249.

Author's short biography



Pradip

Pradip, currently the Group Leader, Materials and Minerals Processing Technology Group at Tata Research Development & Design Centre (TRDDC), Pune, received his B.Tech in Metallurgical Engineering from IIT, Kanpur in 1975 and M.S. and Ph.D. in Materials Science and Mineral Engineering from University of California at Berkeley in 1977 and 1981 respectively. He also spent three years as a scientific officer at Bhabha Atomic Research Centre (BARC) before joining TRDDC in 1984. His main areas of research include particle science & technology, mineral processing, design and development of performance chemicals based on molecular modeling, applied surface and colloid chemistry, mathematical modeling & simulation of particulate processing systems, colloidal processing of advanced ceramics, waste recycling and cement chemistry.

With more than 120 publications and eight patents to his credit, Pradip is the recipient of several honors including National Metallurgist Award, Kuczynski Prize of IISS. Pradip is Fellow, Indian National Academy of Engineering (FNAE) and Fellow, Institute of Materials (FIMMM), UK. He is associate editor of International Journal of Mineral Processing, Bulletin of Materials Science and Transactions, Indian Institute of Metals. He has edited several special issues of international journals, the latest being the Special Issue of Ferroelectrics on Selected Topics in Advanced Materials Research (2004).



Beena Rai

Beena Rai is a research scientist at Tata Research Development and Design Centre, Pune, India. She received her Ph.D. in synthetic organic chemistry from the University of Pune in 1996. Her research interests are synthetic organic chemistry, colloids and surface science computational chemistry and nanotechnology. Recently, she has been working in the area of reagent design wherein molecular modeling techniques are used to design specialty chemicals for various industrial applications.



P. Sathish

Received a master degree in chemical engineering from Indian Institute of Science, Bangalore, India in 2002. Currently he is working as scientist at Tata Research Development and Design Centre, Pune, India. His research interests include adsorption of organics/polymers at the surfaces/interfaces, solid-solid/solid-liquid separations, colloidal processing, crystallization, nanotechnology and rheology of complex fluids. His focus is more towards applying molecular modeling techniques to study these processes.

Surface Structure and Photocatalytic Activity of Ti Supported on Alumina Powder[†]

Masayoshi Fuji^{*1}, Yoshio Sugiyama^{*2},
Takashi Takei^{*2}, Masatoshi Chikazawa^{*2},
Katsuyuki Tanabe^{*3}
and Kohei Mitsuhashi^{*3}

*Ceramics Research Laboratory, Nagoya Institute of
Technology^{*1}*

*Department of Applied Chemistry, Graduate School
of Engineering, Tokyo Metropolitan University^{*2}*

*Research and Development Center, Nittetsu Mining
Co. Ltd.^{*3}*

Abstract

Surface modified alumina powder that has photocatalytic activity was studied. To control the amount of Ti introduced on the surface at the molecular level, the powder was prepared by chemical surface modification with a monofunctional titanate-based coupling agent, followed by partial oxidation of the modification group. The surface density of Ti introduced onto the surface was quantitatively increased with the concentration of the modifying reagent, and/or repetition of the modification. Furthermore, the relationship between the surface structure and the occurrence of photocatalytic activity was examined. The surface structure was measured by XPS and UV-Visible absorption spectrometry. The photocatalytic activity was determined by measuring the degradation of Methylene Blue molecules in water solution with UV irradiation. Photocatalytic activity was realized at a Ti surface density of 3.7 nm^{-2} . The optical absorption edge in UV of the sample shifted to longer wavelengths. The ability as a photocatalyst increased with the amount of Ti-O-Ti. Photocatalytic activity was recognized to be related to the amount of Ti-O-Ti on the alumina surface and the ability of UV absorption.

Key words: Alumina powder, Photocatalyst, Photodegradation, Surface modification, Titanate-based coupling agent

1. Introduction

TiO₂ of anatase type is a typical photocatalyst that is capable of degrading contaminants with the aid of sunlight or artificial illumination without requiring demanding conditions such as high temperature or high pressure. For this reason, this substance is now expected to be used in diverse industrial fields¹⁾.

In particular, there is a strong demand for adoption of the substance to address environmental issues. Accordingly, many reports are available about its degradation mechanism with organic pollutants²⁻⁶⁾ and development of a highly active photocatalyst⁷⁻⁸⁾. For development of a highly active photocatalyst, much research about binary metal oxides has already been carried out. As early as 1985, Kakuta et al. reported that the photocatalytic activity of ZnS-CdS/SiO₂ excels in comparison to that of ZnS/SiO₂ or CdS/SiO₂ compounds⁹⁾. Recently, Anderson et al., Fu et al., Yu et al., Do et al. and Papp et al. have investigated the photocatalytic activity of TiO₂/SiO₂, TiO₂/Al₂O₃, TiO₂/ZrO₂, TiO₂/WO₃, and TiO₂/MoO₃ systems¹⁰⁻¹⁴⁾. These researchers demonstrated that enhanced photocatalytic activity is obtainable with a binary metal oxide system.

^{*1} Corresponding author
10-6-29, Asahigaoka, Tajimi, 507-0071, Japan
TEL: +81-572-27-6811 FAX: +81-572-27-9963
E-mail: fuji@nitech.ac.jp

[†] This report was originally printed in J. Soc. Powder Technology, Japan **39**, 102-107 (2002) in Japanese, before being translated into English by KONA Editorial Committee with the permission of the editorial committee of the Soc. Powder Technology, Japan.

Focusing on alumina as a base material, the authors researched the possibility of using it as a photocatalyst. Due to its basic characteristics, including high hardness, heat resistance and chemical resistance, alumina is commonly used as an industrial material. Expanding the functionality of this substance will produce much applicability of the substance. Anderson et al., in their research into $\text{TiO}_2/\text{Al}_2\text{O}_3$ photocatalysts prepared by a sol-gel process, reported on the effects of the $\text{TiO}_2:\text{Al}_2\text{O}_3$ ratio, TiO_2 region size within particles and adsorptivity on the photocatalytic activity of $\text{TiO}_2/\text{Al}_2\text{O}_3$ ¹⁰. Incidentally, the photocatalytic activity of binary metal oxides is strongly governed by the conditions of presence and surface structure of TiO_2 ; these two factors greatly affect whether or not TiO_2 can function as a photocatalyst. For $\text{TiO}_2/\text{SiO}_2$ systems, this tendency was studied with a CVD process¹⁵, an ion injection process¹⁶ and a surface modification process¹⁷. However, a similar study was still lacking for $\text{TiO}_2/\text{Al}_2\text{O}_3$ systems. To address this issue, the authors have attempted atomic level surface design for alumina powder by employing a surface modification processes in order to allow TiO_2 to be supported on Al_2O_3 ¹⁷⁻¹⁸. With this technique, the authors introduced Ti atoms onto the surface of alumina particles (the base material) to increase gradually Ti sites on the alumina particles, thereby transforming Al_2O_3 into a photocatalyst. XPS measurements, UV absorption edge measurements, and Methylene Blue degradation tests were measured to evaluate the properties of the prepared samples at every stage of the procedure. The relationship between the surface structure of the prepared samples, especially the Ti-supporting state, and the photocatalysis expression mechanism with the supported Ti was discussed.

2. Experimental

2.1 Sample preparation

Fine alumina powder (aluminum oxide C; Nippon Aerosil) was used as the base material, while the modifier used to introduce Ti was isopropyltriisostearoyl titanate $(\text{CH}_3)_2\text{CHO-Ti}(\text{OCOC}_{17}\text{H}_{35})_3$ (KEN-REACT KKR-TTS; Kenrich Petro-chemicals Co.). The molecule of this modifier includes three stearyl groups as hydrophobic side-chain organic functional groups and one hydrophilic hydrolytic degradable group. For this reason, the single modifier reacts with a hydroxyl group on the surface of the alumina particles without polymerization among modifiers. At the same time, owing to steric hindrance with the stearyl groups, individual Ti atoms appeared to exist on the surface

of the alumina particles, separated from each other at a regular specific distance between the atoms¹⁷⁻¹⁸. In order for these features to be utilized for accurate surface design of alumina powder, the authors chose the above-mentioned modifier.

Introduction of Ti was achieved through a process comprised of chemical surface modification and organic chain combustion by oxidation. First, alumina was added in a modifier solution using n-hexane (analytical grade; Kanto Kagaku) as a solvent, and then surface modification was performed through the reflux method to introduce the modifier group onto the surface of the alumina particles. Next, the sample was filtered off under increased pressure, rinsed with n-hexane, and oxidized by combustion with flowing oxygen to remove the organic chains (stearyl groups) in the modifier group. This process, comprised of chemical surface modification and organic chain combustion by oxidation, was taken as one modification procedure, and this procedure was repeated eight times in order to prepare nine samples that included one unmodified (original) alumina and eight alumina samples that underwent the modification procedure from one to eight times.

For surface modification, the saturation modification-capable conditions were investigated in advance, and 12 g of alumina powder and 12 g of modifier (at saturation modification conditions) were added to 830 mL of n-hexane and the mixture was refluxed for 1 hour at the boiling point of hexane. Pressure filtration and rinsing were performed with a membrane filter of pore diameter 0.1 μm (Type JV; Nihon Millipore) at a pressure of 5 kgf/cm². Note that the modified samples were thoroughly rinsed with hexane in order to remove any unreacted modifier (modifier that had been physically adsorbed). Combustion by oxidation was achieved in 10 hours at 450°C with oxygen supplied at a rate of 500 mL/min by an electric furnace (Super Burn; Motoyama). The removal of unreacted modifier by rinsing and burning of organic chains through combustion by oxidation is a particularly important step in ensuring accurate particle surface design. Therefore, the modification procedure was started only after determining the relevant requirements for the necessary rinsing thoroughness, and the temperature and duration of combustion. The necessary rinsing thoroughness was determined based on the trend in weight decrease of the modifier as a result of combustion by using the TG-DTA described below. The rinsing step was repeated until variation in the weight of the modifier was no longer detected and this was taken as the rinsing thorough-

ness point at which unreacted modifier was satisfactorily removed. Note also that combustion by oxidation was attempted only after determining the temperature and duration at which the organic chains in the modifier could be oxidized and removed, by adopting the FT-IR technique.

2.2 Evaluation of physical properties

For estimation of the introduced Ti on the prepared samples, TG-DTA (Thermo Plus; Rigaku Denki) was used. The samples that had not yet undergone combustion by oxidation were subjected to this test; thereby quantification was achieved based on the decrease in weight resulting from combustion of the organic chains. In addition, the physical properties of the samples were evaluated by subjecting the samples to specific surface area measurements, verification of structural variation by using XRD (MX Labo 2; Bunker AXS), observation of fine particle surfaces using TEM (JEM-2000FX; JEOL) analysis of the state of electrons on the surfaces of particles using XPS (ESCA3400; Shimadzu), UV absorption edge measurement, and evaluation for photocatalytic activity. Specific surface area measurement was performed by the nitrogen adsorption method using the GEMINI2360 (Shimadzu). The UV absorption edge of the samples was measured with a UV visible spectrophotometer (UV-3100C; Shimadzu) through diffuse reflectance spectroscopy. The photocatalyst function of the samples was evaluated based on their Methylene Blue (MB) degradation activity. The amount of Methylene Blue degraded was measured by using a UV visible spectrophotometer (U-3210; Hitachi), wherein 0.1 g of sample was added to 25 mL of aqueous Methylene Blue solution whose concentration was 2.0×10^{-5} mol/L. The mixture was irradiated with UV rays for 6 hours while being stirred. Then the solution was filtered off from the suspension and the degree of degradation was analyzed. For filtration of the suspension, a membrane filter of pore diameter 0.2 μm (Type LG; Nihon Millipore) was used. For irradiation with UV rays, two 6 W UV lamps (Black Light; Matsushita Electric Industrial Co., Ltd.) with wavelength ranges of 300 to 400 nm (peak wavelength 352 nm) were used.

3. Results

3.1 Determination of the amount of Ti introduced

Determination of the amount of Ti introduced is graphically plotted in **Figure 1**. As the modification

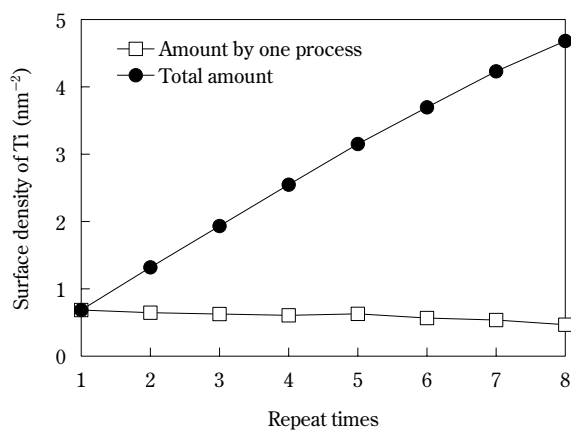


Fig. 1 The relationship between repetitions and surface density of Ti; \square indicates the amount from each process while \bullet is the total accumulated amount.

procedure of chemical surface modification and organic chain combustion by oxidation was repeated, roughly the same amount of Ti was introduced each repetition, although the amount introduced somewhat decreased as the number of repetitions increased. More specifically, an average of 0.6 atoms/nm² of Ti was introduced onto the alumina surface each modification procedure repetition, with a total of approximately 4.7 atoms/nm² of Ti introduced through eight repetitions. In summary, it was understood that the introduction of Ti atoms onto the surface of alumina particles can be quantitatively controlled.

3.2 Effect of transformation into a photocatalyst on surface and bulk structure

As a result of specific surface area measurements, it was understood that the BET specific surface area of untreated alumina powder was 107.8 m²/g, while that of the sample that underwent eight repetitions of the modification procedure was 108.6 m²/g. In other words, there was no significant change in the specific surface area due to transformation into a photocatalyst. In addition, from this result, it was also apparent that micro surface sintering (that is, change in the surface structure of alumina particles) did not occur as a result of the combustion by oxidation process at 450°C.

Next, the XRD patterns of each sample are illustrated in **Figure 2**. The crystal structure of the untreated sample consisted predominantly of δ -alumina. There was no significant variation in the XRD pattern among the samples, from the untreated one to the eight-repetition one. Consequently, it was understood

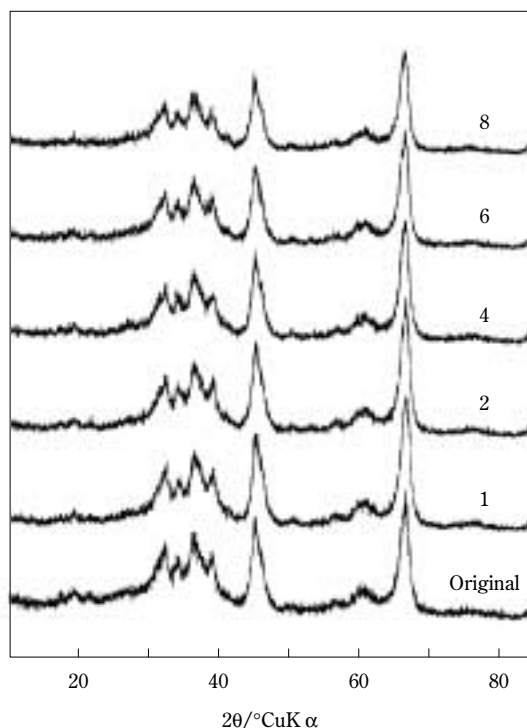


Fig. 2 X-ray diffraction patterns for original and modified alumina. The number is the number of repetitions.

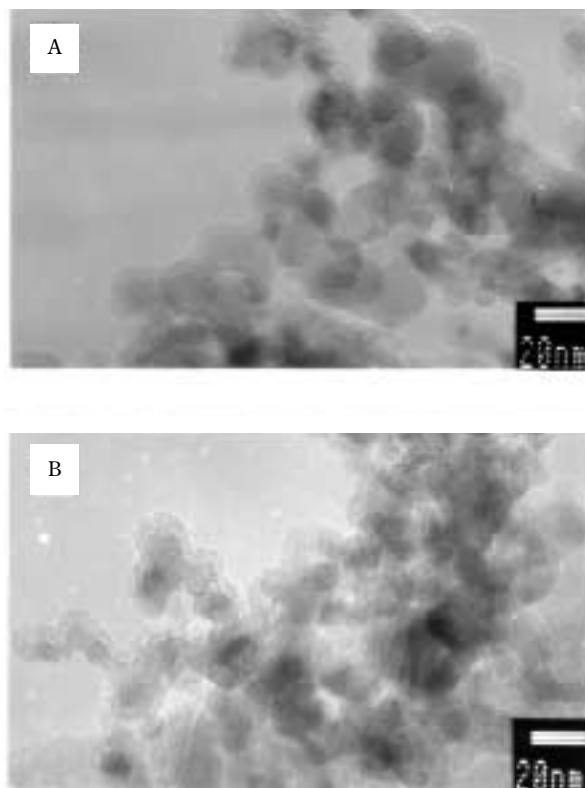


Fig. 3 TEM micrographs of samples: (A) original alumina and (B) modified alumina (Repeat times 8).

that repetition of the modification procedure does not significantly affect the crystallinity or crystal structure of the alumina. Incidentally, no XRD pattern associated with TiO_2 (anatase, rutile, brookite) was found.

TEM images of the untreated sample and the sample that underwent eight modification procedure repetitions are given in **Figures 3A** and **3B**, respectively. The primary particle diameter of the alumina powder measured from 10 to 20 nm. There was no significant difference in the diameter of primary particles between the unmodified and modified samples. In the appearance, the difference such that finer particles attached on modified alumina particles wasn't found between the unmodified and modified samples. In addition, no fine particles that appeared to be TiO_2 were observed on the modified samples.

The above results of specific surface area measurements, XRD measurements and TEM observations show that the proposed process of transformation into a photocatalyst test did not adversely affect the properties of the alumina as a base material.

3.3 Analysis of surface electron state by XPS

The $\text{Ti}2p$ and $\text{O}1s$ spectra for the samples are shown in **Figures 4A** and **4B**, respectively. The $\text{Ti}2p$

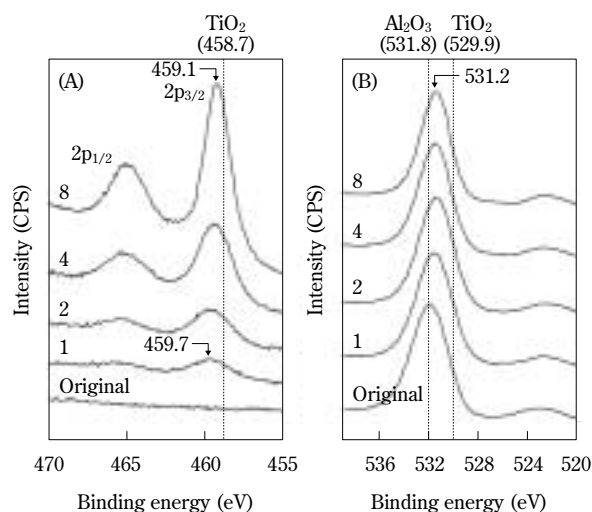


Fig. 4 X-ray photoelectron spectra of the repeatedly modified samples: (A) $\text{Ti}2p$ and (B) $\text{O}1s$. The number is the number of repetitions.

spectra in **Fig. 4A** shows that, as the modification procedure was repeated, the amount of introduced Ti increased and the peak shifted to a lower energy

level. For example, the $Ti2p_{3/2}$ peak of the sample that underwent modification once occurred at 459.7 (eV), while the peak of the sample that underwent modification eight times was at 459.1 (eV). From this finding it seems that repeated modification caused titanium oxide clusters to occur on the surface of alumina particles and the Ti to eventually take the oxidation state of TiO_2 ($Ti2p_{3/2}$; 458.7 eV)¹⁹.

Next, with the O1s spectrum for untreated Al_2O_3 in **Fig. 4B**, the peak belonging to O1s is present at 531.8 eV. As the number of repetitions of the modification procedure increased, the O1s peak shifted to a lower energy level. The O1s peak of the sample that underwent modification eight times is found at 531.2 eV. This peak shift seems to result from the emergence of O1s belonging to -Ti-O- that was formed by the modification procedures. In other words, it seems that the proportion of alumina at the surface decreased while the proportion of -Ti-O- increased, and that, as a result, the O1s peak shifted to the lower energy level of the O1s of TiO_2 (529.9 eV)¹⁹. In summary, because of being gradually covered with titanium oxide as the modification procedure was repeated, the surface of the alumina particles seemed increasingly to take on the surface state of TiO_2 .

3.4 Result of UV absorption edge measurement

The results of the measurements of the UV absorption edge are shown in **Figure 5**. Virtually no UV absorption was found with the untreated alumina. However, for the sample that underwent the modification procedure once, minor UV absorption was detected for shorter wavelengths, relative to the

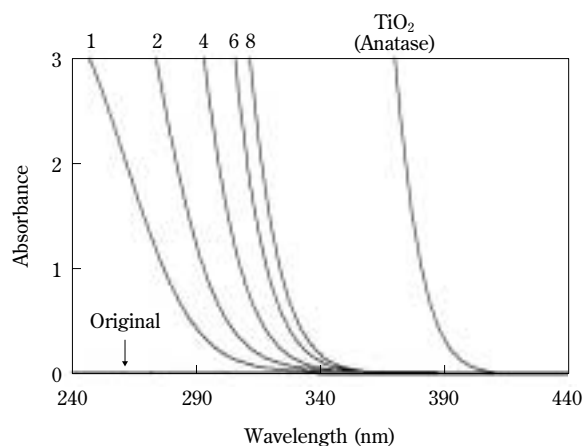


Fig. 5 Solid state diffuse reflectance the UV-VIS spectra of modified samples and Anatase. The number is the number of repetitions.

absorption of TiO_2 (anatase). As the number of repetitions of the modification procedure increased, the UV absorbance gradually increased and the UV absorption edge shifted to relatively longer wavelengths. The magnitude of the absorption edge shift per modification procedure repetition, however, decreased as the number of repetitions increased.

3.5 Evaluation of photocatalytic activity

Figure 6 shows the change of Methylene Blue concentration as an index of the photocatalytic activity. Decreases in Methylene Blue concentrations in the samples not irradiated with UV were from adsorption of Methylene Blue onto the surface of the samples. The amount of adsorption did not differ significantly between the unmodified sample and the samples subjected to the modification procedure for one to eight repetitions. Three possible causes for the decrease in Methylene Blue concentration in the samples not subjected to UV irradiation are adsorption, photocatalytic degradation, and direct degradation of Methylene Blue by normal UV exposure. As is clear in **Fig. 6**, among the samples irradiated with UV, those having undergone the modification procedure six or more times exhibited significant decreases in Methylene Blue concentration. As mentioned previously, there was no significant variation in the amount of adsorbed Methylene Blue, and the effectiveness of direct degradation of Methylene Blue by normal UV exposure appears to be constant regardless of whether the sample is modified or not. In summary, the authors have verified that photocatalytic action is achieved by repeating the modification procedure six or more

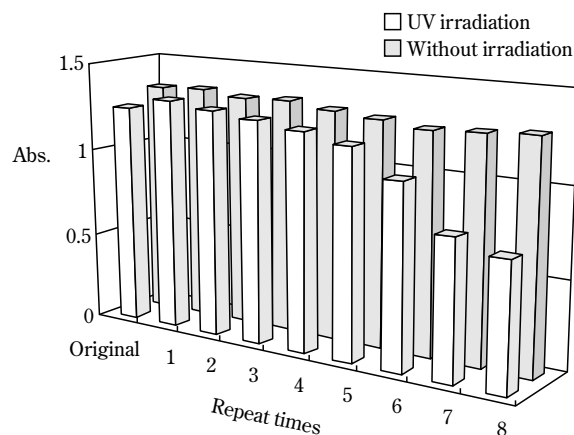


Fig. 6 Photocatalytic degradation and adsorption of MB in water using modified samples.

times under the authors' test conditions, resulting in the total introduction of at least 3.7 atoms/nm² Ti from the modification procedure repetitions. The photocatalytic action intensified as the Ti amount introduced increased.

4. Discussion

4.1 Change in alumina surface structure and hydroxyl group number

From the measurement results obtained with the Grignard reagent method²⁰, the number of hydroxyl groups on the surface of untreated alumina was approximately 7.07 groups/nm². It is apparent that a sufficiently large number of reaction sites were present compared with the number of Ti atoms (0.69 atoms/nm²) introduced as a result of the first modification procedure. From the feature of the proposed modification technique, every Ti atom appears to have been introduced onto the surface of alumina particles as a result of the first modification procedure, with the Ti atoms being spaced a specific regular distance apart from each other. Assuming that three hydroxyl groups occur on Ti atoms as a result of removal of organic chains by oxidation, the total number of hydroxyl groups on each alumina particle will increase by 1.38 groups/nm² because of the decrease in Al-OH groups and the formation of Ti-OH groups on the reaction sites. Accordingly, the number of hydroxyl groups is calculated as 7.07+1.38=8.45 groups/nm². Under this assumption, the number of Al-OH groups after the first modification procedure is 6.38 groups/nm² and the number of Ti-OH groups is 2.07 groups/nm², making the ratio of Al-OH groups to Ti-OH groups approximately 3:1. However, the measured value of the surface hydroxyl groups in the sample after the first modification procedure was 6.75 groups/nm². The presumed cause for why the number of surface hydroxyl groups in the sample after the first modification procedure was smaller than the calculated value is dehydration condensation between Al-OH and Al-OH as well as between Al-OH and Ti-OH.

As a result of the second modification procedure repetition onwards, the modifier was introduced not only to the existing Al-OH groups but also into the newly formed Ti-OH groups, thereby Ti-O-Ti bonds were formed. Apparently, the proportion of Ti-OH groups among the total number of surface hydroxyl groups increased and dehydration condensation occurred between Ti-OH and Ti-OH. Also, it is clear that the shift of O1s peak to a lower energy level, as

shown in **Fig. 4B**, resulted from the increase of Ti-O-Ti bonds formed in the above two ways.

4.2 Surface structure of modified alumina and mechanism of photocatalysis

Because the modifier groups are introduced to the hydroxyl groups on the surface of alumina particles as a result of the first modification procedure, the Al-O-Ti bonds occur on the surface of alumina particles. Hydroxyl groups appear to exist on the introduced Ti after combustion of organic chains. As a result of the second modification procedure repetition onwards, modifier groups are introduced to the hydroxyl groups remaining on the surface of alumina particles and to the hydroxyl groups on the introduced Ti. Consequently, not only Al-O-Ti bonds but also Ti-O-Ti bonds seem to be formed. Note that Ti-O-Ti bonds are also formed as a result of dehydration condensation of hydroxyl groups on Ti. However, as described earlier, because each Ti atom is introduced separated from other Ti atoms at a specific distance as a result of the first modification procedure, the hydroxyl groups on each Ti do not seem to dehydrate and form Ti-O-Ti bonds. Ti-O-Ti bonds seem to have formed from repetition of the modification procedure, as well as through the growth of the so-formed Ti-O-Ti bonds, and this caused the UV absorption edge to shift to the red end of the spectrum. The expansion of the range of absorbable wavelengths resulting from this "red shift" of the UV absorption edge appears to contribute to the expression of photocatalytic activity.

5. Conclusion

The procedure to introduce Ti onto the surface of alumina particles with their surface modification technique was investigated. The surface structure, physical properties, and the photocatalytic activity of the prepared samples were discussed, and reached the following conclusions:

- 1) Introduction of Ti onto the surface of alumina particles by surface modification techniques can be quantitatively controlled with the concentration of the modifier and/or the number of modification procedure repetitions.
- 2) The process for transformation into a photocatalyst (chemical surface modification and organic chain combustion by oxidation) does not significantly affect the bulk structure and characteristics of alumina.
- 3) As the modification procedure was repeated, Ti-O-Ti bonds occurred on the surface of alumina particles, and, at the same time, the UV absorption made

red shift. The oxidation state of Ti seemed to resemble that of the Ti in titanium oxide.

4) By introducing a total of 3.7 atoms/nm² Ti with six modification procedure repetitions, the alumina achieved photocatalytic activity. It was considered that the appearance of photocatalytic activity related with the increased amount of photons being absorbed due to the shift of the absorption edge to the red.

Appendix

Several interesting results were found out after the related studies have been done. Here, I introduce a few of them as a supplement. Two kinds of photocatalyst based on CaCO₃ and SiO₂ were prepared using the same procedure of Al₂O₃ as I mentioned in this paper. One of the studies, photocatalyst based on CaCO₃ showed almost the same results of Al₂O₃, in other word, the photocatalytic activity appeared after the formation of titania-like layer on the surface of CaCO₃. On the other hand, the result of photocatalyst based on SiO₂ was totally different from that of Al₂O₃ and CaCO₃. Although the sample treated by only one procedure had no Ti-O-Ti structures but Si-O-Ti structures, photocatalytic activity was occurred on the sample of SiO₂. A similar result was also obtained from other silicate materials.

References

- Ollis, D. F., E. Pelizzetti and N. Serpone: "Photocatalyzed destruction of water/contaminants," *Environ. Sci. Technol.*, **25**, 1523-1529 (1991).
- Chuang, C., C. Chen and J. Lin: "Photochemistry of Methanol and Methoxy Groups Adsorbed on Powdered TiO₂," *J. Phys. Chem. B*, **103**, 2439-2444 (1999).
- Muggli, D. S., J. T. McCue and J. L. Falconer: "Mechanism of the Photocatalytic Oxidation of Ethanol on TiO₂," *J. Catal.*, **173**, 470-483 (1998).
- Zhuang, J., C. N. Rusu and J. T. Yates: "Adsorption and Photooxidation of CH₃CN on TiO₂," *J. Phys. Chem. B*, **103**, 6957-6967 (1999).
- Ferry, J. L. and W. H. Glaze: "Photocatalytic Reduction of Nitroorganics over Illuminated Titanium Dioxide: Role of the TiO₂ Surface," *Langmuir*, **14**, 3551-3555 (1998).
- O'Shea K. E., S. Beightol, I. Garcia, M. Aguilar, D. V. Kalen and W. J. Cooper: "Photocatalytic decomposition of organophosphonates in irradiated TiO₂ suspensions," *J. Photochem. Photobiol. A: Chem.*, **107**, 221-226 (1997).
- Kosuge, K. and P. S. Singh: "Synthesis of Ti-containing Porous Silica with High Photocatalytic Activity," *Chem. Lett.*, **1**, 9-10 (1999).
- Kominani, H., S. Murakami, Y. Kera and B. Ohtani: "Titanium (IV) Oxide Photocatalyst of Ultra-High Activity: A New Preparation Process Allowing Compatibility of High Adsorptivity and Low Electron-Hole Recombination Probability," *Catal. Lett.*, **56**, (2, 3), 125-129 (1998).
- Kakuta, N., K. H. Park, M. F. Finlayson, A. Ueno, A. J. Bard, A. Campion, M. A. Fox, S. E. Webber and J. M. White: "Photoassisted Hydrogen Production Using Visible Light and Coprecipitated ZnS-CdS without a Noble Metal," *J. Phys. Chem.*, **89**, 732-734 (1985).
- Anderson, C. and A. J. Bird: "Improved Photocatalytic Activity and Characterization of Mixed TiO₂/SiO₂ and TiO₂/Al₂O₃ Materials," *J. Phys. Chem. B*, **101**, 2611-2616 (1997).
- Fu, X., L. A. Clark, Q. Yang and M. A. Anderson: "The Enhanced Photocatalytic Performance of Titania-Based Binary Metal Oxides: TiO₂/SiO₂/ZrO₂," *Environ. Sci. Technol.*, **30**, 647-653 (1996).
- Yu, J. C., J. Lin and R. W. M. Kwok: "Ti_{1-x}Zr_xO₂ Solid Solutions for the Photocatalytic Degradation of Acetone in Air," *J. Phys. Chem. B*, **102**, 5094-5098 (1998).
- Do, Y. R., W. Lee, K. Dwight and A. Wold: "The Effect of WO₃ on the Photocatalytic Activity of TiO₂," *J. Solid State Chem.*, **108**, 198-201 (1994).
- Papp, J., S. Soled, K. Dwight and A. Wold: "Surface Acidity and Photocatalytic Activity of TiO₂, WO₃/TiO₂, and MoO₃/TiO₂ Photocatalysts," *Chem. Mater.*, **6**, 496-500 (1994).
- Anpo, M., N. Aikawa, Y. Kubokawa, M. Che, C. Louis, and E. Giamello: "Photoluminescence and Photocatalytic Activity of Highly Dispersed Titanium Oxide Anchored onto Porous Vycor Glass," *J. Phys. Chem.*, **89**, 5017-5021 (1985).
- Yamashita, H., M. Honda, M. Harada, Y. Ichihashi, M. Anpo, T. Hirao, N. Itoh and N. Iwamoto: "Preparation of Titanium Oxide Photocatalysts Anchored on Porous Silica Glass a Metal Ion-Implantation Method and Their Photocatalytic Reactivities for Degradation of 2-Propanol Diluted in Water," *J. Phys. Chem. B*, **102**, 10707-10711 (1998).
- Fuji, M., N. Maruzuka, T. Takei, T. Watanabe, M. Chikazawa, K. Tanabe and K. Mitsunashi: "Surface properties and photoactivity of silica prepared by surface modification," *Studies in Surface Science and Catalysis*, **132**, 853-856 (2000).
- Fuji, M., N. Maruzuka, J. Yoshimori, T. Takei, T. Watanabe, M. Chikazawa, K. Tanabe and K. Mitsunashi: "Surface Active Sites Introduced onto Calcium Carbonate Powder by a New Preparation Process," *Adv. Powder Technol.*, **11**, (2), 199-210 (2000).
- Wang, R., N. Sasaki, A. Fujishima, T. Watanabe and K. Hashimoto: "Studies of Surface Wettability Conversion on TiO₂ Single-Crystal Surfaces," *J. Phys. Chem. B*, **103**, 2188-2194 (1999).
- Morimoto, T and H. Naono: "Water Content on Metal Oxides. I. Water Content on Silica Gel, Magnesium Oxide, Zinc Oxide, and Titanium Dioxide," *Bulletin of the Chemical Society of Japan*, **46**, (7), 2000-2003 (1973).

Author's short biography



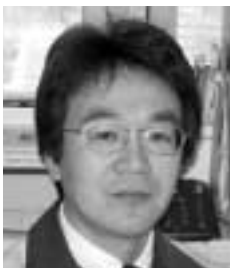
Masayoshi Fuji

Masayoshi Fuji is Associate Professor of Ceramics Research Laboratory, Nagoya Institute of Technology, Gifu. A graduate of Tokyo Metropolitan University, he received his B.S. from the Dept. of Industrial Chemistry in 1989, his M.S. from the Faculty of Engineering in 1991, and his Dr. Eng. from the Faculty of Engineering in 1999. He joined the Department of Industrial Chemistry, Tokyo Metropolitan University, as a Research Associate in 1991. He was Visiting Researcher at Engineering Research Center, University of Florida from 2000 to 2001. He joined Nagoya Institute of Technology since 2002. His research interests are surface chemistry, ceramic processing and powder technology.



Yoshio Sugiyama

Yoshio Sugiyama received his B.E. from the Dept. of Industrial chemistry in 2000, his M.E. from the Faculty of Engineering in 2002 at Tokyo Metropolitan University. After graduating, he began working at Technology Development Center, Toyota Industries Corporation.



Takashi Takei

Takashi Takei is Associate Professor in the Faculty of Engineering of Tokyo Metropolitan University. A graduate of Tokyo Metropolitan University, he received his B.S. from the Dept. of Industrial Chemistry in 1981, his M.S. from the Faculty of Engineering in 1983. He worked in the Central Research Laboratory of Nissan Chemical Industry, Co. Ltd from 1983 to 1986. He received his Doctor of Engineering in 2001 from Tokyo Metropolitan University. He joined the Dept. of Industrial Chemistry, Tokyo Metropolitan University, as a Research Associate in 1987. His research includes preparation and surface chemistry of nano-particles and nanoporous materials.



Masatoshi Chikazawa

Masatoshi Chikazawa is Honorary Professor in Tokyo Metropolitan University. A graduate of Nagoya Institute Technology, he received his B.S. from the Dept. of Industrial Chemistry in 1965, his M.S. from the Faculty of Engineering in 1967. He received his Doctor of Engineering in 1978 from Tokyo Metropolitan University. In 1986, he was promoted Professor in the Faculty of Engineering of Tokyo Metropolitan University. He received the 1983 Jotaki Award of the Society of Powder Technology, Japan. He was involved in research including chemistry of powder surfaces, surface modification of powder particles, adhesion and aggregation of particles.

Author's short biography



Katsuyuki Tanabe

Katsuyuki Tanabe is a manager of Resource Materials Development Section at Nittetsu Mining Co., Ltd. He received his B.S. from Institute of Earth Sciences, School of Education, Waseda University in 1979, and his M.S. from Department of Earth Sciences, Chiba University in 1981. His interest for research and development now is powder technology.



Kohei Mitsuhashi

Kohei Mitsuhashi is an engineer at Nittetsu Mining Co., Ltd. He received his B.S. from Department of Earth Sciences, School of Education, Waseda University in 1995, and his M.S. from Department of Resources Engineering, Graduate School of Science and Engineering, Waseda University in 1997.

Effects of Oxidization and Adsorbed Moisture on Time Change in Tribo-electrification of Powder Particles[†]

Hiroaki Masuda

*Dept. of Chem. Eng., Kyoto Univ.**

Daisuke Yasuda

Mitsubishi Rayon Co., Ltd.

Akihiko Ema

Nisshin Engineering Co., Ltd.

Ken-ichiro Tanoue

*Dept. of Mech. Eng., Yamaguchi Univ.***

Abstract

Tribo-electrification between aluminum target and glass beads has been studied experimentally based on the current generated by the electrification of glass beads. Effect of tangential velocity of impact on the current is investigated. As far as the velocity is low enough, the current shows positive value. However, for higher velocity, the current changes from positive to negative as the time elapses. Sudden increase or decrease in the velocity gives a respective current corresponding to each velocity. The fact means that the polarity of the current is solely determined by the tangential velocity as far as the target is not exchanged. Preservation conditions of the metal target affect on the polarity of the current. If the target is preserved in atmospheric condition for a day, positive current is generated firstly, decreased with time elapsed and finally negative current is generated. Two different experiments support that the polarity change found in this study is not related to the surface oxidization. Effect of water molecules adsorbed on the target surface has been investigated through heat treatment of the target. Higher temperature of the treatment causes the sharper decrease in the initial current, which suggests that the water molecules adsorbed on the target surface causes the change in the polarity of the tribo-electrification. Contact potential difference between particles and target also changes by heat treatment of the target.

Key words: Tribo-electrification, Time change, Adsorbed moisture, Oxidization, Heat treatment

1. Introduction

Particles in powder handling processes usually contact the wall of equipment and rebounding from it.

During these contacting and rebounding, charge transfer takes place between the particles and the wall surface. This brings about electrification of particles and may sometimes cause troubles such as dust explosion, deposition or blockage of pipelines and so on. On the other hand, electrically charged powders are utilized effectively in modern processes such as in electro-photography and electrostatic powder coating [1].

Influences of many factors on tribo-electrification, such as contact potential difference (or work functions) between metal target and particle [2-3], contact area (which depends on particle size, impact velocity) [4-5], relative humidity [5], condition of surface properties [4], have been investigated.

In our previous reports [6-7], effect of the tangen-

* Katura, Nishikyo-ku, Kyoto 615-8510

Tel: 075-383-2665

Fax: 075-383-2655

**corresponding author

Tel: 0836-85-9122

Fax: 0836-85-9101

E-Mail: tano@yamaguchi-u.ac.jp

[†] This report was originally printed in J. Soc. Powder Technology, Japan, **40**, 860-867 (2003) in Japanese, before being translated into English by KONA Editorial Committee with the permission of the editorial committee of the Soc. Powder Technology, Japan.

tial component of impact velocity on the tribo-electrification was investigated using a rotating metal target system. Ema et al. were able to study the tribo-electrification in a wide range of impact angle from 0 to 88° by using the system. The result showed that tribo-charge had a maximum value at a certain impact angle. In order to explain this phenomenon, we have suggested a model from the viewpoint of the effective contact area in charge transfer. This model includes the rolling and the slipping of the particle on the metal target. In the experiments, polarity of the tribo-electrification did not change even if the charge decreases with time elapsed.

Moreover, there were some reports that a polarity of the tribo-electrification was changed by experimental conditions. Commonly, it seems that the polarity is decided by the contact potential difference [2-3]. Nifuku et. al. reported that the change of the polarity occurred if particulate coal introduced into brass pipe over certain air velocity. [8] Masuda et. al. reported that the polarity of tribo-electrification between morundum and some metal plates (iron or nickel) was changed with time elapsed. [9] However, the phenomenon of the polarity change has not been investigated minutely.

In this report, effects of oxidization, preservation ways of the metal target and adsorbed moisture, on the change in the polarity of the tribo-electrification have been investigated. Contact potential differences (CPD) between the various targets and particles are measured. Furthermore, relationship between the CPD and the change in the polarity is investigated.

2. Experimental apparatus and procedure

Figure 1 shows an experimental set-up. Particles are stored in a hopper, which is made of glass in order to reduce initial charge of particles. For $t > 0$, the particles fall through an orifice that is settled at the hopper exit. An ejector having a decompression part is joined with air supplied line. The particles are introduced into the decompression part through a glass funnel and gas-solids two phase flow is generated. The particles in the flow impact on a rotating metal target that causes the charge transfer. The current generated is measured by a digital electrometer (TR8652; Advantest) and recorded in a memory of a personal computer. Metal target is rotated by a motor (SC-VS; Matsushita Electric Industrial Co., Ltd.). The number of revolutions per minute $n (=60\omega/2\pi)$ of the metal target is measured by a tachometer (POCKET TACHOMETER MOEL 3632; Yokogawa Electric Cor-

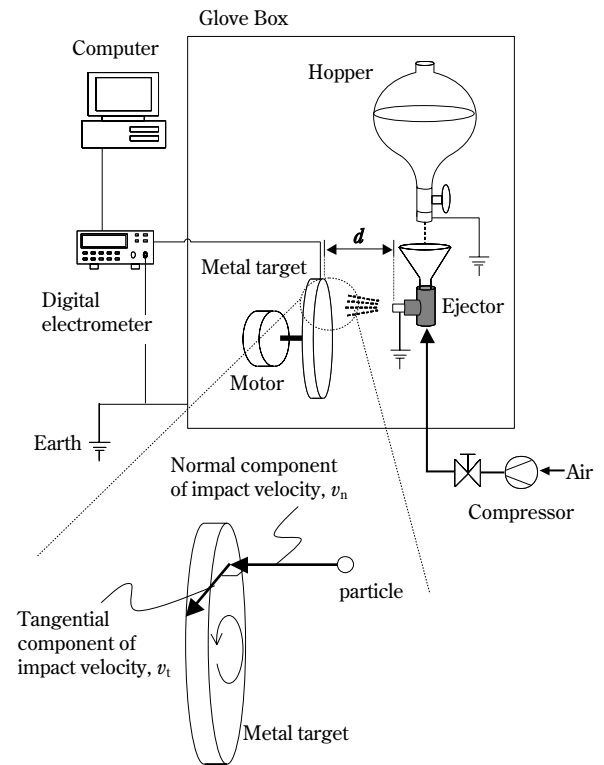


Fig. 1 Experimental apparatus for tribo-electrification between glass beads and rotating metal target.

poration). Both of the hopper and the motor with metal target are set in a glove box and enveloped in a grounded metal wire-net in order to avoid noises. The current caused by noises is less than about $1 \times 10^{-11} \text{A}$ in this experiment. The particles used are glass beads. The mass median diameter D_{P50} of them is $550 \mu\text{m}$. Before the experiments, metal bins with particles are reserved in an auto-desiccator. In order to decrease the initial charge of particles, grounded wires are introduced into the bins. The target is made of aluminum plate with $D_T = 120 \text{mm}$ in diameter and $\delta = 0.5 \text{mm}$ or 1mm in thickness. Preliminary examinations revealed that the generated current hardly change for $0.5 < \delta < 1 \text{mm}$. The target is fixed on an electric insulator made of PMMA (poly methyl methacrylate) in order to prevent current leakage to the motor shaft. The physical properties of the glass beads and the aluminum target are shown in **Table 1**. Particle velocity is measured through particle trajectories obtained using a high-speed camera (FAST-CAM - Net C; PHOTRON). Other experimental conditions are shown in **Table 2**.

Table 1 Physical properties of glass beads and Al-plate

		glass beads	Al-plate
D_{p50}	(μm)	220	–
δ	(mm)	–	0.5, 1.0
ρ	(kg/m^3)	2710	2500
$V_{C/Au}$	(V)	0.16	0.94
T_m	($^{\circ}\text{C}$)	730	659

Table 2 Experimental conditions

T	($^{\circ}\text{C}$)	21~22
φ	(%)	33~63
W	(g/s)	1.12
D_T	(cm)	12
r	(cm)	5 ± 0.5
d	(cm)	2.0
n	(rpm)	0~8000
ΔP	(MPa)	0.4

3. Theory and definition of impact velocity

From conservation law of charge, an electrical current from the metal target to the earth, I , is given by [10]

$$I = -\frac{W}{m_p} \Delta q \quad (1)$$

where W and m_p are mass flow rate of particles and mass of a particle, respectively.

Transferred charge by impact of a particle on a metal target, Δq ($=q_a - q_0$), is given by [10]

$$\Delta q = C V_{P/M} S_{\text{eff}} \quad (2)$$

where C , $V_{P/M}$ and S_{eff} are a proportional constant in charge transfer, the contact potential difference between the particle surface and the metal target surface and the effective contact area in charge transfer [4-7], respectively. Tangential component of impact velocity is changed by rotational speed, n , of metal target. Impact velocity, v_0 , and tangential component of the velocity, v_{t0} , are given by,

$$v_0 = \sqrt{v_{n0}^2 + v_{t0}^2} \quad (3)$$

$$v_{t0} = 2\pi r \omega \quad (4)$$

where r and ω are the distance from the rotating

metal target center to the impact point of particles and the rotational speed of metal target, respectively.

4. Results and discussion

4.1 Effect of tangential component of impact velocity on tribo-electrification

Figure 2 shows current generated by particles impacting on a rotating metal target as a function of time elapsed under various rotational speeds. In the experiments, tangential component of impact velocity changes from 0 to 31.4m/s. Normal component of impact velocity v_{n0} is 6m/s. The current generated decreases with time and approaches a constant value. The more the tangential component of impact velocity is, the faster the decrease in the current. The current approaches to a negative constant value for $n > 4000\text{rpm}$ ($v_{t0} > 21\text{m/s}$) while the polarity of current keeps positive for $n < 4000\text{rpm}$.

In this report, the cause why the polarity changes with increasing the tangential component of impact velocity is investigated through; a) change in the current under quick change in the tangential component of the impact velocity, b) change in the current by preservation ways of target, c) effect of adsorbed moisture, and d) contact potential difference.

4.2 Change in polarity of current generated by particles impacting on a rotating metal target

4.2.1 current under quick change in tangential component of impact velocity

It was reported that the current was changed by contamination of target with particle-component,

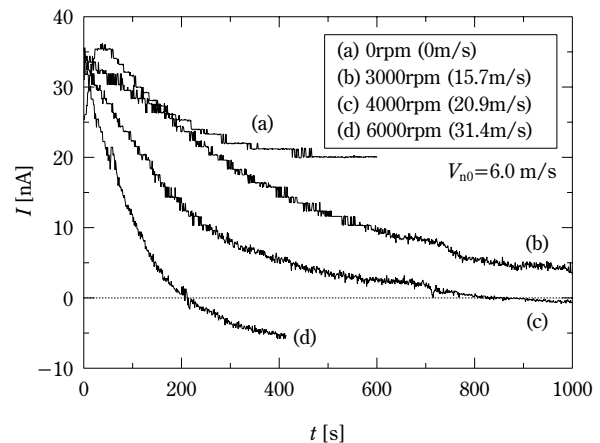


Fig. 2 Change in current generated by particles impacting on a rotating metal target as a function of time elapsed under various tangential velocities of impact. ($T=21^{\circ}\text{C}$, $\varphi=49\%$)

roughness of target-surface and hardness of target [4-5]. After the particles impact on the target with enough time (for example, 10minutes), state of the target surface hardly changes.

If the change in the polarity of the current is caused only by the above phenomena, the polarity seems not to be changed by the quick exchange of rotational speed. The examined results are shown in **Figure 3**. After the particles impact on the target for about 10min, the rotational speed of the target is changed into another speed in stepwise. **Fig. 3a** shows the current where the rotational speed of the target is changed from $n=6000\text{rpm}$ ($v_{t0}=31.4\text{m/s}$) to $n=3000\text{rpm}$ ($v_{t0}=15.7\text{m/s}$) at about $t=700\text{s}$. The negative current increases dramatically to the positive one as soon as the speed is changed. On the other hand, in **Fig. 3b**, positive current decreases dramatically to

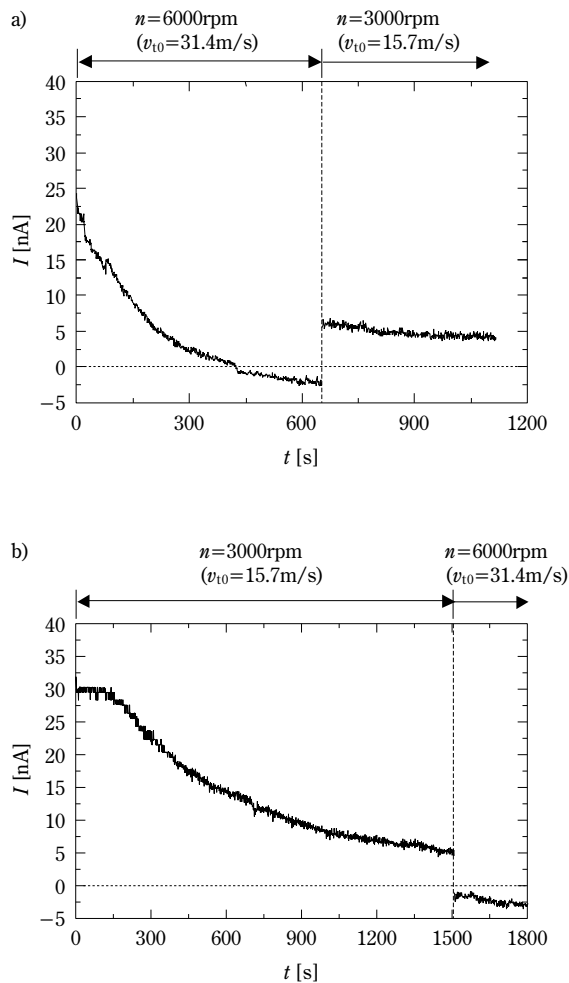


Fig. 3 Change in current generated by particles impacting on a rotating metal target with sudden change in tangential velocity. ($T=22^\circ\text{C}$, $\phi=63\%$)

the negative value as soon as the speed is increased from $n=3000\text{rpm}$ to $n=6000\text{rpm}$. Therefore, the polarity change of the current depends not on the condition of the target surface such as contamination, surface roughness and hardness [4-5] but strongly on the rotational speed.

4.2.2 Effects of preservation ways of target on a polarity of the current

Masuda et al. reported that the current generated by a brass target, which was reserved in normal atmosphere for a day after impacted by particles, returned to the value generated by a virgin brass target [9].

Here the effects of preservation of target on a polarity of the current are investigated. The particles impact on the aluminum target at $n=6000\text{rpm}$ ($v_{t0}=31.4\text{m/s}$) for 1000s and then the target is reserved in the atmospheric condition for a day. After that the particles impact again on the target at $n=6000\text{rpm}$. The result is shown in **Figure 4**. By reserving the target in the atmosphere for a day, the original negative current changes to the positive one. The fact means the state of the target surface changes gradually for a day and then the polarity of the current returns to that of the virgin one. It seems that the target surface in the atmosphere may be changed through chemical reaction, formation of oxidized film, or adsorption of moisture content.

In order to investigate the effect of the oxidized film on the polarity, the target is oxidized in dilute sulfuric acid after the particles impact on it for 10min. Concentration of the sulfuric acid is about 30wt%. The current is measured again by the particles impacting on

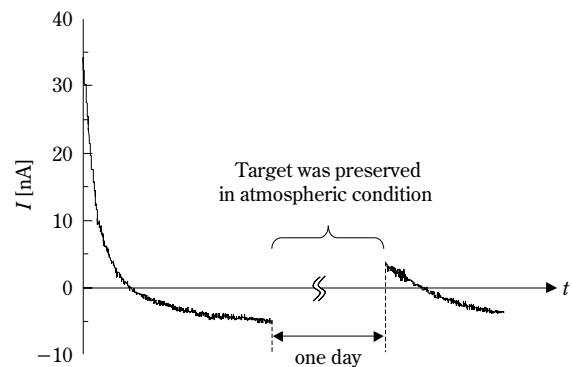


Fig. 4 Effect of preservation of a metal target on current generated as a function of time elapsed. Target was preserved in atmospheric condition for a day. ($T=21^\circ\text{C}$, $\phi=57\%$, $n=6000\text{rpm}$, $v_{t0}=31.4\text{m/s}$)

the target with oxidized film. The result is shown in **Figure 5**. The current hardly changes even if the target is oxidized. By a tester measurement, electric resistance of the target before oxidization is almost 0 while the resistance of the target with oxidized film is infinity. Namely, although the resistance of the surface differs drastically with and without oxidization film, the current hardly changes. Oxidized film of the target hardly affects on the change in the polarity of the current.

In order to investigate the effect of the chemical reactions between the target surface and gaseous contents in the atmosphere on the polarity of the current, the target is reserved in vacuum chamber with silica gels for a day after the particles impact on the target. The result is shown in **Figure 6**. In this case, the polarity of the current does not change as seen in the case that shown in **Fig. 4**, but the current holds negative value as the case shown in **Fig. 5**. Namely the change in the polarity does not occur for the target reserved in the vacuum chamber.

Therefore, contents of adsorbed moisture on the target seem to affect the current on the polarity change seen in **Fig. 4**.

4.2.3 Effect of adsorbed moisture on the current

It seems that there are two contents of adsorbed moisture on the target in the experiments. One is the surface water which depends on environmental conditions. The other is the crystal water that is adsorbed in the surface of the target. In this section, effect of the moisture contents on the polarity of the current is investigated. Virgin target is heated by a furnace (Drying Oven DX41; Yamato Co. Ltd.) at a certain temperature T_h , $50 < T_h [^{\circ}\text{C}] < 250$, for a certain time t_h , $1 < t_h [\text{hr}] < 70$.

Changes in the current with time are measured using three targets; a) without heat treatment, b) with heat treatment ($T_h=150^{\circ}\text{C}$, $t_h=24\text{hr}$) and c) with heat treatment under higher temperature ($T_h=250^{\circ}\text{C}$, $t_h=24\text{hr}$). The results are shown in **Figure 7**. The target is heated in the furnace at certain time and cooled for about 5minutes in the vacuum chamber. After that it is set on the motor and then the particles impact on it. For target without heat treatment in **Fig. 7a**, the current decreases with time elapsed. On the other hand, for targets with heat treatment in **Fig. 7b** and **c**, the currents at $t=0$ have negative values and hardly change with time. An initial current I_0 changes with heating temperature T_h . In these experiments, the current approaches to an almost the same constant value with time elapsed.

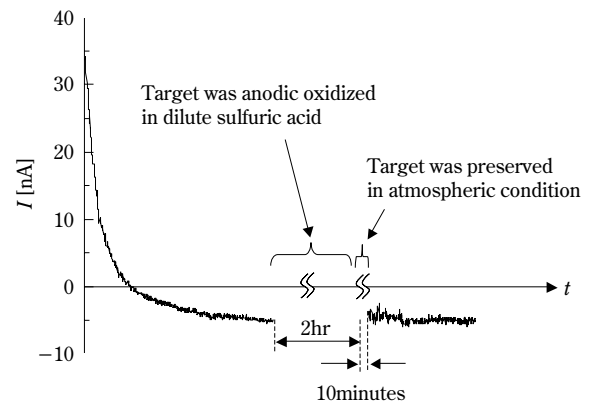


Fig. 5 Effect of anodic oxidation of a metal target in dilute sulfuric acid on current generated as a function of time elapsed. ($T=21^{\circ}\text{C}$, $\phi=57\%$, $n=6000\text{rpm}$, $v_{i0}=31.4\text{m/s}$)

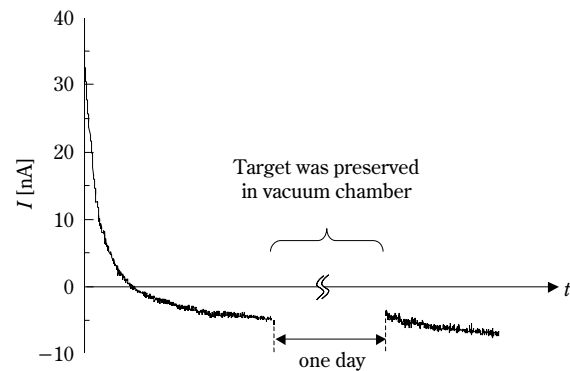


Fig. 6 Effect of preservation of a metal target on current generated with time elapsed. Target was preserved in vacuum chamber for a day. ($T=21^{\circ}\text{C}$, $\phi=57\%$, $n=6000\text{rpm}$, $v_{i0}=31.4\text{m/s}$)

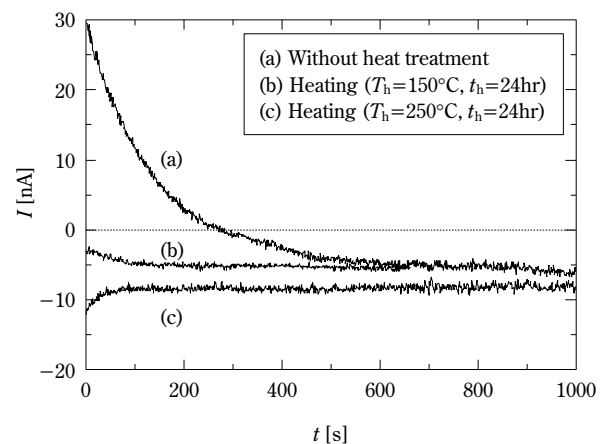


Fig. 7 Effect of heating-up of a metal target on current generated as a function of time elapsed. ($T=21^{\circ}\text{C}$, $\phi=42\sim 46\%$, $n=6000\text{rpm}$, $v_{i0}=31.4\text{m/s}$)

Figure 8 shows change in the initial current for various heating temperature T_h and various heating time t_h . For $T_h=50^\circ\text{C}$, the initial current I_0 hardly changes with any heating times. On the other hands, for $T_h=100, 150, 250^\circ\text{C}$, the initial current I_0 decreases with increasing heating time t_h and then approaches to respective constant value. The initial current decreases with heating temperature and changes from positive value to negative one for $T_h > 150^\circ\text{C}$ and certain heating time t_h^* . Therefore, it suggests that a factor, which changes the polarity of the current, is the decrease in moisture contents (surface water or crystal water) on the target surface.

In order to investigate the effect of heat treatment of the target on the moisture contents, the targets on which the particles impacted are reserved by the following three ways; a) preservation in the atmosphere for 5minutes, b) preservation in the atmosphere for 24hours, c) preservation in distilled water. Before the preservation, the targets are heated at $T_h=250^\circ\text{C}$ for 24hours. For the way c), the heated target reserved in the distilled water is pulled out from the water and dried in the atmosphere for a few minutes. The experiment of particle-impact is conducted using the target on which there are no water drops apparently. The results are shown in **Figure 9**. For the preservation way b), the initial current at $t=0$ has negative value. Absolute value of the current at $t=0$ for the way b) is smaller than that for the way a). It seems that water molecules in the atmosphere are adsorbed on the target surface during 24hour preservation. As for the

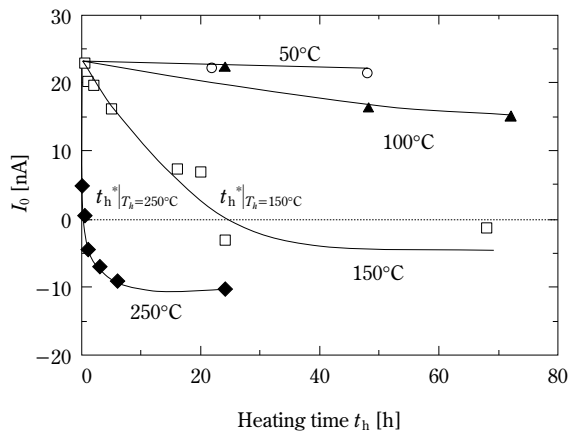


Fig. 8 Influence of heating time on initial current generated by particles impacting on a rotating metal target under various heating temperatures. ($T=21^\circ\text{C}$, $\varphi=33\sim 52\%$, $n=6000\text{rpm}$, $v_{t0}=31.4\text{m/s}$)

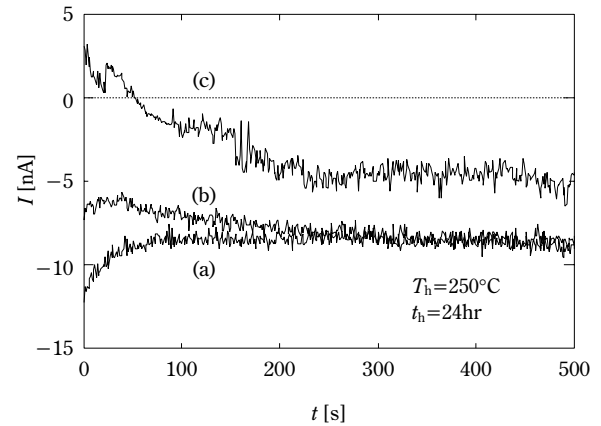


Fig. 9 Change in current generated by impact particles on a rotating metal target with time elapsed for various preserved conditions. ($T=21^\circ\text{C}$, $\varphi=46\%$, $n=6000\text{rpm}$, $v_{t0}=31.4\text{m/s}$) a) Heating only, b) Heating and then preservation in atmospheric condition ($T_a=19.5^\circ\text{C}$, 24hr), c) Heating and then preservation in water ($T_w=25^\circ\text{C}$, 24hr)

experimental result shown in **Fig. 4**, it seems that there are both surface water and crystal one, because a part of the crystal water is remained on the target surface under no heat treatment. On the other hand, there is little crystal water on the target surface for the preservation way b) under the heat treatment in **Fig. 9**. Therefore, the current b) in **Fig. 9** holds the negative value while the current in **Fig. 4** changes from positive to negative. For the preservation way c), the initial current I_0 has positive value because there seems to be crystal water on the target surface again through the dipping into the distilled water.

It suggests that there is a little crystal water, which affects on the change in the polarity of the tribo-electrification, on the target surface. Measurement of crystal water on the target surface is conducted using a Karl Fischer's measuring machine (KYOTO ELECTRONICS MANUFACTURING CO., LTD; MKA-510N). However, the water content is too small to be detected. It needs another method to measure such a small amount of water.

4.2.4 Effect of contact potential differences on current

The contact potential difference (CPD) has been suggested as an index of tribo-electrification [2-3]. From Eqs. (1) and (2), the current is proportional to the CPD. It seems that polarity of the contact potential differences will be one of the causes for the polarity change of the current. The contact potential differences between gold plate and the following

three targets are measured by a contact potential difference measuring machine [2-3]; a) a target without heat treatment, b) a target with heat treatment ($T_h=100^\circ\text{C}$, $t_h=72\text{hr}$) and c) a target with heat treatment under higher temperature ($T_h=250^\circ\text{C}$, $t_h=24\text{hr}$). The results are shown in **Table 3**. In these experiments, the CPD between gold plate and glass beads $V_{P/Au}$ is 0.16 V. The contact potential difference between a metal plate and particles is given by,

$$V_{P/M} = V_{P/Au} - V_{M/Au} \quad (5)$$

CPD values $V_{P/M}$ are also listed in the **Table 3**. Absolute value of CPD decreases with the heat treatment of the target. In other words, it has a tendency that the CPD approaches to the positive value by the heat treatment. However, the polarity of CPD does not change under the heat treatment and the polarity change of the current can not be explained solely by the CPD. As a possible reason for the polarity change, slip of particles on the target surface and resulting local temperature increase may be suggested here.

Table 3 Contact potential difference between target and Au

	$V_{M/Au}$ (V)	$V_{P/M}$ (V)
a: Target without heat treatment	0.94	-0.78
b: $T_h=100^\circ\text{C}$, $t_h=72\text{hr}$	0.82	-0.66
c: $T_h=250^\circ\text{C}$, $t_h=24\text{hr}$	0.29	-0.13

5. Conclusions

Change in a polarity of tribo-electrification of particles by impacting on a rotating metal target has been investigated using glass beads as the particles and aluminum as the target. Main conclusions obtained are as follows:

- 1) If tangential velocity of impact v_{t0} is greater than 20m/s, current generated by tribo-electrification changes from positive to negative as time elapses.
- 2) Sudden increase or decrease in the tangential velocity gives a respective current corresponding to each velocity. The fact means that the polarity of the current is solely determined by the tangential velocity.
- 3) After the particles impact on the target under the condition; $v_{t0} > 20\text{m/s}$ and the target is preserved in the atmospheric condition for a day, then the particle impact experiment showed that positive

current is generated firstly, decreased with time elapsed and finally negative current is generated. Two different experiments support that the polarity change found in this study is not related to the surface oxidization.

- 4) With heat treatment of the target, initial current decreases with increasing the heating temperature T_h and heating time t_h . For $T_h=250^\circ\text{C}$, the initial current changes to a negative value at $t_h > 1$. Higher temperature of the treatment causes the sharper decrease in the initial current. It suggests that the water molecules adsorbed on the target surface causes the polarity change of the tribo-electrification.
- 5) Contact potential difference between particles and target changes by heat treatment of the target. However, the change in the polarity of the current can not be fully explained by the CPD. Therefore, it seems that slip of particles on the target surface caused by increasing the tangential velocity will also affect the polarity change.

Acknowledgement

This work was partly supported by a Grant-in-Aid for Scientific Research A2 (No. 13305054) from the Ministry of Education, Science, Culture and Sports of Japan. Our special thanks are extended to Hideaki Mizutani in Kyoto University for the experiments.

Nomenclature

C	: constant in charge transfer between metal and particle surface	$(\text{CV}^{-1} \text{m}^{-2})$
D_{P50}	: mass median diameter of particles	(m)
d	: distance between ejector and metal target	(m)
I	: current from target to the earth generated by impact of particles	(A)
I_0	: initial current from target to the earth generated by impact of particles	(A)
m_P	: mass of a particle ($=\rho_P\pi D_P^3/6$)	(kg)
n	: number of revolution per minute	(rpm)
ΔP	: air pressure from compressor to ejector	(MPa)
Δq	: charge transferred from target surface to particle	(C)
D_T	: target diameter	(m)
r	: distance from rotating target center to impact point of particles	(m)
S_{eff}	: effective contact area in charge transfer between target and particle	(m)

T	: temperature	(°C)
T_h	: heating temperature	(°C)
T_m	: temperature of melting point	(°C)
t	: elapsed time	(s)
t_h	: heating time	(s)
$V_{A/B}$: contact potential difference between A and B	(V)
v	: particle impact velocity relative to target	(ms ⁻¹)
W	: mass flow rate rate of particles	(gs ⁻¹)

Greek symbol

δ	: thickness of target	(m)
φ	: relative humidity	(%)
ρ	: density	(kg m ⁻³)
ω	: rotational speed of metal target	(rads ⁻¹)

Subscript

M	: metal
P	: particle
n	: normal
t	: tangential

References

- 1) J. F. Hughes: "Electrostatic Powder coating", *Research Studies Press* (1984)
- 2) Itakura, T., H. Masuda, C. Ohtsuka and S. Matsusaka: "The Contact Potential Difference of Powder and the Tribo-electrification", *J. Electrostatics*, **38**, 213-226 (1996)
- 3) Tanoue, K., K. Morita, H. Maruyama and H. Masuda: "Influence of Functional Group on the Electrification of Organic Pigments," *AIChE Journal*, **47**, 2419-2424 (2001)
- 4) Tanoue, K., A. Ema, H. Masuda: "Effect of Material Transfer and Work hardening of Metal Surface on the Current Generated by Impact of Particles", *J. Chem. Eng., Jpn.*, **32**, 544-548 (1999)
- 5) Ema, A., K. Tanoue, H. Maruyama and Hiroaki Masuda: "Impact Electrification of Particles with Metal Plate in Nitrogen Atmosphere", *J. Soc. Powder Technol., Japan*, **38**, 695-701 (2001)
- 6) Ema, A., S. Sugiyama, K. Tanoue, H. Masuda: "Effect of Horizontal Component of Impact Velocity on Impact Electrification of Particles", *J. Inst. Electrostat. Japan*, **26**, 130-136 (2002)
- 7) Ema, A., D. Yasuda, K. Tanoue and H. Masuda: "Tribocharge and Rebound Characteristics of Particles Impact on Inclined or Rotating Metal Target", *Powder Technol.*, **135**, 2-13 (2003)
- 8) Nifuku, M., T. Ishikawa and T. Sasaki: "Static electrification phenomena in pneumatic transportation of coal", *Journal of Electrostatics*, **23**, 45-54 (1989)
- 9) Masuda, H.: "Electrification and Adhesion Phenomena of Powder Particles", *Kagaku Kogaku*, **54**, 41-46 (1990)
- 10) Masuda, H., K. Iinoya: "Electrification of Particles by impact on inclined Metal Plates", *AIChE Journal*, **24**, 950-956 (1978)
- 11) R. Gupa, D. Gidaspow and D. T. Wasan.: "Electrostatic separation of powder mixtures based on the work functions of its constituents", *Powder Tech.* **75**; 79-87 (1993)
- 12) The Chemical Society of Japan: *Kagaku Binran II: Maruzen*, pp. 493-494 (1984)

Author's short biography



Hiroaki Masuda

Professor Masuda obtained his B.Sc. and M.Sc. degrees from Hiroshima University in 1966 and 1968, respectively. In 1973 he obtained his Ph.D. from Kyoto University, which appointed him a research associate that same year. In 1979 he accepted a post as an associate professor at Hiroshima University and then took a chair in 1986. He returned to Kyoto University in 1989 as a full professor, where he has remained ever since. He is now the president of the Society of Powder Technology, Japan. Professor Masuda's current research interests are in the electrostatic phenomena and characterization, the deposition and reentrainment of fine particles, dry dispersion of powder particles, and classification of submicrometer particles.



Daisuke Yasuda

Daisuke Yasuda received B.Sc. (2002) degrees and M.Sc. degrees (2004) from Kyoto University, respectively. Since 2004, he has been working at Mitsubishi Rayon Co., Ltd.



Akihiko Ema

Dr. Akihiko Ema received B.Sc. (1998) degrees and M.Sc. degrees (2000) from Kyoto University, respectively. In 2003, he obtained his Ph.D. from Kyoto University. Since 2003, he has been working at Nisshin Engineering Co., Ltd.



Ken-ichiro Tanoue

Dr. Ken-ichiro Tanoue obtained his B.Sc. degrees from Kagoshima University in 1992. He obtained his M.Sc. degrees (1994) from Kyushu University and received his Ph.D. (1997) from Kyushu University. He then took a research associate at Kyoto, and studied the electrostatic particle deposition and tribo-charging of particles for about 7 years. Since 2003 he has been working in the Department of Mechanical Engineering at Yamaguchi University. Dr. Tanoue's current research interests are in the electrostatic phenomena in corona charging, the electrostatic particle deposition and formation of fine powder particles using a flame method.

Effect of Mixing Condition on Sol-Gel Synthesis of Barium Titanate Ultrafine Particles[†]

Kenjiro GOMI, Kenji TANAKA

Murata Manufacturing Co., Ltd.*

Hidehiro KAMIYA

Graduate School of Bio-Applications and Systems Engineering, BASE,

Tokyo University of Agriculture & Technology**

Abstract

We investigated the sol-gel synthesis process of barium titanate ultrafine particles with using barium hydroxide aqueous solution and titanium alkoxide solution. Emphasis was placed on the relationship between the mixing condition of both solutions and the properties of the particles. A static mixer was used as reactor and the mixing condition was quantitatively characterized by the flow rate of solutions in a static mixer. Mean particle size and the width of size distribution of cubic barium titanate ultrafine particles decreased with increasing flow rate, because the initial concentration of nuclei increased by rapidly mixing the solutions. Since the density of the hydroxyl group in the lattice of cubic barium titanate increased with increasing flow rate, barium titanate had a lattice structure of expanded cubic perovskite.

Key words: Barium titanate, Sol-gel, Mixing condition, Flow rate, Particle size, Lattice parameter, Hydroxyl group

1. Introduction

Barium titanate (BaTiO_3), which is a typical electronic material, is widely used for multilayer ceramic capacitors because of its high dielectric constant and ferroelectric properties¹⁾⁻³⁾. For the miniaturization and high capacitance of multilayer ceramic capacitors, it is necessary that the particle diameter of BaTiO_3 powders is less than 100 nm and have a narrow size distribution and high purity. The conventional BaTiO_3 powder has been synthesized from a solid phase mixture of barium carbonate and titanium oxide fine powders by high temperature heat treatment. A fine grinding process is needed to prepare fine powder that is less than several hundred nanometers in diameter using this solid phase process. However, because of the contamination from the grinding media and the

vessel in the powder and the relatively wide range size distribution of the obtained particles, the abnormal grain growth during sintering¹⁾ and the decrease of electric properties⁴⁾ occur easily.

In recent years, many researchers have been working on the new processes for synthesizing ultrafine BaTiO_3 particles from high-purity raw materials, such as sol-gel method⁵⁾⁻⁷⁾, oxalate method^{8), 9)} and hydrothermal method¹⁰⁾⁻¹²⁾. Using these processes, it is rather easy to prepare ultrafine BaTiO_3 powder that is less than 100 nm in diameter and uniform in stoichiometric composition and has a single phase. In particular, BaTiO_3 ultrafine particles with several 10 nm in diameter were easily prepared by sol-gel method. Two methods are known of obtaining BaTiO_3 powders, including the mixed alkoxide route and the hydroxide-alkoxide route. The hydroxide-alkoxide route has the merit that BaTiO_3 ultrafine particles are easily prepared with a simple synthesis apparatus and at a low temperature below 100°C¹³⁾.

In the sol-gel synthesis process of fine particles, various researches have been studied on the control of the powder properties such as a composition, a size of particles and their size distribution, by synthetic

* 2-26-10, Tenjin, Nagaokakyo-shi, Kyoto 617-8555

** 2-24-16, Naka-cho, Koganei-shi, Tokyo 184-8588

[†] This report was originally printed in J. Ceramic Society of Japan, **111**(1), 67-72 (2003) in Japanese, before being translated into English by KONA Editorial Committee with the permission of the editorial committee of The Ceramic Society of Japan.

conditions; a kind of alcoholic solvent, the solution concentration, a mixed method. In particular, many researches on TiO_2 ¹⁴⁾ and ZrO_2 ¹⁵⁾ particles have been reported. Only batch techniques have been utilized in the lab for precipitation of narrow-sized particles, because the uniformity of mixing and the concentrations of reactants can be easily controlled. As an industrial process, sequential batch precipitation is generally undesirable because of high operating costs, low production rates and batch-to-batch produce variation. The continuous stirred tank reactor is often used for industrial precipitation of powders. However broad particle size distributions are obtained because of the difficulty of the perfect mixing of solutions and the broad residence time distributions. Therefore, to produce narrow-sized powders continuously, a reactor must have narrow residence time distribution and mix uniformly. Ring et al. developed continuous flow reactors, using a glass-bead-packed bed and a static mixer, for preparation of monodispersed titania particles by the hydrolysis of titanium alkoxide^{16, 17)}. Ogihara et al. concluded that important factors to prepare narrow-sized powders in sol-gel process were a rapid stirring, an aging at a fixed temperature and the suitable concentration of the solution^{18, 19)}. The effects of Taylor number and residence time on the particle size, particle size distribution of monodispersed alumina particles by sol-gel process were investigated²⁰⁾.

In the sol-gel synthesis process of BaTiO_3 particles, the effect of chemical factors like alkoxide concentrations and a kind of solvents on characteristics of the powders were investigated²¹⁾. A patent²²⁾ of the preparing method with using a static mixer was obtained. However, the effect of the mixing condition of solutions on characteristics of prepared BaTiO_3 powders is rarely reported. The present study focuses on the quantitative relationship between the mixing condition and characteristics of prepared BaTiO_3 powders by the sol-gel synthesis. We used a static mixer as a continuous flow reactor. The effect of a flow rate of the solution in a static mixer on characteristics of the BaTiO_3 powders was investigated.

2. Experimental

2.1. Preparation of BaTiO_3 particles by sol-gel method

BaTiO_3 powder used in the present study was prepared by the sol-gel method. Barium hydroxide octahydrate and titanium tetraisopropoxide were used as starting materials for the ultrafine BaTiO_3 powder

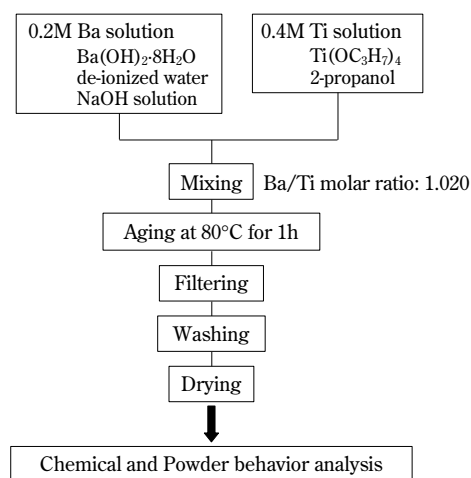


Fig. 1 Flow chart of experimental procedure.

and were prepared by Wako Pure Chemicals Industries, Japan. **Figure 1** illustrates the preparation procedure of ultrafine BaTiO_3 powder. The 0.4M isopropyl alcohol solution of titanium tetraisopropoxide was prepared by diluting the titanium tetraisopropoxide into isopropyl alcohol (nacalai tesque, Japan). The 0.2M barium hydroxide aqueous solution was prepared by mixing the barium hydroxide octahydrate, the distilled water and 12N sodium hydroxide solution (Wako Pure Chemicals Industries, Japan). Additive content of sodium hydroxide was four times of titanium in molar.

A schematic diagram of a synthesis apparatus is shown in **Figure 2**. The apparatus consists of two reservoirs of starting solutions, pumps, Teflon tubes, 250 mm-long Teflon static mixers (Kenics Type N60, Noritake Co., Limited) with 12 steps and a reservoir for aging of BaTiO_3 suspension. The inner diameter

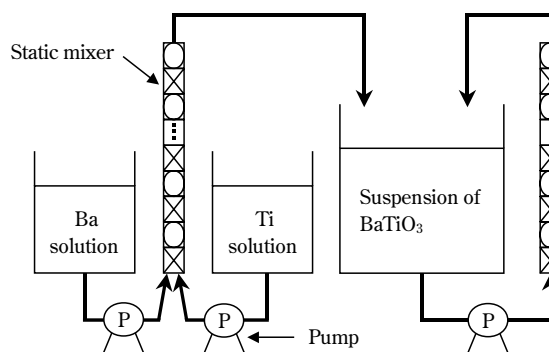


Fig. 2 Schematic diagram of a synthesis apparatus.

of static mixers is 13 mm.

The temperature of barium hydroxide aqueous solution with sodium hydroxide was kept at 80°C with stirring. In order to prevent the generation of BaCO₃ by the reaction between barium hydroxide in solution and CO₂ in air, the nitrogen gas was blown into the solution for 10 min and CO₂ was purged.

The two reactant solutions were introduced to a static mixer by the pump at equal flow rates, and were mixed in a static mixer. The amount of isopropyl alcohol solution of titanium tetraisopropoxide for barium hydroxide aqueous solution was adjusted so that the molar ratio of Ba/Ti would be equal to 1.02. The stoichiometric composition of BaTiO₃ was 1.00. The excess barium hydroxide was added, in order to compensate the unreacted barium ions removed by filtering. Samples of BaTiO₃ suspension were collected in the reservoir and aged with heating to keep above 80°C. After aging for 60 min, BaTiO₃ suspension was filtered by a centrifugal separator and washed with deionized water three times to remove sodium ions in the filtered cake. This filtered cake was dried at 100°C for 12 h.

2.2. Quantification of the mixing condition

The flow rate of solutions in a static mixer was used as an index of mixing condition of barium hydroxide aqueous solution and isopropyl alcohol solution of titanium tetraisopropoxide. The flow rate was determined by the volume of starting solutions, the time for introducing the whole starting solution to a static mixer, and an area of cross section of a static mixer. The flow rate was 0.12-1.24 m/s and the relationship between the flow rate and characteristics of obtained powders was investigated.

2.3. Characterization of the prepared particles

The powder characteristics of the obtained BaTiO₃ by sol-gel process were measured by the following method. The size and the shape of the particles were observed using field emission scanning electron microscopy (FE-SEM: JSM-6340F, JEOL). To evaluate the size distribution of the particles, Feret's diameter was measured by an image analysis of SEM micrographs. In microscopy, Feret's diameter is the measured distance between parallel lines that are tangent to an object's profile and perpendicular to the ocular scale. The number of the particles for measuring the particle size distribution was 75-109. The crystalline phase was identified by X-ray diffraction (RAD-RX, Rigaku) and the lattice parameter of BaTiO₃ was calculated by Rietveld analysis. The specific surface area

of the powders was measured by nitrogen gas adsorption (single-point BET method). The weight loss of the particles and the gas generated with heating were measured with Thermogravimetry / Mass Spectrometry (TG-MS). Hydroxide groups in the particles heated at various temperatures were measured by using a Fourier transform infrared spectrometer (FT-IR : Magna 750, Nicolet).

3. Results

3.1. Effect of aging time on powder properties

To determine an aging time of suspension prepared by mixing barium hydroxide aqueous solution and the isopropyl alcohol solution of titanium tetraisopropoxide, the relationship between the aging time and the powder properties was investigated. The flow rate was 0.73 m/s. The specific surface area and the Ba/Ti molar ratio of prepared BaTiO₃ particles at different aging time are shown in **Figure 3**. The specific surface area of prepared particles decreases with an increase of aging time and was almost constant at 40-60 min. The decrease in the specific surface area suggested the elimination of an alkoxide-derived amorphous TiO₂ gel by reaction with barium ion. On the other hand, the Ba/Ti molar ratio was almost constant when an aging time was longer than 20 min. From these results, an aging time was fixed at 60 min.

3.2. Effects of the flow rate on the specific surface area and the particle size

The Ba/Ti molar ratio and the specific surface area of the synthesized BaTiO₃ particles with a static

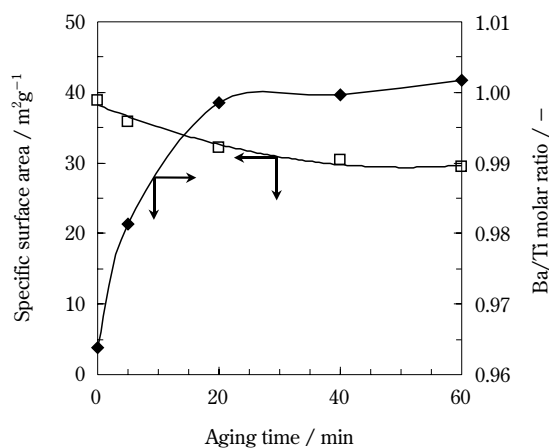


Fig. 3 Effect of aging time on the surface area and the Ba/Ti molar ratio of BaTiO₃ particles prepared by sol-gel method (Flow rate=0.73 m/s).

mixer at various flow rates were determined by X-ray fluorescence analysis and nitrogen gas adsorption method, respectively. These results are shown in **Figure 4**. The specific surface area of BaTiO₃ parti-

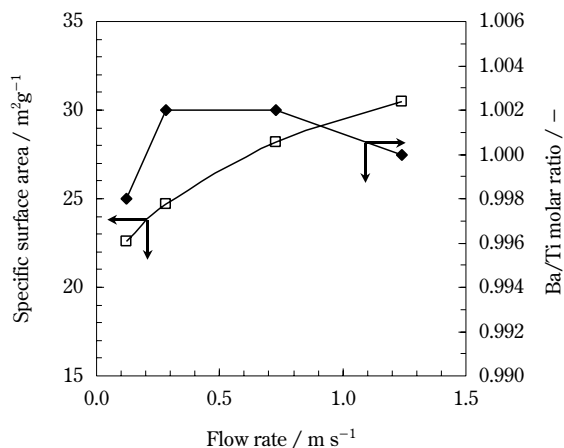


Fig. 4 Effect of mixing condition on the specific surface area and the Ba/Ti molar ratio of BaTiO₃ particles prepared by sol-gel method.

cles increased with increasing flow rate. The relationship between the flow rate and Ba/Ti molar ratio is described later.

SEM micrographs of powders synthesized at various flow rates are shown in **Figure 5**. BaTiO₃ ultra-fine particles with several 10 nm in diameter were obtained in all cases and the particle size decreased with an increase of the flow rate. **Figure 6** shows the size distribution of BaTiO₃ particles at various flow rates. Particles for the flow rate up to 0.28 m/s showed a bimodal particle size distribution. Large and small particles were about 90 nm and 50 nm, respectively. The peak intensity of large particles decreased with increasing flow rate and the peak at 70 nm appeared. The decrease in average particle size and the narrow size distribution were observed with increasing in flow rate.

3.3. Effects of the flow rate on the composition, crystal phase and thermal properties of BaTiO₃ particles

The relationship between the flow rate and the Ba/Ti molar ratio of synthesized BaTiO₃ particles is

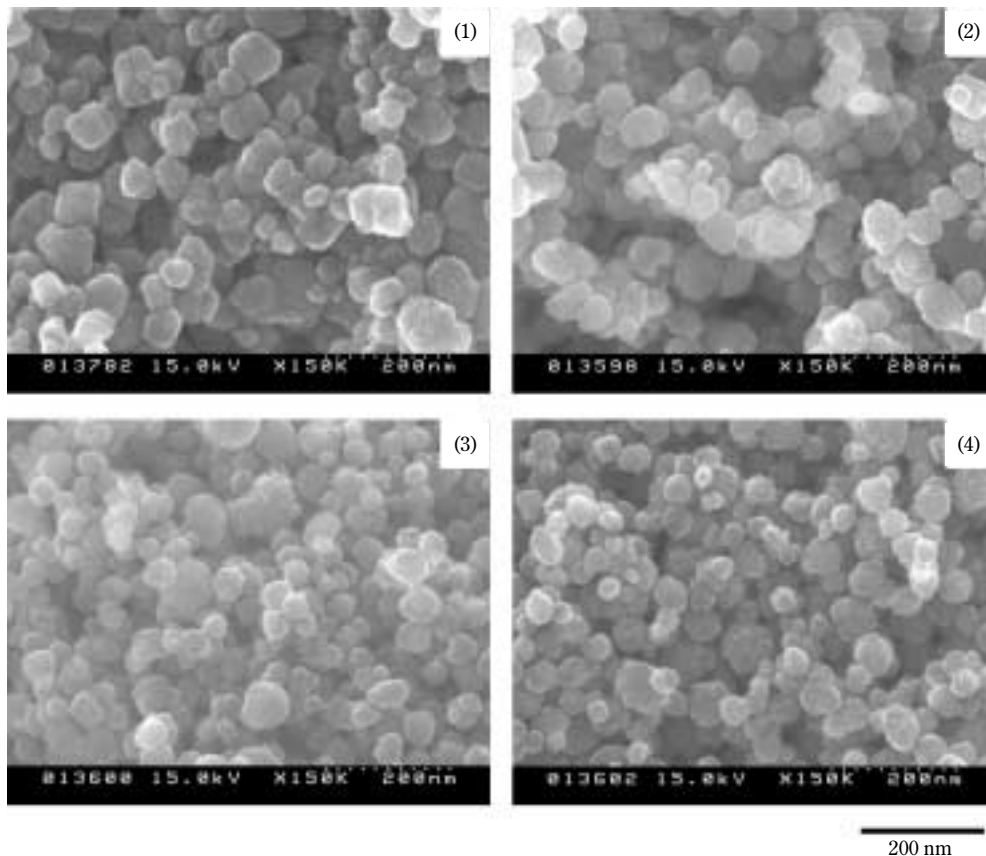


Fig. 5 SEM micrographs of BaTiO₃ particles prepared by different mixing condition: Flow rate (1) 0.12 m/s (2) 0.28 m/s (3) 0.73 m/s (4) 1.24 m/s.

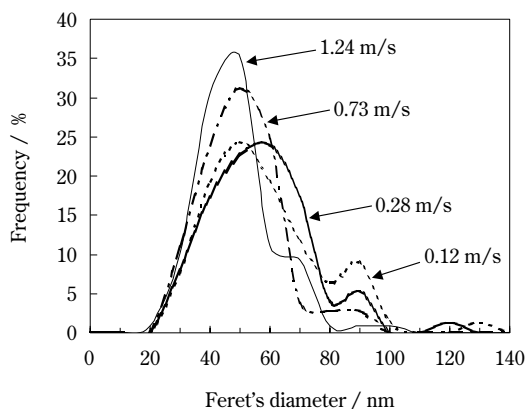


Fig. 6 Effect of mixing condition on particle size distribution of BaTiO₃ particles by sol-gel method.

shown in **Fig. 4**. The Ba/Ti molar ratio was almost 1.0, that is a stoichiometric composition of BaTiO₃, and was not significantly influenced by the flow rate.

Figure 7 shows the XRD patterns of synthesized BaTiO₃ powders and the effect of the flow rate on the crystal phase. In all powders, the diffraction peaks of cubic perovskite phase of BaTiO₃ and BaCO₃ were observed. BaCO₃ would be a reactant between barium ions in the solution and CO₂ gas in air. The peak intensity of BaCO₃ was not influenced by the flow rate. Although a small amount of BaCO₃ was observed in BaTiO₃ particles, no peaks of unreacting titanium compound was detected by XRD analysis. This suggested the formation of the alkoxide-derived TiO₂ gel

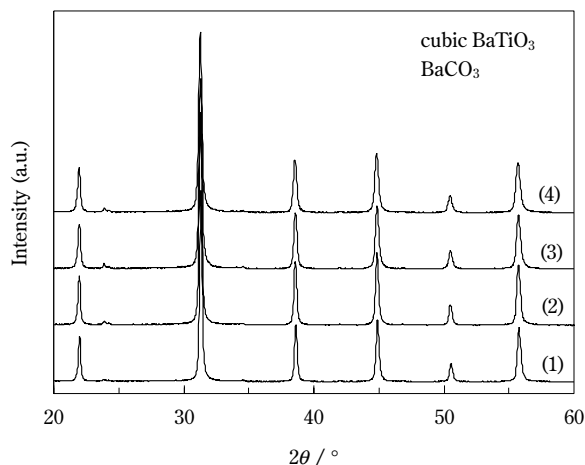


Fig. 7 XRD patterns of BaTiO₃ particles prepared by different mixing condition: (1) 0.12 m/s (2) 0.28 m/s (3) 0.72 m/s (4) 1.24 m/s.

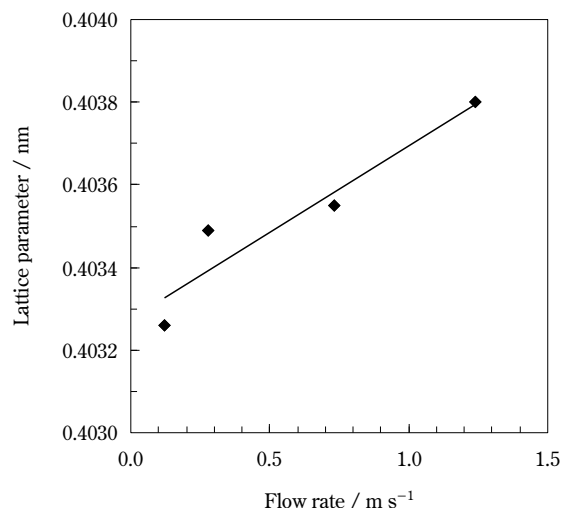


Fig. 8 Effect of mixing condition on the lattice parameter of cubic-BaTiO₃ unit cell prepared by sol-gel method.

in the synthesis process of BaTiO₃. **Figure 8** shows the lattice parameters of prepared BaTiO₃ as a function of the flow rate. The lattice parameter of cubic BaTiO₃ increased with an increase in flow rate.

BaTiO₃ particles at various flow rates were analyzed by thermogravimetry and the results are shown in **Figure 9**. The weight loss of particles increased with increasing flow rate and was performed in the following four steps: (1) room temperature-150°C, (2) 150°C-300°C, (3) 300°C-750°C, and (4) above 750°C. To investigate the cause of the weight loss, gases generated with heating were identified by TG-MS. Gases

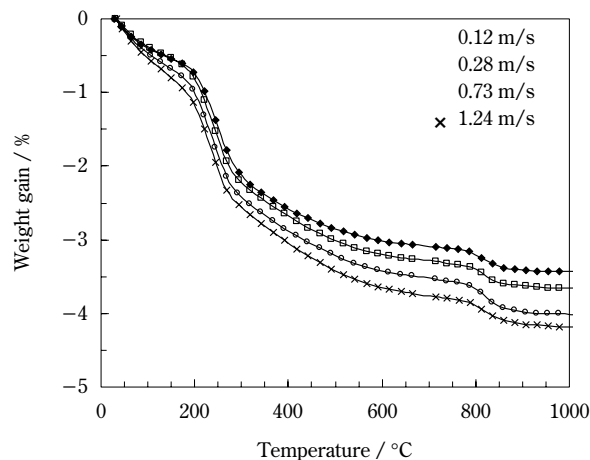


Fig. 9 TG curves of BaTiO₃ particles prepared by sol-gel method with different mixing condition.

were determined to H_2O ($m/z=18$) and CO_2 ($m/z=44$) by measuring the relative mass to charge ratios (m/z). **Figure 10** shows the ion chromatogram of the particles obtained by mixing solutions at the flow rate of 1.24 m/s. H_2O was detected in the next three temperature regions: (1) below 130°C, (2) 130°C-300°C, and (3) 300°C-700°C. CO_2 was detected in the temperature range between 740°C and 900°C. This result was in agreement with the result of TGA as shown in **Fig. 9**. These experimental results indicate that the weight losses in the first step and the fourth step are attributed to the dehydration of the physically adsorbed water and the thermal decomposition of BaCO_3 , respectively. The cause of the weight losses in the second step and the third step, possibly attributed to the chemically adsorbed hydroxyl groups, was investigated later.

Figure 11 shows the effect of the flow rate on the weight loss of BaTiO_3 particles with heating. The weight loss in the first step, attributed to the surface-adsorbed water, increased with an increase in the flow rate, because of an increase in the specific surface area of the particles as shown in **Fig. 4**. The weight loss in the second step was increased with an increase in the flow rate. In the third step and the fourth step, attributed to the thermal decomposition of a very small amount of BaCO_3 , on the other hand, no significant relationship between the weight loss and the flow rate was observed.

Figure 12 shows FT-IR spectra of BaTiO_3 particles (flow rate=1.24 m/s), heated isothermally at temperatures between 300°C and 900°C for 60 min. A small sharp shoulder band at around 3500 cm^{-1} and a large

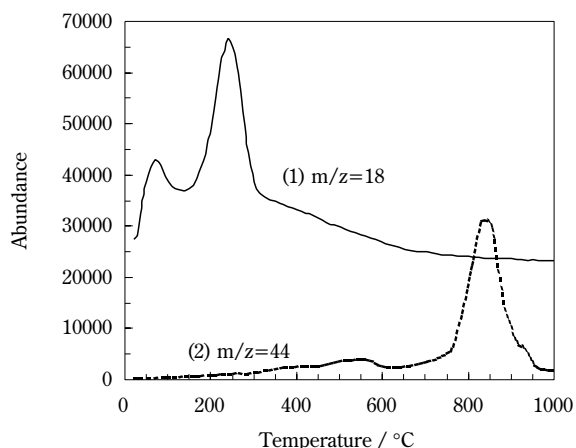


Fig. 10 TG-MS measurement of BaTiO_3 prepared by sol-gel method (Flow rate=1.24 m/s).

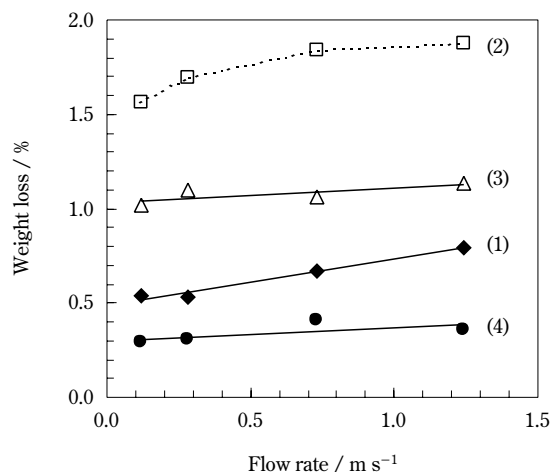


Fig. 11 Effect of mixing condition on the quantity of weight loss of BaTiO_3 particles in TG profile: (1) room temperature-150°C (2) 150°C-300°C (3) 300°C-750°C (4) 750°C-900°C.

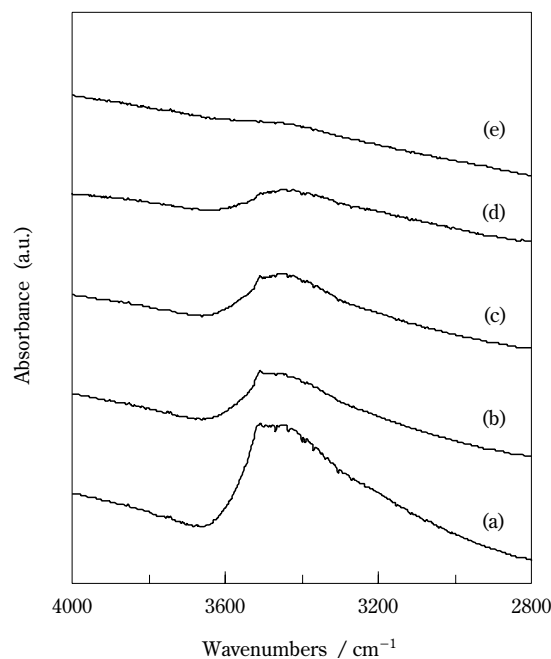


Fig. 12 FT-IR spectra of the stretching vibration of H_2O and hydroxyl group in BaTiO_3 particles by sol-gel method (Flow rate=1.24 m/s): (a) as prepared, and treated for 60 min at (b) 300°C, (c) 500°C, (d) 700°C and (e) 900°C.

broad band at around 3400 cm^{-1} were assigned to the stretching vibration of the lattice hydroxyl group and the stretching vibration of the surface-adsorbed hydroxyl group, respectively²⁴. Both absorption bands

were observed for the as-prepared sample, but were decreased suddenly by the thermal treatment at 300°C for 60 min. A large broad band attributed to the surface-adsorbed hydroxyl group remained at higher temperature. No hydroxyl groups in the sample heated at 900°C were observed. From the results of TGA (**Fig. 9**) and TG-MS (**Fig. 10**), the rapid weight loss at low temperature region was mainly attributed to the dehydration of the lattice hydroxyl group in BaTiO₃.

4. Discussion

BaTiO₃ particles with different powder characteristics were prepared by mixing barium hydroxide aqueous solution and isopropyl alcohol solution of titanium tetraisopropoxide at various flow rates. In this section, the relationship between the flow rate and the powder characteristics was studied.

BaTiO₃ particles with small size and narrow size distribution were prepared by an increase of the flow rate, as shown in **Fig. 6**. This phenomenon can be explained by the mechanism of the nucleation and the growth of nanoparticles. The basic model to explain the mechanism of the formation of fine and monodispersed particles with liquid phase process was proposed by LaMer and Dinegar²³. Generally, the formation of nanoparticles from the solution involves two processes: the nucleation and growth of nuclei. It is known that rapid nucleation relative to the growth results in small and monodispersed particle size. If the nucleation occurs as the solution concentrates, the solution must be diluted rapidly below the minimum concentration of nucleation to prepare the monodispersed particles. There are two approaches to synthesize the particles under such condition. One approach is that a solution is kept at about the minimum concentration of nucleation. If the solute in a solution is consumed by the formation of nuclei, the concentration decreases below the minimum concentration of nucleation and no nucleation can occur. Another approach is a forcible decrease of concentration by addition of the solvent. Generally, the former is used for producing monodispersed particles. In the present study, the fast flow rate increased the number of reaction fields between barium ions and titanium ions in the solution, so that the initial concentration of nucleation increased rapidly. Therefore, the particle size of obtained BaTiO₃ particles decreased with increasing flow rate. Moreover, since the molar ratio of H₂O to titanium tetraisopropoxide was about 300, the solution was diluted and the concentration of alkoxide

in solution decreased rapidly when the solutions were mixed. Therefore, the rapid flow rate resulted in the formation of BaTiO₃ ultrafine particles with the small size and the narrow size distribution.

Effects of the flow rate on the lattice constant of cubic-BaTiO₃ and the weight loss with heating were studied. In the wet synthesis process of particles, the lattice defects due to the hydroxyl groups incorporated in the perovskite lattice is also detected. In the hydrothermal synthesis process of BaTiO₃ particles, the formation of the cation vacancies, due to the incorporation of the hydroxyl groups in the crystal lattice, is reported¹¹. Two kinds of hydroxyl groups in the BaTiO₃ particles were composed of the surface-adsorbed hydroxyl group and the lattice hydroxyl group²⁴. In general, the surface-adsorbed hydroxyl groups have various bonding energies with the surface because of their adsorption on several surface sites with different coordination numbers, while the lattice hydroxyl groups have only specific bonding energy in BaTiO₃ lattice. Therefore, the surface-adsorbed hydroxyl groups were desorbed gradually over the wide temperature range from room temperature to 600°C and the lattice hydroxyl groups desorbed over the narrow temperature range from 300°C to 400°C. Consequently, the weight losses in the second and third steps, as shown in **Fig. 9**, are mainly due to the lattice hydroxyl groups and the surface-adsorbed hydroxyl groups, respectively. As shown in **Fig. 11**, the weight loss in the second step, which was assigned to the lattice hydroxyl groups, increased with increasing flow rate, indicating the amount of the lattice hydroxyl groups can be controlled by the mixing condition. As the lattice hydroxyl groups were desorbed with heating, unit cell volume of cubic-BaTiO₃ decreased, as reported by Hennings et al¹¹, and Wada et al.²⁴. This decrease in unit cell volume is explained by the increase of the Coulomb attractive forces between ions controlling ionic bonding strength. The lattice hydroxyl group OH⁻ in the BaTiO₃ can exist as substitutional in the lattice position of oxygen O²⁻. Therefore the presence of cation vacancies is required in order to satisfy the electroneutrality condition in the particles. The increase of cation vacancies reduced the Coulomb attractive force and result in an enlargement of BaTiO₃ unit cell. Consequently, the lattice constant decreased with an increase of the temperature, by desorbing the lattice hydroxyl groups.

Figure 13 shows the variation in the unit cell volume of cubic-BaTiO₃ heated at various temperatures between room temperature and 800°C. The unit cell

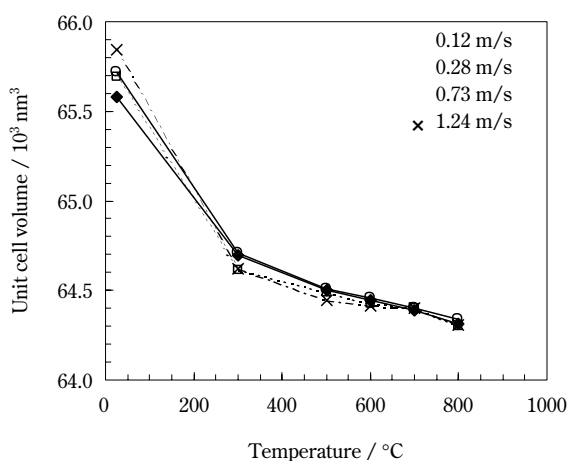


Fig. 13 Variation in unit cell volume of cubic-BaTiO₃ prepared by different mixing condition with temperature.

volume was calculated from the lattice constants determined by XRD analysis. The crystalline structure of BaTiO₃ particles was cubic perovskite in this temperature range. The lattice constant decreased with an increase of annealing temperature, particularly decreased rapidly near 300°C at which the lattice hydroxide groups desorbed. Therefore, unit cell volume of BaTiO₃ particles in the present study was enlarged also by the hydroxyl groups introduced into the lattice. By an increase in the flow rate of solutions, barium hydroxide aqueous solution and isopropyl alcohol of titanium tetraisopropoxide, the amount of the hydroxide groups incorporated to the crystal lattice was increased, so that the unit cell of cubic-BaTiO₃ was enlarged. On the other hand, the lattice constant decreased slightly in the temperature range above 300°C, because the lattice defects decreased gradually by diffusion of ions with heating.

5. Conclusion

We investigated the sol-gel synthesis process of barium titanate ultrafine particles with using barium hydroxide aqueous solution and isopropyl alcohol solution of titanium tetraisopropoxide. Emphasis was placed on the relationship between mixing condition of both solutions and the properties of the particles. A static mixer was used as a reactor and the mixing condition was quantitatively characterized by flow rate of solution in a static mixer. Summary was as follows.

(1) The mixing condition (=flow rate) had no influence on the composition of BaTiO₃ ultrafine particles prepared by sol-gel method.

(2) BaTiO₃ particles with small size and narrow size distribution were prepared by an increase of the flow rate. The fast flow rate increased the number of reaction fields between barium ions and titanium ions in solution, so that the initial concentration of nucleation increased rapidly and the particles size decreased with the flow rate. Moreover, the rapid dilution of solution resulted in the formation of BaTiO₃ ultrafine particles with the small size and the narrow size distribution.

(3) The lattice parameter of cubic BaTiO₃ increased with an increase in the flow rate. By an increase in the flow rate of solutions, the amount of the hydroxide groups incorporated to the crystal lattice was increased, so that the unit cell of cubic-BaTiO₃ was enlarged.

References

- Hilton, A. D. and Frost, R., "Key Engineering Materials", Vols. 66 & 67, Copyright Trans Tech Publications (1992), pp. 142-83.
- Cross, L. E., Am. Ceram. Soc. Bull., 63, 586-90 (1984)
- Pandy, D., Singh, A. P. and Tiwari, V. S., Bull. Mater. Sci., 15, 391-402 (1992)
- Nelson K. E. and Cook R. L., Am. Ceram. Soc. Bull., 38, 499-500 (1959)
- Ikeda, M., Lee, S. K., Shinozaki, K. and Mizutani, N., J. Ceram. Soc. Jpn., 100, 680-84 (1992)
- Kirby, K. W., Mat. Res. Bull., 23, 881-90 (1988)
- Bruno, S. A. and Swanson, D. K., J. Am. Ceram. Soc., 76, 1233-41 (1993)
- Clabaugh, W. S., Swiggard, E. M. and Gilchrist, R., J. Research of the National Bureau of Standards, 56, 289-91 (1956)
- Stockenhuber, M., Mayer, H. and Lercher, J. A., J. Am. Ceram. Soc., 76, 1185-90 (1993)
- Vivekanandan, R., Philip, S. and Kutty, T. R. N., Mater. Res. Bull., 22, 99-108 (1986)
- Hennings, D. and Schreinemacher, S., J. Eur. Ceram. Soc., 9, 41-46 (1992)
- Dutta, P. K., Asiaie, R., Akbar, S. A. and Zhu, W., Chem. Mater., 6, 1542-48 (1994)
- Chaput, F. and Boilot, J. P., J. Am. Ceram. Soc., 73, 942-48 (1990)
- Barringer, E. A. and Bowen, H. K., J. Am. Ceram. Soc., 65, C199-C201 (1982)
- Fegley Jr., B., White, P. and Bowen, H. K., Am. Ceram. Soc. Bull., 64, 1115-20 (1985)
- Jean, J. H., Goy, D. M. and Ring, T. A., Am. Ceram. Soc. Bull., 66(10) 1517-20 (1987)
- Ring, T. A., Chem. Engng., Sci., 39(12), 1731-34 (1984)
- Ogihara, T., Ikeda, M., Kato, M. and Mizutani, N., J. Am. Ceram. Soc., 72, 1598-1601 (1989)
- Ogihara, T., Yabuuchi, M., Yanagawa, T., Ogata, N., Yoshida, K., Nagata, N., Ogawa, K. and Maeda, U., J.

- Soc. Powder Technol., Japan, 31, 620-25 (1994) [in Japanese]
- 20) Ogihara, Y., Ogata, N., Fujita, K., Sato, S., Nomura, M. and Horinouchi, K., J. Soc. Powder Technol., Japan, 37, 722-27 (2000)
- 21) Kiss K., Madger J., Vukasovich M. S., and Lockhart R. J., J. Am. Ceram. Soc., 49, 291-95 (1966)
- 22) Okabe, S., Tsukioka, Y., Kuze, S., Hamaji, Y. and Sakabe, Y., Kokai-Tokkyo-Koho, Heisei 5-85727 [in Japanese]
- 23) La Mer V. K. and Dinegar R. H., J. Am. Chem. Soc., 72, 4847 (1950)
- 24) Wada, S., Suzuki, T. and Noma, T., J. Ceram. Soc. Japan, 103, 1220-27 (1995)

Author's short biography



Kenjiro GOMI

Kenjiro GOMI received his B.Eng. in 1994 and M.Eng. in 1996 from the Department of Applied Chemistry at Keio University. He has been working at Murata Manufacturing Co. Ltd. since 1996. He received his D.Eng. in 2003 from the Graduate School of Bio-Applications and Systems Engineering (BASE) at Tokyo University of Agriculture & Technology.



Kenji TANAKA

Kenji TANAKA received his B.S. in 1966 and M.S. in 1968 from Kyoto Institute of Technology. He has been working at Murata Manufacturing Co. Ltd. since 1968. He received his Ph. D. from Kyoto University in 1990. He got the Technology Award of the Ceramic Society of Japan in 1992 and the Technology Progress Award of the Japan Society of Powder and Powder Metallurgy in 1993, for his establishment of a submicron grinding technique. He is a consultant engineer.



Hidehiro KAMIYA

Hidehiro KAMIYA is full professor of Graduate School of Bio-Applications and Systems Engineering, Tokyo University of Agriculture and Technology since 2003. He received his BE, ME and PhD degrees from Nagoya University (Department of Chemical Engineering) in 1981, 1983 and 1986, respectively. He was Research Associate from 1986 to 1993 at Department of Material Engineering in Nagoya Institute of Technology and Department Chemical Engineering, Nagoya University, and was Associate Professor at Department Chemical Engineering and Graduate School of Bio-Applications and Systems Engineering, Tokyo University of Agriculture and Technology from 1993 to 2003. His scientific activity is mainly concerned with fine powder science and technology, characterization and control of surface interaction between nano-particle in gas and liquid phase. Based on such fundamental research, his application field is material powder processing, ash behavior control in energy and environmental systems, and recently expand to the new field, for example, pharmaceutical and cosmetic etc..

Preparation of the Composite Thermoelectric Materials with Small Particles Dispersion by MA[†]

Shigeru Katsuyama*¹, Mikio Ito*² and Hiroshi Nagai

Department of Materials Science and Processing,
Graduate School of Engineering, Osaka University*

Abstract

We have prepared the thermoelectric materials, where the small particles are dispersed in the matrix, by mechanical grinding (MG) or alloying (MA). Si and C powders were added to the p-type $Fe_{0.92}Mn_{0.08}Si_2$ or n-type $Fe_{0.98}Co_{0.02}Si_2$ powders, and they were mechanically milled followed by being hot-pressed. The amounts of the β -phase, ϵ -phase, α -SiC and C in the sintered samples depend on the amount of the added (Si+C) and Si/C molar ratio, which affect the values of the Seebeck coefficient and electrical resistivity of the samples. A lot of fine α -SiC particles around 20nm were dispersed in the samples, which decreases the thermal conductivity of the samples. The maximum figure of merit values appear at Si/C=1.5 for p-type $Fe_{0.92}Mn_{0.08}Si_2$ containing 4 mass%(Si+C) and Si/C=1.75 for n-type $Fe_{0.98}Co_{0.02}Si_2$. We have also prepared the $CoSb_3$ - $FeSb_2$ composite where the $FeSb_2$ particles are dispersed in the $CoSb_3$ matrix. The dispersed $FeSb_2$ particles contributed to decreasing the thermal conductivity and maintaining the moderate Seebeck coefficient and electrical resistivity of the samples. As a result, the composite whose molar ratio $CoSb_3/FeSb_2$ is 0.7/0.3 and milling time is 25h has a maximum value of figure of merit of $6.1 \times 10^{-4} K^{-1}$ at 756K, which is much larger than that of $3.2 \times 10^{-4} K^{-1}$ for $CoSb_3$.

Key words: Seebeck coefficient, electrical resistivity, thermal conductivity, iron disilicide, skutterudite

1. Introduction

In the face of the impending energy and environmental problems, thermoelectric materials have recently attracted the attention of many researchers. The energy conversion system constructed from the thermoelectric materials can directly convert heat to electricity, and it has the following features; (1) there are no mechanical vibration, noise and exhaust gas during operation, (2) there is no maintenance required and (3) it is compact and light. But, at present the efficiency of the energy conversion is very small com-

pared to the conventional energy conversion systems.

The performance of the thermoelectric material is estimated by the figure of merit, $Z (=S^2/(\rho \times \kappa))$. Here, S , ρ and κ are the Seebeck coefficient, electrical resistivity and thermal conductivity, respectively. The product of Z and T (operating temperature), ZT , is called as the dimensionless figure of merit. The material with high Z or ZT shows high performance as thermoelectric material, and so in order to obtain high performance material, large S and small ρ are required as well as low κ . These parameters are closely related to the carrier density of the materials. In general, the material with large carrier density has small ρ , but it has small S . κ is consisted of κ_{car} and κ_{ph} ; here κ_{car} is the carrier contribution and κ_{ph} is the lattice contribution to the thermal conductivity, respectively. κ_{car} is affected by the carrier density; the material with high carrier density shows small κ_{car} . On the other hand, κ_{ph} is not directly affected by the carrier density. And so, in order to raise the performance of the thermoelectric material, it is necessary to reduce κ_{ph} maintaining the moderate S and ρ .

* 2-1 Yamadaoka, Suita Osaka 565-0871, Japan

¹ TEL (81) 6-6879-7507

E-mail: katsuyama@mat.eng.osaka-u.ac.jp

² TEL (81) 6-6879-7506

E-mail: ito@mat.eng.osaka-u.ac.jp

[†] This report was originally printed in J. of the Japan Soc. of Powder and Powder Metallurgy, **50**, 451-457 (2003) in Japanese, before being translated into English by KONA Editorial Committee with the permission of the editorial committee of the Japan Society of Powder and Powder Metallurgy.

The phonon is scattered by the vacancy, the disordered or substituted atoms in the crystal¹⁾, as well as the grain boundary and the precipitated impurities²⁾, and as a result the conduction of heat is disturbed. The degree of the scattering of the phonon is in proportion to the density of the above microscopic formations, and so it is effective for the reduction of κ_{ph} to introduce more disordered and substituted atoms, increase the density of the crystal grain boundary and more disperse the impurities. The ideal microscopic structure for the low κ_{ph} is shown in **Figure 1**. We show the fundamental procedure for preparing the high performance thermoelectric materials by the metallurgical method, in **Figure 2**. This procedure is

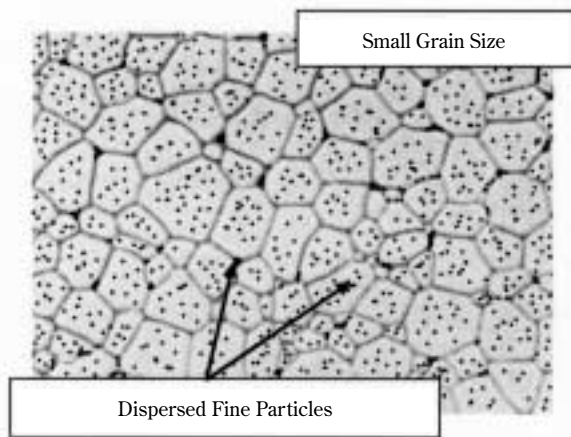


Fig. 1 Ideal microscopic structure for the low κ_{ph} .

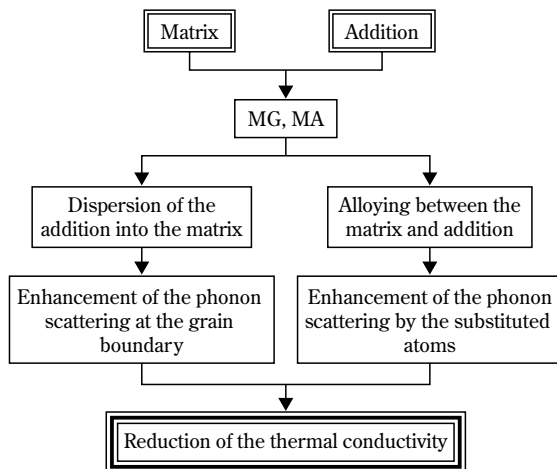


Fig. 2 Fundamental procedure for preparing the high performance thermoelectric materials by metallurgy.

based on the control of the microscopic structure of the materials by MG (Mechanical Grinding) and MA (Mechanical Alloying). MG and MA are mechanical milling processes of the materials by use of Ball mill etc. During milling process, the crystal grain is refined and the added materials are dispersed in the matrix³⁾. Sometimes, a part of the atoms in the matrix is substituted by the atoms in the addition, i.e., alloying between the matrix and addition has been proceeding. When we want to control the microscopic structure of the thermoelectric materials by MG or MA, an appropriate selection of the addition is also important, since there exists the moderate carrier density. Up to now, we have applied the MG and MA methods to the study of the improvement of the performance of the various thermoelectric materials. In this paper, we will report the results on the transition metal disilicide β -FeSi₂ and skutterudite CoSb₃.

The performance of β -FeSi₂ as a thermoelectric material is relatively low, but owing to its low raw materials costs and non-toxicity, it is expected as one of the potential candidates for practical use^{4, 5)}. **Figure 3** shows a part of the phase diagram for the Fe-Si binary system⁶⁾. It is known that there exist the various intermetallic compounds such as ϵ -FeSi, β -FeSi₂ and α -Fe₂Si₅ in the Fe-Si binary system. Both ϵ - and α -phase show the metallic conductivity, and β -phase shows the semiconducting property. As shown in the figure, β -FeSi₂ is stable above 1255K, and it is formed through the peritectic reaction of α - and ϵ -phase. The diffusion of the atoms in the inter-

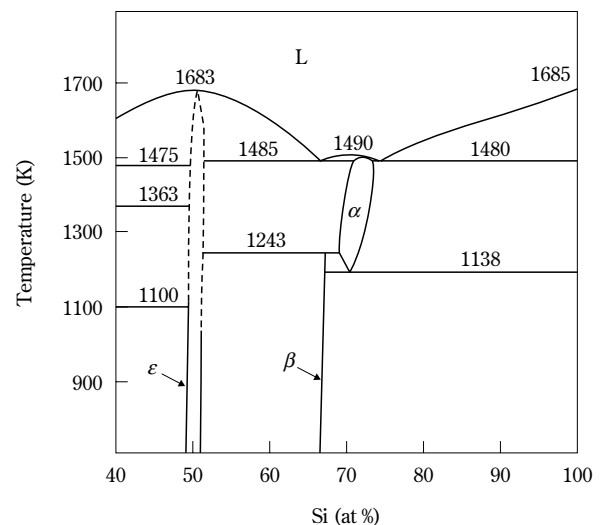


Fig. 3 Phase diagram for the Fe-Si system.

metallic compounds are generally slow, and so when we want to synthesize the β -FeSi₂ by the heat treatment or sintering process, annealing for long time below 1255K is necessary⁷. The MA technique, which is useful for the preparation of minute or amorphous particles, may enable the sintering of the intermetallic compounds at low temperature or the promotion of the peritectic reaction. We have investigated the effect of the SiC dispersion by MA on the performance of β -FeSi₂^{8, 9}.

Skutterudite compounds are represented by MX₃, where M is Co, Rh or Ir and X is P, As or Sb. This structure is composed of a cubic lattice; space group *Im3* and the unit cell contains 8 MX₃ groups, i.e., a total of 32 atoms. In 1959, Dudkin et al. first reported its thermoelectric properties^{10, 11}, and in 1993 Caillat et al. showed its potential as a high performance thermoelectric material¹². Owing to relatively high carrier mobility of 2000 cm²/V/s, the skutterudite compounds possess reasonably large Seebeck coefficient and good electrical conductivity¹³, but their thermal conductivity remains too high to make these materials efficient thermoelectrics¹⁴. As mentioned above, the phonon is scattered by the vacancy, disordered and substituted atoms in the crystal, as well as the grain boundary and precipitated impurities. MG and MA are useful methods for controlling the microscopic structure of the materials. The improvement of the performance of the skutterudite compounds can be expected by the reduction of the thermal conductivity. We have reported the results of the investigation of the thermoelectric properties of CoSb₃-FeSb₂ composite with FeSb₂ particles dispersion¹⁵.

2. Experiment

2.1 Preparation of β -FeSi₂-Si, C composite

Mixtures of Fe, Si, Mn and Co powders in the desired molar ratio for Fe_{0.92}Mn_{0.08}Si₂ (p-type) and Fe_{0.98}Co_{0.02}Si₂ (n-type)^{4, 5} were pressed into pellets and arc-melted in an Ar gas atmosphere. The button was mechanically ground to -60 mesh with mortar and pestle. The obtained powders were mixed with 0-8mass% of (Si+C) powders at various Si/C ratios (Si/C=0.5-2.0). About 20g of these powder mixtures were mechanically ground with a high energy vibration mill (SPEX 8000) for 20h, using stainless steel container (volume; 7×10⁻⁵ m³) and five balls (diameter; 1.2×10⁻² m) under an Ar gas atmosphere. For sintering and transformation to β -phase, about 1g of MA powders were hot-pressed using a carbon die and punch at 1173K for 1h at a pressure of 25MPa under a

vacuum of 10⁻² Pa. The phases, microstructure and compositions of the samples were examined by XRD, SEM, TEM and EDX. Electrical resistivity and Seebeck coefficient were measured from room temperature to 1173K by the standard four probe DC method in a flowing Ar gas atmosphere. Thermal conductivity was measured by the laser flash method from room temperature to 1073K under vacuum.

2.2 Preparation of CoSb₃-FeSb₂ composite

The compounds CoSb₃ and FeSb₂ were prepared by the direct reaction of their elements. For CoSb₃, Co and Sb powders with the desired composition were mixed and evacuated in a quartz ampoule, then heated at 1073K for 24h. For FeSb₂, Fe and Sb powders were heated at 973K for 48h. After the reaction was completed, the ampoule was opened and the products were ground by mortar and pestle into fine powders. The obtained CoSb₃ and FeSb₂ powders were weighed in the desired ratios of CoSb₃ to FeSb₂ of 1-x:x, where x=0, 0.16, 0.2, 0.3 and 0.4. About 10g of mixed powder was put in an agate vial (volume; 4.5×10⁻⁵ m³) with twenty agate balls (diameter; 7×10⁻³ m). MG was carried out for 30min-40h using SPEX 8000 vibration mill under a vacuum of 10⁻³ Pa. The powders after MG were packed into carbon die and hot-pressed at 923K for 1h at a pressure of 10MPa under a vacuum of 10⁻³ Pa. The identification of the samples and the measurement of the thermoelectric properties of the samples were carried out in a similar manner with β -FeSi₂ composite system.

3. Results and Discussions

3.1 Thermoelectric properties of β -FeSi₂-Si, C composite

The X-ray diffraction patterns of p-type Fe_{0.92}Mn_{0.08}Si₂ and n-type Fe_{0.98}Co_{0.02}Si₂ after hot-pressing consisted of mostly β -phase with small amount of ϵ -phase. The amount of ϵ -phase decreases with increasing the amount of (Si+C). The presence of the ϵ -phase means that the composition of the samples has shifted to lower Si content than the stoichiometric, which is resulted from the selective oxidation of Si and/or the introduction of Fe from the stainless container and balls during MA. It has been found by TEM observation and electron diffraction that a lot of fine α -SiC particles with about 20nm size are synthesized in all β -FeSi₂ with the addition of (Si+C).

Figure 4 shows the temperature dependence of the Seebeck coefficient of hot-pressed p-type Fe_{0.92}Mn_{0.08}Si₂ with addition of x mass%(Si+C), where Si/C=1 and

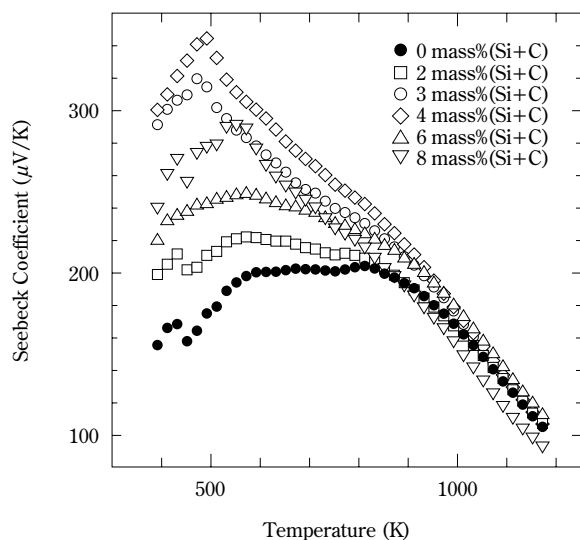


Fig. 4 Temperature dependence of the Seebeck coefficient for the sintered p-type $\text{Fe}_{0.92}\text{Mn}_{0.08}\text{Si}_2$ with addition of x mass% (Si+C).

$x=0-8$. It is surprisingly of interest that the addition of (Si+C) markedly increases the Seebeck coefficient. It is considered that the increase in the Seebeck coefficient might be resulted from the decrease in the amount of the metallic ε -phase due to the fact that some part of the additional Si reacts with the ε -phase to form $\beta\text{-FeSi}_2$ phase. The Seebeck coefficient is decreased by further addition of (Si+C) more than 3-4 mass% probably due to the increase in the amount of SiC, whose Seebeck coefficient is smaller than that of $\beta\text{-FeSi}_2$.

Figure 5 shows the temperature dependence of the electrical resistivity of hot-pressed p-type $\text{Fe}_{0.92}\text{Mn}_{0.08}\text{Si}_2$. The electrical resistivity increases with increasing amount of (Si+C) addition, which is probably due to the decrease in the amount of the dispersed metallic ε -phase with low resistivity^{16, 17)} and the increase in the amount of $\alpha\text{-SiC}$ with high resistivity than that of $\beta\text{-FeSi}_2$ ¹⁸⁾.

Figure 6 shows the temperature dependence of the thermal conductivity of hot-pressed p-type $\text{Fe}_{0.92}\text{Mn}_{0.08}\text{Si}_2$. The addition of (Si+C) markedly decreases the thermal conductivity. It is considered that the decrement in the thermal conductivity is due to the increasing phonon scattering, which is resulted from the dispersion of the ultra-fine $\alpha\text{-SiC}$ particles and small crystal grain.

The calculated Z from the measured Seebeck coefficient, electrical resistivity and thermal conductivity for p-type $\text{Fe}_{0.92}\text{Mn}_{0.08}\text{Si}_2$ with addition of x mass%

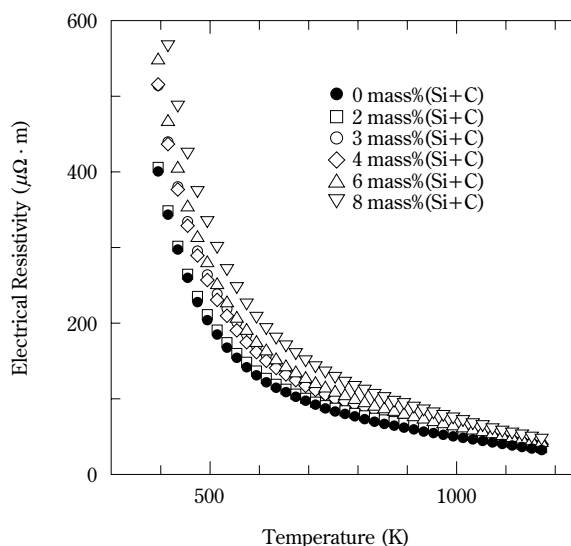


Fig. 5 Temperature dependence of the electrical resistivity for the sintered p-type $\text{Fe}_{0.92}\text{Mn}_{0.08}\text{Si}_2$ with addition of x mass% (Si+C).

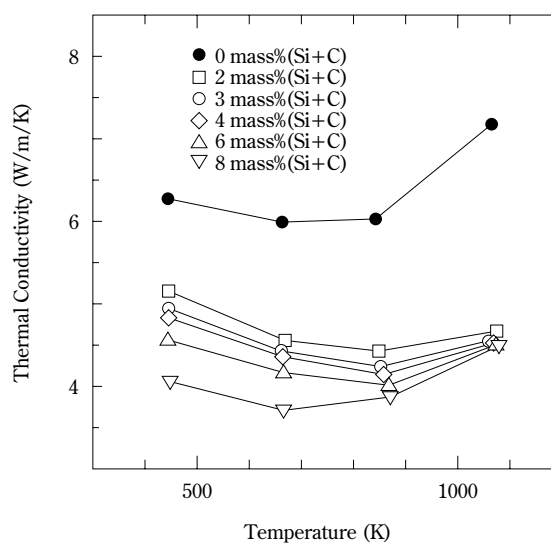


Fig. 6 Temperature dependence of the thermal conductivity for the sintered p-type $\text{Fe}_{0.92}\text{Mn}_{0.08}\text{Si}_2$ with addition of x mass% (Si+C).

(Si+C) are shown in **Figure 7**. It has been found that the addition of (Si+C) markedly increases Z , which shows maximum value at 4 mass%(Si+C). Similar results on the Seebeck coefficient, electrical resistivity, thermal conductivity and Z are also obtained about n-type $\text{Fe}_{0.98}\text{Co}_{0.02}\text{Si}_2$.

Next, in order to more improve the thermoelectric

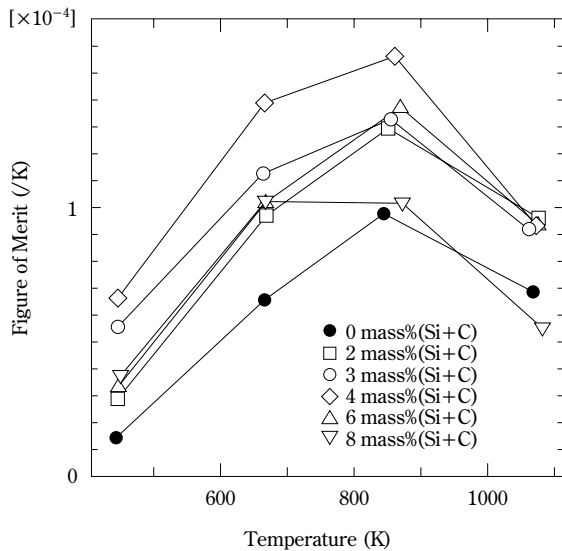


Fig. 7 Temperature dependence of the figure of merit for the sintered p-type $\text{Fe}_{0.92}\text{Mn}_{0.08}\text{Si}_2$ with addition of x mass% (Si+C).

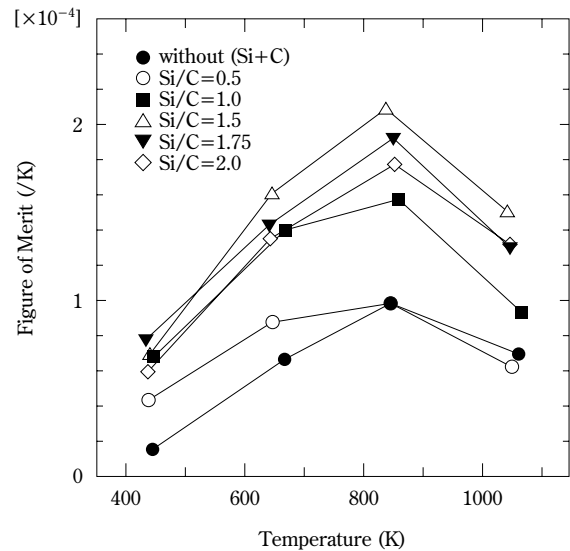


Fig. 8 Temperature dependence of the figure of merit for the sintered p-type $\text{Fe}_{0.92}\text{Mn}_{0.08}\text{Si}_2$ with 4 mass% (Si+C) at various Si/C ratios.

performance of this composite system, the effect of the molar ratio of Si to C ($\text{Si}/\text{C}=0.5\text{--}2$) in the additional 4 mass% (Si+C) on the thermoelectric properties of the hot-pressed p-type $\text{Fe}_{0.92}\text{Mn}_{0.08}\text{Si}_2$ and n-type $\text{Fe}_{0.98}\text{Co}_{0.02}\text{Si}_2$ has been investigated. As a result, the maximum Z appeared at $\text{Si}/\text{C}=1.5$ for p-type $\text{Fe}_{0.92}\text{Mn}_{0.08}\text{Si}_2$ and at $\text{Si}/\text{C}=1.75$ for n-type $\text{Fe}_{0.98}\text{Co}_{0.02}\text{Si}_2$, respectively. The temperature and Si/C ratios dependence of Z for p-type $\text{Fe}_{0.92}\text{Mn}_{0.08}\text{Si}_2$ are shown in **Figure 8**. The maximum Z for p-type $\text{Fe}_{0.92}\text{Mn}_{0.08}\text{Si}_2$ with $\text{Si}/\text{C}=1.5$ is about 1.5 times larger than that with $\text{Si}/\text{C}=1$. The increase of Z by the addition of Si and C is much dependent on the volume fraction of each phase and the morphology of the dispersed α -SiC. **Figure 9** shows the effect of the Si/C molar ratio in the additional 4 mass% (Si+C) on the volume fraction of the β - FeSi_2 , ϵ - FeSi , α -SiC and C. As can be seen from the figure, the volume fraction of the β -phase steeply increases with an increase of Si/C ratio, and becomes almost constant at higher than $\text{Si}/\text{C}=1.5$, which corresponds to the fact that the Seebeck coefficient reaches at maximum at about $\text{Si}/\text{C}=1.5$. It is also seen that the amount of the ϵ -phase, α -SiC and C decreases with the increasing Si/C ratio, and at $\text{Si}/\text{C}=1.5$ ϵ -phase almost disappears. The above results show that for the improvement of the thermoelectric performance of β - FeSi_2 it is necessary to stabilize the β -phase, decrease the ϵ -phase and disperse the moderate amounts of α -SiC particles.

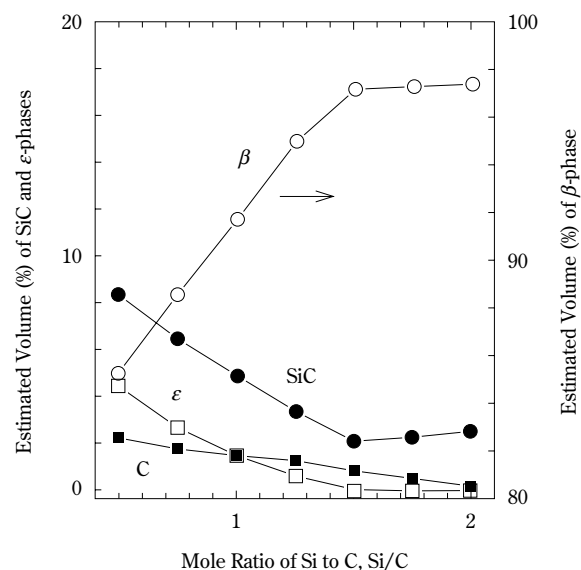


Fig. 9 Estimated volume fraction of β -phase and second phase vs molar ratio of Si/C in the additional (Si+C).

3.2 Thermoelectric properties of $\text{CoSb}_3\text{-FeSb}_2$ composite

The linewidth of the X-ray diffraction peaks of the CoSb_3 and FeSb_2 mixed powders becomes broader as the MG time increased, but in the sample after the MG treatment for 40h, we can still observe the diffraction peaks of CoSb_3 and FeSb_2 . The X-ray diffrac-

tion patterns of the sintered samples consist of the sharp diffraction peaks of CoSb_3 and FeSb_2 , but the diffraction peaks of FeSb_2 become smaller with an increase of MG time and in the samples with an MG time greater than 7h the diffraction peaks of FeSb_2 disappear. The disappearance of the FeSb_2 diffraction peaks is ascribed to the minute dispersion of the FeSb_2 particles into the CoSb_3 matrix.

Figure 10 shows the SEM photographs of the sintered CoSb_3 - FeSb_2 composite whose molar ratio of CoSb_3 to FeSb_2 is 0.6:0.4. It is observed that the grain size of the samples becomes smaller and the dispersion of FeSb_2 particles into CoSb_3 matrix proceeds with an increase of the MG time. The grain size of the dispersed FeSb_2 particles with a MG time of 30min is about 3 or 4 μm , while that with a MG time of 25h is less than 1 μm . The analysis by EDX shows that alloying between CoSb_3 and FeSb_2 proceeds, i.e., Co atoms in CoSb_3 are partly substituted by Fe, and Fe atoms in FeSb_2 are partly substituted by Co.

Figures 11(a) and **(b)** show the temperature and MG time dependence of the Seebeck coefficient and electrical resistivity for CoSb_3 and CoSb_3 - FeSb_2 composite with the CoSb_3 to FeSb_2 molar ratio of 0.8:0.2, respectively. All the Seebeck coefficients are positive, i.e., the CoSb_3 - FeSb_2 composite system is p-type. The Seebeck coefficient for the composite is smaller than that for CoSb_3 especially at low temperature, which is due to the low Seebeck coefficient of FeSb_2 as shown in the figure. The Seebeck coefficient increases with an increase of the MG time. The electrical resistivity for the composite is much smaller than that for CoSb_3 at high temperature, which is also due to the low electrical resistivity of FeSb_2 . The electrical resistivity increases with an increase of MG time, which is due to the enhancement of the carrier scattering at the grain boundaries as the grain size of the composite decreases with MG time. However, the electrical resistivity for the composite with a MG time of 40h is much smaller than that for CoSb_3 at high temperature.

The thermal conductivity is shown in **Figure 12** as a function of temperature and MG time for CoSb_3 and CoSb_3 - FeSb_2 composite. The thermal conductivity is much reduced by MG treatment. This is due to the enhancement of the phonon scattering at the grain boundaries, which is caused by the proceeding of the minute dispersion of the FeSb_2 particles into the CoSb_3 matrix.

Figure 13 (a) shows the temperature dependence of figure of merit Z , which was calculated from the Seebeck coefficient, electrical resistivity and thermal

conductivity. The Z for CoSb_3 shows a maximum value at about 500K, while that for the composite monotonously increases with temperature. In the low temperature range, the Z for the composite is smaller than that for CoSb_3 , but it increases with an increase of MG time, and the composite whose MG time is 25h has a maximum Z of $5.5 \times 10^{-4} \text{ K}^{-1}$ at 750K. We have also prepared the samples whose molar ratio of CoSb_3

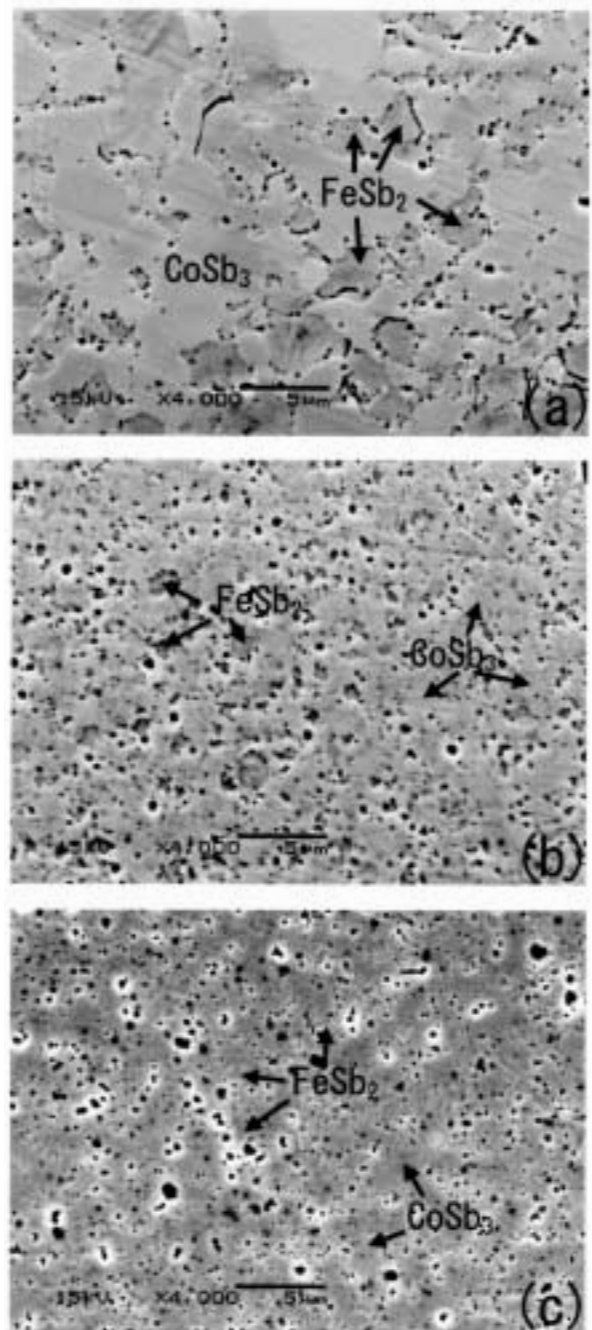


Fig. 10 SEM photographs for the sintered CoSb_3 - FeSb_2 composite whose molar ratio of CoSb_3 to FeSb_2 is 0.6:0.4. (a) MG 30min, (b) MG 7h and (c) MG 25h.

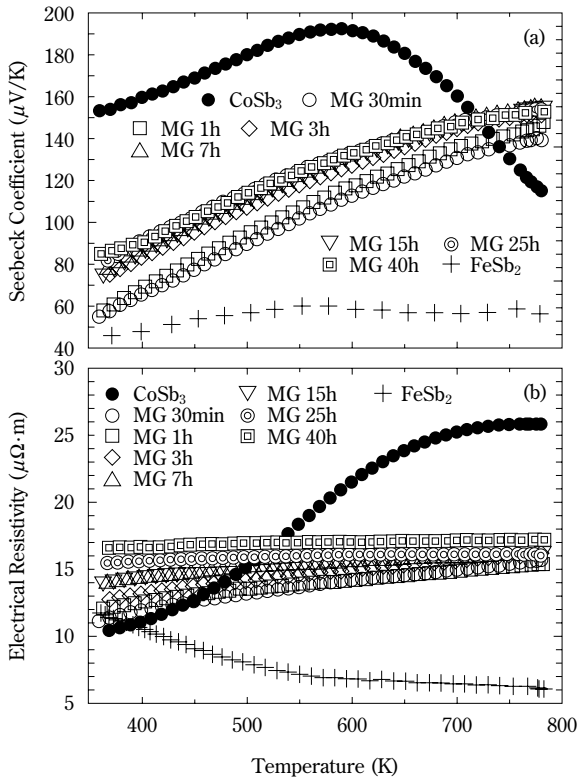


Fig. 11 (a) Seebeck coefficient and (b) electrical resistivity for the CoSb₃-FeSb₂ composite whose molar ratio of CoSb₃ to FeSb₂ is 0.8:0.2 as a function of the temperature and MG time.

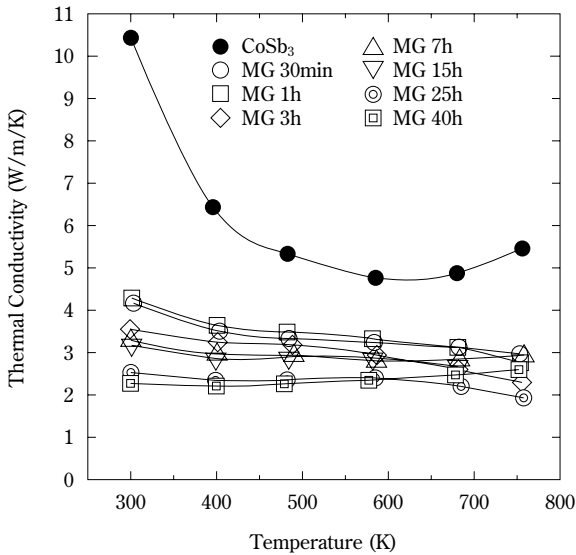


Fig. 12 Thermal conductivity for the CoSb₃-FeSb₂ composite whose molar ratio of CoSb₃ to FeSb₂ is 0.8:0.2 as a function of the temperature and MG time.

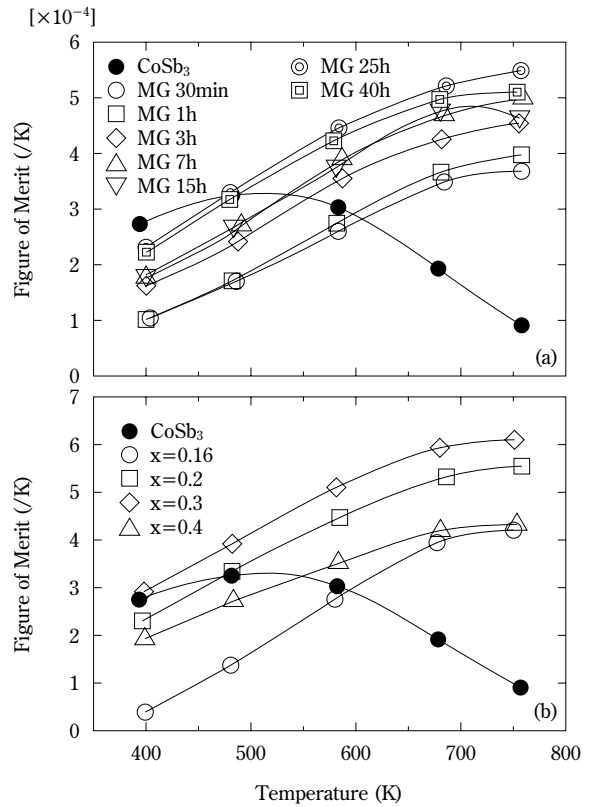


Fig. 13 (a) Figure of merit for the CoSb₃-FeSb₂ composite whose molar ratio of CoSb₃ to FeSb₂ is 0.8:0.2 as a function of the temperature and MG time. (b) Figure of merit for the CoSb₃-FeSb₂ composite whose MG time is fixed at 25h and molar ratio of CoSb₃ to FeSb₂ is 1-x:x as a function of the temperature.

to FeSb₂ varied from 0.84:0.16 to 0.6:0.4. MG time was fixed at 25h. **Figure 13 (b)** shows the temperature and molar ratio dependence of the Z for the CoSb₃-FeSb₂ composite. The sample whose molar ratio of CoSb₃ to FeSb₂ is 0.7:0.3 has a maximum Z of $6.1 \times 10^{-4} \text{ K}^{-1}$ at 756K.

4. Summary and Conclusion

We have synthesized the β -FeSi₂-Si, C and CoSb₃-FeSb₂ composites where the small particles are dispersed in the matrix, and investigated their thermoelectric properties. The key point in this study is to give the milling process to the mixture of the matrix and additional compounds. During milling process, the crystal grain is refined and the added materials are dispersed in the matrix, and sometimes alloying between the matrix and addition has been proceeding, which enhances the phonon scattering at the grain boundaries resulting in the reduction of the

thermal conductivity. On the other hand, the stabilization of the matrix phase induces the increase of the Seebeck coefficient. From the synergism of the above effects, the performance of the thermoelectric materials is raised. There are many problems to be examined such as the possibility of the incorporation of the impurities during milling process and the appropriate selection of the addition, but the MG or MA technique is a very effective method for producing the thermoelectric materials with high performance and more developments can be expected.

References

- 1) B. Abeles, *Phys. Rev.*, **131** (1963) 1906-1911.
- 2) C. M. Bhandari and D. M. Rowe, *Proceeding of the 2nd International Conference on Thermoelectric Energy Conversion*, Arlington, USA, (1978) 32.
- 3) J. S. Benjamine, *Met. Trans.*, **1** (1970) 2943-2951.
- 4) T. Kojima, M. Okamoto and I. Nishida, *Proceeding of the 5th International Conference on Thermoelectric Energy Conversion*, Arlington, USA, (1984) 56.
- 5) T. Kojima and N. Hiroyama, *Tech. Report Tokyo Salesian Polytechnic*, **12** (1986) 15.
- 6) R. Hultgren, P. D. Desai, D. T. Hawkins, M. Gleise and K. K. Kelley, *American Soc. For Metals*, Ohio, (1973) 873.
- 7) T. Sakata, Y. Sakai, H. Yoshio, H. Fugii and I. Nishida, *J. Less-Comm. Met.*, **61** (1978) 301-308.
- 8) H. Nagai, K. Nagai, T. Katsura, S. Katsuyama, K. Majima and M. Ito, *Mat. Trans., JIM*, **39** (1998) 1140-1145.
- 9) H. Nagai, T. Katsura, M. Ito, S. Katsuyama and K. Majima, *Mat. Trans., JIM*, **41** (2000) 287-292.
- 10) L. D. Dudkin and N. Kh Abrikosov, *Soviet Physics Solid State Physics*, **1** (1959) 126-133.
- 11) B. N. Zobrina and L. D. Dudkin, *Soviet Physics Solid State Physics*, **1** (1960) 1668-1674.
- 12) T. Caillat, A. Borshchevsky and J.-P. Fleurial, *Proceedings of 12th International Conference on Thermoelectrics*, Yokohama, Japan, (1993) 132-136.
- 13) K. Matsubara, T. Sakakibara, Y. Notohara, H. Anno, H. Shimizu and T. Koyanagi, *Proceedings of 15th International Conference on Thermoelectrics*, Pasadena, CA, (1996) 96-99.
- 14) J. W. Sharp, E. C. Jones, R. K. Williams, P. M. Martin and B. C. Sales, *J. Appl. Phys.*, **78** (1995) 1013-1018.
- 15) S. Katsuyama, Y. Kanayama, M. Ito, K. Majima and H. Nagai, *J. Appl. Phys.*, **88** (2000) 3484-3489.
- 16) T. Watanabe, M. Hasaka, T. Miyase, *J. Japan Inst. Met.*, **58** (1994) 353-358.
- 17) H. Nagia, S. Katsuyama, S. Nakayama, H. Kobayashi, K. Majima and M. Ito, *Mat. Trans., JIM*, **39** (1998) 515-521.
- 18) G. A. Slack, *J. Appl. Phys.*, **35** (1964) 3460-3468.

Author's short biography



Shigeru Katsuyama

Shigeru Katsuyama received his Dr. S degrees from the Department of Chemistry at Kyoto University in 1992. He was research associate from 1990 to 2003 at the Department of Materials Science and Engineering, Osaka University, and currently he is associated professor. His research interests include the processing and microfabrication of functional materials by chemical and metallurgical routes and the estimation of their physical properties. His current research activities are focused on the development of the thermoelectric materials with high performance.



Mikio Ito

Dr. Mikio Ito has been working as an Assistant Professor of the Department of Material Science and Processing at the Graduate School of Engineering, Osaka University, since 1997. He received his BE, ME, and Dr. E degrees in materials science and engineering from Osaka University in 1992, 1994 and 1997, respectively. His current research activities are focused on the fabrication and development of energy materials, such as thermoelectric materials, hydrogen storage materials etc., through metallurgical and chemical powder processing.

Hiroshi Nagai

Late professor Hiroshi Nagai was a director of the Japan Society of the Powder and Powder Metallurgy. He received his Dr. E degrees at Osaka University in 1971. He left a lot of honorable achievements on the study of functional materials, especially oxygen resistant alloys, permanent magnets and thermoelectric materials. He devoted his life into both teaching and doing research and wrote more than 200 papers on powder metallurgy.

Size Effect for Barium Titanate Nano-particles[†]

Tomoya Ohno, Daisuke Suzuki,
and Hisao Suzuki

Shizuoka University, Faculty of Engineering*

Takashi Ida

Nagoya Institute of Technology, Ceramic Research
Laboratory**

Abstract

Barium titanate (BT) nano-particles with different diameters were prepared by Sol-Gel method. The particle diameter was determined by XRD, and the lattice constants of nano-particles were also determined by XRD. We also measured the lattice vibration for BT nano-particles by raman scattering to discuss on the size effect. As a result, we successfully calculated the intrinsic dielectric constants for BT nano-particles by analyzing the lattice vibration. Moreover, we confirmed the shift of curie temperature by the size effect.

1. Introduction

Barium titanate (BT) is one of the most important dielectric materials for the electronic devices, such as MLCC (Multi Layer Ceramic Capacitor). The thickness of the barium titanate thin film in MLCC has become thinner and reached about 1 μm . Further down sizing is required for the higher performance. For this reason, we should take into account for the size effect of BT nano particles. The critical size for BT has been reported to be spread out in the wide range between 25 and 110 nm, depending on the measurement technique [1], [2]. On the other hand, the change in the electrical properties by the size effect has not been reported.

In this study, we measured the critical particle diameter by XRD and raman scattering in detail to show the phase transition by the size effect. In our previous works, the intrinsic dielectric constants for a lead titanate and lead zirconate titanate nano-particles were calculated by analyzing the raman spectra [3], [4]. In this study, we tried to use the same technique

to observe the dielectric behavior for BT nano-particles.

2. Experimental Procedure

Barium titanate nano-particles were prepared by Sol-Gel method. The starting reagents for barium titanate precursor solution are the metal barium and titanium iso-propoxide. At first, metal barium was refluxed in ethanol at 80°C for 1 hour to prepare the barium alkoxide solution. Next, titanium iso-propoxide was mixed in the barium alkoxide solution, and was refluxed at 80°C for 1 hour to prepare BT precursor solution. The BT precursor particle was prepared by evaporating the solvent from the precursor solution. The BT nano-particles with different diameter were prepared by calcining the BT precursor particle at 350°C to remove the residual organics followed by the annealing at different temperatures to deposit the BT nano-particles with different diameters.

The particle diameter was determined by XRD analysis by using Scherrer's equation. The phase transition by the size effect was observed by raman scattering, as well as the intrinsic dielectric constant. The shift of curie temperature was determined by raman analysis. The raman spectra were measured using JASCO Co., NR-1800, Rev.1.00 raman spectrometer in backscattering geometries. The 488 nm line of an argon ion laser was used as the excitation

* 3-5-1 Johoku, Hamamatsu, Shizuoka 432-8561, Japan

** 10-6-29, Asahigaoka, Tajimi, Gifu 507-0071

[†] This report was originally printed in J. Soc. Powder Technology, Japan, **41**(2), 86-91 (2004) in Japanese, before being translated into English by KONA Editorial Committee with the permission of the editorial committee of the Soc. Powder Technology, Japan.

source at a power level of 50 mW. Each spectrum was the result of the addition of several scans.

3. Results and Discussion

3.1. Change in lattice constant with particle diameter

The particle diameter was measured by XRD analysis using deconvolution technique [5] because the lattice constants for BT nano-particles along a- and c-axes exhibited very near values. Thus the observed XRD patterns were fitted by the Lorentz function to determine the half band width and peak angle, giving rise to the precise calculation of the lattice constants and the particle diameters. The particle diameter was calculated by using Scherrer's equation (equation 1).

$$D = \frac{K\lambda}{\beta \cos\theta} \quad (1)$$

where, $K(=0.9)$ is Scherrer's constant, λ the wavelength of X-ray and β the FWHM.

Figure 1 shows the lattice constant dependence as a function of particle diameter. It was found from this figure that the tetragonality decreased abruptly with decreasing particle diameter at around 30 nm, showing the abrupt phase transition of BT nano-particles compared with the phase transition of a lead titanate nano-particles [6]. In addition, the tetragonality of the 100 nm particle was considered to be lower than that of a single crystal at room temperature. Abrupt change in the lattice constants shown in **Fig. 1** and/or the size effect is ascribed to the rapid overdamping of soft modes [7] and the size dependence in the lattice constants for BT nano-particles exhibited almost same behavior as that reported by Uchino et. al. [2].

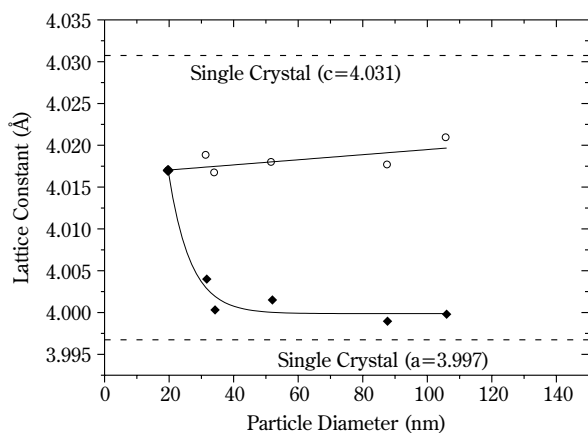


Fig. 1 The lattice constant with particle diameter

3.2. Raman analysis

In this study, accurate phase symmetry change with particle diameter or critical size was determined by the raman scattering because it was very difficult to determine the critical size for BT only by the XRD analysis due to the small difference in the lattice constants along a- and c-axes. By the raman scattering technique, it is easier to identify the crystal symmetry because tetragonal BT particle has the raman active crystal symmetry of C_{4v}^1 to show the distinguishable raman peaks at ambient temperature in contrast to the cubic BT nano-particles of the raman inactive O_h symmetry, leading to the peak disappearance at the critical particle diameter and critical temperature of curie point. Therefore, we can identify the crystal symmetry of BT nano-particles in principle by the existence of raman peaks at the measuring temperature. However, in the case of BT, it is reported that some phonon modes remain even for the cubic structure, because of the lattice relaxation and the secondary raman scattering [8]. Therefore in this study, raman spectrum of a BT single crystal was measured at above the curie temperature of 120°C to confirm the residual peak positions by the lattice relaxation and the secondary scattering. By comparing this raman spectrum of a BT single crystal measured at above the curie temperature and the measured raman spectra of the BT nano-particles, we can easily identify the crystal symmetry of BT nano-particles.

Figure 2 shows the raman spectra for the barium titanate nano-particles with different diameters at room temperature. The observed raman spectra were fitted by simply the sum of damped harmonic oscillators and a Debye relaxation mode. The lattice mode was assigned by analyzing the single crystal data. However, it was very difficult to determine the exact mode frequencies for BT because of their very small difference in the mode frequencies. Therefore, we used polarized laser to assign the accurate mode frequencies for a BT single crystal. **Table 1** listed the index in space group for tetragonal BT. From **Table 1**, only A(LO) modes are detected in raman scattering under the condition of X(ZZ)X (enter the Z-axis polarized incident laser from the X plane of BT single crystal, and then measure the reflected scattering polarized along Z-axis; hereafter the measuring condition is denoted such like this). In this study, A(TO), A(LO) and E(LO) modes were measured under the conditions of Z(YY)Z, X(ZZ)X and X(ZY)X, respectively. Here, a sharp peak was observed at 308 cm^{-1} when measured under the condition of Z(YX)Z to confirm a silent mode. The peak near

200 cm^{-1} was confirmed by the measurements under the conditions of X(ZZ)X and X(ZY)X to be the superimpose of E(1LO) and A1(1LO) modes. Furthermore, it has been reported that the peak near 200 cm^{-1} was also observed by the raman analysis under the X(ZY)Z condition. Therefore, we assigned at last the peak near 200 cm^{-1} to be the superimpose of three peaks of E(1LO), A(1LO) and E(2TO). The observed results in this study were in good agreement with those of the results for a BT single crystal by another reports.

Figure 3 shows the raman spectra for a BT single crystal using the polarized laser under the different conditions. However, raman spectrum under the

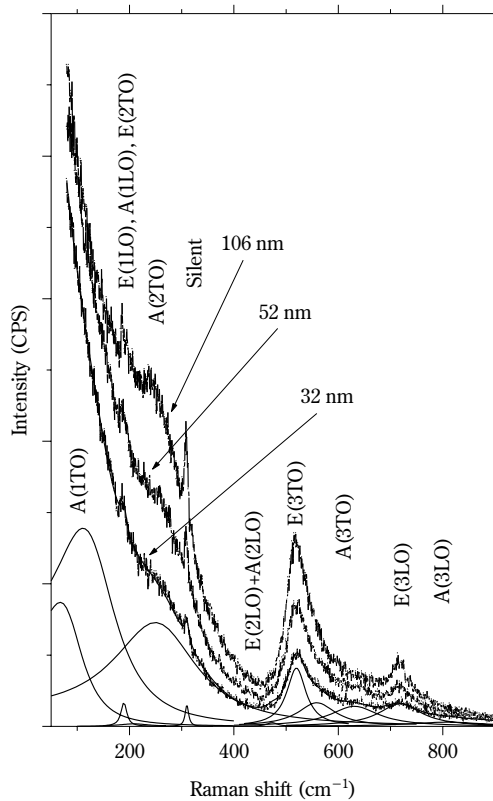


Fig. 2 Raman spectra for BT nano-particles with different particle diameters.

Table 1 Index for tetragonal system in space group

Space Group: C_{4v}^1	
A_1	$\alpha_{xx} + \alpha_{yy}, \alpha_{zz}$
B	α_{xy}
E	$(\alpha_{yz}, \alpha_{zx})$

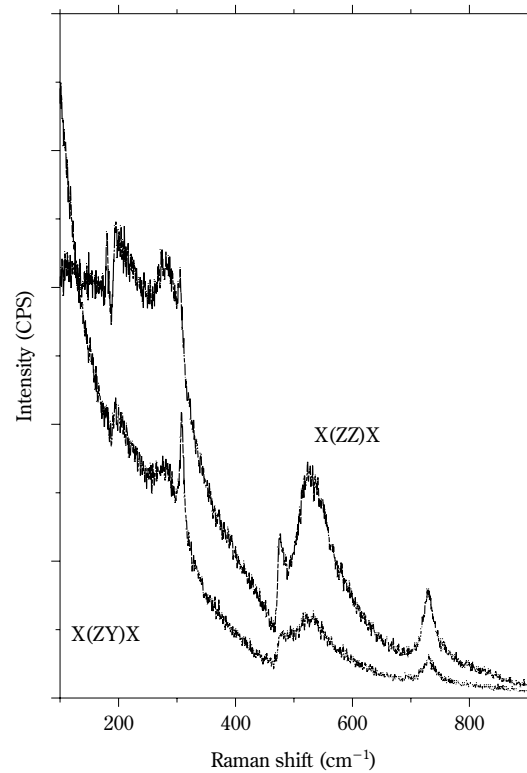


Fig. 3 (a) Raman spectra of BT single crystal (1)

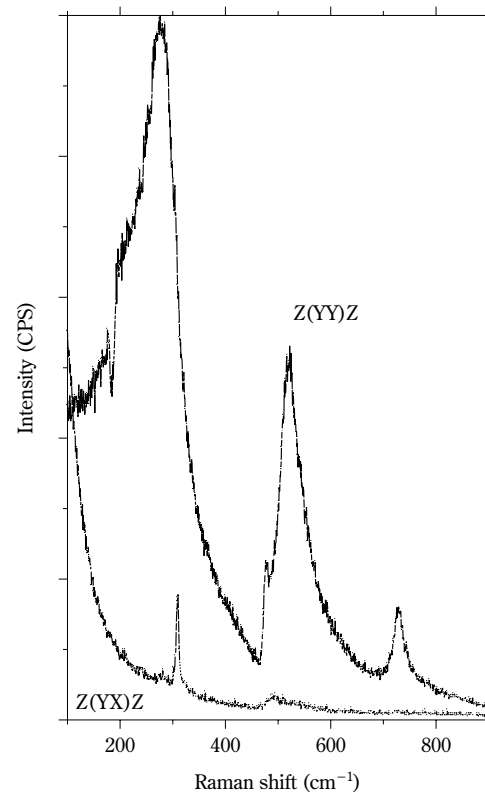


Fig. 3 (b) Raman spectra of BT single crystal (2)

X(ZY)Z condition (90° scattering) could not be observed in this measurement to assign only the E(TO) mode because of the sample limitation. Therefore, we used the reported value for E(TO) mode [7], [9] to analyze the raman spectra for a BT single crystal, leading to the accurate raman analysis for BT nanoparticles. These analyses enabled the calculation of the intrinsic dielectric constant for a BT single crystal by using the LST relation. As a result, the intrinsic dielectric constants of a BT single crystal along a- and c-axes were calculated to be 1247 and 44, respectively. These values were in good agreement with those reported for a BT single crystal ($\epsilon_a=1500$, $\epsilon_c=38$) [7], [9], indicating the accuracy of the measurement technique.

3.3. Change in curie temperature with particle diameter

Generally, the size effect for ferroelectric materials results in the curie temperature shift to the lower temperature. Therefore, the curie temperature shift for BT nano-particles was investigated in this study. **Figure 4** shows the curie temperature shift as a function of the particle diameter. As already pointed out, some lattice vibration remained above the curie temperature by the secondary scattering and so on, in the case of BT. Hence, the raman spectrum for a BT single crystal was measured at above curie temperature of 140°C to assign the residual peaks by the secondary scattering and so on. By this treatment, it was found that the curie temperature for BT nano-particles was shifted to the lower temperature at around 20-30 nm of particle diameter. This tendency was

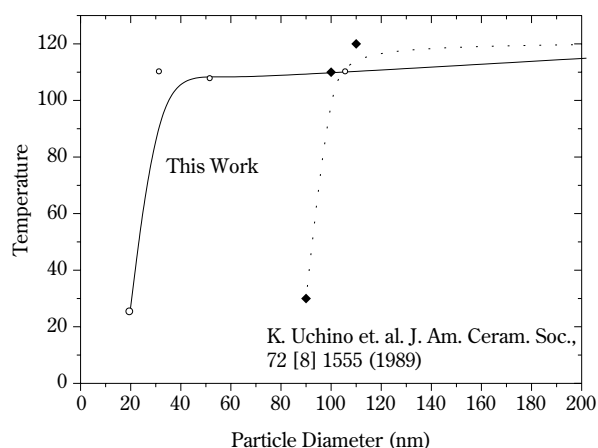


Fig. 4 Change in the curie temperature as a function of particle diameter

almost same as that of the result of Uchino et. al. measured by the change in the lattice constants as a function of the particle diameter using XRD. However, their result showed that the curie temperature shift to the lower temperature began at around 100 nm of particle diameter. This difference in the critical size for BT was ascribed to the measurement techniques of the particle diameter and the crystal symmetry.

3.4. Change in dielectric constant with particle diameter

Whereas there have been many reports on the size effect for ferroelectric materials, there is no report about size effect on the electrical properties for ferroelectric nano-particles. This was ascribed to the difficulty in the measurement of the electrical properties for nano-particles. For example, in the case of the dielectric measurement, the impedance analyzer is used to measure the capacitance of the materials to calculate the dielectric constant. However, by this measurement technique, only the extrinsic dielectric constant including the effect of pores, space charge and so on was estimated, leading to the misunderstanding of the dielectric behavior in the case of the ferroelectric nano-particles which could not be compacted into the dense green body. The measurement of the extrinsic dielectric constant is useful to apply the ferroelectric materials to the electronic devices, however, the intrinsic dielectric constant could not be measured by this method. Therefore, in this research, the intrinsic dielectric constant, not including the effect of pores, space charge and so on, was estimated from the raman spectra by using the LST relation (equation 2).

$$\frac{\epsilon}{\epsilon_{\infty}} = \frac{\omega_{1LO}^2}{\omega_{1TO}^2} * \frac{\omega_{2LO}^2}{\omega_{2TO}^2} * \frac{\omega_{3LO}^2}{\omega_{3TO}^2} \quad (2)$$

where, ω is the mode frequency for each phonon modes, and ϵ_{∞} is optical dielectric constant ($a=5.22$, $c=5.07$). **Table 2** lists the observed mode frequencies for A mode (c-axis direction) of a BT nano-particle with 105 nm. The mode frequencies were calculated by the fitting the spectrum using the damped harmonic oscillators [4], [8]. From these calculation, the intrinsic dielectric constant for BT nano-particle with

Table 2 Mode frequencies from the BT nano crystal with 105 nm diameter

A(1TO)	A(2TO)	A(3TO)	A(1LO)	A(2LO)	A(3LO)
159.3 cm ⁻¹	262.0 cm ⁻¹	548.1 cm ⁻¹	193.3 cm ⁻¹	460.5 cm ⁻¹	739.5 cm ⁻¹

105 nm diameter along c-axis was calculated to be $\epsilon_c=42.0$. In addition, intrinsic dielectric constant for BT nano-particle with 105 nm diameter along a-axis was calculated to be $\epsilon_a=1254.6$ by the calculation for E modes.

In the previous section, the curie temperature was confirmed to shift to the lower temperature by the size effect. This suggests that the dielectric behavior should change according to that illustrated in **Figure 5**. Therefore, it is speculated that the intrinsic dielectric constant increases at room temperature by the size effect. In this study, the intrinsic dielectric constant of BT nano-particles calculated from the equation (2) increased with decreasing particle diameter at around 40 nm as shown in **Figure 6**. Further-

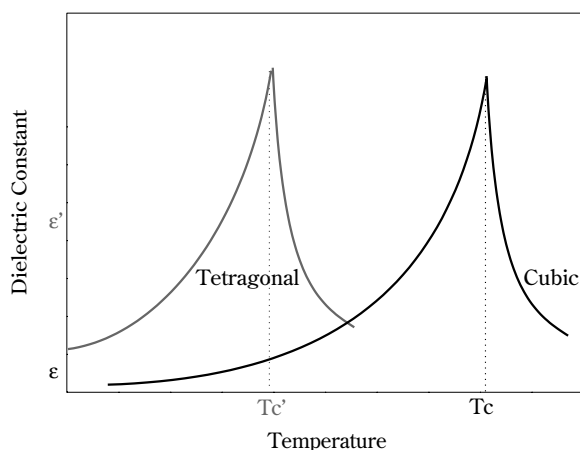


Fig. 5 Schematic illustration for the curie temperature shift of BT nanocrystals

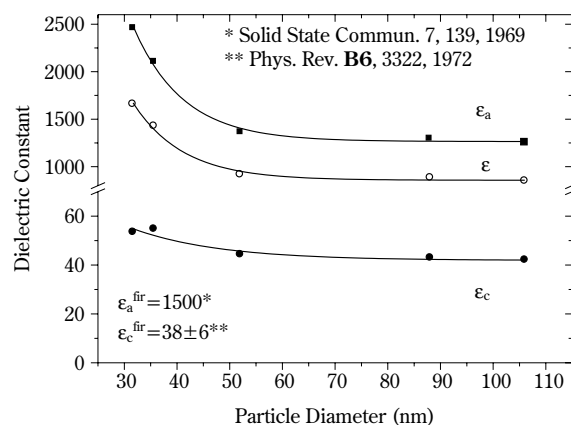


Fig. 6 Change in the intrinsic dielectric constant for BT nanocrystals estimated by raman scattering with particle diameter

more, the intrinsic dielectric constant for a BT nano-particle with 30 nm particle diameter exhibited a larger value than that for a single crystal. These results demonstrate that the intrinsic dielectric constant increases drastically with decreasing particle diameter according to the equation (2), which suggests the possibility for high K (dielectric) materials with thin layers of ferroelectric nano-particles.

3.5. Evaluation of critical size for BT

From the **Figs. 1** and **4**, the tetragonality for BT nano-particles decreased dramatically at around 40 nm of particle diameter, and finally the crystal structure changed to cubic phase at 20 nm. In addition, the intrinsic dielectric constant started to increase at around 40-50 nm, and reached larger value than that for a single crystal if the particle diameter was below 40 nm. Furthermore, it was also confirmed from the raman analysis that the crystal structure was perfectly transformed to the cubic phase at 20 nm of particle diameter. Zhong et. al. has been reported that the onset of the surface relaxation was calculated to start at the size of 43 nm based on the surface relaxation model, in which the surface part of the particles were consisted of the cubic phase [10]. This theoretical consideration will sustain our experimental results. Therefore, we concluded that the critical size determined by the raman analysis together with the XRD analysis was reasonable and the raman analysis was the powerful tool for analyzing the ferroelectric materials.

4. Conclusion

In this study, we demonstrated that the size effect for BT nano-particles could be estimated by using the raman analysis together with the XRD analysis. As a result, the phase transition by the size effect for a BT was successfully confirmed to start at around 20-30 nm of particle diameter. Therefore, the critical size of BT was considered to be about 20 nm. On the other hand, we succeed to separate the exact phonon mode frequencies in raman spectra of BT nano-particles by measuring the fundamental mode frequencies for a single crystal. In addition, the intrinsic dielectric constants for BT nano-particles were successfully calculated by substituting the exact phonon mode frequencies for a LST relation. These results successfully demonstrated that the raman scattering is the powerful tool not only for the analysis of the size effect but also the measurement of the intrinsic dielectric behavior of ferroelectric materials.

5. References

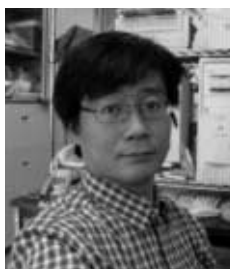
- [1] Kenji Ishikawa and Takatosho Uemori, "Surface relaxation in ferroelectric perovskites", *Phys. Rev.*, **B60**, pp.11841-11845 (1999)
- [2] Kenji Uchino, Eiji Sadanaga and Terukiyo Hirose, "Dependence of the Crystal Structure on Particle Size in Barium Titanate", *J. Am. Ceram. Soc.*, **72**, pp.1555-1558, (1989)
- [3] Hisao Suzuki and Tomoya Ohno, "Characterization of the Ferroelectric Nano Particles by Raman Scattering", *Jpn. J. Soc. Powder Technol.*, **39**, pp.877-884, (2002)
- [4] Tomoya Ohno, Takayuki Mori, Hisao Suzuki, Desheng Fu, Wilfried Wunderlich, Minoru Takahashi and Kenji Ishikawa, "Size Effect for Lead Zirconate Titanate Nanopowders with $\text{Pb}(\text{Zr}_{0.3}\text{Ti}_{0.7})\text{O}_3$ Composition", *Jpn. J. Appl. Phys.*, **41**, pp.6985-6988, (2002)
- [5] Ida, T. and H. Toraya: "Deconvolution of the instrumental functions in powder X-ray diffractometry" *J. Appl. Cryst.*, **35**, 58 (2002)
- [6] Ishikawa, K., K. Yoshikawa and N. Okada: "Size effect on the ferroelectric phase transition in PbTiO_3 ultrafine particles" *Phys. Rev. B: Condens. Matter.* **37**, 5852 (1988)
- [7] Scalabrin, A., A. S. Chaves, D. S. Shim and S. P. S. Porto: "Temperature Dependence of the A_1 and E optical phonons in BaTiO_3 " *Phys. Stat. Sol. (b)*, **79**, 731 (1977)
- [8] Fu, D. S., H. Iwazaki, H. Suzuki and K. Ishikawa: "Phonon mode behaviors of PbTiO_3 thin films deposited on Pt/Si substrates" *J. Phys.: Condens. Matter.*, **12**, 399 (2000)
- [9] Domenico, M., S. H. Wemple, S. P. S. Porto and R. P. Bauman: "Raman Spectrum of Single-Domain BaTiO_3 " *Phys. Rev.* **174**, 522 (1968)
- [10] Zhong, W. L., Y. G. Wang, P. L. Zang and B. D. Qu: "Phenomenological study of the size effect on phase transitions in ferroelectric particles" *Phys. Rev.* **B50**, 698 (1994)

Author's short biography



Hisao Suzuki

Prof. Hisao Suzuki has been at Department of Materials Science, Shizuoka University, Japan since 1994. He was also a Prof. at Mechanical System Engineering of Toyota Technological Institute from 1982 to 1994. He is now one of the *advisory* committee of the Society of Sol-Gel Science and the Society of Powder Technology and was one of the editorial board of the Journal of the Powder Technology, Japan and Journal of Advanced Powder Technology. He was also one of the editorial board of the Bulletin of Ceramics. His major research areas lie in the chemical processing of advanced nano-materials and thin films to apply the nano-devices, especially through the alkoxide route. His current activities are focused on the preparation of hybrid nano-particles by the nano-coating and hybrid integration of ferroelectric thin films with electrode and other nano-layers with controlled nano-structures for Micro(nano)-Electro-Mechanical Systems.



Takashi Ida

Prof. Takashi Ida has been at Ceramic Research Laboratory, Nagoya Institute of Technology, Japan since 1999. He was also a Research Associate at Department of Science, Himeji Institute of Technology from 1991 to 1999 and at Institute for Molecular Science from 1989 to 1991. His major research area lies in the development of a novel analytical method of X-ray diffraction. His current activities are focused on the analyses of the inorganic materials and powders.



Tomoya Ohno

Dr. Tomoya Ohno has been working at the innovative joint research center in Shizuoka University since 2004, as Post Doctoral Fellow under the direction of Prof. M. Fujimoto. He received Ph.D from Shizuoka University in 2004. His main research area lies in the raman analysis for ferroelectric nano-particles and thin films, as well as the electrophoresis control of DNA using nano-spheres.



Daisuke Suzuki

Daisuke Suzuki received his BE degree from the Department of Material Science at Shizuoka University in 2003 under direction of Prof. H. Suzuki. His main research area lies in the size effect for ferroelectric nano-particles.

Information Articles

The 38th Symposium on Powder Technology

The 38th Symposium on Powder Technology was held on September 7, 2004 at the Hotel Floracion Aoyama in Tokyo under the sponsorship of the Hosokawa Powder Technology Foundation and with the support of Hosokawa Micron Corporation. The

symposium in this year was also very successful with the attendance of 160 including about 21 academic people. The main subject of this year was “Towards Further Progress in Powder Industry through Nanostructure Control.”

The 38th Symposium on Powder Technology

Subject: “Towards Further Progress in Powder Industry through Nanostructure Control”

Session 1 Chairperson: Prof. Yutaka Tsuji (Osaka Univ.)

<ul style="list-style-type: none"> • Mass-Production, Functions and Applications of Carbon Nanotubes • Stability of nano particles in solutions and the microstructures of their surfaces (KONA Award Commemorative Lecture) 	<p>Prof. Morinobu Endo (Sinshu Univ.)</p> <p>Prof. Ko Higashitani (Kyoto Univ.)</p>
--	---

Session 2 Chairperson: Prof. Kiyoshi Nogi (Osaka Univ.)

<ul style="list-style-type: none"> • Pharmaceutical design of nano-particulate systems for controlled drug delivery • Novel polymer colloids by environmental-benign processing 	<p>Ph.D. Hirofumi Takeuchi (Gifu Pharm. Univ.)</p> <p>Prof. Hidekazu Yoshizawa (Okayama Univ.)</p>
---	--

Session 3 Chairperson: Prof. Makio Naito (Osaka Univ.)

<ul style="list-style-type: none"> • Design and application of photonic fractal structure using nanoparticles • Nanostructure control for particles and materials, and its application — New machines for nano technology and their application — 	<p>Prof. Yoshinari Miyamoto (Osaka Univ.)</p> <p>Dr. Takehisa Fukui (Hosokawa Powder Technology Research Institute)</p>
---	---



The 12th KONA Award

Dr. Ko Higashitani, Professor of Kyoto University, was selected as the winner of the 12th KONA Award, which is sponsored by Hosokawa Powder Technology Foundation and given to the scientists or groups who have achieved distinguished research works in the field of particle science and technology.

Professor Ko Higashitani graduated from Department of Chemical Engineering, Kyoto University, Japan in 1968, and received a Ph.D. degree in 1973 under the supervision of Prof. A.S. Lodge in Department of Chemical Engineering, University of Wisconsin-Madison, USA. Then he moved to Department of Applied Chemistry, Kyushu Institute of Technology, Japan, as an assistant professor, and became a full professor in 1983. He joined Department of Chemical Engineering, Kyoto University in 1992.

His major research interests have been in the kinetic

stability of colloidal particles in solutions, such as coagulation, breakup, adhesion, detachment of particles in fluids, slurry kinetics, etc. But his recent interests are concentrated on measuring in-situ the molecular-scale structures of particle surfaces by atomic force microscopy, and investigating their correlation with interaction forces between particles and the macroscopic behavior as dispersions.

The KONA award of this year was given to his pioneer works to clarify the correlation between the molecular-scale structures of particle surfaces and their macroscopic behavior in dispersions.

On January 21, 2004, Mr. Masuo Hosokawa, President of the Foundation, handed the 12th KONA Award to Professor Higashitani at the ceremony of presentation held at the R&D Center of Hosokawa Micron Corporation in Hirakata.



Academic publication concerning powder technology in Japan (2003)

JOURNAL OF THE SOCIETY OF POWDER TECHNOLOGY, JAPAN VOL. 40 (2003)

- Simultaneous Operations of Fractionation and Concentration of Binary Protein Mixtures with Particles of Superabsorbent Hydrogels
E.Iritani, Y.Mukai, C.Ueki and N.Katagiri 4
- Compression of a Cohesive Powder in a Storage Container by Centrifugal Force
H.Tsunakawa 11
- Rheology of Fine Particle Suspension from Low to High Concentration – Static Properties –
Y.Nagase, K.Okada and I.Sugiyama 86
- Observation of Filler Packing Structure in Narrow Channels of Thermosetting Plastics Molding Compound
T.Kawaguchi, M.Suzuki and M.Hirota 93
- Preparation of Micron-Size Monodispersed Hematite Particles by Gel-Sol Method
Y.Yonemochi, M.Kimata, K.Yoshimoto, M.Hasegawa, M.Tsukada and H.Kamoya 150
- Design of Solid Dispersion Particles of Drug with Fine Porous Carriers
H.Takeuchi, S.Nagira, H.Yamamoto and Y.Kawashima 157
- Characterization of Particle Orientation in Tape Cast Alumina Green Body Using a Polarizing Microscopy
H.Abe, K.Okamoto, T.Hotta, M.Naito and K.Uematsu 163
- Fabrication of Cordierite Filter with Corrosion Resistance for High Temperature Dust Collection
M.Fuji, Y.Shiroki, M.Takahashi, H.Suzuki, S.Izuhara and Y.Yokoyama 169
- Fast Algorithm of Distinct Element Method with Contact Force Prediction Method
C.Tokoro, K.Okaya and J.Sadaki 236
- Segregation and Dynamic Behavior of Binary Particles of Different Size in 2-D Gas-Solid Fluidized Beds
J.Oshitani, B.Torisakti and Z.Tanada 246
- Stabilization of Photo Degradable Drug Powder by Dry Coating Agglomeration
R.Ito, A.Maida, K.Shinohara and N.Izawa 330
- Evaluation and Control of the Adhesive Force between Fine Particles by Surface Modification Method
Y.Shimada, Y.Yonezawa and H.Sunada 334
- Relation between Distribution of Compressive Force and Convective Flow in Vibrating Particle Beds
Y.Nakanishi, Y.Yamada and K.Saito 339
- Rheology and Stability of Alumina-Water Slurry
T.Saeki 425
- Analysis of Sedimentation and Settling Process of Dense Alumina Slurries by Hydrostatic Pressure Measurement
J.Tsubaki, K.Kuno, I.Inamine and M.Miyazawa 432
- New Evaluation Technique for Slurry Characterization by Constant Pressure Filtration
J.Tsubaki, H.J.Kim, T.Mori, T.Sugimoto, H.Mori and N.Sasaki 438
- Study of Swirling Pneumatic Transport of Granules in a Vertical Pipe
H.Ueda, J.Li, K.Horii, K.Funatsu and Y.Tomita 482
- Dispersion of Surface Modified Silica Nanoparticles into a Resin by Using a Twin Screw Extruder
K.Matsumoto, T.Yoshida and K.Okuyama 489
- Effects of NaOH Concentration on Zeolite Synthesis from Fly Ash with a Hydrothermal Treatment Method
K.Jukui, Y.Nishimoto, M.Takiguchi and H.Yoshida 497
- Effect of Sieve Opening on Packing Properties of Fine Powder by Tapping under Reduced Pressure
T.Ishikura and H.Nagashima 558
- Preparation of Sub-micron Particles of Fatty Acid Multivalent Metal Salt Using Newly Developed Jet-Mixing Method
K.Sawada and M.Konaka 565
- Characteristics of Dust Collection in Moving Bed with Dust Generation
S.Ogawa, N.Ehara, Y.Bando and M.Nakamura 573
- Shape Separation of Particles by a Newly Developed Separator with Flowing Liquid Film
K.Yamamoto, T.Nishikawa, T.Miyajima, R.Yamazaki and M.Sugimoto 624
- Toner Size Selectivity in Electrophotographic Transfer Process
A.Noda, M.Takeuchi, Y.Yamaguchi, N.Katsuta and T.Fukuhara 631
- Dependence of Toner Charging Characteristics of Toner/Carrier Mixing Ratio
H.Okada and M.Takeuchi 639

● Structure and Properties of Thiol-Functionalized Silica Gels Prepared by Sol-Gel Process H.Tanaka, M.Yokoji and R.Hino	649
● R&D of Milling Technology in Pharmaceutical Industry T.Fukunaka and J.W.Tom	655
● Constitutive Equation and Governing Differential Equation for Filtration Expressed in Moving Coordinate Y.Nagase, K.Okada and S.Qian	712
● Synthesis of Rare Earth Element-Iron-Oxygen Ultrafine Particles by Using Inductively Couple Plasma – Relation between Ionic Radius of Rare Earth Element and Products – M.Sugasawa, N.Kikukawa, Y.Nagano, N.Kayano and T.Kimura	720
● Experimental Verification of Governing Differential Equation for Filtration – Constant Pressure Cake Filtration – Y.Nagase and K.Okada	786
● Dewatering Effect in Variable Pressure Filtration and Simplified Estimation Method of Filtrate Volume Y.Nagase and K.Okada	795
● Collection of Hydrocarbons Generated by Thermal Decomposition of Polystyrene by Ceramic Filters and Their Cleaning by Pulse Jet S.Ogawa, T.Kijima, Y.Bando and M.Nakamura	801
● Effects of Oxidization and Adsorbed Moisture on Time Change in Tribo-electrification of Powder Particles H.Masuda, D.Yasuda, A.Ema, H.Mizutani and K.Tanoue	860
● Effects of Production Conditions on Specific Surface Area of Nickel Ultrafine Particles Produced by DC Plasma Jet K.Saitou	868

KAGAKU KOGAKU RONBUNSHU VOL. 29 (2003)

• Continuous Dry Material Separation from Automobile Shredder Residue J.Oshitani, K.Kiyoshima and Z.Tanaka	8
• Analysis of Bubbles in a Three-Dimensional Fluidized Catalyst Bed Using a Fast X-ray CT Scanner T.Kanda, T.Kai, T.Takahashi, M.Misawa, N.Ichikawa and I.Tiseanu	112
• Captive Particle Imaging and Structural Change on Combustion of Petroleum Cokes Containing Ash M.Yokota, T.Nishimura, M.Hataoka and M.Hayashi	140
• Particle Properties of LiMn_2O_4 Fabricated by Ultrasonic Spray Pyrolysis Method K.Matsuda and I.Taniguchi	232
• Time Dependency of the Pressure Drop in a Flat Type Pulse Jet Fabric Filter C.Kanaoka and Y.Yao	267
• Control of Product Particle Size by Closed-circuit Pulverization System H.Yoshida, A.Miyatake, E.Shinoda, K.Fukui and H.Kanemoto	272
• Particle Size Analysis of Silica Powders in Diluted-Dispersed Suspension by Ultrasonic Attenuation H.Abe, M.Naito, K.Nakahira, T.Hotta, Y.Suzuki, H.Shimada, K.Yonekura and K.Kato	442
• Compression Test of K NEEDED Wed Powder in a Cylinder T.Moriwaki	445
• Influence of Ammonia Concentration on Particle Size Distributions in Seeded Reaction of Hydrolysis and Condensation of Tetraethyl Orthosilicate D.Nagao, E.Mine, T.Katakura and M.Konno	546
• Measurement of Trapping Behavior of Dust Particles during Plasma Process by Suck-Out Method K.Kondo, Y.Imajo, M.Shimada and K.Okuyama	513
• Development of an Airtight Oscillating Fluidized Bed S.Deguchi, M.Deguchi, A.Nishimura and Y.Fujima	493
• Proposal of a New Rheological Model of a Highly Loaded Coal-Water Mixture (CWM) S.Matsuo	526
• Heat Transfer Characteristics in an Airtight Oscillating Fluidized Bed and Their Relation with Bubble Behavior S.Deguchi, M.Deguchi, M.Isobe, A.Nishimura and Y.Fujima	585
• Effect of the Blade Shape on the Performance of a Mechanical Impact Mill S.Akiyama, K.Kozawa and H.Yoshida	607
• Algebraic Expression of the Minimum Gas Velocity Restraining Downward-Flowing Particles through the Contraction Midway of a Circulating Fluidized Bed Riser S.Deguchi, T.Mizuno, K.Matsuoka, A.Nishimura, H.Nasu and Y.Fujima	660
• Model Analysis of Iron Ore Reduction in a Circulating Fluidized Bed Y.Kato and H.Itaya	667
• Estimation of Filtering Velocity and Pressure Drop Parameters from Total Pressure Drop in a Multi-Compartment Bag Filter H.Ikeno, Y.Tada, S.Hiraoka and Y.Shuto	701
• Applicability of the Dilatancy Model to Suspensions in Shear-thinning Medium S.Ookawara and K.Ogawa	714
• Effect of Polyacrylic Acid on Flocculation and Dispersion Behavior of Fine $\alpha\text{-Al}_2\text{O}_3$ Particles J.Shibata, K.Fujii, K.Horai, N.Murayama and H.Yamamoto	753
• Design of Granules for Homogeneous Green Compacts A.Shimosaka, T.Suzukawa, Y.Shirakawa and J.Hidaka	802
• Design of Granules for Green Compacts by Simulation of Spring-back Behavior A.Shimosaka, Y.Yamamoto, Y.Shirakawa and J.Hidaka	811
• Development of a Method for Determination of the Amount of Particles Reaching the Wall of a Coal Gasifier Y.Harada, T.Yamashita, T.Yamamoto, H.Aoki and T.Miura	795

JOURNAL OF AEROSOL RESEARCH VOL.18 (2003)

● Emissions of Organic Carbon from 'In-Use' Diesel Vehicles H.Yokota, S.Tahara, F.Sano and K.Sakamoto	40
● Calculation of Molecule-cluster Collision Cross Sections Y.Okada, S.Yamaguchi and K.Takeuchi	47
● Performance of Electrostatic Precipitator Using Electrospray Charging Method J.H.Ahn, J.U.Yoon, K.Y.Kim and K.H.Ahn	98
● Measurement of Particles in Processing Plasma Area by Using a Sampling Method K.Kondo, M.Shiratani and Y.Watanabe	118
● Numerical Simulation of Aerosol Behavior in Turbulent Natural Convection – Evaluation of Aerosol Behavior by Homogeneous Nucleation in Cover Gas Region of LMFRs – H.Ohira	125
● Reduction of Diesel Exhaust Emissions by Passive Regeneration-type Diesel Particulate Filters Y.Yokota, S.Tahara, H.Ueno and K.Sakamoto	185
● Development of Nitrate Particle Analyser H.Yoshiyama, M.Nimura, R.Yamaguchi and M.Itoh	195
● Elastic Light Scattering Measurement of an Ellipsoid Aerosol Particle S.Yoshiyama	272
● Influences of Fiber Crimp and Cross-sectional Shape on Particle Collection Performance of Cigarette Filter M.Inagaki, N.Namiki and Y.Otani	278

New Products News

NANOCULAR SYSTEMS

Hosokawa Micron has developed a new process technology, Mechano Chemical Bonding (MCB) Technology, which incorporates field energy, such as Plasma or High Magnetic Field Energy, and mechanical energy to create advanced functional composites with nanostructures.



NANOCULAR P™ – Laboratory Model

Laboratory model is to develop a small amount of advanced materials. In conjunction with mechanical energy, the new system utilizes plasma irradiation to clean the particle surfaces, enabling the formation of strong bonds between particles for creating New Functional Materials.

< Technical Specifications >

Model: NC-Lab-P

Motor: 2.2 kW

Effective Capacity: 0.1 liter



NANOCULAR P™ – Continuous Model

Continuous model is for the commercial production of advanced functional materials. Together with the mechanical energy, the new system utilizes plasma irradiation to clean the particle surfaces, enabling the production of New Functional Materials in a continuous operating system.

< Technical Specifications >

Model: NC-400-P

Motor (max): approx. 100 kW

Capacity: 10~100 kg/hr

The system consists of vacuum pump, chiller unit and pre-mixer.

New Products News

MECHANOFUSION® FOR PHARMACEUTICAL cGMP APPLICATION

By applying mechanical forces to the processed materials, **MECHANOFUSION®** can precisely mix different particles together, produce composite materials and modify particle shapes. **MECHANOFUSION®** system has been successfully used for numerous industrial applications. In addition to the standard units, specially designed cGMP models are available with a capacity of 0.1 to 1.0 liter.



AMS-Lab-GMP

For preparing clinical trial batches and commercial production

Motor: 2.2 kW

Effective Capacity: 1.0 liter/batch



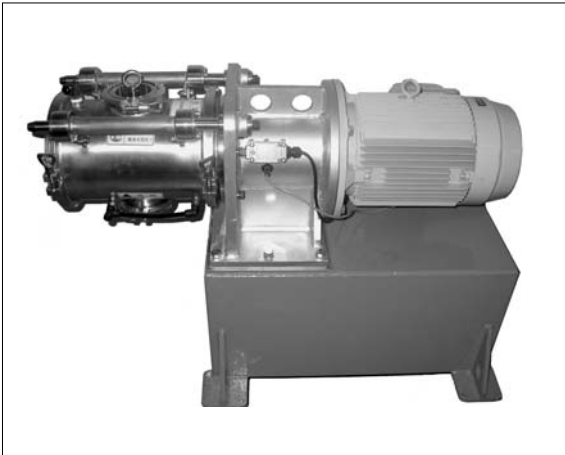
AMS-Mini-GMP

For drug development with small samples

Motor: 0.75 kW

Effective Capacity: 100 ml/batch

New Products News



NOBILTA™ is a new-generation powder processing equipment designed to perform fast precision mixing (Macro to Micro scale), to create composite materials, to modify particle surfaces and to sphericalize particles in accordance to specific product requirements.

< Technical Specifications >

Model: NOB-130, 300, 700 and 1000

Motor: 0.5~200 kW

Capacity: 0.5~300 liters



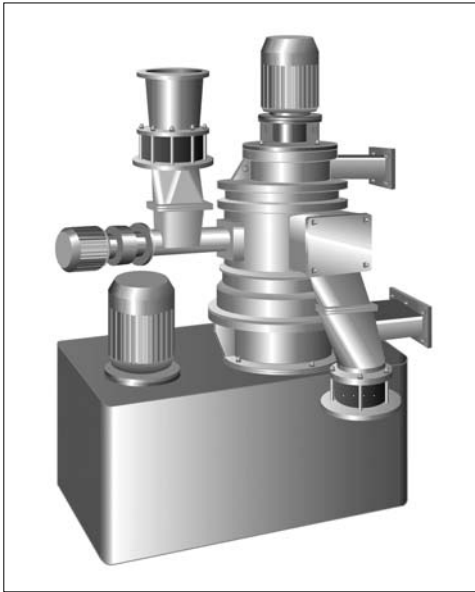
NANOPARADE™ is a lab-scale nozzle-free ink jet system for producing micro-structural thin films by spraying liquid suspension of nanoparticles onto a substrate. It can also be applied to develop functional gradient materials and composites by varying the components and material properties of the liquid suspension. Experiments can continuously be carried out without the limitations of nozzle-type devices.

< Technical Specifications >

System Component: Software loaded PC, supersonic wave generator (standard 10 MHz), oscillator for supersonic wave, high frequency amplifier, etc.

System Size: 620(W) × 450(D) × 540 (H) mm

New Products News



FACULTY is a multi-functional equipment for particle design. By applying the mechanical energy to the particles and separating the coarse from the fine particles, various functional materials can be produced by the **FACULTY**. Combining the fines separation and particle sphericalization, the unit can increase the bulk density of the powder and remove its no-value ingredients, which improve the filling quantity and functionality of the value-added powder.

< Technical Specifications >

Model: F-Lab, F-300, F-400 and F-600

Motor: 1.0~55.0 kW

Scale up Factor: 1, 2, 4

For more information, please contact: **International Sales Dept.**
Hosokawa Micron Corporation
9, 1-Chome, Shodai Tajika, Hirakata Shi, Osaka 573-1132, Japan
Tel: +81-72-855-2224
Fax: +81-72-855-2679
Email: info@hmc.hosokawa.com

C.C. Huang, Ph.D.
Hosokawa Nano Particle Technology Center (USA)
10 Chatham Road, Summit, NJ 07901, U.S.A.
Tel: +1-908-277-9245
Fax: +1-908-277-9329
Email: chuang@hmii.hosokawa.com

R&D Dept.
Hosokawa Alpine A. & Co., OHG
Peter-Doerfler-Strasse 13-25, D-86199, Augsburg, Germany
Tel: +49-821-5906-221
Fax: +49-821-5906-466
Email: mail@alpine.hosokawa.com

HOSOKAWA MICRON

Hosokawa Micron Ltd. is a member of the Hosokawa Micron Group, responding to global needs through an emphasis on materials science and engineering. The Group is an international provider of equipment and Technology for powder and particle processing, product recovery, plastics processing and confectionery products. The Group maintains facilities for research, engineering, manufacturing, and service in each of the world's major industrial markets.



Process Technologies for Tomorrow



HOSOKAWA MICRON

Headquarter Locations;
HOSOKAWA MICRON CORPORATION

<http://www.hosokawamicron.co.jp>